

Electrically Conductive Adhesives

Edited by

R. Gomatam
K.L. Mittal

Electrically Conductive Adhesives

This page intentionally left blank

Electrically Conductive Adhesives

Edited by

R. Gomatam and K. L. Mittal

///VSP///

LEIDEN • BOSTON
2008

CRC Press
Taylor & Francis Group
6000 Broken Sound Parkway NW, Suite 300
Boca Raton, FL 33487-2742

© 2008 by Koninklijke Brill NV Leiden The Netherlands
CRC Press is an imprint of Taylor & Francis Group, an Informa business

No claim to original U.S. Government works
Version Date: 20120525

International Standard Book Number-13: 978-9-00-418782-5 (eBook - PDF)

This book contains information obtained from authentic and highly regarded sources. Reasonable efforts have been made to publish reliable data and information, but the author and publisher cannot assume responsibility for the validity of all materials or the consequences of their use. The authors and publishers have attempted to trace the copyright holders of all material reproduced in this publication and apologize to copyright holders if permission to publish in this form has not been obtained. If any copyright material has not been acknowledged please write and let us know so we may rectify in any future reprint.

Except as permitted under U.S. Copyright Law, no part of this book may be reprinted, reproduced, transmitted, or utilized in any form by any electronic, mechanical, or other means, now known or hereafter invented, including photocopying, microfilming, and recording, or in any information storage or retrieval system, without written permission from the publishers.

For permission to photocopy or use material electronically from this work, please access www.copyright.com (<http://www.copyright.com/>) or contact the Copyright Clearance Center, Inc. (CCC), 222 Rosewood Drive, Danvers, MA 01923, 978-750-8400. CCC is a not-for-profit organization that provides licenses and registration for a variety of users. For organizations that have been granted a photocopy license by the CCC, a separate system of payment has been arranged.

Trademark Notice: Product or corporate names may be trademarks or registered trademarks, and are used only for identification and explanation without intent to infringe.

Visit the Taylor & Francis Web site at
<http://www.taylorandfrancis.com>

and the CRC Press Web site at
<http://www.crcpress.com>

Contents

Preface

vii

Part 1: Introduction and Recent Developments

Using Electrically Conductive Inks and Adhesives as a Means to Satisfy European PCB Manufacturing Directives

H. J. Lewis and A. Ryan

3

An Overview of the Use of Electrically Conductive Adhesives (ECAs) as a Solder Replacement

H. J. Lewis and F. M. Coughlan

25

Electrically Conductive Adhesives for Electronic Packaging and Assembly Applications

L. J. Matienzo, R. N. Das and F. D. Egitto

39

Anisotropic Conductive Adhesives for Flip-Chip Interconnects

W. Wang, Y. C. Chan and M. Pecht

57

Review of Recent Advances in Electrically Conductive Adhesive Materials and Technologies in Electronic Packaging

M. J. Yim, Y. Li, K.-s. Moon, K. W. Paik and C. P. Wong

79

Recent Advances in Developing High Performance Isotropic Conductive Adhesives

D. D. Lu and C. P. Wong

117

Recent Advances in Nano-conductive Adhesives

D. D. Lu, Y. G. Li and C. P. Wong

135

Part 2: Mechanical Durability and Reliability Aspects

Reliability of Anisotropic Conductive Adhesive Joints in Electronic Packaging Applications

Y. C. Lin and X. Chen

157

Drop Test Performance of Isotropic Electrically Conductive Adhesives

J. E. Morris and J. Lee

185

Mechanics of Adhesively Bonded Flip-Chip-on-Flex Assemblies.

Part I: Durability of Anisotropically Conductive Adhesive Interconnects

J. Haase, D. Farley, P. Iyer, P. Baumgartner, A. Dasgupta and J. F. J. Caers

203

Mechanics of Adhesively Bonded Flip-Chip-on-Flex Assemblies.	
Part II: Effect of Bump Coplanarity on Manufacturability and Durability of Non-conducting Adhesive Assemblies	
<i>D. Farley, A. Dasgupta and J. F. J. Caers</i>	227
Fatigue Behavior of Electrically Conductive Adhesives	
<i>B. Su and J. Qu</i>	251
Aspect Ratio and Loading Effects of Multiwall Carbon Nanotubes in Epoxy for Electrically Conductive Adhesives	
<i>J. Li, J. K. Lumpp, R. Andrews and D. Jacques</i>	271
Part 3: Characterization and Properties	
Novel Techniques for Characterization of Fast-Cure Anisotropic Conductive and Non-conductive Adhesives	
<i>M. Teo</i>	287
Chemorheology of Epoxy/Nickel Conductive Adhesives During Processing and Cure	
<i>J. Zhou and E. Sancaktar</i>	301
Temperature Characterization in Anisotropic Conductive Film Adhesive Bonding	
<i>R. L. D. Zenner, C. T. Murray and C. Fisher</i>	327
Operating Temperature of Anisotropic Conducting Film Adhesives	
<i>R. Divigalpitiya</i>	345
Geometric Effects on Multilayer Generic Circuits Fabricated Using Conductive Epoxy/Nickel Adhesives	
<i>J. Zhou and E. Sancaktar</i>	357
Stable and Unstable Capillary Flows of Highly-Filled Epoxy/Nickel Suspensions	
<i>J. Zhou and E. Sancaktar</i>	367
Electrical Properties of Copper-Filled Electrically Conductive Adhesives and Pressure-Dependent Conduction Behavior of Copper Particles	
<i>Y.-S. Lin and S.-S. Chiu</i>	387
Experimental Investigation and Micropolar Modelling of the Anisotropic Conductive Adhesive Flip-Chip Interconnection	
<i>Y. Zhang, J. Liu, R. Larsson and I. Watanabe</i>	411

Preface

These days the mantra is ‘Go Green, Think Green’. Every industry is trying earnestly to switch to green products, green processes and green manufacturing and the electronics/microelectronics industry is no exception. With all the environmental concerns and constraints today and stricter future regulations, there is a patent need to replace materials noxious to the environment by environmentally-friendly alternatives. Electrically conductive adhesives (ECAs) is one such example. ECAs offer an excellent alternative to lead–solder interconnects for microelectronic packaging applications. ECAs are used in electronics for laptop computers, camcorders, watch electronics, hard-drive suspensions and a myriad of electronic equipments. Environmentally-friendly ECAs offer many advantages vis-à-vis solder, such as simple and low-temperature processing conditions, better thermo-mechanical performance and finer pitch. Even though ECAs have excellent potential for being an efficient and less costly alternative to lead–solder interconnects, they still possess a number of problems with regard to durability and design to meet specific needs. Thus there has been a flurry of R&D activity in surmounting these problems and concerns.

An ECA is essentially composed of a polymer resin (commonly an epoxy) and an electrically conductive filler. Many different kinds of filler materials, ranging from silver (commonly used) to carbon nanotubes, have been explored. Also they are available in different formulations as Anisotropically Conductive Adhesives (ACAs), Anisotropically Conductive Films (ACFs) and Isotropically Conductive Adhesives (ICAs). So a user has a broad spectrum of products from which he/she can choose the optimum formulation depending on performance requirements.

So in light of the current intense research activity in ameliorating the existing formulations or designing new and improved ECAs we decided to bring out this special volume, which reflects the cumulative wisdom of many world-class researchers in this burgeoning field.

This book is based on the two Special Issues of the *Journal of Adhesion Science and Technology (JAST)* (Vol. 22, Nos 8–9, pp. 795–1015 (2008) and Vol. 22, No. 14, pp. 1593–1797 (2008)) dedicated to this topic. Based on the widespread interest in and tremendous importance of ECAs, we decided to make this book available as a

single and easily accessible source of information. The papers as published in the above-mentioned issues have been re-arranged more logically in this book.

The book contains a total of 21 papers (reflecting overviews and original research) and are divided into three parts as follows: Part 1: Introduction and Recent Developments; Part 2: Mechanical, Durability and Reliability Aspects; and Part 3: Characterization and Properties. Topics covered include: various forms of ECAs, viz., anisotropically conductive adhesives, anisotropically conductive films and isotropically conductive adhesives; electrically conductive adhesives and inks in PCB (Printed Circuit Board) manufacturing; ECAs as a solder replacement; high performance isotropically conductive adhesives; ECAs in electronic packaging; nano-conductive adhesives; mechanical, durability, reliability and performance aspects of ECAs; fatigue behavior of ECAs; carbon nanotubes for ECAs; bulk characterization of ECAs using a variety of techniques; electrical properties of ECAs and their conduction behavior; and modelling of ECA flip-chip interconnection.

It is obvious that many different aspects and ramifications of ECAs are accorded due coverage in this book and thus this book represents a comprehensive treatise on this subject.

We certainly hope that this book containing bountiful up-to-date information will be of great interest and value to anyone interested in or passionate about finding ‘green’ alternatives in the electronics/microelectronics industry. Also we further anticipate that this book, representing a commentary on current research activity in this important arena, will serve as a fountainhead for new ideas and concomitantly new vistas will emerge.

Now comes the pleasant task of thanking those who helped in materializing this book. First and foremost our thanks go to the authors for their interest, enthusiasm, cooperation and contribution without which this book would not have been in the hands of the readers. We profusely thank the unsung heroes (reviewers) for their time and efforts in providing many valuable comments as comments from peers are *sine qua non* to maintain the highest standard of a publication. Finally, our appreciation goes to the appropriate individuals at Brill (publisher) for giving this book a body form.

RAJESH GOMATAM

Adjunct Professor

Department of Mechanical Engineering and Mechanics

Lehigh University, Bethlehem, PA 18015

USA

and

K. L. MITTAL

P.O. Box 1280

Hopewell Jct., NY 12533

USA

Part 1

Introduction and Recent Developments

This page intentionally left blank

Using Electrically Conductive Inks and Adhesives as a Means to Satisfy European PCB Manufacturing Directives

H. J. Lewis^{a,*} and A. Ryan^b

^a College of Engineering, University of Limerick, Limerick, Ireland

^b Department of Manufacturing & Operations Engineering, University of Limerick, Limerick, Ireland

Abstract

The European Union implemented the WEEE (Waste Electrical and Electronic Equipment) and RoHS (Restriction of Hazardous Substances) directives in July 2006. The aim of the WEEE directive is to reduce the quantity of electrical/electronic equipment being disposed of in landfill, by promoting reduction, reuse, and recycling of equipment/component parts; with the RoHS directive eliminating a number of hazardous substances from the manufacturing process of such equipment that may eventually end up in landfill.

The main effect on the manufacture of Printed Circuit Boards has thus been to identify a drop-in replacement for leaded solders, and the replacement of other banned substances in the manufacturing process, i.e. compliance to the RoHS directive, with limited attention being paid to the WEEE directive.

A system of manufacturing a PCB has been evolved by utilising the principle of reducing manufacturing processes in the development of the PCB substrate and the possibility of recovering components at end of life by degradation of the substrate. A test vehicle was developed based on a currently mass manufactured board, but using a substrate of paper card, with interconnecting tracks added using conductive inks *via* a printing process. Components were bonded to the tracks using electrically conductive adhesives *via* an industry-based manufacturing line. The scope of this paper will be confined to the ability to utilise an ECA as the connecting medium for single-sided boards with a paper card substrate, thus opening the possibility of producing a WEEE/RoHS compliant environment-friendly PCB.

Keywords

Electrically Conductive Adhesives (ECAs), electrically conductive inks, environment-friendly PCB, WEEE, RoHS, IPC

1. Introduction

The modern Printed Circuit Board (PCB) can be traced back to Paul Eisler in 1936 [1], and has been developed to the current mass manufactured automated process in a relatively few but significant steps. The PCB is a major element in a large number of consumer goods, toys and industrial equipment. However, tech-

* To whom correspondence should be addressed. Tel.: 00 353 61 202647; Fax: 00 353 61 202567; e-mail: huw.lewis@ul.ie

nological progress in electronic circuitry has led to a short product life cycle for many PCBs. It has been estimated that each European Union (EU) citizen (prior to the enlargement of the EU) produces 23 kg of electrical/electronic waste per annum [2], with 90% of this type of waste being deposited in landfill, incinerated or recovered without pre-treatment, thus making its pollutants a major source of the hazardous content found in municipal waste [3]. In order to protect the environment the EU directives on Waste Electrical and Electronic Equipment (WEEE) and Restriction of Hazardous Substances (RoHS) [4, 5] were implemented from July 1, 2006. These directives adopted from the initial proposal of June 2000 restrict the use of disposing of WEEE in landfill, and ban the use of lead, cadmium, mercury, hexavalent chromium, and two flame retardant chemicals: polybrominated biphenyls and polybrominated diphenylethers in the manufacture of electrical and electronic equipment.

The initial effect on PCB manufacturing was the introduction of lead-free solder as a direct replacement for leaded solder, however, higher temperature requirements have led to higher scrap rates [6]. A number of alternatives have been investigated to replace solder as the joining medium between the track and the component, these include a tri-metal system of plating component leads with tin and nickel (to reduce tin whiskering) and directly bonding them to the track [7], and the use of Electrically Conductive Adhesives [8]. In developing an alternative to the joining mechanism between the component and the track, consideration must be given to current PCB manufacturing methods, as any changes must be accommodated by existing equipment. An ECA has been shown to be suitable as a drop-in replacement to solder pastes for surface mount components [8] thus satisfying the RoHS requirement. However, in moving towards satisfying the WEEE directive, the use of ECAs and conductive inks has been shown to be acceptable in the production of a single-sided recyclable PCB using a degradable paper card substrate with printed conductive ink interconnections [9].

The viability of utilising an ECA as a connecting medium between components and a paper-based degradable substrate is presented here.

2. An Alternative Method of Manufacturing a Single-Sided PCB

In developing an alternative PCB to meet the EU directives a single-sided rigid circuit board was utilised; as Frey [10] indicates that the value of such boards will increase from \$7.48 Billion in 2005 to \$8.2 Billion in 2010. A rigid printed circuit board consists of a substrate (epoxy resin) populated by various components which are attached to the interconnecting pattern on the board using solder. During the manufacturing process, there are a number of effluent and potential air emissions generated by the process (Table 1a and 1b) [11]. Thus in developing environmentally acceptable PCBs it is necessary to eliminate as many of these potentially damaging areas as possible whilst still maintaining the integrity of the final product.

Table 1(a).

Effluents from PCB manufacture [11]

Organic solvents	Tin
Vinyl polymers	Lead
Stannic oxide	Palladium
Copper	Gold
Nickel	Cyanides
Iron	Sulphates
Chromium	Acids

Table 1(b).

Potential air emissions in PCB manufacture [11]

Sulphuric acid	Ammonia
Hydrochloric acid	Organic solvent vapours
Phosphoric acid	Isopropanol
Nitric acid	Acetone
Acetic acid	Petroleum distillates
Chlorine	Ozone-depleting substances

Table 2(a).

Effluents in paper manufacture [12]

Cellulose fibre	Carbohydrate starch
Hemi-cellulose	Organochlorine products*
Acidic compounds (biodegradable)	Chlorophenolics
Chloroform	Neutral chlorinated products

* Organochlorines: a wide range of organic chemicals that include chlorine, commonly used as pesticides.

The alternative method of producing a PCB involves using a sustainable, degradable fibre-based (paper) substrate to replace the existing thermoplastic epoxy substrate. The fibre-based (paper) substrate was a standard matte card with a surface roughness of 1.6 µm for a 80 g/m² paper quality, and of a similar thickness as the epoxy board it was to clone. The environmental advantages of using paper as a substrate can be seen in Table 2a and 2b [12].

This substrate was used in conjunction with commercially available conductive inks and screen printing to produce the interconnecting track and screen printed conductive adhesives for component connection to generate a comparative PCB (Fig. 1) [13]. Both sets of boards were populated with surface mount components on the same production line. The single-sided board produced was used to examine the

Table 2(b).

Potential air emissions in paper manufacture [12]

Carbon dioxide	Hydrogen sulphide**
Sulphur dioxide**	Volatile organics
Chloroform	Other organochlorines*

* Organochlorines: a wide range of organic chemicals that include chlorine, commonly used as pesticides.

** Only in the KRAFT process of paper manufacture.

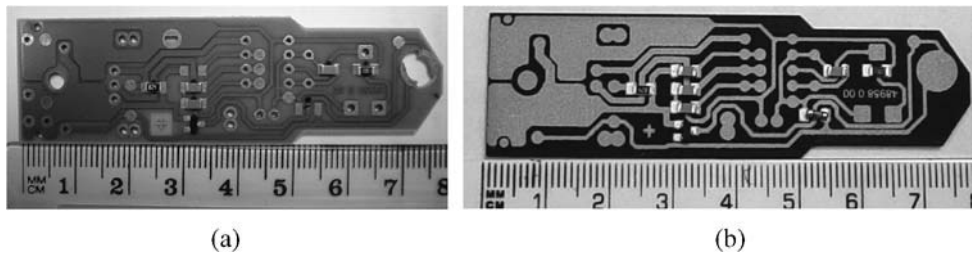


Figure 1. (a) Standard epoxy-based PCB with solder connections and (b) cloned paper-based PCB with ECA connections.

Table 3.

Properties of electrically conductive adhesive used [14]

Details	
Name	Emerson & Cuming, Ablebond 8175
Type	Isotropic
Filler	Silver flakes
Binder material	Epoxy
Glass transition temperature	80°C
Volume resistivity	0.0005 Ω cm
Viscosity@25°C	70 000 cP
Cure condition	3 min@ 150°C
Cure option	6 min@ 130°C

structural, electrical and mechanical properties of the conductive ink, the conductive adhesive, and the interaction between these two and the paper-based substrate.

An isotropic adhesive using a silver filler [14] (Table 3) was selected for this application due to its ability to retain conductivity as the silver particles oxidise [15] together with a thermosetting binder polymer as it exhibits higher shear strength than those manufactured from thermoplastic binder material [16].

Eight components were bonded to the board (Fig. 2) with the adhesive being printed using a 150 µm thick stainless steel stencil with desired laser cut aper-



Figure 2. Component positioning.



Figure 3. ECA spread after printing.

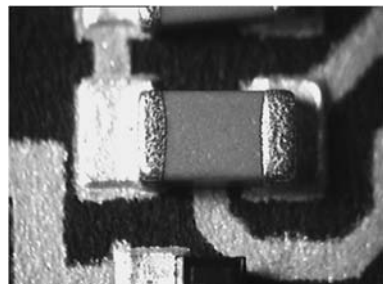


Figure 4. ECA printed correctly.

tures as suggested by the manufacturers. It was found, through experimentation, that a printing speed of 89 mm per second, and a squeegee pressure of 0.97 bar allowed for successful printing of the adhesive, with over 200 paper substrate boards being successfully populated.

Errors in the application of the ECA can include the incorrect positioning of the adhesive, hence the component not bonding to the board; or excess adhesive being deposited resulting in bridging of tracks thus damaging the circuit (Fig. 3). Excess adhesive can be deposited if the adhesive is at an incorrect viscosity (100 000 cP is recommended [17], although 70 000 cP was used here) or temperature as it will not flow smoothly across the stencil and will result in the adhesive being dragged through the apertures of the stencil and along the substrate. However when the ECA is deposited correctly (Fig. 4), the component sits on the substrate forming a suitable electrical and mechanical bond with the board.

Having produced the boards with a paper-based substrate, an investigation into the bonds formed between the component and conductive ink track was undertaken in accordance with a number of standards.

3. Testing Boards to Existing Standards

The alternative boards were tested according to the Standards indicated in Table 4 before and after being exposed to the different environmental conditions indicated in Table 5.

Table 4.

Requirements of proposed circuit assemblies

Parameter	Standard requirement	Source
Electrical requirements		
Volume resistivity	$<1 \times 10^{-3} \Omega \text{ cm}$ (1 megohm cm)	National Centre for Manufacturing Sciences (NCMS), Wong and Lu [18]
Shift of joint resistance	$<20\%$ (after 500 h at $85^\circ\text{C}/85\% \text{ RH}$)	Lu, Tong and Wong [23]
Mechanical requirements		
Impact strength	Required to sustain 6 drops from 152.4 cm	NCMS, Wong and Lu [18]
Applied shearing force	$>30 \text{ N}$	Coughlan and Lewis [8]
Structural requirements		
Joint structure	Section 12 of IPC-A-610C	Institute for Interconnection and Packaging Electronic Components (IPC) [19]

Table 5.

Environmental test parameters

Test	Reason	Parameters	Source
Temperature cycling	Extreme temperature differences and shock	-40°C to 120°C ramp profile of 15 min i.e. -40°C for 15 min, ramp to 120°C in 15 min hold for 15 min, ramp down to -40°C in 15 min	Mil-STD 883F [20] Jagt [21] Coughlan and Lewis [8]
Temperature storage	Joint degradation at elevated temperature	125°C for 500 h	Mil Std 883F [22]
Humidity aging	High temperature damp conditions	$85^\circ\text{C}/85\% \text{ RH}$ for 500 h	Wong and Lu [18]

The objectives of the tests are as follows:

- To examine the effect of different environmental exposures on the mechanical, electrical and structural properties of the bond between the component and the board.
- To examine the joint resistance of the conductive adhesive bonds to industrial specifications.
- To examine the adhesion strength of the conductive material bonds using both a drop test as per Lu and Wong [24] and a shear test as per Coughlan and Lewis [8].
- To examine the structure of the conductive adhesive bonds using the international standard IPC-A-610C [19], thereby establishing if it was possible to produce boards, which conformed to manufacturing standards.
- To use existing manufacturing functionality testing techniques to establish if the developed boards performed to current production requirements.

3.1. Electrical Requirements

3.1.1. Volume Resistivity

The volume resistivity of the ECA utilised in the test was $0.5 \times 10^{-3} \Omega \text{ cm}$ as stated by the manufacturer, which was within the required specification as indicated in Table 4.

3.1.2. Examination of Joint Resistance of the Conductive Adhesives

Joint resistance is the resistance of the joint between the component and the interconnection pad. It is obvious that any replacement of the current joining medium (i.e. solder) must have similar performance levels as the current medium or at least satisfy current manufacturing standards (Table 4).

A 4-probe tester was used to analyse the joint resistance of the ECA. This technique involves placing 2 probes onto the component and 2 probes onto the pad and measuring the resistance across the pad and component, Fig. 5. Four joint positions were chosen with the average value of joint resistance indicated in Table 6, before and after environmental tests.

It is apparent that exposure to hostile environmental conditions will result in an increase in joint resistance. In Table 4 it has been shown that a change in resistance greater than 20% will result in it being deemed a failure. The percentage change in resistance for temperature cycled components was almost 800%, while the percentage change in joint resistance for those components stored at elevated temperatures for 500 h was 754%. These results are obviously well outside the acceptable tolerance of a 20% change in joint resistance; thus exposure to elevated temperatures and temperature cycling will negatively impact the joint resistance of the assemblies and will result in the assemblies failing this particular criterion.

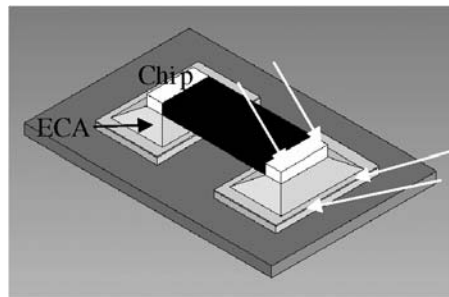


Figure 5. Placement of probes to measure joint resistance.

Table 6.

Average joint resistance prior to and after environmental tests

Sample	Joint 1 (Ω)	Joint 2 (Ω)	Joint 3 (Ω)	Joint 4 (Ω)
Pre-test values	0.13	0.07	0.15	0.06
Temp. cycling	0.61	0.65	0.63	0.90
500 h storage	0.93	0.64	0.63	0.69

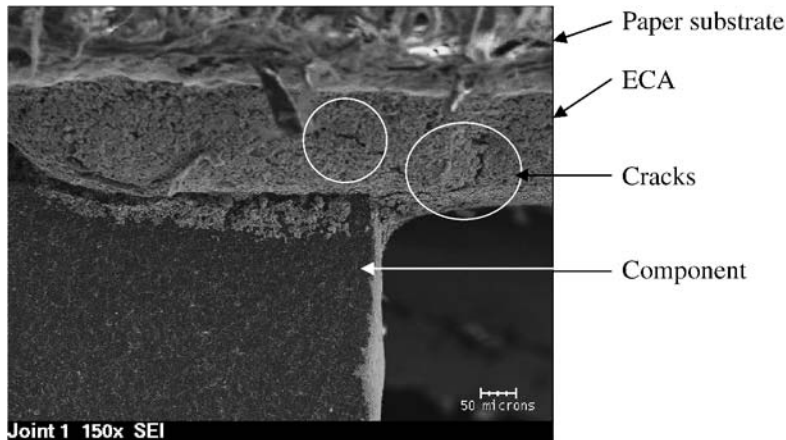


Figure 6. Cracks formed in ECA after environmental conditioning.

Jagt [25] has shown that cracking can occur between the adhesive and the component because both materials have different coefficients of thermal expansion, the CTE for conductive adhesives is typically 40 ppm/ $^{\circ}\text{C}$ while that of a tinned component is 25 ppm/ $^{\circ}\text{C}$ [16]. Thus the stress in the materials due to the difference in expansion of the component lead and the adhesive can lead to the growth of interfacial cracks. These cracks reduce the conductive ability of the adhesive as it forces the silver platelets farther apart thus increasing the joint resistance, Fig. 6.

3.2. Mechanical Properties

3.2.1. Shear Tests

Shear testing was used to measure the adhesion strength of the conductive adhesive bond that had secured the surface mount component to the interconnecting pattern. In order for the proposed manufacturing process to be deemed successful the assemblies must withstand a shearing force greater than 30 N [8]. Tests in both the horizontal and vertical directions were carried out (Fig. 7).

This investigation fulfilled a number of objectives:

- It established the adhesion strength of the ECA bond between a component and a pad formed by printing silver conductive ink on a paper substrate.
- It facilitated a comparison between existing solder and ECA joints.
- It quantified the effect of environmental aging techniques on the adhesion strength of alternative boards.

For the purpose of analysis the components on the board were labelled 1–7, as per Fig. 8, with the results of the tests being shown in Table 7.

A secondary factor in the strength of the bond between component and substrate is the placement of the component onto the substrate. If the component was poorly placed so that not all the termination of the component was in contact with the

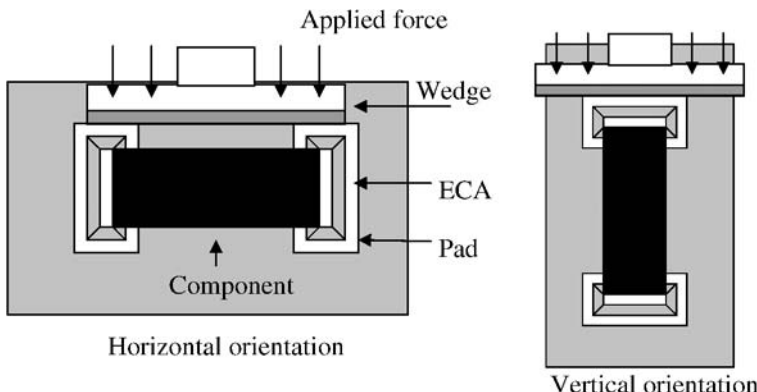


Figure 7. The direction of the applied shearing force on individual components.

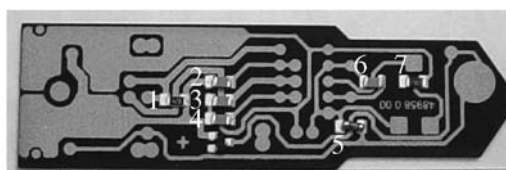


Figure 8. Alignments of components on board.

Table 7.

Applied shearing forces that cause components to dislodge, pre- and post-environmental testing

Exposure	Applied force required to dislodge component (N)						
	1	2	3	4	5	6	7
Untreated	10.9	7.9	7.6	10.4	6.6	9.1	12.3
200 h storage	13.9	11.1	10.9	13.3	5.5	14.2	10.6
300 h storage	18.0	16.2	18.3	13.5	5.3	13.7	14.7
400 h storage	16.1	12.5	13.7	16.9	9.2	14.2	9.8
500 h storage	12.6	9.2	9.5	11.5	7.4	10.0	12.3
Temp cycling	14.7	15.1	12.7	14.6	5.4	16.3	20.0
200 h 85°C/85% RH	11.2	10.8	8.5	12.8	5.0	15.2	14.6
300 h 85°C/85% RH	11.7	11.3	9.1	12.6	4.2	14.8	15.5
400 h 85°C/85% RH	14.2	12.2	7.9	13.5	6.5	13.7	11.1
500 h 85°C/85% RH	10.5	10.4	8.5	12.5	5.7	13.8	13.4

**Figure 9.** An example of a misaligned component that will exhibit lower bond strength.

electrically conductive adhesive, then these components had significantly reduced bond strength (Fig. 9).

From Table 7 it is apparent that exposing the environmentally friendly assemblies to temperature storage or temperature cycling does not negatively impact the shear strength of the conductive adhesive-conductive ink bond. Whilst cracks within the adhesive reduced its conductive ability, they did not negatively impact the shear strength of the adhesive. There is in fact an increase in shear strength after exposing the samples to elevated temperatures due to the binder material being evaporated away, thus allowing the silver particles to nestle tighter together forming a stronger mechanical bond. Having identified that exposure to environmental conditions did not negatively impact the shear strength of the assemblies it is necessary to compare the shear forces required to dislodge a component bonded using conductive adhesive with current industrially used lead-free solder pastes. Three variations of board were used: ECA and epoxy substrate, lead-free solder and epoxy substrate, and ECA and paper substrate (Table 8).

Table 8.

Comparison of average shear forces required to dislodge components

Component no. (Fig. 8)	1 (N)	2 (N)	3 (N)	4 (N)	5 (N)	6 (N)	7 (N)
ECA & PCB	35.5	42.9	38.8	35.3	20.8	46.1	52.0
Solder & PCB	33.8	25.9	28.5	24.2	26.7	25.0	31.7
ECA & degradable substrate	10.9	7.9	7.6	10.4	6.6	9.1	12.3

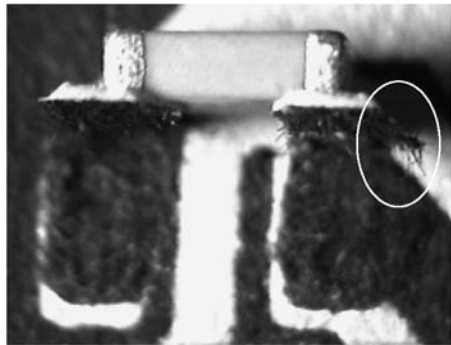
**Figure 10.** Paper substrate failure indicated by paper fibres attached to component.**Figure 11.** Paper substrate failure indicated by the visibility of the substrate where pad should be.

Table 8 shows that the average shear forces to dislodge a component using ECA on an epoxy substrate is higher than that of the lead-free solder. However, for the ECA on the paper-based board it is significantly reduced, approximately a third of the other boards. This is due to the paper tearing. It can be seen from Figs 10–13, that it is the substrate that fails with the ECA adhering to both the component and the surface of the paper. Fibres from the paper are still attached to both the ECA and component. This is in contrast to the epoxy-based boards in Figs 14 and 15, where the ECA has sheared.

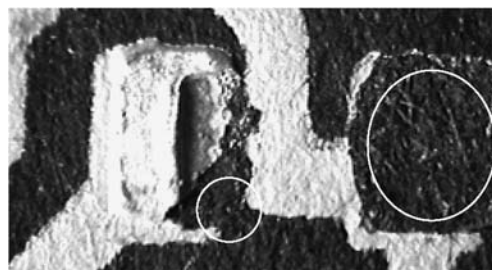


Figure 12. Paper substrate failure indicated by the visibility of substrate where pad should be.

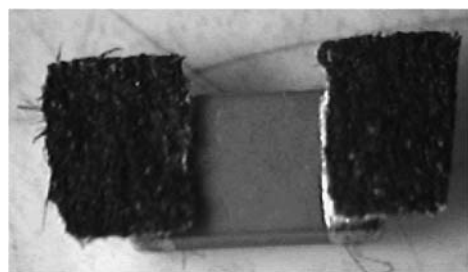


Figure 13. Paper substrate and adhesive still attached to component.

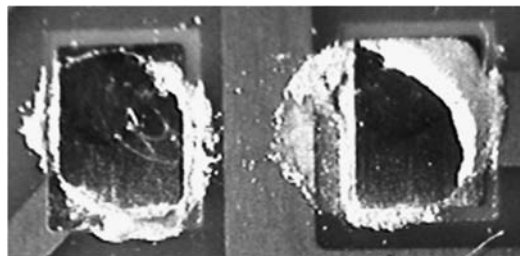


Figure 14. Failure of ECA used on an epoxy substrate.

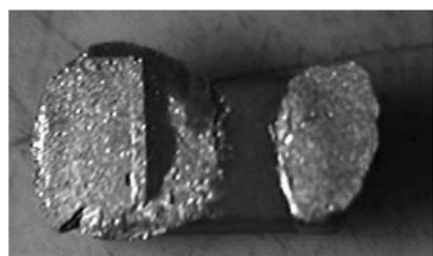


Figure 15. ECA still attached to component after failure using an epoxy substrate.

In summary the shear strength of the alternative board assemblies is primarily limited by the strength of the paper rather than the strength of the adhesive employed. It has been established that utilising a conductive adhesive to join a component to a printed conductive silver ink pad on a paper substrate performs poorly when compared to utilising a conductive adhesive to join a component to a copper pad on an epoxy-based substrate. The average shear force of 9.2 N for the alternative boards did not compare well with the required 30 N [8]. The relatively poor performance is due to the strength of the paper substrate rather than the strength of the bond between the ink and the adhesive, which remained intact (Fig. 13). When the adhesive was used on an epoxy substrate an average shear strength of 38.7 N was found, which is within the acceptable tolerance. Although the shear strength of an individual joint is indicative of the bond formed, it is not a direct indication of the mechanical functionality of the board. Rarely a specific component on a board will encounter a shear force. However, the board may endure impact forces by being dropped. The boards were thus subjected to a drop test as indicated by Wong and Lu [18] and Lu and Wong [24].

3.2.2. Drop Test Procedure to Analyse Impact Strength of the Adhesive

A total of 36 electronic circuits were subjected to impact investigation (Table 4) i.e. withstand a drop from 152.4 cm (6 ft) (Fig. 16); prior and after environmental treatment (Table 5). The boards were dropped 3 times on their edges and 3 times on their backs. The criterion for pass or fail was the dislodgement of components. The resulting tests indicate that with no failures, the bond strength between the ECA and the paper substrate is sufficiently strong to pass this particular requirement when dropped on their back. However, when dropped on their edge there was an 11% failure rate. As only a limited number of tests were performed, it is not conclusive whether these failures indicate a significant enough number to warrant rejection of

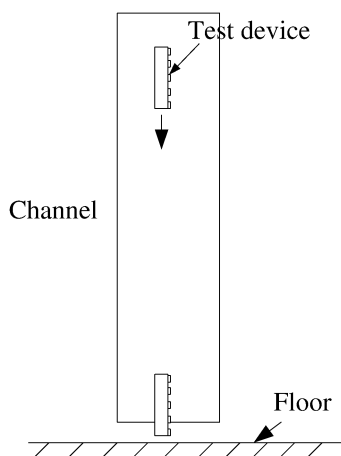


Figure 16. A schematic of drop test setup [24].

the use of ECA on a paper substrate. Further investigation indicated that the failures resulted from dislodgement of Component 7.

There are two possible reasons as to why this component became detached:

- Insufficient adhesive,
- Poor alignment of component.

If insufficient adhesive is applied to the substrate before component placement then the component will detach itself from the board upon impact. However, as this was the only component dislodged, and it was not in a difficult position in regard to the printing of the ECA, then it is assumed that in this particular case, poor alignment could be the underlying cause of failure (Fig. 9).

A similar success rate was found after environmental conditioning and in general all circuits withstood drops from the prescribed height. The circuits that failed did so due to the dislodgement of 1 component representing 3% of all the components tested, which can be explained as an alignment problem rather than an ECA failure.

The mechanical properties of the ECA and paper-based substrate satisfy the defined tests (Table 4), with the exception of the shear test, where substrate failure was the problem. It is also evident that the environmental conditioning has no effect on the mechanical properties of the developed system. Having examined the mechanical requirements of the alternative printed circuit boards according to industrial and international standards, the next section examines the structure of conductive adhesive bonds using IPC international standard requirements [19]. Electrical test are described in Section 3.4, with boards that had not been subjected to drop tests.

3.3. Examining the Structure of the ECA Bonds Using IPC Standards

The structure of the bond between the conductive adhesive and the interconnecting pattern of conductive ink is examined under Section 12.2.2 of the IPC-A-610C Standard, Acceptability of Electronic Assemblies [19]. This standard is a collection of visual quality acceptability requirements for electronic assemblies.

When examining the bond structure there are 3 classifications or tolerance levels into which the board can fall:

- Class 1 includes consumer products, some computer and computer peripherals where cosmetic imperfections are not important and the major requirement is the function of the completed electronic assembly.
- Class 2 includes communication equipment, sophisticated business machines, and instruments where high performance and extended life are required and for which uninterrupted service is desired but not critical. Certain cosmetic imperfections are allowed.
- Class 3 includes the equipment and products where continued performance or performance-on-demand is critical. Equipment downtime cannot be tolerated

and must function when required, such as in life support items or flight control systems.

The developed assemblies will be examined under Class 1 criterion, in order to establish whether or not the developed boards can be manufactured to current standards. Table 9 illustrates the desired bond targets, the acceptable tolerance range, and the percentage of circuits which failed, and also outlines the failure mechanisms experienced. The failure rate under the IPC standard based on a production run of 208 boards, with 7 components, is small, with 34 components failing out of a possible 1456 (2.3%). It is thus apparent that it is possible to use current industrial equipment to print electrically conductive adhesive and automatically place surface mount components onto a degradable substrate and achieve a finished assembly which is deemed acceptable under international standards.

3.4. Functionality Examination

It has been illustrated that the developed boards are compatible with existing surface mount technology and that it is possible to produce a printed circuit board on paper, to international standards, using existing processes and equipment. This examination focuses on determining if the assemblies are in line with the manufacturer's specifications. By using a board which is currently in production it was possible to compare the developed board to the required manufacturing standard (Fig. 17, Table 10).

The results obtained from the functionality analysis of 25 completed electronic assemblies are shown in Table 11.

Whilst surface mount components were populated on the boards using an industrial line, the through-hole components needed to complete Tests 1 and 2 were manually assembled, due to the lack of line time available to the project. On close inspection some bridging had occurred between the component leads of the manually assembled through-hole components (Fig. 18). In general the development of an alternative PCB can be seen to be feasible based on current manufacturing standards and functionality.

4. Discussion

The RoHS and WEEE directives have been implemented in EU member states. The RoHS directive has led to the substitution of banned materials with acceptable materials as drop-in replacements. Thus the manufacturing processes to produce electrical equipment and specifically printed circuit boards have not changed, although some of their parameters (e.g. reflow temperature) have.

Thus when developing an environment-friendly PCB, the current manufacturing equipment and processes should not need significant alteration for the implementation of the new board. Here we have discussed the use of an ECA on a degradable paper-based substrate, with conductive ink interconnections. The boards produced

Table 9.

Examinations of circuits according to IPC-A-610C

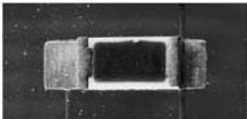
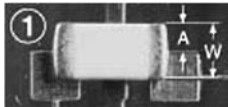
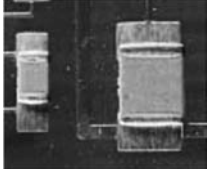
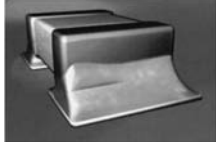
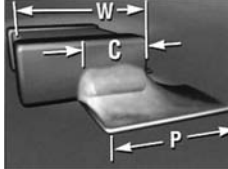
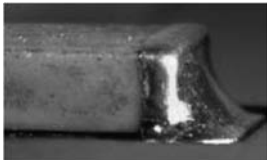
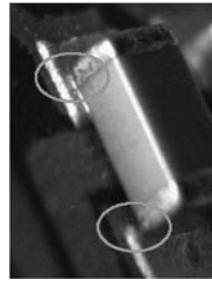
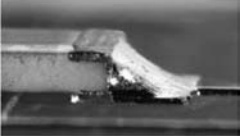
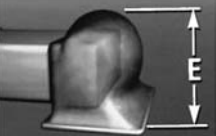
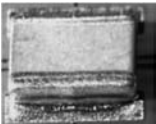
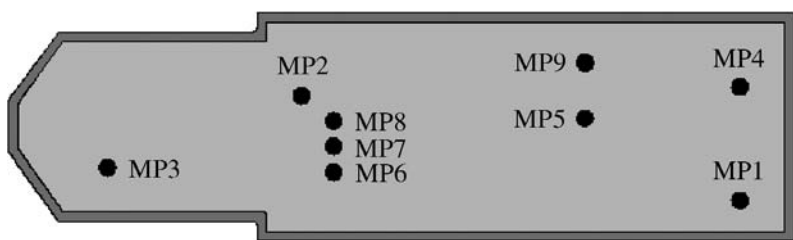
Test	Target	Tolerance/range	% fail	Example
Side overhang		 ① Side overhang (A) is greater than 50% component termination width (W) or 50% land width (P), whichever is less	4.81 (10 of 208 circuits)	
End overhang		No tolerance, no overhang required for circuit to be deemed a pass	0.96 (2 of 208 circuits)	
End joint width		 End joint width (C) is at least 50% of component termination width (W) or 50% of land width (P), whichever is less	3.37 (7 of 208 circuits)	
Side joint length		Side joint length is not required. However, bond between the component and pad must be evident	0.96 (2 of 208 circuits)	 Image shows acceptable bonding

Table 9.

(Continued.)

Test	Target	Tolerance/range	% fail	Example
Maximum fillet height			1.92 (4 of 208 circuits)	
Minimum fillet height	Maximum fillet height is the solder thickness plus component termination height	Maximum fillet height (E) may overhang the land or extend onto the top of the end cap metallisation, but not extend further onto the component body	3.37 (7 of 208 circuits)	
End overlap		No tolerance specified but a deposition of adhesive must be evident	0.96 (2 of 208 circuits)	

**Figure 17.** Location of the points specified by the manufacturer for functionality tests.

were built as clones of an existing production board, and populated on the same equipment. Current standards were used to test the boards (Table 12).

It is apparent that the new boards will meet the majority of the required standards, with the exception of shear strength, and shift of joint resistance after environmen-

Table 10.

The resistance values set by the manufacturer at specified positions on the circuit to deem the circuit acceptable

Test number	Defined measuring points (Fig. 17)	Requirements
1	MP2 against MP9	150 Ω , $\pm 5\%$
2	MP4 against MP5	820 k Ω , $\pm 5\%$
3	MP5 against MP6	>10 k Ω
4	MP6 against MP7	>10 k Ω
5	MP7 against MP8	>10 k Ω

Table 11.

The resistance values measured on the paper substrate boards at the manufacturer's specified positions

Circuit number	Test 1 Ω	Test 2 k Ω	Test 3 k Ω	Test 4 M Ω	Test 5 M Ω
1	150.7	822.0	60.4	40.0	40.0
2	150.7	821.0	60.6	4.1	40.0
3	3.0	818.0	60.6	3.9	40.0
4	153.9	820.0	60.6	3.9	40.0
5	150.0	31 400.0	60.7	40.0	40.0
6	151.0	820.0	60.7	40.0	40.0
7	151.6	819.0	61.2	40.0	40.0
8	161.4	40 000.0	58.9	40.0	40.0
9	150.9	822.0	61.1	3.8	40.0
10	151.6	821.0	59.9	40.0	40.0
11	8.5	820.0	61.1	20.9	40.0
12	150.6	813.0	60.7	20.7	33.5
13	151.2	819.0	60.8	3.8	40.0
14	151.2	822.0	59.8	40.0	40.0
15	151.2	822.0	60.7	40.0	40.0
16	150.7	820.0	60.9	203	40.0
17	151.2	823.0	61.2	40.0	40.0
18	151.9	823.0	60.7	3.9	40.0
19	151.3	816.0	59.9	18.9	40.0
20	151.8	819.0	59.3	40.0	40.0
21	1.8	6000.0	60.8	40.0	40.0
22	5200.0	822.0	59.9	40.0	40.0
23	151.0	822.0	61.0	40.0	40.0
24	166.2	820.0	60.8	40.0	40.0
25	151.9	822.0	60.8	3.8	40.0

tal treatment. In the case of shear tests, the substrate was the cause of the failure rather than the ECA. The standard set for the shear testing could be questioned, as the boards passed the drop tests (ignoring poor component placement). A similar

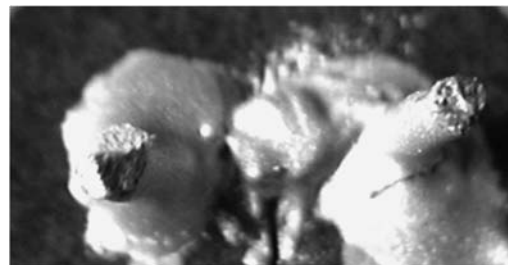


Figure 18. Bridging of ECA joints.

Table 12.

Performance of assembled alternative boards

Parameter	Standard requirement	Pass/fail	
Electrical requirements		Conductive ink	Pass
Volume resistivity	$<1 \times 10^{-3} \Omega \text{ cm}$ (1 milliohm cm)	Conductive adhesive	Pass
Shift of joint resistance	$<\pm 20\%$ change (after environmental exposure)	Conductive ink	Pass
		Conductive adhesive	Fail
Mechanical requirements			
Impact strength	Required to sustain 6 drops from 152.4 cm	Prior to environmental exposure	Pass
		Post-environmental exposure	Pass
		Prior to environmental exposure	Fail
Applied shear force	$>30 \text{ N}$	Post-environmental exposure	Fail
Structural requirements			
Joint structure	Section 12 of IPC-A-610C	Result of examination of joint structure	Pass
Functionality		Test 1	84%
Functionality performance	Tests as per company datasheet, Appendix G	Test 2	88%
		Test 3	100%
		Test 4	100%
		Test 5	100%
Flammability			
Flammability Examination	BS 61189-2	Pass subject to coating with flame retardant	

argument could be made for the shift in joint resistance after conditioning, in that the boards passed the manufacturer's functionality tests.

The development of a paper-based PCB, with conductive ink interconnection, and an ECA as a component connection has been shown to be feasible for single-sided SMT boards of IPC class 1 status.

5. Conclusion

It has been shown that a paper substrate PCB can be manufactured utilising conductive silver inks for the interconnecting track pattern, and ECAs as the connecting medium for bonding SMT components. Further to this, environmental conditioning of the boards had only limited effect on the mechanical properties of the ECA joints. However, the environmental conditioning did affect the shift joint resistance by over the defined 20%, deeming the connections to be unacceptable. Further to this the applied shearing force to dislodge a component was approximately 30% of that of the lead-free solder joint, falling short of the 30 N deemed acceptable. Whilst the boards failed on these two parameters, they passed both drop and manufacturers functionality tests, thus questioning the tolerance of the standards. Further work is being carried out on the recovery of components and materials from the circuit boards at end of life by the degradation of the paper substrate.

References

1. P. Eisler, *My Life with the Printed Circuit*. Lehigh University Press, Bethlehem, PA (1989).
2. A. Kosloff, *Screen Printing Electronic Circuits*, 2nd ed. The Signs of the Times Publishing Company, Cincinnati, OH (1980).
3. B. Kopacek, *Taking the Life-Cycle Approach to Electronic Waste Management*. Research Directorate General-Growth Programme, European Commission, Brussels (2000).
4. Directive 2002/96/EC of the European Parliament and of the Council of 27 January 2003 on Waste Electrical and Electronic Equipment (WEEE), *Official Journal of the European Union* **46(L 37)**, 24–38 (2003).
5. Directive 2002/95/EC of the European Parliament and of the Council of 27 January 2003 on the Restriction of the Use of Certain Hazardous Substances in Electrical and Electronic Equipment, *Official Journal of the European Union* **46(L 37)**, 19–23 (2003).
6. G. C. Munie, L. Turbini, J. Gamalski, D. Bernier and D. W. Bergman, *J. Surface Mount Technol.* **13**(1), 15 (2000).
7. F. M. Coughlan and H. J. Lewis, *J. Mater. Process. Technol.* **153–154**, 241–246 (2004).
8. F. M. Coughlan and H. J. Lewis, *J. Electronic Mater.* **35**, 912–921 (2006).
9. A. Ryan and H. Lewis, in: *Proc. 16th International Conference On Flexible Automation and Intelligent Manufacturing*, pp. 669–676, University of Limerick (2006).
10. M. Frey, AT&S Annual Report 2005/2006, The Annual Report of Austria Technologie & Systemtechnik Aktiengesellschaft AG (2006).
11. Electronics Manufacturing, in: *Pollution Prevention and Abatement Handbook*, pp. 302–306. World Bank Group (1998).
12. The Environmental Consequences of Pulp and Paper Manufacture, Friends of the Earth Briefing sheet. Available at <http://www.foe.co.uk/pubsinfo/briefings/html/19971215150024.html>
13. A. Ryan, *An alternative manufacturing system for printed circuit boards*, PhD Thesis, University of Limerick (2006).
14. Ag-510 Silver filled Electrically Conductive Screen Printable Ink/Coating. Datasheet., Conductive Compounds Inc., Londonderry, NH (2007).
15. J. Felba, K. Friedel and R. Kisiel, in: *Proc. of XXIV International Microelectronics and Packaging Society (IMAPS) Meeting*, pp. 24–45, Ryto, Poland (2000).

16. H. Hvims and H. Ronsberg, C2.3.3 Thermal Conductivity, Chapter C: *Polymer Bonding*, The Nordic Electronics Packaging Guideline (2007). Available at <http://extra.ivf.se/ngl/>
17. J. Liu and P. Lundstrom, in: *Conductive Adhesives for Electronic Packaging*, J. Liu (Ed.), Chapter 9. Electrochemical Pubs Ltd, Isle of Man (1999).
18. C. P. Wong and D. Lu, in: *Proc. 4th International Conference on Adhesive Joining & Coating Technology in Electronics Manufacturing*, pp. 121–129, Espoo, Finland (2000). Available at <http://csdl2.computer.org/persagen/DLabsToc.jsp?resourcePath=/dl/proceedings/&toc=comp/proceedings/adhes/2000/6460/00/6460toc.xml> (2008).
19. IPC-A-610C Acceptability of Electronic assemblies. A Standard issued by IPC-Association Connection Electronics Industries, Northbrook, Illinois (2000). Available at www.ipc.org
20. MIL-STD-883 F, Method 1010.8 Temperature Cycling. A standard issued by the Department of Defence USA (2004).
21. J. C. Jagt, *IEEE Trans. Components, Packaging and Manufacturing Technol. — Part A* **21**, 215–224 (1998).
22. MIL-STD-883 F, Method 1008.2 Stabilisation Bake. A standard issued by the Department of Defence USA (2004).
23. D. Lu, Q. K. Tong and C. P. Wong, *IEEE Trans. Electronic Packaging Manufacturing* **22**, 228–232 (1999).
24. D. Lu and C. P. Wong, *IEEE Trans. Components and Packaging Technol.* **23**, 620–626 (2000).
25. J. C. Jagt, in: *Conductive Adhesives for Electronic Packaging*, J. Liu (Ed.), Chapter 11. Electrochemical Pubs Ltd., Isle of Man (1999).

This page intentionally left blank

An Overview of the Use of Electrically Conductive Adhesives (ECAs) as a Solder Replacement

H. J. Lewis^{a,*} and F. M. Coughlan^b

^a College of Engineering, University of Limerick, Limerick, Ireland

^b Department of Manufacturing and Operations Engineering, University of Limerick, Limerick, Ireland

Abstract

Electrically conductive adhesives (ECAs) have been utilised in the internal bonding of leads to chips for some time. With the need to replace leaded solder, ECAs are an obvious candidate as a drop-in replacement.

This paper discusses the general make-up of ECAs and the Standards to which these might be compared when using them as a replacement for solder.

Keywords

Electrically conductive adhesives (ECAs), leaded solder replacement, European Waste Electronic and Electrical Equipment directive (WEEE), European Reduction of Hazardous Substances directive (RoHS)

1. Introduction

On 13 June 2000, the European Union (EU) adopted two proposals to deal with the problem of waste management and environmental pollution in Europe. The Waste Electrical and Electronic Equipment (WEEE) directive [1] was aimed at reducing electrical waste, increasing recovery, recycling and minimising environmental impact; whilst the Restriction of Hazardous Substances (RoHS) directive [2] introduced a substitution requirement for those substances in electronic equipment, which pose the main environmental problems during disposal and recycling of such waste.

The RoHS directive stated that lead, mercury, cadmium, hexavalent chromium and two types of flame-retardants, polybrominated biphenyls (pbb) and polybrominated diphenyl ethers (pbde), had to be substituted by July 1, 2006. This instigated a move in the industry towards the use of lead-free solder. However, some limitations exist with lead-free solder, including the requirement of a relatively high

* To whom correspondence should be addressed. Tel.: 00 353 61 202647; Fax: 00 353 61 202913; e-mail: huw.lewis@ul.ie

soldering temperature (30–40°C higher than lead-based solder), which may cause an increased scrap rate due to damaged boards.

An alternative to lead-free solder is the use of electrically conductive adhesives (ECAs). These consist of a polymer binder and conductive filler which have been utilised in the semiconductor industry for chip-to-die connections [3], and are considered as environmentally friendly. Although conductive adhesives have become commercially available and have the advantage of a lower processing temperature, they have not been extensively used as a general solder replacement. This is due to limitations such as high joint resistance and low mechanical strength, especially when exposed to various environmental conditions [4].

The electrical, mechanical and structural formulation of ECAs, together with the properties that they would need to become comparable to solder is presented here.

2. Electrically Conductive Adhesives

2.1. Adhesive Formulation

The formulation of an electrically conductive adhesive consists of a binding material and a conductive filler, the combination of which determines the strength and electrical characteristics of the adhesive (Fig. 1).

(1) Binding material: Epoxy is the most commonly used material as an ECA binder with silicone being the most unacceptable. Tests carried out by the Danish environmental protection agency (EPA) concluded that silicone variants showed unacceptable interconnection resistance and very low shear strength values on a variety of substrates. However, from an environmental point of view, the EPA recommends that the choice of the adhesive resin should be made according to the following preference [5]:

- Polyester.
- One-component/two-component silicone.
- Acrylate/two-component epoxy/one-component epoxy.

With two-component adhesives, the resin and curing agent are separate, usually to prolong pot-life, and need to be mixed prior to use.

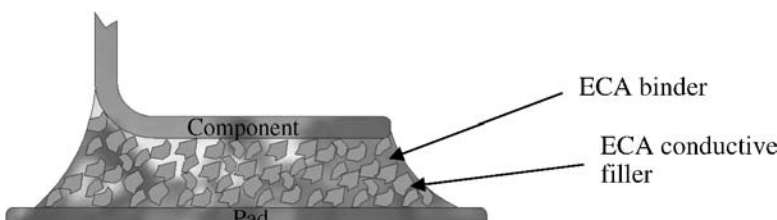


Figure 1. Schematic of an electrically conductive adhesive indicating the bond between the component lead and the printed circuit board pad.

- (2) Filler material: The most commonly used metals in conductive adhesives are silver, aluminium, gold and copper. Each one has different properties that determine how suitable the metal is for a particular application. Examples of these determining properties include electrical conductivity, ageing mechanisms, health risk and cost [3]. Silver is the most commonly used conductive filler for conductive adhesives with 80 wt% being the limit in epoxy adhesives [6]. Although it is an expensive material, its most important property is its ability to retain high conductivity as the silver particles oxidise. The stability of the electrical characteristics of conductive adhesives is dependent on the type and geometry of the metal filler [7]. There are three different filler geometries, namely, spheres, flakes and needles. The filler metal should be of optimum geometry that provides minimum critical filler concentration for low resistance, the best contact between neighbouring metallic particles, and the strongest adhesion to the resin. Filler flakes have more contact points and tend to be more conductive than spheres, however, Shimada *et al.* [8] claim that mixed type filler shows the highest conductivity and may be the best option.

2.2. Adhesive Curing

Thermoplastic conductive adhesives are based on a polymer dispersed in a solvent which cures when the solvent has evaporated. Thermosetting conductive adhesives, such as epoxy, cure because of a chemical reaction between the polymer resin and curing agent [6]. This chemical reaction makes it difficult to determine the exact point at which a joint is fully cured. An incomplete cure will result in weak adhesion whereas over-curing may cause bond degradation [9]. When an epoxy resin begins to cure, cross-linking of epoxide groups proceeds rapidly. This is because there are many unreacted groups ready to form bonds. After a certain period, most groups have bonded and thus the rate at which cross-links form significantly reduces. At this point, the proportion of unreacted material begins to decrease exponentially with time. Any unreacted material present at the end of the cure cannot contribute to the mechanical strength of the adhesive; thus Boyle *et al.* [9] claim that an accepted degree of cure occurs when 95% of the adhesive has reacted.

Boyle *et al.* went on to explain that since the thermal mass of the adhesive deposit is smaller than the materials being bonded, any heat produced by the epoxy during curing will be conducted away into the surrounding materials. This will prevent a rise in temperature of the epoxy and therefore it is assumed that the epoxy cures at the same temperature as its surroundings. The rate at which this reaction proceeds is exponentially dependent on temperature and can be accelerated by elevating the temperature according to the Arrhenius equation (1):

$$A_f = e^{\left\{ \frac{\theta}{k} \left(\frac{1}{T_2} - \frac{1}{T_1} \right) \right\}}, \quad (1)$$

where A_f is the acceleration factor between the Kelvin temperatures, T_1 and T_2 , θ is the activation energy of the reaction and k is Boltzmann's constant.

This theory implies that for any given reaction, there are pairs of values of temperature and time that will cure the reaction to the same degree. This is reflected in the conductive adhesive manufacturers cure schedules for conductive epoxies since manufacturers generally quote several alternative sets of cure times and temperatures for the same adhesive, for example, 150°C for 1 h or 175°C for 30 min.

2.3. Adhesive Conduction

Electrically conductive adhesives can be either isotropic or anisotropic based on the concentration of filler material.

2.3.1. Isotropic Conductive Adhesives (ICAs)

Isotropic conductive adhesives electrically conduct in all directions and have already been used in the electronics industry, primarily as die-attach adhesives [4]. They can be categorised as non-filled or filled adhesives depending on how the polymer is made conductive.

- (1) Non-filled isotropic conductive adhesives: Non-filled adhesives are polymers that are inherently electrically conductive or doped and are known as intrinsically conductive polymers (ICPs). Doping is the process of adding a small percentage of foreign atoms to a regular crystal lattice for the development of new properties.

They are mainly polymerised compounds that derive their electrical properties from their molecular structure [4]. The most common conductive polymers are based on polyacetylene, polyaniline and polypyrrole.

Gilleo [10] claims that a few of these materials have been commercialised for end applications such as battery electrodes and that doped polyacetylene has been found to have achieved a conductivity level of nearly 70% that of copper. However, Gilleo also explains that conductive polymers are extremely brittle and sensitive to oxidation and are thus not useful as a solder replacement.

- (2) Filled isotropic conductive adhesives: Filled adhesives consist of approximately 70–80% metallic particles in a polymer binder. When the adhesive is cured, the particles are uniformly distributed and form a network within the polymer structure (Fig. 2). By this network, electrons can flow across the particle contact points by direct metallic contact making the mixture electrically conductive. Due to the nature of the network formed, paths are made available for the current to flow in all directions [4]. Application areas for isotropic adhesives include the attachment of dies to lead-frames and the attachment of surface mount devices to flexible circuits and ceramics [12].

2.3.2. Anisotropic Conductive Adhesives (ACAs)

Anisotropic conductive adhesives can be of either paste or film form (ACAF) and provide unidirectional electrical conductivity in the vertical or Z-axis. This directional conductivity is achieved by using relatively low volume loading of the conductive filler well below the percolation threshold [13].

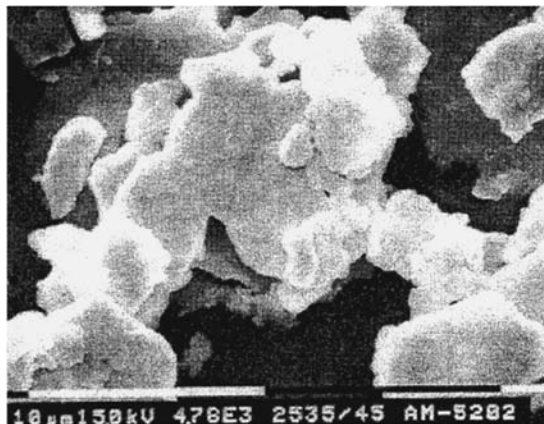


Figure 2. SEM image of direct contact between filler flakes [11].

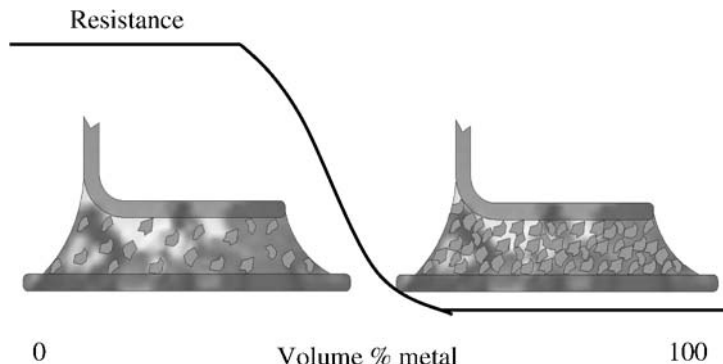


Figure 3. Schematic of percolation theory indicating the reduction in joint resistance at a specific point as more conductive filler material is added; conductivity of the ECA increases marginally after this point [14].

Percolation theory predicts a ‘critical’ filler concentration at which a three-dimensional network is established and conductivity increases suddenly by several orders. Thereafter, conductivity changes slowly with increase in filler concentration.

Thus, the percolation threshold, P_c , is reached when a sufficient amount of filler has been loaded into the polymer to transform the composite from an insulator to a conductor (Fig. 3) [14].

In ACAs, the low volume loading of filler (normally between 5 and 10 volume percent) is insufficient for inter-particle contact and prevents conductivity in the $X-Y$ plane of the adhesive (Fig. 4). This is opposite to ICAs that usually have a filler amount greater than that required to reach percolation threshold.

Prior to component placement, the ACA adhesive is placed between the surfaces to be connected. Heat and pressure are simultaneously applied until the particles bridge the two surfaces creating an electrical connection (Fig. 5). Once electrical

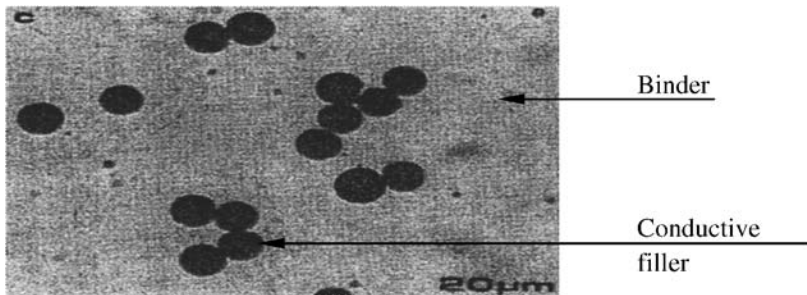


Figure 4. SEM image of an anisotropic conductive adhesive having a low filler to binder ratio, indicating the chain effect of the filler particles through the application of heat and pressure [3].

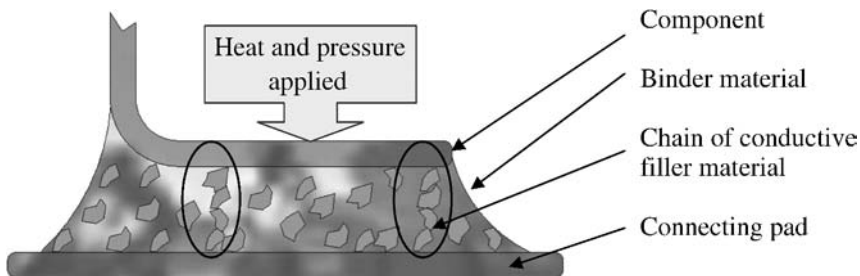


Figure 5. Schematic of curing of an anisotropic conductive adhesive, indicating the application of heat and the direction of applied pressure required to develop filler contact for conductivity in one direction.

continuity is produced, the polymer binder is hardened by a thermally initiated chemical reaction (for thermosets) or by cooling (for thermoplastics) [6].

ACAs have been used for a number of years in attaching chips to package lead frames. The advantages offered by this method of connection are high density interconnect, a low temperature process and low cost. More recently, ACAs have been used to connect flip-chips to other substrate materials, with varying degrees of success [12]. The main driver towards the use of ACAs in the area of SMT is the prospect of achieving extremely fine pitch connections at low cost. A major disadvantage, however, is that pressure and heat must be simultaneously applied while the polymeric matrix is hardened. Otherwise, the conductive pathway is lost. Isotropic conductive adhesives are easier to cure and are thus more common than ACAs, as direct solder replacement.

3. Electrical Properties of Electrically Conductive Adhesives

Electrical conductivity and joint resistance are the two main electrical properties of conductive adhesives. Electrical conductivity is the conductivity of the adhesive (conversely known as volume resistivity) and is measured in $\Omega \text{ cm}$. Joint resistance,

measured in $\text{m}\Omega$, is the resistance through the adhesive between the lead of the component and the pad on the board.

3.1. Electrical Conductivity

In general, conductive adhesives have a low conductivity before curing. This is increased after curing where cure shrinkage of the polymer binder increases contact between the filler particles, with adhesives of higher cure shrinkage showing better conductivity. However, although thermosetting materials shrink a small degree upon curing, too much shrinkage may cause bond failure [15].

Lu and Wong [16] claim that although cure shrinkage is the main mechanism for determining conductivity, a lubricant layer present on the adhesive flakes (specifically silver), also influences conductivity. In polymers with silver flakes, there is a thin layer of organic lubricant on the silver particle surface, which is electrically insulating [17]. Wong and Lu [18] show that this organic layer is a silver salt formed between the flake surface and the lubricant, which is typically a fatty acid such as stearic acid. The removal of this layer can be carried out with a lubricant remover, such as acetic acid. This increases conductivity but also increases the viscosity of the adhesive that is essential for screen-printing. They also found that a lubricant remover changed the volume resistivity of an isotropic conductive adhesive from approximately $6 \times 10^{-4} \Omega \text{ cm}$ to $1 \times 10^{-4} \Omega \text{ cm}$.

3.1.1. Joint Resistance

Joint resistance is not an adhesive property like conductivity but is a characteristic that is dependent on the termination and pad metals being joined. The type of metals used with conductive adhesives is an important criterion since joint resistance between a conductive adhesive and a non-noble metal increases dramatically during elevated temperatures, humidity ageing ($85^\circ\text{C}/85\% \text{ RH}$) and temperature cycling (-40 to $+125^\circ\text{C}$) [8]. Although this increase particularly applies to adhesives with silver filler flakes and tinned component and pad surfaces, work by Morris and coworkers [19] claims that this can also be applied to bare copper terminations.

Other factors that increase joint resistance include:

- Oxidation and corrosion.
- Galvanic corrosion.
- Interfacial crack formation.

3.1.1.1. Oxidation and Corrosion. Galvanic corrosion rather than simple oxidation of a non-noble metal (at the interface between the adhesive and the non-noble metal pad) is the mechanism responsible for joint resistance changes [20]. A galvanic corrosion process only happens under wet conditions with the presence of an electrolyte and is more prominent in adhesives of high moisture absorption. During humidity ageing, moisture accumulates at the interface between the metal filler and

pad. Different metals with dissimilar electrochemical potentials form an electrochemical cell in the presence of the water.

The metal with higher electrochemical potential, silver filler, acts as the cathode and the metal with lower electrochemical potential, non-noble metal pad, acts as the anode. During the electrochemical process, the anode is eroded.

Jagt [11] utilised noble terminations and tinned copper pads for joint resistance analysis. He describes the presence of a copper oxide layer, approximately 100 nm thick on the pads after humidity ageing ($85^{\circ}\text{C}/85\% \text{ RH}$) and states that the formation of this copper oxide layer was considered the cause for resistance increase. Research carried out by Liu and Lundstrom [21] also supports this claim.

3.1.1.2. Interfacial Crack Formation. Large increases in resistance values after humidity ageing ($85^{\circ}\text{C}/85\% \text{ RH}$) and a rapid change in temperature (-40 to $+125^{\circ}\text{C}$) may be explained by interfacial crack formation between the adhesive and tinned components (Fig. 6) [11]. Cracking usually occurs between the adhesive and substrate due to a difference in the coefficient of thermal expansion (CTE) between the two materials. For a tinned surface, the CTE is approximately $25 \text{ ppm}^{\circ}\text{C}$. For a conductive adhesive it is typically higher than $40 \text{ ppm}^{\circ}\text{C}$ and dramatically increases when the adhesive is heated above its glass transition temperature (T_g) [6]. At high temperatures, conductive adhesives are known to show fatigue behaviour due to viscoelastic and viscoplastic properties of the polymer matrix [22]. When cracks appear at the interface, they seem to be due to the thermo-mechanical fatigue of the adhesive joint, which leads, at low temperatures, to the brittle and premature fracture at the interface.

Although, component and pad metals, galvanic corrosion and interfacial cracking all have an effect on joint resistance, the overall internal structure of the adhesive is important in determining the electrical properties of the adhesive. For low resistance, the filler flakes should be in close contact to form a conductive path, there should be full attachment between the flakes and the terminations, and there should

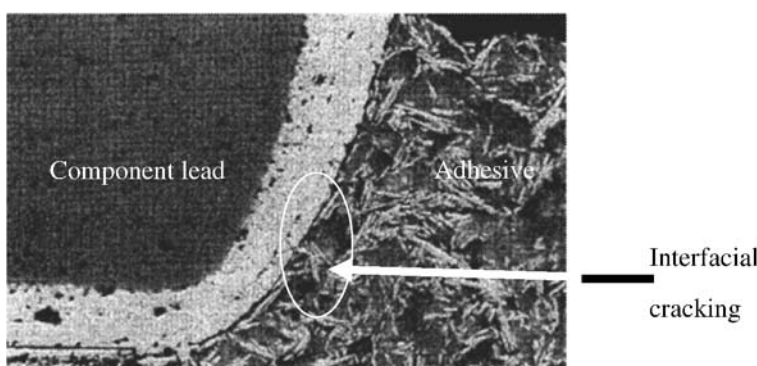


Figure 6. SEM image of interfacial cracking ($\times 700$) between a component lead and ECA due to the differences in the coefficient of thermal expansion of the materials after humidity aging [11].

be a sufficient amount of adhesive between the component lead and the pad with a high percentage of filler flakes.

4. Mechanical Properties of Electrically Conductive Adhesives

Adhesion strength is the main mechanical property of electrically conductive adhesives and can be categorised as either cohesion or bond adhesion strength. Different factors that affect the joint adhesion strength are material, joint size, the thickness of the adhesive layer, temperature of cure, presence of fillers, age and environmental conditions.

4.1. Cohesion Strength

The cohesion strength of a conductive adhesive refers to the internal strength of the adhesive, which is dependent on the type of polymer used and the amount of filler present. Research by Wong and Lu [4] reported the development of an alternative conductive adhesive, which uses a resin of low modulus that absorbs impact energy. It can be demonstrated that a high amount of conductor filler within the adhesive reduces adhesion strength. Conversely, a reduction of conductor filler will improve cohesion strength but will reduce conductivity.

4.2. Bond Adhesion Strength

The bond adhesion strength of a conductive adhesive refers to the adhesion strength between the pad and component termination.

Perichaud and Deletage [22] explain that thermosetting materials, such as epoxy, have a higher adhesion strength than thermoplastics. Thermosetting polymers can produce both strong covalent and secondary bonds where thermoplastics can only form secondary bonds. Thus, thermosetting polymers form a better hold with the component termination and metal pad. However, a reduction in adhesion strength can be a result of the manufacturing parameters (too little adhesive printed), environmental conditions, or materials used.

Lu and Wong [23] reported that non-noble metals, due to oxide formation on the pads, showed a significant reduction in adhesion strength after humidity ageing (500 h 85°C/85% RH). Rorgren and Liu [24] also illustrated a reduction in adhesion strength when using tinned circuit board pads, however similar adhesion strength on both the tinned and passivated copper surfaces was observed.

5. Utilisation of Conductive Adhesives as a Solder Replacement

The previous sections introduced the structure and properties of electrically conductive adhesives and outlined the research detailing their use in electronic manufacture. In order to assess their suitability as a solder replacement, a set of standards or requirements need to be defined for the electrical, mechanical and structural properties of ECAs, together with a set of manufacturing parameters.

5.1. Electrical Requirements

Wong and Lu [4] explain that the National Centre for Manufacturing Sciences (NCMS) in conjunction with seven industry collaborators established a set of criteria for a successful electrically conductive adhesive. These criteria, outlined below, are what each conductive adhesive must possess if it is used as a solder replacement.

- Volume resistivity lower than $1 \times 10^{-3} \Omega \text{ cm}$ (1 milliohm cm).
- Shift of joint resistance less than 20% (after 500 h 85°C/85% RH).

The volume resistivity is a property that is inherent to the adhesive. However, a shift in joint resistance after humidity ageing may be due to moisture penetration, a metal oxide layer, or interfacial cracking.

5.2. Mechanical Requirements

Wong and Lu [4] also outlined the mechanical requirements for the use of electrically conductive adhesives as a solder alternative. This NCMS requirement is used to examine the adhesion strength between the components and the circuit boards using drop tests (6 drops at 152.4 cm); with Coughlan and Lewis [25] indicating that a shear force greater than 30 N is needed.

5.3. Structural Requirements

The structures of the conductive adhesive joints can be examined with the use of IPC definitions [26]. These grade the joints into different acceptance classes.

6. Manufacturing Parameters

Conductive adhesives can be applied to a circuit board using screen-printing. The choice of stencil and squeegee used in the printing process is pertinent to a good adhesive joint. Researchers generally recommend metal stencils with apertures 80% of the pad size.

The thickness of the stencil should be smaller for adhesives than for solder, as a thinner joint is favourable. However, it is recommended that conductive adhesives should have a thicker printed deposit than solder. Components being soldered experience wetting forces due to the molten solder which helps align the component to the connecting pad. The lack of wetting forces when using ECAs requires the margin of error in the placement of a component to be reduced [27]. The pad thickness should also be higher due to the large weight tolerance of different components [28]. Compared to the viscosity of solder paste (typically 500 000 cP [29]), the viscosity of adhesives is lower (55 000 and 70 000 cP for the adhesives examined) thus less adhesive is required as the adhesive will easily slump and cause bridging [21]. A typical stencil thickness is 0.10–0.15 mm but is dependent on application. Liu and Lundstrom [21] used a stencil thickness of 0.11 mm but found that the adhesive adhered to the stencil apertures.

Contact printing is preferred over non-contact as less adhesive is printed. A metal squeegee is preferred as rubber squeegees are too soft and tend to scoop out the adhesive from the apertures during printing. Recommended squeegee speed varies from 45 to 75 mm/s and the angle from 20 to 45° [21].

In component placement, the effect of the mounting pressure on an adhesive is of great importance since conductive adhesives do not self-align or contract. Too high a pressure may cause the adhesive to flow out and create a short circuit after curing. Reducing stencil thickness or the component footprint can reduce this flow-out by reducing the amount of adhesive printed. In addition, a high mounting force may cause deflection of the circuit board and thus create bridging. Too low a mounting force may cause a high joint resistance in the connection or open joints [21].

In curing, an extended schedule is recommended to ensure a complete cure. Research carried out by Rorgen and Liu [24] suggested that a curing schedule chosen for a particular conductive adhesive should greatly exceed the minimum times recommended by the supplier. This will ensure that lag effects caused by thermal mass of the assembled board will be reduced and the risk of under-curing minimised.

7. Summary of Electrically Conductive Adhesives

Electrically conductive adhesives have been used as a medium for semiconductor die to lead frame connections for several years. It is logical, therefore, to utilise this technology when investigating a solder replacement in circuit board manufacturing.

This paper described the structure together with the electrical and mechanical properties of conductive adhesives and introduced the test criteria required for them to become a solder replacement. In addition, in order to facilitate their use as a solder substitute, it was necessary to define the manufacturing parameters required, with an aim to determine these for an optimal adhesive performance.

7.1. Further Developments in ECA Technology

Whilst the development of ECAs began in the 1980s [30] recent developments have focused on increasing the electrical properties of ECAs. These include the low temperature sintering of nano-silver particles [31], the use of silver–tin fillers [32], and the addition of short chain difunctional acids [33]. The strength of the adhesive joint has also been investigated by utilising silver-coated particles and short fibres [34], the use of plasma cleaning and vacuum processes, coupling agents and the roughening of contact surfaces [35].

The authors whilst acknowledging the need for a drop in replacement for solder have developed a tri-metal system for the connection of chip leads directly to pads. The use of a nickel then tin coating over the chip lead, allows for direct bonding to the pad, with the absence of tin whiskering [36].

References

1. Directive 2002/96/EC of the European Parliament and of the Council of 27 January 2003 on Waste Electrical and Electronic Equipment (WEEE), *Official Journal of the European Union* **46(L 37)**, 24–38 (2003).
2. Directive 2002/95/EC of the European Parliament and of the Council of 27 January 2003 on the Restriction of the Use of Certain Hazardous Substances in Electrical and Electronic Equipment, *Official Journal of the European Union* **46(L 37)**, 19–23 (2003).
3. D. D. Chang, P. A. Crawford, J. A. Fulton, R. Mc. Bride, M. B. Schmidt, R. E. Sinitski and C. P. Wong, *IEEE Trans. on Components, Hybrids and Manuf. Technol.* **16**, 828–835 (1993).
4. C. P. Wong and D. Lu, in: *Proc. 4th International Conference on Adhesive Joining and Coating Technology in Electronics Manufacturing*, Espoo, Finland, pp. 121–129 (2000). Available at: <http://csdl2.computer.org/persagen/DLAbsToc.jsp?resourcePath=/dl/proceedings/&toc=comp/proceedings/adhes/2000/6460/00/6460toc.xml> (2008).
5. H. Hvims and H. Ronsberg, C1.5 Basic types of conductive adhesives, Chapter C: Polymer bonding, *The Nordic Electronics Packaging Guideline* (2007). Available at: <http://extra.ivf.se/ngl/>
6. H. Hvims and H. Ronsberg, C2.3.3 Thermal conductivity, Chapter C: Polymer bonding, *The Nordic Electronics Packaging Guideline* (2007). Available at <http://extra.ivf.se/ngl/> (2008).
7. F. M. Christensen, T. Jorgensen and I. R. Nielson, Environmental and technical characteristics of conductive adhesives *versus* soldering, Working Report No. 16, Danish EPA (2000).
8. Y. Shimada, D. Lu and C. P. Wong, in: *Proc. IMAPS, International Symposium on Advanced Packaging Materials*, Braselton, Georgia, pp. 336–343 (2000). Available at <http://www.ecampus.com/book/9780930815592> (2008).
9. O. Boyle, D. C. Whalley and D. J. Williams, in: *Proc. 30th International Society for Hybrid Microelectronics (ISHM) Nordic Conference*, Oslo, pp. 139–149 (1992). Available at <http://www.worldscinetarchives.com/cgi-bin/details.cgi?id=pii:S0960313192000145&type=html> (2008).
10. K. Gilleo, in: *Conductive Adhesives for Electronic Packaging*, J. Liu (Ed.), Chapter 1. Electrochemical Pubs Ltd., Isle of Man (1999).
11. J. C Jagt, in: *Conductive Adhesives for Electronic Packaging*, J. Liu (Ed.), Chapter 11. Electrochemical Pubs Ltd., Isle of Man (1999).
12. L. Li, C. Lizzul, H. Kim, I. Sacolick and J. E. Morris, *IEEE Trans. on Components, Hybrids and Manuf. Technol.* **16**, 843–850 (1993).
13. C. Bastecki, *A Benchmark Process for the Lead-Free Assembly of Mixed Technology PCBs*, a report for Alphametals Corp. (1999). Available at www.alphametals.com/leadfree/pdfs/leadfree.pdf
14. J. E. Morris, in: *Conductive Adhesives for Electronic Packaging*, J. Liu (Ed.), Chapter 3. Electrochemical Pubs Ltd., Isle of Man (1999).
15. C. Christuk, *Adhesives & Sealants Industry (ASI) Magazine* (February, 2002). Available at <http://www.adhesivesmag.com/CDA>
16. D. Lu and C. P. Wong, *Intl. J. Adhesion Adhesives* **20**, 189–193 (2000).
17. D. Lu, Q. K. Tong and C. P. Wong, *IEEE Trans. Components, Packaging and Manuf. Technol. — Part A* **22**, 365–371 (1999).
18. C. P. Wong and D. Lu, in: *Proc. of 4th International Conference on Adhesives Joining & Coating Technology in Electronic Manufacturing*, Espoo, Finland, pp. 121–129 (2000). Available at <http://csdl2.computer.org/persagen/DLAbsToc.jsp?resourcePath=/dl/proceedings/&toc=comp/proceedings/adhes/2000/6460/00/6460toc.xml> (2008).
19. L. Li, J. E. Morris, J. Liu, Z. Lai, L. Ljungkrona and C. Li, in: *Proc. 45th IEEE Electronic Components and Technology Conference*, Las Vegas, pp. 114–119 (1995). Available at http://ieeexplore.ieee.org/xpl/freeabs_all.jsp?arnumber=514370 (2008).

20. C. P. Wong, D. Lu, L. Meyers, S. A. Vona and Q. K. Tong, in: *Proc. 1st IEEE International Symposium on Polymeric Electronics Packaging*, Norrkopingpp, pp. 80–85 (1997). Available at http://ieeexplore.ieee.org/xpl/freeabs_all.jsp?arnumber=868842 (2008).
21. J. Liu and P. Lundstrom, in: *Conductive Adhesives for Electronic Packaging*, J. Liu (Ed.), Chapter 9. Electrochemical Pubs Ltd., Isle of Man (1999).
22. M. G. Perichaud and T. Y. Deletage, *Microelectronics Reliability* **40**, 1227–1234 (2000).
23. D. Lu and C. P. Wong, *J. Appl. Polym. Sci.* **74**, 399–406 (1999).
24. R. S. Rorgen and J. Liu, *IEEE Trans. Components, Packaging and Manuf. Technol. — Part B* **18**, 305–312 (1995).
25. F. M. Coughlan and H. J. Lewis, *J. Electronic Mater.* **35**, 912–921 (2006).
26. IPC-A-610C Acceptability of Electronic assemblies, *A Standard issued by IPC Association Connection Electronics Industries*. Northbrook, Illinois (2000). Available at www.ipc.org
27. D. Terstagge, Available at <http://www.smtinfo.net/docs/Electronic%20Production/5.htm> (2007).
28. O. D. Hennemann, H. Mieskes and B. Dorbath, *Interconnection Technology in Electronics* (Translated from Verbindungstechnik in der Elektronik) **129**, 30–47 (1990).
29. Tutorialsweb, *SMT Components and Assembly — Chapter 3* (Online). Available at: <http://www.tutorialsweb.com/smt/chapter5c.htm> (2007).
30. K. Gilleo, *Polymer Thick Films*. Springer (1996).
31. Y. Li, K. Moon and C. P. Wong, *J. Appl. Polym. Sci.* **99**, 1665–1673 (2005).
32. M. Yamashita and K. Suganuma, *Microelectronics Reliability* **46**, 850–858 (2006).
33. Y. Li, K. Moon and C. P. Wong, *IEEE Trans. on Components, Packaging Manuf. Technol. — Part A* **29**, 173–178 (2006).
34. I. Novak, I. Krupa and I. Chodak, *Synthetic Metals* **144**, 13–19 (2004).
35. Y. Li and C. P. Wong, *Mater. Sci. Eng. R* **51**, 1–35 (2006).
36. F. M. Coughlan and H. J. Lewis, *J. Mater. Process. Technol.* **153–154**, 240–246 (2004).

This page intentionally left blank

Electrically Conductive Adhesives for Electronic Packaging and Assembly Applications

L. J. Matienzo*, R. N. Das and F. D. Egitto

Endicott Interconnect Technologies, Inc. Endicott, NY 13760, USA

Abstract

Some recent advances in materials, structures and properties that affect the mechanical and electrical characteristics and reliability performance of electrically conductive adhesives (ECAs) are discussed. This is done in the context of electronic packaging and assembly applications. Micro-silver-filled epoxy ECAs (with an average silver particle size of 5 μm) modified by addition of a conducting polymer, low melting point (LMP) alloys, or nanoparticles (average particle size of 80 nm) are described and compared with respect to volume resistivity, tensile strength and adhesion to copper. To understand the conduction and sintering behaviors of the various ECA formulations, SEM, optical microscopy and X-ray photoelectron spectroscopy (XPS) are used to investigate the micro-structure and chemical nature of the cured ECAs. Volume resistivity of the specially formulated adhesives is in the range of 10^{-4} to 10^{-6} Ohm cm. Adhesives formulated with a conducting polymer exhibit the greatest tensile strength with copper when compared to the other formulations investigated. The conducting polymer-modified ECA exhibited electrical conductivity on the order of that achieved with conventional ECAs. Hence, good electrical performance is achieved concurrent with superior mechanical properties. It was found that with increasing curing temperature, the volume resistivity of all ECAs decreased. This is attributed to sintering of metal particles at higher temperatures. Incorporation of nanoparticles reduces sintering temperature. Sintering of ECAs with micrometer-scale silver particles was further evaluated using high temperature/pressure lamination. A continuous metallic network resulted when the lamination temperature was greater than 300°C. Electrical stability of ECA joints with aluminum was evaluated by stress testing in an environment of elevated temperature and humidity. A thin layer of silane-based coupling agent on the aluminum surfaces retards the degradation of the electrical properties of the joint. In general, proper preparation of the metal surface to which an ECA is mated is critical for maintaining both electrical and mechanical performances.

Keywords

Electrically conductive adhesives (ECAs), electronic packaging, sintering, materials characterization

1. Introduction

Electronic packaging is the technology of electrically and mechanically interconnecting a multiplicity of components into an integrated system. The electronic pack-

* To whom correspondence should be addressed. Tel.: (607)-755-3188; Fax: (607)-755-6151; e-mail: matienzo@eitny.com

age provides a framework for mounting of and physical support for the electronic components, provides protection of devices from the environment and enables removal of heat from devices. The primary function of the package is electrical interconnection of components (e.g., integrated circuit chips, printed wiring boards, etc.) for input, distribution and output of electrical signals and power. Interconnection within a component has traditionally been made using copper circuitry, typically circuit traces for connections within a wiring plane and plated holes for connection between planes. Interconnection among components (assembly) is commonly made using solder, most often tin–lead alloys. Low-cost tin–lead solders have been used as interconnecting materials in electronics for many decades. These alloys have good electrical and mechanical properties, reasonably low melting point and good reliability, but they are not nature-friendly. The use of lead (Pb) in electronics has been controversial. Indeed, its toxic effects are well documented. As the quantity of waste related to electronic products increases, global legislative initiatives and corporate marketing strategies are driving a reduction in the use of such toxic substances in electronics. One solution is the use of lead-free solders [1]. These solders generally possess relatively higher melting points than their tin–lead counterparts. The higher reflow temperatures required for assembly with lead-free solders can compromise the integrity of an organic substrate, thus limiting the number of suitable organic packaging substrate materials that are available.

During the past few years, there has been increasing interest in the use of electrically conductive adhesives (ECAs) as interconnecting materials in the electronics industry [2, 3]. Conductive adhesives are composites of polymer resin and conductive fillers. Metal-to-metal contact between conductive fillers provides electrical conductivity [4–7], whereas the polymer resin provides favorable processing attributes and mechanical robustness [8]. A number of investigations have been reported related to formulation and processing of ECAs [9–17]. These include studies related to curing behavior, shrinkage due to solvent evaporation, thermal annealing, organic binder material, metal filler material and size of metal filler. ECAs that are available for use in advanced packaging applications can have a broad distribution of particle sizes, including nano- and micro-filled adhesives [11, 12, 16]. ECAs have found application in microelectronics as alternatives to electrical interconnections otherwise produced by soldering, brazing, or welding methods. Applications for bonding with ECAs include die attach to circuit boards and surface mount technology of components [18, 19]. As is the case for any joining method, mechanical and electrical reliability are critical.

The demand for high-performance, lightweight, portable computing power is continually driving the electronics packaging industry toward miniaturization. New packaging designs need to be able to integrate more IC chips with greater function, higher I/O counts, smaller pitches and greater heat densities, while being pushed into smaller and smaller footprints. Traditionally, greater wiring densities have been achieved by reducing the dimensions of circuit lines and plated holes, increasing the number of wiring layers, and sequentially building up these structures with layer-

to-layer interconnection made using shallow plated holes that span only one or two layers (blind and buried vias). As opposed to the situation with traditional plated-through-hole (PTH) connections, blind and buried vias do not occupy space on circuit layers situated above or below the layers that they connect. This space is, therefore, available for additional wiring. These approaches for achieving greater wiring density possess inherent limitations, for example, those related to drilling and plating of high aspect ratio vias, reduced conductance of narrow circuit lines, and increased cost of fabrication related to additional wiring layers. As a result, the microelectronics industry is moving toward alternative, innovative approaches as solutions for squeezing more function into smaller packages.

Replacement of conventional plated-through holes with vertically-terminated vias opens up additional wiring channels on layers above and below the terminated vias, facilitating a more space-efficient package design. Egitto *et al.* [20] have reported on the use of ECAs to replace the more traditional PTH technology for making vertical interconnections in electronic packages. This structure for z-axis electrical interconnection employs an ECA to interconnect thin cores (sub-composites). The cores are processed, aligned and laminated to form a composite structure. The net effect is a composite laminate having vertical interconnections with small diameter holes that can be terminated arbitrarily at any layer within the cross-section of the package (Figs 1 and 2). Integral to the methodology described in Ref. [20] is the use of core building blocks that can be laminated in a manner such that electrical interconnection between adjacent cores is achieved. The cores can be structured to contain a variety of arrangements of signal, voltage and ground planes. In addition, signal, voltage and ground features can reside on the same plane. One of the building blocks is a “signal core” that contains circuit traces having metal pads for electrical connection to adjacent cores. The second building block is a joining core constructed with holes in the core that are filled with an ECA. By stacking cores of these two types in an alternating fashion prior to lamination, the conductive paste electrically connects copper pads on the signal cores that reside on either side of the joining cores. Two signal layers are added to the composite structure each time one adds an additional signal core and an additional joining core. A structure with four signal layers composed of five sub-composites (two signal cores and three joining cores) is shown schematically in Fig. 1. Optical photographs of composite laminate structures are shown in cross-section in Fig. 2.

In the present paper, the materials and parameters that control ECA characteristics and reliability performance, as related to electronic packaging, are described. In addition, the techniques used for materials characterization (chemical, electrical and mechanical) are addressed, as are the results of these characterizations. Among the ECA characteristics discussed are resistivity, viscosity, morphology, particle distribution and interaction and chemical composition. A detailed description of some analytical techniques applied to the characterization of ECAs including SEM, laser scanning microscopy, Auger electron spectroscopy, X-ray photoelectron spectroscopy (XPS) and mass spectroscopy can be found in Refs [21, 22].

Fabrication of core building blocks...

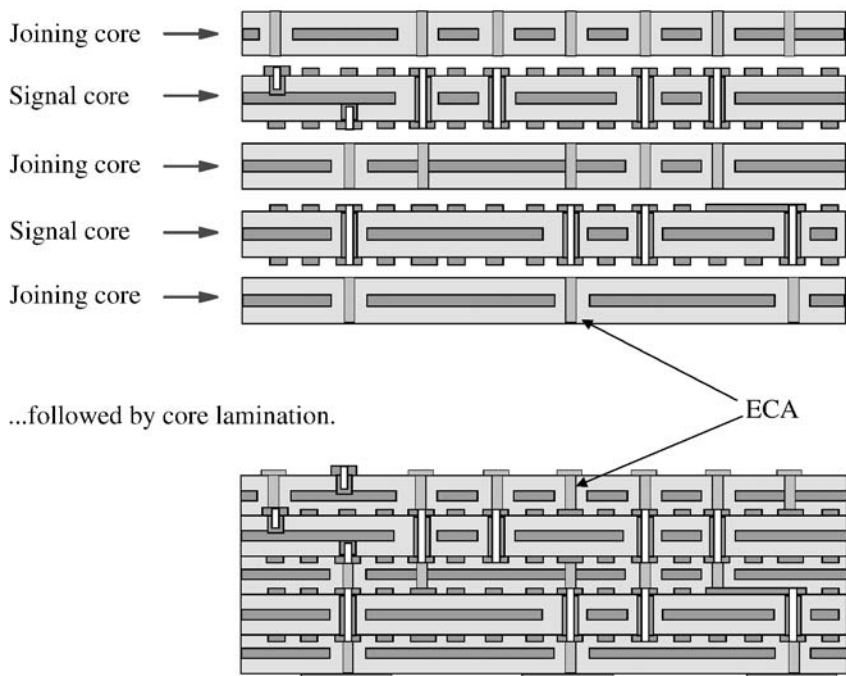


Figure 1. Composite structure formed by lamination of five cores. Vertical electrical interconnections are made using an ECA. Controlled-depth vias increase wiring density and eliminate *via* stubs.

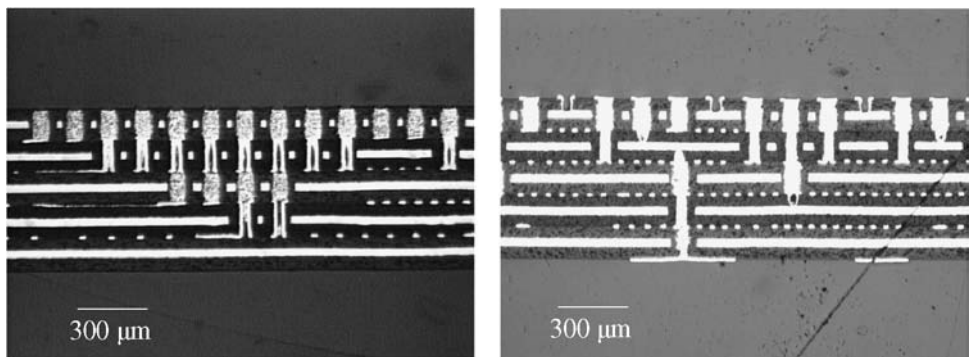


Figure 2. Optical photographs showing cross-sectional views of a multilayer laminate chip carrier constructed using an ECA for vertical electrical interconnections. Diameter of the ECA-filled vias is around 75 μm. The pitch between vias is 150 μm. Two different areas of the same carrier are shown.

2. Paste (ECA) Formulation, Characteristics and Behavior

2.1. Paste (ECA) Components

Conductive adhesives are composites of polymer resin and conductive fillers. Common polymer matrices are epoxy-forming resins and silicones with a high loading

of conductive particles [9]. The particles themselves can be composed of a single metal, mixtures of metals, or metal-coated particles. More recently, silver particles coated with self-assembled monolayers (SAMs) have been used in ECA formulations [23]. Other ECA components that enhance their mechanical and/or electrical performance include use of conducting polymers and low-melting-point (LMP) particles.

Conducting polymers, such as polyaniline, are generally doped with protonic acids such as aqueous hydrochloric acid (HCl) to give conductivity on the order of 1 S/cm². Polyanilines are generally [24–26] environmentally stable soluble polymers that are fabricated by a one-step synthesis involving inexpensive raw materials [27]. Other conducting polymers typically used in organic electronics are poly(3,4-ethylenedioxythiophene) doped with polystyrene sulfonic acid (PEDOT/PSS), dodecyl benzene sulfonic acid doped polyaniline (DBSA/PANI), camphor sulfonic acid doped polyaniline (CSA/PANI) and a polyaniline doped with di-nonyl naphthalene sulfonic acid (DNNSA). A variety of conducting polymers, blended with appropriate matrix polymers (such that the conducting polymer dilutes the relative amount of silver filler in the ECA) and cured at ~190°C for 2 h, showed low volume resistivity, in the range of 10⁻⁵ Ohm cm, which is similar to that of the micro-silver filled epoxy adhesive to which the conducting polymer was added.

In a typical LMP system, the LMP metals, or LMP-coated particles, melt and reduce inter-particle resistance among the metallic particles by producing a continuous metallic network. The use of LMP particles can be coupled with some conductive polymers to produce new formulations with some attractive properties.

2.2. Preparation and Characterization of ECAs

One cannot always find a suitable commercially-available ECA for advanced printed wiring board (PWB) applications requiring electrical interconnections. To this end, a variety of silver and LMP-based nano- and microparticles and their dispersions into epoxy resins were prepared. A reference ECA, suitable for advanced PWB applications, and previously described in the literature [20], was prepared by thoroughly mixing 88 g of silver flakes with average particle size of 5.0 µm with 12 g of an epoxy pre-polymer. When cured, the ECA exhibits an electrical resistivity on the order of 10⁻⁵ Ohm cm.

For comparison with this reference ECA, another ECA containing 88 g of silver nanoparticles with an average particle size 80 nm mixed with 12 g of epoxy pre-polymer and 15 g of propylene glycol methyl ether acetate (PGMEA) was prepared.

A similar process was used for a mixture of silver nano- and microparticles, and LMP-based systems where the silver microparticles were replaced by a mixture of silver nano- and microparticles (nanoparticle percentage up to 50%) and about 5.0 µm size LMP–Cu mixed particles. To compare the electrical and mechanical properties of the various ECA formulations, the ECAs were deposited

onto a PWB substrate and cured or laminated at different temperatures ranging from 150 to 365°C.

For some investigations discussed in this work, Ablebond® 8175 (Ablebond® is a registered trademark of National Starch and Chemical Company, Billerica, MA), a silver-loaded (about 80% silver by weight), commercially available electrically conductive amine-cured epoxy adhesive was used to characterize bonding between metal surfaces for PWB applications. This ECA contains relatively large silver flakes. Some flakes having dimensions greater than 75 µm have been observed. Hence, this ECA does not lend itself to fine feature PWB applications.

Adhesives were characterized by SEM and optical microscopy to ascertain particle dispersion and their interconnection mechanism. A Keithley micro-ohmmeter was used for electrical characterization. Room temperature (25°C) viscosity was measured using a MALVERN C-VOR Rheometer operating in the oscillation mode using 50 Pa stress at 1 Hz. Heat of curing reaction of adhesives was studied using differential scanning calorimetry (DSC). Practical adhesion (90° peel test) and tensile strength were measured using an Instron (Model 1122) and an MTS tensile tester, respectively.

2.3. Effect of Processing Parameters

Exposure of ECAs to ambient conditions before curing can affect paste properties of the final product. Figure 3 shows viscosity as a function of exposure time at room temperature for a micro-silver-filled epoxy ECA. Viscosity measurement was done using a 50 Pa stress under N₂. Adhesive viscosity increased by about 30% after 40 h

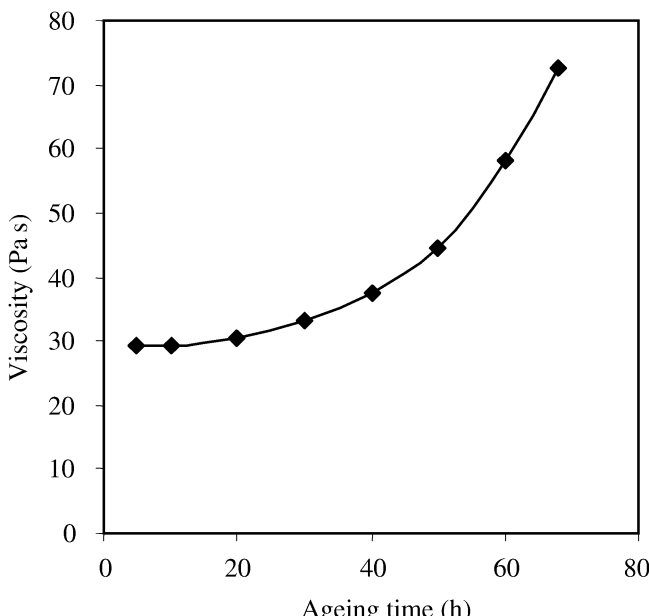
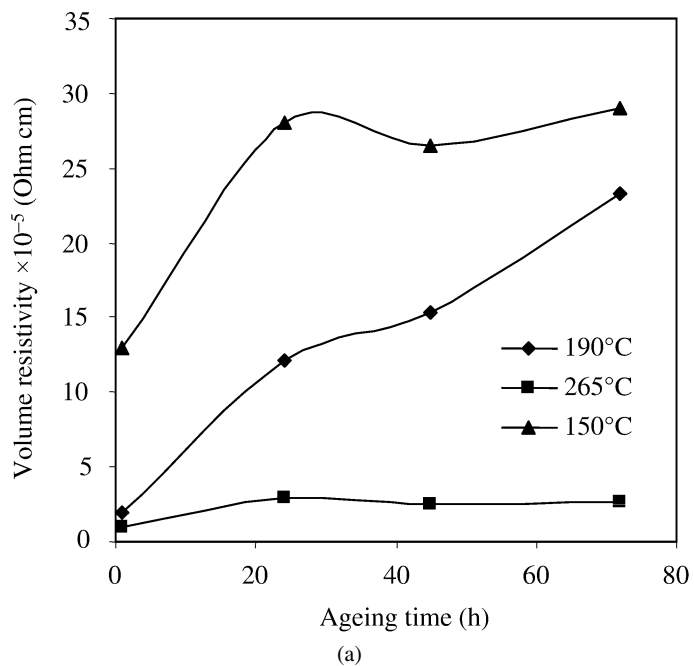
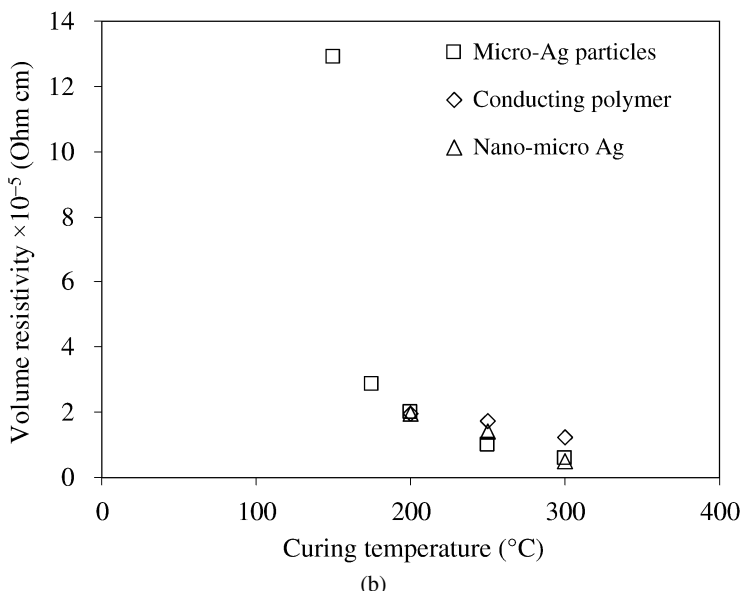


Figure 3. Viscosity as a function of exposure time at room temperature for a silver-epoxy ECA.

and doubled after 70 h. Differential Scanning Calorimetry (DSC) measurements indicated that this change was the result of polymer cross-linking. Figure 4a presents



(a)



(b)

Figure 4. (a) Volume resistivity of micro-scale silver-filled adhesive with ageing time as a function of curing temperature. (b) Volume resistivity of three ECA formulations as a function of curing temperature.

volume resistivity values for the same adhesive, cured at various temperatures, as a function of aging time at room temperature prior to their thermal curing. After 72 h, curing of the ECA at 50, 190 and 265°C resulted in values of 50×10^{-5} , 32×10^{-5} and 2×10^{-5} Ohm cm, respectively. Change in resistivity with aging was significant when cured below 200°C, but it was not significant when cured at or above 250°C. Figure 4b shows volume resistivity of the same silver-filled (micro-scale) adhesive as a function of curing temperature. Figure 4b also includes data for an ECA fabricated using a conducting polymer, and a third ECA in which nanoparticles of Ag were added to the micro-sized Ag particles.

2.4. Sintering

Sintering is the process of fusing or welding adjacent surfaces of particles in a powder by heating to a temperature below the melting-point of the components. A number of factors affect the degree of sintering that can be achieved at a given temperature. Elevated temperatures can enhance sintering of the metallic particles in ECAs, even those with micro-scale Ag particle fillers. One may postulate that the decrease in volume resistivity observed with increased curing temperature of the ECA (Fig. 4) is due, to a large extent, to sintering of metal particles.

2.4.1. High Temperature Sintering

In an effort to understand the behavior of conductive paste (ECA) as a function of curing temperature (under pressure), a silver–epoxy ECA containing about 88% (wt/wt) silver flakes was laminated at three different temperatures (at high pressure) between two sheets of copper. The copper foil was chemically removed before analyses. The selected temperatures included laminations at 190, 275 and 365°C.

XPS analyses were performed on the etched surfaces to follow the evolution with lamination temperature of signals from carbon (C_{1s}) and silver (Ag_{3d}) in the exposed areas (Fig. 5). The C_{1s} spectra are similar to each other with the exception of the level of carbonyl contributions, ca. 288 eV, as a function of temperature. The Ag_{3d} XPS spectra show that polymer flow during curing at the lower lamination temperature does not allow for the appearance of silver atoms at the surface of the cured film. These experiments also indicate that the silver–organic mixture is capable of surviving at temperatures as high as 365°C. Although epoxies are generally known to decompose at temperatures below 300°C, DSC analysis has shown that the decomposition temperature for this ECA is 339.7°C in a nitrogen atmosphere. The XPS analyses show that these high temperatures enhance exposure of silver particles at the surface of the cured ECA. This may promote better electrical contact of the silver particles to a conductive surface to which it may be connected, e.g., metal contact pads in the circuit traces of an electronic packaging component (Figs 1 and 2).

Argon ion etching for depth profiling was used on the exposed surface to determine if organic residues were present below the surfaces of the samples as measured by XPS. The oxygen content is limited to the top surface of the samples. In all cases, the silver particles co-exist with organic residues below the initial surface.

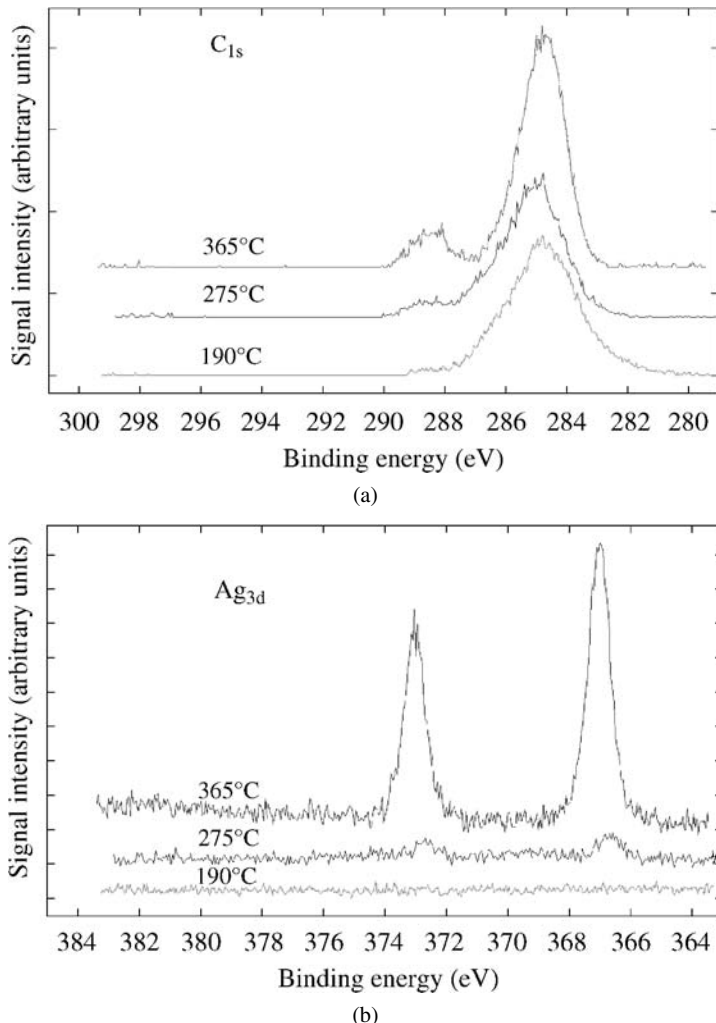


Figure 5. C_{1s} XPS spectra (a) and Ag_{3d} XPS spectra (b) of an ECA with micro-scale Ag flakes, cured at various temperatures.

Further understanding of these results was obtained by analyzing the particles through optical views of their cross-sectional areas (Fig. 6) and SEM imaging (Fig. 7). These two figures contain a general view of the morphological variations of the ECA cured at the various selected temperatures. Both views of the ECA cured at the highest temperature (Figs 6c and 7c) indicate an appreciable change in morphology which is consistent with sintering of silver particles. At the lower temperature, the silver particles are separated by larger areas of polymer. It is only at the highest temperature that the silver phase appears more consolidated. However, there are areas of polymer interspersed throughout the continuous silver network.

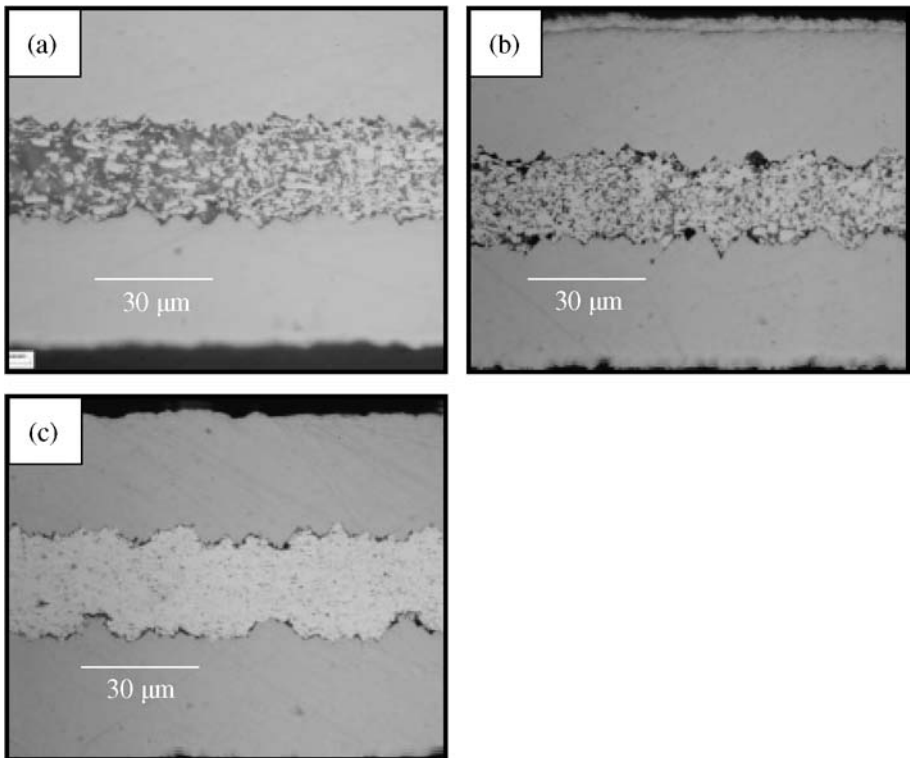


Figure 6. Optical photographs of cross-sections taken from laminates processed at (a) 190, (b) 275 and (c) 365°C. Bondline thicknesses are 30, 20 and 30 μm, respectively.

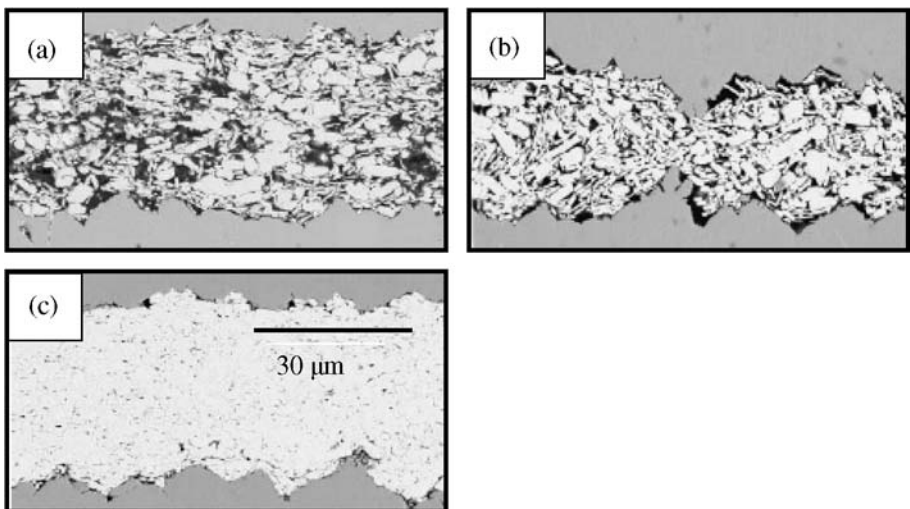


Figure 7. SEM micrographs of cross-sections taken from laminates processed at (a) 190, (b) 275 and (c) 365°C. Bondline thicknesses are 30, 20 and 30 μm, respectively. The dimension marker shown in (c) applies to all three micrographs.

This ECA was used to fabricate two z -axis interconnection structures as described above (Fig. 1), by performing laminations at 200 and 365°C, respectively. Lamination at the higher temperatures requires suitable high-temperature dielectric materials. In this instance, PTFE-based dielectric materials were employed. Optical photographs and SEM micrographs taken from cross-sections of the ECA-filled *via* structures are shown in Fig. 8. Laminating at the higher temperature produced a sintered and connected network of silver.

2.4.2. Low Temperature Sintering: Use of Silver Nanoparticles

As shown by the experiment at 365°C, the sintering process is achievable using micro-scale particles. However, it is well known that change in grain size has a direct impact on the electronic properties of a system as well as on the sintering behavior [28]. Consolidation of particles may be achievable more efficiently with reduction of the average silver particle size. In view of this, Das *et al.* [29] carried out a systematic investigation of electrical resistance behavior of ECAs fabricated using silver nanoparticles. Figure 9 shows an SEM micrograph of an ECA fabricated using a mixture of silver nanoparticles and microparticles and cured at 275°C. At this temperature, below the decomposition temperature of typical epoxies, sintering is observed. Comparable sintering was not observed at this temperature for ECAs fabricated without the addition of nanoparticles (Figs 6b and 7b). It appears that at a sufficiently high concentration, nanoparticles are more prone to immediate particle–particle contact, facilitating sintering.

2.5. Adhesives with Low Melting Point (LMP) Particles

An LMP system is a mixture of low melting point particles, and a higher melting point metal(s) in a polymer matrix. In a typical LMP system, the LMP particles melt and react with the metallic particles to form a continuous network. Das *et al.* [29] discussed the importance of LMP coating of various metal particles relative to providing a uniform, continuous conducting LMP network. It was demonstrated that excessive amounts of LMP material could melt and spread, a potential cause of shorting between adjacent electrical circuit traces. During the cure of the polymer matrix at temperatures above the melting point of LMP particles, LMP particles melt and react with higher melting point metal particles. Electrical conduction is enhanced through a plurality of metallurgical connections formed *in situ* from the two powders in the polymer binder.

2.6. Joint Reliability

2.6.1. Stability in Humid Environments

Electrically conductive interfaces between metal surfaces, including aluminum, are commonly formed by means of bonding with an ECA. Humid environments have been shown to induce an increase in electrical resistance between aluminum objects bonded in this manner [30]. However, joints that are electrically stable through stress testing in environments of elevated temperature and humidity (85°C and 80% RH for up to 137.5 h) can be obtained by treating the aluminum surface with

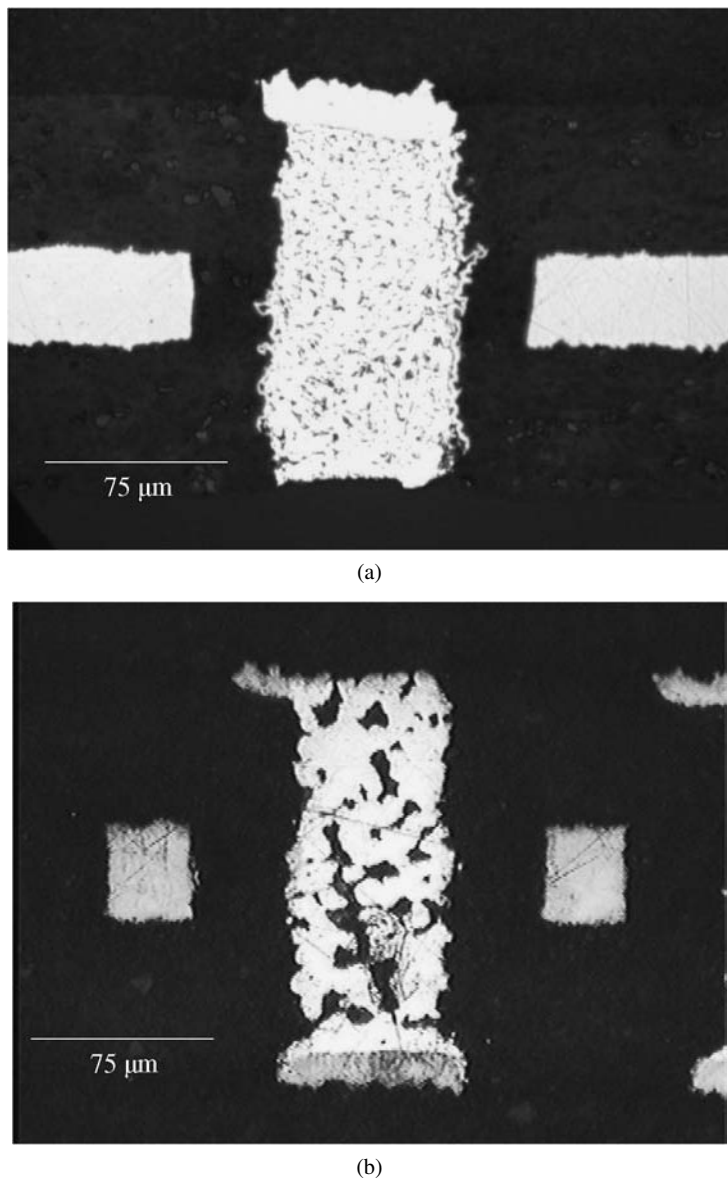


Figure 8. Optical photographs of cross-sections of ECAs with micro-scale silver flakes, laminated into a composite structure at (a) 200 and (b) 365°C. SEM micrographs of the same constructions laminated at (c) 200 and (d) 365°C.

a thin layer (<5 nm) of an organo-silane coupling agent, i.e., a material capable of bonding chemically with the aluminum oxide surface layer, and potentially bonding with the polymer binder in the adhesive. Organo-silanes can act as corrosion inhibitors of aluminum surfaces to stabilize electrical performance [31].

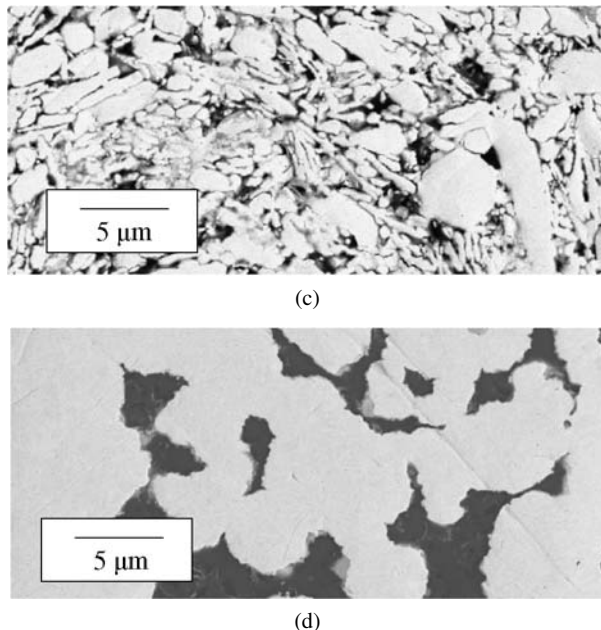


Figure 8. (Continued.)

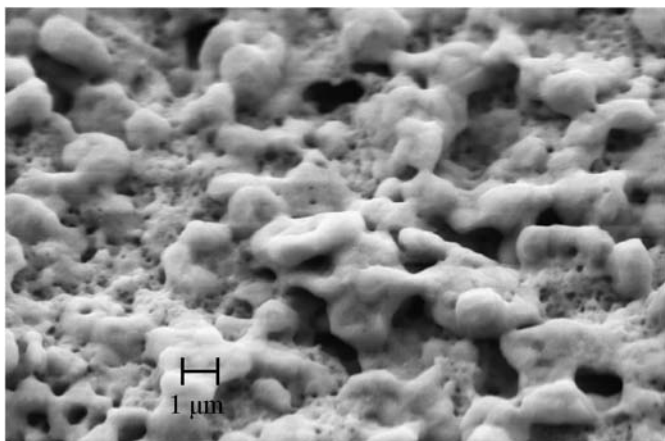


Figure 9. SEM micrograph of an ECA fabricated using a mixture of silver nanoparticles and microparticles and laminated at 275°C. Sintering is observed.

Matienco *et al.* [32] measured electrical resistance as a function of time in T&H environment (85°C and 80% relative humidity) for a silver–epoxy ECA on aluminum surfaces that were processed using three different treatments prior to bonding; (1) vapor blasting, (2) vapor blasting followed by application of a thin (<5 nm) layer of amino-terminated silane and (3) vapor blasting followed by application of a thin layer of an epoxy-terminated silane. Their results are shown in Fig. 10. Elec-

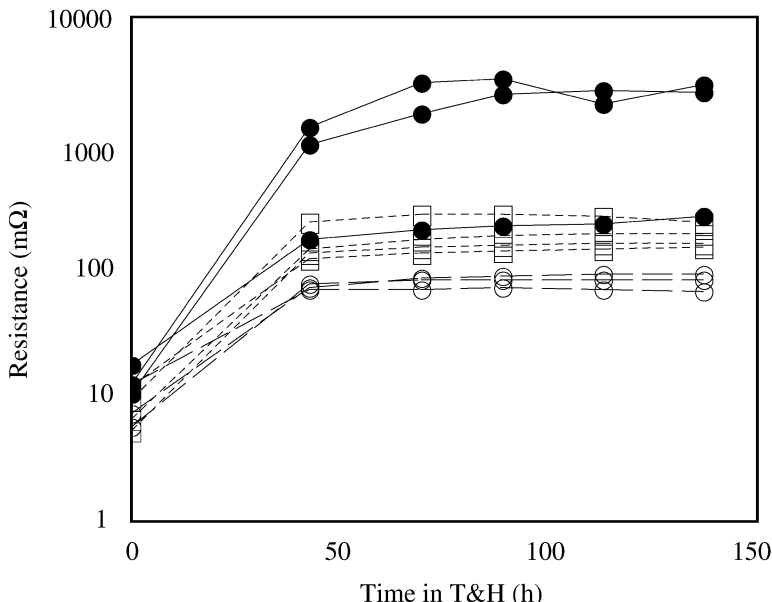


Figure 10. Resistance as a function of time in T&H (85°C and 80% relative humidity) for a silver-loaded, commercially-available conductive epoxy formulation and aluminum surfaces processed using three different treatments prior to bonding; (1) vapor blasting (●), (2) vapor blasting followed by application of a thin layer of A1100 amino-terminated silane (□) and (3) vapor blasting followed by application of a thin layer of Z6040 epoxy-terminated silane (○). For each treatment, a separate curve is shown for each of three individual samples. From Ref. [32]. Reproduced with permission from Springer, Germany.

trical stability of joints formed using the organo-silane-treated surfaces was better than that for the untreated surfaces, and the epoxy-terminated silane imparted better stability than the amino-terminated silane. This may be because the amino functionality has a propensity toward proton incorporation in solution to make a quaternary ammonium end group. This increases the surface pH which places the aluminum surface in its electrochemically active region, rendering aluminum less resistant to corrosion [33].

2.6.2. Stability of Joints as Multilayer Interconnects

For multilayer printed wiring applications, as described above, the need for high density wiring must be satisfied without compromising electrical, thermal and reliability performance. Adhesion between the ECA and the substrate to which it is mated is critical to the reliability of the electronic package. Surface finish of the metal to which an ECA is mated has a definite impact on the reliability of the joint at that interface. Careful preparation of the metal contact surfaces to which an ECA is mated is required to provide robust and reliable joints. Figure 11a shows a photograph of a cross-section taken from a laminate for which metal surfaces were not properly prepared to provide robust mating with a silver–epoxy ECA. Following exposure of this laminate to four thermal cycles that simulated solder reflow con-

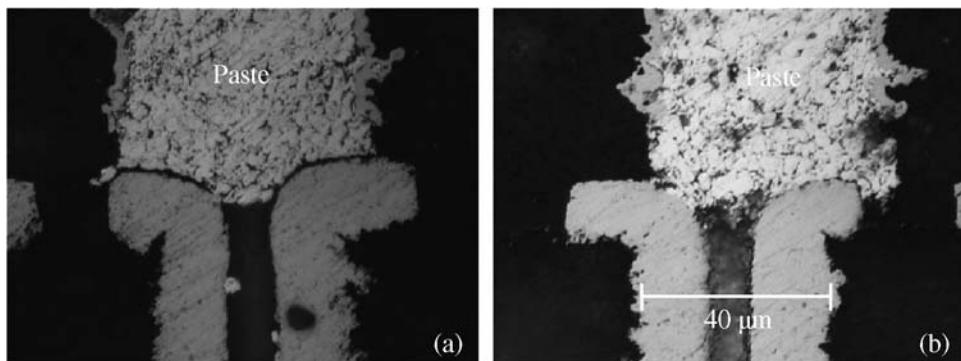


Figure 11. Photographs of cross-sections taken from temperature-cycled metal–paste joints for which the metal mating surfaces were untreated (a) and treated using a proprietary process (b).

Table 1.

Tensile strength and failure modes for a variety of ECA formulations. In all cases, silver filler particles were micro-size. Cohesive failures occurred within the ECA

ECA	Tensile strength (MPa)	Failure mode
LMP-modified Ag–epoxy	4.14	Cohesive
(Conducting polymer + LMP)-modified Ag–epoxy	12.4–13.8	Cohesive
Conducting polymer-modified Ag–epoxy	>26.2	Glue for fixturing ruptured
Ag–epoxy	23.3	Cohesive

ditions, the ECA separated from the opposing metal surface. Figure 11b illustrates the result, after similar thermal cycling, for metal surfaces that had been properly prepared. These joints are very robust.

2.6.3. ECA Formulation and Mechanical Strength

Although excess filler loading in ECAs can enhance their electrical performance, this condition can weaken their overall mechanical strength. Strength of adhesive joints formed using a variety of ECA formulations was evaluated using tensile strength measurements. Tensile strength was measured using an MTS tensile testing machine at a pull rate of 0.063 cm/min, and measuring until the joint ruptured. Micro-particle filled adhesives show high tensile strength with copper foils, resulting in cohesive failure within the ECA. Conducting polymer doped samples did not show any failure within the ECA. In this case, the glue used to attach laminates to test fixtures ruptured. This improvement in mechanical performance is likely due to the reduced metal particle loading in these samples. LMP-based ECA samples showed mechanical strength on the order of 4.14 MPa. Addition of conducting polymer to the LMP-based ECA enhanced the mechanical strength to a value of 12.4–13.8 MPa. Table 1 summarizes the tensile strength measurements for

these ECAs. Conducting polymer modified silver-filled ECA yielded the maximum mechanical strength. Based on the electrical properties of these ECAs, reported above, good mechanical strength can be obtained without compromising electrical performance.

3. Summary

A wide variety of ECA formulations are available for electronic packaging and assembly applications. The requirements that drive the use of a specific ECA are application-specific. For a given application, optimization of the electronic system can be achieved by altering the ECA formulation, control of processing conditions (e.g., lamination temperature and pressure), and treatment of surfaces to which the ECA is bonded. Judicious selection of materials, processing conditions, and treatments yields interconnections that can withstand the rigors of environmental stresses, e.g., temperature and humidity.

A variety of ECAs modified with nanoparticles, conducting polymer, and LMP particles were investigated and evaluated for these interconnection applications. ECA formulations with conducting polymer show good mechanical strength without compromising electrical conductivity. Incorporation of nanoparticles into ECAs reduces sintering temperature. LMP particles melt at low temperature and also reduce interparticle resistance.

The volume resistivity of ECAs decreases with increasing curing temperature. In addition, this may be attributed to a greater degree of sintering at elevated temperatures. ECAs have been shown to be useful even when processed at temperatures above those at which they are conventionally believed to degrade. Enhancement of electrical stability of ECA/metal joints has been demonstrated by use of several different treatments, prior to bonding, of the metal surface to which the ECA is mated.

Acknowledgements

The authors acknowledge the contributions of B. L. Pennington, S. Hurban, M. Shay, G. Kohut, D. Thorne and V. Markovich.

References

1. I. Artaki, D. Noctor, J. Mather, S. Schroeder, D. Napp, C. Desantis, W. Desaulnier, L. Tsung-Yu Pan Felton, M. Palmer, J. Rosser, J. Felty, P. Vianco, J. Greaves, G. Whitten, Y. Zhu and C. A. Handwerker, in: *Proceedings of EcoDesign'99: First International Symposium*, Tokyo, Japan, pp. 602–605 (1999).
2. Y. Li and C. P. Wong, *Mater. Sci. Eng. R* **15**, 1 (2006).
3. J. Liu, R. Rorgren and L. Ljungkrona, *J. Surface Mount Technol.* **8**, 30 (1995).
4. L. Ye, Z. Lai, J. Liu and A. Tholen, *IEEE Trans. Electron. Packag. Manuf.* **22**, 299 (1999).
5. K. Yasuda, J. M. Kim, M. Rito and K. Fujimoto, in: *Proc. Int. Conf. on Electronic Packaging*, Maui, HI, pp. 149–154 (2003).

6. K. Yasuda, J. M. Kim, M. Yasuda and K. Fujimoto, in: *Proc. Int. Conf. on Solid State Devices and Materials*, Tokyo, Japan, pp. 390–391 (2003).
7. K. Yasuda, J. M. Kim and K. Fujimoto, in: *Proc. 3rd Int. IEEE Conf. on Polymers and Adhesives in Microelectronics and Photonics*, Montreux, Switzerland, pp. 5–10 (2003).
8. Q. Yao and J. Qu, *J. Electron. Packag.* **124**, 127 (2002).
9. J. Xiao and D. D. L. Chung, *J. Electronic Mater.* **34**, 625 (2005).
10. W. J. Jeong, H. Nishikawa, H. Gotoh and T. Takemoto, *Metall. Mater. Trans. A* **46**, 704 (2005).
11. W. J. Jeong, H. Nishikawa, D. Itou and T. Takemoto, *Metall. Mater. Trans. A* **46**, 2276 (2005).
12. H. H. Lee, K. S. Chou and Z. W. Shih, *Intl. J. Adhesion Adhesives* **25**, 437 (2005).
13. C. F. Goh, H. Yu, S. S. Yong, S. G. Mhaisalkar, F. Y. Boey and P. S. Teo, *Thin Solid Films* **504**, 416 (2006).
14. M. Inoue and K. Suganuma, *Soldering Surface Mount Technol.* **18**, 40 (2006).
15. Y. Fu, M. Willander and J. Liu, *J. Electronic Mater.* **30**, 866 (2001).
16. E. Sancaktar and N. Dilsiz, *J. Adhesion Sci. Technol.* **13**, 679 (1999).
17. H. J. Jiang, K. S. Moon, J. X. Lu and C. P. Wong, *J. Electronic Mater.* **34**, 1432 (2005).
18. R. L. Keusseyan, B. S. Speck and J. L. Dilday, *Intl. J. Microcircuits Electronic Packaging* **17**, 236 (1994).
19. O. Boyle, D. C. Whalley and D. J. Williams, in: *Proceedings of 9th ISHM European Hybrid Microelectronics Conference*, Nice, France, pp. 75–82 (1993).
20. F. D. Egitto, S. R. Krasniak, K. J. Blackwell and S. G. Rosser, in: *Proc. IEEE 55th Electronic Components and Technology Conference*, Lake Buena Vista, FL, pp. 1132–1138 (2005).
21. M. A. Gaynes, L. J. Matienzo, J. A. Zimmerman and D. C. Van Hart, *Mater. Res. Soc. Symp. Proc.* **445**, 139 (1997).
22. D. M. Sarno, S. Prasad, L. J. Matienzo and W. E. Jones Jr, *Mater. Res. Soc. Symp. Proc.* **734**, 181 (2003).
23. Y. Li, K. S. Moon and C. P. Wong, *J. Electronic Mater.* **34**, 1573 (2005).
24. M. Angelopoulos, A. Ray, A. G. MacDiarmid and A. J. Epstein, *Synth. Metals* **21**, 21 (1987).
25. M. Angelopoulos, G. E. Asturias, S. P. Ermer, A. Ray, E. M. Scherr and A. G. MacDiarmid, *Mol. Cryst. Liq. Cryst.* **160**, 151 (1988).
26. K. T. Tzou and R. V. Gregory, *Synth. Metals* **69**, 109 (1995).
27. A. G. MacDiarmid, J. C. Chiang, A. F. Richter, N. L. D. Somasiri and A. J. Epstein, in: *Conducting Polymers*, L. Alcacer (Ed.), pp. 105–120. Reidel, Dordrecht (1985).
28. P. Pramanik and R. N. Das, *Mater. Sci. Eng. A* **304**, 775 (2001).
29. R. N. Das, K. I. Papathomas, J. M. Lauffer and F. D. Egitto, in: *Proc. IEEE 57th Electronic Components and Technology Conference*, Reno, NV, pp. 74–81 (2007).
30. J. D. Venables, D. K. McNamara, J. M. Chen and T. S. Sun, *Appl. Surface Sci.* **3**, 88 (1979).
31. L. J. Matienzo, D. K. Shaffer, W. C. Moshier and G. D. Davis, *J. Mater. Sci.* **21** 1601 (1986).
32. L. J. Matienzo, F. D. Egitto and P. E. Logan, *J. Mater. Sci.* **38**, 4831 (2003).
33. M. Pourbaix, *Atlas of Electrochemical Equilibria in Aqueous Solutions*. NACE, Houston, TX (1974).

This page intentionally left blank

Anisotropic Conductive Adhesives for Flip-Chip Interconnects

Weiqiang Wang^a, Y. C. Chan^b and Michael Pecht^{a,*}

^a Center for Advanced Life Cycle Engineering (CALCE), University of Maryland, College Park, MD 20742, USA

^b Department of Electronic Engineering, City University of Hong Kong, Tat Chee Avenue, Kowloon Tong, Hong Kong

Abstract

Anisotropic conductive adhesive films consist of an epoxy adhesive with dispersed conductive particles. They are used as electrical–mechanical interconnecting materials for flip-chip to flexible substrates and flip-chip to glass substrates. Contact resistance and adhesion strength are two important features of anisotropic conductive adhesive film joints. Contact resistance is affected by the curing degree of the adhesive, the bump characteristics, the reflow process and the environmental application conditions. Adhesion strength is affected by bonding temperature, bonding pressure, bubbles in the joints and particle characteristics. To assess reliability, anisotropic conductive adhesive film joints were tested under thermal cycling tests, autoclave tests and mechanical shock tests.

Keywords

ACF, flip-chip, reliability test

1. Introduction

Flip-chip technology has emerged as a high-density, high-performance interconnection method. A revolutionary technology to attach flip-chip devices without solder bumps or balls and underfill uses anisotropic conductive adhesive films (ACFs). Conductive adhesives avoid the toxicity and environmental concerns of lead and chlorofluorocarbon-based flux cleaners, but also have technological advantages over tin–lead (Sn/Pb)-based solder interconnects: (1) the lower curing temperature required for the adhesive reduces joint fatigue and stress cracking problems, enabling the use of heat-sensitive or non-solderable materials; (2) fewer processing steps enable an increase in production throughput; (3) the higher flexibility and the closer match in the coefficient of thermal expansion (CTE) enable a more compliant

* To whom correspondence should be addressed. Tel.: (01)301-405-5323; Fax: (01)301-314-9269; e-mail: pecht@calce.umd.edu

connection, while minimizing failures and (4) the smaller filler particle size facilitates finer line resolution [1]. Anisotropic conductive adhesives can also provide short electrical paths, good horizontal gap insulation, low joint stress and sufficient mechanical adhesion. Moreover, no cleaning/flux is required, secondary underfill is not necessary, and placement of the anisotropic conductive adhesives is not critical.

2. ACF Bonding Process

ACF consists of an epoxy adhesive and the conductive particles (3–10% volume fraction) dispersed in an adhesive matrix. The specifications of a typical commercial ACF are shown in Table 1. The bonding process for the ACF interconnection involves the simultaneous application of heat and pressure. During the bonding process, the adhesive resin is squeezed out and the conductive particles are trapped between the bump of the chip and the pad of the substrate. Due to the applied pressure, conductive particles are deformed between the bump and the pad as shown in Fig. 1.

In order to remove any organic contaminant that might have an adverse effect on the ACF interconnection, substrates must be carefully washed using an organic

Table 1.
Specifications of a typical commercial ACF

Property	
Thickness (μm)	7–74
Conductive particle type	Resin + Ni/Au plating, Cu plating, Ag plating or Al plating
Particle diameter (μm)	0.5–30
Insulation coating on particle surface	Yes

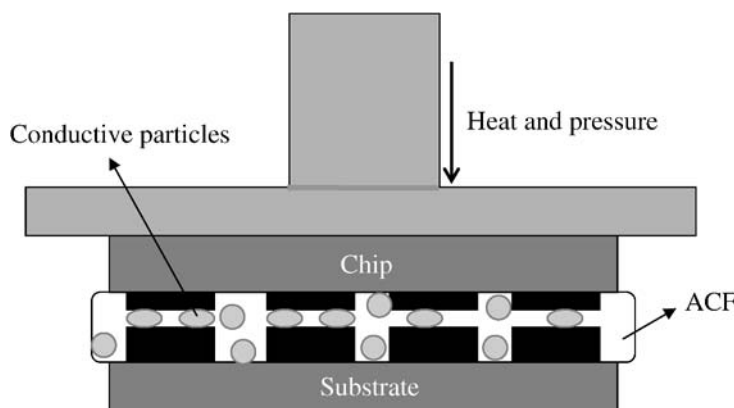


Figure 1. Schematic diagram showing bonding using ACF.

solvent before bonding. The ACF is cut to the correct size in order to cover the area for bonding. Pre-bonding is performed at a low pressure and low temperature. The final bonding is conducted at a high pressure and high temperature. The substrate pads and the chip bumps are aligned in order to obtain high-precision bonding. Finally, the chip is bonded onto the substrate by applying heat and pressure.

As integrated circuits get smaller and advanced materials are used, contaminant-free active surfaces are crucial in order to obtain high-yield, reliable products. A specific challenge for flip-chip bonding by ACF is the poor bond strength with the flex caused by surface contamination and the delamination of the chip and/or ACF by contaminants from the flex. Contaminants that degrade adhesion include organic or oxide layers. These impurities must be thoroughly removed before the bonding process is started. The surface finish or surface treatment of the flex must enable good adhesion. An efficient and cost-effective method of preparing the substrate materials prior to bonding is plasma etching [2].

Since pressure is applied to “force” the conductive particles to make contact between the flip-chip and the flexible substrate, the degree of deformation of the conductive particles can affect the performance of ACF interconnects. Ideally, the conductive particles should be pressed until just before the metallic layers begin to break. At this point, the contact area between the bonding surfaces is the largest. However, if the pressure is too high, the particles will spread out between adjacent bumps or pads and end up contacting each other, creating a short circuit. If the bonding pressure is too low, the particles may not be able to make contact between the connecting bumps and pads [3]. The required pressure is, therefore, dependent on the bump co-planarity. This has been studied using nonlinear finite element models, as well as with simple semi-analytical models for non-conductive adhesives [4, 5].

Conventionally, thermal heating is used to initiate and carry out curing. Thermal curing during die bonding is costly, which means it is always desirable to find an alternative curing process in ACF technology. An alternative to thermal curing is to use microwave radiation [6]. The alternating electrical field of a microwave causes re-orientation of the long-chain molecules of polymers. This results in friction among molecules, which converts the microwave energy into thermal heat [7, 8]. High heating and a uniform temperature distribution can be easily obtained because all molecules are heated simultaneously without the requirement of thermal conduction.

A microwave-activated bonding process can be used to reduce the final bonding temperature. To study the effect of microwave preheating on the bonding performance, samples were preheated at 80 and 240 W for 2 or 3 s, and then finally bonded at 150, 160 and 170°C and 60 N load for ten seconds. It was found that this method could reduce the maximum curing temperature by 10–170°C if microwave preheating of the ACF was used for 2–3 s prior to final bonding. When high bond strength was not required, 160°C curing could also be used as the final bonding temperature after microwave preheating of the ACF for two seconds at very low power (80 W). The benefits of reducing the final bonding temperature up to 10–20°C are

reductions in the operation cost and processing time. As an example, the contact resistance for samples bonded at 170°C with a microwave preheating of ACF was 0.015 Ω (microwave: 3 s at 80 W), which was even lower than for the samples bonded at 180°C without any microwave preheating. The shear force measured at breakage in the die shear test was found to be 176.8 N maximum, which was higher than that of ACF joints bonded at 180°C without any microwave preheating (173.3 N). Optical microscopy investigation of this joint revealed a low concentration of air bubbles, which is beneficial for creating high bond strength. The samples bonded at 160°C with a preheating time of two seconds also showed low contact resistance (0.022–0.032 Ω), which was very close to that of ACF joints bonded at 180°C without any microwave preheating (0.017 Ω). But the bond strength was not satisfactory due to the considerable amount of air bubble entrapment.

3. Contact Resistance of ACF Joints

Electrical conduction in ACF interconnections is restricted to the z (out-of-plane) direction, while electrical insulation in the x – y plane is maintained. When an electronic assembly is subjected to temperature changes, thermal stresses develop in the assembly [9]. The stresses generated due to the CTE mismatch of the materials may lead to warpage [10] in the assembly. The thermally-induced warpage directly affects the interconnection between the chip and the substrate, causing poor integrity in the assembly [11]. During thermally-induced warpage, the conductive particles in the ACF, which provide the actual interconnection path, experience different types of stresses. These stresses can delaminate the chip bump from the substrate pad. As a result, the contact areas between the conductive particles and the bumps and between the conductive particles and the pads decrease and the contact resistance increases.

3.1. Contact Resistance Monitoring

The contact resistance of the flip-chip on a flexible or glass substrate (FCOF or FCOG) can be measured using the four-point probe method. This method is conducted by driving an electrical current through two of the connections, while monitoring the corresponding electrical potential at the other two connections, as shown in Fig. 2.

In one case, the first three bumps of the chip were interconnected in each set of five bumps. Electrical current was passed through bumps 1 and 4 and the corresponding output voltage was measured between bumps 2 and 3. The initial contact resistance was measured by passing 1–5 mA of DC current (I) to obtain the corresponding output voltage (V) using a FLUKE multimeter. The contact resistance (R) was then calculated using Ohm's Law. Connections between the multimeter and bumps for the contact resistance measurement were through heat resistance wires that were soldered to the output terminals of the bumps.

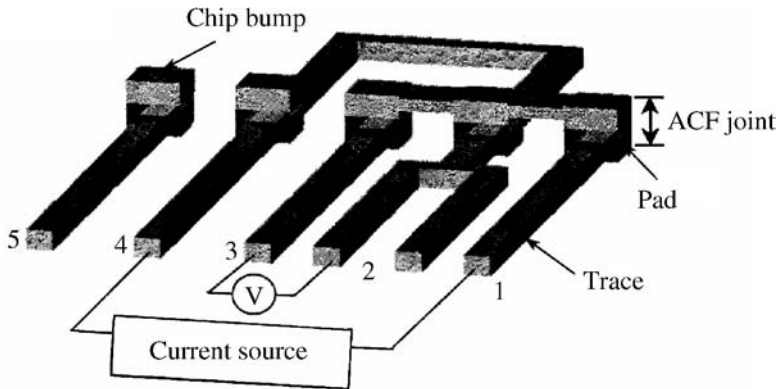


Figure 2. Schematic diagram of circuitry to measure the contact resistance using the four-point method.

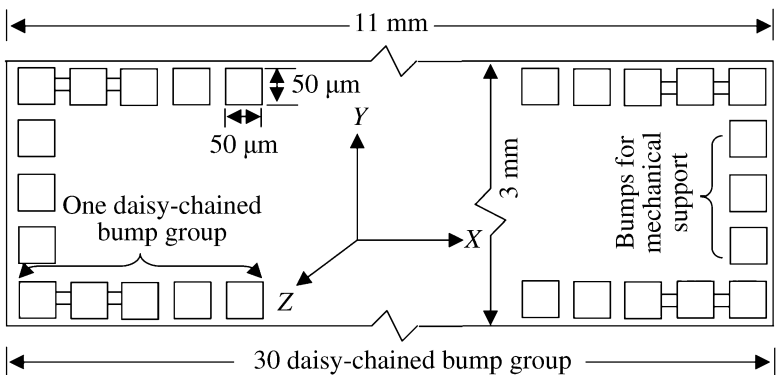


Figure 3. Schematic diagram of a test chip, showing groups of daisy-chained bumps.

Usually, test chips use the design shown in Fig. 3. Sixty sets of bumps are daisy-chained. These groups of bumps run parallel along both of the long sides of the chip for electrical connection.

3.2. Effect of Temperature on Contact Resistance

Contact resistance of ACF joints is affected by temperature. Thus, tests are necessary to study the effect of temperature variation on the contact resistance. For example, an FCOF assembly was placed in a thermal chamber, and the contact resistance was measured as a function of temperature from 30 to 150°C. At each measurement temperature, the sample was held for three hours to allow equilibrium to be reached. The contact resistance was also measured before and after high-temperature exposure. The contact resistance of ACF joints changed with the environmental temperature. The contact resistance increased with an increase of environmental temperature, as shown in Fig. 4.

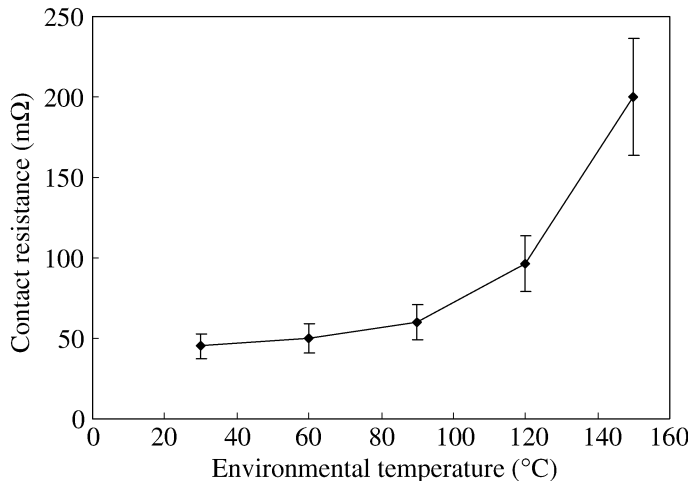


Figure 4. Average contact resistance measured at different environmental temperatures.

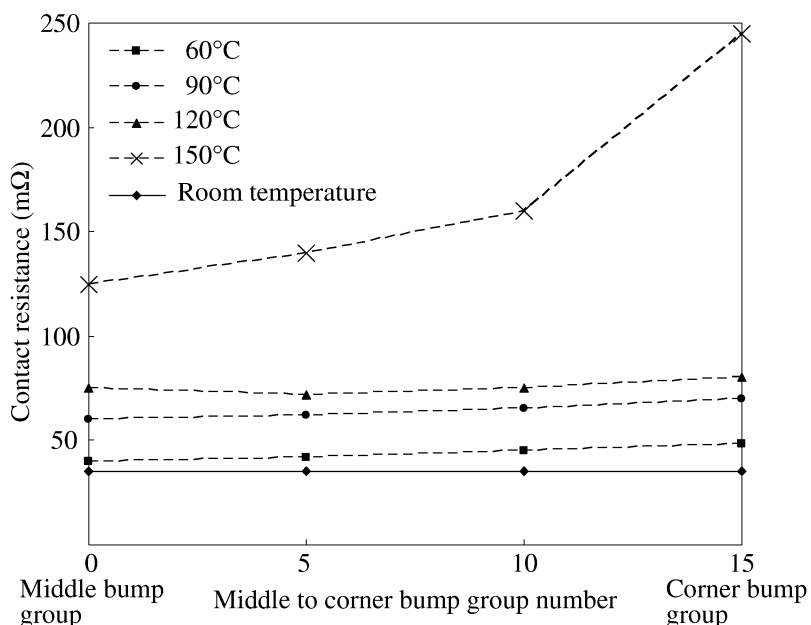


Figure 5. Contact resistance measured at different environmental temperatures for different interconnect positions.

The contact resistance increased from the middle to the corner of the package at high temperature, as shown in Fig. 5. The middle bumps of the chip experienced only the stress developed in the z direction, while the corner bumps experienced stress developed in all directions; therefore, the greatest cumulative stresses were

generated at the corner side of the interconnections. An ACF with a low CTE and high T_g value is essential to make the contact resistance stable.

3.3. Effect of Curing Degree of Adhesive on Contact Resistance

The physical, electrical and mechanical properties of the cured conductive adhesives depend, to a large extent, on the degree of curing of the epoxy composition of the conductive adhesive. Successful bonding involves the selection of proper parameters, during which chemical reactions proceed to completion. The curing degree of adhesives affects the contact resistance of ACF joints in terms of the microstructure.

Based on the assumption that the exothermic heat evolved during the cure is directly proportional to the extent of cure, the curing degree, α , can be expressed as:

$$\alpha = \frac{Q_T - Q_R}{Q_T}, \quad (1)$$

where Q_T is the total exothermic heat of the raw material and Q_R is the residual or exothermic heat of the previously cured material. These were measured with dynamic differential scanning calorimeter (DSC) scans of the uncured and cured samples at different temperatures. The curing degree of ACF for different bonding temperatures is shown in Fig. 6. During the bonding process, the temperature was maintained to increase the fluidity of the ACF and then to quickly cure while maintaining constant pressure on the chip [12]. In this thermal process of the epoxy-based adhesive, higher temperature initiated and accelerated the cross-linking reaction by providing higher energy. Therefore, the curing degree of the ACF also increased with the increase in curing temperature.

Figure 7 shows that the contact resistance of FCOF assemblies decreases with the increase in bonding temperature up to 210°C and then increases when the bonding temperature is above 210°C. FCOF packages assembled at 210°C show the lowest contact resistance compared to those assembled at other temperatures.

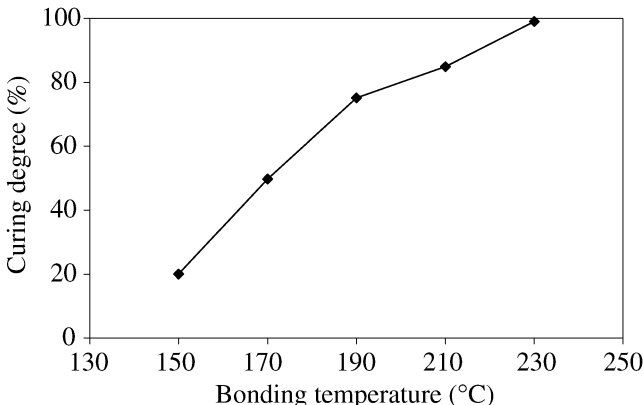


Figure 6. Curing degree at different bonding temperatures [13].

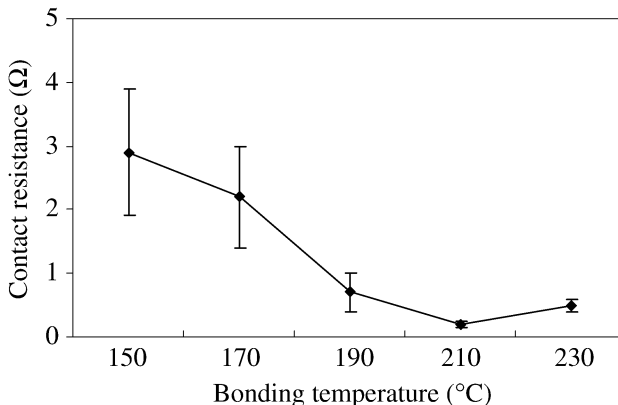


Figure 7. Contact resistance of FCOF assemblies at different bonding temperatures [13].

During the early stage of the bonding process, the ACF becomes soft and rubbery, which allows the conductive particles to move within the ACF. When the curing process is complete, the ACF becomes hardened and the mobility of the conductive particles is lost. Higher bonding temperature results in higher curing, and the ACF becomes stiffer with a higher modulus. After the bonding process, the conductive particles recoil slightly to create more contact areas with pads for highly cured ACF. Thus the higher contact area of the deformed particles to the pads remains stable and the contact resistance is relatively low.

3.4. Effects of Bump Characteristics on Contact Resistance

Two types of bumps were used to test the effect of bump height on contact resistance: gold/nickel (Au/Ni), which is a 4 μm -thick nickel bump with gold coating, and a 1 μm -thick aluminum pad [14]. After bonding, the online contact resistance is measured for different thermal cycling profiles (-55 to 125°C , -40 to 150°C and -65 to 150°C). The initial contact resistance of the Au/Ni bump chips is usually found to be less than that of the bumpless chip, but the increase of online contact resistance during thermal shock is higher in the Au/Ni bump chips than in the bumpless chips. It is clear that the chip with high bump height could suffer a maximum increase in contact resistance during thermal shock. During thermal cycling, the online contact resistance increase is higher in the Au/Ni bump. During thermal warpage, the bump height is typically high in the Au/Ni bump, which suggests the probability that the conductive particles will escape when the joint is high or when bending occurs. In that case, the chip bump and substrate pad tend to move in opposite directions, causing a failure. The failure rate is higher when the height of the interconnections is higher.

It has been observed that after a certain number of thermal cycles, there can be an abrupt change in the online contact resistance. The time/cycle taken for such a change can be termed as the “incubation time/cycle”. After such an incubation period, the ACF joint loses its reliability. It is proposed that during the incubation

period, a critical transition occurs in the ACF joints and the ACF fails to hold bumps and pad at their original positions.

3.5. Effect of Reflow Process on Contact Resistance

Reflow soldering processes, such as vapor phase soldering and infrared soldering, have become the common method for mounting integrated circuit packages. In these soldering processes, the package needs to be heated to above 200°C, which is much higher than the final bonding temperature of the ACF interconnection. The ability of an ACF to withstand multiple solder reflows is a major milestone in its growing acceptance by the semiconductor packaging industry.

The effect of the reflow process on the contact resistance of ACF joints has been studied [15]. In one series of tests, FCOF assemblies were fixed on FR4 substrate and passed through the reflow oven. The reflow profiles were defined in advance using a thermocouple, according to the specifications of lead-tin solder paste and lead-free solder paste. Three different reflow profiles were used with different peak temperatures — 210, 230 and 260°C. The samples were placed into the reflow oven directly without any protection. The test results of contact resistance are summarized in Table 2. When the peak temperature was 210°C, no open joints were found and the contact resistance was increased by 23 mΩ. When the peak temperature was 230°C, only 5% of the joints were open, and the contact resistance variation increased to 29 mΩ. When the peak temperature was 260°C, nearly 40 open joints were found, and the contact resistance was increased by 60 mΩ.

Conductive particles deformed very well and had good contact with conductive metallization surfaces before reflow, as shown in Fig. 8. Although no conduction gap was found after the reflow process with peak temperatures of 210 and 230°C, the contact area between the particles and conductive metallization surfaces decreased to some degree. This should be the main reason that contact resistance increased after reflow. The formation of a conduction gap was obvious after the reflow process with a peak temperature of 260°C, as indicated by the arrow in Fig. 8.

The apparent CTE mismatch between the polymer particles and the epoxy resin matrix seemed to be the major reason for the contact resistance change. Finite element analysis showed that the highest stress occurred at the interface between the

Table 2.

Contact resistance under different reflow profiles with different peak temperatures

Profile No.	Peak temperature (°C)	Time above melting point (s)	No. of test joints	Electrical resistance (mΩ), mean value (standard deviation)		No. of open joints
				Before reflow	After reflow	
1	210	60	53	124 (24)	147 (31)	0
2	230	60	36	126 (28)	155 (41)	2
3	260	60	48	123 (26)	183 (55)	16

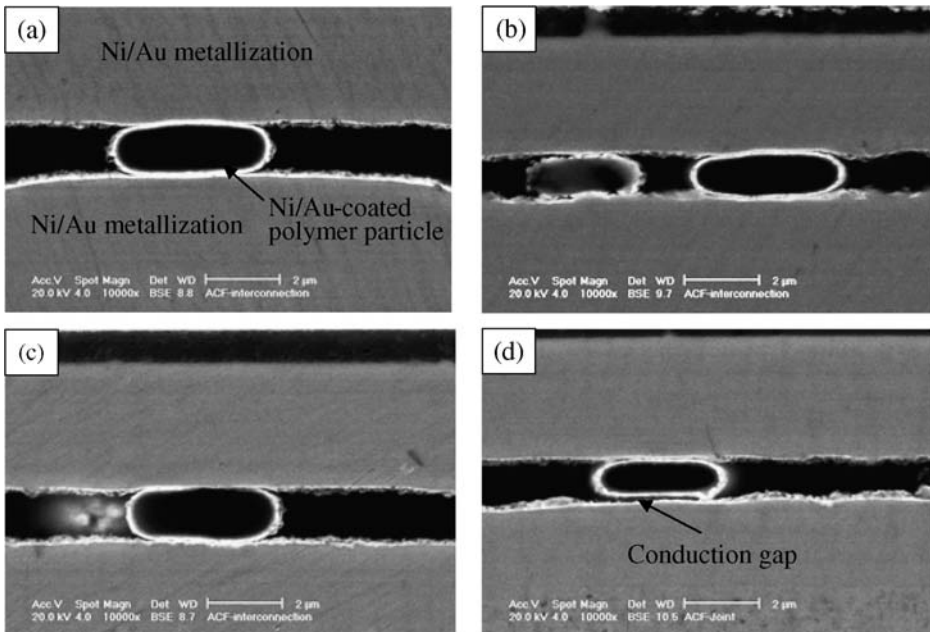


Figure 8. SEM images showing the ACF interconnection through conductive particles (a) as-bonded at 200°C, 80 N, 10 s and after reflow with peak temperature at (b) 210°C, (c) 230°C and (d) 260°C [15].

polymer particle and the epoxy resin matrix during the reflow process [16]. The CTE mismatch caused the loss of contact area during the reflow process, which would cause a contact resistance increase or even open joints. The polystyrene used in the conductive particles was claimed to be stable up to 250°C but began to degrade rapidly above that temperature [17]. The chemical structure scissoring in the polystyrene caused it to soften and changed its physical properties. The thermal gravimetric analysis showed that although the maximum decomposition rate of epoxy used in the ACF was found to occur at over 400°C, some initial decomposition already occurred between 200 and 300°C [18]. All these changes contributed to the contact resistance change in the ACF solder joints during the reflow process.

A reliability test was conducted at 85°C and 85% relative humidity for 500 h to study the effect of the reflow process with a 210°C peak temperature on the reliability of ACF joints with two different bump metallizations, Au and Au/Ni. It was found that the ACF joints with gold bumps were more sensitive to the reflow process and exhibited more than 100% increase in contact resistance after the reflow process. However, when the Au/Ni bump chip was used, the contact resistance increased about 20% during the reflow process and exhibited better performance than the original ACF joints during the reliability test. The reason for the difference between the two metallizations was the higher height of the gold bump than the Au/Ni bump.

4. Adhesion Strength of ACF Joints

Adhesion strength is a critical parameter of fine-pitch ACF interconnects, which are vulnerable to shocks encountered during assembly, handling and service life. Various factors, including bonding temperature, bonding pressure, air bubbles and particle characteristics, affect the adhesion strength. Two different types of commercial ACFs (ACF1 for FCOG and ACF2 for FCOF) were used to study the effects of these parameters on the adhesion strength. ACF1 is $35 \pm 5 \mu\text{m}$ thick with Ni/Au-plated resin particles with a diameter of $3.5 \mu\text{m}$. ACF2 is $30 \mu\text{m}$ thick with gold-plated resin particles with a diameter of $3.5 \mu\text{m}$.

A dynamic impact test was designed to study the adhesion strength of the ACF joints. The test equipment was an air-cylinder-driven instrument, as shown in Fig. 9. The substrate was fixed to a sensor gauge for recording, and the chip was clamped with a rigid head to apply the load. When the compressed air in the cavity of the cylinder was released through the air pipe, the piston (valve stem) drew back quickly, providing rapid loading and causing stress between chip and substrate. The average speed of the piston was about 0.1 m/s . Six samples for each condition were tested to obtain an average and the extent of deviation of the impact strength values for FCOG and FCOF.

4.1. Effect of Bonding Temperature on Adhesion

Under a bonding pressure of 60 MPa , the impact load required to debond for both of the packages rose with the bonding temperature up to 190°C , and then decreased. Impact test results on different ACFs showed a similar trend for both FCOF and FCOG, which indicated that bonding temperature had a major effect on adhesion strength. The increase in bonding temperature increased the curing degree of the adhesive, which increased the adhesion strength. However, using a very high temperature (230°C) in the bonding process decreased the impact strength of the ACF joints.

4.2. Effect of Bonding Pressure on Adhesion

It was found that the adhesion strength increased only very slightly as the bonding pressure increased. Pressure changed the thickness of the ACF between the bump (of the chip) and the pad (of the substrate), which was limited by the extent of the deformation of the conductive particles. The thickness of ACF materials between

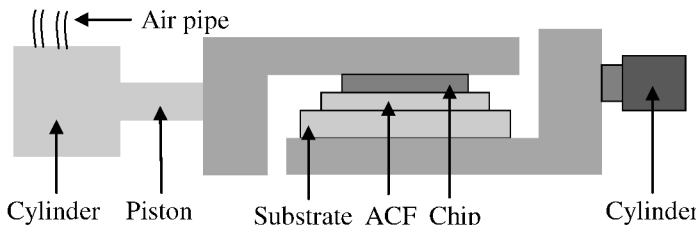


Figure 9. Schematic diagram of dynamic impact test [19].

the chip and the substrate remained more or less the same, because the thickness depended on the sum of the height of the bump, the deformed particle and the pad.

Although pressure is not important with respect to adhesion, it is necessary for reliable bonding. First, adequate pressure was applied to assure intimate intermolecular contact between adhesive and adherend (chip and substrate) so that van der Waals interaction, electrostatic interaction, and other bonds at the interface could take place. Then suitable deformation of the particles was needed to obtain sufficient contact between the input/output of the chip (i.e., the bump) and the pad of the substrate to maintain stable electrical conduction between the particles and the conductors. Too high a pressure causes excessive deformation of the core of the particles and can crack the Au/Ni layer of the particles, which is not desirable from the point of view of electrical conduction.

4.3. Effect of Air Bubbles on Adhesion

An air bubble entrapped at the adhesive/adherend interface can degrade the adhesion. Air bubbles and voids generally exist in an ACF and at the ACF/substrate interface, as shown in Fig. 10. This phenomenon can be explained by looking at the bonding process. During prebonding of the ACF on the substrate, some air is entrapped at the corner of the pads and conductors at the ACF/substrate interface. During chip bonding, the ACF becomes a thick liquid, then flows between the pads and between the bumps. The ACF near the chip becomes viscous and cures earlier than that near the substrate, so air bubbles that are entrapped during the ACF lamination process cannot escape. If ACFs are cured too quickly at much higher temperatures, more air bubbles remain. This kind of defect reduces the contact area and provides a stress propagation path for a crack, resulting in premature delamination along the ACF/substrate interface under low force.

4.4. Effects of Particle Characteristics on Adhesion

Typically, 5–15% volume fraction of the ACF consists of metal-coated spherical particles with diameters ranging from 3 to 10 μm . They change the electrical, thermal and mechanical properties of the ACF material. Specifically, they reduce the

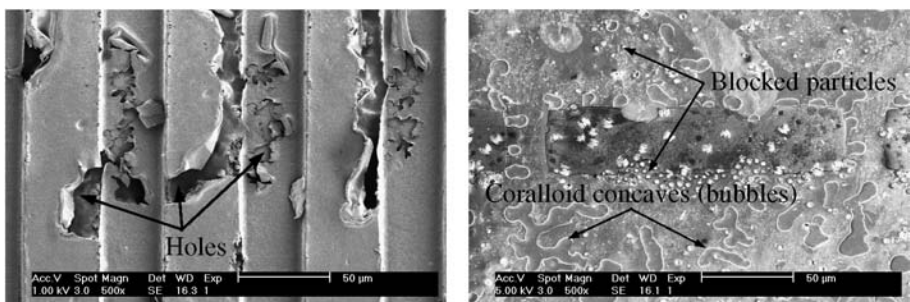


Figure 10. (a) Air bubbles and voids in the adhesive in FCOF (chip side) and (b) air bubbles at the ACF/substrate interface in FCOG (chip side) [19].

CTE, increase the elastic modulus, increase the brittleness, and increase the T_g [20]. In the ACF matrix, random dispersion of particles introduces asymmetry and discontinuity in the whole material. The particles act as voids to weaken the material's impact resistance. Thus, the adhesion is influenced by the particle size and distribution in the ACF. There are gaps between the particles and the polymer, which makes the particles loose and moveable under external loading. Many reasons contribute to this kind of separation. First, when bonding pressure is applied, the particles between bump and pad are compressed into an elliptical shape. However, after the pressure is released, the elastic recovery leaves interspaces between the particles and the cured polymer. Second, due to the CTE mismatch among the particle core, the coating, and the ACF matrix, different expansion and shrinkage during the curing process produces gaps between the coating and the ACF matrix, as well as between the core and the coating. The higher the bonding temperature, the larger is the gap between the particle and the adhesive matrix. Third, poor adhesion between the coating and the polymer core is responsible for interface detachment when the material is subjected to mechanical force.

5. Reliability Test of ACF Joints

Although the ACF technology for flip-chip seems to be a breakthrough in fine-pitch interconnections, the ACF interconnections also have some problems that jeopardize the reliability of the packages. As already noted, voids trapped inside the epoxy matrix during the bonding process affect the reliability performance of ACF interconnections. As the material of the chip, the substrate, and the ACF have different CTEs, there is always the problem of stress formation due to CTE mismatches in the assembly during manufacturing and curing. Due to the mismatch of CTEs of different materials, warpage can be induced during life operation, which can affect the conductive resistance of the interconnection [20]. The moisture absorption of ACFs contributes to the thermal stress and raises the susceptibility of packages to popcorn cracking [21]. The galvanic corrosion process can also cause failure in the presence of moisture and non-noble metal interfaces.

5.1. Online Contact Resistance of ACF Joints During Thermal Cycling Test

Many unbalanced stresses in the assembly can decouple the chip bump and substrate pad. To assess this, a FCOF package bonded with a 35 μm ACF was tested under temperature cycling. The chip had 368 Al (2 μm) pads — the same design as that shown in Fig. 3. The metal pads on flexible film consisted of Au (0.5 μm)/Ni (4.0 μm)/Cu (12 μm). The conductive particles were Ni/Au-plated with a diameter of 3.5 μm . The package was prebonded at 100°C with a pressure of 0.3 MPa for seven seconds and finally bonded at 180°C with a pressure of 80 N for 15 s. Three temperature cycling profiles were used for the tests, as shown in Table 3. The high extreme temperature of profile No. 2 (125°C) is below the T_g of the ACF matrix (131°C), while the other two are above the T_g .

Table 3.

Details of temperature cycling profiles used in the experiment

Profile No.	High temperature (°C)	Low temperature (°C)	Dwell time (min)	Time for interchange (min)
1	140	-40	30	5
2	125	-55	15	2
3	150	-65	15	3

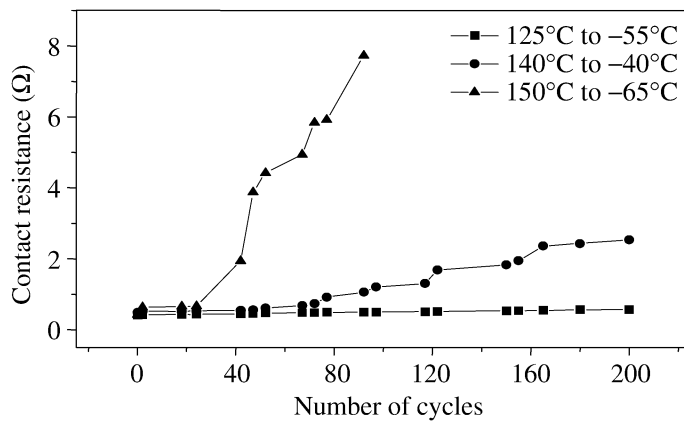


Figure 11. Variation of online contact resistance with number of cycles for 3 different high temperature cycling profiles (corner joints).

The online contact resistance was measured for ACF joints at the four corners as well as in the middle of the chip. Before temperature cycling, the contact resistance was around $0.4\ \Omega$. It was found that for the temperature cycling profiles with high temperatures above the T_g , the ACF expanded, lost its rigidity, and thus became vulnerable to the shear force generated by thermal stresses. Results showed that for the temperature cycling condition 150 to -65°C , the online contact resistance increased to the maximum of $8.2\ \Omega$ in 100 cycles, as shown in Fig. 11, whereas for the temperature cycling profile 125 to -55°C , the online contact resistance increased to only $1\ \Omega$ in 500 cycles. It was also clear that the online contact resistance was lower for the temperature cycling profile of 125 to -55°C than for the other two temperature cycling profiles. Below the T_g , the ACF was stiff enough to hold the interconnection firmly, even at corner positions. However, as 125°C is close to the T_g , viscoelastic deformation in the ACF matrix occurred due to the stress generated by the thermal mismatch between the chip and the flexible substrate. Thus contact resistance increased, although it was very low compared to other thermal conditions above the T_g .

It was found that the chip bump and substrate pad moved in opposite directions, causing the conductive particles to move and/or damage easily. The incubation time

was also found to occur earlier for temperature cycling conditions above the T_g . Incubation time occurred at around 40 cycles for the temperature cycling condition 150 to -65°C and 120 cycles for the temperature cycling profile 140 to -40°C , whereas there was no incubation time noticed for the temperature cycling profiles of 125 to -55°C . The ACF joint lost its rigidity and online contact resistance increased sharply after the incubation time. There were many open joints identified after temperature cycling.

From the cross-sectional microstructures shown in Fig. 12, it is clear that conductive particles deformed to different extents with the Al pad and the Au/Ni/Cu pad. In the as-bonded sample, there was a gap between the bump and the pad, as shown in Fig. 12(a), and the conductive particles had good contact between the two pads, as in Fig. 12(b). However, the gap between the bump and the pad was filled due to oxidation during temperature cycling, as shown in Fig. 12(c), and the conductive particle lost contact with the bump, as in Fig. 12(d). The oxidation layer, formed due to prolonged thermal exposure, limited the chip Al pad and substrate pad from moving away from each other when shear stress was generated due to warpage in the assembly. This effect decreased with the increase in contact resistance in bumpless chips, compared with the gold/nickel bumps.

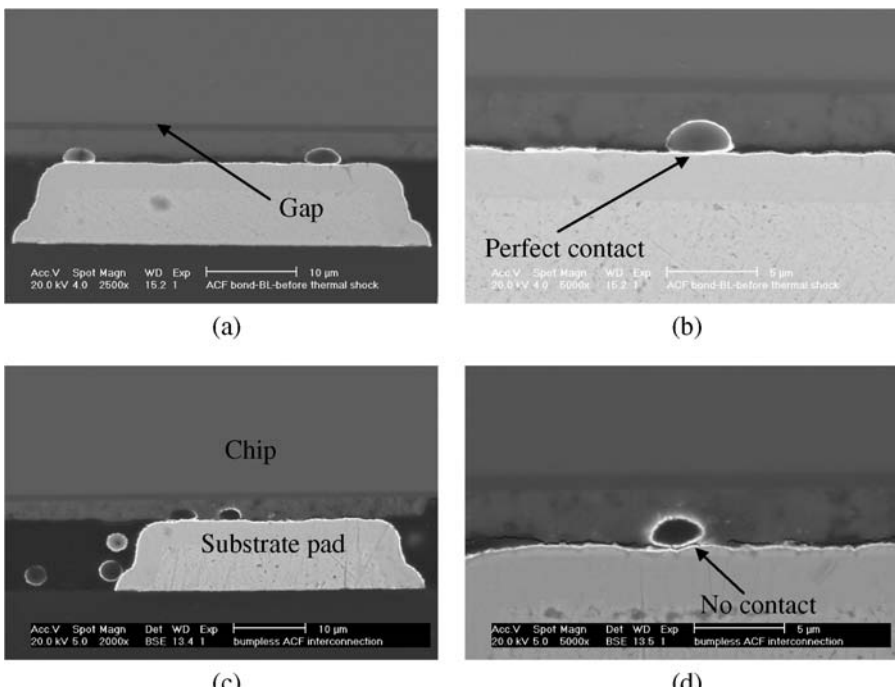


Figure 12. SEM micrographs showing the ACF interconnections: (a) and (b) sample as bonded, (c) and (d) sample after thermal shock.

In order to decrease the thermal warpage in the assembly it is recommended that an ACF with a lower CTE and a higher T_g be used. It is also vital to select a substrate material with a CTE similar to that of the silicon. From this work comes a recommendation to avoid longer chips for ACF joints, since the joints at the corners of a long chip are susceptible to failure during temperature cycling.

5.2. Electrical Performance and Mechanical Behavior of ACF Joints During Autoclave Testing

An autoclave test was applied on 84 samples of FCOF packages. The ACF joint was prebonded at 90°C with a pressure of 0.3 Pa, followed by a final bonding at 200°C with a pressure of 160 N for ten seconds. The autoclave test was designed according to the JEDEC Standard No. 22 Method A 102-B, with the test conditions set at 121°C, 100% relative humidity and 1 atm. The test readout points were selected at 0, 48, 96, 144, 192, 240, 288, 336 and 384 h. Contact resistance was measured at these readouts. These samples were then subjected to the die shear tests.

The contact resistance measurement results showed an increment in contact resistance from about 110.5 mΩ at zero hour to about 823.2 mΩ after 48 h in the autoclave test, as shown in Fig. 13. A slower increment of contact resistance was observed when the autoclave test time was getting close to 300 h. These increments in contact resistance were not recoverable. The first open circuit was observed at 192 h. However, a growth in the percentage of open circuits was observed at 336 h, increasing from about 5% to over 15%.

There were two potential causes for the increase in contact resistance for samples that had undergone the autoclave test: debonding at the ACF joints, and corrosion of the aluminum metallization. The increment of contact resistance in the accelerated test was mainly due to shrinkage of the contact area induced by the growth of corrosion or oxidation film, and/or by hygroscopic swelling in the contacts. Moisture absorption by the ACF and/or flexible substrate accelerated the corrosion process

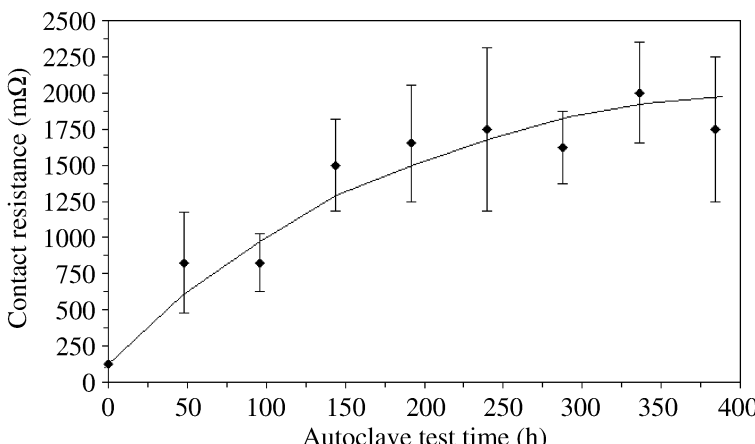


Figure 13. Contact resistance after an autoclave test (121°C, 100% RH, 1 atm).

of the aluminum metallization. Aluminum atoms contributed their electrons to oxygen atoms to form aluminum oxide film that led to a reduction in the number of free electrons on its surface, and consequently, an increase in electrical resistance. Aluminum oxide film is a passive layer that prevents further growth, and thus showed a slower increment in contact resistance at 336 h in the autoclave test.

The shear strength of the ACF joints was about 12.60 MN/m^2 . After 48 h in the autoclave test, the shear strength degraded about 22% to 9.79 MN/m^2 . The shear strength degraded and decreased below the lower control limit after 336 h, which suggested that 336 h was the critical cut-off time for maintaining the adhesion strength of the anisotropic conductive joints in the autoclave test. Elongation of the ACF joints decreased 20% after 48 h in the autoclave test and an almost linear degradation trend was observed in the autoclave test from 48 to 384 h. The elastic modulus of the ACF joints degraded about 16% in 48 h of autoclave time. The adhesion strength of the ACF joints degraded due to weakening of the adhesion at the ACF/copper trace interface. Because the copper base metallization could not withstand the corrosive test conditions, separation occurred between the copper trace and flexible substrate.

Hydrolysis at the ACF outer surface and oxidation at the surface of the copper trace was observed in samples that had undergone 336 h of the autoclave test. The combined effects of hygroscopic swelling-induced stress and corrosion of the metal surfaces in this test environment introduced a failure mechanism in the ACF joints — stress-corrosion cracking — as shown in Fig. 14. Oxide layer growth was detected at the Ni/ACF interface. These oxides grew from the copper trace/flexible substrate interface not covered by the gold coating. The oxide growth broke the bonding between the ACF and the copper trace, and reduced its adhesion area, thus weakening its mechanical strength.

5.3. Effect of Mechanical Shock on Contact Resistance of ACF Joints

High mechanical shock resistance is a critical parameter for the high-performance ACF joint used in products like cell phones [22]. The components joined by an ACF become detached from the printed circuit board when the assemblies experience significant shocks during handling and service life. To assess the shock resistance of the ACF joints, FCOF packages were studied under mechanical shock. The effect of mechanical shock combined with the heat and humidity was also studied. The mechanical shock tests were carried out using a CEAST (a supplier whose head-quarter is in Italy) instrumented drop weight impact tester with a drop weight of 3.164 kg, following the ASTM Standard D3029, which is suitable for thin specimens [23]. The drop height varied from 0.2 to 0.5 m, while the number of drops varied from one to six. For each condition, five samples were tested. After each drop, the contact resistance of the samples was measured. The relative humidity tests were conducted in an autoclave with test conditions set at 85°C , 85% RH and 1 atm. The readout times were 48, 96, 192, 288, 336 and 384 h. At these time points,

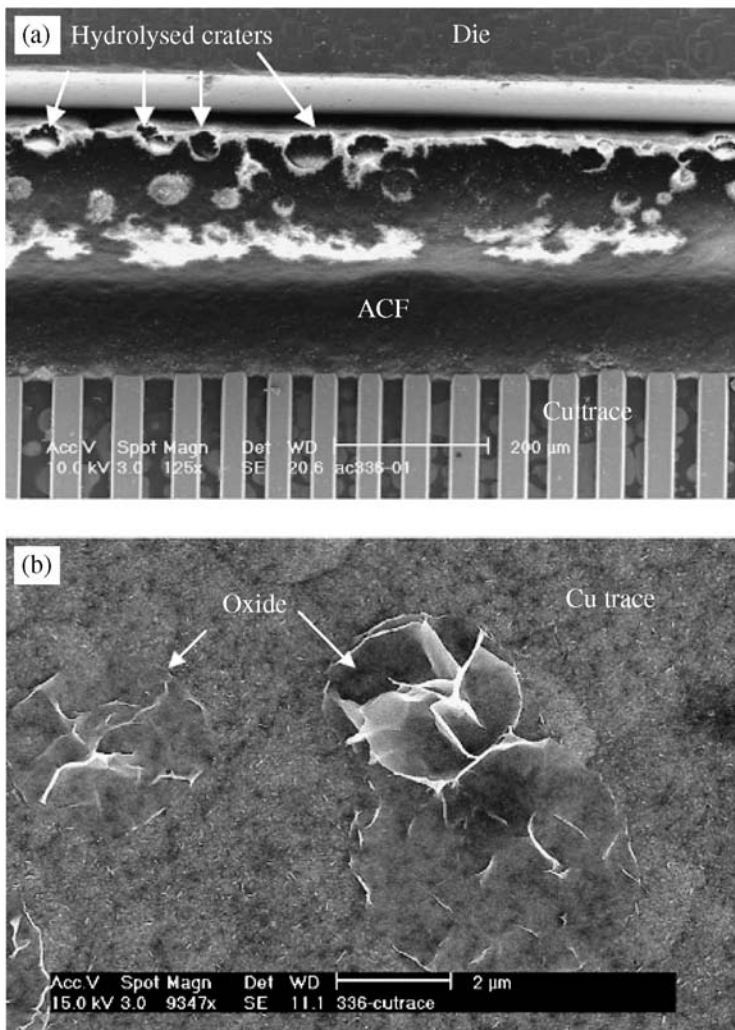


Figure 14. SEM micrographs showing corrosion after 336 h of autoclave testing (a) ACF-hydrolysis and (b) Cu trace-oxidation.

a weight of 3.164 kg was dropped from various heights (0.2–0.4 m) several times (1–4). The contact resistance was measured following the ASTM Standard D3029.

It was found that the contact resistance increased as the drop height increased and also increased with the number of drops, as shown in Fig. 15. From cross-sectional analysis under a scanning electron microscope (SEM), it was found that the conductive particles changed their shape under mechanical shock. After bonding, the particle shape was likely to be oval, but after several shocks, the particles became deformed. As the chip package suffered mechanical shock, the substrate was prone to move upward causing shear stress in the ACF joints. The extreme abrasion loosened the particle in such a way that the central polymeric portion spalled

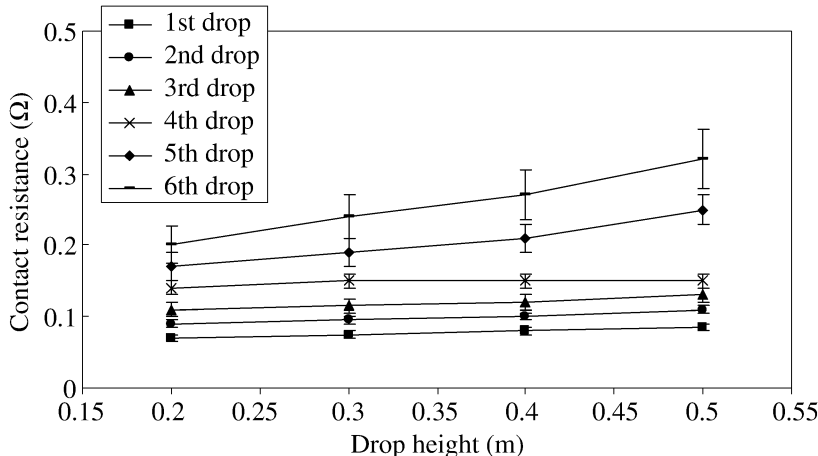


Figure 15. Variation of contact resistance with drop height as a function of number of drops.

out, leaving the conductive portion attached to the bump and pad. Sometimes, under drop weight impact, the conductive layer of the particles broke, exposing the polymer. Under a mechanical shock, the bump and pads also tended to become eroded and deformed. The shock applied during testing of FCOF packages affected the deformation and erosion of the conductive layer within the ACF, which in turn affected the electrical performance of the interconnects. When the shock was large enough, the absorbed energy burst the outermost layer of the conductive particles, exposing the polymer sphere, which is an insulator. As a result, the conductivity of the ACF was lost and it became an insulator that resisted the current flow between the two pads. Also, with excessive abrasion, a large amount of local heat was generated between the bumps and pads. There was a significant difference in the CTEs of the bump (4–10 ppm at 160–190°C) and the ACF (133 ppm at 160–190°C), which probably helped to cause delamination of the ACF from the chip surface. This kind of delamination led to reliability problems in the service life. During bonding between the chip and the flexible substrate, a localized elastic stress was stored in the joint and when the joint experienced a further significant level of energy, this residual stress was released; ultimately the joint became weak and failed.

The contact resistance after mechanical shock for samples that went through the humidity test is shown in Fig. 16 for a drop height of 0.2 m. For drop heights of 0.3 and 0.4 m, the plots showed a similar trend. The results show an increase in contact resistance by 50% from zero to 48 h in the autoclave without any mechanical shock. Almost a constant rate of change in contact resistance was observed up to 143.5 mΩ at 384 h in the autoclave test condition. A maximum of 25% open circuits were found under the most severe conditions. The contact resistance was found to increase from 62 mΩ at the as-bonded condition to 478 mΩ when the samples were kept under the temperature–humidity conditions (85°C, 85% RH, 1 atm) for a load dropped from 0.4 m height four times. It was observed that an ACF joint could

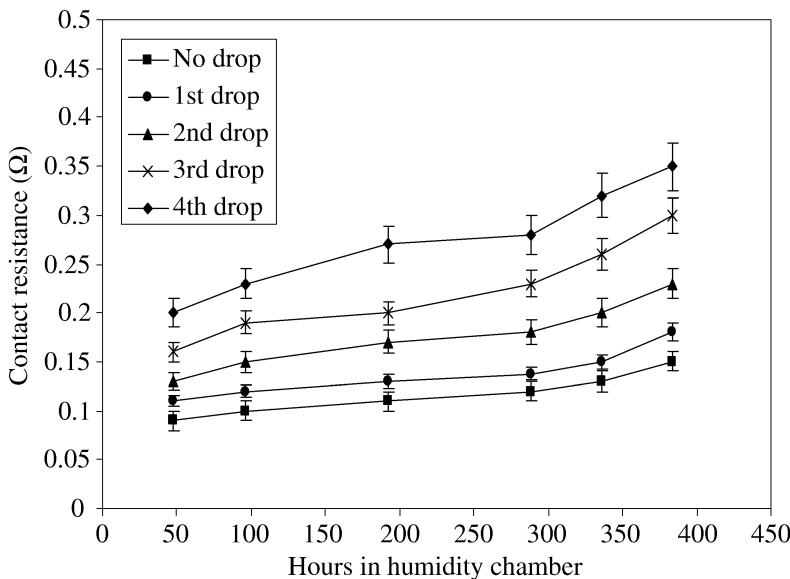


Figure 16. Variation of contact resistance with hours in humidity chamber as a function of number of drops (height = 0.2 m).

survive a mechanical shock up to three or four times in the absence of temperature–humidity conditions, but after that it became vulnerable. The survival time lessened when humidity and heat were applied prior to mechanical shock.

5.4. Short-Circuiting of Adjacent Leads in ACF Joints

Instability of joints is frequently found over time when voltage is applied, particularly in situations where clusters of conductive particles are trapped between bump gaps. It was found that the possibility of short-circuiting was dependent on the curing degree of the ACF matrix. FCOG packages were used to study the effect of curing degree on the possibility of short-circuiting [24]. A Perkin–Elmer Spectrum One FT-IR Spectrometer was used to obtain spectra from ACF samples to calculate their curing degree. ACF samples were prepared at $T = 180^\circ\text{C}$ for five different curing times ($t = 0, 5, 10, 15$ and 20 s).

When a cluster of particles was trapped between adjacent bumps and exposed to an electric field, the particles were likely to be charged. If the applied field was high enough, the forces acting on the charged particles could become strong enough to overcome the holding forces established by the adhesive matrix (such as viscous drag), which meant the particles were likely to start to move and pull adjacent particles closer to form conductive chains, causing shorting. From the results of the insulation resistance test, short-circuiting failures were found only in samples cured at $t = 5$ s (less than 50% cured). Samples cured at both $t = 10$ and 20 s (more than 80% cured) survived the test, which lasted for 24 h. Apparently, the curing degree of ACFs influenced the chance of short-circuiting between adjacent joints under an

electric field effect. Thus, proper curing of ACFs is necessary to form reliable ACF joints.

6. Conclusions

ACF joints have been developed as an alternative to solder joints in flip-chip packages. This technology vitiates environmental concerns by avoiding lead and chlorofluorocarbon-based flux cleaners. The lower curing temperature and higher flexibility of ACF joints and the closer CTE match of the materials reduce joint fatigue and stress cracking. Using this technology involves fewer steps, enabling an increase in throughput. Small filler particle size facilitates finer line resolution of flip-chip packages.

The contact resistance of ACF joints increases with temperature and bump height. The higher curing degree of the adhesive, achieved by a high bonding temperature and longer bonding time, can result in lower and more stable resistance, higher adhesion strength, and a reduced possibility of short-circuiting. But too high a bonding temperature (such as 230°C) will cause oxidation of the contact area, which can increase the contact resistance. Bonding pressure has little effect on adhesion strength, but a certain amount of bonding pressure is necessary to obtain a reliable interconnection. Air bubbles incorporated during the bonding process can cause delamination of ACF joints.

ACF joints can maintain their low contact resistance within the incubation time during thermal cycling tests, but after the incubation time, the contact resistance will increase quickly. Most likely, ACF joints can survive general mechanical shocks up to three or four times in the absence of high temperature and humidity, but under autoclave test conditions, the survival time will decrease substantially. Temperature-humidity conditions also cause stress corrosion of ACF joints, which degrades the conductivity of the joints.

References

1. H. K. Kim and F. G. Shi, *Microelectronics J.* **32**, 315–321 (2001).
2. M. A. Uddin, M. O. Alam, Y. C. Chan and H. P. Chan, *J. Electronic Mater.* **32**, 1117–1124 (2003).
3. Y. C. Chan and D. Y. Luk, *Microelectronics Reliability* **42**, 1195–1204 (2002).
4. D. Farley, A. Dasgupta and J. Caers, in: *Proceedings of the 6th International Conference on Thermal, Mechanical and Multi-physics Simulation and Experiments in Micro-electronics and Micro-systems* (EuroSimE 2005), pp. 471–477 (2005).
5. D. Farley, A. Dasgupta and J. F. J. Caers, in: *Proceedings of the ASME InterPACK2005* (2005).
6. T. Wang and J. Liu, *J. Electronics Manufacturing* **10**, 181–189 (2000).
7. M. Chen, E. J. Siochi, T. C. Ward and J. E. McGrath, *Polym. Eng. Sci.* **33**, 1092–1109 (1993).
8. T. Wang, Y. Fu, M. Becher and J. Liu, in: *Proceedings of the 51st IEEE Electronic Components and Technology Conference*, pp. 593–597 (2001).
9. J. Nysaether, Z. Lai and J. Liu, *IEEE Trans. Advanced Packaging* **23**, 743–749 (2000).
10. M. Yim, Y. Joen and K. Paik, *IEEE Trans. Electronics Packaging Manufacturing* **23**, 171–176 (2000).

11. S. Rzepka, B. Waidhaus and E. Meusal, *Microsystem Technol.* **1**, 129–133 (1995).
12. Y. C. Chan and D. Y. Luk, *Microelectronics Reliability* **42**, 1185–1194 (2002).
13. M. A. Uddin, M. O. Alam, Y. C. Chan and H. P. Chan, *Microelectronics Reliability* **44**, 505–514 (2004).
14. L. Ali, Y. C. Chan and M. O. Alam, *J. Electronic Mater.* **33**, 1028–1035 (2004).
15. C. Y. Yin, M. O. Alam, Y. C. Chan, C. Bailey and H. Lu, *Microelectronics Reliability* **43**, 625–633 (2003).
16. C. Y. Yin, H. Lu, C. Bailey and Y. C. Chan, *IEEE Trans. Electronics Packaging Manufacturing* **27**, 254–259 (2004).
17. A. P. Mathew, S. Packirisamy and S. Thomas, *Polymer Degradation Stability* **72**, 423–439 (2001).
18. S. C. Tan, Y. C. Chan, Y. W. Chiu and C. W. Tan, *Microelectronics Reliability* **44**, 495–503 (2004).
19. Y. P. Wu, M. O. Alam, Y. C. Chan and B. Y. Wu, *Microelectronics Reliability* **44**, 295–302 (2004).
20. H. Kristiansen and J. Liu, in: *Proceedings of the 5th High Density Packaging and Component Failure Analysis in Electronics Manufacturing Conference*, pp. 111–114 (2002).
21. E. H. Wong, R. Rajoo, S. W. Koh and T. B. Lim, *J. Electronic Packaging* **124**, 122–126 (2000).
22. M. Zwolinski, J. Hickman, H. Rubon and Y. Zaks, in: *Proceedings of the 2nd International Conference on Adhesive Joining and Coating Technology in Electronic Manufacturing*, pp. 333–340 (1996).
23. ASTM D 3029: “Standard Test Methods for Impact Resistance of Flat, Thin, Rigid, Plastic Specimen by Means of Falling Weight”.
24. Y. W. Chiu, Y. C. Chan and S. M. Lui, *Microelectronics Reliability* **42**, 1945–1951 (2002).

Review of Recent Advances in Electrically Conductive Adhesive Materials and Technologies in Electronic Packaging

Myung Jin Yim^a, Yi Li^a, Kyoung-sik Moon^a, Kyung Wook Paik^b and C. P. Wong^{a,*}

^a School of Materials Science and Engineering, Georgia Institute of Technology, 771 Ferst Drive, Atlanta, GA 30332-0245, USA

^b Materials Science and Engineering, Korea Advanced Institute of Science and Technology, 373-1, Kusong-dong, Yusong-gu, Taejon, Korea 305-701

Abstract

Electrically Conductive Adhesives (ICAs: Isotropic Conductive Adhesives; ACAs: An-isotropic Conductive Adhesives; and NCAs: Non-conductive Adhesives) offer promising material solutions for fine pitch interconnects, low cost, low-temperature process and environmentally clean approaches in the electronic packaging technology. ICAs have been developed and used widely for traditional solder replacement, especially in surface mount devices and flip chip application. These also need to be lower cost with higher electrical/mechanical and reliability performances. ACAs have been widely used in flat panel display modules for high resolution, lightweight, thin profile and low power consumption in film forms (Anisotropic Conductive Films: ACFs) for last decades. Multi-layered ACF structures such as double and triple-layered ACFs were developed to meet fine pitch interconnection, low-temperature curing and strong adhesion requirements. Also, ACAs have been attracting much attention for their simple and lead-free processing as well as cost-effective packaging method for semiconductor packaging applications. High mechanical reliability, good electrical performance at high frequency level and effective thermal conductivity for high current density are some of required properties for ACF materials to be pursued for a wide usage in flip chip technology. Recently, NCAs are becoming promising for ultra-fine pitch interconnection and low cost joining materials in electronic packaging applications.

In this paper, an overview of the recent developments and applications of electrically conductive adhesives for electronic packaging with focus on fine pitch capability, electrical/mechanical/thermal performance and wafer level packaging application is presented.

Keywords

Electrically conductive adhesives, ICA, ACA, NCA, electronic packaging, fine pitch joint, flat panel display, flip chip, reliability, wafer-level packaging

* To whom correspondence should be addressed. Tel.: 404-894-2846; Fax: 404-894-9140; e-mail: cp.wong@mse.gatech.edu

1. Introduction

Today, resin-based interconnection materials for electronic packaging and interconnection technologies are widely used in manufacturing of electronic devices such as flat panel displays and semiconductor/system package modules [1]. They are attractive as traditional solder alternative due to advantages of low-temperature and low cost process, finer pitch capability and environmentally clean solutions. Electrically conductive adhesives are generally composite materials composed of an insulating adhesive binder resin and a conductive filler. Depending on the conductive filler loading level, they are divided into ICAs, ACAs or NCAs. The differences based on the percolation theory between an ICA and an ACA/NCA is shown in Fig. 1. For an ICA, the electrical conductivity is provided in all x -, y - and z -directions due to high filler content, exceeding the percolation threshold.

For an ACA or NCA, the electrical conductivity is provided only in the z -direction between the electrodes of the assembly. Figure 2 shows the schematics of the interconnect structures and typical cross-sectional images of flip chip joints by ICA, ACA and NCA materials illustrating the bonding mechanism for all three adhesives. Especially, ICA materials, typically silver-filled conductive adhesives, have been recommended as solder replacement materials in a surface mount technology (SMT), flip chip, chip scale package (CSP) and ball grid array (BGA) applications. There are still challenging technical issues for full commercialization of ICAs such as low conductivity and reliability, high material cost, and poor impact strength, etc. and extensive research is being performed to enhance the electrical performance and reliability of adhesive joints [2–6].

Interconnection technologies using ACFs are major packaging methods for flat panel display modules with high resolution, lightweight, thin profile and low consumption power [7], and have already been successfully implemented in the forms of Outer Lead Bonding (OLB), flex to PCB bonding (PCB), reliable direct chip

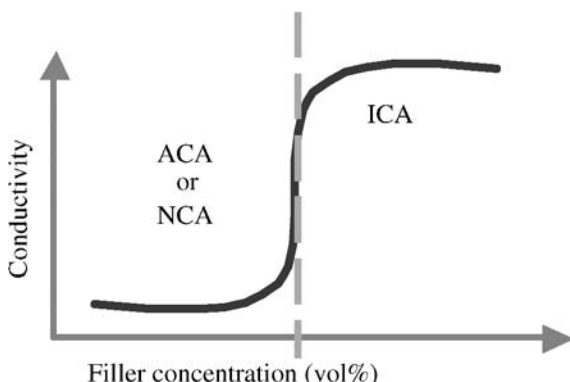


Figure 1. A typical percolation curve showing the abrupt increase in conductivity at the percolation threshold.

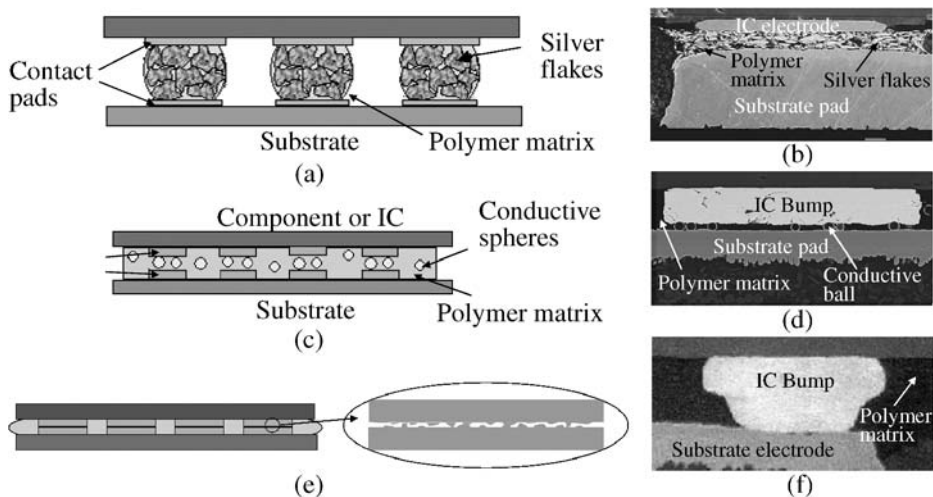


Figure 2. Schematic drawings and cross-sectional views of (a, b) ICA, (c, d) ACA and (e, f) NCA flip chip bonding.

attach such as Chip-On-Glass (COG), Chip-On-Film (COF) for flat panel display modules [8–11], including liquid crystal display (LCD), plasma display panel (PDP) and organic light emitting diode display (OLED). As for the small and fine pitched bump of driver ICs to be packaged, fine pitch capability of ACF interconnection is much more desired for COG, COF and even OLB assemblies. There have been advances in development works for improved material systems and design rules for ACF materials to meet fine pitch capability and better adhesion characteristics of ACF interconnection for flat panel displays. Alternative resin-based interconnection materials such as anisotropic conductive pastes (ACPs) and non-conductive films/pastes (NCFs/Ps) have been developed and introduced due to their advantages in terms of process, cost and ultra-fine pitch capability where a conventional ACF has limitations.

It is obvious that electrically conductive adhesive materials are required for advanced packaging materials, but formulation, material design and process should be optimized and developed for high electrical, mechanical and thermal performance as well as enhanced reliability performance.

In this paper, an overview on recent issues, developments and applications of conductive adhesives for electronic packaging applications with fine pitch capability, high electrical, mechanical, and reliability performance, and wafer level flip chip package applications is presented.

2. Isotropic Conductive Adhesives (ICAs) for Electronic Packaging

ICAs are being used to replace the traditional eutectic SnPb solder alloys in electronic packaging and interconnects. They are composites of polymer resins and

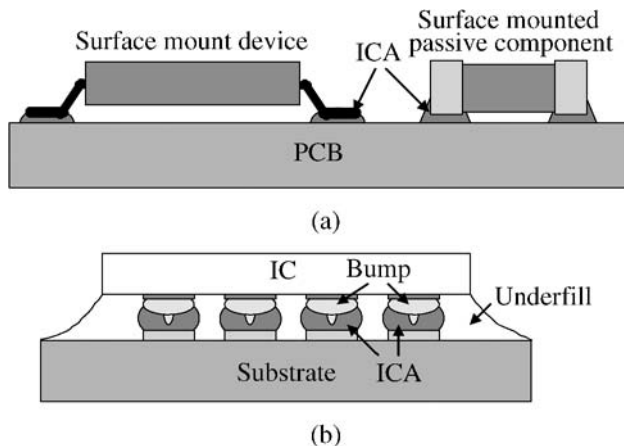


Figure 3. Schematic structures of (a) surface mount interconnection using ICA and (b) flip chip interconnection using ICA.

conductive fillers. The polymer resins, thermoplastic or thermosetting resins, are generally cured at high temperature and provide the shrinkage force, adhesion strength, and chemical and corrosion resistances. Epoxy, cyanate ester, silicone, polyurethane are thermosetting resins, and phenolic epoxy, polyimide are common thermoplastics for an ICA matrix resin. Conductive fillers include silver (Ag), gold (Au), nickel (Ni), copper (Cu) and Sn, SnBi or SnIn coated Cu in various sizes and shapes. Ag is the most common conductive filler for an ICA due to its high conductivity and easy processing, but its high cost is one of drawbacks for wide use of Ag-filled ICAs. ICAs have been used for die attach adhesives [12, 13], adhesives for SMT [14, 15], and flip chip [16] and other applications. Figure 3 shows the schematics of SMT components and flip chip devices interconnected by ICAs instead of solder alloy.

2.1. ICAs for Surface-Mount Technologies

Surface-mount technology (SMT) is the main technique for interconnecting chip components to substrate by packing and placing the components on the printed circuit board and using the reflow furnace to melt the solder alloy for the electronic system interconnection. Tin–lead (Sn–Pb) solder has been exclusively used as the interconnection material in surface-mount technology, because current commercial ECAs, in spite of their numerous advantages, cannot be used as drop-in replacements for solder in all applications due to some challenging issues. Due to the extreme toxicity of lead and legislations for lead-free electronics, world-wide efforts have been put in the study of ICAs. Significant progress has been made to address different materials properties and reliability issues for the development of high performance ICAs as a potential replacement for lead-containing solders in SMT application as well.

2.2. ICAs for Flip Chip Interconnects

Isotropic conductive adhesive materials use much higher loading than ACAs to give electrical conduction isotropically or in all directions throughout the material. In order for these materials to be used for flip chip applications, it is necessary to apply them selectively onto those areas which are to be electrically interconnected, and to ensure that spreading of the materials does not occur during placement or curing which would cause electrical shorts between the separate pathways. ICAs are generally supplied in paste form. To precisely deposit the ICA paste, screen or stencil printing is most commonly used. However, to do this to the scale and accuracy required for flip chip bonding would require very accurate pattern alignment. To overcome this requirement, the transfer method may be used. For this technique, raised studs or pillars are required on either the die or the substrate. The ICA is then selectively transferred to the raised area by contacting the face of the die or the substrate to a flat thin film of the ICA paste. This thin film may be produced by screen printing and the transfer thickness may be controlled by controlling the printed film thickness. This method confines the paste to the area of the contact surfaces and the quantity may be adequately controlled so as to prevent spreading between pathways when the die is placed. Pressure during bonding is not required in this technique, which gives the option of oven curing the assembly.

In a high volume environment, the high precision screen printing techniques to print the ICA paste directly onto the I/O pads of the substrate can be used. This would remove the requirement for stud pillars on the substrate track terminations and also quite possibly the need for bumping of the flip chip pads. Once such a process is in place, the ICA technique could then compete with the ACA method on the basis of speed and ease of processing, however, substantial improvements in bond strength will need to be made before the technique can be realistically considered. Unlike ACA flip chip bonding, however, a separate underfilling step would be required with ICA flip chip bonding to improve long-term reliability of the bond. It is shown that reliability is quite good with ICA flip chip joining on rigid substrates [17]. The difficulties with the ICA flip chip joining technology are the poor processibility and small process window in handling of the flip chip module directly after assembly.

Although there are many technical advantages of ICAs compared with traditional solder materials, current ICAs still have some limitations on the electrical, thermal, and reliability properties compared with SnPb solders for full replacement for solder. Table 1 shows a general comparison of various properties between SnPb solders and conventional ICAs [18]. Therefore, much research effort has been focused on the improvement of electrical conductivity of ICAs and reliability enhancement of ICA joints, electrically and mechanically. Also the replacement of expensive Ag flakes by new metal flakes is required for wide use of ICAs instead of solder materials. Copper can be a conductive filler metal due to its low resistivity, low cost and improved electromigration performance, but oxidation causes this metal to lose its conductivity [19].

Table 1.

Comparison between a Conductive Adhesive and Eutectic Solders [18]

Characteristic	SnPb solder	ICA
Volume resistivity ($\Omega \text{ cm}$)	0.000015	0.00035
Typical junction resistance ($\text{m}\Omega$)	10–15	<25
Thermal conductivity (W/mK)	30	3.5
Shear strength (psi)	15.2 MPa	13.8 MPa
Min. processing temperature ($^{\circ}\text{C}$)	215	150–170
Environmental impact	Negative	Very minor

Table 2.

Relationship of shrinkage and electrical conductivity of ECAs [27]

Formulation	Cross-link density (10^{-3} mol/cm^3)	Shrinkage (%)	Bulk resistivity ($10^{-3} \Omega \text{ cm}$)
ECA1	4.50	2.98	3.0
ECA2	5.33	3.75	1.2
ECA3	5.85	4.33	0.58

2.3. Electrical Conductivity Improvement of ICAs

To enhance the electrical conductivity of metal-filled ICAs, polymer–metal composite properties are controlled and maximized. Typically, increasing cure shrinkage of matrix polymer binder [20], the intimate metallic contacts by removal of lubricant layer on Ag flakes [21], and oxidation layer removal [22], metallurgical bonding between the conductive particles by low melting point alloy coating on Cu powder [23, 24] are representative methods for improvement of ICA conductivity. Recently, nano-sized Ag particles are added as conductive fillers instead of highly loaded micro-sized Ag flakes and the electrical conductivity is enhanced by sintering nano-sized Ag fillers [25].

2.3.1. Increase of Polymer Matrix Shrinkage

In general, ICA pastes exhibit insulative property before cure, but the conductivity increases dramatically after curing. ICAs achieve electrical conductivity during the polymer curing process caused by the shrinkage of polymer binder. Accordingly, ICAs with high cure shrinkage generally exhibit higher conductivity. Table 2 shows the relationship between shrinkage and conductivity for three different cross-link density ECAs, ECA1, ECA2 and ECA3 [26]. With increasing cross-link density of ECAs, the shrinkage of the polymer matrix increased, and, consequently, an obviously decreased resistivity of ECAs was observed. Therefore, increasing the cure shrinkage of the polymer binder could improve electrical conductivity. For epoxy-based ICAs, a small amount of a multi-functional epoxy resin can be added

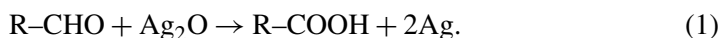
into the ICA formulation to increase cross-link density, shrinkage, and thus increase electrical conductivity.

2.3.2. In Situ Removal of Lubricant on Ag Flakes

An ICA is generally composed of a polymer binder and Ag flakes. There is a thin layer of organic lubricant on the Ag flake surface. This lubricant layer plays an important role for the performance of ICAs, including the dispersion of the Ag flakes in the adhesives and the rheology of the adhesive formulations [21, 28–30]. This organic lubricant layer, typically a fatty acid such as stearic acid, forms a silver salt complex between the Ag surface and the lubricant [21]. However, this lubricant layer affects conductivity of an ICA because it is electrically insulating. To improve conductivity, the organic lubricant layer should be partially or fully removed or replaced during the curing of ICA. A suitable lubricant remover is a short chain dicarboxylic acid because of the strong affinity of carboxylic functional group ($-COOH$) with silver and stronger acidity of such short chain dicarboxylic acids. With the addition of only a small amount of short chain dicarboxylic acid, the conductivity of an ICA can be improved significantly due to the easier electronic tunneling/transport by the intimate flake–flake contacts in the Ag flake networks [25, 31].

2.3.3. Incorporation of Reducing Agents

Silver flakes are by far the most used fillers for conductive adhesives due to the high conductivity of silver oxide compared to other metal oxides, most of which are insulative. However, the conductivity of silver oxide is still inferior to metal itself. Therefore, incorporation of reducing agents would further improve the electrical conductivity of ICAs. Aldehydes were introduced into a typical ICA formulation and obviously improved conductivity was achieved due to reaction between aldehyde and silver oxide that exists on the surface of metal fillers in ECAs during the curing process:



The oxidation product of aldehydes, carboxylic acids, which are stronger acids and have shorter molecular length than stearic acid, can also partially replace or remove the stearic acid on Ag flakes and contribute to the improved electrical conductivity [22].

2.3.4. Low-Temperature Transient Liquid-Phase Fillers

Another approach for improving electrical conductivity is to incorporate transient liquid-phase metallic fillers in ICA formulations. The filler used is a mixture of a high-melting-point metal powder (such as Cu) and a low-melting-point alloy powder (such as Sn–Pb or Sn–In). The low-melting-alloy filler melts when its melting point is reached during the cure of the polymer matrix. The liquid phase dissolves the high melting point particles. The liquid exists only for a short period of time and then forms an alloy and solidifies. The electrical conduction is established through

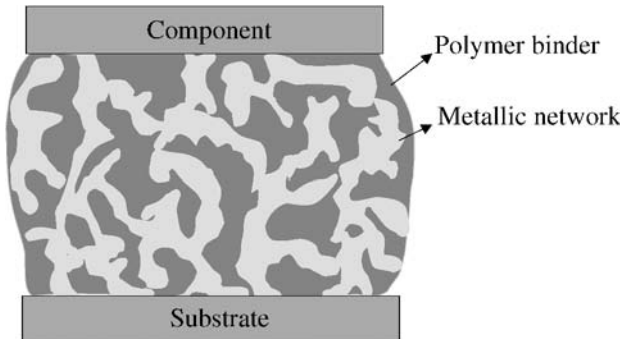


Figure 4. Schematic of an ECA joint with metallurgical connections in conductive filler network by transient liquid phase sintering.

a plurality of metallurgical connections *in situ* formed from these two powders in the polymer binder (Fig. 4).

The polymer binder with an acid functional ingredient fluxes both the metal powder and the metals to be joined and facilitates the transient liquid bonding of the powders to form a stable metallurgical network for electrical conduction, and also forms an interpenetrating polymer network providing adhesion. High electrical conductivity can be achieved using this method [32, 33].

2.3.5. Low-Temperature Sintering of Nano-silver Fillers

Recently, nano-sized conductive particles have been proposed as conductive fillers in ICAs for fine pitch interconnects. Although the nano-silver fillers in ICAs can reduce the percolation threshold, there has been concern that incorporation of nano-sized fillers may introduce more contact spots due to high surface area and consequently induce higher resistivity compared to micro-sized fillers. A recent study showed that nano-silver particles could exhibit sintering behavior at curing temperature of ICAs [34]. Typically, application of nano-fillers increases the contact resistance and reduces the electrical performance of the ICAs. The number of contacts between the small particles is larger than that between the large particles. The overall resistance of an isotropic conductive adhesive (ICA) formulation is the sum of the resistance of filler, the resistance between filler particles, and the resistance between filler and pads (equation (2)). In order to decrease the overall contact resistance, the reduction of the number of contact points between the particles may be obviously effective. If nano-particles are sintered together, then the number of contacts between filler particles will be fewer. This will lead to smaller contact resistance. By using effective surfactants on these nano-sized silver fillers for better filler dispersion in ECAs, obvious sintering behavior of the nano-filters can be achieved. The sintering of nano-silver fillers improved the interfacial properties of conductive fillers and polymer matrices, and reduced the contact resistance between fillers. Therefore, an improved electrical conductivity of nano-silver-filled

ICAs can be achieved at a lower loading level than that of micro-filler-ICAs with a filler loading of 80 wt% or higher:

$$R_{\text{total}} = R_{\text{btw fillers}} + R_{\text{filler to bond pad}} + R_{\text{fillers}}. \quad (2)$$

2.4. Reliability Enhancements of ICA Interconnects

Critical reliability concerns of ICA joints in electronic packaging applications are mainly due to unstable contact resistance between ICA and metal finished components under environmental attacks, such as humidity and temperature cycling/aging. For high temperature and humidity aging environment, the galvanic corrosion rather than simple thermal oxidation at the interface between metallic fillers in ICA and non-noble metal finish is known as the most detrimental underlying mechanism for unstable contact resistance [35]. Therefore, most research works for improving the stability of electrical conductivity of ICA joints have focused on the methods to avoid or minimize the unstable contact resistance mechanism of ICA joints. Several possible methods are: development of polymer matrix resin with low moisture absorption [36], use of oxygen scavengers [35] and corrosion inhibitors [36] in the ICA formulation, the corrosion control by adding metal fillers with low corrosion potential, sacrificial anode [37], and oxide-penetrating particles in the ICA formulation [38]. Also, for the reliability improvement of Ag-based ICA joints, Ag migration is most serious concern. Several methods are proposed to reduce Ag migration and improve the reliability of ICA joints such as Ag alloying with an anodically stable metal [39], hydrophobic polymer coating over the PWB [40], surface coating of tin, nickel, gold or organic compounds on silver particles.

2.4.1. ICA With Low Moisture Absorption

Moisture in polymer composites has been known to have an adverse effect on both mechanical and electrical properties of epoxy laminates [41, 42]. Effects of moisture absorption on conductive adhesive joints include degradation of bulk mechanical strength; decrease of interfacial adhesion strength causing delamination; promoting the growth of voids present in the joints, giving rise to swelling stress in the joints; and inducing the formation of metal oxide layers resulted from corrosion. The water condensed from the adsorbed moisture at the interface between an ECA and metal surface forms the electrolyte solution required for galvanic corrosion. Therefore, one way to prevent galvanic corrosion at the interface between an ICA and the non-noble metal surface and achieve high reliability is to select ICAs with lower moisture absorption. ICAs with a low moisture absorption generally exhibit more stable contact resistance on non-noble metal surfaces compared with those with high moisture absorption [36].

2.4.2. ICA With Oxygen Scavengers

Since oxygen accelerates galvanic corrosion, oxygen scavengers could be added into ECAs to slow down the corrosion rate [35]. When ambient oxygen molecules diffuse through the polymer binder, they react with the oxygen scavenger and are consumed. The main mechanism for oxygen scavengers to inhibit the corrosion

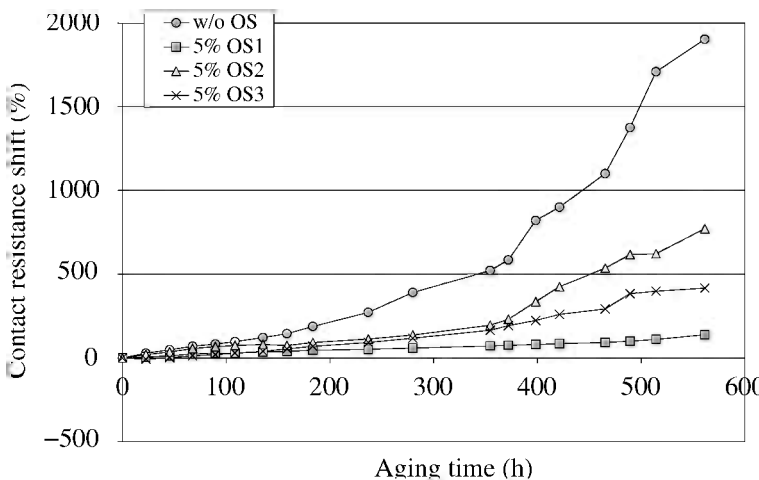


Figure 5. Shifts of contact resistance of conductive adhesives on Sn/Pb surface with and without oxygen scavengers.

is the cathodic mechanism which is based on the lowering of oxygen concentration. Therefore, the reactivity of an oxygen scavenger with oxygen is an important consideration. Some commonly used oxygen scavengers include sulfates such as sodium sulfate (Na_2SO_4), hydrazine ($\text{H}_2\text{N}-\text{NH}_2$), carbohydrazide ($\text{H}_2\text{N}-\text{NH}-\text{CO}-\text{NH}-\text{NH}_2$), diethylhydroxylamine ($(\text{C}_2\text{H}_5)_2\text{N}-\text{OH}$), and hydroquinone ($\text{HO}-\text{C}_6\text{H}_4-\text{OH}$) [43–46]. Figure 5 shows the effect of oxygen scavengers on the contact resistance between an ICA and a Sn/Pb surface. The application of oxygen scavengers reduces the contact resistance increase obviously, especially in the first 200 h test time. However, with continuing aging test when the oxygen scavenger within the ECA is depleted, oxygen can again diffuse into the interface and accelerate the corrosion process. Therefore, oxygen scavengers can only delay the galvanic corrosion process, but do not solve the corrosion problem completely.

2.4.3. ICA With Corrosion Inhibitors

Another method of preventing galvanic corrosion and stabilizing contact resistance is the use of corrosion inhibitors in ICA formulations [35, 36, 47, 48]. In general, organic corrosion inhibitors are chemicals that adsorb on metal surfaces and act as a passivation barrier layer between the metal and the environment by forming an inert film over the metal surfaces [49–52]. Thus, the metal finishes can be protected. Some chelating compounds are especially effective in preventing metal corrosion [51]. Appropriate selection of corrosion inhibitors can be very effective in protecting the metal finishes from corrosion. However, the effectiveness of the corrosion inhibitors is highly dependent on the types of contact surfaces. Effective corrosion inhibitors have been discovered for Sn/Pb, Cu, Al and Sn surfaces [35, 47, 53].

2.4.4. ICA With Sacrificial Anode

To improve the contact resistance stability, applying a sacrificial anode is another efficient method. For galvanic corrosion of ECAs during aging, the larger the dif-

ference in electrochemical potentials, the faster the corrosion develops. Also, the self-corrosion rates of both metals are different: the comparably active metal (the anode) corrodes faster while the other (the cathode) corrodes slower. Generally, metals with a low potential tend to corrode faster and show increased contact resistance than those with a high potential value. Therefore, when applying sacrificial materials with lower electrochemical potential than those of electrode-metal pads into ECAs, the sacrificial materials are preferentially corroded first and, thus, can protect the metal finishes [37]. This corrosion control is very important in reliability issues of the conductive adhesive joints. The addition of individual metals with low corrosion potential, metal mixtures or metal alloys greatly reduces the electrode potential of ECAs, or, in other words, narrows down the potential gap between the ECA and the metal finishes. Thus, these sacrificial anode materials act as an anode in this configuration and they are corroded first instead of the metal finishes, resulting in protecting the surfaces at the cathode [37, 54, 55].

2.4.5. ICA With Oxide-Penetrating Particles

Another approach for improving contact resistance stability during aging is to incorporate some electrically conductive particles, which have sharp edges, into the ICA formulations. Such particle is called oxide-penetrating filler. Force must be provided to drive the oxide-penetrating particles through the oxide layer and hold them against the adherend materials. This can be accomplished by employing polymer binders that show high shrinkage when cured as shown in Fig. 6 [38]. This concept is used in polymer-solder which has good contact resistance stability with standard surface-mounted devices (SMDs) on both solder-coated and bare circuit boards.

2.5. Adhesion Strength and Mechanical Reliability Enhancement of ICA Interconnects

Another critical reliability issue regarding conductive adhesives is their low adhesion strength. High adhesion strength is a critical parameter in fine pitch interconnection that is fragile to shocks encountered during assembly, handling and lifetime.

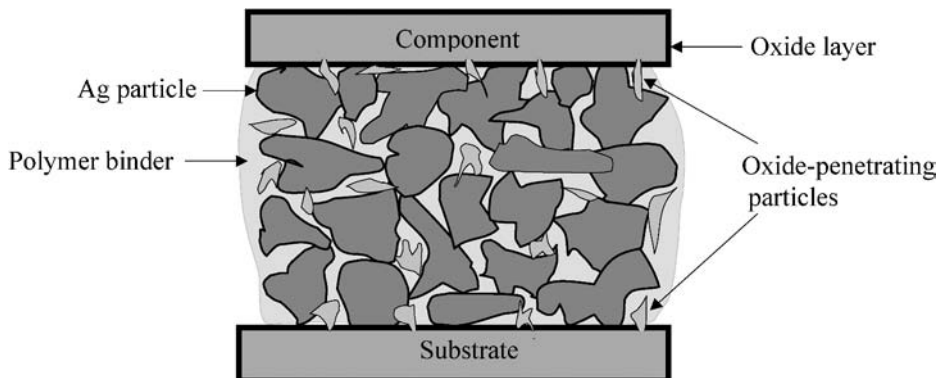


Figure 6. A joint connected with an ICA containing oxide-penetrating particles and silver particles.

There are two types of adhesion mechanisms, physical bonding and chemical bonding, which contribute to the overall adhesion strength of a polymer on a surface [56]. Chemical bonding involves the formation of covalent or ionic bonds to link the polymer and the substrate [56]. In other words, a chemical reaction must take place for the formation of chemical bonds. Physical bonding involves mechanical interlocking or physical adsorption between the polymer and surface of substrate. In cases where the molecules of the polymer are highly compatible with the molecules of the substrate, they interact to form an inter-diffusion layer. In mechanical interlocking, polymer and substrate interact on a more macroscopic level, where the polymer flows into the crevices and the pores of substrate surface to establish adhesion [56]. Therefore, a polymer is expected to have better adhesion on a rougher surface because there is more surface area and “anchors” to allow for interlocking between the polymer and the substrate. Under thermal cycling (TC) environment, the failure mechanisms of unstable ICA performance are generally the thermal stress in the ICA joint and the interfacial delamination due to the adhesion degradation. The TC performance of ICA joints can be improved by reducing the thermal stress by incorporating flexible molecules in the epoxy resin [57].

2.5.1. Adhesion Improvement by Coupling Agents in ICAs

The most useful approach to improve the adhesion of ICA joints is by using coupling agents [58]. Coupling agents are organofunctional compounds based on silicon, titanium, or zirconium. Their general structure is $R-X-(O-R')_3$, where $X = Si, Ti$ or Zr , R = organic group that interacts with the polymer, and R' = a hydrolysable methoxy or ethoxy group that interacts with the substrate. A coupling agent consists of two parts and acts as intermediary to “couple” the inorganic substrate and polymer.

Silane coupling agents have been commonly used to improve the adhesion performance [59]. For example, chemically etched 304 stainless steel can react with γ -aminopropyltrimethoxysilane. The methoxy groups of the silane coupling agent can first hydrolyze to hydroxyl groups which are quite reactive and can react with the metal surface hydroxyl groups, forming an $M-O-Si$ chemical bond. The other organo-reactive group (e.g., amine end of the coupling agent) can react with poly(amic acid), a precursor of the polyimide polymer, to form a strong polymer–metal interfacial bond. As such, it produces mechanically stronger polyimide/stainless steel interfaces [60]. Other approaches use the formation of a thick metal oxide layer prior to application of the silane coupling agent to improve the adhesion to organic films [61]. In conductive adhesives, application of specific silane coupling agents with appropriate concentration can increase the adhesion strength on different metal surfaces [58]. As an example of effect of coupling agents on adhesion strength of ECAs, Fig. 7 shows the adhesion data of polyarylene ether derivative (PAE-2E) with a coupling agent (CA-4), and the obvious increase in adhesion strength on Ni/Au and Sn surfaces was observed.

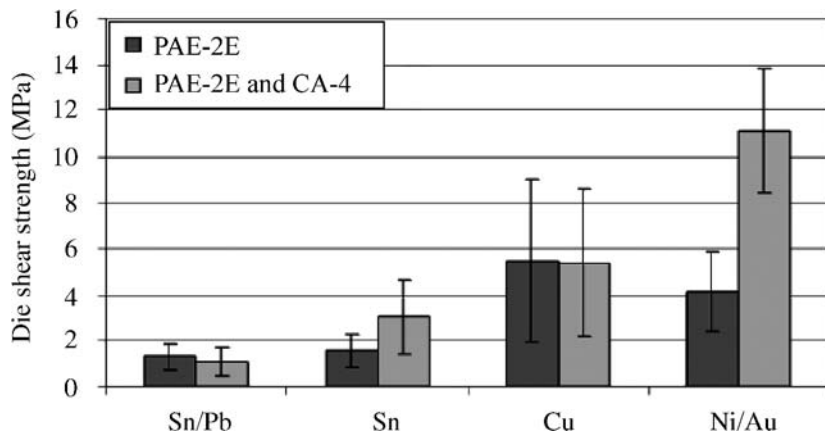


Figure 7. Adhesion data of PAE-2E with coupling agent (CA-4) [58].

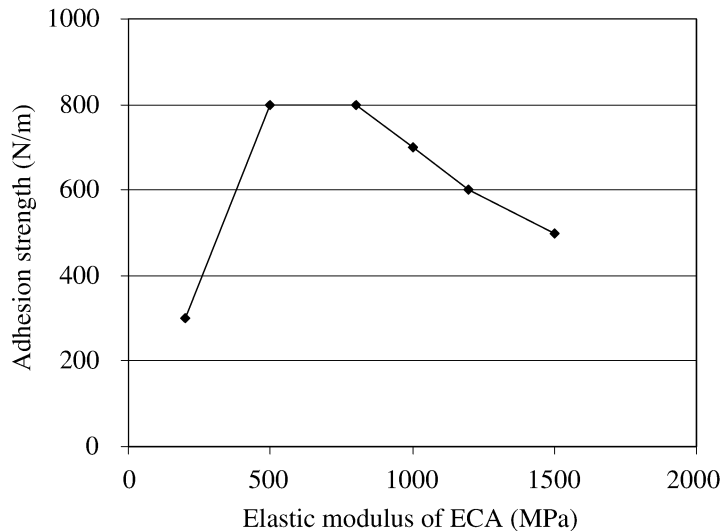


Figure 8. The relationship between the adhesion strength and the elastic modulus of ECA [63].

Although silane coupling agents are mostly used, some other coupling agents with various functional groups, such as thiol, carboxylate coupling agents, are also used [60].

2.5.2. Adhesion Improvement by Optimization of Elastic Modulus of the Adhesive
 In order to enhance the adhesion, another approach is to lower the elastic modulus of adhesive resins. By using low elastic modulus resins, the thermal stress at the adhesion interface can be reduced which should result in improved adhesion strength [61, 62]. Figure 8 shows the relationship between the adhesion strength against COF (Chip on flex) and the elastic modulus. The adhesion strength increases with lowering the elastic modulus value deteriorates the cohesive

force and, thus, decreases the adhesion strength. Therefore, the elastic modulus needs to be optimized to improve the adhesion properties.

In addition to the methods listed above, some other factors such as curing conditions and structures of IC packaging may also affect the adhesion strength of conductive adhesives.

2.5.3. Improving the Thermo-cycling Reliability of ICA Interconnects

The poor thermal cycling (TC) performance of the ECA joints has been another reliability issue for board level interconnects. Generally, the failure of the electrical interconnection during the TC test can be caused by many factors such as coefficient of thermal expansion (CTE) mismatch between the IC component chip/the interconnection materials/the substrates, elastic moduli difference of these components, adhesion strength of the interconnect materials on the IC chip and the substrate, the mechanical properties of the IC chips, the glass transition or the softening point of the ECA materials, moisture uptake both at the interface and in the bulk ECAs, the surface or interface property change and so forth. Especially, the thermal stress in the ECA joints generated by a huge temperature difference during the TC and the interfacial delamination due to the adhesion degradation could be the critical reasons. In this aspect, a feasible solution to the TC failure problem is to introduce flexible molecules into the epoxy resin matrix. By releasing the thermal stress with the flexible molecules, the thermomechanical stresses can be dramatically reduced and the ECA/component joint interfaces can stay intact through the thermal cycling test [64].

3. Anisotropic Conductive Adhesives (ACAs) for Electronic Packaging

Anisotropic conductive adhesives (ACAs) or anisotropic conductive films (ACFs) provide uni-directional electrical conductivity only in the vertical or Z-axis. This directional conductivity is achieved by using a relatively low volume loading of conductive filler (5–20 volume percent) [65–67]. The low volume loading is insufficient for inter-particle contact and prevents conductivity in the X-Y plane of the adhesive. The ACA, in film or paste form, is interposed between the surfaces to be connected. Heat and pressure are simultaneously applied to this stack-up until the particles bridge the two conductor surfaces. Because of the anisotropy, an ACA/ACF can be deposited over the entire contact region, greatly facilitating materials application. Also, an ultra-fine pitch interconnection (<0.04 mm) can be achieved easily. The fine pitch capability of ACA/ACF would be limited by the particle size of the conductive filler, which can be a few micrometers or a few nanometers in diameter.

3.1. ACAs for Flat Panel Displays

ACF materials are mostly wide used in connecting the tape-carrier packages (TCPs) with driver IC to the LCD glass panel and PCB boards, as well as other interconnection areas for flat panel display manufacturing. Figure 9 shows various packaging

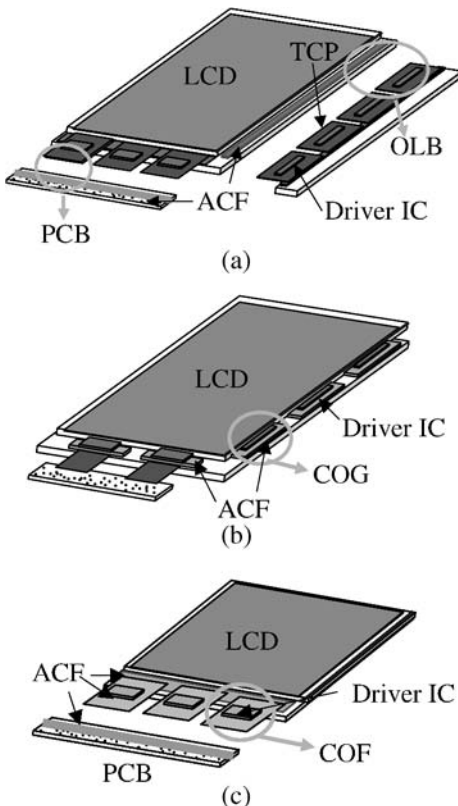


Figure 9. Various packaing technologies using an ACF in LCD modules (a) TCP: Outer Lead Bonding (OLB) and PCB bonding, (b) COG bonding and (c) COF bonding.

technologies using ACFs for LCD modules: TCP, COG and COF bonding. Since the interconnection input/output (I/O) pitch of driver IC electrode has been decreased and the number of output electrodes per IC increased for the high resolution LCD modules, ACF materials and packaging technologies have also been developed to meet high density interconnection capability.

ACF bonding process is a thermo-compression bonding as shown in Fig. 10. In case of TCP bonding, the ACF material is attached on glass substrate after release film is removed and TCP with driver IC is pre-attached. Then final bonding is established by thermal cure of ACF resin, typically at 180°C, 20 s and 30 kgf/cm² and conductive particle deformation between the electrodes of TCP and glass substrate by applied bonding pressure.

The kind, size, and density of conductive filler, and adhesive resin system are different according to packaging technology for LCD module. When TCP is mounted using an ACF on LCD glass substrate, the CTE mismatch between TCP and the panel should be considered for thermal bonding, and this is more serious for finer pitch TCP bonding, i.e., below 50 µm. For flex to glass bonding below 50 µm pitch,

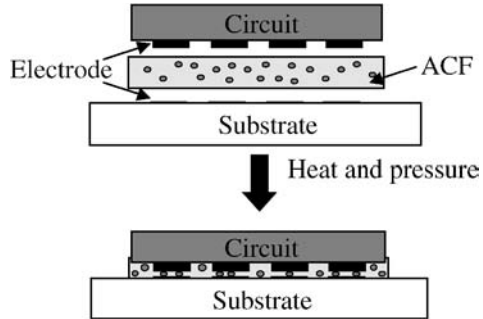


Figure 10. Thermo-compression bonding using an ACF.

COF using an ACF becomes more attractive due to several advantages like fine pitch capability, design flexibility and low CTE base material. ACFs are also used in attaching fine-pitched driver IC on COF substrates. The geometry of COF is very similar to that of TCP. However, the substrate is different, i.e., it is a two-layer structure, normally Cu and polyimide (PI) which is thinner, higher density, better flexible and more durable in high temperature than TCP with a three-layer structure (Cu, adhesive and PI). COF's two-layer structure without adhesive layer normally has weak adhesion property with ACF materials. Therefore, there has been development in ACF adhesion improvement to two-layer COF substrate.

In COG technology, the bare driver ICs are flip chip bonded on glass substrate using an ACF, and it is most advantageous technology for low cost and compact size LCD module production [68]. The CTE difference between driver IC and glass substrate is relatively small compared with that in TCP applications and it provides more reliable COG connections.

3.2. ACFs for Fine Pitch Interconnections

As the function of driver IC for high-resolution LCD modules increases, the bump density on IC is also increased and this means that bump size and pitch are reduced. For fine pitch COG connection using an ACF, the number of conductive particles trapped between the bump and the substrate pad should be sufficient. Therefore, conductive particle density in the ACF for COG is much higher than that of ACF for TCP OLB. But due to high density of conductive particles, there is high possibility of electrical short between adjacent bumps, mainly due to electrical path formed by a chain of conductive particles accumulated after being flowed into the bump gap during COG bonding process. Therefore, a double-layer ACF, which is composed of an ACF layer and an NCF layer without conductive filler, was developed for high electrical conductivity between the bump and ITO electrode and electrical insulation between adjacent bumps [69]. As bump size and pitch of driver IC decreased more and more, insulating layer coated conductive particles were introduced instead of conventional conductive particles in the ACF layer, and non-conductive

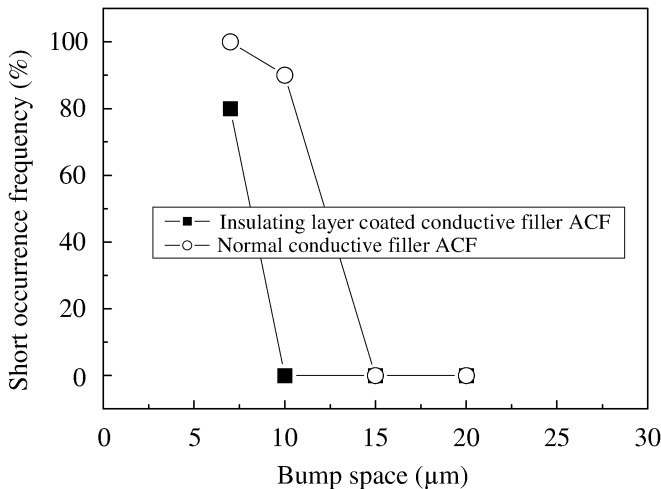


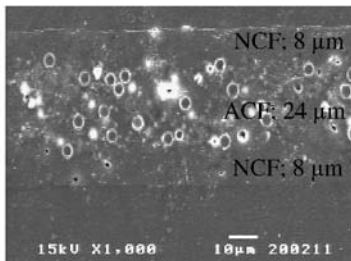
Figure 11. The relationship between the short occurrence frequency and the type of conductive particle [70].

fillers were incorporated together with conductive particles to ensure electrical insulation [70].

Figure 11 shows the relationship between the short occurrence frequency and the type of conductive particle. The double-layer ACF with conventional conductive particle and insulating layer coated conductive particle, both in 4 μm diameter size and 35 000/mm² density. Insulating layer coated conductive filler ACF is more advantageous than normal conductive particle ACF by reducing electrical shorts more effectively, and it achieves insulation capability at 10 μm gap level. In double-layer ACF structure, ACF and NCF layer thicknesses are 7 μm and 18 μm, respectively. The viscosity, formulation, thickness of adhesive layers, conductive filler density, type and hardness should be optimized for high performance COG package.

COF, another fine pitch ACF bonding area, is a relatively new technology compared with COG and COB in the production of flat panel modules. LCD module production using COF technology is accelerated due to its advantages of fine pitch interconnection, low contact resistance and pre-test capability compared with COG in the high-density, multi-functional LCD modules. In COF technologies, there are several alternatives for interconnect materials and processes, such as Au–Sn joining [71], stud bump bonding (SBB) joining [72], ACF joining [73], and NCF and NCP joining [74]. Among them, ACF joining method has been applied as the main bonding method similar to COG technology.

As mentioned before, COF's substrate is a two-layer structure without the adhesive layer, and, therefore, normally has weak adhesion property with ACF materials. It is necessary to improve the adhesion property between IC chip, ACF and two-layer flex substrate for ever-increasing reliability requirement of COF modules. In addition, fine pitch interconnection is the basic requirement in COF using ACF for driver IC packaging. A triple-layered ACF has been developed, which has func-



(a)

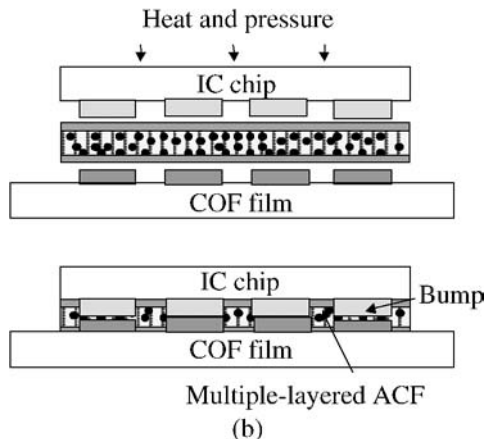


Figure 12. (a) Cross-sectional view of triple-layered ACF obtained by SEM and (b) COF bonding process using a triple-layered ACF [75].

tional layers on both sides of conventional ACF layer to improve interface adhesion and control bonding property for fine pitch application during thermo-compression bonding as shown in Fig. 12, and the resulting reliability enhancement of COF module assembly [75].

3.3. ACAs for Reliability Enhancement in Flip Chip Assembly

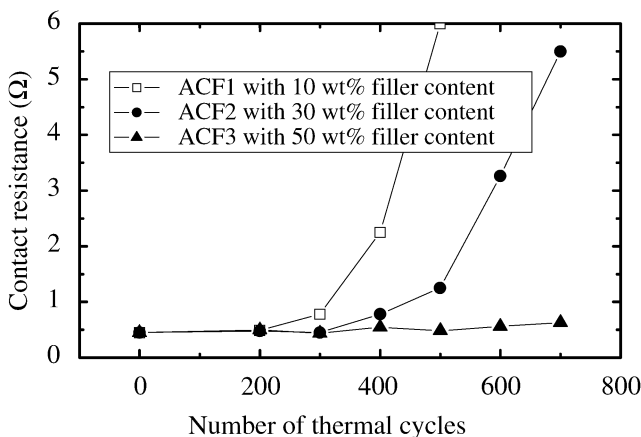
Flip chip assembly on organic board using anisotropic conductive adhesives (ACAs) has received much attention due to many advantages such as simple and lead-free processing, low cost, fine pitch interconnection and low-temperature processing [76–78]. Especially highly improved electrical and thermal performance as well as high frequency characteristics are anticipated due to reduced interconnection distances.

Most of all, flip chip using an anisotropic conductive adhesive should provide acceptable reliability level in harsh environment together with good processability. This requires the use of polymer materials which have CTE value close to the chip and the board, and strong adhesion for better reliability. For better mechanical properties without degradation of strong adhesion, non-conductive fillers are incorporated and optimized. As the content of filler increased, CTE values decreased

Table 3.

The Tg, CTE and modulus of ACA composites [79]

ACA composite	T_g^{TMA} (°C)	CTE (ppm/°C)		Modulus (GPa@25°C)
		α_1	α_2	
ACA 1 with 10 wt% filler	87.6	87.9	3960	5.3
ACA 2 with 30 wt% filler	93.5	76.1	3630	3.2
ACA 3 with 50 wt% filler	98.8	60.7	3920	2.5

**Figure 13.** Contact resistance of flip chip interconnects using ACAs with different filler contents during thermal cycling test from -60°C to 150°C for 700 cycles [79].

and storage moduli increased, but the DSC behavior did not change. Table 3 summarizes the material properties of ACA composites with different filler contents showing lower CTE and higher modulus as filler content increases [79].

For the test IC chip and substrate, gold stud bumps were formed on each I/O pad of test chips and 1-mm thick FR-4 substrates were prepared. Flip chip assembly was performed by bonding the chip on the substrate with an appropriate bonding pressure of 50 kgf/cm^2 at 180°C for 30 s. The chip was electrically connected to the substrate *via* the contacts between compressed gold stud bumps and conductive fillers in the ACA. Non-conductive fillers with smaller size than conductive fillers do not contribute the electrical contacts and affect other properties such as Young's modulus and CTE because the electrical path is formed by the conductive fillers larger than non-conductive fillers which are dispersed in the polymer resin.

Reliability tests in terms of temperature cycling, high humidity and temperature, and high temperature and dry condition tests were performed by measurement of contact resistance variation. Figure 13 shows that flip chip assembly using modified ACA composites with lower CTEs and higher modulus by loading non-conducting fillers exhibits more stable contact resistance behavior than conventional ACAs

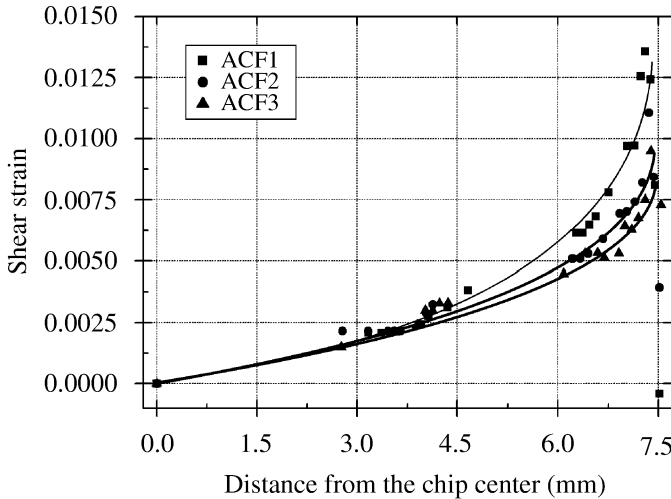


Figure 14. Thermal shear strain of ACF layers between the chip and FR-4 substrate of flip chip assembly [79].

without non-conducting fillers during the temperature cycling test. An ACF with a lower CTE and higher modulus can reduce the thermally induced shear strain in the ACF layer as measured by Moiré interferometry during thermal cycling environment as shown in Fig. 14, and thus can increase the overall thermal cycling lifetime of ACF joints [79]. There are still more demanding requirements for reliability enhancements such as low moisture absorption, high temperature electrical stability during reflow process, low degree of process-induced voids, high cure density, and stability of interface adhesion strength in an ACA [80–85].

3.4. ACAs for High Frequency Interconnections

Recently, high frequency modeling and characterization for ACA flip chip interconnects have been performed to understand high frequency characteristic of flip chip interconnect using ACFs, and thereby design better ACF and bump materials for enhanced high frequency performance of the ACF joint [86–88].

The effect of low dielectric filler incorporation on high frequency behavior of ACFs was investigated. The extracted impedance model parameters for a $100 \times 100 \mu\text{m}$ bonding pad are presented in Fig. 15 for a conventional ACF with conductive particle only, and ACF with conductive particle and SiO_2 filler. In an ACF flip chip interconnect at high frequency, interconnection capacitance formed between CPW of PCB and the test chip pad is relatively high due to the high dielectric constant of the ACF resin and the large area, small gap of the parallel metal line structure in the test vehicle, compared with the solder ball flip chip structure. Therefore, the resonance frequency of the ACF flip chip interconnect is lower than that of the solder ball flip chip interconnect.

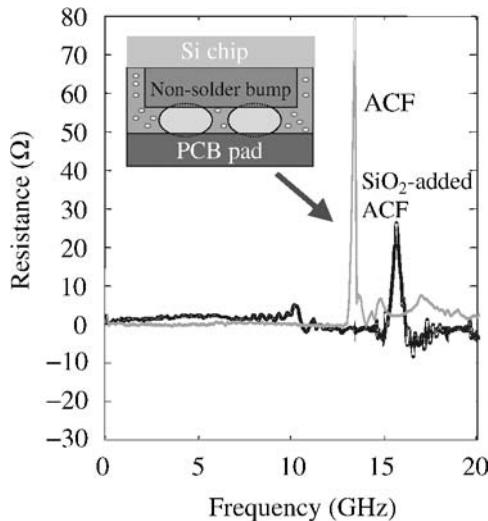


Figure 15. Impedance parameter, resistance (R) of flip chip interconnect using electroless Ni/Au bumped chip and two different ACFs in high frequency range [89].

Both ACFs show resonance frequencies, around 13 GHz for the conventional ACF and 15 GHz for the SiO_2 containing ACF. This resonance phenomenon is dominantly affected by the inductance of conductive particles and capacitance of polymer matrix. In particular, capacitance of polymer matrix is induced by the proximity effect between chip and substrate. Interestingly, the ACF with SiO_2 has resonance frequency slightly higher than the conventional ACF. ACF containing SiO_2 filler exhibited the resonance phenomenon around 15 GHz. This difference originated from dielectric constant change of polymer matrix. By adding SiO_2 filler into the ACF formulation, dielectric constant of polymer matrix in the ACF was lowered and the ACF resonance frequency was shifted to higher frequency [89].

The effect of bump metallurgy on high frequency behavior of ACF interconnects was also investigated. Figure 16 shows the impedance parameter of Au stud bumped chip packaged by ACF method, and compared with Ni/Au bumped chip. As shown in Fig. 16, Au stud bumped chip does not exhibit resonance phenomenon up to 20 GHz. This means that Au stud bumps maintain a constant impedance in the high frequency range up to 20 GHz. Capacitive coupling of the Au stud bump interconnect between the chip and substrate is relatively low due to the different bonding structure such as large gap of epoxy resin and the small area in the parallel pad structure, compared to the ACF flip chip using Ni/Au bumped chip. Consequently, the resonance frequency of the Au stud bump interconnects using an ACF is higher than that of ACF flip chip interconnect using electroless Ni/Au bump, and it was not observed up to 20 GHz.

High frequency performances of several flip chip interconnects using ACFs at RF and high frequency range were demonstrated and ACF flip chip assembly was shown as a simple and cost-effective method for high frequency devices [89].

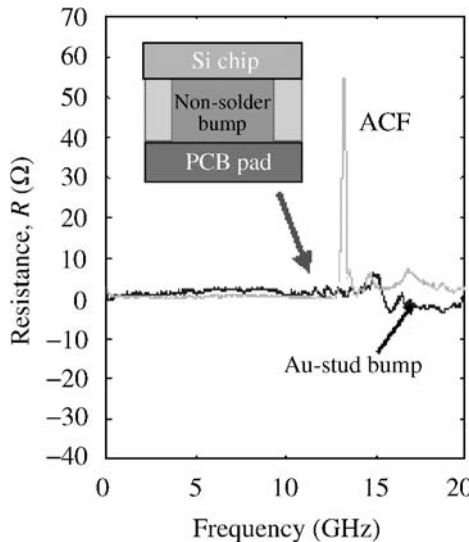


Figure 16. Impedance parameter, resistance (R) of flip chip interconnect using ACF without silica and two different chips, electroless Ni/Au bumped and Au stud bumped chips in high frequency range [89].

3.5. ACAs With Improved Thermal Properties for High Current Density Interconnections

As the current density for the ACA flip chip assembly is increasing for high current and high power dissipation device applications, the current carrying capability of the ACA is one of the important properties which have been characterized [90]. An ACA, normally a thermally poor conductor, is required to be a thermal transfer medium which allows the board to act as new heat sink for the flip chip package and improve the lifetime of ACA flip chip joint under high current density application. The effect of thermal conductivity of ACA on the current carrying capability of flip chip joints was investigated [91]. Figure 17 shows comparison results of I–V characteristics for two different ACA materials: one is a conventional ACA without any thermal filler and the other is the thermally conductive ACA with 100 phr SiC filler. The ACA flip chip joint was bias-stressed at a pair of ACA joints with Au stud bumps and the I–V curves were plotted. The conventional ACA flip chip joint shows the typical I–V curve with maximum allowable current level of 4.53 A. In contrast, the flip chip joint using a thermally conductive ACA shows almost linear increase of current with increase of voltage and the maximum allowable current level is 6.71 A. Therefore, the current carrying capability of the ACA flip chip joint was improved by using thermally conductive ACA material. Figure 18 shows the resistance changes of flip chip joints using a conventional ACA and a thermally conductive ACA as a function of time under constant current of 4.1 A. The contact resistance of the conventional ACA flip chip joint increased abruptly as time passed 50 h and had open circuit before 100 h. But the thermally conductive ACA flip chip joint showed stable contact resistance behavior without any open circuit.

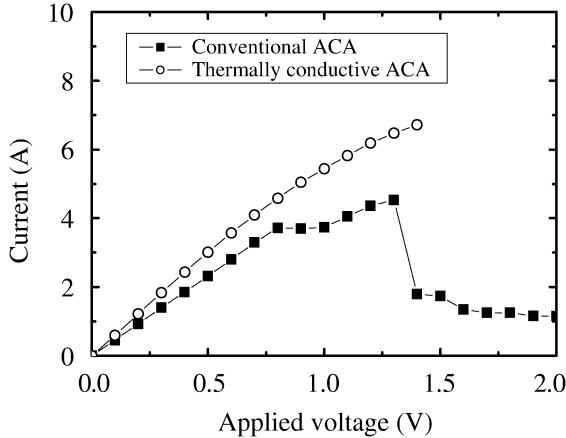


Figure 17. I–V test (bias stressing) results at flip chip joints with Au stud bumps for a conventional ACA and a thermally conductive ACA [90].

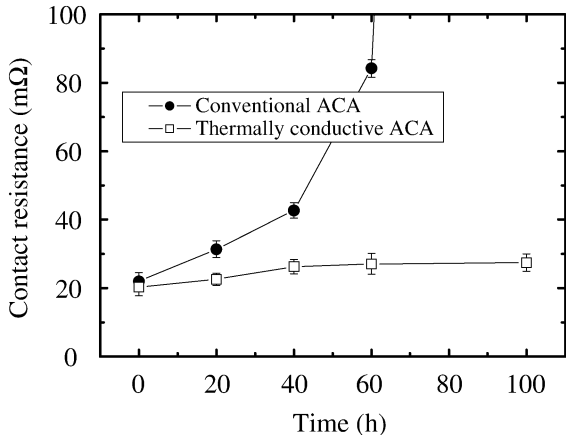


Figure 18. Contact resistance changes of flip chip joints with Au stud bump using a conventional ACA and a thermally conductive ACA after 20, 40, 60 and 100 h under current stressing [90].

The failure or degradation mechanism of ACA flip chip joints under current biasing test is suggested as follows; (1) Au–Al intermetallic compounds (IMCs) formation, (2) Crack formation and propagation along the Au/IMC interface, and (3) Al or Au depletion due to electromigration [92]. All these causes of electrical degradation of ACA flip chip joints are due to the heat accumulation at the Au stud bumps/PCB pads and thermal degradation of the adhesive due to Joule heating under high current bias. Similar discussion on the heat induced failure mechanism of flip chip joints using isotropic conductive adhesives (ICAs) under high current density was presented [93].

If the local temperature of the flip chip joint by ACA/Au stud bump is relatively low due to effective heat dissipation throughout the thermally conductive ACA, the

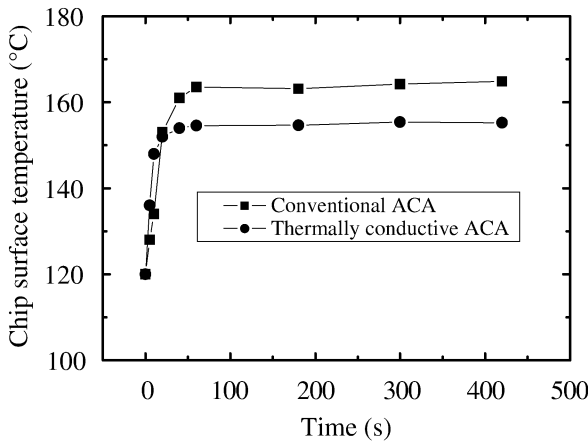


Figure 19. Chip surface temperature of flip chip assemblies using conventional and thermally conductive ACAs as a function of time under high current application condition [90].

thermal degradation process due to local Joule heating and the electrical degradation of the ACA flip chip joint are slowed down, and electrical stability is obtained. This is verified by the behavior of junction temperature on the surface of flip chip IC assemblies under current stressing condition as a function of time in Fig. 19.

The chip surface temperature increases sharply and becomes stable at around 50 s of high current application time. The chip surface using a thermally conductive ACA became hot faster than the conventional ACA joint, which means that the thermally conductive adhesive dissipates the heat from the source more easily than the conventional ACA. The maximum temperature of the chip surface of the flip chip joint using a thermally conductive ACA is lower than that of conventional ACA under constant current stressing. Therefore, the electrical reliability of a flip chip joint under high current bias condition can be improved by dissipating the heat from the hot spot and keeping the chip temperature as cool as possible.

3.6. ACAs With Improved Electrical Properties

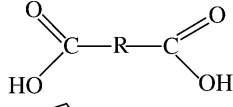
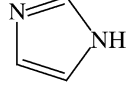
As the conductivity of ACA joints is directly determined by the mechanical contact between the terminals of chips and the electrodes on chip carriers, the bonding force plays a critical role in the electrical performance. High bonding pressure is certainly favorable to an intimate contact, and thus to a low contact resistance. In addition, all ACA flip chip joints should have uniform electrical conductivity, requiring the bonding situation of every joint to be completely the same because the bonding of all the bumps of a chip is performed simultaneously.

3.6.1. Enhancement by Organic Self-Assembly Monolayers (SAMs)

In order to enhance the electrical performance of ACA materials, organic monolayers have been introduced at the interface between metal filler and metal-finished bond pad of ACAs [94, 95]. These organic molecules adhere to the metal surface

Table 4.

Potential organic monolayer interfacial modifiers for different metal finishes

Formula	Compounds	Metal finish
H-S-R-S-H*	Dithiols	Au, Ag, Sn, Zn
N≡C-R-C≡N	Dicyanides	Cu, Ni, Au
O=C=N-R-N=C=O	Diisocyanates	Pt, Pd, Rh, Ru
	Dicarboxylates	Fe, Co, Ni, Al, Ag
	Imidazole and derivatives	Cu
R-SiOH*	Organosilicone derivatives	SiO2, Al2O3, quartz, glass, mica, ZnSe, GeO2, Au

* R denotes alky or aromatic groups.

and form physi-chemical bonds, which allow electrons to flow, and thus, it reduces electrical resistance and enables a high current flow. The unique electrical properties are due to their tuning of metal work functions by these organic monolayers. The metal surfaces can be chemically modified by the organic monoalyers and reduced work functions can be achieved by using suitable organic monolayer coatings. An important consideration when examining the advantages of organic monolayers pertains to the affinity of organic compounds to specific metal surfaces. Table 4 gives the examples of molecules preferred for maximum interactions with specific metal finishes; although only molecules with symmetrical functionalities for both head and tail groups are shown, molecules and derivatives with different head and tail functional groups can also be used for interface modification of different metal surfaces.

Dicarboxylic acids and dithiols have been introduced into ACA joints for silver-filled and gold-filled ACAs, respectively. For dithiol containing ACAs with micro-sized gold fillers, significantly lower joint resistance and higher maximum allowable current (highest current applied without inducing joint failure) were achieved for low-temperature curable ACAs (<100°C). For high curing temperature ACAs (150°C), the improvement is not as significant as for low curing temperature ACAs, due to the partial degradation of organic monolayer coating at the relatively high temperature. However, when dicarboxylic acid or dithiol was introduced into the interface of nano-silver-filled ACAs, significantly improved electrical properties could be achieved for high temperature curable ACAs, suggesting the coated organic monolayers did not suffer degradation on silver nanoparticles at the curing temperature (150°C) (Fig. 20). The enhanced bonding could be attributed to the larger surface area and higher surface energy of nano-particles, which enabled

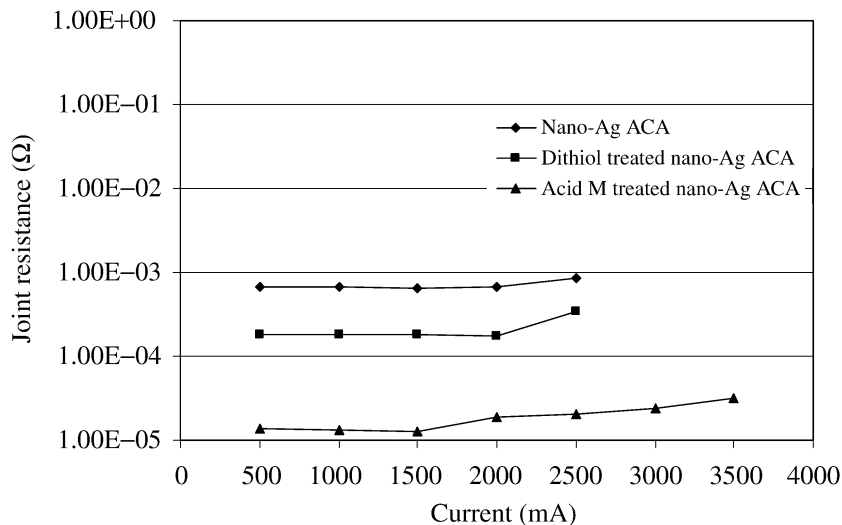


Figure 20. Joint resistance of nano-Ag-filled ACA with dithiol or dicarboxylic acid (acid M) [95].

the monolayers to be more readily coated and be relatively thermally stable on the metal surfaces [95].

3.6.2. Low-Temperature Sintering of Nano-Silver (Ag)-filled ACA

One of the concerns for an ACA/ACF is the higher joint resistance since interconnection using an ACA/ACF relies on mechanical contact, unlike the metal bonding in soldering. An approach to minimize the joint resistance of an ACA/ACF is to make the conductive fillers fuse with each other and form metallic joints such as metal solder joints. However, to fuse metal fillers in polymers does not appear feasible, since a typical organic printed circuit board ($T_g \sim 125^\circ\text{C}$), on which the metal filled polymer is applied, cannot withstand such a high temperature; the melting temperature (T_m) of Ag, for example, is around 960°C . Research showed that the T_m and sintering temperature of materials could be dramatically reduced by decreasing the particle diameter size of the materials [96, 97]. It has been reported that the surface pre-melting and sintering processes are a primary mechanism of the T_m depression of the fine nano-particles (<100 nm). For nano-sized particles, sintering could occur at much lower temperatures, and, thus, the use of fine metal particles in ACAs would be promising for fabricating high electrical performance ACA joints through eliminating the interface between metal fillers. The application of nano-sized particles can also increase the number of conductive fillers on each bond pad and result in more contact area between the fillers and bond pads. Figure 21 shows the SEM micrographs of nano-Ag particles annealed at various temperatures. Although very fine particles (20 nm) were observed for as synthesized (in Fig. 21a) and 100°C treated particles (in Fig. 21b), dramatically larger particles were observed after heat treatment at 150°C and above. With increasing temperature, the particles became larger and appeared as a solid matter rather than as porous parti-

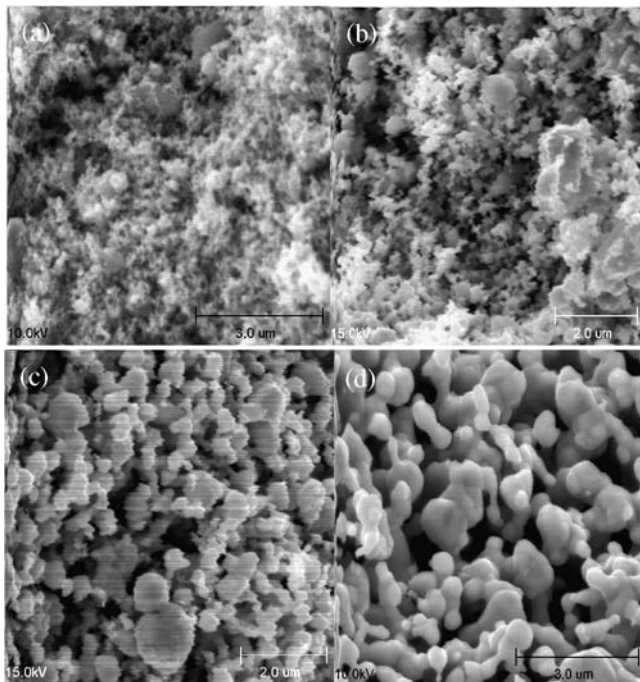


Figure 21. SEM micrographs of 20 nm-sized Ag particles annealed at different temperatures for 30 min: (a) room temperature (no annealing); (b) annealed at 100°C; (c) annealed at 150°C and (d) annealed at 200°C [94].

cles or agglomerates. The particles shown in Fig. 21c–d were fused through their surface and many dumbbell type particles could be found. The morphology was similar to a typical morphology of the initial stage in the typical sintering process of ceramic, metal and polymer powders. This low-temperature sintering behavior of the nano-particles is attributed to the extremely high inter-diffusivity of the nano-particle surface atoms, due to the significantly energetically unstable surface status of the nano-sized particles with large proportion of the surface area to the particle volume.

For the sintering reaction in any material system, temperature and duration are the most important parameters, in particular, the sintering temperature. Current–resistance (I – R) relationship of the nano-Ag-filled ACAs is shown in Fig. 22. As can be seen from the figure, with increasing curing temperature, the resistance of the ACA joints decreased significantly, from $10^{-3} \Omega$ to $5 \times 10^{-5} \Omega$. Also, higher curing temperature ACA samples exhibited higher current carrying capability than the low-temperature samples. This phenomenon suggested a higher degree of sintering of nano-Ag particles and consequently superior interfacial properties between nano-Ag filler particles and metal surfaces of the bond pads were achieved at higher temperatures [98], yet the x – y direction of the ACF maintained an excellent electrical insulation.

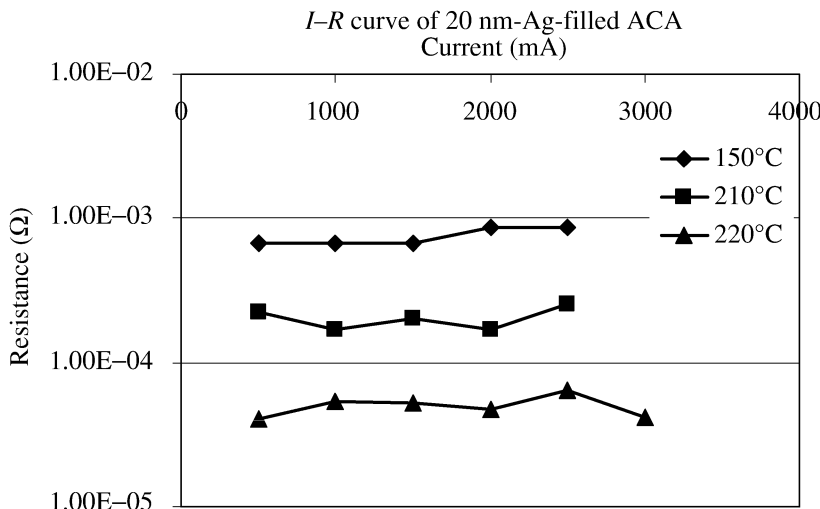


Figure 22. Current–resistance (I – R) relationship of nano-Ag-filled ACAs with different curing temperatures [98].

3.7. ACAs for Wafer Level Packaging Applications

Flip chip technology is extending its applications to the fields of smart cards, displays, computers, mobile phones, communication systems, etc. However, the flip chip technology has a drawback that the production efficiency is poor in terms of process complexity and product cost because it requires conventional solder-using complex connection processes, i.e., solder flux coating, chip/board arranging, solder bump reflowing, flux removing, underfilling and cure process. In order to reduce these complex processes, particular attention has recently been paid to wafer-level packaging technology in which wafers are coated with polymeric materials having flux and underfill functions [99, 100]. More recently, in developing new, improved flip chip connection technology, advantage has been taken of conductive adhesives, which are of lower price than solders and enable the formation of ultra-fine pitches with the potential to realize environmentally friendly, fluxless and low-temperature processes.

In spite of extensive research activity, flip chip technology using these environmentally friendly ACFs or ACAs as connecting materials suffers from the disadvantage of being inefficient in production costs requiring many processes, including chip design and bump formation for ACA flip chip packaging, mass production of connecting materials, and automation of connecting processes. Therefore, wafer level flip chip package using ACAs was developed to provide advantages in terms of production cost by simplifying the processes steps compared to the fabrication of conventional solder bump flip chip packages [101, 102].

Fabrication of wafer-level flip chip package using ACAs is comprised of forming a low priced non-solder bump on an I/O pad of each chip of a wafer, coating the ACA over the wafer, dicing the ACA-coated wafer into individual chips using

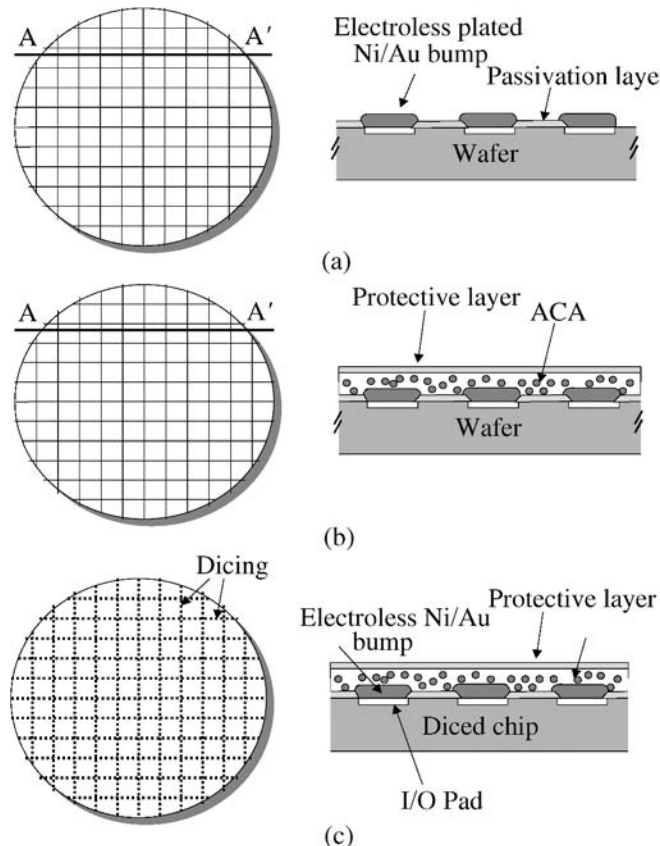


Figure 23. (a) Schematic views showing a wafer with non-solder bump formation and cross-sectional view along the line A–A', (b) schematic views showing a wafer after ACA deposition on the wafer with non-solder bump and its cross-sectional view and (c) schematic views showing a dicing process and cross-section of diced chip with ACA deposition [101].

a wafer dicing machine, and subjecting the individual chips to flip chip bonding as shown in Fig. 23. The application of ACA to the wafer with non-solder bumps can be achieved by a spraying, a doctor blade, or a meniscus coating process using ACP solution, and lamination of ACF. The film was laminated on the wafer to a thickness of 20–50 μm .

In wafer dicing process, the wafer with pre-applied ACA is mounted on a wafer dicing machine to check the scribe line of the wafer through pre-applied ACA layer, after which the wafer is diced into individual chips. In this regard, the ACA layer is required to be transparent and to have such high adhesion so as not to exhibit delamination during the process. After removing the protective layer from the diced chips, it is heat pressed against a circuit board so that the individual chips are electrically connected *via* the conductive particles of the ACA onto the substrate pads. Wafer level flip chip package using ACAs is economically favorable owing to its simplicity and environmentally friendly process.

4. Non-conductive Adhesives (NCAs) for Electronic Packaging

Electrically conductive adhesive joints can be formed using non-filled organic adhesives, i.e. without any conductive filler particles. The electrical connection with an NCA is achieved by sealing the two contact partners under pressure and heat. Thus, the small gap contact is created by approaching the two surfaces to the distance of the surface asperities. The formation of contact spots depends on the surface roughness of the contact partners. Under small bonding pressure, the two surfaces enable only a small number of contact spots to form which allow the electric current to flow. When the parts are pressed together under large bonding pressure during the sealing process, the number and area of the single contact spots are increased according to the macroscopic elasticity or flexibility of the parts and the microhardness and plasticity of the surfaces, respectively.

4.1. NCAs for Improved Electrical Properties

Since the electrical conductivity of an NCF is achieved through physical/mechanical contact and no metallurgical joints are formed, it has limited electrical conductance and current carrying capability. Low contact resistance and high current carrying capability of NCF joints are demanding properties for lead-free solder alternatives and high current density application. To ensure low contact resistance and high current density, the interface between electrodes plays an important role. The interfaces between electrodes for NCF joints must be defect free and occupy a stable contact area even under high electrical current and harsh environments. This interface control in NCF joints contributes to their performance and reliability in electronic packaging. In most NCF joints, electrical conductance between contacts depends on the constriction resistance and tunneling resistance due to the presence of ultra-thin insulating film between contacts. The control of the tunneling resistance is important in reducing the contact resistance for NCF joints [103–105]. Self-assembled monolayers (SAMs) have been extensively studied in the last decade, and recent discoveries on the capability of SAMs to functionalize materials and tune their physical and chemical properties have attracted great interest in this research area [106–110]. In particular, conjugated molecules which have a small gap between the highest occupied molecular orbital (HOMO) and the lowest unoccupied molecular orbital (LUMO) and possess delocalized π -electrons can contribute to conduction. In semiconductors, self-assembled molecular wires have been shown to be effective in tuning the metal work function (Φ) and electrical conduction of metal-molecule contact [111–115].

To enhance the electrical performance of non-conductive adhesives, conjugated molecular wires are incorporated into the NCF formulation, and the current-resistance ($I-R$) relationships of NCF joints are shown in Fig. 24 [116]. The untreated NCF joints showed a contact resistance of $0.15 \times 10^{-3} \Omega$ and current carrying capability (maximum current below which the I-V relationship remains linear) of 2.7 A. After incorporating conjugated molecular wires, the joint resistance of NCF could be reduced to $0.1 \times 10^{-3} \Omega$ and $0.05 \times 10^{-3} \Omega$ with benzo-

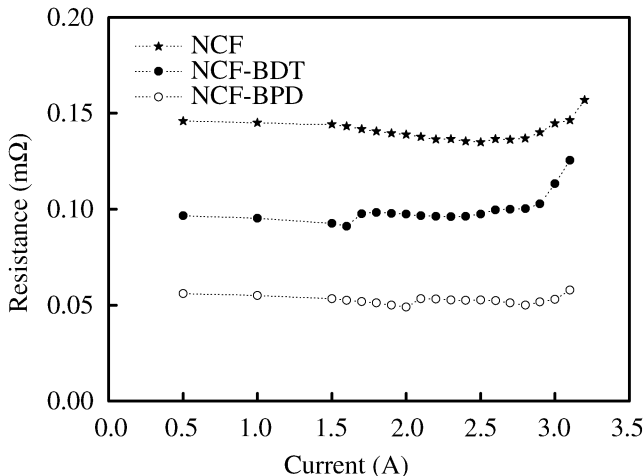


Figure 24. Electrical properties (I – R relationship) of NCF joints with molecular wires [116].

dithiol (BDT) and biphenyl dithiol (BPD), respectively. BDT containing NCF decreased the joint resistance by 1/3 and BPD containing NCF decreased the joint resistance by 2/3. In addition, the current carrying capabilities of BDT and BPD containing NCFs were increased to 2.9 A and 3.1 A, respectively. The significantly improved electrical properties of NCFs could be attributed to the enhanced interface properties, such as reduced tunneling resistance with molecular wires and the conjugated molecular wires assisted electron tunneling and current flow between the joints [117].

4.2. NCAs With Improved Reliability Properties for Flip Chip Assembly

NCAs, materials basically composed of an adhesive polymer resin and a curing agent, have attracted much attention as an alternative for ACAs for flip chip on organic boards due to the advantages of low cost and ultra-fine pitch capability [118–121]. For more wide use of flip chip technology using NCAs, it is necessary to provide good reliability data to prove the advantages of NCAs flip chip technology. The most commonly observed flip chip failure occurs during the thermal cycling test, which is due to the thermal expansion mismatch between chip and substrate. Therefore, the problem of CTE mismatch between chip and substrate becomes serious with the NCAs flip chip assembly because of high CTE of NCA materials without any filler. For this reason, novel NCAs that have low CTE for underfill-like function have been developed. Figure 25 shows the schematic drawing of flip chip chip size package (FCCSP) using an NCF for first level interconnection and its cross-sectional view of NCF joint with Au stud bump.

The addition of non-conducting silica filler in the NCA composite materials has control on the curing behavior, thermo-mechanical properties, and reliability for the NCA flip chip assembly on an organic substrate. The content of non-conducting filler was optimized for the desirable thermo-mechanical properties of NCA com-

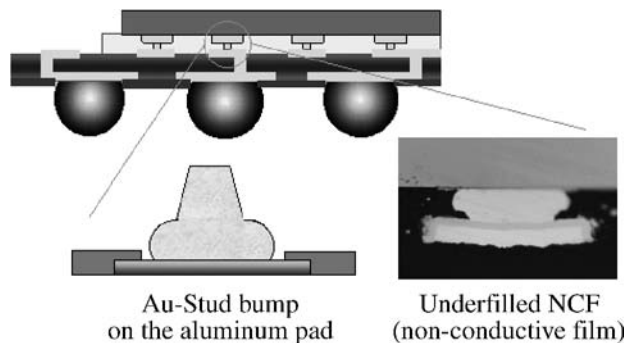


Figure 25. Schematics of flip chip CSP using an NCF and cross-section of NCF interconnection [122].

posite materials, such as proper curing profile, high Tg, low CTE and modulus, and strong adhesion. These effects of non-conducting filler addition on the NCA material properties were verified by reliability tests. The reliability of an NCA flip chip assembly using modified NCA with non-conducting filler is significantly better than that of flip chip assembly using commercial ACFs as shown in Fig. 26. Therefore, the incorporation of non-conductive fillers in the NCA composite material significantly improves the reliability of flip chip CSP using NCA materials [122, 123]. NCA materials continue to increase their applications because of their low cost, finer pitch interconnection, high reliability and processability. But the technical concerns for processing and performance of NCAs such as high bonding pressure required and electrical instability at high temperatures should be resolved [124]. Recently, nano-sized metallic fillers have been incorporated into NCA formulations for improved electrical and thermal conductivity, and reduced bonding pressure [95].

5. Conclusion

This review paper has described the recent developments, research activity and applications of electrically conductive adhesives as one of promising lead-free alternatives for electronic packaging and interconnection applications in terms of materials, processing, and reliability concerns. Electrically conductive adhesive materials have evolved to meet the higher electrical/mechanical/thermal performance, fine pitch capability, low-temperature processing and strong adhesion/reliability requirements for electronic packaging modules and assemblies. ICAs are becoming attractive in replacing SnPb or Pb-free solder alloys in die attach, SMT and flip chip assemblies with electrical, mechanical and reliability enhancements. More research investigations in improving these performances of ICAs together with comparable material cost to solder are being pursued for electronics manufacturing without solder. ACAs have been successfully used for fine pitch and Pb-free interconnection areas for flat panel displays and semiconductor packaging. New material systems for conductive fillers and adhesive matrices are being developed for ever-increasing

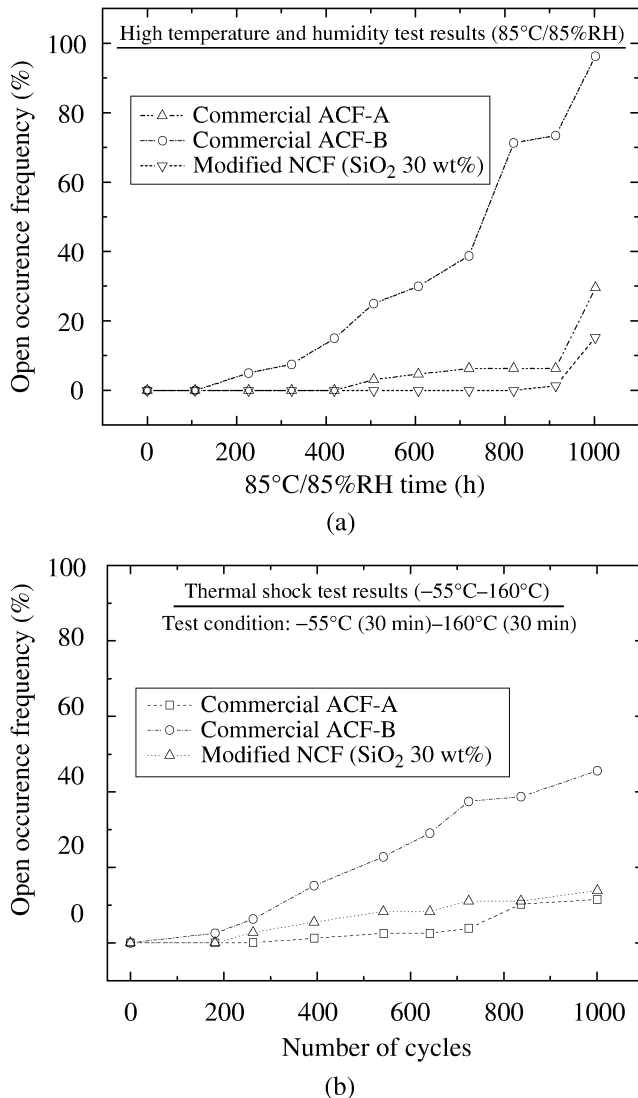


Figure 26. Open occurrence frequency of NCA flip chip interconnects (a) during $85^{\circ}\text{C}/85\%\text{RH}$ test and (b) -55°C – 160°C thermal shock test [122].

demands of electrical, thermal, and reliability performances with fine pitch, low-temperature and fast cure ability, etc. Especially multi-layered ACF structures such as double and triple-layered ACFs for fine pitch COG and COF package technologies have been developed, and underfill-like ACA/F and thermally conductive ACAs have been developed for the reliable flip chip assembly under thermal cycling and high current density environments. High frequency characteristic of ACF flip chip interconnects was also investigated and was found to be useful for RF and high frequency interconnects. Wafer level flip chip package using pre-applied ACFs was

demonstrated for wide use of ACF flip chip technology in mass production. For cost and ultra-fine pitch reasons, NCAs/NCFs are emerging materials as Pb-free and fine pitch conductive adhesive choices, and electrical performance and reliability enhancements have been achieved through materials and process optimization. Research and developments for high performance and low cost conductive adhesives are in active stage.

Electrically conductive adhesives and packaging technologies using them are expanding their applications and are offering great potential for Pb-free interconnection materials for electronic packaging applications.

References

1. J. Liu (Ed.), *Conductive Adhesives for Electronics Packaging*. Electrochemical Publications Ltd., British Isles (1999).
2. M. Jwolinski, J. Hickman, H. Rubin, Y. Zaks, S. McCarthy, T. Hanlon, P. Arrowsmith, A. Chaudhuri, R. Hermansen, S. Lan and D. Napp, *IEEE Trans. Comp. Packag. Manuf. Technol. — Part C* **19**, 241 (1996).
3. D. Lu and C. P. Wong, *IEEE Trans. Comp. Packag. Technol.* **23**, 620 (2000).
4. Y. Li, K. Moon and C. P. Wong, *Science* **308**, 1419 (2005).
5. J. C. Jagt, P. J. M. Beris and G. F. C. M. Lijten, *IEEE Trans. Comp. Packag. Manuf. Technol. — Part B* **18**, 292 (1995).
6. Y. Li and C. P. Wong, *Mater. Sci. Eng. Report* **51**, 1 (2006).
7. I. Watanabe, Y. Gotoh and K. Kobayashi, in: *Proc. Asia Display/IDW*, Nagoya, Japan, pp. 553–556 (2001).
8. H. Nishida, K. Sakamoto and H. Ogawa, *IBM J. Res. Develop.* **42**, 517 (1998).
9. D. J. Williams, D. C. Whalley, O. A. Boyle and A. O. Ogunjimi, *Soldering & Surface Mount Technol.* **5**, 4 (1993).
10. J. Liu, A. Tolvgard, J. Malmodin and Z. Lai, *IEEE Trans. Comp. Packag. Manuf. Technol.* **22**, 186 (1999).
11. P. Clot, J. F. Zeberli, J. M. Chenuz, F. Ferrando and D. Styblo, in: *Proc. Electronics Manuf. Technol. Symp., 24th IEEE/CPMT*, Austin, TX, p. 36 (1999).
12. R. L. Dietz, D. Peck, P. J. Robinson, M. G. Firmstone, P. M. Bartholomew and G. Paterson, *Soldering & Surface Mount Tech.* **9**, 55 (1997).
13. J. Miragliotta, R. C. Benson, T. E. Phillips and J. A. Emerson, in: *Proc. Mater. Res. Soc. Symp.*, Boston, MA, p. 245 (1998).
14. D. Cavasin, K. Brice-Heams and A. Arab, in: *Proc. 53rd IEEE Electronic Components and Technology Conf.*, New Orleans, LA, pp. 1404–1407 (2003).
15. R. Kisiel, *J. Electronic Packag.* **124**, 367 (2002).
16. H. de Vries, J. van Delft and K. Slob, *IEEE Trans. Comp. Packag. Technol.* **28**, 499 (2005).
17. J. Liu, Z. Lai, H. Kristiansen and C. Khoo, in: *Proc. 3rd Int'l Conf. on Adhesive Joining and Coating Technology in Electronics Manufacturing*, Binghamton, NY, pp. 1–17 (1998).
18. K. Gilleo, in: *Environment-friendly Electronics: Lead-free Technology*, J. S. Hwang (Ed.), p. 590. Electrochemical Publications Ltd., Port Erin, UK, Chapter 24 (2001).
19. S. G. Hong and M. D. Ho, *J. Environmental Sci. Health A* **34**, 2043 (1999).
20. D. Lu and C. P. Wong, *Int. J. Adhesion Adhesives* **20**, 189 (2000).
21. D. Lu, Q. K. Tong and C. P. Wong, *IEEE Trans. Comp. Packag. Technol.* **22**, 365 (1999).

22. Y. Li, K. S. Moon, A. Whitman and C. P. Wong, *IEEE Trans. Comp. Packag. Technol.* **29**, 758 (2006).
23. K. S. Moon, J. Wu and C. P. Wong, *IEEE Trans. Comp. Packag. Technol.* **26**, 375 (2003).
24. S. K. Kang, S. Buchwalter and C. Tsang, *J. Electronic Mater.* **29**, 1278 (2000).
25. Y. Li, K. S. Moon and C. P. Wong, *IEEE Trans. Comp. Packag. Technol.* **29**, 173 (2006).
26. D. Lu, Q. K. Tong and C. P. Wong, *IEEE Trans. Comp. Packag. Manuf. Technol. — Part C* **22**, 223 (1999).
27. B. Rosner, J. Liu and Z. Lai, in: *Proc. of the 46th IEEE Electronic Components and Technology Conference*, May 28–31, Orlando, FL, pp. 578–581 (1996).
28. L. Smith-Vargo, *Electronic Packaging & Production* (August), 48–49 (1986).
29. E. M. Jost and K. McNeilly, in: *Proc. of Int'l Soc. for Hybrid Microelectrncis*, Minneapolis, MN, pp. 548–553 (1987).
30. S. M. Pandiri, *Adhesives Age* (October), 31–35 (1987).
31. Y. Li, K. Moon, H. Li and C. P. Wong, in: *Proc. of 54th IEEE Electronic Components and Technology Conf.*, Las Vegas, NV, pp. 1959–1964 (2004).
32. C. Gallagher, G. Matijasevic and J. F. Maguire, in: *Proc. of 47th IEEE Electronic Components and Technology Conf.*, San Jose, CA, pp. 554–560 (1997).
33. J. W. Roman and T. W. Eagar, in: *Proc. Int'l Soc. for Hybrid Microelectrncis*, San Francisco, CA, p. 52 (1992).
34. H. J. Jiang, K. Moon, J. Lu and C. P. Wong, *J. Electronic Mater.* **34**, 1432 (2005).
35. D. Lu, Q. K. Tong and C. P. Wong, *IEEE Trans. Electr. Packag. Manuf.* **22**, 228 (1999).
36. D. Lu and C. P. Wong, *J. Appl. Polym. Sci.* **74**, 399 (1999).
37. H. Li, K. S. Moon and C. P. Wong, *J. Electronic Mater.* **33**, 106 (2004).
38. D. Durad, D. Vieau, A. L. Chu and T. S. Wei, US patent No. 5,180,523 (1989).
39. M. Hrovat, D. Belavlic and I. Hipot, *Electrotechnical Review* **58**, 93 (1991).
40. H. Schonhorn and L. H. Sharpe, US Patent No. 4,377,619 (1983).
41. M. K. Antoon, J. L. Koenig and T. Serafini, *J. Polym. Sci.* **19**, 1567 (1981).
42. M. K. Antoon and J. L. Koenig, *J. Polym. Sci.* **19**, 197 (1981).
43. P. A. Reardon, in: *Proc. Corrosion'86*, NACE, Houston, TX, p. 175 (1986).
44. M. G. Noack, in: *Proc. Corrosion'89*, NACE, Houston, TX, p. 436 (1989).
45. P. A. Reardon and W. E. Bernahl, in: *Proc. Corrosion'87*, NACE, Houston, TX, p. 438 (1987).
46. S. Romaine, in: *Proc. of the American Power Conf.*, Chicago, IL, pp. 1066–1073 (1986).
47. Y. Li, K. Moon and C. P. Wong, *J. Adhesion Sci. Technol.* **19**, 1427 (2005).
48. Y. Li, K. Moon and C. P. Wong, U.S. Patent pending (October), application date (2005).
49. C. Cheng, G. Fredrickson, Y. Xiao, Q. K. Tong and D. Lu, US Patent No. 6,344,157 (2002).
50. G. Trabanelli and V. Carassiti, in: *Advances in Corrosion Science and Technology*, G. Fontana and R. W. Staehle (Eds). Plenum Press, New York, NY (1970).
51. G. Trabanelli, in: *Corrosion Mechanisms*, F. Mansfeld (Ed.). Marcel Dekker, New York, NY (1987).
52. O. L. Riggs Jr, in: *Theoretical Aspects of Corrosion Inhibitors and Inhibition*, C. C. Nathan (Ed.). The National Association of Corrosion Engineers (NACE), Houston (1973).
53. L. J. Matienzo, F. D. Egitto and P. E. Logan, *J. Mater. Sci.* **38**, 4831 (2003).
54. H. Li, K. Moon and C. P. Wong, *J. Electronic Mater.* **33**, 106 (2004).
55. H. Takezawa, T. Mitani, T. Kitae, H. Sogo, S. Kobayashi and Y. Bessho, in: *Proc. of 8th IEEE Int'l Symp. on Adv. Packag. Mater.*, Atlanta, GA, pp. 39–143 (2002).
56. A. N. Gent and G. R. Hamed, in: *Encyclopedia of Polymer Science and Technology*, J. I. Kroschwitz, H. F. Mark, N. M. Bikales, C. G. Overberger and G. Menges (Eds). Wiley, New York, NY (1985).

57. J. Caers, X. Zhao, E. Wong, C. Ong, Z. X. Wu and R. Ranjan, in: *Proc. of the 53rd IEEE Electronic Components and Technology Conference*, New Orleans, LA, pp. 1176–1180 (2003).
58. S. Liong, C. P. Wong and W. F. Burgoyne, *IEEE Trans. Comp. Packg. Technol.* **28**, 327 (2005).
59. K. L. Mittal (Ed.), *Silanes and Other Coupling Agents*, Vol. 4. VSP/Brill, Leiden (2007).
60. K. Moon, C. Rocket and C. P. Wong, *J. Adhesion Sci. Technol.* **18**, 153 (2004).
61. A. Nagai, K. Takemura, K. Isaka, O. Watanabe, K. Kojima, K. Matsuda and I. Watanabe, in: *Proc. 2nd IEMT/IMC Symp.*, Tokyo, Japan, pp. 353–357 (1998).
62. I. Watanabe, T. Fujinawa, M. Arifuku, M. Fujii and Y. Gotoh, in: *Proc. of 9th IEEE Int'l Symp. on Adv. Packag. Mater.*, Atlanta, GA, pp. 11–16 (2004).
63. G. D. Davis and J. D. Venables, in: *Durability of Structural Adhesives*, A. J. Kinloch (Ed.), p. 43. Applied Science Essex, UK (1983).
64. H. Li, K. S. Moon, Y. Li, L. Fan, J. Xu and C. P. Wong, in: *Proc. 54th IEEE Electronic Components and Technology Conf.*, Las Vegas, NV, pp. 165–169 (2004).
65. J. Liu, *Circuit World* **19**, 4 (1993).
66. J. Liu, *Soldering & Surface Mount Technol.* **13**, 39 (2001).
67. K. Gilleo, *Soldering & Surface Mount Technol.* **7**, 12 (1995).
68. R. Joshi, *Microelectronics J.* **29**, 343 (1998).
69. I. Watanabe, K. Takemura, N. Shiozawa and T. Ohta, in: *Flip Chip Technologies*, J. H. Lau (Ed.), Chapter 9, p. 301. McGraw Hill (1996).
70. M. J. Yim, J. S. Hwang and K. W. Paik, *Int'l J. Adhesion Adhesives* **26**, 304 (2006).
71. J. Tjandra, C. L. Wong, J. How, S. Peana, M. Mita and G. Murakami, in: *Proc. Electronic Packag. Technol. Conf. EPTC*, Singapore, pp. 52–57 (1997).
72. Y. Kumano, Y. Tomura, M. Itagaki and Y. Bessho, *Microelectronic Reliab.* **41**, 525 (2001).
73. S. M. Chang, J. H. Jou, A. Hsieh, T. H. Chen, C. Y. Chang, Y. H. Wang and C. M. Huang, *Microelec. Reliab.* **41**, 2001 (2001).
74. R. Aschenbrenner, J. Gwiasda, J. Eldring, E. Zakel and H. Reichl, *Int. J. Microcircuits Electronic Packag.* **18**, 154 (1995).
75. M. J. Yim, J. Hwang, J. Kim, J. Y. Ahn, H. J. Kim, W. Kwon and K. W. Paik, *J. Electronic Mater.* **33**, 76 (2004).
76. R. Miessner, R. Aschenbrenner and H. Reichl, in: *Proc. 49nd IEEE Electronic Components and Technology Conf.*, San Diego, CA, pp. 595–601 (1999).
77. G. Sarkar, S. Mridha, T. T. Chong, W. Y. Tuck and S. C. Kwan, *J. Mater. Process Technol.* **89**, 484 (1999).
78. J. Liu and Z. Lai, *J. Electronic Packag.* **124**, 240 (2002).
79. M. J. Yim and K. W. Paik, *IEEE Trans. Comp. Packag., Manuf. Technol.* **24**, 24 (2001).
80. C. Y. Yin, H. Lu, C. Bailey and Y. C. Chan, *Soldering & Surface Mount Technol.* **18**, 27 (2006).
81. C. Yin, H. Lu, C. Bailey and Y. C. Chan, *Circuit World* **111**, 20 (2005).
82. C. Yin, H. Lu, C. Bailey and Y. C. Chan, *IEEE Trans. Electronic Packg. Manuf.* **27**, 254 (2004).
83. L. Cao, Z. Lai and J. Liu, *J. Electronic Packg.* **127**, 43 (2005).
84. M. J. Rizvi, Y. C. Chan, C. Bailey, H. Lu and A. Sharif, *Soldering & Surface Mount Technol.* **17**, 40 (2005).
85. K. K. Lee, N. H. Yeung and Y. C. Chan, *Soldering & Surface Mount Technol.* **17**, 4 (2005).
86. M. J. Yim, W. H. Ryu, Y. D. Jeon, J. H. Lee, S. Y. Ahn, J. H. Kim and K. W. Paik, *IEEE Trans. Comp. Packag. Manuf. Technol.* **22**, 575 (1999).
87. R. Sihlbom, M. Dernevnik, M. Lindgren, J. P. Starski, Z. Lai and J. Liu, *IEEE Trans. Comp. Packag. Manuf. Technol.* **21**, 469 (1998).

88. G. Dou, Y. C. Chan, J. E. Morris and D. C. Whalley, *Soldering & Surface Mount Technol.* **18**, 3 (2006).
89. M. J. Yim, I. H. Jeong, H. K. Choi, J. S. Hwang, J. Y. Ahn, W. S. Kwon and K. W. Paik, *IEEE Trans. Comp. Packag. Technol.* **28**, 789 (2005).
90. S. H. Fan and Y. C. Chan, *J. Electronic Mater.* **32**, 102 (2003).
91. M. J. Yim, H. J. Kim and K. W. Paik, *J. Electronic Mater.* **34**, 1165 (2005).
92. H. J. Kim, W. S. Kwon and K. W. Paik, in: *Proc. 5th Int'l Conference on Electronic Materials and Packaging*, Tokyo, Japan, pp. 203–208 (2003).
93. J. Haberland, B. Pahl, S. Schmitz, C. Kallmayer, R. Aschenbrenner and H. Reichl, in: *Proc. 52nd IEEE Electronic Components and Technology Conf.*, pp. 144–149 (2002).
94. Y. Li, K. Moon and C. P. Wong, *J. Electronic Mater.* **34**, 266 (2005).
95. Y. Li, K. Moon and C. P. Wong, *J. Electronic Mater.* **34**, 1573 (2005).
96. K. Moon, H. Dong, R. Maric, S. Pothukuchi, A. Hunt, Y. Li and C. P. Wong, *J. Electronic Mater.* **34**, 132 (2005).
97. M. Y. Efremov, F. Schietekatte, M. Zhang, E. A. Olson, A. T. Kwan, R. S. Berry and L. H. Allen, *Phys. Rev. Lett.* **85**, 3560 (2000).
98. Y. Li, K. Moon and C. P. Wong, *J. Appl. Polym. Sci.* **99**, 1165 (2006).
99. P. Garrou, *IEEE Trans. Adv. Packag.* **23**, 198 (2000).
100. Q. Tong, B. Ma, S. Hong, L. Nguyen, H. Nguyen and A. Negasi, in: *Proc. 52nd IEEE Electronic Components and Technology Conf.*, San Diego, CA, pp. 1366–1372 (2002).
101. K. W. Paik and M. J. Yim, US Patent No. 6,518,097 (2003).
102. H. Y. Son, C. K. Chung, M. J. Yim, J. S. Hwang, G. J. Jung, J. K. Lee and K. W. Paik, *IEEE Trans. Electr. Packg. Manuf.* **30**, 221 (2007).
103. R. Holm, *Electrical Contacts*. Springer, New York, NY (1967).
104. M. Chin, K. A. Iyer and S. J. Hu, *IEEE Trans. Comp. Packag. Technol.* **27**, 317 (2004).
105. L. Kogut and K. Komvopoulos, *J. Appl. Phys.* **95**, 576 (2004).
106. A. Ulman, *Chem. Rev.* **96**, 1533 (1996).
107. J. H. Cho, J. A. Lim, J. T. Han, H. W. Jang, J.-L. Lee and K. Cho, *Appl. Phys. Lett.* **86**, 171906 (2005).
108. G. Parthasarathy, P. E. Burrows, V. Khalfin, V. G. Kozlov and S. R. Forrest, *Appl. Phys. Lett.* **72**, 2138 (1996).
109. Y. Hirose, A. Kahn, V. Aristov and P. Soukiassian, *Appl. Phys. Lett.* **68**, 217 (1996).
110. P. G. Piva, G. A. Dilabio, J. L. Pitters, J. Zikovsky, M. Rezeq, S. Dogel, W. A. Hofer and R. A. Wolkow, *Nature* **435**, 658 (2005).
111. B. de Boer, A. Hadipour, M. M. Mandoc, T. van Woudenberg and P. W. M. Blom, *Adv. Mater.* **17**, 621 (2005).
112. T. Dadash, Y. Gordin, R. Krahne, I. Khivrich, D. Mahalu, V. Frydman, J. Sperling, A. Yacoby and I. Bar-Joseph, *Nature* **436**, 677 (2005).
113. A. Nitzan and M. A. Ratner, *Science* **300**, 1384 (2003).
114. C. Joachim, J. K. Gimzewski and A. Aviram, *Nature* **408**, 541 (2000).
115. A. V. Tivanski, Y. He, E. Borguet, H. Liu, G. C. Walker and D. H. Waldeck, *J. Phys. Chem. B* **109**, 5398 (2005).
116. Y. Li, M. J. Yim and C. P. Wong, *J. Electronic Mater.* **36**, 549 (2007).
117. H. Dong, Y. Li, M. J. Yim and C. P. Wong, *Appl. Phys. Lett.* **29**, 092102 (2007).
118. H. Yu, S. G. Mhaisalkar, E. H. Wong, L. K. Teh and C. C. Wong, *IEEE Trans. Comp. Packag. Technol.* **29**, 71 (2006).
119. W. K. Chiang, Y. C. Chan, B. Ralph and A. Holland, *J. Electronic Mater.* **35**, 443 (2006).

120. Z. W. Zhong, *J. Electronic Packag.* **127**, 29 (2005).
121. L. K. Teh, C. C. Wong, S. Mhaisalkar, K. Ong, P. S. Teo and E. H. Wong, *J. Electronic Mater.* **33**, 271 (2004).
122. M. J. Yim, J. S. Hwang, W. S. Kwon, K. W. Jang and K. W. Paik, *IEEE Trans. Electr. Packg. Manuf.* **26**, 150 (2003).
123. K. W. Paik and M. J. Yim, US patent No. 6,930,399 (2005).
124. H. C. Cheng, C. L. Ho, K. N. Chiang and S. M. Chang, *IEEE Trans. Comp. Packag. Technol.* **27**, 398 (2004).

Recent Advances in Developing High Performance Isotropic Conductive Adhesives

Daoqiang Daniel Lu^{a,*} and C. P. Wong^b

^a Intel Corporation, 5000 W. Chandler Blvd, Chandler, AZ 85226, USA

^b School of Materials Science and Engineering and Packaging Research Center, Georgia Institute of Technology, Atlanta, GA 30332-0245, USA

Abstract

Recently, significant advances have been made to improve isotropic conductive adhesive (ICA) technology. This paper provides an overview of research achievements in both electrical and mechanical aspects including electrical conductivity improvement, contact resistance mechanism elucidation and approaches to stabilize the contact resistance, and mechanical impact performance enhancement.

Keywords

Isotropic conductive adhesive, conductivity improvement, contact resistance, corrosion, corrosion inhibitor, low melting point alloy, impact performance, epoxide-terminated polyurethane

1. Introduction to Conductive Adhesive Technology

Electrically conductive adhesive (ECA) technology is one of the lead-free alternatives to soldering technology. ECAs can offer numerous advantages such as fewer processing steps which reduces processing cost, lower processing temperature which makes the use of heat-sensitive and low cost substrates possible, and fine pitch capability [1].

There are two main types of conductive adhesives, anisotropic conductive adhesives (ACAs) and isotropic conductive adhesives (ICAs) [2–8]. All of the electrically conductive adhesives consist of a polymer binder and a conductive filler. ACAs provide uni-directional electrical conductivity in the vertical or Z-axis. The discussion in this paper mainly focuses on isotropic conductive adhesives. ICAs consist of metallic particles (normally in flake form) in a polymer matrix. Typical filler loadings are 25–30 volume %. At these loadings, the materials have achieved the percolation threshold and are electrically conductive in all directions after the materials are cured. The most common ICAs are silver flake-filled thermosetting

* To whom correspondence should be addressed. Tel.: (480) 5522909; Fax: (480) 5521295.

epoxies which are typically provided as one-part thixotropic pastes. They can provide both electrical and mechanical interconnections between components after they are cured [5–8].

However, there are many limitations of the current ICA technology. The main limitations include lower conductivity, unstable contact resistance with non-noble metal finished components, and poor mechanical impact performance. The electrical conductivity of an ICA is lower than that of Sn/Pb solder. Although this conductivity might be adequate for low power electronics applications, the electrical conductivity of ICAs must be improved. Contact resistance between an ICA and non-noble metal (such as Sn or Ni) finished components increased dramatically especially under elevated temperature and humidity aging conditions [9–14]. In addition, electronic packages are subject to significant shocks during assembly, handling and throughout product life. The packages cannot survive without adequate impact performance. Most of the current commercial ICAs have poor impact performance. Components assembled using ICAs tend to fall apart from the substrate when the package experiences a sudden shock. For conductive adhesive technology to find universal appeal as a solder replacement, new conductive adhesives with desirable overall properties must be developed [12].

2. Electrical Conductivity of ICAs

The electrical conductivity of ICAs is inferior to that of solders [15]. Even though the conductivity of ICAs is adequate for most applications, higher electrical conductivity of ICAs is still needed. To develop a novel ICA for modern electronic interconnect applications, a thorough understanding of the materials is needed.

An ICA is generally composed of a polymeric matrix and a filler such as Ag flakes. There is a thin layer of organic lubricant, typically a fatty acid such as stearic acid, on the Ag flake surface. This lubricant layer plays an important role in the performance of ICAs, including the dispersion of the Ag flakes in the adhesives and the rheology of the adhesive formulations [15–18]. This organic layer is a Ag salt formed between the Ag surface and the lubricant [18, 19]. This lubricant layer affects conductivity of an ICA because it is electrically insulating. To improve conductivity, the organic lubricant layer must be partially or fully removed. Some chemical substances can be used to dissolve the organic lubricant layer [18–20]. However, the viscosity of an ICA paste might increase if the lubricant layer is removed. An ideal chemical substance (or lubricant remover) should be latent (does not remove the lubricant layer) at room temperature, but be active (capable of removing the lubricant layer) at a temperature slightly below the cure temperature of the polymer binder. The lubricant remover can be a short chain acid, a high boiling point ether such as diethylene glycol monobutyl ether and diethylene glycol monoethyl ether acetate, and a poly(ethylene glycol) with a low molecular weight [18–20]. These chemical substances can improve electrical conductivity of ICAs by removing the lubricant layer on the Ag flake surfaces and providing intimate flake–

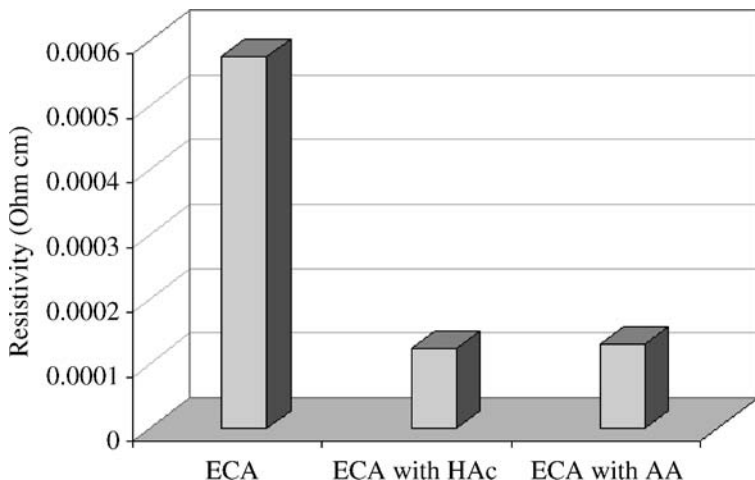


Figure 1. Effect of adding short chain acids (HAc and AA) on the resistivity of an ICA.

Table 1.

Effect of curing shrinkage on resistivity of ICAs

Formulation	Cross-link density (10^{-3} mol/cm 3)	Shrinkage (%)	Bulk resistivity (mOhm cm)
ICA1	4.50	2.98	3.0
ICA2	5.33	3.75	1.2
ICA3	5.85	4.33	0.58

flake contact [18, 19]. Figure 1 shows the impact of two short chain acids such as acetic acid (HAc) and adipic acid (AA) on the resistivity of an ICA.

In general, an ICA paste has low conductivity before cure, but the conductivity increases dramatically after the ICA is cured. The ICA achieves conductivity during the cure process, mainly through more intimate contact between Ag flakes caused by cure shrinkage of the polymer binder [21]. Cure shrinkage of the polymer binder affects the electrical conductivity of an ICA. An ICA that has higher cure shrinkage generally shows higher conductivity [21]. Therefore, increasing cure shrinkage of the polymer binder is another method for improving electrical conductivity (as shown in Table 1). For ICAs based on epoxy resins, a small amount of a multi-functional epoxy resin can be added into the ICA formulation to increase cross-link density, shrinkage, and thus increase conductivity [21, 22].

Electrical conductivity of ICAs can be improved by applying an electrical field before or during curing. An applied electrical field could improve electrical conductivity significantly; however, the exact reasons for this improvement are not yet clear [23].

Another approach for improving conductivity is to incorporate transient liquid-phase sintering metallic fillers in ICA formulations. The filler used is a mixture of a high melting point metal powder and a low melting point alloy powder. The electrical conduction is established through a plurality of metallurgical connections formed *in situ* from these two powders in a polymer binder. When heated at a specific high temperature, the low melting point alloy powder melts and diffuses rapidly into the high melting point filler and eventually solidifies at that temperature. The polymer binder fluxes both the metal powder and the metal to be joined and facilitates the transient liquid bonding of the powder particles to form a stable metallurgical network for electrical conduction and also to form an interpenetrating polymer network providing adhesion. High electrical conductivity can be achieved using this method [24–26]. One critical limitation of this technology is that the number of combinations of lower melting point filler and high melting point filler is limited. Only certain combinations of these two metallic fillers can dissolve each other and form metallurgical interconnections.

3. Contact Resistance of ICA Joints

3.1. Mechanism Underlying the Unstable Contact Resistance

The total contact resistance of an ICA joint consists of the bulk resistance of metals (R_{metal}), bulk resistance of the ICA material (R_{bulk}), and the interfacial resistance (R_{int}) between the ICA and the metal (refer to Fig. 2). The bulk resistance of the metals does not change during aging. Therefore, changes of bulk resistance of an ICA and the interfacial resistance will cause total contact resistance shifts. The change of bulk resistance of an ICA material during aging was studied first.

Bulk resistance shifts of five commercial conductive adhesives (ECA-1, ECA-2, ECA-3, ECA-4 and ECA-5) during 85°C/85% RH aging were studied and results are shown in Fig. 3. All of the five ICAs were silver flake filled and epoxy-based conductive adhesives and were from four different manufacturers. As can be seen from this figure, bulk resistance of all the ECAs decreased in the early stage of the aging and remained stable thereafter. The initial decrease of bulk resistance may

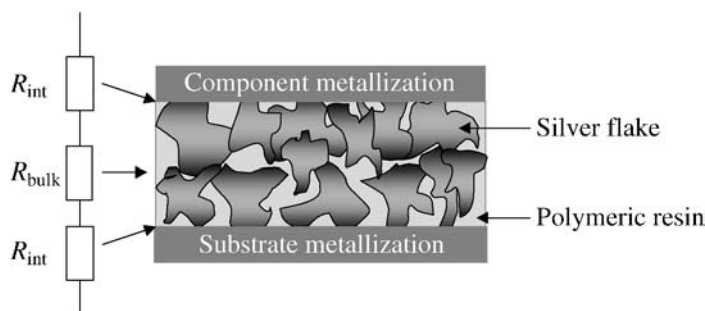


Figure 2. Contact resistance model of an ICA joint.

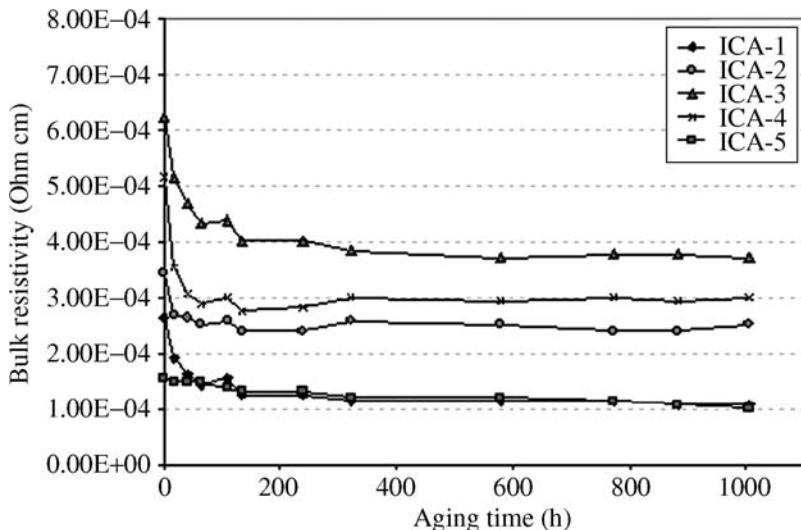


Figure 3. Bulk resistivity shifts of ICAs during 85°C/85% RH aging.

be due to further cure of the ECA. The bulk resistance of silver-filled ICAs did not change during aging because silver flakes are not susceptible to oxidation or corrosion and silver oxide is still highly electrically conductive even after silver is oxidized. It can be concluded from this study that a conductive adhesive showed stable bulk resistance during an elevated temperature and humidity aging as long as the ICA was filled with silver flakes. In other words, silver flake-filled conductive adhesives have stable bulk resistance during aging.

Contact resistance between the above ICAs and non-noble metal finished components increases dramatically during an elevated temperature and humidity aging, especially at 85°C/85% relative humidity. National Center of Manufacturing and Science (NCMS) has set a criterion for solder replacement conductive adhesives. The criterion is if the contact resistance shift after 500-h 85°C/85% RH aging is less than 20%, then the contact resistance is defined as “stable” [27]. The fact that bulk resistance of all these ECAs remained stable and contact resistance of these ICAs on non-noble metals increased during aging indicated that the contact resistance increase was caused by the increase of the interfacial resistance (R_{in}) between the ICA and the metal.

Corrosion was suggested as the possible mechanism for resistance shift in several papers [10, 11, 28–30]. A recent study confirmed that galvanic corrosion rather than simple oxidation of the non-noble metal at the interface between an ICA and the non-noble metal was the main mechanism for the shift in contact resistance of ICAs (Fig. 4) [31, 32]. The non-noble acts as an anode, and is reduced by losing electrons, and then turns into a metal ion ($M - ne^- = M^{n+}$). The noble metal acts as a cathode, and its reaction generally is $2H_2O + O_2 + 4e^- = 4OH^-$. Then M^{n+} combines with OH^- to form a metal hydroxide or metal oxide. After corrosion,

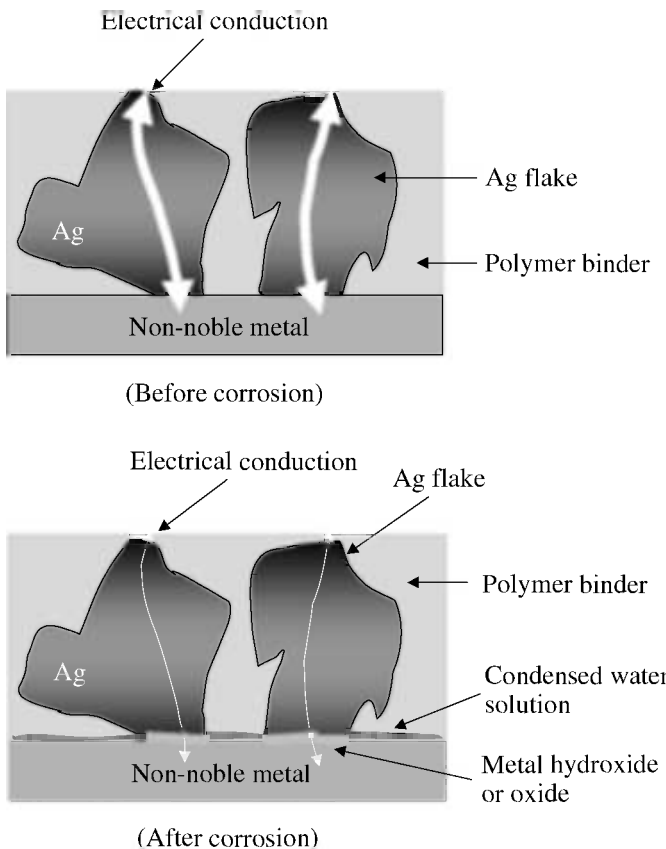


Figure 4. Metal hydroxide or oxide formation after galvanic corrosion.

a layer of metal hydroxide or metal oxide is formed at the interface. Because this layer is electrically insulating, the contact resistance increases dramatically [31, 32]. A galvanic corrosion process has several characteristics: (1) happens only under wet conditions, (2) an electrolyte must be present and (3) oxygen generally accelerates the process. Based on this finding, several methods can be employed to stabilize the contact resistance.

3.2. Effects of Electrolytes on Contact Resistance Shifts

An electrolyte solution is one of the requirements for galvanic corrosion. Electrolytes should increase the electrical conductivity of the solution, accelerate galvanic corrosion, and cause larger contact resistance increase.

The effects of four electrolytes, sodium chloride (NaCl), sodium acetate (NaAc), ammonium chloride (NH_4Cl), ammonium sulfate ($(\text{NH}_4)_2\text{SO}_4$), on contact resistance shifts of an ECA on Sn/Pb metal were investigated. The concentration of each electrolyte was 0.5 part of each electrolyte per 100 parts of the resin of the ECA.

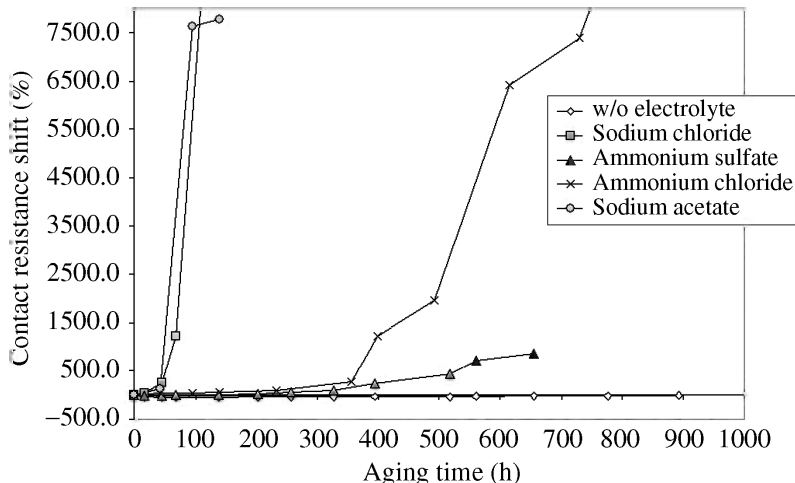


Figure 5. Effect of electrolyte on contact resistance shift of ICAs on Sn/Pb surface.

The contact resistance of the ECAs with and without the electrolytes was measured periodically during 85°C/85% RH aging. The results are shown in Fig. 5.

As can be seen from Fig. 5, the ICAs with the electrolytes showed faster increase of contact resistance than the ECA without electrolytes. Electrolytes can increase electrical conductivity of the solution and accelerate galvanic corrosion. It can be concluded from this study that, in order to stabilize contact resistance during aging, resins, hardeners, and other ingredients with low impurity contents should be used to formulate ICAs.

3.3. Effect of Moisture Adsorption on Contact Resistance Shifts

The water condensed from the adsorbed moisture at the interface between an ECA and the metal formed the electrolyte solution which was required for galvanic corrosion. Therefore, an ICA with lower moisture absorption should show slower contact resistance shift during aging due to its slower corrosion rate at the interface.

Three ICA formulations were formulated with different epoxy resins but the same hardener and catalyst. These three ICAs had similar properties but different levels of moisture absorption. The moisture absorption of the cured resins of these ICAs is shown in Fig. 6. The contact resistance shifts of these ICAs on Sn/Pb were compared and are shown in Fig. 7. Comparing Figs 6 and 7, it was found that the ICA with the highest moisture absorption (ECA-III) showed the fastest contact resistance shift and the ICA with the lowest moisture absorption (ECA-I) showed the slowest contact resistance shift during aging. Thus, there is a correlation between moisture absorption and contact resistance shift. Therefore, one of the approaches to formulate an ICA with more stable contact resistance is to select epoxy and hardener combinations which can provide ICAs with lowest moisture absorption.

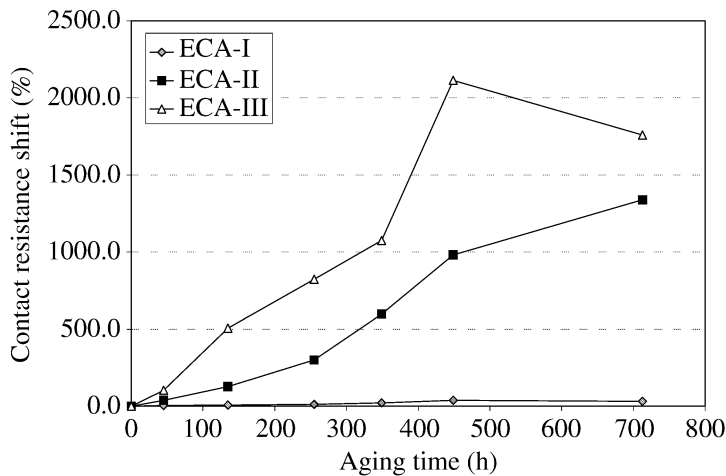


Figure 6. Moisture absorption of three ICAs (ECA-I, ECA-II and ECA-III).

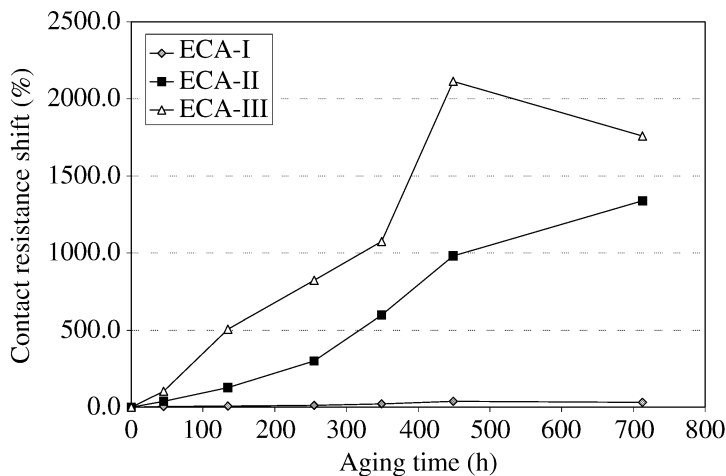


Figure 7. Contact resistance shift of three ICAs (ECA-I, ECA-II and ECA-III).

3.4. Approaches to Improve Contact Resistance Stability

Galvanic corrosion happens only in wet conditions. An electrolyte solution must be formed at the interface before galvanic corrosion can happen. Therefore, one way to prevent galvanic corrosion at the interface between an ICA and the non-noble metal surface is to lower the moisture pickup of the ICA. ICAs that had low moisture absorption generally showed more stable contact resistance on non-noble surfaces [33, 34]. Without an electrolyte, galvanic corrosion rate is very low. The electrolyte in this case is mainly from the impurity of the polymer binder (generally epoxy resins). Therefore, ICAs formulated with resins of high purity should perform better.

The second method of preventing galvanic corrosion is to incorporate some organic corrosion inhibitors into ICA formulations [32, 34, 35]. In general, organic corrosion inhibitors act as a barrier layer between the metal and the environment by being adsorbed as a film over the metal surfaces [36–39]. Some chelating compounds are especially effective in preventing metal corrosion [38]. Most organic corrosion inhibitors can react with epoxy resin at certain temperatures. Therefore, if an ICA is epoxy-based, the corrosion inhibitor must not react with the epoxy resin when the epoxy resin is cured. Otherwise, the corrosion inhibitors are consumed by reacting with the epoxy resin and lose their effect. Organic corrosion inhibitors are thoroughly summarized in the literature [37–39].

Two corrosion inhibitors (INH1) and (INH2) were used in this study. The shifts of contact resistance of the ICAs without and with corrosion inhibitors on Sn/Pb during 85°C/85% RH aging were measured and the results are shown in Fig. 8. From the figure, it can be seen that both inhibitors could slow the contact resistance increase. The ICA with INH1 showed stable contact resistance after the initial decrease even after 1400-h 85°C/85% RH aging. INH2 was not as effective as INH1.

The main mechanism of chelating corrosion inhibitors such as INH1 is that they may adsorb on a specific metal surface and form a complex film which plays an essential role in the inhibition of the metal corrosion.

The absorbance of each of corrosion inhibitor solutions was scanned for the wavelength from 600 nm to 190 nm. It was found that the INH1 and INH2 showed characteristic absorbance peaks at wavelengths of 235 nm and 263 nm, respectively. These two wavelengths were selected as the fixed wavelengths in the later measurement of the corrosion inhibitor concentrations.

A small amount (2 g) of a Sn/Pb powder was placed into 8 ml aqueous solution of INH1 and INH2 (concentration was 3×10^{-5} g/ml). The mixtures were kept at room temperature for 24 h. After the Sn/Pb powder settled down, the upper clear solution

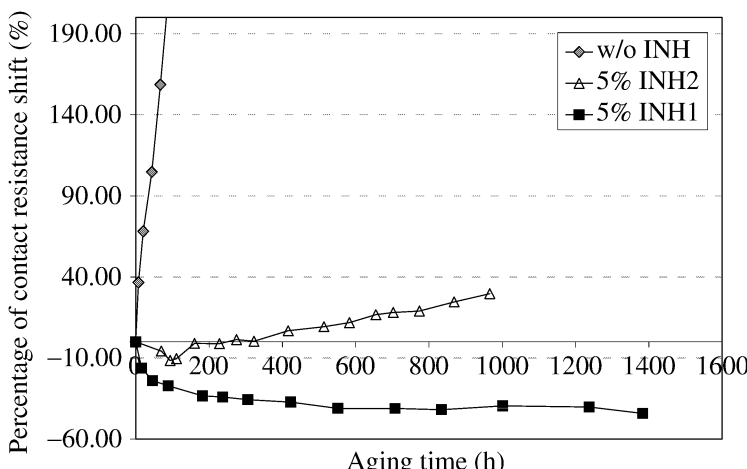


Figure 8. Contact resistance shifts of conductive adhesives with and without corrosion inhibitors.

was studied using the UV-visible spectrometry. The absorbance of the original solutions of these corrosion inhibitors, and the upper solutions from the mixtures was measured and compared. Three samplings were collected for each solution, and results are shown in Table 2. From the absorbance data in this table, it can be clearly seen that INH1 concentration in the solution decreased significantly after mixing with Sn/Pb powder for some time but INH2 concentration did not change much. This result indicated that INH1 was adsorbed on the Sn/Pb surface easily but INH2 did not. The strong absorbance of INH1 on Sn/Pb may be the reason that INH1 could effectively stabilize the contact resistance of ECAs on Sn/Pb surfaces.

Electrochemical study can elucidate the effects of corrosion inhibitors on decreasing the corrosion rate. Polarization resistance (R_p) was determined as the slope of the potentiostatic polarization curves of Sn/Pb, measured in the vicinity of the zero current. The polarization conductance ($1/R_p$), which is directly proportional to the corrosion current, was measured on Sn/Pb electrodes in the solutions. Therefore, if the Sn/Pb shows a higher polarization conductance in a solution, it is more susceptible to corrode in that solution. The polarization resistance and polarization conductance of the Sn/Pb in the electrolyte solutions without or with the inhibitors are shown in Table 3. As can be seen from the table, Sn/Pb had a much lower polarization conductance in the electrolyte solution with INH1 added than the one without an inhibitor. But Sn/Pb showed a slightly lower polarization conductance in

Table 2.

Absorbance from the UV spectra of INH1 and INH2 solutions

Sample ID	INH1 (at 235 nm)		INH2 (at 263 nm)	
	INH1 solution before mixing with Sn/Pb powder	INH1 solution after mixing with Sn/Pb powder	INH2 solution before mixing with Sn/Pb powder	INH2 solution after mixing with Sn/Pb powder
1	3.59	0.85	3.49	3.29
2	3.56	0.85	3.40	3.29
3	3.58	0.86	3.44	3.30
Average	3.57	0.85	3.44	3.29

Table 3.

Polarization resistance (R_p) and polarization conductance ($1/R_p$) of Sn/Pb in electrolyte solutions with and without inhibitors

Electrolyte solution	R_p ($\Omega \text{ cm}^2 \times 10^{-3}$)	$1/R_p$ ($\Omega^{-1} \text{ cm}^{-2} \times 10^6$)
0.2 M NaCl	3.27	306
0.2 M NaCl + 0.001 M INH2	4.10	244
0.2 M NaCl + 0.001 M INH1	7.46	134

INH2 electrolyte solution than in the electrolyte solution without an inhibitor. The results clearly indicated that Sn/Pb showed a much slower corrosion rate in NaCl solution with INH1 than INH2. Therefore, INH1 could stabilize contact resistance of ECAs on Sn/Pb much more effectively than INH2.

Some silane coupling agents, besides their traditional use as surface modifiers for adhesion improvement, can act as corrosion inhibitors to stabilize electrical contact resistance of conductive adhesive joints. Matienzo *et al.* [40] demonstrated that conductive adhesive joints were electrically stable for up to 137.5 h under 85°C/85% RH condition by treating the aluminum substrate surface with a thin layer (less than 5 nm) of an organo-silane coupling agent, which is a material capable of bonding chemically with the aluminum oxide surface layer and potentially bonding with the polymer binder in the adhesive.

Oxygen can accelerate galvanic corrosion. Therefore, another way to slow down the corrosion process is to incorporate some oxygen scavengers into ICA formulations [41]. When an oxygen molecule diffuses through the polymer binder, it reacts with the oxygen scavenger and is consumed. However, when the oxygen scavenger is depleted completely, then oxygen still can diffuse into the interface and accelerate the corrosion process. Therefore, oxygen scavengers can only delay galvanic corrosion process for some time. Similarly, the oxygen scavengers used must not react with epoxy resin at its cure temperature. Common oxygen scavengers include hydrazine, carbohydrazide, hydroquinone, gallic acid, propyl gallate, hydroxylamines and related compounds, dihydroxyacetone, 1,2-dihydro-1,2,4,5-tetrazines, erythorbic acid and oximes [41–44].

Incorporating a low melting alloy (LMA) filler into Ag-filled ICA can stabilize the contact resistance [45]. For comparison purpose, another ICA (ICA-1) was formulated using the same resin but only with silver flakes. As shown in Fig. 9, metallurgical connections between the Ag particles were formed in the ICA filled with LMA, but only physical contacts between Ag flakes were found in the ICA-1. An acid was incorporated in the ICA formulations to act as a fluxing agent. During the cure of the ICAs, the fluxing agent removed the oxide on the Ag flake surfaces, and the LMA particles melted and wetted the silver flakes and connected the silver flakes together. Due to this metallurgical connection, a lower bulk resistance was expected for the LMA-filled ICA than the ICA-1. The interconnection between the ICA and the Ni metal surface was also observed using the SEM. From Fig. 10, it can be seen that a good metallurgical connection was formed at the interface between the ICA and the Ni surface. However, for ICA containing only silver flakes (ICA-1), only physical contacts between the Ag flakes and the Ni metal were observed. Therefore, a lower contact resistance should be expected for the LMA-filled ICA than the ICA-1. It was found that the ICA with the LMA filler showed much lower initial contact resistance (0.15 Ohm) than the ICA with only the silver flakes (8.90 Ohm). The metallurgical interconnection formed between the silver flakes and the substrate (Ni) resulted in a lowered contact resistance.

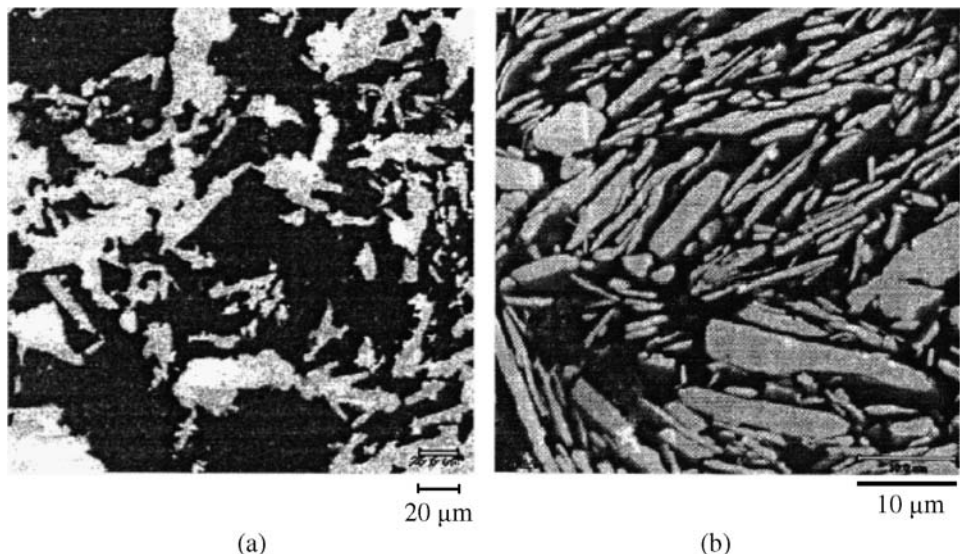


Figure 9. SEM micrographs of (a) an ICA filled with Ag flakes and an LMA filler and (b) an ICA filled only with Ag flakes.

The contact resistance shift during 85°C/85% RH aging of these two ICAs was also compared and the results are shown in Fig. 11. As can be seen from the figure, the ICA filled with silver flakes and LMA filler showed much more stable contact resistance on Ni than the ICA filled with silver flakes only. The resistance increase of the ICA filled only with silver flakes was also due to the metal oxide formation caused by galvanic corrosion during aging. However, because there were metallurgical connections between the silver flakes and the substrate (Ni), the contact resistance remained stable during the elevated temperature and humidity aging.

4. Impact Performance

Impact performance is a critical property of solder replacement ICAs. There have been continuing efforts in developing ICAs that have better impact strength and will pass the drop test, a standard test used to evaluate the impact strength of ICAs.

Nano-sized metal particles were used in ICAs to improve the electrical conduction and mechanical strength. Using nano-sized particles, agglomerates are formed due to surface tension effect [46]. Another approach is simply to decrease the filler loading to improve the impact strength [47]. However, such a process reduces the electrical properties of the conductive adhesives. A recent development was reported where conductive adhesives were developed using resins of low modulus so that this class of conductive adhesives could absorb the impact energy developed during the drop test [48]. However, the electrical properties of these materials were not mentioned in the paper. Conformal coating of the surface-mounted devices was

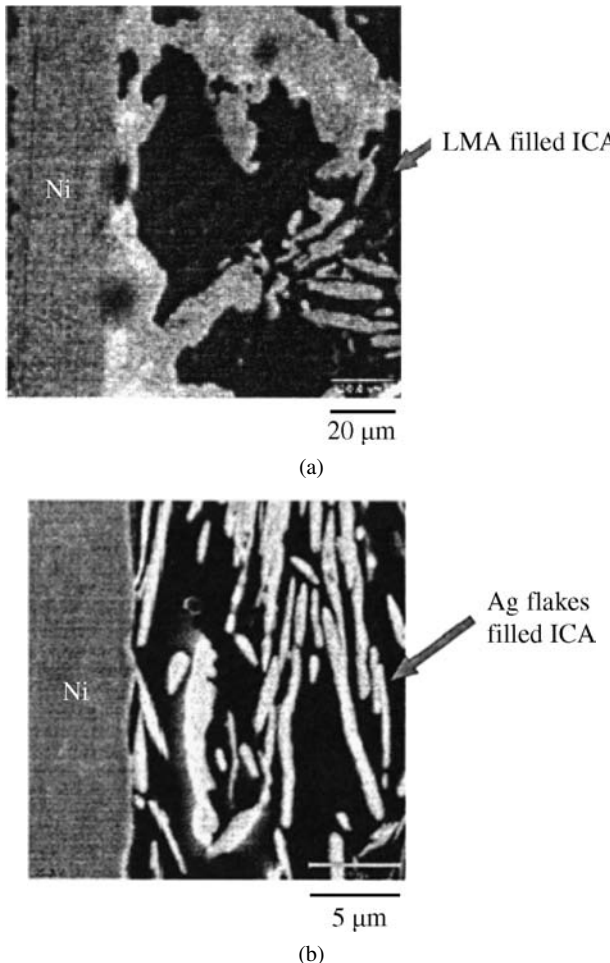


Figure 10. SEM micrographs of joints formed between (a) a Ni substrate and an ICA filled with Ag flakes and LMA and (b) an ICA filled with only Ag flakes.

used to improve mechanical strength. It was demonstrated that conformal coating could improve the impact strength of conductive adhesives joints [49].

More recently, a new class of conductive adhesives which is based on an epoxide-terminated polyurethane (ETPU) has been developed [50–52]. This class of conductive adhesives has the properties of polyurethane materials, such as high toughness and good adhesion. The modulus and glass transition temperature of the ICAs can be adjusted by incorporating some epoxy resins such as bisphenol-F epoxy resin. Conductive adhesives based on the ETPU showed a broad loss factor ($\tan \delta$) peak with temperature and a high $\tan \delta$ value at room temperature. The $\tan \delta$ value of a material is a good indication of the damping property and impact performance of the material. In general, the higher the $\tan \delta$ value, the better the damping property (impact strength) of the material. As an example, changes in $\tan \delta$ and modulus

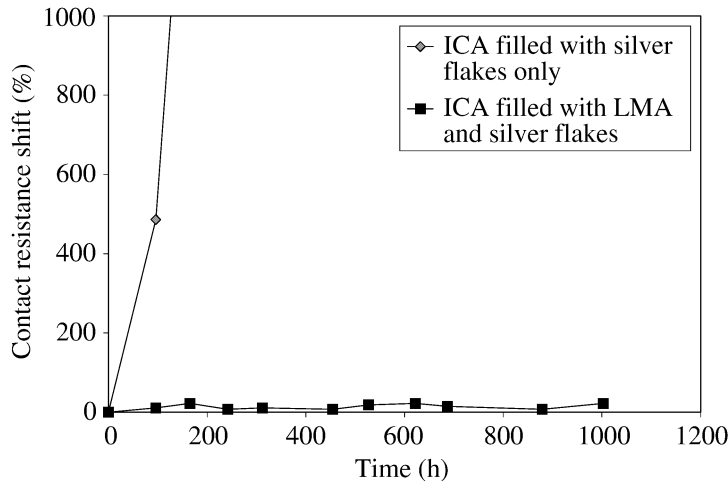


Figure 11. Contact resistance shifts of ICAs on nickel surface.

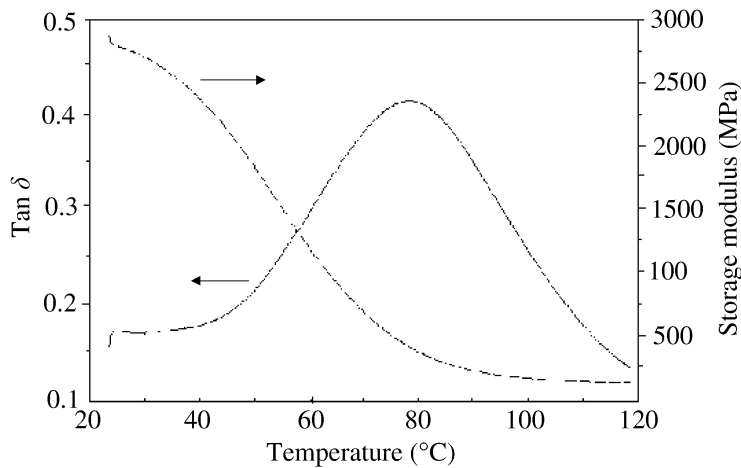


Figure 12. Changes of $\tan \delta$ and storage modulus with temperature of an ETPU-based conductive adhesive.

with temperature of an ETPU-based ICA which were Measured by a Dynamic Mechanical Analyzer (DMA) are shown in Fig. 12. ICA based on ETPU resin also showed much higher loss factor ($\tan \delta$) in a wide frequency range than the ICA based on bisphenol-F epoxy resin (Fig. 13). This indicated that the ICAs based on ETPU resin should exhibit good damping property and improved impact performance in different electronic packages. This class of conductive adhesives showed superior impact performance and substantially stable contact resistance with non-noble metal surfaces, such as Sn/Pb, Sn and Cu [50–52].

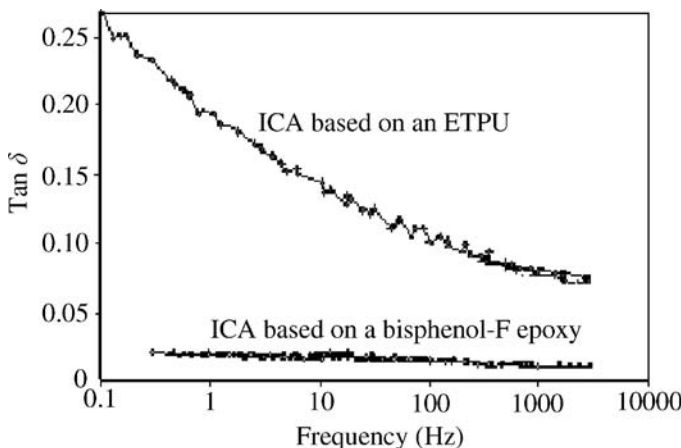


Figure 13. Loss factor ($\tan \delta$) *versus* frequency of two ICA materials.

5. Summary

Significant progress has been made in the last few years to address various issues of ICA technology. Conductivity mechanism was studied and different effective approaches such as adding silver flake lubricant removers and increasing resin curing shrinkage to enhance the conductivity of ICAs were demonstrated. The mechanism underlying the unstable contact resistance of ICAs was clearly elucidated. Based on this understanding, various ways to stabilize contact resistance of ICAs, such as utilizing pure resin with low moisture pickup, adding oxygen scavengers, adding corrosion inhibitors, and incorporating low melting alloy filler, were studied. An effective corrosion inhibitor was identified and its mechanism was elucidated too. Finally, an epoxy-terminated polyurethane resin was demonstrated to be an effective resin to dramatically enhance the mechanical impact performance of an ICA.

References

1. R. Cdenhead and D. DeCoursey, *Intl. J. Microelectronics* **8**(3), 14 (1985).
2. J. C. Jagt, *IEEE Trans. Components, Packaging, Manufacturing Technol. (Part A)* **21**, 215 (1998).
3. A. O. Ogunjimi, O. Boyle, D. C. Whalley and D. J. Williams, *J. Electronics Manuf.* **2**, 109 (1992).
4. P. G. Harris, *Soldering Surface Mount Technol.* **20**, 19 (1995).
5. K. Gilleo, *Soldering Surface Mount Technol.* **19**, 12 (1995).
6. J. Liu, Z. Lai, H. Kristiansen and C. Khoo, in: *Proceedings of the 3rd International Conference on Adhesive Joining & Coating Technology in Electronics Manufacturing*, pp. 1–17, Binghamton, NY (1998).
7. S. Corbett and M. J. Dominano, *Surface Mount Technol.* **48**, 48–52 (1997).
8. J. Bolger and S. Morano, *Adhesives Age* **17**, 17–20 (1984).
9. M. A. Gaynes, R. H. Lewis, R. F. Saraf and J. M. Roldan, *IEEE Trans. Components, Packaging, Manufacturing Technol. (Part B)* **18**, 299 (1995).
10. G. Nguyen, J. Williams, F. Gibson and T. Winster, in: *Proceedings of International Electronic Packaging Conference*, pp. 479–486, Binghamton, NY (1993).

11. J. C. Jagt, P. J. M. Beric and G. F. C. M. Lijten, *IEEE Trans. Components, Packaging, Manufacturing Technol. (Part B)* **18**, 292–298 (1995).
12. M. Zwolinski, J. Hickman, H. Rubon and Y. Zaks, in: *Proceedings of the 2nd International Conference on Adhesive Joining & Coating Technology in Electronics Manufacturing*, pp. 333–340, Stockholm, Sweden (1996).
13. H. Botter, in: *Proceedings of the 2nd International Conference on Adhesive Joining & Coating Technology in Electronics Manufacturing*, pp. 30–37, Stockholm, Sweden (1996).
14. C. P. Wong, D. Lu, S. Vona and Q. K. Tong, in: *Proceedings of the 1st IEEE International Symposium on Polymeric Electronics Packaging*, pp. 80–85, Norrkoping, Sweden (1997).
15. L. Smith-Vargo, *Electronic Packaging & Production* **48**, 48–49 (1986).
16. E. M. Jost and K. McNeilly, in: *Proceedings of ISHM*, pp. 548–553, Bournemouth, England (1987).
17. S. M. Pandiri, *Adhesives Age*, 31 (Oct.) (1987).
18. D. Lu, Q. K. Tong and C. P. Wong, *IEEE Trans. Components, Packaging, Manufacturing Technol. (Part A)* **22**, 365 (1999).
19. D. Lu, Q. Tong and C. P. Wong, in: *Proceedings of 1998 International Symposium on Advanced Packaging Materials*, pp. 256–260, Braselton, GA (1998).
20. A. J. Lovinger, *J. Adhesion* **10**, 1 (1979).
21. D. Lu, Q. K. Tong and C. P. Wong, *IEEE Trans. Components, Packaging, and Manufacturing Technol. (Part C)* **22**, 223 (1999).
22. D. Lu and C. P. Wong, *Intl. J. Adhesion Adhesives* **20**, 189 (2000).
23. J. Morris and C. Cook, in: *Proceedings of the 2nd IEEE International Symposium on Polymeric Electronic Packaging*, pp. 15–26, Gothenburg, Sweden (1999).
24. C. Gallagher, G. Matijasevic and J. F. Maguire, in: *Proceedings of the 47th IEEE Electronic Components and Technology Conference*, pp. 554–560, San Jose, CA (1997).
25. J. W. Roman and T. W. Eagar, *Proceedings of ISHM*, 52–57 (Nov.) (1992).
26. C. Gallagher, G. Matijasevic and A. Capote, US Patent No. 5,863,622 (1998).
27. M. Zwolinski, J. Hickman, H. Rubin Y. Zaks, S. McCarthy, T. Hanlon, P. Arrowsmith, A. Chaudhuri, R. Hermansen, S. Lan and D. Napp, *IEEE Trans. Components, Hybrids Manufacturing Technol. (Part C)* **19**, 241 (1996).
28. H. Botter, in: *Proceedings of the 2nd International Conference on Adhesive Joining & Coating Technology in Electronics Manufacturing*, pp. 30–37, Stockholm, Sweden (1996).
29. K. Gilleo, *Circuits Assembly*, 50 (Feb.) (1994).
30. K. Gilleo, *Circuits Assembly*, 52 (Jan.) (1994).
31. D. Lu, Q. K. Tong and C. P. Wong, *IEEE Trans. Components, Packaging, Manufacturing Technol. (Part C)* **22**, 228 (1999).
32. Q. K. Tong, G. Fredrickson, R. Kuder and D. Lu, in: *Proceedings of the 49th IEEE Electronic Components and Technology Conference*, pp. 347–352, San Diego, CA (1999).
33. D. Lu and C. P. Wong, *J. Appl. Polym. Sci.* **74**, 399 (1999).
34. D. Lu and C. P. Wong, in: *Proceedings of 4th International Symposium and Exhibition on Advanced Packaging Materials, Processes, Properties and Interfaces*, pp. 288–294, Braselton, GA (1999).
35. Q. K. Tong, A. Xiao and D. Lu, US Patent No. 6,344,157 (2002).
36. H. Leidheiser, Jr., *J. Coatings Technol.* **53**, 29 (1981).
37. G. Trabanelli and V. Carassiti, in: *Advanced Corrosion Science and Technology*, M. G. Fontana and R. W. Staehle (Eds), Vol. 1, pp. 147–229. Plenum Press, New York, NY (1970).

38. G. Trabanelli, in: *Corrosion Mechanisms*, F. Mansfeld (Ed.), pp. 119–164. Marcel Dekker, New York, NY (1987).
39. O. L. Riggs, Jr., in: *Corrosion Inhibitors*, C. C. Nathan (Ed.), pp. 2–27. NACE, Houston (1973).
40. L. J. Matienzo, F. D. Egitto and P. E. Logan, *J. Mater. Sci.* **38**, 4381 (2003).
41. P. A. Reardon, *Proc. Corrosion'86*, Paper no. 175, NACE, Houston, TX (1986).
42. M. G. Noack, *Proc. Corrosion'89*, Paper no. 436, NACE, Houston, TX (1989).
43. P. A. Reardon and W. E. Bernahl, *Proc. Corrosion'87*, Paper no. 438, NACE, Houston, TX (1987).
44. S. Romaine, in: *Proceedings of the American Power Conference*, pp. 1066–1073, Chicago, IL (1986).
45. D. Lu and C. P. Wong, *IEEE Trans. Electronics Packaging Manufacturing* **23**, 185 (2000).
46. S. Kotthaus, R. Haug, H. Schafer and O. D. Hennemann, in: *Proceedings of 1st IEEE International Symposium on Polymeric Electronics Packaging*, pp. 64–69, Norrkoping, Sweden (1997).
47. S. Macathy, in: *Proceedings of Surface Mount International*, pp. 562–567, San Jose (1995).
48. S. A. Vona and Q. K. Tong, in: *Proceedings of 4th International Symposium and Exhibition on Advanced Packaging Materials, Processes, Properties and Interfaces*, pp. 261–267, Braselton, GA (1998).
49. J. Liu and B. Weman, in: *Proceedings of the 2nd International Symposium on Electronics Packaging Technology*, pp. 313–319, Shanghai, China (1996).
50. D. Lu and C. P. Wong, *IEEE Trans. Components, Packaging, Manufacturing (Part C)* **22**, 324 (1999).
51. D. Lu and C. P. Wong, US Patent No. 6,740,192 (2004).
52. Y. Rao, D. Lu and C. P. Wong, *Intl. J. Adhesion Adhesives* **24**, 449 (2004).

This page intentionally left blank

Recent Advances in Nano-conductive Adhesives

Daoqiang Daniel Lu^{a,*}, Yi Grace Li^b and C. P. Wong^b

^a Intel Corporation, 5000 W. Chandler Blvd., Chandler, AZ 85226, USA

^b School of Materials Science and Engineering, Georgia Institute of Technology,
Atlanta, GA 30332, USA

Abstract

Nano-conductive adhesives have been attracting more and more interest in microelectronic packaging field due to their unique electrical and mechanical properties compared to conventional conductive adhesives. There has been extensive research on nano-conductive adhesives which contain nano-fillers such as nanoparticles, nano-wires or carbon nano-tubes. This paper provides a comprehensive review of most recent advances in nano-conductive adhesives.

Keywords

Isotropic conductive adhesives, anisotropic conductive adhesives, nano-wires, nano-particles, carbon nano-tubes, conductivity, self-assembled monolayers, silver migration, fine pitch flip chip interconnection

1. Introduction

Electrically conductive adhesives (ECAs) are composites of polymeric matrices and electrically conductive fillers. Polymeric matrices have excellent dielectric properties and thus are electrical insulators. The conductive filler provides the electrical properties and the polymeric matrix provides mechanical properties. Therefore, electrical and mechanical properties are provided by different components, which is different from metallic solders that provide both the electrical and mechanical properties. ECAs have been available for some time. Metal-filled thermoset polymers were first patented as electrically conductive adhesives in the 1950s [1–3]. Recently, ECA materials have been identified as one of the major alternatives for lead-containing solders for microelectronic packaging applications. There are two types of conductive adhesives: isotropically conductive adhesives (ICAs) and anisotropically conductive adhesives/films (ACAs/ACFs).

Isotropic conductive adhesives, also known as “polymer solder”, are conductive in all directions. The conductive fillers provide the composite with electrical con-

* To whom correspondence should be addressed. Tel.: (480) 5522909; Fax: (480) 5521295; e-mail: daniellu66@gmail.com

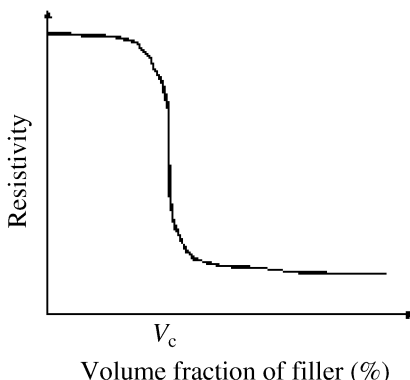


Figure 1. Effect of filler volume fraction on the resistivity of ICA systems.

ductivity through contact between the conductive particles. With increasing filler concentration, the electrical properties of an ICA transform it from an insulator to a conductor. Percolation theory has been used to explain the electrical properties of ICAs. At low filler concentrations, the resistivity of ICAs decreases gradually with increasing filler concentration. However, the resistivity drops dramatically above a critical filler concentration, V_c , called the percolation threshold (as shown in Fig. 1). It is believed that at this concentration, all the conductive particles contact each other and form a three-dimensional network. The resistivity decreases only slightly with further increase in the filler concentration [4–6]. In order to achieve conductivity, the volume fraction of conductive filler in an ICA must be equal to or slightly higher than the critical volume fraction. Similar to solders, ICAs provide the dual functions of electrical connection and mechanical bond in an interconnection joint. In an ICA joint (Fig. 2), the polymer resin provides mechanical stability and the conductive filler provides electrical conductivity. Filler loading levels that are too high cause the mechanical integrity of adhesive joints to deteriorate. Therefore, the challenge in formulating an ICA is to maximize conductive filler content to achieve a high electrical conductivity without adversely affecting the mechanical properties. In a typical ICA formulation, the volume fraction of the conductive filler is about 25 to 30% [7, 8].

Recently, anisotropic conductive adhesives/films (ACAs/ACFs) has become popular as one of promising candidates for lead-free interconnection solutions in microelectronic packaging application due to their technical advantages such as fine pitch capability (<40 μm pitch), low temperature processing ability, low cost and environmentally-friendly materials and processing, etc. ACAs/ACFs consist of conducting particles (typically 5–10 μm in diameter) and a polymer matrix which provide both attachment and electrical interconnection between electrodes [9–11]. In particular, ACFs are widely used for high-density interconnection between liquid-crystal display (LCD) panels and tape carrier packages (TCPs) to replace the traditional soldering or rubber connectors. In LCD applications, traditional soldering may not be as effective as ACFs in interconnecting materials

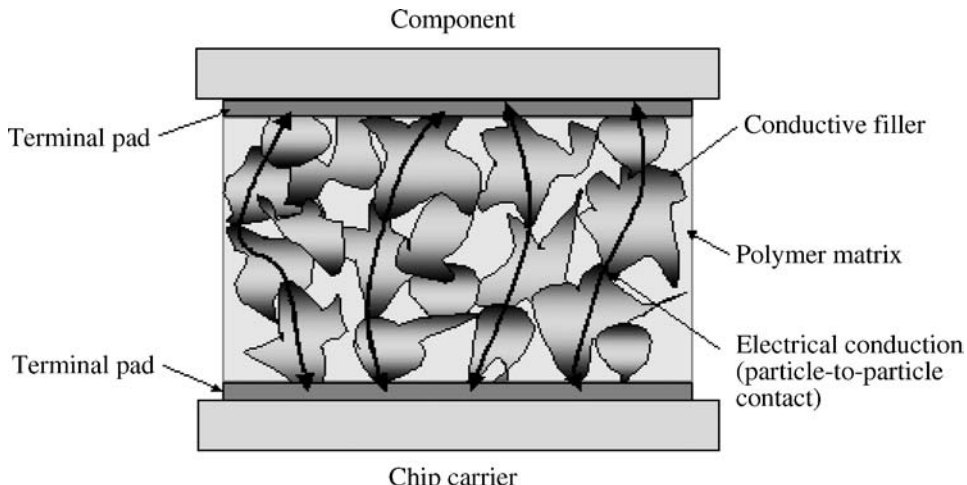


Figure 2. Schematic illustrating how electrical conduction paths are established by uninterrupted particle-to-particle contact between the component and chip carrier terminal pads in an ICA joint.

between indium tin oxide (ITO) electrodes and TCP. ACFs have also been used as an alternative to soldering for interconnecting TCP input lead bonding to printed circuit boards (PCBs). ACAs/ACFs provide uni-directional electrical conductivity in the vertical or Z-axis. This directional conductivity is achieved by using a relatively low volume loading of conductive filler (5–20 volume percent). The low volume loading is insufficient for inter-particle contact and thus prevents conductivity in the X-Y plane of the adhesive. The ACA/ACF is interposed between the two surfaces to be connected. Heat and pressure are simultaneously applied to this stack until the conductive particles bridge the two conductor surfaces. Figure 3 shows the configuration of a component and a substrate bonded with an ACA. Once the electrical continuity is produced, the polymer matrix is hardened by thermally initiated chemical reaction (for thermosets) or by cooling (for thermoplastics). The hardened dielectric polymer matrix holds the two components together and helps maintain the pressure contact between component surfaces and conductive particles. Because of the anisotropy, ACA/ACF can be deposited over the entire contact region without electrically shorting adjacent electrical contacts, greatly facilitating materials application. Also, an ultrafine pitch interconnection (<40 µm) can be achieved easily. The fine pitch capability of ACA/ACF would be limited by the particle size of the conductive filler, which can be a few micrometers or only a few nanometers in diameter.

To meet the requirements for future fine pitch and high-performance interconnects in advanced packaging, ECAs with nano-materials are attracting more and more interest due to their specific electrical, mechanical, optical, magnetic and chemical properties. There has been extensive research on nano-conductive adhesives which contain nano-fillers such as nano-particles, nano-wires or carbon

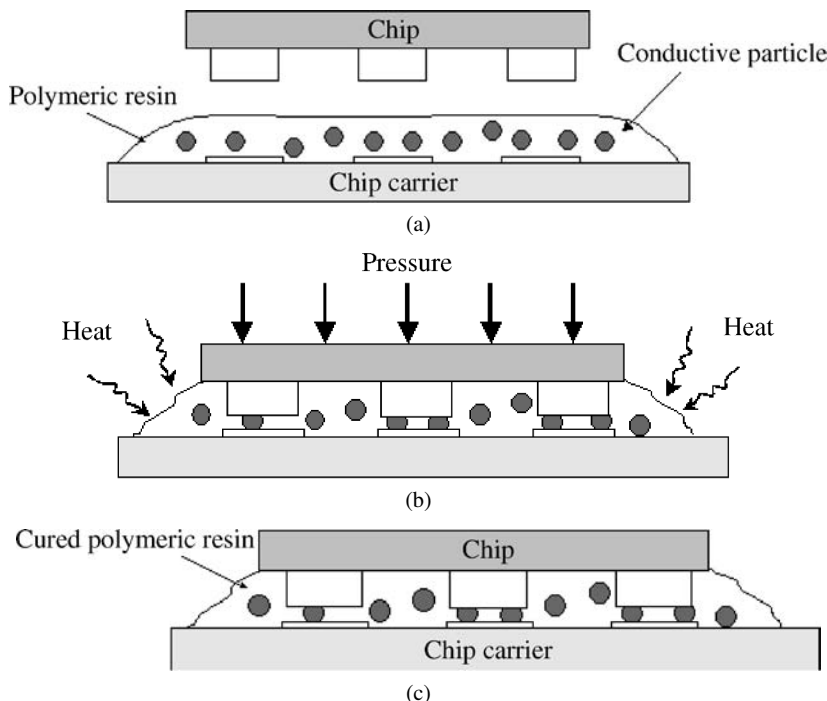


Figure 3. A series of schematics illustrating the steps in forming an ACA joint. (a) Component parts: a bumped die and mating carrier with ACA spread over the surface. (b) Die is mounted with the carrier and held in place when cured. (c) Side view of the completed assembly.

nano-tubes. This paper provides a comprehensive review of most recent research results on nano-conductive adhesives.

2. Recent Advances in Nano-isotropic Conductive Adhesives (Nano-ICAs)

2.1. ICAs with Silver Nano-wires

Wu *et al.* [12] developed an epoxy-based ICA filled with silver nano-wires, and compared the electrical and mechanical properties of this nano-ICA to two other ICAs filled with micrometer-sized (roughly 1 μm and 100 nm) silver particles. The nano-wires had a diameter of roughly 30 nm and a length up to 1.5 μm , and the nano-wires were polycrystalline in nature. It was found that at a low filler loading (e.g., 56 wt%), the bulk resistivity of ICA filled with the Ag nano-wires was significantly lower than the ICAs filled with 1 μm or 100 nm silver particles. The better electrical conductivity of the ICA filled nano-wires was contributed by the lower contact resistance between nano-wires and a more significant contribution from the tunneling effect among the nano-wires [12].

It was also found that at the same filler loading (e.g., 56 wt%), the ICAs filled with Ag nano-wires showed shear strength similar to that of the ICAs filled with the 1 μm and 100 nm silver particles. However, to achieve the same level of electrical conductivity, the filler loading must be increased to at least 75 wt% for the ICA filled with micrometer-sized Ag particles, and the shear strength of these ICAs is then decreased (lower than that of the ICAs filled with 56 wt% nano-wires) due to the higher filler loading.

2.2. Effect of Nano-sized Silver Particles on the Conductivity of ICAs

Lee *et al.* [13] studied the effect of nano-sized filler on the conductivity of conductive adhesives by substituting nano-sized Ag colloids for micro-sized Ag particles partially or wholly in a polymeric system (poly(vinyl acetate) — PVAc). Electrical resistivity was then measured as a function of silver volume fraction.

It was found that when nano-sized silver particles were added into the system at 2.5 wt% increment, the resistivity increased in almost all cases, except when the quantity of micro-sized silver was slightly lower than the percolation threshold value. At that point, the addition of the about 2.5 wt% brought about significant decrease in resistivity. Near the percolation threshold, when the micro-sized silver particles are still not connected, the addition of a small amount of nano-sized silver particles helps to build the conductive network and thus lowers the resistivity of the composite. However, when the filler loading is above the percolation threshold and all the micro-sized particles are connected, the addition of nano-particles seems only to increase the relative contribution of contact resistance between the particles. Due to its small size, for a fixed amount of addition, the nano-sized silver colloid contains a larger number of particles when compared with micro-sized particles. This large number of particles should be beneficial to the interconnection between particles. However, it also inevitably increases the contact resistance. As a result, the overall effect is an increase in resistivity upon the addition of nano-sized silver colloids.

Ye *et al.* [14] also reported a similar phenomenon, i.e. the addition of nanoparticles showed a negative effect on electrical conductivity. They proposed two types of contact resistance, i.e. restriction resistance due to small contact area and tunneling resistance when nano-particles are included in the system. It was believed that the conductivity of micro-sized Ag particle filled adhesives was dominated by constriction resistance, while that of the nano-particle-containing conductive adhesives was controlled by tunneling and even thermionic emission. Fan *et al.* [15] also observed a similar phenomenon (adding nano-size particles reduced both electrical and thermal conductivities).

Lee *et al.* [13] also studied the effect of temperature on the conductivity of ICAs. Heating the composite to a higher temperature can reduce the resistivity quite significantly. This is likely due to the high activity of nano-sized particles. For micro-sized paste, this temperature effect was considered negligible. The interdiffusion of silver atoms among nano-sized particles helped to reduce the contact resistance

quite significantly and the resistivity reached 5×10^{-5} Ohm cm after treatment at 190°C for 30 min. Jiang *et al.* [16] showed that when suitable surfactant was used in the nano-Ag containing ICA, the dispersion and interdiffusion of silver atoms among nano-sized particles could be facilitated and the resistivity of ICA could be reduced to 5×10^{-6} Ohm cm.

2.3. ICAs Filled with Aggregates of Nano-sized Ag Particles

To improve the mechanical properties under thermal cycling conditions while still maintaining an acceptably high level of electric conductivity, Kotthaus *et al.* [17] studied an epoxy-based ICA material system filled with aggregates of nano-sized Ag particles. The idea was to develop a new filler material which did not deteriorate the mechanical property of the polymer matrix to a great extent. A highly porous Ag powder was attempted to fulfill this requirement. The Ag power was produced by the inert gas condensation (IGC) method. The powder consisted of sintered networks of ultra-fine particles in the size range from 50 to 150 nm. The mean diameter of these aggregates could be adjusted up to some micrometers. The as-sieved powder was characterized by a low level of impurity content, an internal porosity of about 60%, and a good ability for resin infiltration.

Using the above nano-sized Ag power instead of Ag flakes is more likely to retain the properties of the resin matrix because of the infiltration of the resin into the pores. Measurements of the shear stress-strain behavior indicated that the thermo-mechanical properties of bonded joints could be improved by up to a factor of 2, irrespective of the chosen resin matrix.

Resistance measurements on filled adhesives were performed in a temperature range from 10 to 325 K. The specific resistance of the nano-sized Ag power filled adhesive was about 10^{-2} Ohm cm and did not achieve the typical value of commercially available adhesives of about 10^{-4} Ohm cm. The reason may be that Ag nano-particles are more or less spherical in shape, which provides fewer conduction paths than Ag flakes, and have the intrinsically lower specific conductivity. For certain applications where mechanical stress plays an important role, this conductivity may be sufficient, and therefore, the porous Ag could be suitable as a new filler material for conductive adhesives.

2.4. ICAs Filled with Nano-sized Ni Particles

It is generally known that metal powders present properties that are different from those of bulk metals when their particle size is made as small as nanometer size. Powders are classified into particles, micro-particles and nano-particles according to size. Although the classification criterion is not clear, particles with diameter smaller than 100 nm are generally called nano-particles. This classification is based on the fact that when particle size is smaller than 100 nm, the particle possesses properties that are not found in the micro-particles larger than 100 nm. For example, when the particle diameter of such magnetic materials as iron and nickel is near 100 nm, their magnetic domains change from multiple to single, and their magnetic

properties also change [18]. Majima *et al.* [18] reported an application example of metal nano-particles to conductive pastes, focusing on the properties of a new conductive adhesive that were not found in conventional ICAs.

Sumitomo Electric Industries, Ltd. (SEI) has developed a new liquid-phase deposition process using plating technology [18]. This new nano-particle fabrication process achieves purity greater than 99.9% and allows easy control of particle diameter and shape. The particle's crystallite size calculated from the results of X-ray diffraction measurement is 1.7 nm, which leads to an assumption that the size of primary particles is extremely small. When the particle size of nickel and other magnetic metals becomes smaller than 100 nm, they change from multi-domain particles to single-domain particles, and thus their magnetic properties change. That is, if the diameter of nickel particles is around 50 nm, each particle acts like a regular magnet, and magnetically connects with each other to form chain-like clusters. When the chain-like clusters are incorporated into a conductive paste, electrical conduction of the paste is expected to be better than the original paste. The chain-like nickel particles developed were mixed with a pre-defined amount of poly(vinylidene fluoride) (PVdF) that acted as an adhesive. Then, *n*-methyl-2-pyrrolidone was added to this mixture to make a conductive paste. This paste was applied on a polyimide film and then dried to make a conductive sheet. Specific volume resistivity of the fabricated conductive sheet was measured by the quadrupole method. The same measurement was also conducted on the conductive sheet that used paste made of conventional spherical nickel particles. Measurement of the sheet resistance immediately after paste application indicated that the developed chain-like nickel powder had low resistance of about one-eighth of that of the conventionally available spherical nickel particles. This result showed that when the newly developed chain-like nickel particles were incorporated in the conductive paste, high conductivity could be achieved without pressing the sheet. SEI tested and developed the metal nano-particles and investigated the possibility of their application in a conductive paste.

2.5. Nano-ICAs Filled with CNT

2.5.1. Electrical and Mechanical Characterization of CNT-Filled ICAs

The density of commercially available silver-filled conductive adhesives is around 4.5 g/cm³ after cure. Metal-filled electrically conductive adhesives offer an alternative to typical lead–tin soldering with the advantages of being simple to process at lower temperatures without toxic lead or corrosive flux. The disadvantage of conventional metal-filled conductive adhesives is that a high loading of filler decreases the mechanical impact strength, while a low filler loading results in poor electrical properties. Carbon nano-tubes are a new form of carbon, which was first identified in 1991 by Sumio Iijima of NEC, Japan [20]. Nano-tubes are sheets of graphite rolled into seamless cylinders. Besides growing single wall nano-tubes (SWNTs), nano-tubes can also have multiple walls (MWNTs)—cylinders inside other cylinders. A carbon nano-tube can be 1–50 nm in diameter and up to few mm in length,

with each end “capped” with half of a fullerene dome consisting of five or six member rings. Along the sidewalls and cap, additional molecules can be attached to functionalize the nano-tube to adjust its properties. CNTs are chiral structures with a degree of twist such that the graphite rings join into cylinders. The chirality determines whether a nano-tube will conduct in a metallic or semiconducting manner. Carbon nano-tubes possess many unique and remarkable properties. The measured electrical conductivity of metallic carbon nano-tubes is in the order of 104 S/cm [20]. The thermal conductivity of carbon nano-tubes at room temperature can be as high as 6600 W/mK [22]. The Young’s modulus of carbon nano-tubes is about 1 TPa. The maximum tensile strength of carbon nano-tubes is close to 30 GPa, with some reported at TPa [23]. The density of MWNTs is 2.6 g/cm³ and the density of SWNTs ranges from 1.33 to 1.40 g/cm³ depending on the chirality [24]. Since carbon nano-tubes have very low density and long aspect ratios, they have the potential of reaching the percolation threshold at very low weight percent loading in the polymer matrix.

Wu *et al.* [25] developed a process to prepare silver-coated carbon nano-tubes (SCCNTs), and then used the SCCNTs to formulate an ICA and compared its electrical and mechanical properties to ICAs filled with traditional multi-walled carbon nano-tubes (CNTs) and micrometer-sized Ag particles. It was found that the ICA filled with SCCNTs had a lower bulk resistivity (2.21×10^{-4} Ohm cm), and higher shear strength than that of the Ag particle filled ICA at the same filler volume content (28%).

Experiments conducted by Qian *et al.* [26] showed 36–42% and 25% increases in elastic modulus and tensile strength, respectively, in polystyrene (PS)/CNT composites. The TEM observations in their experiments showed that cracks propagated along weak CNT–polymer interfaces or relatively low CNT density regions and caused failure. If the outer layer of MWNTs can be functionalized to form strong chemical bonds with the polymer matrix, the CNT/polymer composites can be further improved in mechanical strength and have controllable thermal and electrical properties.

2.5.2. Effect of Adding CNTs to the Electrical Properties of ICAs

Lin and Lin [27] studied the effect of adding CNTs on the electrical conductivity of silver-filled conductive adhesives which had epoxy as the base resin and had various filler loadings. It was found that the CNTs could enhance the electrical conductivity of the conductive adhesives greatly when the silver filler loading was still below the percolation threshold. For example, the 66.5 wt% filled silver conductive adhesive without CNTs had a resistivity of 10⁴ Ohm cm, but showed a resistivity of 10⁻³ Ohm cm after adding 0.27 wt% CNTs. Therefore, it is possible to achieve the same level of electrical conductivity by adding a small amount of CNTs instead of the silver fillers.

2.5.3. Composites Filled with Surface Treated CNTs

Although CNTs have exceptional physical properties, incorporating them into other materials has been very challenging due to their non-polar and hydrophobic surfaces. Problems such as phase separation, aggregation, poor dispersion in the matrix, and poor adhesion to the matrix must be overcome. Zyxex Corporation [28] claimed that they had overcome these restrictions by developing a new surface treatment technology that optimizes the interaction between CNTs and the host matrix. A multifunctional bridge was created between the CNT sidewalls and the host matrix. The power of this bridge was demonstrated by comparing the fracture behavior of the polycarbonate, polystyrene or epoxy composites filled with untreated and surface treated nano-tubes. It was observed that the untreated nano-tubes interacted poorly with the polymer matrix, and thus left behind voids in the matrix after fracture. However, for the composite filled with treated nano-tubes, the nanotubes remained in the matrix even after the fracture, indicating strong interaction with the matrix. Due to their superior dispersion in the polymer matrix, the treated nanotubes achieved the same level of electrical conductivity at much lower loadings than the untreated nano-tubes [28].

2.6. Inkjet Printable Nano-ICAs and Inks

Inkjet printing of very fine pitch matrix is very attractive for many applications such as fine pitch paths, antennas, etc. But there are special requirements for inkjet printing materials, namely the most important ones are low viscosity and very homogeneous structure (like a molecular fluid) to avoid sedimentation and separation during the process. Additionally, for electrical conductivity of printed structures, the liquid has to contain conductive particles, with nano-size dimensions to avoid blocking the printing nozzle as well as to prevent sedimentation phenomenon. The nano-sized silver seems to be one of the best candidates for this purpose, especially when its particle size is less than 10 nm.

Inkjet is an accepted technology for dispensing small volumes of material (50–500 pl). Currently traditional metal-filled conductive adhesives cannot be processed by ink jetting (due to their relatively high viscosity and large size of filler material particles). The smallest droplet size achievable by traditional dispensing techniques is in the range of 150 µm, yielding proportionally larger adhesive dots on the substrate. Electrically conductive inks are available on the market with metal particles (gold or silver) < 20 nm suspended in a solvent at 30–50 wt%. After deposition, the solvent is eliminated and electrical conductivity is enabled by a high metal ratio in the residue. Some applications include a sintering step. However, these traditional nano-filled inks do not offer an adhesive function [29].

There are many requirements for an inkjettable, Ag particle filled conductive adhesive. The silver particles must not exceed a maximum size determined by the diameter of the injection needle used. At room temperature the adhesive should resist sedimentation for at least eight, preferably 24 h. A further requirement by the end-user for the adhesive properties is a two-stage curing mechanism. In the first

curing step the adhesive surface is dried and remains meltable. In this state the product may be stored for several weeks. The second curing step involves bonding the components with the previously applied adhesive. By heating and applying pressure the adhesive is re-melted and cured. Thus the processing operation is similar to that required for soldering. A conductivity in the range of 10^{-4} Ohm cm in the bulk material is required. An adhesive less prone to sedimentation was formulated by using suitable additives. Furthermore, the formation of filler agglomerations during deflocculation and storage was reduced. This effect was achieved by making the additives adsorb onto the filler particle surfaces. This requires a very delicate balance. If the insulation between individual silver particles becomes too strong, overall electrical conductivity is significantly reduced.

Kolbe *et al.* [30] and Moscicki *et al.* [31] demonstrated feasibility of an inkjet-table, isotropically conductive adhesive in the form of a silver-loaded resin with a 2-step curing mechanism. To enable the 2-step curing process, an acrylate-methacrylate-epoxy resin matrix was formulated and provided with commercially available initiators for the UV and thermally activated curing stages. In the first step, the adhesive was dispensed (jetted) and pre-cured leaving a “dry” surface. In this pre-curing stage, the double bonds of acrylate and methacrylate groups react to give a thermoplastic with epoxy sidegroups. In this state, the adhesive may be stored in a refrigerator for more than 4 weeks without losing its application-related properties. In the second step, a heated stamp was used to position the component on the pre-applied adhesive at a temperature of 180°C and a pressure of 2 MPa for 10 s. Afterwards the adhesive was post-cured in an oven at an elevated temperature (e.g., 130°C for 30 min). The attainable droplet size was in the range of 130 μm , but could be further reduced by using smaller (such as 50 μm) and more advanced nozzle shapes.

3. Recent Advances in Nano-ACAs/ACFs

3.1. Low Temperature Sintering of Nano-Ag-Filled ACAs/ACFs

One of the concerns for ACAs/ACFs is the higher joint resistance since interconnection using an ACA/ACF relies on mechanical contact, unlike the metal bonding of soldering. An approach to minimize the joint resistance of an ACA/ACF is to make the conductive fillers fuse to each other and form metallic joints such as metal solder joints. However, to fuse metal fillers in polymers does not seem feasible, since a typical organic printed circuit board ($T_g \sim 125^\circ\text{C}$), on which the metal-filled polymer is applied, cannot withstand such a high temperature; the melting temperature (T_m) of Ag, for example, is around 960°C. Research showed that the T_m and sintering temperatures of materials could be dramatically reduced by decreasing the size of the materials [32, 33]. It has been reported that the surface pre-melting and sintering processes are a primary mechanism for the T_m depression of the fine nano-particles (<100 nm). For nano-sized particles, sintering could occur at much lower temperatures and, as such, the use of the fine metal particles in

ACAs would be promising for fabricating high electrical performance ACA joints through eliminating the interface between metal fillers. The application of nano-sized particles can also increase the number of conductive particles on each bond pad and result in more contact area between the particles and bond pads. Figure 4 shows SEM micrographs of Ag nano-particles annealed at various temperatures. Although very fine particles (20 nm) were observed for as synthesized (in Fig. 4a) and 100°C treated particles (in Fig. 4b), dramatically larger particles were observed after heat treatment at 150°C and above. With increasing temperature, the particles became larger and appeared as solid matter rather than porous particles or

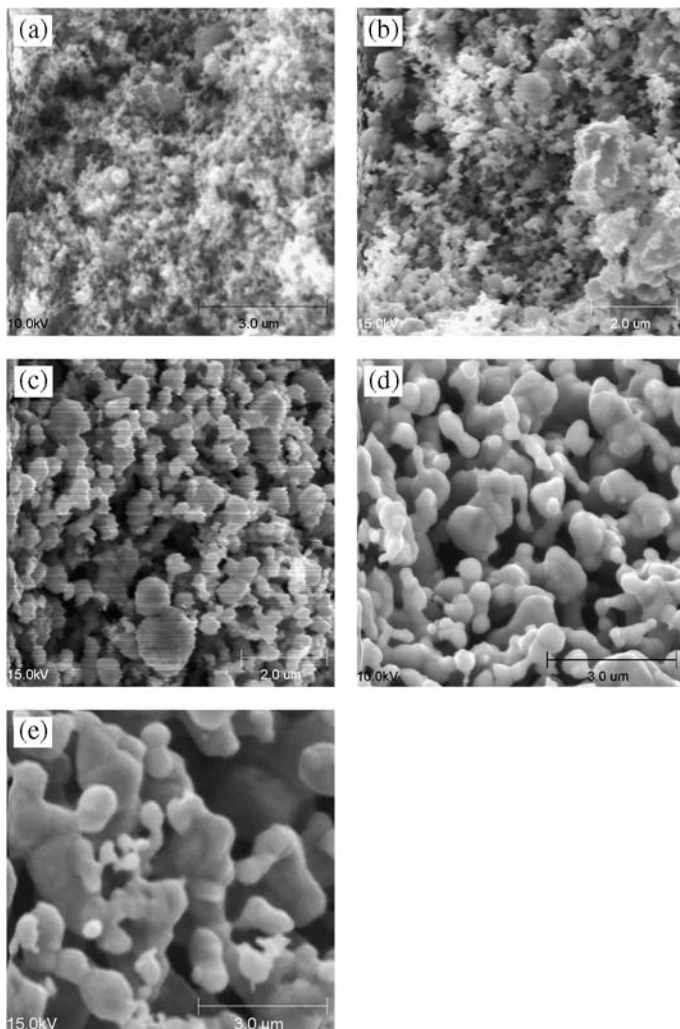


Figure 4. SEM micrographs of 20 nm-sized Ag particles annealed at different temperatures for 30 min: (a) room temperature (no annealing); (b) annealed at 100°C; (c) annealed at 150°C; (d) annealed at 200°C and (e) annealed at 250°C [32].

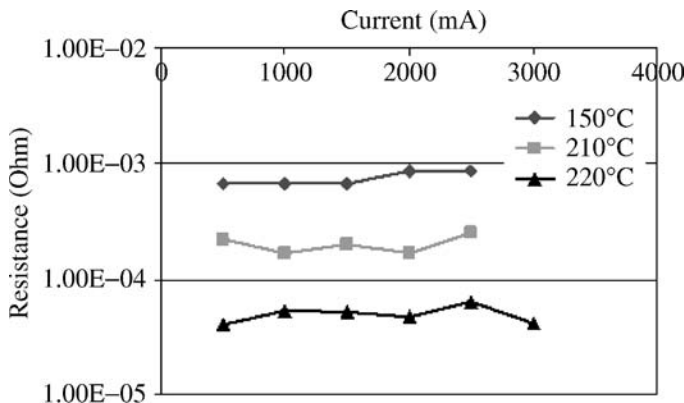


Figure 5. Current–resistance (I–R) relationship of ACAs filled with Ag nano-particles at different curing temperatures [34].

agglomerates. The particles shown in Fig. 4c–e were fused through their surface and many dumbbell type particles could be found. The morphology was similar to a typical morphology of the initial stage in the typical sintering process of ceramic, metal and polymer powders. This low temperature sintering behavior of the nano-particles is attributed to the extremely high inter-diffusivity of the nano-particle surface atoms, due to the significantly energetically unstable surface condition of the nano-sized particles with large proportion of the surface area to the entire particle volume.

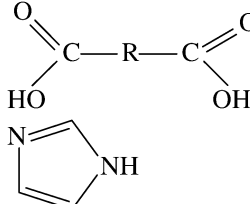
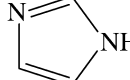
For the sintering reaction in a material system, temperature and duration are the most important parameters, in particular, the sintering temperature. Current–resistance (I–R) relationship of ACAs filled with Ag nano-particles is shown in Fig. 5. As can be seen from the figure, with increasing curing temperature, the resistance of the ACA joints decreased significantly, from 10^{-3} to 5×10^{-5} Ohm. Also, higher curing temperature ACA samples exhibited higher current carrying capability than the low-temperature samples. This phenomenon suggested that more sintering of Ag nano-particles and subsequently improved interaction between the nano-particles and metal bond pads were achieved at higher temperatures [34], yet the X–Y direction of the ACA maintains an excellent dielectric property for electrical insulation.

3.2. Self-Assembled Monolayers for Nano-ACAs/ACFs

In order to enhance the electrical performance of ACA/ACF materials, self-assembled monolayers (SAMs) have been introduced into the interface between metal fillers and metal-finished bond pad of ACAs [35, 36]. These organic molecules adsorb onto the metal surface and form physico-chemical bonds, which allow electrons to flow. As such, they reduce electrical resistance and enable a high-current flow. The unique electrical properties are due to the tuning of metal work-function by these organic monolayers. Metal surfaces can be chem-

Table 1.

Potential organic monolayer interfacial modifiers for different metal finishes

Chemical structure	Compounds	Metal finish
H-S-R-S-H	Dithiols	Au, Ag, Sn, Zn
N≡C-R-C≡N	Dicyanides	Cu, Ni, Au
O=C=N-R-N=C=O	Diisocyanates	Pt, Pd, Rh, Ru
	Dicarboxylates	Fe, Co, Ni, Al, Ag
	Imidazole and derivatives	Cu
R-SiOH	Organosilicone derivatives	SiO2, Al2O3, quartz, glass, mica, ZnSe, GeO2, Au

R denotes alky or aromatic groups.

ically modified by the organic monoalyers and reduced work-functions can be achieved by using suitable organic monolayer coatings. An important consideration when examining the advantages of organic monolayers pertains to the affinity of organic compounds to specific metal surfaces. Table 1 gives the examples of molecules preferred for maximum interactions with specific metal finishes; although only molecules with symmetrical functionalities for both head and tail groups are shown, molecules and derivatives with different head and tail functional groups are possible for interfaces concerning different metal surfaces.

Different organic self-assembled monolayers (SAMs), e.g., dicarboxylic acids and dithiols, have been introduced into ACA/ACF joints. For ACAs with SAMs and micrometer-sized gold/polymer or gold/nickel fillers, lower joint resistance and higher maximum allowable current (highest current applied without inducing joint failure) were achieved for low temperature curable ACAs (<100°C). For high curing temperature ACAs (150°C), however, the improvement was not as significant as low curing temperature ACAs, due to the partial desorption/degradation of organic monolayer coating at the relatively high temperature [37]. However, when dicarboxylic acid or dithiol was introduced into the interface of nano-silver-filled ACAs, significantly improved electrical properties could be achieved for a high-temperature curable ACA/ACF, suggesting the coated molecular wires did not suffer degradation on silver nano-particles at the curing temperature (Fig. 6). The enhanced bonding could be attributed to the larger surface area and higher surface energy of nano-particles, which enabled the monolayers to be more readily coated and relatively thermally stable on the metal surfaces [38].

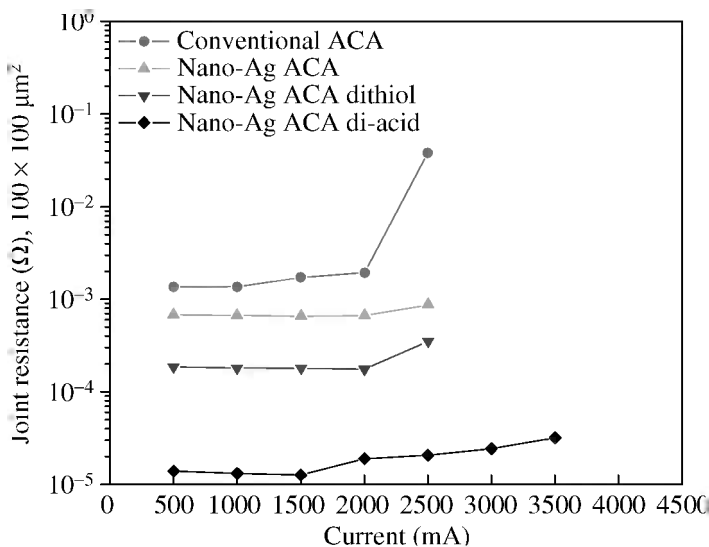


Figure 6. Electrical properties of nano-Ag-filled ACAs with dithiol or dicarboxylic acid [38].

3.3. Silver Migration Control in Nano-silver-Filled ACAs

Silver is the most widely used conductive filler in ICAs and exhibits exciting potential in nano-ACAs/ACFs due to many unique advantageous properties of silver. Silver has the highest room temperature electrical and thermal conductivities among all the conductive metals. Silver is also unique among all the cost-effective metals because of its conductive oxide (Ag_2O). In addition, silver nano-particles are relatively easily formed into different sizes (a few nano-meters to 100 nm) and shapes (such as spheres, rods, wires, disks, flakes, etc.) and are well dispersed in a variety of polymeric matrix materials. Also the low-temperature sintering and high surface energy makes silver one of the promising candidates as a conductive filler in nano-ACAs/ACFs. However, silver migration has long been a reliability concern in the electronics industry. Metal migration is an electrochemical process, whereby, metal (e.g., silver), in contact with an insulating material, in a humid environment and under an applied electric field, leaves its initial location in ionic form and deposits at another location [39]. It is considered that a threshold voltage exists above which the migration starts. Such migration may lead to a reduction in electrical spacing or cause a short circuit between interconnections. The migration process begins when a thin continuous film of water forms on an insulating material between oppositely charged electrodes. When a potential is applied across the electrodes, a chemical reaction takes place at the positively-biased electrode where positive metal ions are formed. These ions, through ionic conduction, migrate toward the negatively charged cathode and, over time, they accumulate to form metallic dendrites. As the dendrite growth increases, a reduction of electrical spacing occurs. Eventually, the

dendrite silver growth reaches the anode and creates a metal bridge between the electrodes, resulting in an electrical short circuit [40].

Although other metals may also migrate under specific environments, silver is more susceptible to migration, mainly due to the high solubility of silver ions, low activation energy for silver migration, high tendency to form dendrite shape and low possibility to form stable passivation oxide layer [41–43]. The rate of silver migration is increased by: (1) an increase in the applied potential; (2) an increase in the time of the applied potential; (3) an increase in the level of relative humidity; (4) an increase in the presence of ionic and hygroscopic contaminants on the surface of the substrate and (5) a decrease in the distance between electrodes of opposite polarity.

In order to reduce silver migration and improve the reliability, several methods have been reported. These methods include: (1) alloying the silver with an anodically stable metal such as palladium [40] or platinum [44] or even tin [45]; (2) using hydrophobic coating over the printed wiring board (PWB) to shield its surface from humidity and ionic contamination, since water and contaminates can act as a transport medium and increase the rate of migration; (3) plating of silver with metals such as tin, nickel or gold, to protect the silver fillers and reduce migration; (4) coating the substrate with polymer [46]; (5) applying benzotriazole (BTA) and its derivatives in the polymeric matrix [47]; (6) employing siloxane epoxy polymers as diffusion barriers due to their excellent adhesion to conductive metals [48] and (7) chelating silver fillers in ECAs with molecular monolayers [49]. As an example shown in Fig. 7 [50], with carboxylic acids forming chelating compounds with silver ions, the silver migration behavior (leakage current) could be significantly reduced and controlled.

3.4. ACF with Straight-Chain-Like Nickel Nano-particles

Sumitomo Electric Industries (SEI) recently developed a new-concept ACF using nickel nano-particles with a straight-chain-like structure as a conductive filler [51]. They applied the formulated straight-chain-like nickel nano-particles and solvent in a mixture with epoxy resin on a film substrate. Then the particles were aligned toward the vertical direction of the film surface and fixed in the resin by evaporating the solvent. In the evaluation using 30- μm pitch IC chips and glass substrates (the area of Au bumps was 2000 μm^2 , the distance between neighboring bumps was 10 μm), this new ACF showed excellent reliability of electrical connection after high-temperature, high-humidity (60°C/90% RH) test and thermal cycle test (between –40 and 85°C). The samples were also exposed to high-temperature, high-humidity (60°C/90% RH) for surface insulation resistance (SIR) study. Although the distance between two electrodes was only 10 μm , ion-migration did not occur and insulation resistance was maintained at over 1 G Ω for 500 h. This result showed that the new ACF has superior insulation reliability. This indicates that this new ACF has potential for application in very fine interconnections.

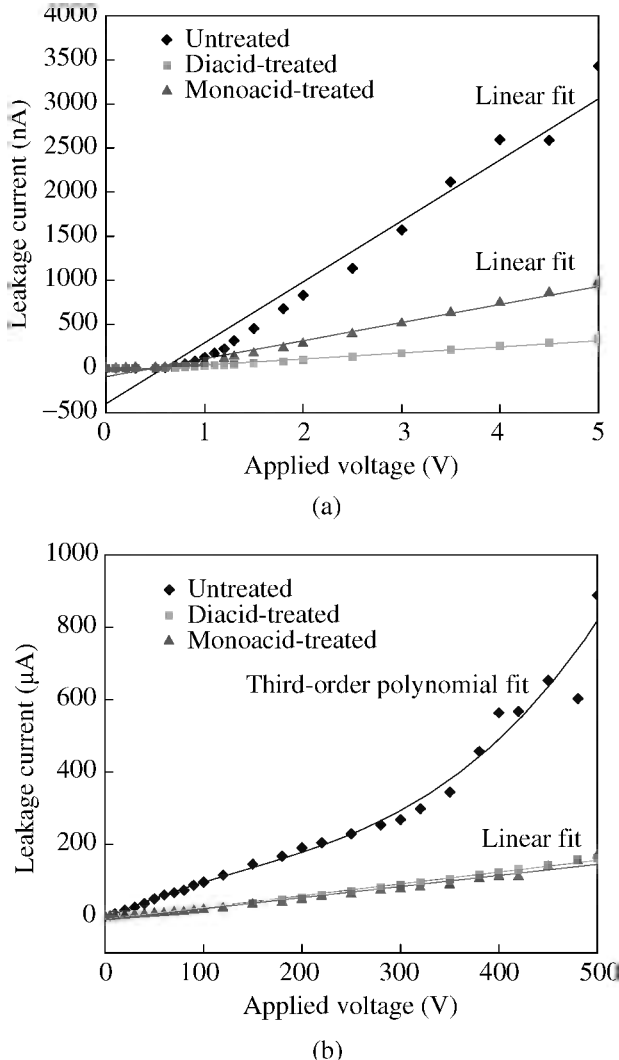


Figure 7. Leakage current–voltage relationships of nano-Ag-filled conductive adhesives at (a) low voltages and (b) high voltages [49].

3.5. Nano-wire ACFs for Ultra-Fine Pitch Flip Chip Interconnection

In order to satisfy the reduced I/O pitch and avoid electric shorting, a possible solution is to use high-aspect-ratio metal posts. Nano-wires exhibit high possibilities due to the small size and extremely high aspect ratio. In the literature, it is shown that nano-wires could be applied in FET sensors for gas detection, magnetic hard-disks, nano-electrodes for electrochemical sensors, thermal–electric devices for thermal dissipation and temperature control, etc. [52–54]. To prepare nano-wires, a template for growing nano-wires needs to be fabricated. Many expensive

methods such as e-beam, X-ray or scanning probe lithographies have been used but micrometer length nano-wires have not been obtained. Another less expensive alternative is electrodeposition of metal into nano-porous template such as anodic aluminum oxide (AAO) [58] or block-copolymer self-assembly template [56]. The disadvantages of a block-copolymer template include its small thickness (which means only short nano-wires can be made from the template), nonuniform distribution and poor parallelism of nano-pores. However, AAO has benefits of higher thickness ($>10\text{ }\mu\text{m}$), uniform pore size and density, larger size and very parallel pores. Lin *et al.* [57] developed a new ACF with nano-wires. They used AAO templates to obtain silver and cobalt nano-wire arrays by electrodeposition. And then a low viscosity polyimide (PI) was spread over and filled into the gaps of nano-wires after surface treatment. The bi-metallic Ag/Co nano-wires could stay parallel during fabrication by magnetic interaction between the cobalt and the applied magnetic field. The silver and cobalt nano-wires/polyimide composite films could be obtained with nano-wire diameter of about 200 nm and maximum film thickness up to 50 μm . The $X-Y$ insulation resistance was about 4–6 G Ω and the Z -direction resistance including the trace resistance (3 mm length) was less than 0.2 Ω .

3.6. In situ Formation of Nano-conductive Fillers in ACAs/ACFs

One of the challenging issues in the formation of nano-filler ACAs/ACFs is the dispersion of nano-conductive fillers in the ACA/ACF. A considerable amount of research has been conducted in recent years to address the dispersion issue of nano-composites because nano-fillers tend to agglomerate. For the fine pitch electronic interconnects using nano-filler ACAs/ACFs, the dispersion issues need to be solved. The efforts usually include physical approaches such as sonication and chemical approaches such as use of surfactants. Recently, a novel ACA/ACF containing *in situ* formed conductive nano-particles was proposed for the next generation high performance fine-pitch electronic packaging applications [58, 59]. This novel interconnect adhesive combines the electrical conduction along the Z -direction (ACA-like) and the ultrafine pitch ($<100\text{ nm}$) capability. Instead of adding the conductive nano-fillers in the resin, the nano-particles can be *in situ* formed during the curing/assembly process. By using *in situ* formation of nano-particles, during the polymer curing process, the filler concentration and dispersion actually could be better controlled and the drawback of surface oxidation of the nano-fillers could be easily overcome.

4. Summary

Ag nano-wires were shown to be able to provide ICAs with similar conductivity as traditional Ag flakes at a much lower filler loading, and thus provide ICAs with better mechanical performance. Adding Ag nano-particles into an ICA filled with Ag flakes generally showed a negative effect on electrical conductivity. However, some factors such as high-temperature annealing and adding certain surfactants on

the surfaces of nano-particles can enhance the interdiffusion of Ag atoms among nano-particles and thus improve the conductivity. Incorporating CNTs into ICAs filled with Ag flakes enhanced the conductivity greatly only when the Ag filler loading was still below the percolation threshold. Functionalizing CNT surfaces to improve the interaction between the CNTs and the matrix significantly improved the mechanical performance of CNT-filled ICAs.

ACAs/ACFs filled with Ag nano-particles showed low resistance due to the sintering of the nano-particles at relatively low temperatures, and lower resistance was observed for ACAs/ACFs sintered at a higher temperature. By introducing self-assembled monolayers (SAMs) into the interfaces between the metal fillers and metal contact pads, lower joint resistance and higher maximum allowable current were observed for low-temperature curable ACAs (curing temperature <100°C). By chelating silver fillers with an organic compound such as a carboxylic acid, the silver migration was greatly reduced. ACAs filled with Ag/Co nano-wires were developed with acceptable electrical performance. *In situ* formation of Ag nano-particles during ACA curing was demonstrated, and better filler dispersion was achieved.

References

1. H. Wolfson and G. Elliot, US Patent 2,774,747 (1956).
2. K. R. Matz, US Patent 2,849,631 (1958).
3. D. P. Beck, US Patent 2,866,057 (1958).
4. P. B. Jana, S. Chaudhuri, A. K. Pal and S. K. De, *Polym. Eng. Sci.* **32**, 448 (1992).
5. A. Malliaris and D. T. Turner, *J. Appl. Phys.* **42**, 614 (1971).
6. G. R. Ruschau, S. Yoshikawa and R. E. Newnham, *J. Appl. Phys.* **73**, 953 (1992).
7. K. Gilleo, *Soldering Surface Mount Technol.* **19**, 12 (1995).
8. P. G. Hariss, *Soldering Surface Mount Technol.* **20**, 19 (1995).
9. Y. Li, K. Moon and C. P. Wong, *Science* **308**, 1419 (2005).
10. Y. Li and C. P. Wong, *Mater. Sci. Eng. R.* **51**, 1 (2006).
11. J. Lau, C. P. Wong, N. C. Lee and S. Lee (Eds), *Electronics Manufacturing: With Lead-Free, Halogen-Free, and Conductive-Adhesive Materials*. McGraw Hill, New York, NY (2002).
12. H. Wu, X. Wu, J. Liu, G. Zhang, Y. Wang, Y. Zeng and J. Jing, *J. Composite Mater.* **40**, 1961 (2006).
13. H. S. Lee, K. S. Chou and Z. W. Shih, *Intl. J. Adhesion Adhesives* **25**, 437 (2005).
14. L. Ye, Z. Lai, J. Liu and A. Tholen, *IEEE Trans. Electronics Packaging Manuf.* **22**, 299 (1999).
15. L. Fan, B. Su, J. Qu and C. P. Wong, in: *Proceedings of IEEE Electronic Components and Technology Conference*, Las Vegas, NV, pp. 148–154 (2004).
16. H. Jiang, K. Moon, Y. Li and C. P. Wong, *Chem. Mater.* **18**, 2969 (2006).
17. S. Kotthaus, B. H. Günther, R. Haug and H. Schafer, *IEEE Trans. Components, Packaging, Manuf. Technol. (Part A)* **20**, 15 (1997).
18. M. Majima, K. Koyama, Y. Tani, H. Toshioka, M. Osoegawa, H. Kashihara and S. Inazawa, *SEI Technical Review* **54**, 25 (2002).
19. R. N. Das, J. Lauffer and F. Egitto, in: *Proceedings of IEEE Electronic Components and Technology Conference*, San Diego, CA, pp. 112–118 (2006).

20. S. Iijima, *Nature* **354**, 56 (1991).
21. A. Thess, R. Lee, P. Nikolaev, H. Dai, P. Petit, J. Robert, C. Xu, Y. H. Lee, S. G. Kim, A. G. Rinzler, D. T. Colbert, G. Scuseria, D. Tománek, J. E. Fischer and R. E. Smalley, *Science* **273**, 483 (1996).
22. S. Berber, Y. K. Kwon and D. Tománek, *Phys. Rev. Lett.* **84**, 4613 (2000).
23. M. F. Yu, B. S. Files, S. Arepalli and R. S. Ruoff, *Phys. Rev. Lett.* **84**, 5552 (2000).
24. G. Gao, T. Cagin and W. A. Goddard III, *Nanotechnology* **9**, 184 (1998).
25. H. Wu, X. Wu, M. Ge, G. Zhang, Y. Wang and J. Jiang, *Composites Sci. Technol.* **67**, 1182 (2007).
26. D. Qian, E. C. Dickey, R. Andrews and T. Rantell, *Appl. Phys. Lett.* **76**, 2868 (2000).
27. X. C. Lin and F. Lin, in: *Proceedings of High Density Microsystem Design and Packaging, Conference*, Shanghai, China, pp. 382–384 (2004).
28. M. Rutkofsky, M. Banash, R. Rajagopal and J. Chen, Zyxex Corporation Application Note 9709 (2006). Available at <http://www.zyxex.com/Documents/9709.PDF> 28.
29. A. Kamyshny, M. Ben-Moshe, S. Aviezer and S. Magdassi, *Macromol. Rapid Commun.* **26**, 281 (2005).
30. J. Kolbe, A. Arp, F. Calderone, E. M. Meyer, W. Meyer, H. Schaefer and M. Stuve, in: *Proceedings of IEEE Polytronic 2005 Conference*, Wroclaw, Poland, pp. 1–4 (2005).
31. A. Moscicki, J. Felba, T. Sobierajski, J. Kudzia, A. Arp and W. Meyer, in: *Proceedings of IEEE Polytronic 2005 Conference*, Wroclaw, Poland, pp. 40–44 (2005).
32. K. Moon, H. Dong, R. Maric, S. Pothukuchi, A. Hunt, Y. Li and C. P. Wong, *J. Electronic Mater.* **34**, 132 (2005).
33. M. Y. Efremov, F. Schietekatte, M. Zhang, E. A. Olson, A. T. Kwan, R. S. Berry and L. H. Allen, *Phys. Rev. Lett.* **85**, 3560 (2000).
34. Y. Li, K. Moon and C. P. Wong, *J. Appl. Polym. Sci.* **99**, 1665 (2006).
35. Y. Li, K. Moon and C. P. Wong, in: *Proceedings of 54th IEEE Electronic Components and Technology Conference*, Las Vegas, NV, pp. 1968–1974 (2004).
36. Y. Li and C. P. Wong, in: *Proceedings of 55th IEEE Electronic Components and Technology Conference*, Lake Buena, FL, pp. 1147–1154 (2005).
37. Y. Li, K. Moon and C. P. Wong, *J. Electronic Mater.* **34**, 266 (2005).
38. Y. Li, K. Moon and C. P. Wong, *J. Electronic Mater.* **34**, 1573 (2005).
39. G. Davies and J. Sandstrom, *Circuits Mfg.* **56** (Oct. 1976).
40. G. Harsanyi and G. Ripka, *Electrocomponent Sci. Technol.* **11**, 281 (1985).
41. G. Di Giacomo, in: *Electrochemistry of Semiconductors and Electronics: Processes and Devices*, J. McHardy and F. Ludwig (Eds), pp. 255–295. Noyes Publications, Park Ridge, NJ (1992).
42. R. Manepalli, F. Stepniak, S. A. Bidstrup-Allen and P. Kohl, *IEEE Trans. Advanced Packaging* **22**, 4 (1999).
43. G. Di Giacomo, *Reliability of Electronic Packages and Semiconductor Devices*, Chapter 9. McGraw-Hill, New York, NY (1997).
44. R. J. Klein Wassink, *Microelectronics Intl.* **9**, 9–12 (1987).
45. Y. Shirai, M. Komagata and K. Suzuki, in: *Proceedings of the 1st International IEEE Conference on Polymers and Adhesives in Microelectronics and Photonics*, Potsdam, Germany, pp. 79–83 (2001).
46. H. Schonhorn and L. H. Sharpe, US Patent 4,377,619 (1983).
47. V. Brusic, G. S. Frankel, J. Roldan and R. Saraf, *J. Electrochem. Soc.* **142**, 2591 (1995).
48. P. I. Wang, T. M. Lu, S. P. Murarka and R. Ghoshal, US Patent 7,285,842 (2007).
49. Y. Li and C. P. Wong, US Patent pending (2005).
50. Y. Li and C. P. Wong, *Appl. Phys. Lett.* **81**, 112 (2006).

51. H. Toshioka, M. Kobayashi, K. Koyama, K. Nakatsugi, T. Kuwabara, M. Yamamoto and H. Kashihara, *SEI Technical Review* **62**, 58 (2006).
52. C. M. Lieber, *Science* **293**, 1289 (2001).
53. G. A. Prinz, *Science* **282**, 1660 (1998).
54. C. R. Martin and V. P. Menon, *Anal. Chem.* **67**, 1920 (1995).
55. J. M. Xu, *Appl. Phys. Lett.* **79**, 1039 (2001).
56. T. P. Russell, *Science* **290**, 2126 (2000).
57. R. Lin, Y. Hsu, Y. Chen, S. Cheng and R. Uang, in: *Proceedings of 55th IEEE Electronic Components and Technology Conference*, Lake Buena, FL, pp. 66–70 (2005).
58. Y. Li, K. Moon and C. P. Wong, in: *Proceedings of 56th IEEE Electronic Components and Technology Conference*, San Diego, CA, pp. 1239–1245 (2006).
59. Y. Li, Z. Zhang, K. Moon and C. P. Wong, US Patent pending (2006).

Part 2

Mechanical Durability and Reliability Aspects

This page intentionally left blank

Reliability of Anisotropic Conductive Adhesive Joints in Electronic Packaging Applications

Y. C. Lin^{a,b} and X. Chen^{a,*}

^a School of Chemical Engineering & Technology, Tianjin University, Tianjin 300072, P. R. China

^b School of Mechanical and Electrical Engineering, Central South University, Changsha 410083, P. R. China

Abstract

New interconnection materials are always necessary as a result of evolving packaging technologies and increasing performance and environmental demands on electronic systems. In particular, anisotropic conductive adhesives (ACAs) have gained popularity as a potential replacement for solder interconnects. Despite numerous benefits, ACA-type packages pose several reliability problems. During the last 10 years, tremendous research and development efforts have been spent on improving the reliability of ACA joints. In this paper, the effects of the bonding process (including the bonding temperature, bonding pressure, curing conditions and reflow processes) on the reliability of ACA joints are presented. Then the effects of the environmental factors (including high temperature, humidity, thermal cycling, impact load, etc.) on the reliability of ACA joints are discussed. Finally, the effects of the properties of the components (including properties of substrates, ACAs, conductive particles and the bump height) on the reliability of ACA joints are reviewed. Additionally, future research areas and remaining issues are pointed out.

Keywords

Anisotropic conductive adhesives (ACA), bonding process, hygrothermal aging, reliability

1. Introduction

Electronic packages nowadays are becoming smaller, lighter with higher in/out (I/O) count and better performance and must be cost competitive. The trend in electronic packaging runs from bulky plastic ball grid arrays (PBGAs) with solder joints to miniature flip-chips with anisotropic conductive adhesive interconnects. Meanwhile, the environmentally-friendly manufacturing is another important goal for the electronic packaging industry. In particular, the use of anisotropic conductive adhesives (ACAs) instead of soldering and underfill encapsulation helps to achieve such goals. The interest in using an ACA, instead of solder, comes partly from the fact

* To whom correspondence should be addressed. Tel.: +86-22-27408399; Fax: +86-22-87893037; e-mail: xchen@tju.edu.cn

that the use of an ACA for the direct interconnection of flipped silicon chips to printed circuits (flip-chip packaging), offers numerous advantages such as reduced thickness, improved environmental compatibility, lower assembly process temperature, increased metallization options, reduced cost, and decreased equipment needs [1–9]. There are also several review papers on the topic of ACAs [10, 11]. The application of ACA joints in such cases as smart cards, disk drives, and driver chips for electronic assemblies has attracted much interest and has been widespread, including on glass substrates [12–16], flexible circuits [17–20], rigid board [21, 22], and ceramic substrate [23, 24].

An ACA is a composite composed of fine conductive particles that are uniformly dispersed in a thermosetting epoxy matrix, and it has been widely used for interconnecting microelectronic elements. Generally, there are two main forms of ACA: (1) paste, referred to hereafter simply as an anisotropically conductive adhesive (ACA); (2) an anisotropically conductive film (ACF). In an ACA joint, the filler particles normally constitute between 5 and 10 volume percent, and do not cause any direct metallic contact before the assembly process is completed. The principle of ACA joints is that the electrical connections are established through conductive particles and the mechanical interconnections are established by the cured adhesive. For example, Fig. 1 shows a typical chip-on-glass (COG) assembly based on

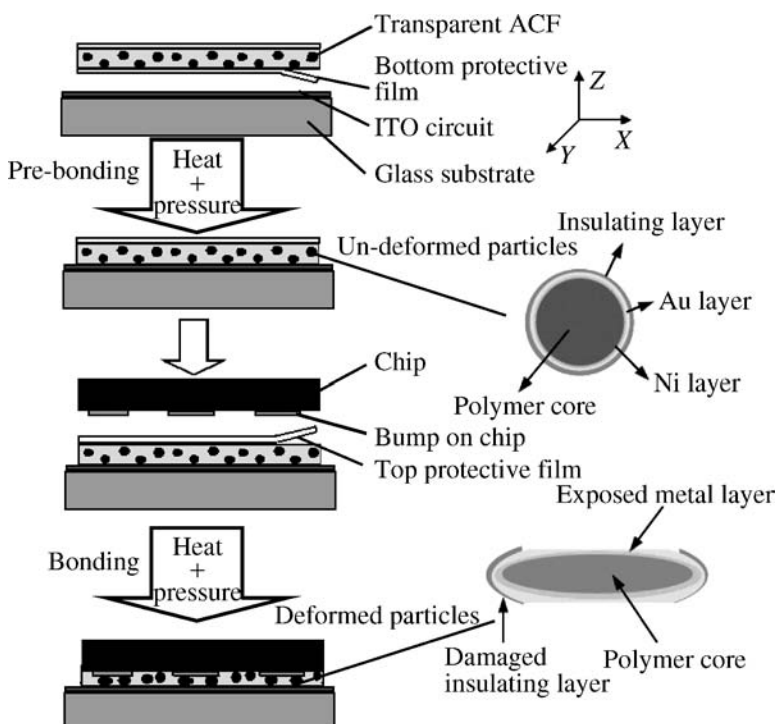


Figure 1. Interconnection process for a COG assembly.

ACF interconnection techniques. First, an ACF is laminated to a glass substrate with ITO (indium tin oxide) tracks. Pressure and temperature are applied during the lamination process to ensure positioning accuracy, uniformity, etc. Then, the bumps on integrated circuits (ICs) are aligned with the tracks on the glass. Finally, the IC chip is pressed onto the glass at a specified high temperature and pressure. The conductive particles are trapped between the bumps and tracks, while the adhesive resin is squeezed out. The interconnections are established by the compressive force between the electrodes due to the shrinkage of the adhesive after curing. Consequently, the electrical conduction is restricted to the z -direction and the electrical isolation is maintained in the $x-y$ plane. Additionally, it is necessary to know the deformation of conductive particles during die mounting process. Generally, the conductive particles consist of a polymer core material coated with a thin metal layer (nickel or/and gold), and then insulated again with a polymer material on its exterior surface. The conductive particles in an ACF are of ball shape before die bonding. When the IC chip is pressed onto the glass at a high temperature and pressure, the particles are entrapped and deformed between the bumps of the chip and the glass substrate, and then the external insulation layer of the particle is damaged and the interior metal layer is exposed. Thus, the electrical connections are established through conductive particles.

Despite numerous benefits, ACA-type packages pose several reliability problems. During the last 20 years, tremendous research and development efforts have been spent on understanding the ACA joints. The results of these studies would allow development of ACA joints using fine pitch flip-chips on flexible/rigid substrates with better reliability and performance. The purpose of this paper is to review the recent investigations on the reliability of ACA joints in electronic packaging applications. Additionally, this paper highlights the important papers that have played significant role in the advancement of the ACA technology.

2. Effect of Bonding Process on the Reliability of ACA Joints

In the bonding process of ACA joints, temperature, pressure and curing conditions are the critical bonding parameters for optimal bonding conditions. Also, the effects of reflow and alignment process are significant. Many investigators have studied the effects of these critical factors during flip-chip-on-substrate assembly in relation to the performance of the ACA interconnect.

2.1. Effect of Bonding Temperature on the Reliability of ACA Joints

Epoxy resin based ACAs are temperature sensitive; therefore, their structure is highly dependent on the bonding temperature chosen. When temperature increases, the ACA will melt and transform into a low viscosity liquid, and finally cross-links will be created to form three-dimensional networks which contributes to its stable physical properties. The cross-link density of ACA is very important in determining its reliability performance. Due to the temperature sensitive characteristics of the

ACA, the mobility of the conductive particles is different at different ACA curing stages. During the bonding process of ACA joints, as the ACA is being cured it becomes soft and rubbery. This transformation allows the ACA to flow, which, in turn, allows the conductive particles to move and distribute themselves evenly throughout the ACA joint. When the curing process is completed, the ACA becomes hardened and the conductive particles are trapped by bump and pad. A reliable interconnection should have sufficient amount of conductive particles between the bump and pad in close contact [25, 26]. Therefore, the root cause of the instability of contact resistance may be due to the incorrect selection of bonding temperature during ACA bonding, and some investigations have been carried out to understand the effects of the bonding temperature on the reliability of flip-chip assemblies using ACAs [27–35].

The effects of different bonding temperatures during flip-chip-on-flex (FCOF) assembly in relation to the performance of the anisotropically conductive film (ACF) interconnection were investigated [27]. The results showed that Ni bumps formed better interconnections than bumpless FCOF packages. Aluminum oxide was observed and was thought to be the main cause of the increased contact resistance after the moisture-soak tests. The conductive particles were not fully compressed by the bumps and pads, and gaps were observed between the conductive particles and Cu pads in bumpless packages. Conductive particles in the Ni bump FCOF packages were tightly trapped and hence gave better connections. The performance of the ACF interconnection was affected by the degree of curing of the ACF, which was determined by the bonding temperature.

In 2002, Luk *et al.* [28] developed a low cost method to manufacture hard disk drive (HDD) head using ACF bonding for flex-to-flex interconnection. Critical process bonding temperatures were identified and characterized to find out the optimal bonding temperature for the lowest resistance and hence a reliable ACF joint. Acceptance criterion for complete curing of adhesive was determined at level of more than 85% of adhesive curing.

Zhang *et al.* [29] systematically discussed the influence of bonding temperature and bonding pressure on the adhesion of bumpless die (aluminum surface) with two kinds of Anisotropic Conductive Films (ACFs). The results showed that the adhesion strength between the ACFs and aluminum was not affected much by bonding pressure but it increased with increasing bonding temperature.

Wu *et al.* [30] studied the effects of bonding temperature on the behavior of ACF joint in flip-chip-on-glass (COG) and flip-chip-on-flexible (COF) substrate packages by impact tests. The results showed that the impact strength increased with the bonding temperature, but after a certain temperature, it decreased. Higher degree of curing at higher bonding temperature was accountable for the increase of the adhesion strength, while too high temperature caused overcuring of ACF and degradation at the ACF/substrate interface — thus decreased the adhesion strength. Higher extent of air bubbles was found at the ACF/substrate interface of the sample

bonded at the higher temperature. These air bubbles reduced the actual contact area and hence reduced the impact strength.

Tan *et al.* [31] investigated the effect of different bonding temperatures on the thermal stability of ACFs. The experimental results showed that the temperature for maximum decomposition rate of ACF decreased with increasing bonding temperature. Some network scissoring occurred on the C–N bond during the bonding process, which was the main reason why the ACF bonded at high temperature, 225°C, gave relatively low thermal stability. The contact resistance results suggested that the ACF bonded for 10 s at 205°C, yielding a curing degree of 85.0%, was the best bonding condition to obtain a low contact resistance after thermal aging. FT-IR results showed there was a significant increase in the absorbance peak of carbonyl group after thermal aging. Thermal oxidation reactions which had taken place at high bonding and aging temperature had broken the polymer networks in the ACF and caused electrical failure.

A systematic study was carried out to clarify the effects of the bonding temperature on the cross-linking of the ACF matrix which, in turn, affects the performance of the interconnection [32]. The results showed that the high temperature cured samples had higher reaction rate and a greater curing degree as well as high adhesion strength compared with low temperature cured samples. Contact resistance was also found to be strongly dependent on the curing degree. The contact resistance decreased with the curing degree and achieved a minimum value at 87% of curing.

Rizvi *et al.* [33] focused on the effect of bonding temperature on the curing of ACFs, and their adhesion strength and electrical performances after high temperature aging. The results showed that higher bonding temperatures had resulted in higher ACF curing and stronger adhesion. After ageing, the adhesion strength increased for the samples bonded at lower temperatures and decreased for the samples bonded at higher temperatures. ACF assemblies with higher degrees of curing showed smaller increases in contact resistance after ageing. Conduction gaps at the bump-particle and/or particle-pad interfaces were found and were thought to be the essential cause for the increase in contact resistance.

Chen and coworkers [34, 35] investigated the effects of different bonding temperatures and bonding temperature ramp on the electrical performance and the adhesion strength of ACF interconnection. The test results showed that the contact resistance changed only slightly, but the adhesion strength increased with the increase in bonding temperature. The optimum temperature range for ACF bonding was found to be between 180–200°C.

2.2. Effect of Bonding Pressure on the Reliability of ACA Joints

The deformation degree of conducting particles during bonding determines the contact area and the electrical characteristics of the interconnection, because the bonding pressure is applied to force the conductive particles to make contact between the flip-chip and flexible/rigid substrate. Ideally, the conductive particles should be

squashed until the metallic layer begins to break. At this point, the contact area between the bonding surfaces becomes the largest. However, if the pressure applied is too high, the metallic layer of the particles will burst open, exposing the polymer to the bonding surfaces, and hence would not be conductive [37]. But there is no report to determine how much the conductive particles should deform for the best interconnections. Meanwhile, the distribution of the particles, which greatly influences the contact resistance of the ACF joints, is determined, to some extent, by the amount of pressure applied during the bonding process. This is because if the particles are too spread out between adjacent bumps or pads, caused by too much pressure applied, they might end up contacting each other creating the same effect as short-circuiting; whereas, if the bonding pressure is too low, the particles may not be able to make contact between the connecting bumps and pads [36]. Therefore, much research and development effort has been spent in understanding the effect of the bonding pressure on the reliability of ACA joints in flip-chip assemblies. Kang *et al.* [37] reported an assembly and interconnection technology for micromechanical structures using an ACF which provides many advantages. The results showed that the optimum bonding conditions were bonding at 180°C with a pressure of 5 kg/cm² applied for 10 s.

A theoretical electrical conduction model with a physical contact mechanism was simulated and experimentally verified to understand the efficiency of electrical conduction in an ACF by Yim and coworkers [38, 39]. It was shown that the electrical contact resistance of ACF depends on the external pressure, and the number, the size, and mechanical and electrical properties of particles. The model was in good agreement with experimental results except at higher bonding pressures. In general, as bonding pressure increased, a sharp decrease of contact resistance followed by a constant value was observed after reaching the critical bonding pressure. However, an excessive bonding pressure rather increased the connection resistance of the ACF interconnection.

Pinardi *et al.* [40] carried out a deformation study of the PCB during the flip-chip assembly process using an ACA. It was shown that the process-induced stress was much higher than the bonding pressure applied. The results also showed that by varying the bonding load and the temperature, the process induced stress in the structures could be optimized, so that the failure of the structure could be minimized.

Yim and Paik [41] published a paper where the effects of bonding pressure on the electrical and mechanical properties of ACF joint between FPC and ITO glass substrate using 5 μm diameter Ni-filled ACF and Au-coated polymer-filled ACF were investigated. The results showed that as bonding pressure increased, decrease of contact resistance followed by a constant resistance increase was observed after reaching the critical bonding pressure of 3 kg/cm². An excessive applied bonding pressure led to contact resistance increase and induced internal elastic stress buildup at the bonding interface. This stress was released under temperature and humidity

tests and resulted in gaps at the interface which led to contact resistance increase and open circuits.

Prabhakumar and Constable [42] studied the issue of using an ACA as a flex-to-card interconnection to interconnect the polyimide flexible circuit from a flat panel display to the FR4 circuit card. The results showed that over the range of bonding pressures, a systematic variation in the average bond thickness was found, but no variation was found in the number of particles in the bond or the resistance.

Chan and Luk [36] investigated the effect of bonding pressure during flip-chip-on-flex (FCOF) assembly in relation to the performance of an ACF interconnection, and they focused on the effect of bonding pressure on the contact resistance of ACF joints. Two types of ACFs were used in their study. ACF 1 was designed to create good interconnection when the connecting bumps and pads were in close contact while ACF 2 could give good connections when the conductive particles were in contact with the bumps and pads, hence the deformation of conductive particles within ACF 2 FCOF packages was less than that within ACF 1 packages. The results showed that ACF 2 gave much better interconnection performance as compared to ACF 1 indicating that ACF 2 was more flexible and could tolerate a wider range of bonding pressure.

Luk *et al.* [28] developed a low cost method to manufacture hard disk drive (HDD) head using ACA bonding for flex-to-flex interconnection. Critical process bonding pressure was identified and characterized to find out the optimal bonding pressure for the lowest resistance and hence a reliable ACA joint. Finally, they emphasized that although the ACF bonding technique was a mature process for chip on glass in liquid crystal display applications, there were still many unknown variables such as process parameters settings, substrate materials properties and effects of operating environment to be understood for applications in HDD head manufacturing.

Frisk *et al.* [43] evaluated the effect of bonding pressure on the reliability of ACA flip-chip joints using rigid FR-4 board and flexible liquid crystal polymer (LCP) board by a temperature cycling test. It was found that the different bonding pressures used had clearly different effects on the substrates used. The best reliability using the flexible substrates was achieved with the highest pressure. On the other hand, the lowest pressure used was the best for the rigid substrates. Moreover, the failure mechanisms of the test samples on the different substrates varied. The reliability of the adhesive joints in the case of flexible LCP substrates was much better than that in the case of rigid substrates.

Seppälä and Ristolainen [44] studied the adhesive flip-chip bonding process and failure mechanisms of ACA joints. The results showed that the bonding pressure affected the reliability of the joints significantly. The lower the applied pressure, the higher was the failure percentage. Also, the magnitude of the pad depression into the substrate could be minimized using a low bonding pressure. However, the pressure below the recommended bonding pressure was shown to be inadequate. In order to further minimize the magnitude of the pad depression, two-step heating

process was used. The effect of the degree of depression on the reliability of the joints must be studied in the future.

Lim *et al.* [45] published a paper where a three-factor design of experiments was carried out to investigate the effects of assembly parameters such as bonding pressure, temperature and time on moisture sensitivity level (MSL) performance when reflowed at 260°C. Results showed that higher bond force was undesirable and contributed to delamination at critical interfaces. With process optimization, the flip-chip BGA with large die and high I/O was able to meet the lead-free soldering requirement.

In 2006, Chen *et al.* [35] investigated the effects of bonding pressure on the electrical performance and the adhesion strength of an ACF interconnection. The test results showed that the contact resistance and adhesion strength both improved with the increase in bonding pressure, but the adhesion strength decreased if the bonding pressure was over 0.25 MPa. The optimum pressure range for ACF bonding was concluded to be between 0.15–0.2 MPa.

2.3. Effect of Curing Conditions on the Reliability of ACA Joints

Generally, adhesive materials can be cured in a short time under high curing temperature. High curing temperature usually leads to an increase in cross-link density and heat resistance. Nevertheless, curing process under high temperature can cause problems such as the tendency for shrinking, cracking and voids for the adhesive material, and it would probably lower the dielectric properties. In order to understand the curing kinetics of an anisotropic conductive adhesive film and the effect of curing conditions on the reliability of assemblies using an ACF joint, some investigations have been carried out [35, 46–52].

Miessner *et al.* [49] published a paper where a reliability study of flip-chip on FR4 interconnections with ACA was carried out and the influences of different process parameters such as pre-baking, cure temperature and heating ramp on the properties were investigated. They also found that the bump metallurgy and shape had a strong influence on the reliability of the electrical interconnection. Cao *et al.* [50] established the optimum curing degree and curing temperature to achieve the best performance of an ACA joint. It was shown that the electrical and mechanical performances were dependent on curing conditions.

Lee *et al.* [51] investigated a new type of UV curable ACA for chip-on-flex application. The adhesive bonds of the chip-on-flex application were cured at different curing cycles within a range of UV intensities. The curing cycles in their work were with different periods of time that were needed to cure the ACAs under different UV light intensities. The result showed that the longer the curing time and the higher the UV intensity, the higher the curing degree was obtained. Furthermore, the curing time in the UV curable ACA was much shorter than that of the conventional thermal curable ACAs.

Zhang *et al.* [52] studied the effect of curing conditions on the capability parameter and glass transition temperature (T_g) of the anisotropic conductive film (ACF).

In their study, DSC was used to detect the changes in the T_g of the ACF before and after curing. Also, the changes of T_g with different curing times were investigated. The results showed that the glass transition temperature decrease was one of reasons for the decreasing ACF bonding strength.

In 2006, Chen *et al.* [35] published a paper where the effects of curing time, different teflon thicknesses to form a flat bonding plane and post-processing on the electrical performance and adhesive strength of ACF interconnection were investigated. The test results showed that the curing time had great influence on the adhesive strength of ACF joints, and the optimum curing time range for ACF bonding was concluded to be between 18–25 s. The contact resistance and the adhesive strength both deteriorated with the increasing teflon thickness. The tests on different post-processing conditions showed that the specimens kept in 120°C chamber for 30 min presented the best performance of the ACF joints.

2.4. Effect of the Reflow Process on the Reliability of ACA Joints

As many electrical devices undergo at least one solder reflow process after the ACF bond, i.e., in the process of manufacturing this type of devices, so the first step usually is to use ACF bonding to achieve high accuracy for fine-pitch placement of some components, and then this is followed by a standard solder reflow process for the formation of solder interconnections. Therefore, some investigations have been performed to study the effect of solder reflow on the reliability of ACF interconnections [53–59].

Yin and coworkers [53, 54] indicated that the contact resistance of an ACF interconnection increased after reflow process due to the decrease in contact area of the conducting particles between the mating I/O pads. However, the relationship between the contact resistance and bonding parameters of the ACF interconnection with reflow treatment followed a similar trend to that of the as-bonded (i.e. without reflow) ACF interconnection. The contact resistance also increased as the peak temperature of reflow profile increased. During the reflow process, the entrapped (between the chip and substrate) adhesive matrix tries to expand much more than the tiny conductive particles because of its higher coefficient of thermal expansion, thus the induced thermal stress would try to lift the bump from the pad and decrease the contact area of the conductive path and eventually leading to a complete loss of electrical contact.

Chiang and Chan [55] investigated the influence of reflow process on the reliability of ACF joints using bumpless chips. The contact resistance of the ACF joint was found to increase as the peak reflow temperature increased. The moisture degraded both chemical and physical properties of the ACF joints. In reflow soldering after temperature/humidity test, the ACF joint reliability further deteriorated due to the presence of thermal and hygroscopic stress. Chiang and Chan [56] also studied the reliability of the ACA joint under reflow soldering and environmental test. The results showed that the ACA joint behaved differently under different reflow soldering profiles. The lower reflow temperature resulted in more reliable ACA joints by

maintaining low contact resistance. In contrast, high contact resistance was found in assemblies treated with higher reflow temperature.

Yin *et al.* [57] also investigated the effect of solder reflow process on the reliability of the ACF interconnection for flip-chip on flex (FCOF) applications. The results showed that the contact resistance of ACF interconnections increased after the reflow and the magnitude of the increase was strongly correlated to the peak reflow temperature. The interface between the particle and its surrounding material was significant and the contact resistance was the highest at the interface between the particle and the adhesive matrix.

3. Effects of Environmental Factors on the Reliability of ACA Joints

The effects of the environmental factors, including temperature, humidity, thermal cycling, impact load, etc., on the reliability of ACA joints are also significant. It is well known that the epoxy-based ACA joints are often subjected to high relative humidity environment and are susceptible to moisture sorption, especially at elevated temperatures, which is one of the major reliability concerns for ACA joints. Prolonged hygrothermal aging may lead to irreversible degradation of the epoxy resin system due to susceptibility of the resin polymer to hydrolysis and oxidation, as well as due to the change in the effective average cross-link molecular weight. The absorbed moisture has deleterious effects on the physical properties of epoxies and can, therefore, greatly compromise the performance of an epoxy-based component. Meanwhile, the polymeric materials swell upon absorbing moisture, while other components of the electronic assemblies (such as the ceramic and glass substrates) cannot absorb the moisture. Therefore, the mismatch of the thermal and moisture expansion coefficients of the materials leads to thermal and hygroscopic stresses in the polymeric materials constituting the electronic package. The combined effects are most important for the failures of ACA joints. For example, Fig. 2 shows possible failures of ACA joints in a chip-on-glass (COG) assembly in a mobile telephone under hygrothermal conditions. Obviously, the cracks and delaminations, along with some air bubbles, can be easily found at the interface between the chip and glass substrate. Some researchers have studied the effect of moisture on the epoxy resin properties, including tensile strength, elastic modulus, etc., and the effect of hygrothermal aging on ACA material and ACA joints. Therefore, some investigations have been performed to understand the failure mechanisms of ACA joints under different environmental factors [58–106].

Liu [58] investigated the feasibility of using anisotropic conductive adhesives to join surface-mount devices as solder replacement in one of the earliest work in this field. Based on industrial demands, two anisotropic conductive adhesives were chosen for the experimental study. It was concluded that some anisotropic conductive adhesive joints were stable in the 85°C/85% RH environment and therefore had better corrosion resistance than other ACA joints. But none of them passed

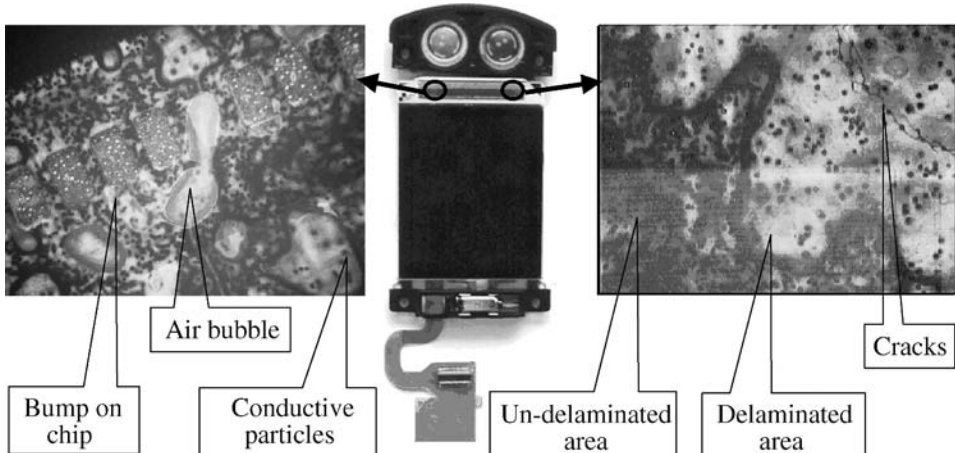


Figure 2. Failures of a COG assembly in a mobile telephone under hygrothermal conditions.

temperature cycling from -55 to 125°C for 1000 cycles required by the military standard.

In 1995, Stam *et al.* [59] carried out a reliability study of ACA joints for fine pitch package assembly. It was shown that although mechanical strength and electrical resistance obtained were similar to those expected for solder assembly, reliability needed to be addressed in greater detail in order to make the application of ACAs a viable alternative to solder, specially in humidity testing.

In 1996, Lai and Liu [60] investigated the ACA joining technology on rigid board, which was also the earliest work in this field. They carried out a systematic experimental study on flip-chip bonding assembly using an ACA on rigid board, including investigation of aging, constant humidity, temperature cycling, humidity cycling, shear, vibration and shock testing. The results indicated that under optimum process conditions, high quality and high reliability joints could be achieved. The analysis showed that the failure was dependent on competition between factors: thermal stress, elastic stress, expansion due to moisture absorption and interatomic force. This paper was the earliest work in this field where ACA was used on rigid board.

In 1999, Liu *et al.* [61] performed an evaluation of environmental impact on reliability using ACAs for flip-chip joining. The results of reliability testing (the temperature cycling test and aging test) showed that relatively only small resistance changes were observed after the reliability test. By using flip-chip ACA joining technology, the quantity of environmentally-risky materials has been reduced more than ten times, and the use of precious metals has been reduced more than 30 times compared to conventional surface mount technology.

Yim and Paik [41] investigated environmental effects such as thermal aging, high temperature/humidity aging and temperature cycling on contact resistance and adhesion strength. The results showed that temperature cycling and temperature-

humidity tests displayed detrimental effects of increased contact resistance and electrical failure in the ACF interconnection. Increased contact resistance and decreased adhesion strength after harsh environmental tests were mainly due to the loss of contact by thermal stress effect and moisture absorption, and also partially due to the formation of metal oxide on the conductive particles.

Weidler *et al.* [62] studied the electrical properties and the reliability of ACA film interconnections between aluminum pads on a glass substrate and electrolytically tin coated copper pads on a polyimide flexible circuit as a function of temperature and humidity aging. It was found that although the interconnections to the aluminum metallurgy preformed well, the weak part of the bond was determined to be the adhesive–aluminum interface. Cracks were observed to originate at this interface, and nearly all electrical resistance was shown to be due to the aluminum metallurgy.

Murray *et al.* [63] studied the environmental reliability of ACFs used in making polyimide flex to LCD interconnection. They examined both the electrical and peel performances of these bonds after environmental aging, including wide ranges of temperature and humidity conditions.

In 2000, Lefebvre [64] revealed that the adhesion between an epoxy and glass was lowered abruptly when the epoxy was equilibrated with air whose relative humidity (RH) exceeded a critical value. The critical humidity marking the onset of adhesion loss was also associated with a sudden increase of water uptake by the epoxy. The critical humidity effect was due to the trapping of water by the hydroxyl groups which became available as inter-chain hydrogen-bonded structures were broken.

In 2001, Liu [65] developed a theoretical model for predicting the number of cycles to catastrophic failure during the temperature cycling for any anisotropic conductive adhesive joint used for electronics interconnecting purposes. The model can predict the resistance increase of the joint as a function of the increasing crack length and also as a function of the number of temperature cycles.

Connection reliability and connection deterioration mechanism regarding a flip-chip attachment method were examined using an anisotropic conductive film to connect Si chips having Au bumps to the printed wiring substrate [66]. A connection reliability of 1000 cycles or more was obtained in a $-30/80^{\circ}\text{C}$ temperature cycle test. An increase in resistance in the temperature cycle test was thought to have been caused by Au plating on the wiring rubbing off due to sliding on the Au bump and wiring interface as a result of the difference in coefficients of linear expansion for the chip and substrate, and this rubbing caused a reduction in contact area.

Zhang *et al.* [29] systematically discussed the influence of humidity on the adhesion of bumpless die (aluminum surface) with two kinds of ACFs. It was found that the adhesion strength at the ACF/aluminum interface increased while the adhesion at the ACF/glass surface decreased after aging in the same high temperature and high humidity environment. Moisture mainly diffused into aluminum

and resulted in oxidation reaction instead of diffusing into the adhesive to swell it. The more the swelling of the adhesive, the lower the delamination strength at the ACF/aluminum interface. So the adhesion strength of shear samples increased after temperature/humidity exposure. In addition, the oxidation reaction can provide fresh rougher surface that may enhance adhesion strength.

Wu and Chau [67] carried out a reliability assessment of adhesive joints using chip-on-glass (COG) technology at various aging temperatures and at high humidity. It was found that aging generally caused a decrease in shear strength when the aging temperature was below the glass transition temperature (T_g) of the ACF. When the aging temperature was slightly above the T_g of the ACF, a significant decrease in shear strength was observed. Moreover, the results revealed the presence of some voids near the component bumps, resulting in high stresses at the high aging temperature, and the ACF was not fully cured, allowing higher moisture absorption than a fully cured ACF and thus leading to joint degradation.

Wei *et al.* [68] carried out a generic study on the reliability performance of the flip-chip in a package using an ACF in the autoclave (AC) test environment. Their studies identified the failure mechanism in ACF interconnection under the AC test environment. It was found that the mismatch in moisture expansion between the epoxy and joints was the root cause for the joint opening. Based on their studies, recommendation to use a higher modulus ACF and lower modulus substrates was proposed.

Tan *et al.* [69] investigated the behavior of ACF joints under high moisture and elevated temperature, under various mechanical loadings (die shear and cyclic fatigue in shear). The results showed that epoxy based ACF exhibited insignificant plastic deformation, especially for samples that had undergone autoclave test. Reduction trend was observed in the shear modulus over autoclave test time for ACF joints. Fracture surface of the ACF joint that failed in the shear test showed spalling and less plastic deformation after exposure to autoclave test. Tan and coworkers [70, 71] also reported that the stress-corrosion cracking induced by autoclave test conditions reduced the mechanical strength of anisotropic conductive joints and also increased the contact resistance by allowing more moisture to reach the aluminum metallization. The results showed that the epoxy-based ACF absorbed moisture and experienced hygroscopic swelling to degrade the adhesion strength and elasticity in hygrothermal environments. Also, contact resistance showed an increasing trend, which was most probably due to the formation of an oxidation layer on top of the aluminum metallization as well as to the hygroscopic swelling of the ACF.

Wang [72] reviewed the current development of chip-on-glass (COG) technology for mobile display applications, with the emphasis on the challenges in the reliability study. It was shown that delamination and Indium-tin-oxide (ITO) corrosion were two major concerns faced by the industry. The former was typically caused by moisture in combination with high temperature. ITO corrosion was typically caused by moisture, contamination, and ionic impurities in the ACF or on the glass surface.

Mercado *et al.* [73] investigated the failure mechanism of an ACF joint using finite element simulation. Simulation results showed that moisture-induced ACF swelling and delamination were the major causes of ACF joint failure. With moisture absorption, the loading condition at the interface was tensile-dominant, which corresponded to lower interface toughness (or fracture resistance). This condition made the joint more prone to interface delamination.

Zhang and coworkers [74, 75] presented the initial contact resistance, electrical performance after reliability tests (such as high humidity and temperature and thermal cycling), and degradation mechanisms of ACF interconnection for flip-chip-on-flex (FCOF) assembly using very-low-height Ni and Au-coated Ni-bumped chips. The results showed that the degradation of electrical performance was mainly related to the oxide formation on the surface of deformed particles with non-noble metal coating, the severe metal oxidation on the conductive surface of bumps, and CTE mismatch between the ACF adhesive and the conductive surface metallization. Additionally, some methods for reducing initial contact resistance and improving ACF interconnection reliability were suggested.

Wu *et al.* [76] studied the impact properties of flip-chip interconnection using an anisotropic conductive film on the glass and flexible substrates. It was found that impact load caused fracture to propagate at the ACF/substrate interface (for COG packages) and in the ACF matrix (for COF packages).

Uddin *et al.* [77] performed systematic experimental work to evaluate the reliability of the ACF joint at high temperature for flip-chip-on-flex (FCOF) assemblies. It was found that initially, the contact resistance increased linearly with increasing temperature, but later, it increased abruptly. This changeover was related to the glass transition temperature (T_g) of the ACF matrix. In addition, as the adhesive strength became lower at temperatures above the glass transition, it was unable to resist the thermal stress of the flex. The cumulative thermal stress at the edges dislodged the particles from the interconnection. Even below the T_g , the thermal stress at the edges was higher than at the middle point. Thus, the contact resistance varied from the middle joint of the chip to that of the corner at the same high temperature. To reduce the contact resistance at the corner joint of the FCOF packages bonded by ACF, a square-shaped chip instead of a chip with a higher aspect ratio should be used. It was also suggested to use an adhesive with a higher glass transition temperature and a lower CTE.

Chen *et al.* [78] studied the failure mechanism of ACF joint in chip-on-glass (COG) by microscopic observation. The evolution of interfacial bubbles and delamination of COG specimens was observed. The experiment showed that the moisture absorption in ACF varied with both temperature and humidity.

The thermally induced deformation and warpage of ACF flip-chip assemblies as a function of distance from the neutral point and ACF materials properties were investigated by Kwon and co-workers [79, 80]. The results indicated that the properties of ACF had a significant role in the thermal deformation and reliability performance during thermal cycling testing. An ACF with a low CTE and a high

modulus can reduce the thermally induced shear strain in the ACF layer, and thus can increase the overall thermal cycling lifetime of ACF joint compared with high CTE and low modulus ACF. During the thermal loading, the shear deformation was more detrimental to the electrical degradation of ACA joints than normal strain. Yang *et al.* [81] also investigated the warpage damage of the chip for ACA film type electronic packages under thermal cycling. The reduction in chip warpage due to increase in delamination length was obtained as a function of thermal fatigue cycles. Finally, a new model to predict damage level of ACA package and remaining life was proposed.

Lin *et al.* [82] studied the effects of hygrothermal aging on anisotropic conductive adhesive joints by both experiments and theoretical analyses recently. The results showed that the strength of ACF joint decreased and the fracture mechanism gradually changed with hygrothermal aging. That is, a transition from cohesive to interfacial mode of debonding occurred. Additionally, they developed an ACF joint aging model with hygrothermal environment by introducing a dimensionless parameter A, which was obtained from the interfacial fracture energy and used to describe the decrease of interfacial fracture energy. It was found that the process of degradation for the interfacial fracture energy could be approximately divided into three phases, i.e., the primary, secondary and tertiary phases. Lin *et al.* [83] also studied the effect of hygrothermal aging on epoxy-based anisotropic conductive film. The results indicated that there were some chemical modifications to the aged ACF materials, which verified the viewpoint that the material was subjected to chemical hydrolysis with increased aging of the ACF under the hygrothermal conditions. Meanwhile, quantitative analysis of the relative absorbance intensities of the epoxy functional groups showed that continuous cure reaction occurred with hygrothermal aging.

The damage to the adhesive interface of the ACA joints was investigated by Zhang *et al.* [84]. In their study, the cohesive zone type interface model was used for the ACF bonded samples, and the interface model could calculate the peel strength for a 90° peel test. The constitutive equation for the interface was modified by introducing the thermal damage factor and humidity damage factor, which were derived from the experimental data. Their calculated results from the interfacial model with damage factors agreed well with those of the 90° peel tests.

Additionally, as anisotropic conductive adhesives (ACAs) are based on the epoxy system, some studies have been carried out to investigate the behavior of the epoxy system under hygrothermal conditions.

In 2002, Luo *et al.* [85] presented a study on the mobility of water and polymer chains in epoxy materials and its influence on the rate of adhesion degradation in a humid environment. The results showed that absorbed water reduced the glass transition temperature of polymeric materials due to the plasticizing effect of water. The higher mobility of absorbed water and the higher mobility of polymer chains in the epoxy led to faster adhesion degradation during aging in a humid environment.

Leung *et al.* published a paper [86] where the subcritical interfacial debonding process was described. The debonding rates of polymers were characterized at different temperatures by shear fracture tests and tapered double cantilever beam tests under mechanical loading and simultaneous exposure to controlled acidic environments. It was found that elevated temperature and acidity had a strong effect on package reliability, but mechanical loading was found to have a minimal effect on the rate of adhesion degradation.

In 2005, Lin and Chen [87, 88] studied the effects of hygrothermal conditions on the mechanical behavior of DGEBA epoxy system, which is commonly used as the adhesive. The results showed that due to the effect of the hygrothermal condition, the tensile strength and tensile elastic modulus of the water-saturated, desorbed and resaturated samples both reduced much, compared to the original unaged or dry samples. This was probably due to the plasticizing effect of absorbed moisture. Also, the moisture sorption–desorption–re-sorption characteristics of the DGEBA/DDA epoxy system were investigated by hygrothermal aging and molecular dynamics (MD) simulation. Lin and Chen [89] also investigated the effect of hygrothermal conditions on epoxy system by fractography and computer simulation. In this work, the tensile fracture surfaces were analyzed for the initially dry, moisture-saturated and completely desorbed specimens. Furthermore, fracture surface patterns were simulated using a computer, based on the theory that the conic-shaped pattern was due to the intersection between a moving planar crack front and a radial growing circular craze or secondary crack front. The results showed that there was a close relationship between the velocity ratio of crack velocity to craze or secondary crack velocity and fracture surface patterns. Additionally, the brittle/ductile transition appeared due to the effect of hygrothermal conditions.

Also, some other intensive research and development works have been carried out in the field of flip-chip on board technology, using ACAs as an alternative to soldering [90–106].

4. Effects of the Properties of Components

4.1. Effect of ACA Material Properties

As the bump size in the flip-chip assembly is reduced, the current density through the bump also increases. This increased current density causes new failure mechanisms, such as interface degradation due to intermetallic compound formation and adhesive swelling resulting from high current stressing. This process is found especially in high current density interconnection in which the high junction temperature enhances such failure mechanisms. Therefore, it is necessary for the ACA to become a thermal transfer medium that allows the board to act as a new heat sink for the flip-chip package and thus improve the lifetime of the ACA flip-chip joint. Fatigue life of ACF interconnection, which is limited by the thermal expansion mismatch between chip and substrate, could be increased by varying the interconnection material properties. In general, the interconnection material between chip

and substrate should have close CTE value to those of the chip and substrate for the reduction of thermally induced strain and stress. So, understanding the effect of CTE value of ACFs on thermo-mechanical properties will help in achieving better performance and reliability of flip-chip packages by choosing the right ACF materials. Some investigations have been carried out in this field [107–115].

Yim and co-workers [107, 108] discussed the flip-chip assembly on organic board using an ACF and electroless Ni/Au bump. Three kinds of ACF materials with different CTE values were prepared by incorporation of nonconductive particles and bonded between Si chips and FR-4 boards for the thermal strain measurement using Moiré interferometry. They found that when the content of nonconductive particles increased the CTE value of cured adhesive film decreased. The thermal strain of the ACF interconnection layer decreased according to the decreased CTEs of ACF materials. This result indicated that the thermal fatigue life of ACF flip-chip assembly on organic boards, limited by the thermal expansion mismatch between the chip and the board, could be increased by low CTE ACF.

In 2002, Liu and Lai published a paper [109] where a reliability study on nine types of ACAs and one nonconductive film (NCF) joints on a Flip-Chip/FR-4 assembly under temperature cycling conditions was carried out. The results showed clearly that under optimized conditions, high reliability flip-chip anisotropic conductive adhesive joints on low-cost substrate could be achieved.

In 2003, Kwon and Paik [110] investigated thermally induced deformations of ACF flip-chip assemblies as a function of Distance to Neutral Point (DNP) and ACF materials properties. The results indicated that the properties of ACF had a significant role in the thermal deformation and overall reliability during thermal cycling testing. Therefore, optimized ACF properties can enhance ACF package reliability during thermal cycling regime.

Teo and co-workers [111, 112] studied the effects of ACA material properties on package reliability performance. In their study, four representative ACA materials with diverse properties were selected. Reliability tests including Moisture Sensitivity Test (MST), Pressure Cooker Test (PCT), Temperature Cycling (TC) and High Temperature Storage (HTS) were performed on the test vehicles. Findings indicated that the best properties for high reliability assemblies were high adhesion strength after subjecting to reliability test conditions (stress aging), low coefficient of moisture expansion (CME) and low elastic modulus of ACA.

In 2005, Hwang *et al.* [113] investigated the effects of thermoplastic resin content of anisotropic conductive films on the pressure cooker test reliability of anisotropic conductive film flip-chip assembly. In their study, the changes in ACF resin morphology due to the phase separation of thermoplastics, and subsequent changes in physical and mechanical properties were investigated as a function of thermoplastic content of the ACF formulation. Furthermore, the pressure cooker test (PCT) reliability of ACF flip-chip assemblies with various thermoplastic contents was also investigated. The results showed that as thermoplastic content increased, the coefficient of thermal expansion (CTE) of the ACF increased, and elastic modulus (E')

of the ACF decreased. In contrast, water absorption amount decreased as thermoplastic content increased. As a result, PCT reliability of ACF flip-chip assembly was improved by adding up to 50 wt% content of thermoplastic.

The effects of the functionality of the epoxy monomer on the composite properties and reliability of ACFs in a flip-chip package were investigated by Hwang *et al.* [114]. The results showed that the ACFs prepared using epoxy monomers with higher functionality resulted in lower molecular weight between crosslinks (M_c). As the M_c decreased, the elastic modulus (E') and coefficient of thermal expansion (CTE) improved. The ACFs prepared using higher functionality epoxy monomers showed improved reliability performance of the flip-chip on organic substrate assemblies.

4.2. Effects of Substrate Properties

Another important issue is the effects of the substrate hardness, geometry and material on the ACA joints, and parallelism of substrates and components remains a major issue in obtaining consistency of conduction across assembly joints. Therefore, some studies have been carried out to understand the mechanisms [24, 60, 115–117].

The planarity of the substrate can have a strong influence on the reliability of the ACA joints. On flexible substrates, in particular, the presence of conductor tracks can cause a non-flat surface. The result is uneven pressure distribution and, therefore, poor bonding quality. In 1996, Lai and Liu [60] studied the reliability of ACA flip-chip bonding on rigid and flexible printed circuit substrates by a number of environmental tests, including aging, constant humidity, temperature cycling, humidity cycling, shear, vibration, and shock testing. The results indicated that the bonding pressure with the flexible board was always uneven. The uneven pressure distribution leads to non-uniform deformation of the contacting pads on the flexible board.

In 1998, Oguibe *et al.* [24] published a paper where successful assembly of 220 μm pitch bumped flip-chips on both FR5 and plated ceramic substrates with 10 μm diameter particle thermoplastic adhesive was achieved. They found that the adhesive containing large particles accommodated planarity errors due to surface roughness and non-flat pad shape better than the smaller diameter particles. On the other hand, it was found to be difficult to obtain 100% consistency in conduction with unbumped flip-chip dies and with small diameter balls.

Liu and Lai [115] observed that on an FR-4 substrate, the electrical conductivity and reliability of the joint depended on the distance to the glass fibre in the substrate. A longer distance means a thicker layer of soft epoxy which may deform during the bonding. Insufficient particle deformation will, therefore, be obtained at that point. A shorter distance gives more resistance to this deformation and thereby results in better electrical conductivity and reliability. Seppälä *et al.* [116] published some important data on the reliability of the flip-chip joining on FR-4 substrate using ACA. It was shown that the co-planarity of the substrate and the chip was important

for the bonding quality. It was also shown that by decreasing the bonding pressure, reliability of the test chip types could be improved.

Fan and Chan [117] investigated the effect of the substrate-pad physical properties (surface roughness and hardness) on the current-carrying capacity of the ACA joints. It was found that the variation in current carrying capacity (or connection resistance) of Au/Cu pad joints was larger than that of Au/Ni/Cu pad joints. The current-carrying capacity was related to the variation of the resistance of ACF joints. For the Au/Cu pad ACF joints, the deformation of the particles' upper and lower sides was nearly symmetrical. The contact between conductive particles and pad had the character of "sliding contact", especially under high pressure. For the Au/Ni/Cu pad ACF joint, the contact between particles and pad determined the conduction characteristics of ACF joint. It has the character of "static contact". Thus, the current-carrying capacity (or connection resistance) of Au/Cu pad joints was more sensitive to the bonding pressure.

4.3. Effect of Bump Height on the Reliability of ACA Joints

Flip-chip joining using ACAs has become a very attractive technique for electronics packaging. The bumps of the flip-chip (FC) technology are usually made from nickel. Since pressure is applied to force the conductive particles to make a contact between the nickel bumps and the copper pads in printed circuit boards (PCBs) or flexible circuits (flex), the deformation of the bump can affect the electrical conductivity. In particular, the height of the bumps can change the deformation characteristics, and hence the reliability of the interconnection in the FC assembly. Therefore, some researchers have investigated the effect of bump height on flip-chip joint reliability using ACAs [118–124].

In 1997, Lam *et al.* [118] investigated the structural reliability of direct-chip-attach bonded with an anisotropic conductive film. The results showed that tall bump height could reduce the potential for electrical failure in ACF interconnects when ACF/bump interfacial fracture was the dominant failure mode.

In 1998, Lai *et al.* [119] studied the effect of bump height on the reliability of ACA flip-chip joining with FR4 rigid and polyimide flexible substrates. In the temperature cycling test, the assemblies on FR4 substrate showed that reliability decreased with increasing bump height. While with the flexible substrate, the electrical performance of the ACA flip-chips did not change. It was also shown that the different mechanisms were attributed to the different stiffness substrates.

Electroless nickel/gold bumps of different heights were used to study the effect of bump height on flip-chip joint reliability using ACAs [120]. The chips were assembled on FR-4 substrates and the samples were subjected to temperature cycling from –40 to 125°C. The results showed that the bump height was important for the quality and reliability of flip-chip joints, and the high bumped joints showed poor reliability, which could be due to the formation of pores.

Pinardi and co-workers [121, 122] also reported on the effect of bump height on the strain variation during thermal cycling test of ACA flip-chip joints. In this work,

the strain development during thermal cycling test of flip-chip joining with different bump heights was studied. The results showed that the effect of bump height was significant at the interface between the bumps and the pads. Their calculations showed that there was practically no effect of the bump height on the strain variation in the bumps and in the pads.

Wu *et al.* [123, 124] also studied the effect of bump height on the reliability of ACF in flip-chip (FC) assemblies. In their study, flip-chip assemblies on printed circuit board (PCB) and flex, with bump heights of 4, 20 and 40 μm , and with a constant copper pad height were compared by modeling the bonding process under thermal cycling from -40 to 125°C . It was shown that the largest stress occurred for the smallest bump height, and stress in the anisotropic conductive film for the FC-on-flex assembly was also found to be generally larger than that for the FC-on-PCB.

Additionally, the planarity of the bumps across a single chip is essential to improve the reliability of the ACA joints. If there is a large variation in bump height across the chip, it will be impossible to exert a uniform pressure over the entire chip. It is important to have bumps of uniform height across the chip. Otherwise bonding quality cannot be guaranteed.

4.4. Effect of the Conductive Particles of ACF

In ACA interconnections, the particles are electrical conductors providing current paths in the fine pitch electronic packaging as well as mechanical parts connecting with the chip bumps and the substrate pads through the mechanical deformation interfaces. However, the particles are randomly distributed in ACF materials which can cause problems, especially in ultra-fine pitch applications. This is because the concentration and deformation of particles within the material vary at different locations, and hence may result in low reliability of the assemblies. In order to understand the effect of the conductive particles on the reliability of the assemblies using anisotropic conductive adhesives, some investigations have been done [39, 60, 125–129].

Yim and Paik [39] studied the relationship between particle content of an ACF and the connection resistance. The results showed that for ACFs with increased particle contents, the connection resistance decreased. However, for more than 4 wt% of conductive particles, the connection resistance did not decrease further, but became stabilized. This is because of two opposing factors: the resistance increase caused by a decrease of contact area per particle and the resistance decrease caused by increasing number of conduction paths at the same bonding pressure. Sarkar *et al.* [126] showed that the number of conductive particles existing on a bump increased as the content of conductive particles increased. The content of the conductive particles can seriously affect the connectability, resulting in short-circuit. The most suitable content is within the range of 2.5–12.5 vol%. Further, the interconnection resistance decreases as the volume content of the conductive particles increases up to 7.5 vol%.

Paik *et al.* [127] investigated the effect of fillers on the thermo-mechanical properties of modified ACA composite materials and the resulting reliability of flip-chip assemblies on organic substrates using modified ACA materials. It was observed that lowering the CTE of the ACA material by adding the fillers significantly enhanced thermal cycling reliability.

In 2003, Dou *et al.* [128] investigated the electrical conduction characteristics of anisotropic conductive adhesive particles. It was stated that the ACA particle resistance was determined by the particle deformation and the particle geometry. However, the deformation and the nickel layer thickness were more sensitive than the resin diameter and the gold layer thickness.

In 2005, Cao *et al.* [129] studied the effects of ACA resin and different curing agents, as well as different conductive particles, on flexible substrate of the flip-chip joints by formulating several ACA pastes and different sized silver (Ag) powders or gold (Au)-coated polymer spheres as conductive particles. The results showed that both the size and type of conductive particle had very limited influence on an ACA flip-chip joint.

5. Summary Conclusions

In this paper, a summary of our understanding of the electrical, physical, thermal, chemical, and environmental behaviors of ACAs in conjunction with various packaging applications is elaborated. The effects of the bonding process, environmental factors, and properties of the components on the reliability of ACA joints are systematically reviewed. The results of these studies would allow development of ACA joints using fine pitch flip-chips on flexible/rigid substrates with better reliability and performance. The literature survey indicates that the following issues of ACA bonding in electronic assemblies need further study:

- (1) There is lack of understanding of the adhesive flow behavior during the bonding process. With the increasing demand for smaller pitch, how the adhesive and conductive balls move in a bonding process becomes critical for the selection and design of the material and process parameters. Sufficient number of conducting particles must be trapped during the bonding process to guarantee electrical contact with both conductor surfaces.
- (2) Fundamental understanding of the performance and features of mini-specimen and material interfaces (e.g. particle, ACA, bump and pad metal) involved in ACA bonding is necessary. But the difficulty is that the testing standards and methodology for characterization of mini-specimen and material interfaces have not been established.
- (3) There is lack of effective numerical finite element methods (FEM) based on interfacial fracture mechanics, which can be used to simulate the fracture characteristic of interface and crack-tip. Understanding of the effects of the induced

stress state after assembly on the mechanical performance under testing conditions and service is needed.

- (4) It is necessary to clarify the failure mechanisms of ACA joints under different environmental conditions. Since conductive balls are mixed with the adhesive, the adhesive film cannot be considered as a homogeneous material. There is no reported study on the effect of conductive balls on the delamination of adhesives. More importantly, moisture appears to be one of the key factors affecting the failure. There is no effective tool to investigate the effect of moisture.
- (5) Further reduction of the pitches in ACA joining technology and wide application in electronics packaging require a major breakthrough in ACF materials and careful reliability design.

Acknowledgements

This work was supported by the National Natural Science Foundation of China (Grant No. 10672118) and the Cheung Kong Scholar Program for Innovative Teams of the Ministry of Education (Grant No. IRT0641). Y. C. Lin thanks for the support from the Postdoctoral Science Foundation of Central South University and the Science Research Foundation Program of Central South University.

References

1. J. Liu (Ed.), *Conductive Adhesives for Electronics Packaging*. Electrochemical Publications, Port Erin, UK (1998).
2. A. Nagai, K. Takemure, K. Isaka, O. Watanabe, K. Kojima, K. Matsuda and I. Watanabe, in: *Proceedings of Joint International Electronic Manufacturing Symposium and the International Microelectronics Conference (IEMT/IMCP)*, Tokyo, pp. 353–357 (1998).
3. D. Lu, Q. K. Tong and C. P. Wong, in: *Proceedings of the 49th IEEE Electronic Components and Technology Conference*, San Diego, CA, pp. 347–352 (1999).
4. J. Liu, *Solder Surface Mount Technol.* **13**, 39–57 (2001).
5. J. Lau, C. P. Wong, N. C. Lee and S. W. R. Lee (Eds), *Electronics Manufacturing: with Lead-free, Halogen-free, and Conductive Adhesive Materials*. McGraw Hill, New York, NY (2002).
6. A. M. Tan, S. P. S. Lim and C. Lee, in: *Proceedings of the 53rd IEEE Electronic Components and Technology Conference*, Singapore, pp. 390–396 (2003).
7. P. Savolainen, I. Saarinen and O. Rusanen, in: *Proceedings of the 4th IEEE International Conference on Polymers and Adhesives in Microelectronics and Photonics*, Portland, OR, pp. 99–104 (2004).
8. Y. Li and C. P. Wong, in: *Proceedings of the 4th IEEE International Conference on Polymers and Adhesives in Microelectronics and Photonics*, Portland, OR, pp. 1–7 (2004).
9. Y. Li, K. Moon and C. P. Wong, *Science* **308**, 1419–1420 (2005).
10. J. Liu, Y. Wang, J. Morris and H. Kristiansen, in: *Proc. of the International Symposium on Advanced Packaging Materials: Processes, Properties and Interfaces*, pp. 193–208 (2005).
11. Y. Li and C. P. Wong, *Mater. Sci. Eng. R* **51**, 1–35 (2006).
12. R. R. Reinke and T. W. Kennedy, in: *Proceedings of the SID International Symposium. Digest of Technical Papers*, pp. 305–308 (1988).

13. D. C. Hu, S. J. Ho and B. Y. Tang, in: *Proceedings of the 13th IEEE/CHMT International Electronics Manufacturing Technology Symposium*, Bulimore, MD, pp. 277–282 (1992).
14. C. H. Lee and K. I. Loh, in: *Proceedings of the 45th IEEE Electronic Components and Technology Conference*, Las Vegas, NV, pp. 21–25 (1995).
15. J. Baumbach, H. Baur, E. Lueder, A. Yamauchi, L. Dorfmüller and P. M. Knoll, in: *Proceedings of the Society for Information Display International Symposium*, San Jose, CA, pp. 848–852 (1999).
16. I. Watanabe, T. Fujinawa, M. Arifuku, K. Kobayashi and Y. Gotoh, in: *Proceedings of the International IEEE Conference on the Asian Green Electronics*, Hongkong, pp. 229–234 (2004).
17. H. Otsuki, H. Morishita, T. Kokogawa, K. Adachi, F. Matsukawa and H. Takasago, in: *Proceedings of the International Symposium on Microelectronics*, San Diego, CA, pp. 86–90 (1991).
18. J. Liu, K. Boustedt and Z. Lai, *Circuit World* **22**, 19–24 (1996).
19. R. Miesner, R. Aschenbrenner, H. Reichl, S. Ling, L. Binh, A. Lew, R. Benson and E. Nhan, in: *Proceedings of the 50th IEEE Electronic Components and Technology Conference*, Las Vegas, NV, pp. 1133–1138 (2000).
20. L. Li and T. Fang, in: *Proceedings of the 4th International Conference on Adhesive Joining and Coating Technology in Electronics Manufacturing*, Espoo, Finland, pp. 129–135 (2000).
21. K. Gustafsson, S. Mannan, J. Liu, Z. Lai, D. Whalley and D. Williams, in: *Proceedings of the 47th IEEE Electronic Components and Technology Conference*, San Jose, CA, pp. 561–566 (1997).
22. R. Miesner, R. Aschenbrenner and H. Reichl, in: *Proceedings of the 49th IEEE Electronic Components and Technology Conference*, San Diego, CA, pp. 595–601 (1999).
23. A. O. Ogunjimi, S. H. Mannan, D. C. Whalley and D. J. Williams, *IEEE Trans. Compon. Packag. Manuf. Technol. Part C* **19**, 257–263 (1996).
24. C. N. Oguibe, S. H. Mannan, D. C. Whalley and D. J. Williams, in: *Proceedings of the 3rd International Conference on Adhesive Joining and Coating Technology in Electronics Manufacturing*, Binghamton, New York, NY, pp. 27–33 (1998).
25. Y. W. Chiu, Y. C. Chan and S. M. Lui, *Microelectron. Reliab.* **42**, 1945–1951 (2002).
26. G. Connell, R. L. D. Zenner and J. A. Gerber, in: *Proceedings of the 47th IEEE Electronic Components and Technology Conference*, San Jose, CA, pp. 274–278 (1997).
27. Y. C. Chan and D. Y. Luk, *Microelectron. Reliab.* **42**, 1185–1194 (2002).
28. C. F. Luk, Y. C. Chan and K. C. Hung, *Microelectron. Reliab.* **42**, 767–777 (2002).
29. J. H. Zhang, Y. C. Chan, Z. M. Zeng and Y. W. Chiu, in: *Proceedings of the 52nd Electronic Components and Technology Conference*, San Diego, CA, pp. 1569–1574 (2002).
30. Y. P. Wu, M. O. Alam, Y. C. Chan and B. Y. Wu, *Microelectron. Reliab.* **44**, 295–302 (2004).
31. S. C. Tan, Y. C. Chan, Y. W. Chiu and C. W. Tan, *Microelectron. Reliab.* **44**, 495–503 (2004).
32. M. A. Uddin, M. O. Alam, Y. C. Chan and H. P. Chan, *Microelectron. Reliab.* **44**, 505–514 (2004).
33. M. F. Rizvi, Y. C. Chan, C. Bailey, H. Lu and A. Sharif, *Solder Surface Mount Technol.* **17**, 40–48 (2005).
34. X. Chen and J. Zhang, *Key Eng. Mater.* **297**, 918–926 (2005).
35. X. Chen and J. Zhang, C. Jiao and Y. Liu, *Microelectron. Reliab.* **46**, 774–785 (2006).
36. Y. C. Chan and D. Y. Luk, *Microelectron. Reliab.* **42**, 1195–1204 (2002).
37. I. B. Kang, M. R. Haskard and B. K. Ju, in: *Proc. SPIE*, San Jose, CA, pp. 280–287 (1996).
38. M. J. Yim, K. W. Paik, Y. K. Kim and H. N. Hwang, in: *Proceedings of the Pacific Rim/ASME International Intersociety Electronic and Photonic Packaging Conference*, New York, NY, pp. 65–72 (1997).

39. M. J. Yim and K. W. Paik, *IEEE Trans. Compon. Packag. Manuf. Technol. Part A* **21**, 226–234 (1998).
40. K. Pinardi, J. Liu, R. Haug, C. Treutler and M. Willander, in: *Proceedings of the 3rd International Conference on Adhesive Joining and Coating Technology in Electronics Manufacturing*, Binghamton, New York, NY, pp. 34–37 (1998).
41. M. J. Yim and K. W. Paik, *IEEE Trans. Advanc. Packag.* **22**, 166–173 (1999).
42. A. Prabhakumar and J. H. Constable, in: *Proceedings of the 51st IEEE Electronic Components and Technology Conference*, Orlando, FL, pp. 580–585 (2001).
43. L. Frisk, A. Seppälä and E. Ristolainen, *Microelectron. Reliab.* **44**, 1305–1310 (2004).
44. A. Seppälä and E. Ristolainen, *Microelectron. Reliab.* **44**, 639–648 (2004).
45. S. P. S. Lim, A. M. Tan and C. Lee, in: *Proceedings of the 6th Electronics Packaging Technology Conference*, Shenzhen, China, pp. 450–454 (2004).
46. Y. C. Chan, M. A. Uddin, M. O. Alam and H. P. Chan, *J. Electronic Mater.* **32**, 131–136 (2003).
47. K. K. Lee, K. T. Ng, C. W. Tan, Y. C. Chan and L. M. Cheng, in: *Proceedings of the International Conference on the Business of Electronic Product Reliability and Liability*, Shanghai, China, pp. 134–139 (2004).
48. K. K. Chan, N. H. Yeung, Y. C. Chan, S. C. Tan and K. K. Lee, in: *Proceedings of the 53rd IEEE Electronic Components and Technology Conference*, New Orleans, pp. 1701–1704 (2003).
49. R. Miesner, R. Aschenbrenner and H. Reichl, in: *Proceedings of the 49th IEEE Electronic Components and Technology Conference*, San Diego, CA, pp. 595–601 (1999).
50. L. Cao, Z. Lai and J. Liu, in: *Proceedings of the 6th IEEE CPMT Conference on High Density Microsystem Design and Packaging and Component Failure Analysis*, Shanghai, China, pp. 254–258 (2004).
51. K. K. Lee, S. C. Tan and Y. C. Chan, *J. Electron. Packag.* **127**, 52–58 (2005).
52. J. Zhang, H. Jia and X. Chen, *Chinese Electron. Packag.* **6**, 33–36 (2006).
53. C. Y. Yin, M. O. Alam, Y. C. Chan, C. Bailey and L. Hua, *Microelectron. Reliab.* **43**, 625–633 (2003).
54. C. Y. Yin, H. Lu, C. Bailey and Y. C. Chan, in: *Proceedings of the International IEEE Conference on the Asian Green Electronics (AGEC)*, Hongkong, pp. 240–245 (2004).
55. W. K. Chiang and Y. C. Chan, in: *Proceedings of the International IEEE Conference on the Asian Green Electronics (AGEC)*, Hongkong, pp. 235–239 (2004).
56. W. K. Chiang and Y. C. Chan, *J. Electron. Packag.* **127**, 113–119 (2005).
57. C. Y. Yin, H. Lu, C. Bailey and Y. C. Chan, *IEEE Trans. Electron. Packag. Manuf.* **27**, 254–259 (2004).
58. J. Liu, *Circuit World* **19**, 4–11 (1993).
59. F. Stam, P. O’Grady and J. Barrett, *J. Electron. Manuf.* **5**, 1–8 (1995).
60. Z. Lai and J. Liu, *IEEE Trans. Compon. Packag. Manuf. Technol. Part B* **19**, 644–660 (1996).
61. J. Liu, A. Tolvgard, J. Malmodin and Z. Lai, *IEEE Trans. Compon. Packag. Manuf. Technol.* **22**, 86–90 (1999).
62. J. D. Weidler, R. D. Burg, J. J. Decker and J. H. Constable, in: *Proceedings of the 50th Electronic Components and Technology Conference*, Las Vegas, NV, pp. 906–913 (2000).
63. C. T. Murray, P. B. Hogerton, T. Chheang and R. L. Rudman, in: *Proceedings of the International Symposium on Microelectronics*, Boston, MA, pp. 820–825 (2000).
64. D. R. Lefebvre, *J. Adhesion Sci. Technol.* **14**, 925–937 (2000).
65. J. Liu, in: *Proceedings of the 1st IEEE International Conference on Polymers and Adhesives in Microelectronics and Photonics*, Potsdam, Germany, pp. 209–212 (2001).

66. S. Fujiwara, M. Harada, Y. Fujita, T. Hachiya and M. Muramatsu, in: *Proceedings of the 52nd Electronic Components and Technology Conference*, San Diego, CA, pp. 1124–1129 (2002).
67. C. M. L. Wu and M. L. Chau, *Solder Surface Mount Technol.* **14**, 51–58 (2002).
68. Z. Wei, L. S. Waf, N. Y. Loo, E. M. Koon and M. Huang, in: *Proceedings of the 4th Electronics Packaging Technology Conference*, Singapore, pp. 133–138 (2002).
69. C. W. Tan, Y. C. Chan and N. H. Yeung, *Microelectron. Reliab.* **43**, 481–486 (2002).
70. C. W. Tan, Y. C. Chan and N. H. Yeung, *Microelectron. Reliab.* **43**, 279–285 (2003).
71. C. W. Tan, Y. W. Chiu and Y. C. Chan, *Mater. Sci. Eng. B* **98**, 255–264 (2003).
72. Z. P. Wang, in: *Proceedings of the 5th Electronics Packaging Technology Conference*, Singapore, pp. 595–599 (2003).
73. L. L. Mercado, J. White, V. Saruhan and T. Y. T. Lee, *IEEE Trans. Component. Packag. Technol.* **26**, 509–516 (2003).
74. J. H. Zhang and Y. C. Chan, *J. Electronic Mater.* **32**, 228–234 (2003).
75. J. H. Zhang, Y. C. Chan, M. O. Alam and S. Fu, *Microelectron. Reliab.* **43**, 1303–1310 (2003).
76. Y. P. Wu, M. O. Alam, Y. C. Chan and B. Y. Wu, in: *Proceedings of the 53rd IEEE Electronic Components and Technology Conference*, New Orleans, LA, pp. 544–548 (2003).
77. M. A. Uddin, Y. C. Chan, H. P. Chan and M. O. Alam, *J. Electronic Mater.* **33**, 14–21 (2004).
78. X. Chen, J. Zhang and Z. P. Wang, in: *Proceedings of the 9th Intersociety Conference on Thermal and Thermomechanical Phenomena in Electronic Systems*, Las Vegas, NV, pp. 453–457 (2004).
79. W. S. Kwon, S. J. Ham, M. J. Yim, S. B. Lee and K. W. Paik, *J. Electron. Packag.* **127**, 86–90 (2005).
80. W. S. Kwon, S. J. Ham and K. W. Paik, *Microelectron. Reliab.* **46**, 589–599 (2006).
81. S. Y. Yang, W. S. Kwon, S. B. Lee and K. W. Paik, *Key Eng. Mater.* **297–300**, 887–892 (2005).
82. Y. C. Lin, X. Chen and Z. P. Wang, *J. Adhesion Sci. Technol.* **20**, 1383–1399 (2006).
83. Y. C. Lin, X. Chen, H. J. Zhang and Z. P. Wang, *Mater. Letters* **60**, 2958–2963 (2006).
84. J. Zhang, X. Chen and X. L. Wei, *Key Eng. Mater.* **324**, 471–475 (2006).
85. S. J. Luo, J. Leisen and C. P. Wong, *J. Appl. Polym. Sci.* **85**, 1–8 (2002).
86. S. Y. Y. Leung, D. C. C. Lam, S. J. Luo and C. P. Wong, *J. Adhesion Sci. Technol.* **18**, 1103–1121 (2004).
87. Y. C. Lin and X. Chen, *Polymer* **46**, 11994–12003 (2005).
88. Y. C. Lin and X. Chen, *Chem. Phys. Lett.* **412**, 322–326 (2005).
89. Y. C. Lin and X. Chen, *Mater. Letters* **59**, 3831–3836 (2005).
90. L. K. Teh, M. Teo, E. Anto, C. C. Wong, S. G. Mhaisalkar, P. S. Teo and E. H. Wong, *IEEE Trans. Component. Packag. Technol.* **28**, 506–516 (2005).
91. J. H. Zhang and Y. C. Chan, in: *Proceedings of the Sixth IEEE CPMT Conference on High Density Microsystem Design and Packaging and Component Failure Analysis*, Shanghai, China, pp. 277–281 (2004).
92. Y. C. Lin, Investigation of Characteristics for Adhesive and Bonding Reliability for COG Assemblies under Hygrothermal Conditions, *Ph.D. Dissertation*. Tianjin University, Tianjin, China (2006).
93. R. R. Gomatam and E. Sancaktar, in: *Proceedings of the 4th IEEE International Conference on Polymers and Adhesives in Microelectronics and Photonics*, Portland, OR, pp. 14–26 (2004).
94. Y. C. Lin, X. Chen and Z. P. Wang, in: *Proceedings of the 10th Intersociety Conference on Thermal and Thermomechanical Phenomena in Electronic Systems*, Las Vegas, NV, pp. 826–832 (2006).

95. Z. Wei, J. Coffin and A. Arvelo, in: *Proceedings of the 10th Intersociety Conference on Thermal and Thermomechanical Phenomena in Electronic Systems*, Las Vegas, NV, pp. 1082–1087 (2006).
96. M. J. Rizvi, Y. C. Chan, C. Bailey and H. Lu, *Microelectron. Reliab.* **45**, 589–596 (2005).
97. Y. C. Lin, X. Chen and Z. P. Wang, in: *Proceedings of the 10th Intersociety Conference on Thermal and Thermomechanical Phenomena in Electronic Systems*, Las Vegas, NV, pp. 946–952 (2006).
98. M. J. Rizvia, C. Bailey, Y. C. Chan and H. Lu, in: *Proceedings of the 10th Intersociety Conference on Thermal and Thermomechanical Phenomena in Electronic Systems*, Las Vegas, NV, pp. 855–860 (2006).
99. A. Lafir, Y. C. Chan and M. O. Alam, *Solder Surface Mount Technol.* **17**, 20–31 (2005).
100. K. W. Paik and W. S. Kwon, in: *Proceedings of the 4th IEEE International Conference on Polymers and Adhesives in Microelectronics and Photonics*, Portland, OR, pp. 141–147 (2004).
101. M. Inoue, T. Miyamoto and K. Suganuma, in: *Proceedings of the 4th IEEE International Conference on Polymers and Adhesives in Microelectronics and Photonics*, Portland, OR, pp. 148–152 (2004).
102. S. J. Ham, W. S. Kwon, K. W. Paik and S. B. Lee, in: *Proceedings of the 2nd IEEE International Conference on Polymers and Adhesives in Microelectronics and Photonics*, Portland, OR, pp. 63–67 (2002).
103. C. Lee and A. Yeo, in: *Proceedings of the 6th Electronics Packaging Technology Conference*, Shenzhen, China, pp. 420–425 (2004).
104. C. Y. Yin, H. Lu, C. Bailey and Y. C. Chan, *Electronics World* **111**, 20–24 (2005).
105. M. Holmberg, J. Lenkeri, M. Lahti and B. Wiik, in: *Proceedings of the 2nd IEEE International Conference on Polymers and Adhesives in Microelectronics and Photonics*, Zalaegerszeg, Hungary, pp. 49–53 (2002).
106. R. A. Islam, Y. C. Chan and B. Ralph, *J. Mater. Res.* **19**, 1662–1668 (2004).
107. M. J. Yim, Y. D. Jeon and K. W. Paik, *IEEE Trans. Electron. Packag. Manuf.* **23**, 171–176 (2000).
108. M. J. Yim and K. W. Paik, *IEEE Trans. Compon. Packag. Manuf. Technol.* **24**, 24–32 (2001).
109. J. Liu and Z. Lai, *J. Electron. Packag.* **124**, 240–245 (2002).
110. W. S. Kwon and K. W. Paik, in: *Proceedings of the 3rd IEEE International Conference on Polymers and Adhesives in Microelectronics and Photonics*, Montreux, Switzerland, pp. 351–356 (2003).
111. M. Teo, S. G. Mhaisalkar, E. H. Wong, P. S. Teo, C. C. Wong, K. Ong and C. F. Goh, in: *Proceedings of the 5th Electronics Packaging Technology Conference*, Singapore, pp. 718–725 (2003).
112. M. Teo, S. G. Mhaisalkar, E. H. Wong, P. S. Teo, C. C. Wong, K. Ong, C. F. Goh and L. K. Teh, *IEEE Trans. Component. Packag. Technol.* **28**, 157–164 (2005).
113. J. S. Hwang, M. J. Yim and K. W. Paik, *J. Electronic Mater.* **34**, 1455–1462 (2005).
114. J. S. Hwang, M. J. Yim and K. W. Paik, *J. Electronic Mater.* **35**, 1722–1727 (2006).
115. J. Liu and Z. Lai, in: *Proceeding of the International, InterSociety, Electronic Packaging Technical/Business Conference & Exhibition*, Maui, HI, pp. 1691–1697 (1999).
116. A. Seppälä, S. Pienimaa and E. Ristolainen, *Int. J. Microcircuits Electron. Packag.* **24**, 148–159 (2001).
117. S. H. Fan and Y. C. Chan, *J. Electronic Mater.* **32**, 101–108 (2003).
118. D. C. C. Lam, C. Shen, J. F. Xie, Z. Karim and P. Tong, in: *Proceeding of Electronic Packaging Materials Science IX. Symposium*, Boston, MA, pp. 297–306 (1997).
119. Z. Lai, R. Lai, K. Persson and J. Liu, *J. Electron. Manuf.* **8**, 217–224 (1998).

120. K. Persson, Z. Lai, A. Zribi, J. Liu and M. Willander, in: *Proceedings of the 3rd International Conference on Adhesive Joining and Coating Technology in Electronics Manufacturing*, Binghamton, NY, pp. 132–136 (1998).
121. K. Pinardi, Z. Lai, D. Vogel, L. K. Yi, J. Liu, S. Liu, R. Haug and M. Willander, *IEEE Trans. Compon. Packag. Manuf. Technol.* **23**, 447–451 (2000).
122. K. Pinardi, Z. Lai, L. K. Yi, J. Liu, S. Liu and R. Haug, in: *Proceedings of the 50th IEEE Electronic Components and Technology Conference*, Las Vegas, NV, pp. 1118–1121 (2000).
123. C. M. L. Wu, J. Liu and N. H. Yeung, in: *Proceedings of 4th International Conference on Adhesive Joining and Coating Technology in Electronics Manufacturing*, Espoo, Finland, pp. 101–106 (2000).
124. C. M. L. Wu, J. Liu and N. H. Yeung, *Solder Surface Mount Technol.* **13**, 25–30 (2001).
125. N. H. Yeung, Y. C. Chan and C. W. Tan, *J. Electron. Packag.* **125**, 624–629 (2003).
126. G. Sarkar, S. Mridha, T. C. Tan, Y. T. Wu and C. K. Sem, *J. Mater. Proc. Technol.* **89–90**, 484–490 (1999).
127. K. W. Paik, M. J. Yim and W. S. Kwon, in: *Proceedings of the Technical Program, Pan Pacific Microelectronics Symposium*, Kauai, HA, pp. 217–223 (2001).
128. G. B. Dou, Y. C. Chan and J. Liu, *J. Electron. Packag.* **125**, 609–616 (2003).
129. L. Cao, S. M. Li, Z. Lai and J. Liu, *J. Electronic Mater.* **34**, 1420–1427 (2005).

This page intentionally left blank

Drop Test Performance of Isotropic Electrically Conductive Adhesives

James E. Morris* and Jeahuck Lee

Department of Electrical and Computer Engineering, Portland State University, Portland,
OR 97207-0751, USA

Abstract

Drop test survival is a crucial element of isotropic conductive adhesive (ICA) reliability. Drop test data are presented for four different ICA materials, with varying cure profiles. Only one of the materials passes the ad hoc standard (including none of the “snap cure” formulations, although performance is improved by extended cure times). Drop test performance deteriorates when the sample has survived a series of smaller drops, leading to a cumulative damage model based on crack initiation at interface bubbles, and is improved by a pre-cure heat soak to drive off the bubbles.

Keywords

Electrically conductive adhesives (ECAs), isotropic conductive adhesives (ICAs), glass transition temperature (T_g), cure temperature, drop test

1. Introduction

Electrically conductive adhesive (ECA) materials are available as anisotropic conductive adhesives (ACAs), anisotropic conductive films (ACFs) and isotropic conductive adhesives (ICAs), and can be used in a wide variety of applications to support both mechanical bonding and electrical interconnection between a device or chip carrier and a circuit board contact pad. ICAs have been researched steadily over the past decade as potential candidates for lead-free replacement of solder in surface mount technology (SMT) applications and flip-chip attachment. Environmental-friendly ICAs offer many advantages over solder, such as simple and low temperature process conditions and better thermo-mechanical performance. However, ICA technology is still in the process of validating reliability performance, compared to the more mature soldering technologies, and even the newer lead-free solders. ICA reliability has continued to be a source of concern for widespread practical implementations in commercial products, and the objective of this paper is to fo-

* To whom correspondence should be addressed. Tel.: 1-503-725-9588; Fax: 1-503-725-3807; e-mail: j.e.morris@ieee.org

cus on drop test ICA reliability studies, including the influence of different curing conditions.

2. Experimental

These studies used Ablebond 8175, 8175A and 84-1 LM1 as the materials for investigation, along with a material from another supplier (denoted by “ICA-X”), and an experimental 136H3 formulation. The “benchmark” adhesive (Ablebond 8175) is a silver-flake filled conductive adhesive with a silver content of about 70 wt%, designed for solder replacement in microelectronic interconnect applications, and 8175A is a “snap-cure” variant. These stress-absorbing adhesives may be used with thick film metallizations or traditional printed circuit board surfaces. In addition, they can achieve fine pitch resolution (0.5 mm) when printed using either a stainless steel mesh screen or a metal mask stencil. They are also syringe dispensable. Ablebond 84-1 LM1 is also a silver-filled electrically conductive epoxy adhesive, designed for microelectronic chip bonding by an automatic dispenser or a hand probe. 136H3 has a low glass transition temperature, T_g , below room temperature, so it has a significant mechanical loss modulus under operating conditions. It is well established that drop test survival correlates with high loss modulus materials [1–3], with improved impact resistance due to energy absorption observed for ICAs with epoxies of T_g less than the test temperature.

2.1. Sequence A (Ablebond 8175 and ICA-X) [4]

Two different “components” were used to provide some variation in the experiments: plastic quad flat pack (PQFP) packages and aluminum dummy components. The aluminum dummies permit greater control of “component” inertial mass and bond area than is possible with actual components, although this feature was not fully exploited in the experiments reported here. The standard aluminum component had dimensions $25.4 \times 38.1 \times 3.18$ mm for a mass of 8.3 g, and the ICA bond pattern is shown in Fig. 1(a), with all segments 7.94×1.59 mm for a bond area of 76 mm^2 . The bond pattern for the 4 g, 25.4×25.4 mm PQFP shown in Fig. 1(b) provides a total lead adhesion area of 140 mm^2 . Three components were mounted

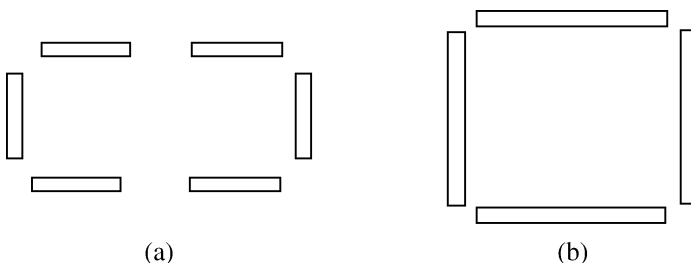


Figure 1. Bond patterns used for Sequence A: (a) aluminum dummy components and (b) PQFP components.

Table 1.

Sequence A drop test data for Ablebond 8175 and ICA-X

Sample	ICA paste	Cure temperature	Component	Number of 5-foot drops to failure	Pass/fail
A1	8175	144°C	Aluminum	>65	Pass
A2	8175	150°C	Aluminum	37	Pass
A3	8175	160°C	Aluminum	10	Pass
A4	8175	144°C	PQFP	19	Pass
A5	8175	150°C	PQFP	10	Pass
A6	8175	160°C	PQFP	13	Pass
B1	8175	144°C	Aluminum	32	Pass
B2	8175	150°C	Aluminum	5	Fail
B3	8175	160°C	Aluminum	28	Pass
B4	8175	144°C	PQFP	7	Pass
B5	8175	150°C	PQFP	10	Pass
B6	8175	160°C	PQFP	10	Pass
C1	ICA-X	144°C	PQFP	1	Fail
C2	ICA-X	150°C	PQFP	9	Pass
C3	ICA-X	160°C	PQFP	6	Fail

on each copper board, with 12.7 mm between components to permit separation after cure, and the boards were placed for 30 min on the stationary belt of a reflow oven, in order to test the effect of curing temperature on drop test performance, at a position where the thermal gradient provided three cure temperatures: 160°C, the nominal 30 min cure temperature of 150°C and 144°C.

The drop tests were performed using a vertical metal track (shown in reference [5]) that guided the samples but did not restrict their fall, so they landed on their edge on the concrete floor. For a sample to “pass” the test, it must survive, i.e. stay securely bonded, for no less than 6 drops from 5 feet (the *de facto* standard test developed by the National Manufacturing Sciences Consortium [6]). The results are shown in Table 1; testing of an individual sample was stopped when it survived 65 5-foot drops.

2.2. Sequence B (Ablebond 8175A, 84-1LM and 136H3) [7]

The next experimental sequence consisted of three series, which employed three different materials, including one “snap-cure”. A number of 7.5 × 7.5 cm circuit boards were fabricated, with stenciled conductive adhesive for a range of chip sizes in the layout shown in Fig. 2. After preparing the boards, the chips were placed on the board with a pair of tweezers and pressed into place. Table 2 lists the components used. In all cases, four samples were made with each adhesive, and two samples of each were dropped from 3 feet and two from 5 feet. The cure schedules used are presented in Table 3, where the snap-cure schedules for drop tests in

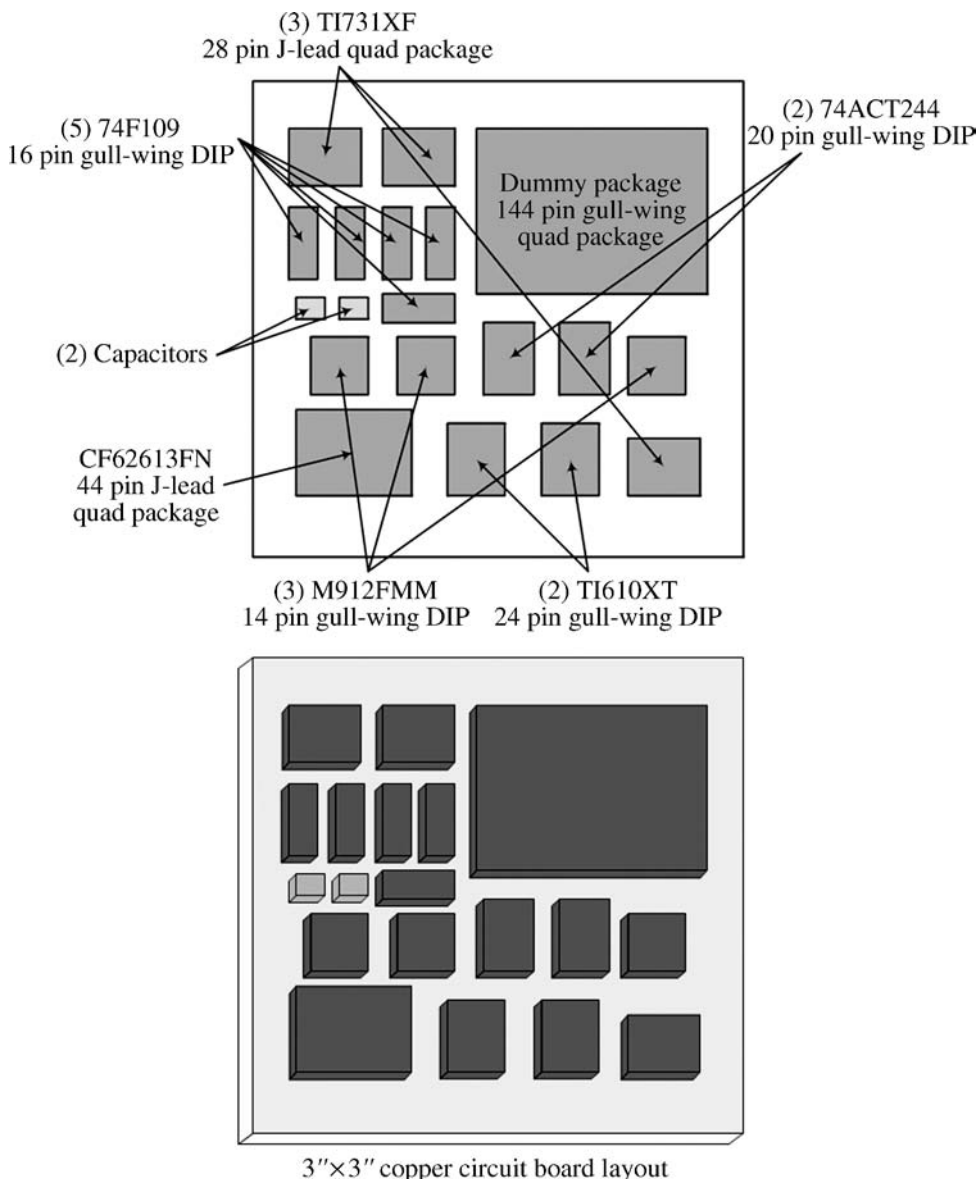


Figure 2. Chip layout on the copper circuit board for Sequence B Series 1.

both Series 1 and 2 are modified from the data sheet recommendations (3 min at 150°C for Ablebond 8175A) based on prior experience. The snap-cure extension for 8175A from 3 min to 5.5 min accommodates the thermal transient as the temperature falls to 140°C and recovers to 150°C within one minute when the samples are put into the box oven, but due to disappointing results at 5.5 min, the curing time was increased to 7 min in Series 2. However, this still seemed to be insufficient for

Table 2.

Board components for Sequence B drop tests; see Fig. 2 for Series 1 layout

Component	Description	Number of components		
		Series 1	Series 2	Series 3
Dummy Package	Large QFP	1		1
CF62613FN	Medium QFP	1		
731XF	Small QFP	3		
TI610XT	Large DIP	2		
H9506	Large DIP		1	
74ACT244	Medium DIP	2	4	
M912FMM	“Square” DIP	3	2	
74F109	Small DIP	5		
74F20	Small DIP		3	
TI749A	Smallest DIL		5	
Capacitor	Std. small SMT Pkg	2		

Table 3.

Cure schedules for Sequence B drop test samples

	Series 1		Series 2		Series 3
	8175A	84-1 LM1	8175A	136H3	136H3
Cure temp. (°C)	150	150	150	150	150
Cure time (min)	5.5	60	7	7	60

drop test survival. The 7-min cure for 136H3 in Series 2 was as per data sheet recommendation, but the manufacturer also donated some 60-min cure samples with one large QFP component per (smaller) board.

2.3. Sequence C (Ablebond 8175) [8]

Ablebond 8175 was chosen for Sequence C, rather than the snap-cure 8175A. The longer cure times offer more control of the thermal profile parameters in order to investigate the effects of thermal cure profiles on ICA properties. The thermal cure process is crucial to the ultimate electrical and mechanical properties of ICAs, and this curing was done in a Heller six-zone hot air reflow oven with profiles which could include a pre-heating period for outgassing (Table 4). These tests used two different packages, SO20GT-7.6 mm and PLCC 68, and four cure profiles. Each sample, with one package per smaller board, was dropped 20 times from 1 foot, and then successively 20 times each from 2, 3, 4, and 5 feet until the sample fell off the board, or, more specifically in a couple of cases, until at least one package lead detached from the board.

Table 4.

Ablebond 8175 cure profiles for Sequence C

Profile	Cure temp. (°C)	Cure time (min)	Belt speed (cm/min)
(i)	150	60	NA
(ii)	175	30	NA
(iii)	70	30	2
	120	30	
	150	60	
	120	30	
	70	30	
(iv)	90	10	4
	140	20	
	175	30	
	140	20	
	90	10	

(i) 150°C ramp and hold, (ii) 175°C ramp and hold,
 (iii) 150°C with pre-heating/post-cooling and (iv) 175°C with pre-heating/post-cooling.

3. Results

3.1. Sequence A [4]

The results of the drop tests can be seen in Table 1, where samples A and B represent two different batches of Ablebond 8175 paste. The sample B2 result seems anomalous, and will be ignored. There seems to be a general trend for 8175, with the exception of samples B4–B6, that under-cured samples survive more drops than those cured to specification, which survive more than over-cured samples. However, no verification of the degree of cure was undertaken, and full cure might be actually achieved at 144°C, or not achieved even at 160°C. Given (i) that drop test resilience corresponds to high loss modulus, (ii) the delay in reaching thermal equilibrium when samples are inserted into the oven, rather than ramping up to the cure temperature on a slowly moving belt, and (iii) the appearance of the ICA surfaces, there is some suspicion that all the samples were actually under-cured to some degree. However, the C sample results for ICA-X are totally different and seem to suggest that the optimum cure lies where expected (at 150°C), or marginally above. Comparison of A and B samples with C sample suggests that the 8175 cure schedule is unexpectedly forgiving for impact resistance. Other interesting observations from the Sequence A drop test results include:

- The aluminum components adhere better than the PQFP components, despite the higher mass, presumably due to rougher surfaces, a postulate supported

by the fact that the point of failure for the Al samples is mainly at the substrate surface, whereas the PQFP failures usually occurred at the lead interfaces.

- PQFP leads bend under impact, and sometimes fail (fracture) before the ICA bond.
- The dispensed ICA thickness was not well controlled, and the paste adhering to the sides of the PQFP leads was more than in a practical case.
- No electrical properties were monitored in these experiments, so it is not possible to infer the cure states from conductivity.

3.2. Sequence B [7]

All four of the boards with Ablebond 8175A adhesive were cured for five and a half minutes at $150 \pm 3^\circ\text{C}$, with the temperature stabilized within the first minute. After performing the drop tests on these boards, it was decided that the adhesive on two boards was not fully cured by the five minute schedule, because the paste was noticed to be still tacky, although most of the smaller components survived one 3-foot drop (Fig. 3(a)). However, the Ablebond 84-1 LM1 appeared to be fully cured to a fully hardened state on all four boards by the one hour process time. It is noted that the copper circuit board was untarnished by the five minute curing process, but that the copper surface oxidized to a reddish-brown color over the one hour cure period.

Figures 3–6 show the first drop test results, presented as the average values for two boards in each figure. Clearly, the larger components fall off first, as previously demonstrated by the variation in drop test survival rate with component mass shown in Fig. 7 for dummy aluminum component blocks [9]. (The larger contact area available with the dummy blocks increases the number of drops to failure and improves the statistical consistency of the results.) The data of Figs 3(a) and 4(a) are not considered to be fully reliable, due to the possibility of incomplete cure, so the only point of interest is the improvement shown in Figs 5(a) and 6(a) for complete cure, despite the higher loss modulus of the tacky specimens. Despite the full cure, the survival rates of Ablebond 84-1 LM1 attachments are actually worse than for the Ablebond 8175A. Only one of the capacitors detached from the board in any of these tests for either adhesive. But note that the adhesive cured along the side of the capacitor, and that the lead attachment area for the capacitor is larger than that of any other leads on the other chip, in addition to the capacitor being smaller, albeit denser.

Figures 5 and 6 show the Series 2 drop test results with the longer Ablebond 8175A cure time than in Series 1, and with the experimental 136H3 replacing the Ablebond 84-1 LM1. The experimental 136H3 formulation is much more impact resistant than either of the others, but none of the Series 1 or 2 tests produced a “pass”.

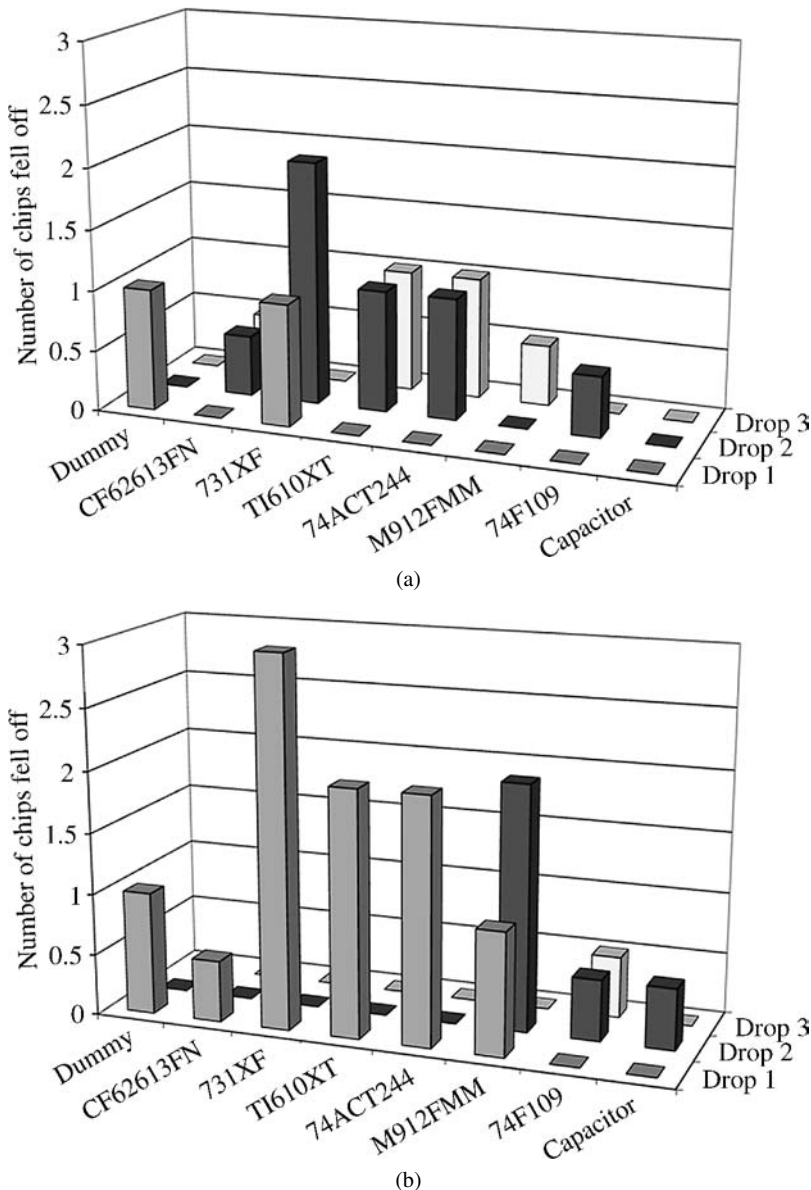


Figure 3. Average drop test results from 3-foot height (Sequence B, Series 1). (a) Ablebond 8175A. (b) Ablebond 84-1 LM1.

The 7-min 136H3 cure time was per specification, but the Series 3 60-min cure samples supplied by the manufacturer performed significantly better, and “passed” with dummy QFP survival rates of 13 to 29 drops from 3 feet and 7–10 drops from 5 feet.

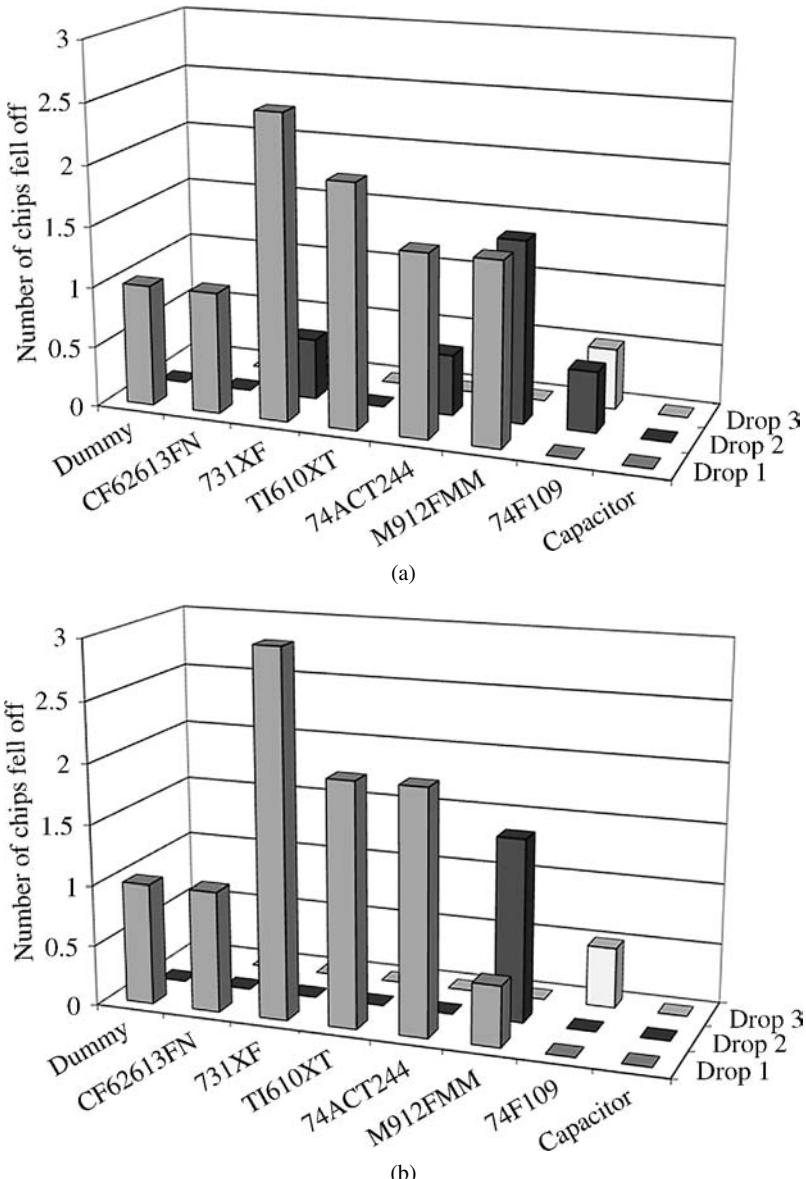


Figure 4. Average drop test results from 5-foot height (Sequence B, Series 1). (a) Ablebond 8175A. (b) Ablebond 84-1 LM1.

Comparison of Figs 3(a) and 4(a) with Figs 5(a) and 6(a) clearly shows that fully cured adhesive performs better than under-cured. Figures 5(b) and 6(b) also clearly demonstrate the benefit of a fully cured low- T_g material to achieve the high loss modulus necessary for impact energy absorption, and that the extended cure time (Sequence B, Series 3) further improves impact resistance.

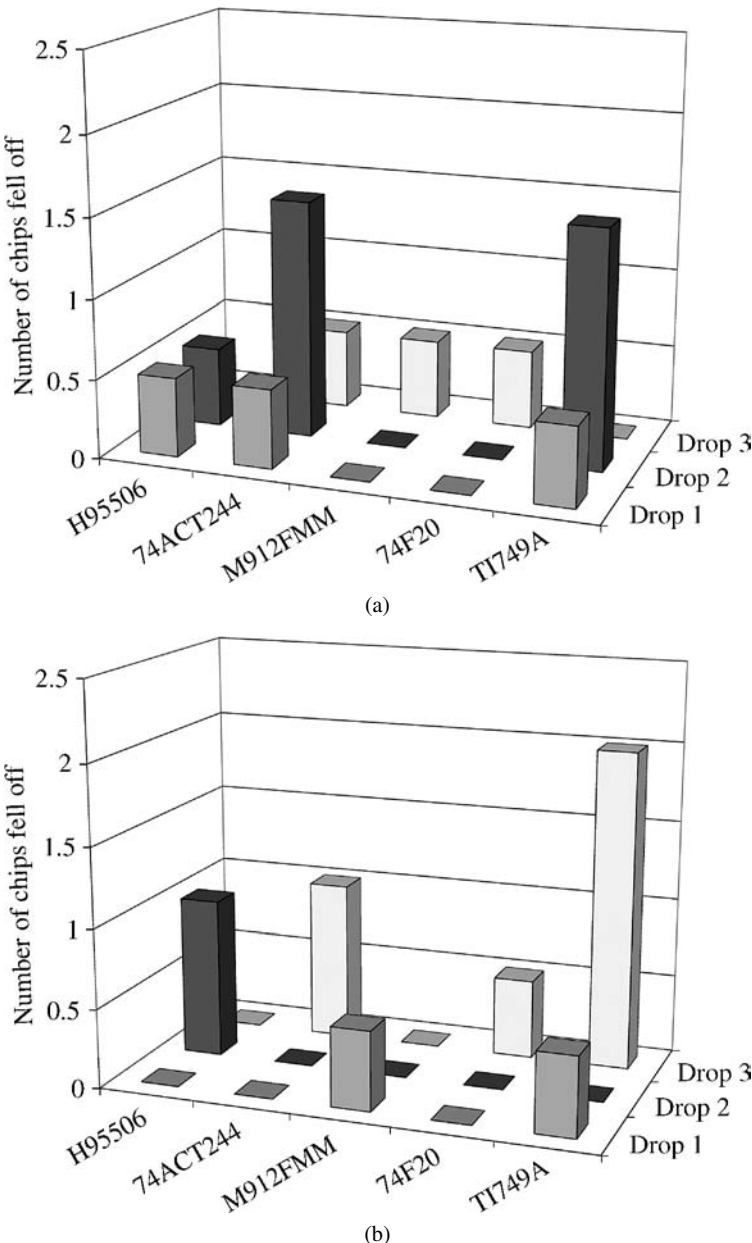


Figure 5. Average drop test results from 3-foot height (Sequence B, Series 2). (a) Ablebond 8175A. (b) 136H3.

3.3. Sequence C [8]

Figures 8–11 show the results of the third drop test sequence, which used only Ablebond 8175. “Ramp and hold” and “pre-heat/post-cool” curing schedules are defined

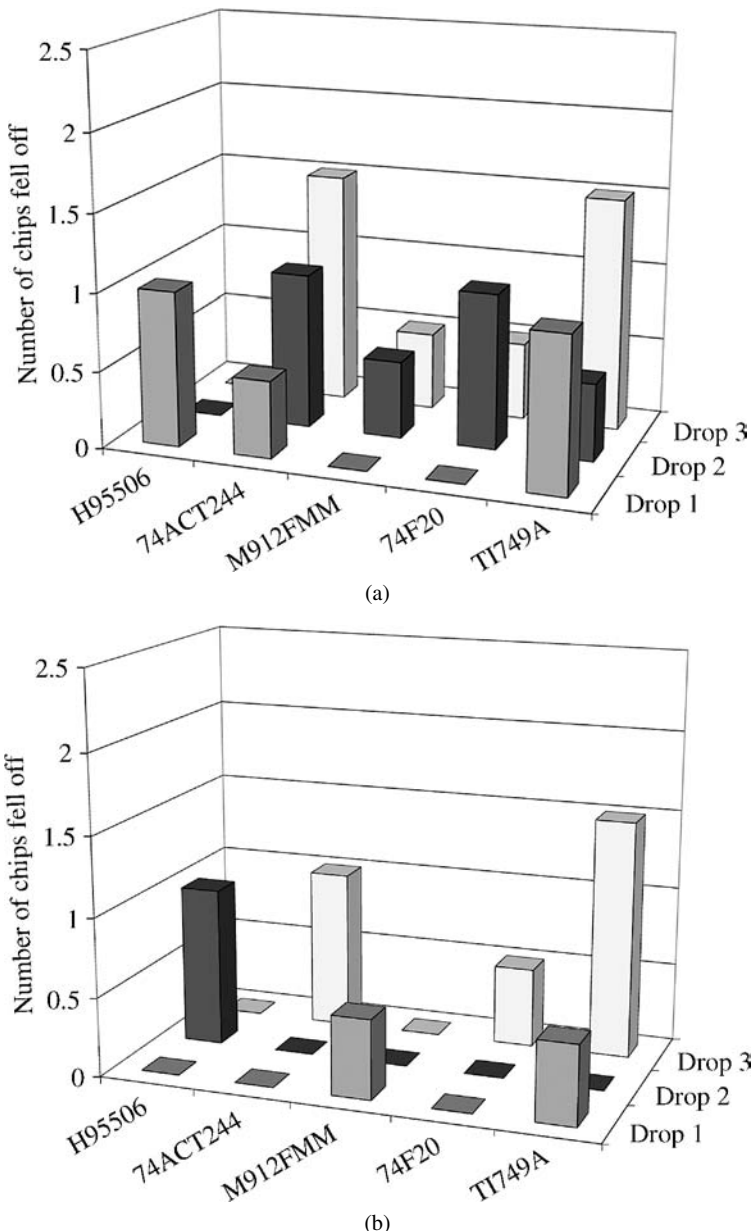


Figure 6. Average drop test results from 5-foot height (Sequence B, Series 2). (a) Ablebond 8175A. (b) 136H3.

in Table 4. The variation in the number of drops survived by multiple samples is indicated in each figure by the relatively small “range”. Note that if a sample failed at two 4-foot drops, for example, this would mean that it had previously survived 20 drops from each of 1, 2 and 3 feet plus the two drops from 4 feet. As shown in

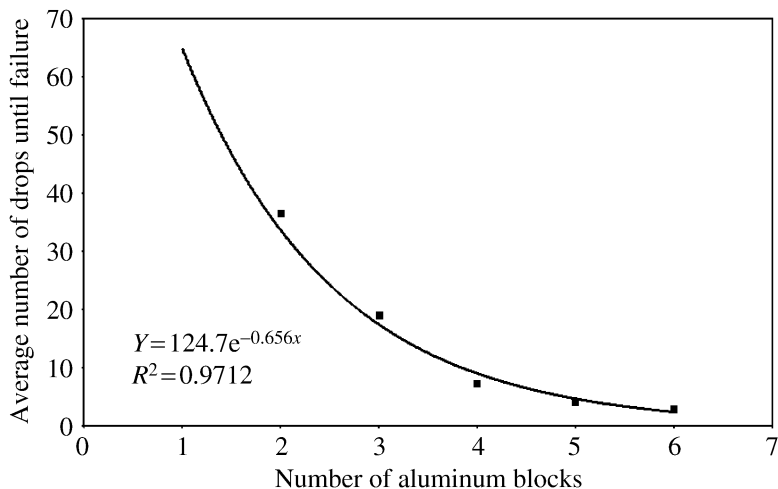


Figure 7. Drop test survival using aluminum blocks as dummy chips (5-foot drops; $2.5 \times 2.5 \times 3$ mm aluminum blocks; 1 cm^2 adhesion area; blocks stacked with cyanoacrylate “super-glue”; single block survived 120 drops without failure).

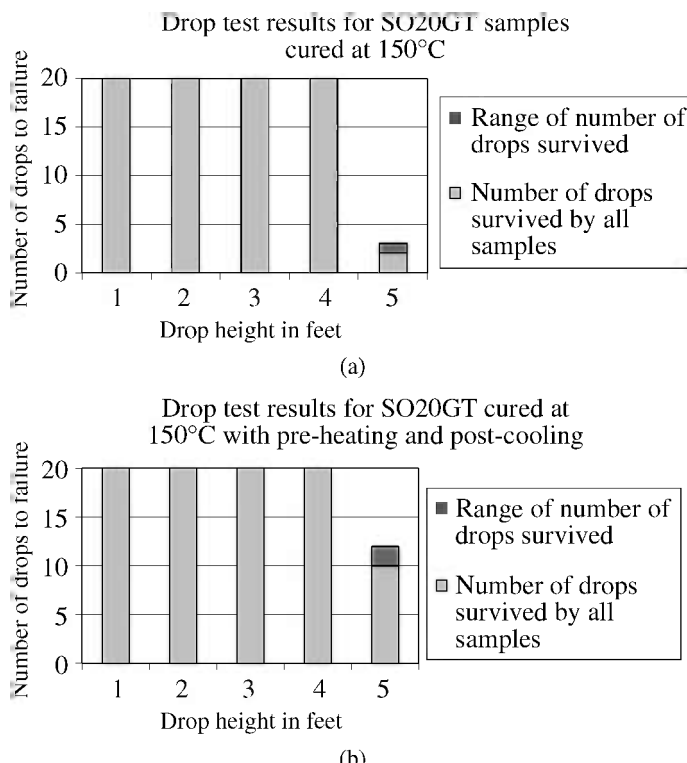


Figure 8. SO20GT 150°C : (a) ramp and hold, and (b) pre-heat/post-cool.

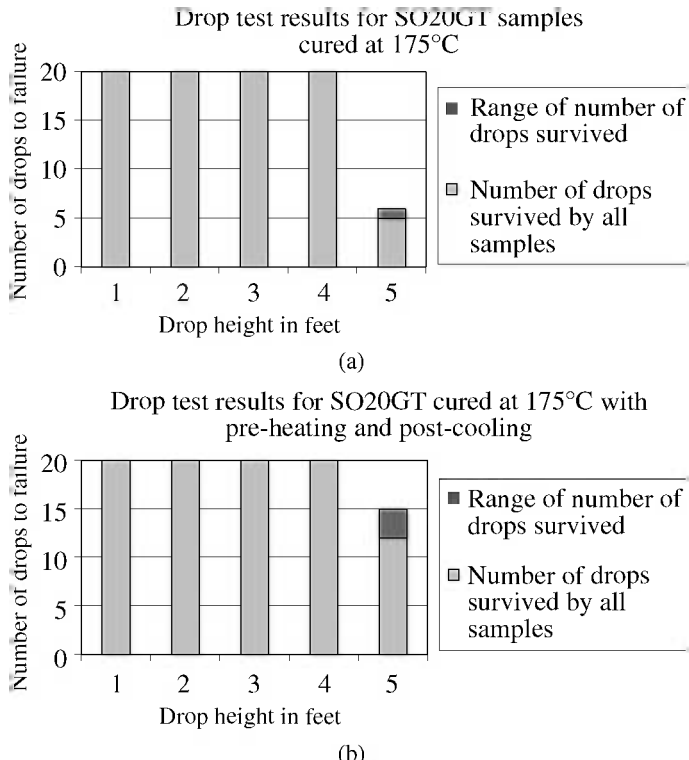


Figure 9. SO20GT 175°C: (a) ramp and hold, (b) pre-heat/post-cool.

Figs 8 and 9, all of the SO20GT samples survived 20 drops from each of 1, 2, 3 and 4 feet, and then some variable number from 5 feet. Comparison of Figs 8 and 9 with Figs 10 and 11 shows again that the larger PLCC68 components fall off sooner than the smaller SO20GTs. The change in cure schedule from 60 minutes at 150°C to 30 min at 175°C apparently produces a small improvement in SO20GT impact resistance, but a significant reduction in PLCC68 impact resistance, for both the simple ramp-and-hold and pre-heat/post-cool profiles. The only explanation proposed for these differences is that the 175°C results in an over-cure, to which the J-lead PLCC68 samples are more susceptible than the SO20GT gull wing configuration due to the smaller contact area observed (Fig. 12). The primary result is that samples with the pre-heating and post-cooling have better impact resistance than without, as shown by comparisons of (a) and (b) in Figs 8–11. Hence, it is asserted that samples cured with pre-heating and post-cooling invariably sustain more drops without failure compared to those that are normally cured, although this result is more evident for the smaller SO20GT packages (Figs 8 and 9) than for the PLCC68 (Figs 10 and 11).

It was also noted that impact damage was cumulative, i.e. the samples which survived multiple small drops would then survive less 5-foot drops than samples

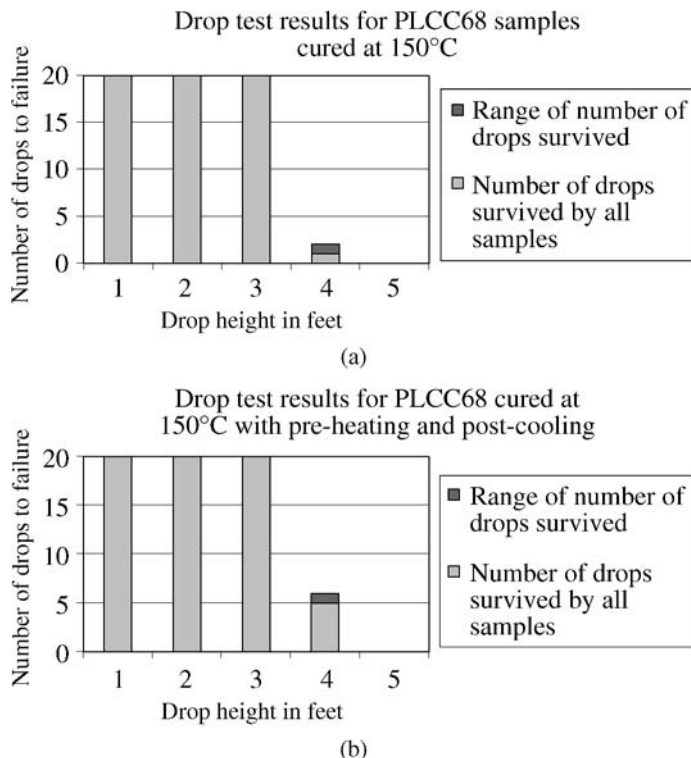


Figure 10. PLCC68 150°C: (a) ramp and hold, (b) pre-heat/post-cool.

which had not undergone the prior sequence of small drops. One can compare the results of Fig. 8 with the 10-drop survival rates observed from 5 feet for PQFP packages with the same adhesive and 150°C cure (Table 1) [4] to conclude that the succession of small drops has damaged the adhesive prior to actual failure.

4. Discussion

In the course of plasma surface treatments for improved adhesion, it was discovered that vacuum exposure of the material prior to cure significantly improved adhesion [10], and that the reason was clearly correlated to bubble escape from the material. If the cure process is too rapid, the organic solvents used to control viscosity to achieve reproducible uniform printing cannot escape, and become entrapped in the epoxy as bubbles. Under vacuum, these bubbles can escape (Fig. 13 [11]). Bubbles at the substrate interface have also been correlated with weak ACF adhesion [12], and would explain why impact failure is almost always interfacial rather than cohesive, despite the governing property being the bulk loss modulus, and this picture is consistent with the cumulative damage mentioned earlier, with crack initiation at the bubbles. Perichaud *et al.* [13] found that bubble content was reduced or eliminated by a pre-cure heat soak at a temperature sufficiently high to drive out volatile

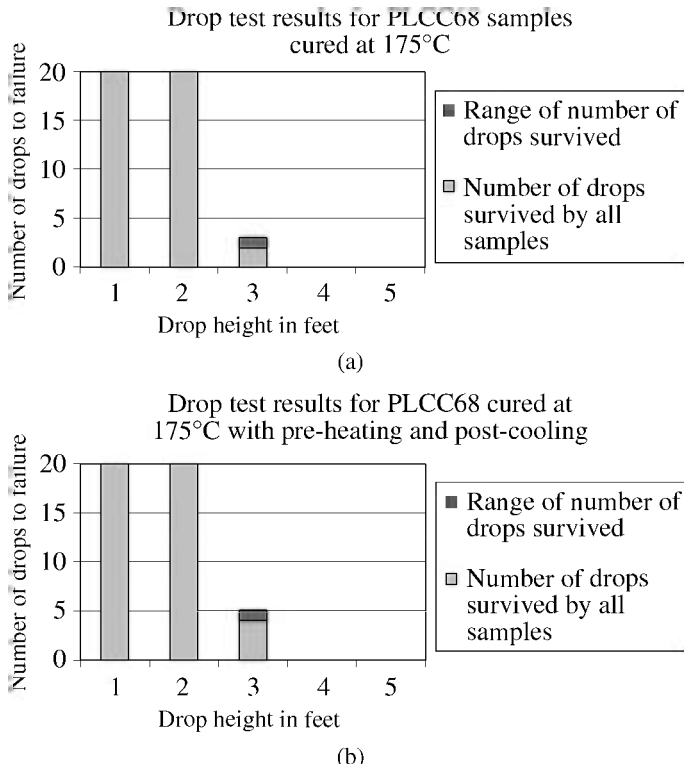


Figure 11. PLCC68 175°C (a) ramp and hold, (b) pre-heat/post-cool.

components, but low enough for a negligibly small cure rate (e.g. 100°C for a 150°C cure schedule). The expected benefit of the pre-cure heat soak is seen in Figs 8–11.

5. Summary and Conclusions

An initial objective of these experiments was to further explore the widely accepted notion that ICA drop test performance correlates with the bulk loss modulus rather than adhesion. With the assumption that the loss modulus should be greater for under-cured materials, the intention was to correlate drop test results with degree of cure, varied by cure temperature. Initial data (samples A1, A2 and A3 in Table 1) appeared to confirm the expectation, but the rest of Sequence A's results are much more ambiguous, without a convincing trend. In addition, the dummy aluminum devices resisted impact better than the lighter PQFPs with greater adhesion area, indicating the importance of surface roughness.

The primary purpose of Sequence B was to confirm the influence of device size, (actually inertial mass) on impact resistance, using real devices rather than the aluminum dummies which had previously confirmed the principle (Fig. 7). At the same time, a range of different materials was used, including especially snap-cure ICAs, and a study of the effects of different drop heights was initiated. The Ablebond

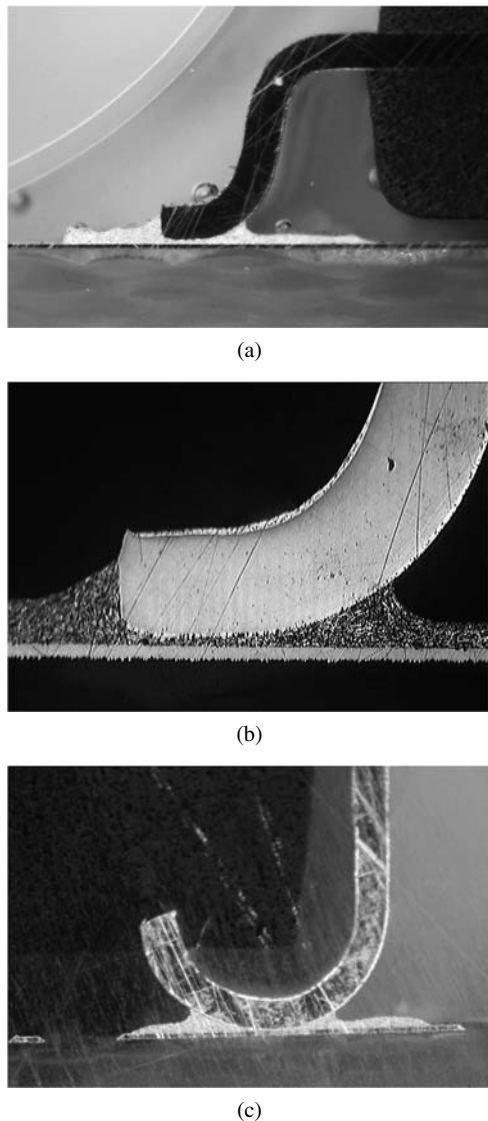


Figure 12. Package leads and Ablebond 8175 (Sequence C) ICA attachment. (a) SO20GT gull-wing lead. (b) Magnified view of (a). (c) PLCC68 J-lead.

8175A (and the 60-min cure 136H3) survived the 3 feet drops better than the 5 feet drops, as one would expect, but even that simple trend was absent for the other materials. The only consistent trend is the higher survival rates of the smaller components.

The device size effect is confirmed again in Sequence C by the greater impact resistance of the smaller SO20GT device over the larger PLCC68 in Figs 8–11. Comparison of these results with the 8175 data in Table 1 indicates that the smaller

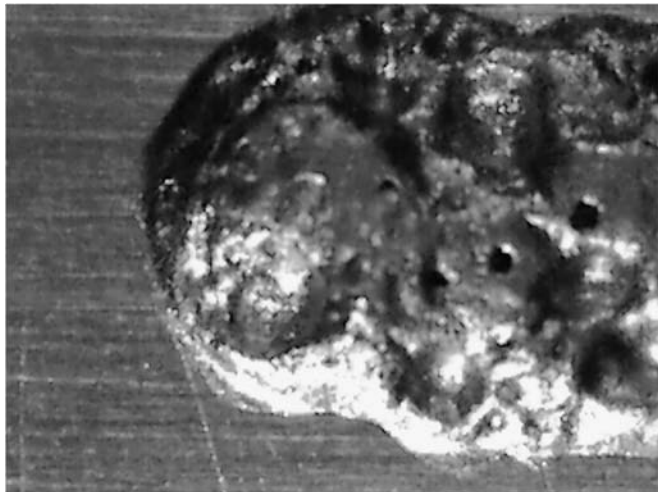


Figure 13. Uncured ICA surface after exposure to vacuum (0.75×0.55 cm).

drop sequences, although survived, weaken impact resistance to the standard 5 feet drops, suggesting a crack propagation fracture mode. Adding pre-heating and post-cooling steps to the cure schedule is known to reduce the incidence of bubbles which would act as crack initiation sites, so the significant improvement in impact resistance gained from the added processing steps was as expected. The relatively poor performance of the over-cured samples of Fig. 11 also seems to confirm that the bulk loss modulus is the determining parameter.

Acknowledgements

The original experimental work described here was performed at Binghamton University by Christina Cook, Falk Anderssohn, Enrico Loos, Sebastian Probstain, Sean MacDavitt, Marcus Armann, Albrecht Kleye, Peter Fruehauf and Santosh Kudtarkar.

References

1. Q. Tong, S. Vona, R. Kuder and D. Shenfield, in: *Proceedings of 3rd International Conference on Adhesive Joining & Coating Technology in Electronic Manufacturing*, Binghamton, NY, pp. 272–277 (1998).
2. S. Luo and C.-P. Wong, in: *Proceedings 8th International Symposium on Advanced Packaging Materials*, Braselton, GA, pp. 226–231 (2002).
3. S. Luo and C.-P. Wong, *IEEE Trans. Components, Packaging Technol.* **24**, 38–42 (2001).
4. S. R. MacDavitt and J. E. Morris, in: *Proceedings of 4th International Conference on Adhesive Joining Technology in Electronics Manufacturing*, Helsinki, Finland, pp. 221–224 (2000).
5. A. Kulkarni and J. E. Morris, in: *Proceedings of 3rd International IEEE Conference on Polymers & Adhesives in Microelectronics & Photonics*, Montreux, Switzerland, pp. 333–336 (2003).

6. M. Zwolinski, J. Hickman, H. Rubin, Y. Zaks, S. McCarthy, T. Hanlon, P. Arrowsmith, A. Chaudhuri, R. Hermansen, S. Lau and D. Napp, *IEEE Trans. Components, Packaging Manuf. Technol. Part C* **19**, 241–250 (1996).
7. J. E. Morris, C. Cook, M. Armann, A. Kleye and P. Fruehauf, in: *Proceedings of 2nd International Symposium on Polymeric Electronics Packaging*, Gothenburg, Sweden, pp. 15–26 (1999).
8. S. A. Kudtarkar and J. E. Morris, in: *Proceedings of 8th International Symposium on Advanced Packaging Materials*, Stone Mountain, GA, pp. 144–150 (2002).
9. J. E. Morris, F. Anderssohn, S. Kudtarkar, E. Loos and J. Liu, in: *Proceedings of 26th International Spring Seminar on Electronics Technology*, High Tatras, Slovakia, pp. 90–94 (2003).
10. J. E. Morris, F. Anderssohn, S. Kudtarkar and E. Loos, in: *Proceedings of 1st International Conference on Polymers & Adhesives in Microelectronics & Photonics*, Potsdam, Germany, pp. 61–69 (2001).
11. S. Probstain and J. E. Morris, in: *Proceedings of 4th International Conference on Adhesive Joining Technology in Electronics Manufacturing*, Helsinki, Finland, pp. 41–45 (2000).
12. H. J. Kim, C. K. Chung, M. J. Yim, S. M. Hong, S. Y. Jang, Y. J. Moon and K. W. Paik, in: *Proceeding of 56th IEEE Electronic Components and Technology Conference*, San Diego, CA, pp. 952–958 (2006).
13. M. G. Perichaud, J. Y. Deletage, D. Carboni, H. Fremont, Y. Danto and C. Faure, in: *Proceedings 3rd International Conference on Adhesive Joining & Coating Technology in Electronics Manufacturing*, Binghamton NY, pp. 55–61 (1998).

Mechanics of Adhesively Bonded Flip-Chip-on-Flex Assemblies. Part I: Durability of Anisotropically Conductive Adhesive Interconnects

J. Haase^a, D. Farley^a, P. Iyer^a, P. Baumgartner^a, A. Dasgupta^{a,*} and J. F. J. Caers^b

^a CALCE, Mechanical Engineering Dept., University of Maryland, College Park, MD 20742, USA

^b Philips Applied Technologies, Electronic Packaging & Thin Film, High Tech Campus 7, WDX-3A 0.262, 5656 AE Eindhoven, The Netherlands

Abstract

This is Part I of a two-part paper on adhesively bonded flip-chip-on-flex (FCOF) microelectronic assemblies. This paper examines the use of anisotropically conductive adhesives (ACAs), and the companion paper (Part II) addresses the use of non-conductive adhesives (NCAs). Two types of FCOF dies, bonded with ACAs, were subjected to temperature cycling and repeated temperature shock durability tests. The specimens have Au-plated bumps and the ACA contains Au-plated polymer particles. Specimens were fabricated with different bonding pressures. Scanning Electron Microscopy (SEM) investigations were performed to characterize the distribution and shape of the conducting particles.

Contact resistance measurements, conducted throughout the temperature cycling durability test for 1000 temperature cycles between 20°C and 115°C, showed that resistance varied cyclically with each temperature cycle, but there was no increase in the average resistance over the duration of the test. In contrast, cyclic thermal shock tests between -50°C and 115°C produced failures within 200–2500 cycles, depending on the specimen configuration.

Studies were conducted to examine the effect of specimen configuration and temperature on: (i) interconnect resistance, based on electro-thermal modeling; and (ii) mechanical contact stresses, based on thermomechanical modeling. Modeling techniques used detailed finite element analysis (FEA) as well as simpler rapid-assessment models based on 2D variational methods (for example, the Raleigh–Ritz method) and 1D electrical resistance networks. These models were used to parametrically investigate the influence of interconnect design, bonding pressure, temperature and interconnect degradation mechanisms, on the contact resistance and contact stresses.

Results suggested that the thermal expansion of the ACA during temperature cycling did not cause any changes in the contact resistance at the contact interface, thus suggesting the possibility of bonding at Au–Au interfaces. During thermal shock, the expansion mismatch stress between the die and Printed Wiring Board (PWB) at the low temperature (-50°C) was probably sufficient to fracture this bond. The issue of gold-to-gold bonding will be addressed in a future paper.

* To whom correspondence should be addressed. Tel.: 301 405 5251; e-mail: dasgupta@umd.edu

Keywords

Flip-chip-on-flex, anisotropically conductive adhesives, thermal cycling test, failure mechanisms, bonding pressure, interconnect resistance, finite element model, Raleigh–Ritz model, parametric studies

1. Introduction

Conductive Adhesives (CAs) are composed of an adhesive polymer matrix with conductive filler particles. There are two categories of CAs: Isotropically Conductive Adhesives (ICAs) and Anisotropic Conductive Adhesives (ACAs). An ICA consists of a polymer matrix with metallic flakes dispersed throughout the polymer. The polymer provides mechanical strength and the metal flakes form conductive paths in all directions.

In contrast, ACAs, which are the subject of this paper, only conduct normal to the surface bond-pad. ACAs are composed of spherical conducting particles dispersed throughout the polymer matrix, as shown schematically in Fig. 1. The conducting particles can be hard or soft, and provide electrical paths between mating gold bumps on the flip-chip die and gold-plated copper tracks on the flex substrate. The coplanarity requirement for these bond-pads is not very stringent because compliant conducting particles compensate for any dimensional variations in pad height. ACAs can be applied under the entire flip-chip die because they do not create lateral conductive paths (shorts) between neighboring contacts [1].

Conductive adhesives have gained popularity as a potential replacement for solder interconnects as they are a lead-free alternative, and are suitable for finer pitch ($<50\text{ }\mu\text{m}$) application than solders [2]. Furthermore, they offer a no-flux process, thus eliminating the need for flux cleaners that are harmful to the environment [3]. ACA bonding is affordable because it is a low-temperature process that avoids the reflow step in manufacturing, thus allowing lower energy consumption and the ability to use low-temperature parts and PWB materials. The fabrication process with ACAs is shorter (and hence cheaper) than the process for solders, because there is no need for fluxing, cleaning, and underfilling. Because of these advantages ACAs are popular in several industries, including in Liquid Crystal Displays

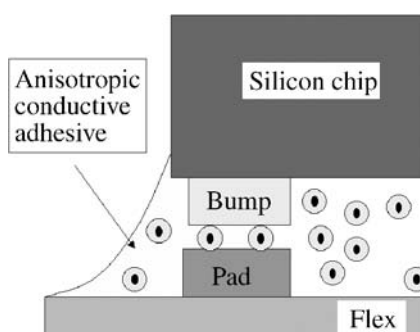


Figure 1. Schematic of how an ACA bonds a flip-chip to a flexible substrate (flex).

(LCDs), smart cards and labels, automotive applications, and portable microelectronics [4]. Finally, adhesive joints are more flexible than solder joints and may be able to withstand mechanical loading better. Much of the work done on conductive adhesives is based on adhesives filled with hard particles such as silver and nickel [5–8]. Among the studies involving soft particles, there has been no systematic approach to determining the true failure mechanism [9–11].

The objective in this paper is to add to the body of published data regarding the durability of ACAs with metal-coated soft polymer conductive particles. In particular, the durability of an ACA FCOF technology needs to be qualified for cyclic thermomechanical environments.

In Section 2, we discuss the temperature cycling and thermal shock experiments. The test results are presented in Section 3 and the accompanying modeling effort is described in Section 4. Summary and future work are discussed in Sections 5 and 6, respectively.

2. Experimental Approach

This section presents details of test setup, specimen fabrication, thermal cycling tests and thermal shock tests.

2.1. Specimen Configuration

The test specimens consisted of 5×5 mm flip-chip dies, attached to a flexible polyimide substrate (10×7.5 cm) with an ACA, as shown in Fig. 2. The conducting particles in the ACA were soft $3\text{--}4 \mu\text{m}$ polymer spheres coated with $0.3 \mu\text{m}$ of pure gold. Two different kinds of dies were used in this study, labeled as Type 1 die and Type 2 die. Table 1 shows the difference between the two dies. Die type 1 has octagonal gold bumps, as shown in Fig. 3a, on a die that was peeled from its flex substrate. Bright gold spheres can also be seen in the bulk of the ACA surrounding the bump. The dark circular spots on the die gold pad are conducting particles adhering to the surface (as shown in Fig. 3b), indicating that there was substantial bonding strength between the gold pads and gold coating on the conducting particle. This bonding can be due to mechanical interlocking caused by large plastic deformations, or due to cold-welding.

The bond-pads in each flip-chip die and matching pads on the flex substrate are daisy-chained for checking continuity. In addition, individual joints were configured separately for four-point resistance measurement of the joint resistance.

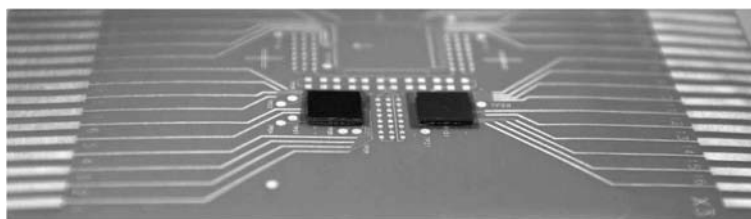


Figure 2. Two daisy-chained flip-chip dies mounted on a daisy-chained flexible substrate.

Table 1.
Specimen characteristics

Type	Die 1	Die 2
Die size	$5 \times 5 \text{ mm}^2$	$5 \times 5 \text{ mm}^2$
Pitch	200 μm	150 μm
Number of bumps	84	118
Dimension of bumps	90 μm octagon	60 \times 75 μm rectangle
Area of bumps	6723 μm^2	4500 μm^2
Bump height	20 μm	15 μm

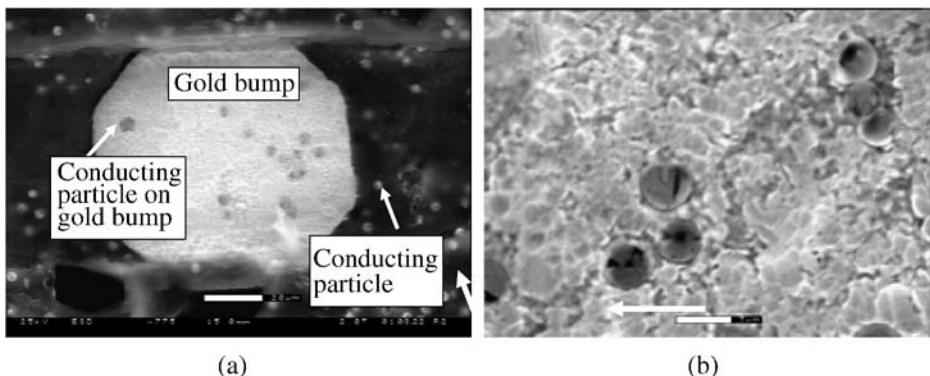


Figure 3. (a) Gold bump on die, showing gold conducting particles and (b) zoomed view.

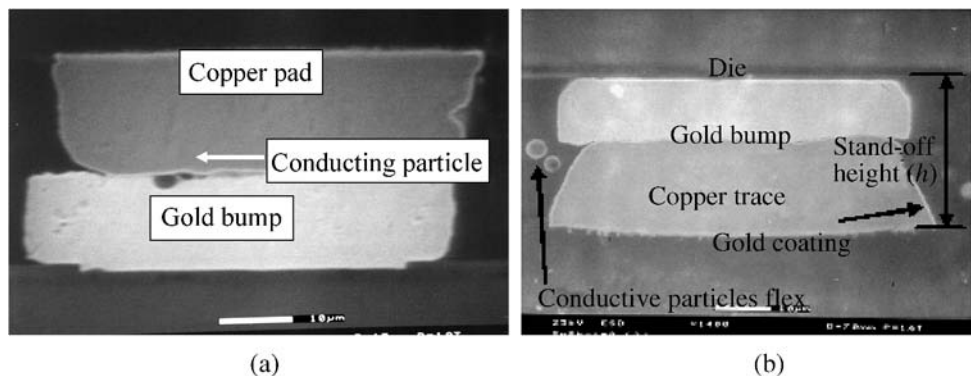


Figure 4. Gold bump bonded on gold-plated copper track, showing (a) trapped conducting particle (flex on top) and (b) no particle between pads (die on top).

The gold bumps on the die were bonded to matching gold-plated copper bond-pads on the flex substrate, with the ACA, as shown in Fig. 4a. The heights of both the gold bump and the copper pad were approximately 20 μm , while the thickness

of the chemically deposited gold on the copper pad was $0.2\text{ }\mu\text{m}$. Figure 4b shows a cross-sectional view without any trapped particles.

2.2. Specimen Fabrication

The standard procedure for ACA bonding consisted of first dispensing the ACA over the flex, aligning the die bumps with the copper tracks on the flex substrate, applying pressure and temperature to cure the adhesive and properly deforming the conducting particles, and finally cooling the assembly to room temperature.

2.2.1. Variation of Bond Pressure in Specimen

The ACA bonding pressure was parametrically varied in the specimen fabrication process. The bonding pressure in specimens for the thermal cycling tests was varied from low values ($2\text{--}4\text{ kgf/mm}^2$ of bump area) to high values ($8\text{--}10\text{ kgf/mm}^2$ of bump area). The bonding pressure in specimens for thermal shock tests was varied over four levels: 4, 8, 10 and 20 kgf/mm^2 .

Figure 5 shows a joint cross-section from a low bond pressure specimen (4 kgf/mm^2 bond pressure). Generally, many conductive particles are trapped between the bump and track in such specimens. The trapped particles cause a moderate indentation in the soft gold bump, and experience moderate flattening where they are in contact with the relatively harder copper track. Figure 6 shows a cross-section of a high bond pressure specimen (10 kgf/mm^2 bonding pressure). High bonding pressure significantly increases the particle deformation near the copper pad, but does not increase the deformation near the gold bump.

These SEM pictures reveal that the conductive particles have no visible asperities on their contact surfaces, and appear to be in good contact with the bump and pad at both low and high pressures. The specimens fabricated with high bond pressure show that in spite of the large deformation the gold coating has not delaminated from its polymer-core sphere. In addition, no cracking is seen in the gold coating due to the large deformation.

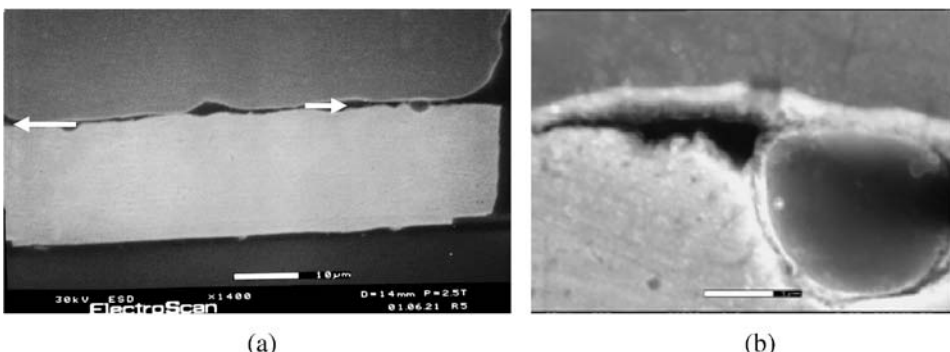


Figure 5. (a) SEM picture of specimen with low bond pressure (conducting particles are seen between bump and track with arrows pointing to them) and (b) zoomed view showing detail of particle deformation and indentation into gold bump.

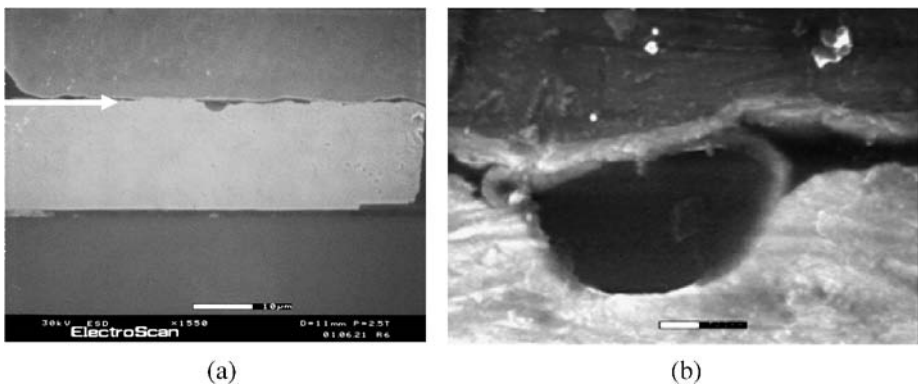


Figure 6. (a) SEM picture of high-bond pressure specimen and (b) zoomed view showing detail of particle deformation and indentation into gold bump.

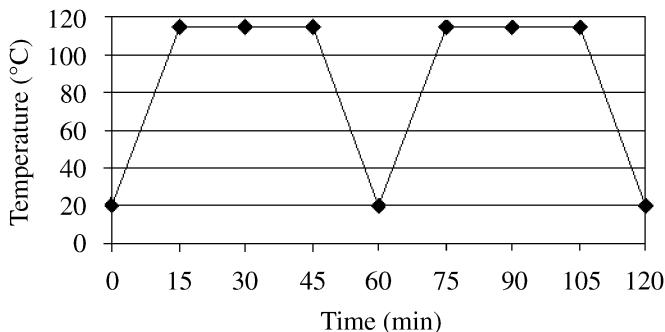


Figure 7. Temperature profile for accelerated thermal cycling durability test.

2.3. Testing — Thermal Cycling and Shock

Selected FCOF specimens were subjected to accelerated temperature cycling to assess their thermomechanical durability. A temperature profile from 20°C to 115°C (shown in Fig. 7), with fifteen-minute ramp times and half-hour dwell times was chosen, to maximize creep and stress-relaxation, thus maximizing the probability of reduction in contact force with a corresponding increase in the contact resistance.

Selected samples were subjected to cyclic liquid-to-liquid thermal shock between -50°C and 110°C, to explore their durability under more severe thermal extremes. The cycle consisted of 10 s dwell time at the extreme temperatures in a commercial perfluoropolyether liquid, as shown in Fig. 8.

2.4. Failure Monitoring

The failure monitoring schemes were somewhat different in the temperature cycling and thermal shock tests. In the cycling test, the resistance of each daisy-chained specimen was continuously monitored, while in the shock test the resistance had

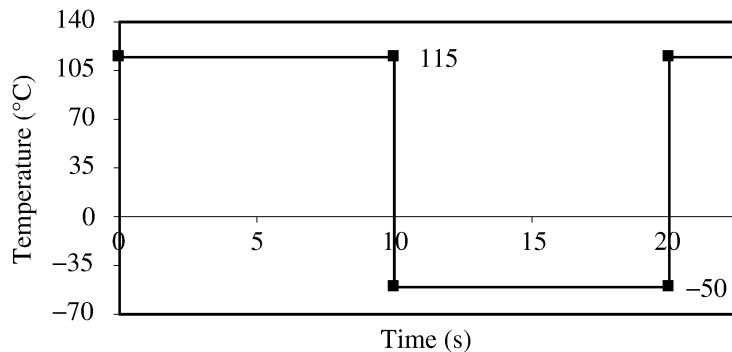


Figure 8. Thermal shock cycle temperature profile.

to be manually monitored at intermittent intervals because the shock chamber does not permit *in situ* resistance measurement.

In the thermal cycling test, the resistance of each specimen was continuously monitored every 10 s. The individual joint resistances had scatter of approximately one milliohm, however this scatter was random and centered about a mean value. A moving-point average was calculated with 20 data points, and was plotted in each data plot as a solid line. The running average of the resistance was found to follow a regular cyclic pattern in phase with the temperature cycle. The large resistance of the daisy-chained net necessitated manual 4-point resistance measurement of individual joints in nets with suspected failures. Failed joints showed infinite resistance.

In the thermal shock tests, the resistance of the daisy-chained nets was manually measured every 50 cycles, since the test chamber configuration did not permit continuous *in situ* monitoring. Specimens were surface dried at room temperature for approximately 20–25 min for the specimen to equilibrate with the room temperature before measuring the resistance. The resistance of each daisy-chain was measured using two probes and a HP 34401A multimeter.

3. Test Results

The results from thermal cycling and thermal shock are reported in this section.

3.1. Thermal Cycling

The resistance history for one thermal cycle is shown in Fig. 9 for an individual joint and in Fig. 10 for an entire daisy-chain net, for a low bond pressure ($2\text{--}4 \text{ kgf/mm}^2$) specimen. The scatter in the data for an individual joint is clearly high because the resistance is very low compared to the resolution of the measurement method. The corresponding 20-point moving average value shown as the solid line in Fig. 9, is clearly proportional to the temperature and varies cyclically in phase with the temperature cycle. The corresponding plots for a high bond pressure specimen, shown in Figs 11 and 12, reveal that the joint resistance in high bond pressure specimen is approximately 5–10% lower than the joint resistance in low bond pressure specimen.

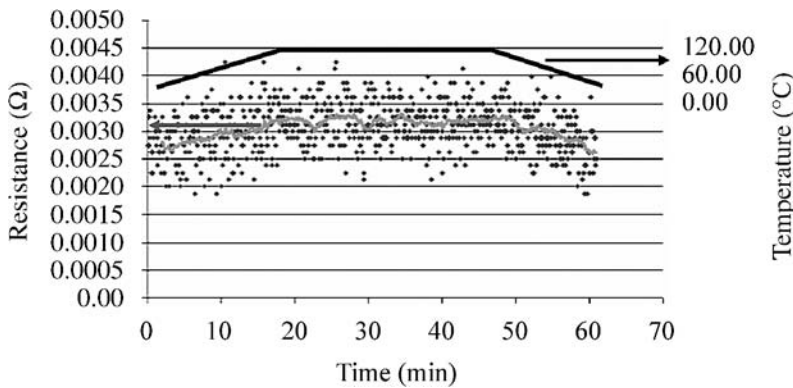


Figure 9. Individual joint resistance in low bond pressure specimen.

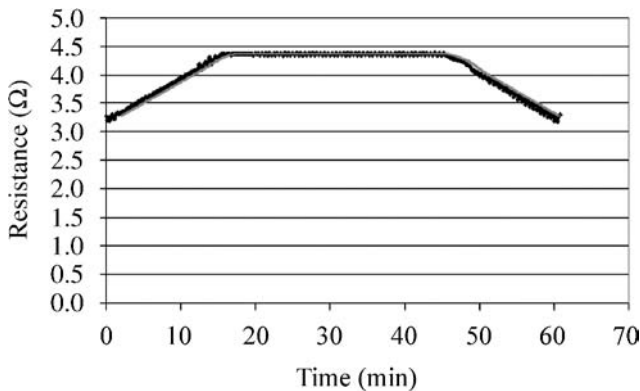


Figure 10. Daisy-chain resistance in low bond pressure specimen.

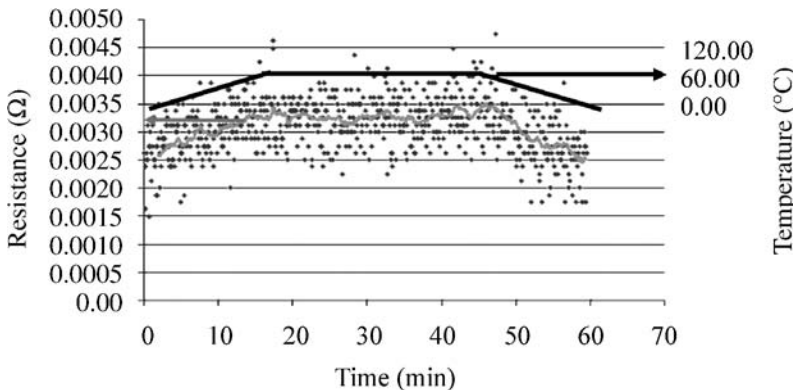


Figure 11. Individual joint resistance in high bond pressure specimen.

None of the specimens failed in the thermal cycling test and the resistance curves were found to remain unchanged for all 1000 cycles of the thermal cycling test (Fig. 13).

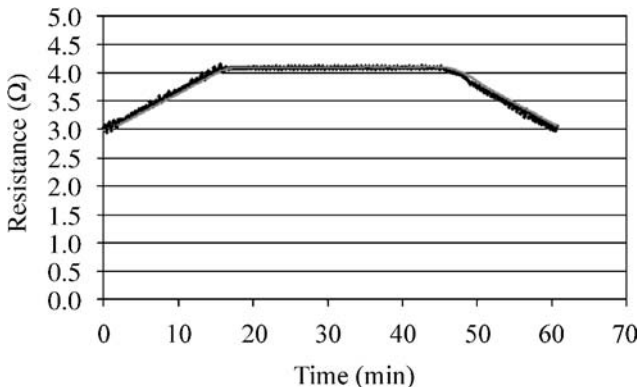


Figure 12. Daisy-chain resistance in high bond pressure specimen.

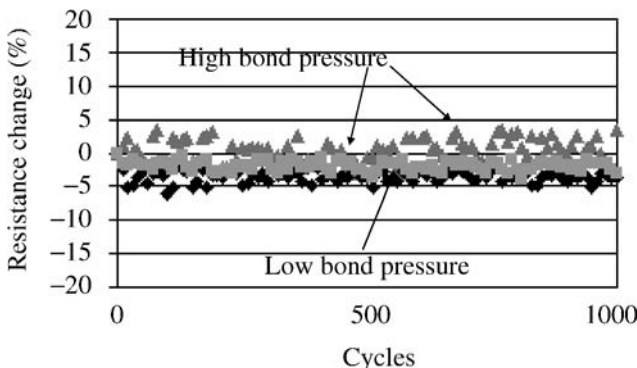


Figure 13. Resistance change for 1000 temperature cycles.

3.2. Thermal Shock

Unlike in thermal cycling, there were many failures in the thermal shock tests, presumably due to the higher thermal expansion mismatch stresses encountered at the low temperature of -50°C . This stress increase occurs as we cool further below the ACA curing temperature. The results of thermal shock testing are presented in Table 2. The plot of cycles-to-failure vs bond pressure, shown in Fig. 14, shows that the durability of FCOF assemblies is weakly proportional to bonding pressure, with Type 1 die being more durable and marginally more sensitive to bond pressure than Type 2 die.

The large amount of scatter seen in the failure data is typical in this architecture. Type 1 dies survive longer during the thermal shock test because although they have fewer bumps, the total bump area is larger because of the larger bumps (see Table 1). Thus, a Type 1 die has more load bearing area to distribute the thermal expansion mismatch stresses, and also has a higher probability of capturing conductive particles between its bumps.

Table 2.
Thermal shock results

Pressure (kgf/mm ²)	Cycles-to-failure	
	Die 1	Die 2
4	950–1000	—
8	—	275–300
10	1525–1575 200–250 850–900 950–1000 2350–2400 >1700 >2100	225–250 250–300 950–1000 450–500 450–500 550–650
20	1650–1700 950–1000	350–400 350–400 500–550

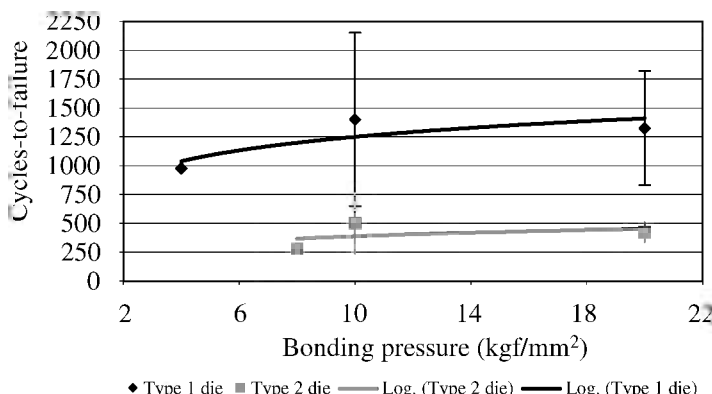


Figure 14. Relation between cycles-to-failure and bonding pressure.

Failed specimens were cross-sectioned and examined under a scanning electron microscope. The most significant and consistent apparent difference between specimens bonded at different pressures is a difference in the stand-off heights. Figure 15 shows the measured values of the stand-off height as a function of the bonding pressure.

The change in durability with bonding pressure is, in part, because the stress in the interconnect changes as a function of this stand-off height and, in part, because the strength of the interconnect changes as a function of the bonding pressure. The effect of stand-off height is discussed in more detail in Section 4, while the effect on bond strength is deferred to a future paper.

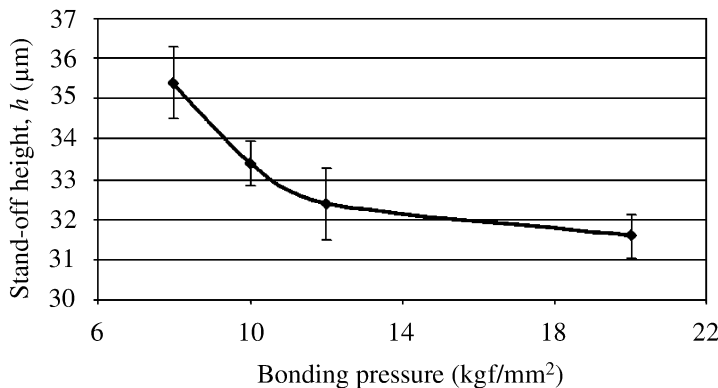


Figure 15. Plot of stand-off height of a Type 2 die vs bonding pressures.

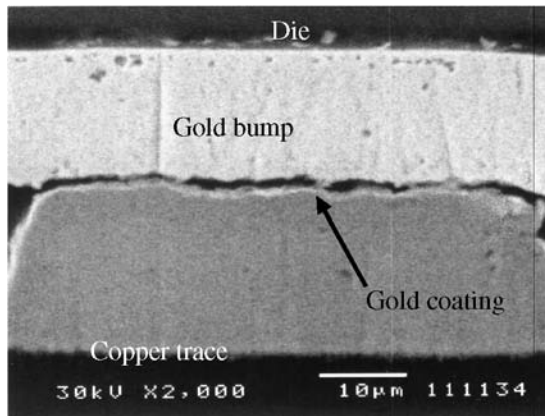


Figure 16. Cross-section of a bump of a Type 2 die (bonding pressure 8 kgf/mm²) showing a spacing of 1–2 μm between the gold bump and the copper trace.

Cross-sections of failed specimens are shown in Figs 16 and 17. In certain cases, misalignment of the bump and the trace has also been observed (see Fig. 17). Misaligned joints and joints without trapped conductive particles are expected to have reduced durability under stress testing.

Failures appear to be due to separation of the Au–Au interface between the bond-pads. It is not immediately clear if the conductive particles are separating by debonding from the pads or by tearing of the gold coating. Both possibilities are modeled later in Section 4.

4. Modeling

The electrical, thermal, and mechanical behaviors of these ACA bonded FCOF joints are investigated with detailed finite element models. Simpler reduced-order models are also developed for parametric studies of joint electrical resistance as

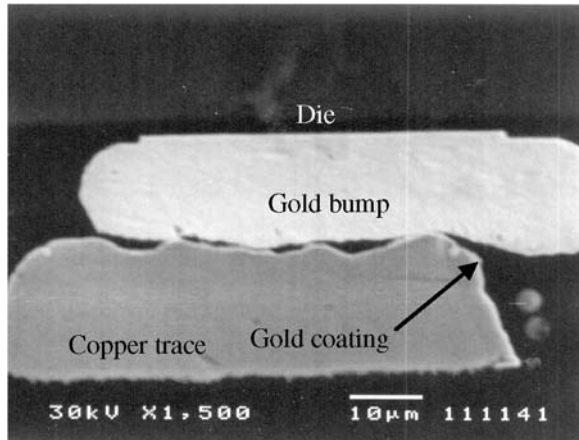


Figure 17. Cross-section of a bump of a Type 2 die (bonding pressure 8 kgf/mm²) showing a misalignment of the gold bump and the copper trace.

a function of temperature and of thermo-mechanical stresses as a function of bonding pressure. The goal is to provide insights into the electrical resistance measurement trends and the failure data observed in the experiments.

The electrical modeling is described first, followed by the thermo-mechanical modeling.

4.1. Electrical Model

As shown in the previous section, the electrical path between each pair of bond-pads is through one or more conductive particles. The performance of each ACA joint is modeled with a simple 1D analytic model as well as with detailed finite element analysis (FEA). Guided by SEM pictures of the disassembled bond-pads, shown in Fig. 3, approximately 20 conductive particles are included between each pair of bond-pads.

4.1.1. Analytic 1D Electrical Model

In order to understand the electrical connection that occurs in an ACA joint, it is important to understand the resistance of each entity individually as a function of temperature. The dominant contribution to the interconnect resistance is from the conductive particle, rather than the bump and pad. The resistance of the conductive particle includes the resistivity of the gold coating and the constriction resistance at the contact points with the bond-pads. Equation (1) accounts for both resistances:

$$R_{\text{total}} = [\rho_0 \cdot b \cdot (T - T_0) + \rho_0] \times \left[\frac{h}{(n \cdot A)} + \left(\frac{1}{2 \cdot n \cdot a} + \frac{1}{2 \cdot \alpha} \right) \right], \quad (1)$$

where:

ρ resistivity ($\Omega \text{ m}$)

h height of deformed conductive particle (m)

A effective cross-sectional area (m^2)

R_{total} resistance (Ω)

n number of conducting spheres

a radius of single contact spot (m)

α radius containing a number of contact spots (m)

ρ_0 resistivity at a reference temperature ($\Omega \text{ m}$)

b temperature coefficient of resistivity

T temperature ($^\circ\text{C}$)

T_0 reference temperature ($^\circ\text{C}$).

Data for the temperature-dependent resistivity of gold are available in the literature [12] and are omitted here for brevity. Results of this analytic electrical model are compared with experimentally collected data and FEM electrical models in the following sections.

4.1.2. Electrical FEA Modeling

FEA is used here to model the temperature-dependent resistance change (within one temperature cycle) of a single ACA joint. The model, shown in Fig. 18, is an axisymmetric representation of a unit cell containing one typical conductive particle sandwiched between the gold and copper mating pads. A typical joint can be considered to behave like twenty such unit cells in parallel. The boundary conditions consist of a unit current at the top surface and a zero potential at the bottom surface. The side surfaces are modeled as electrically insulated.

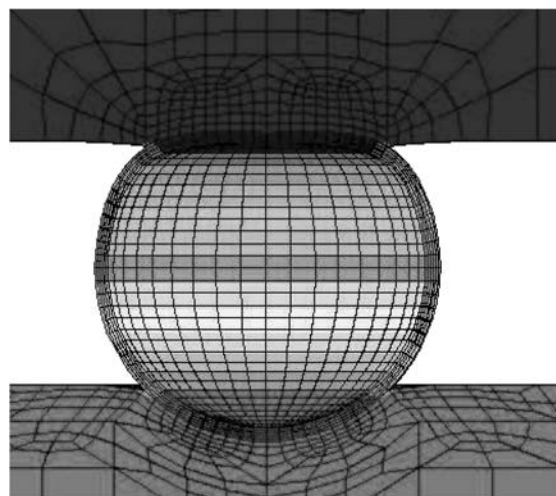


Figure 18. Cross-section showing the equipotential surfaces of the bump (top structure), gold coating of the particle, and the copper pad and its gold coating (bottom structure).

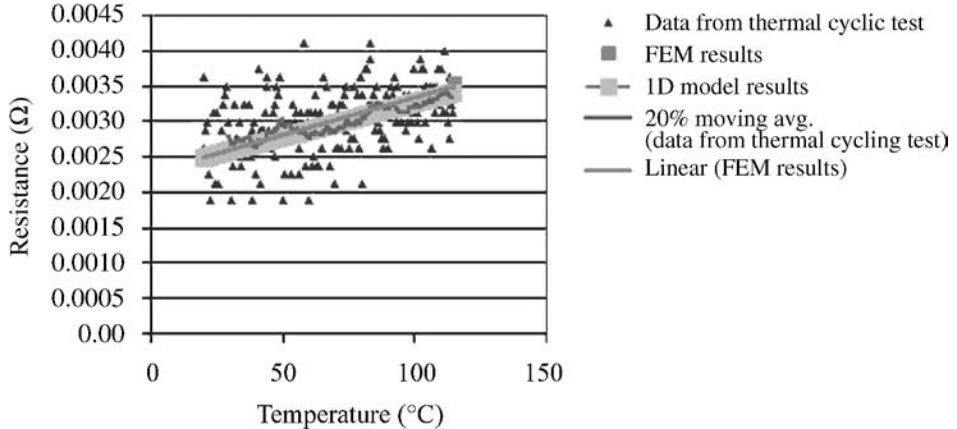


Figure 19. Verification of FEM and 1D model showing a comparison of measured resistance with predictions from FE model and the 1D analytic reduced-order model.

The predicted equipotential contours are also shown in Fig. 18. The voltage drop across the bumps and pads is clearly smaller compared to the voltage drop across the particle. This validates the assumption made in the simple 1D analytic electrical model of Section 4.1.1 that the resistance of the joint is dominated by that of the conductive particle.

The results of the FEA model are compared with the measured data and the prediction from the analytic 1D electrical model. The same assumptions and inputs were used for both the FEA model and the 1D model. The resistance was determined at 20, 40, 60, 75, 100 and 115°C in the FEA simulation and these data points are plotted in Fig. 19 and connected using a linear curve fit. The FEA results agree well with the measurements as well as with the 1D analytic model. Because of this good agreement there is added confidence that the FEA and 1D model provide a reasonable estimate of the resistance of the joint.

The agreement with the experimental data suggests that the observed cyclic resistance changes during the thermal cycles are completely due to the temperature-dependence of the resistivity of the gold material in the conductive particle. In comparison, the contact resistance at the interface with the bond-pad remains constant throughout the test. If this interface was generated by two gold surfaces merely in mechanical contact due to compressive forces generated during the curing of the ACA, then we should have expected the contact resistance to also change with cycling of the contact force caused by ACA thermal expansion during the temperature cycling test. The insensitivity of the interface contact resistance to changes in the contact force lends more credibility to the hypothesis developed in regard to Fig. 3: that a mechanical or metallurgical bond has formed between the pads and the conductive particles. This bonding could either be due to mechanical interlocking caused by large plastic deformations at the surface or metallurgical bonding caused

by gold-to-gold cold welding at the interface. The nature of this bonding will be investigated in a future paper.

4.1.3. Electrical Parametric Study

Because the electrical FEA has shown the ability to correctly predict the resistance as a function of temperature, this model is used to provide parametric insights into changes in the resistance as a function of potential degradation of the electrical connection due to stresses induced by thermal cycling. As discussed in Section 3.2, two types of degradation mechanisms are parametrically modeled: (i) progressive delamination between the gold in the conductive particle and the gold in the bond-pads; (ii) progressive fracture of the gold coating on the conductive particle. The associated change in interconnect resistance can be correlated in future studies to the progression of damage in the interconnects due to thermomechanical stresses.

The model for interface delamination cracking is shown in Fig. 20. The crack is introduced in the FEA model in the region of highest interfacial stresses and is assumed to propagate through the interface. The change in the effective resistance of the joint is parametrically recorded as a function of crack length, as shown in Fig. 21.

The model for progressive axisymmetric tear/fracture through the thickness of the gold coating on the conductive particle is shown in Fig. 22. The thickness of the

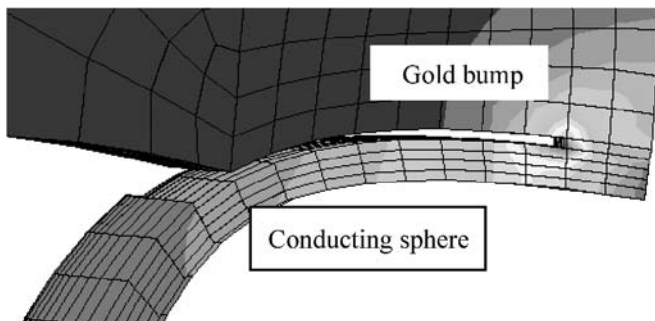


Figure 20. Delamination of conducting sphere.

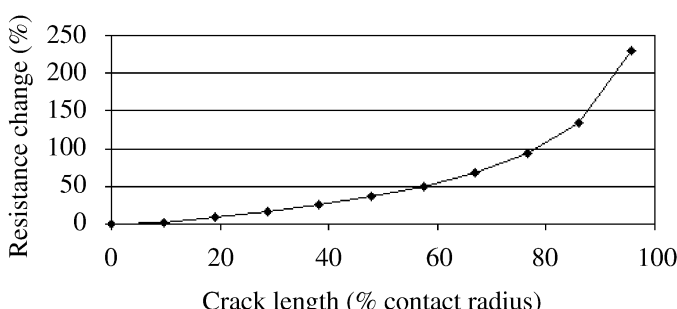


Figure 21. FEA results of parametric study: Delamination of particle from bond-pad and the effect on contact resistance.

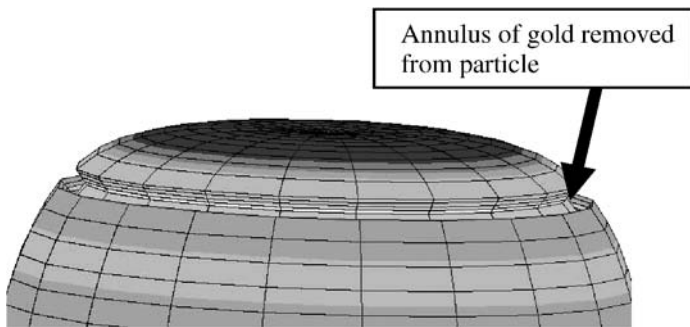


Figure 22. Conducting particle with annular “crack” in gold coating.

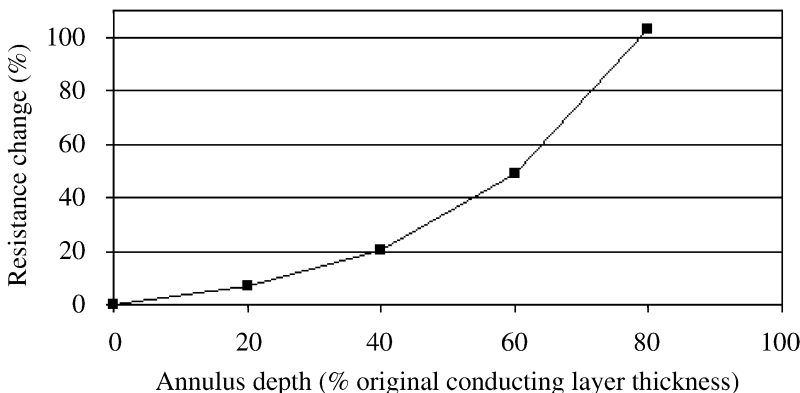


Figure 23. FEA results of parametric study: tearing of gold skin. This plot shows how electrical resistance changes depending on how far a crack goes through the gold layer encasing the particle.

gold coating is progressively reduced where high stresses are expected, to mimic the growth of a crack/tear through the thickness of the gold coating. Figure 23 shows the corresponding resistance change. This potential failure site and failure mode are confirmed later in Section 4.2.1.

4.2. Thermo-Mechanical Model

In order to investigate the thermomechanical deformations occurring in the ACA joint during temperature cycling, the test conditions were simulated using a detailed axisymmetric FEA model and a reduced-order 2D semi-analytic model.

4.2.1. FEA Model

A detailed local axisymmetric model with a single conductive particle was created, similar to the one shown in Fig. 18. This model estimates the stresses in and around a particle at the center of a bond-pad towards the center of the die, where the global CTE mismatch is small. This model showed the location of the greatest von Mises stress when the system was heated from 20°C to 115°C. The results shown

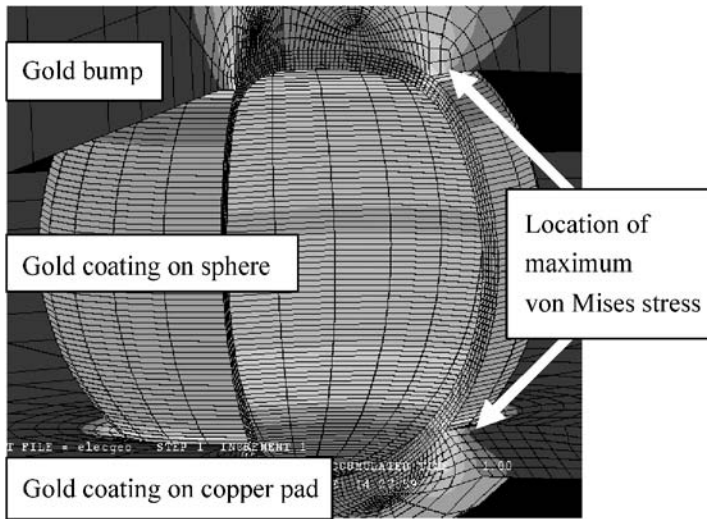


Figure 24. von Mises' stress in a particle when the temperature is raised from 20°C to 115°C.

in Fig. 24 show the stress concentrations at the interface corner, thus confirming the potential location for the damage sites identified earlier in Figs 21 and 23.

4.2.2. Reduced-Order Thermomechanical Model for Parametric Studies

In this section we quantitatively explore some of the reasons why the increased bonding pressure increased the interconnect durability under thermal shock tests (as shown in Fig. 14), and also why the Type 1 die proved to be more durable than the Type 2 die. Since Fig. 15 reveals a strong dependence of the joint height on the bonding pressure, it is instructive to investigate how the interconnect height contributes to the interconnect durability. In order to investigate these issues and to conduct parametric studies for design guidelines, a simple 2D semi-analytic stress analysis model, based on the Raleigh–Ritz method, was developed to predict the stress and strain fields caused by global and local thermal expansion mismatches between the die, flex, bumps and the ACA. For simplicity, the conductive particles are ignored here as their contribution to the total strain energy of the system is negligible.

The Raleigh–Ritz method is a well-known classical technique. In this method an approximate solution of the displacement field is developed as a weighted linear combination of simple known trial functions. The weight functions are unknown parameters whose values are obtained by minimizing the resulting potential energy due to this displacement field. The strain and stress distributions can now be determined from this approximate displacement field in the interconnect.

The analysis was based on the following assumptions/modifications:

- The flexural deformation of the flexible substrate is described with simple trigonometric functions.

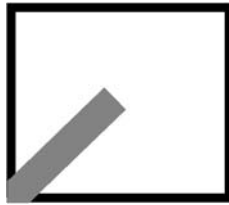


Figure 25. Top view of die showing the diagonal slice model.

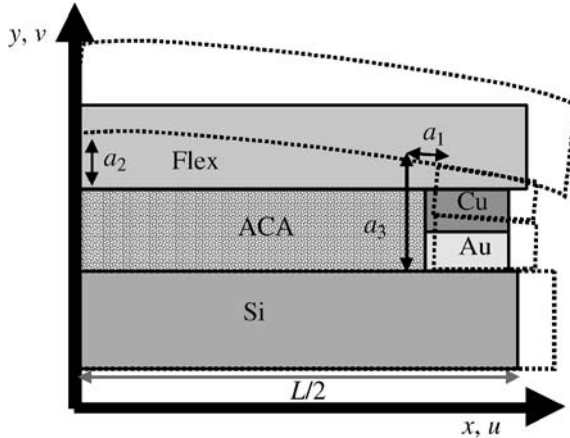


Figure 26. Schematic of a cross-section view of the diagonal slice model.

- All other displacement fields are described with simple linear functions.
- The shear forces exerted by the adhesive on the flexible substrate are negligible.
- Only elastic behavior is considered.

The purpose of this analysis is to examine the shearing and peeling forces on the bumps due to global thermal expansion mismatch between the die and flex. Following common practice in the modeling of electronic assemblies, a diagonal slice of the specimen was chosen and only one half of this symmetric slice was analyzed. This diagonal slice is schematically shown in the top view of the die in Fig. 25. The model includes the silicon die, the gold bumps on the die, the flex with its copper traces and the ACA, as shown in Fig. 26. The model is shown vertically inverted (flex on top) to simplify the displacement expressions in the Raleigh–Ritz model. The material properties used are given in Table 3 and model dimensions are as per Table 1.

The displacement field as per the assumptions listed above can be written as:

$$u = a_1 xy + \alpha_{\text{Si}} x \Delta T, \quad (2)$$

$$v = a_2 y \cos\left(\frac{x\pi}{L}\right) + a_3 y, \quad (3)$$

Table 3.

Properties used to model materials

	Young's modulus (GPa)	Coefficient of thermal expansion (CTE) α ppm/ $^{\circ}$ C	Poisson's ratio
Silicon	131	2.8	0.28
Polyimide	2.78	40	0.32
Gold	77.2	14.4	0.42
Copper	129.5	17	0.3
ACA polymer ($T_g = 145^{\circ}$ C)	1.4	55 ($40\text{--}100^{\circ}$ C) 550 ($100\text{--}140^{\circ}$ C)	—

where u and v are displacements in the x and y directions, respectively, in the flex, ACA and the bond-pads. The deformations in the die are negligible in comparison.

The parameters a_i are the Raleigh–Ritz parameters that are estimated by minimizing the resulting potential energy of this system. The geometric meaning of these parameters is shown in Fig. 26. When estimating the strain energy of this system, the flex substrate is treated as a shell with flexural and membrane strain energies. After the parameters a_i are solved, the strain and stresses are estimated everywhere in the ACA, flex and bond-pads. The parameters of interest are the vertical and horizontal resultant forces on the bond-pads due to the thermal expansion mismatches between the die, flex and adhesive. Details of the analysis are omitted here in the interest of brevity, since the Raleigh–Ritz technique is described in any classical mechanics text.

4.2.3. Results of Raleigh–Ritz Model

The forces and average stresses on the bond-pads were calculated for a temperature change (ΔT) of -190° C which is the temperature difference from the initial stress-free ACA curing temperature (140° C) to the starting point of the thermal shock cycle (-50° C). To estimate the stresses in the next part of the thermal shock cycle, the model was subjected to a temperature cycle (ΔT) of 165° C (difference between the extreme ends of the thermal shock cycle). This calculation was repeated for the different heights shown in Fig. 15 for different bonding pressures. Knowing the forces developed in the bond-pads in one thermal shock cycle, the average bond-pad stresses can now be plotted to assess the effect of bond height on bond stress.

Figure 27 shows the resulting history of the vertical peeling stresses σ_{yy} and Fig. 28 shows the history of the horizontal shearing stresses τ_{xy} , at the interface of the bond-pads, in a Type 1 die and a Type 2 die. The shear stresses are far higher than the peeling stresses. Type 1 die experiences more compressive stresses and smaller shearing stresses than the Type 2 die. This explains why Type 1 die was more durable under thermal shock testing in Section 3.2. Furthermore, the compressive stresses increase as the bonding pressure increases (because of the resulting

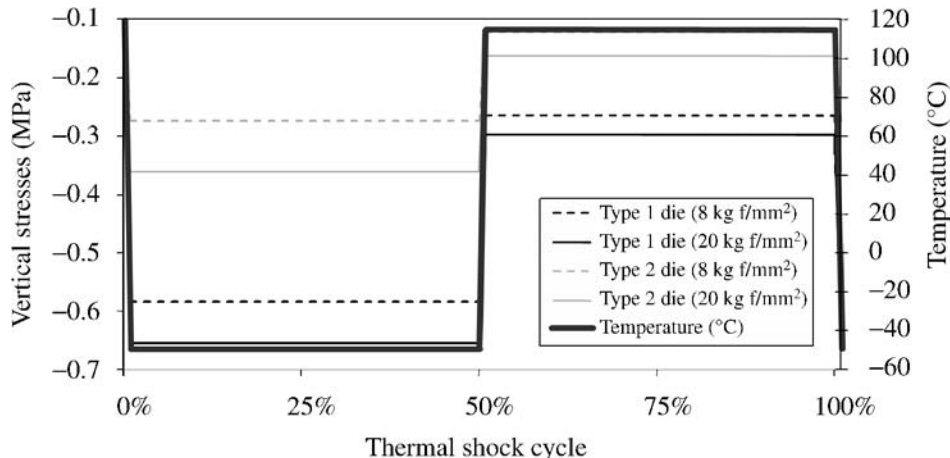


Figure 27. Vertical peeling stresses developed at the interconnect during one thermal shock cycle.

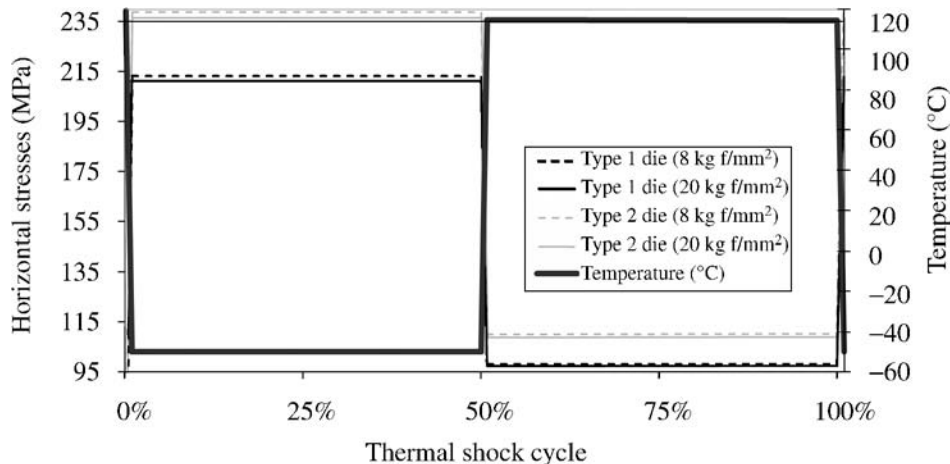


Figure 28. Shear stresses developed at the interconnect during one thermal shock cycle.

decrease in bond height), thus demonstrating the contribution of the bond height to the increasing durability, as a function of bonding pressure (shown in Fig. 14).

4.2.4. Parametric Studies

The Raleigh–Ritz model developed is also useful as it can provide simple design guidelines, regarding the effect of geometry on the interconnect durability. By parametrically altering the geometry of the bumps, die size, height of the flexible substrate, the stress in the package can be determined, which in turn, gives an estimate of the durability of the ACA-bonded FCOF assembly. Similar results are also obtained when material properties such as the modulus or the coefficient of thermal expansion are parametrically varied. This study provides parametric insights into optimization of these design variables, to provide more reliable FCOF assemblies.

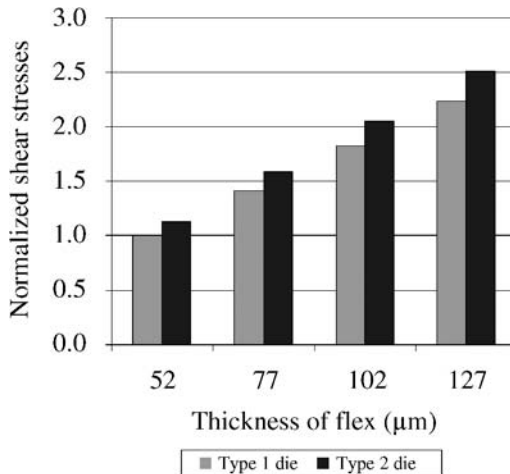


Figure 29. Variation of shear stresses with flex thickness in Type 1 and Type 2 dies, normalized to the value of die Type 1 with 52 μm flex thickness.

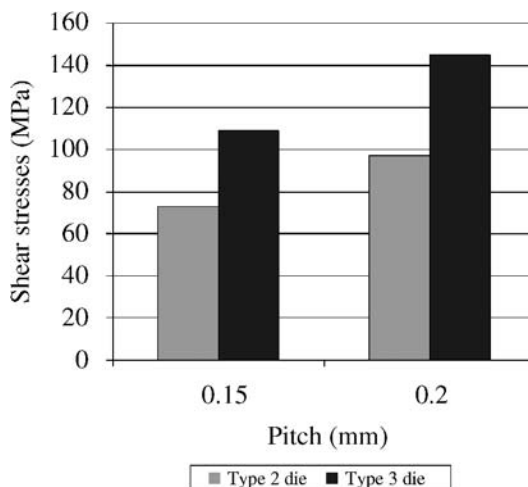


Figure 30. Variation of shear stress with pitch of bumps in Type 1 and Type 2 dies.

As an example, the CTE of the flex was found to have very little effect on the shear stresses in the bond-pads. Representative selections of the most significant results are presented Figs 29–31, where the shear stresses in Type 1 and Type 2 dies are shown for varying flex thickness, bond pitch, and CTE of the ACA. As expected, shear stress in the bond-pad increases with increasing flex thickness, increasing bond pitch and increasing ACA CTE. In general, Type 1 dies are seen to experience lower shear stresses, thus explaining their higher durability in the thermal shock tests in Section 3.2.

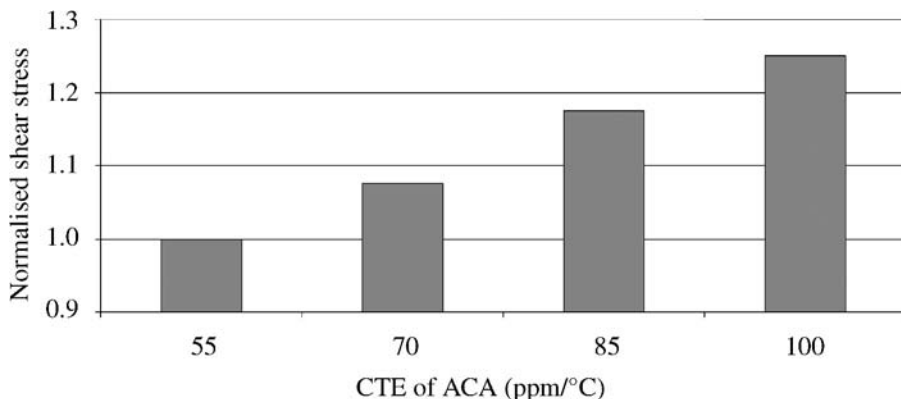


Figure 31. Variation of shear stress with the CTE of the ACA in a Type 2 die, normalized to the stress corresponding to a CTE of 55 ppm/°C.

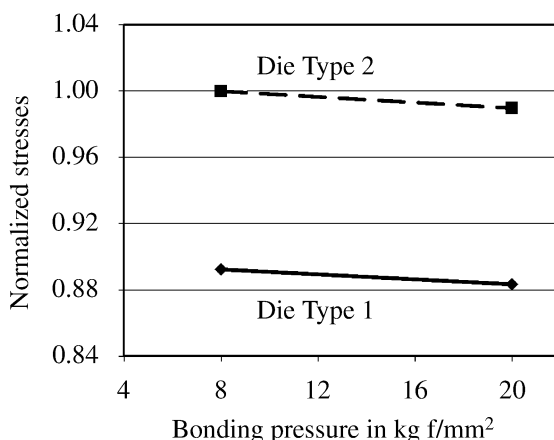


Figure 32. Plot of maximum shear stresses in packages bonded at different bond pressures.

The same model also proves useful in investigating the process window of the package. Process variables such as bonding pressure can be varied (by varying the bond height, as shown in Fig. 15) to estimate the maximum shear stresses that develop. Figure 32 shows the maximum shear stress in packages at different bonding pressures.

Finally, this model can also be used to extract from the durability test results, a S-N fatigue curve, Fig. 33, where the cycles-to-failure is directly related to the von Mises stress at the bond-pad. The specimens used to construct this plot include both die types and bonding pressures of 8 and 20 kgf/mm². The fit shows a power-law that can be used to describe this test data. This is a very useful outcome, which can be used to extrapolate the durability data to other temperature cycles, other loading conditions, and other package configurations.

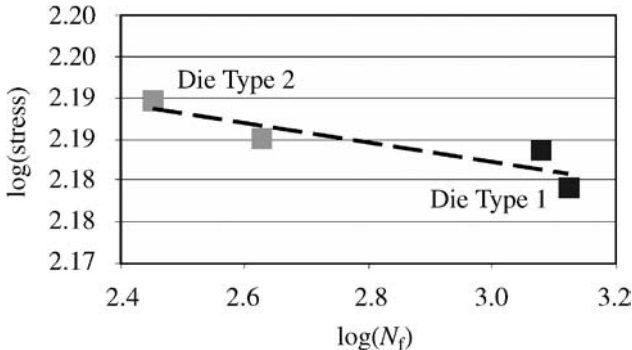


Figure 33. Fatigue S–N plot of interconnect stress *vs* cycles-to-failure (N_f).

5. Summary and Conclusions

The electrical connection in the ACA joints examined in this study is through the conductive gold coating on the soft polymer spheres that connected the bump and the pad. Test specimens were fabricated with two die types. The resistance of all interconnects was found to vary cyclically with temperature cycling, but no permanent degradation was found through 1000 temperature cycles between 20°C and 115°C. Using 3D FEA and simple 1D analytic models, the resistance changes of the interconnect were found to closely track the temperature-dependent resistivity of the gold and copper materials in the interconnect. This suggests that no degradation occurred at the contact interface at the stress levels encountered during this temperature cycling test.

Thermal shock tests between more extreme temperature conditions (−50°C and 115°C) did induce failures on all the tested adhesive joints. To gain insights into the failure mechanisms, electrical degradation of an ACA bonded joint was parametrically modeled with detailed defect-seeded 3D FEA models. The two failure modes examined here are: (i) interfacial delamination between conductive particle and bond-pad; (ii) tearing of the thin gold coating on the polymer sphere used as the conductive particle.

In the thermal shock tests, Type 1 dies were found to fail before Type 2 dies and the durability appeared to increase with increasing bonding pressure. As shown by thermo-mechanical models, the dependence on bonding pressure is due to changes in the bond-pad geometry, bond-pad stress and bond-pad strength. The effects of design and process variables on the bond-pad geometry and stress were examined in this study with the help of thermo-mechanical 3D FEA models and a simple 2D semi-analytic model. The investigation of the dependence of the bond-pad strength on design and process variables is deferred to a future study.

The modeling effort in this study not only provided good parametric insights into the effects of various design and process variables on the reliability of this ACA architecture, but also provided useful material properties like basic fatigue S–N curves of ACA interconnect assemblies.

6. Future Work

This paper is the first in a two-part series and has presented a simple study of some basic durability issues in ACA-bonded FCOF architecture. The second paper in this series will look at a competing FCOF technology that uses non-conducting adhesives (NCAs) to bond the flip-chip die to the flex substrate. There are unique manufacturing challenges in the NCA architecture due to more stringent co-planarity requirements and these will be examined in Part II.

The results presented in this paper revealed that the bonding pressure might affect the thermal cycling durability of adhesively bonded FCOF systems for two reasons. The first is that the bonding pressure affects the stand-off height, which affects the thermomechanical bond-pad stresses. The second is that the bonding pressure affects the bond strength due to mechanical interlocking and/or cold-welding [13, 14]. The first issue has been examined in this paper, the second will be examined in future research.

Acknowledgements

This work was funded by the members of CALCE EPSC, and would not have been possible without the generous help of Dr. J. W. C. de Vries of Philips Centre for Industrial Technology, Dr. B. T. Han of the University of Maryland and K. Rogers of the University of Maryland.

References

1. Z. Zhong, *Microelectronics International* **16**, 6 (1999).
2. M. A. Gaynes, R. H. Lewis, R. F. Saraf and J. M. Roldan, *IEEE Trans. Advanced Packaging* **18**, 299 (1995).
3. L. Loken, in: *Proc. NEPCON WEST*, Anaheim, CA, p. 632 (1994).
4. L. K. J. Vandamme, M. G. Perichaud, E. Noguera, Y. Danto and U. Behner, *Microelectronics Reliability* **39**, 1089 (1999).
5. J. C. Jagt, *Proc. Sem. Electric Conduct. Adhesives Delco Electron.* (1996).
6. J. C. Jagt, P. J. M. Beris and G. Lijten, *IEEE Trans. Advanced Packaging* **18**, 292 (1995).
7. H. Kristiansen and J. Liu, *IEEE Trans. Components, Packaging, and Manufacturing Technology* **21**, 208 (1998).
8. O. Rusanen and J. Lenkkeli, *IEEE Trans. Advanced Packaging* **18**, 320 (1995).
9. R. Aschenbrenner, A. Ostmann, G. Motulla, E. Zakel and H. Reichl, *IEEE Trans. Components, Packaging, and Manufacturing Technology* **20**, 95 (1997).
10. R. Miessner, R. Aschenbrenner and H. Reichl, in: *Proceedings of the 49th IEEE Electronic Components and Technology Conference*, San Diego, CA, p. 595 (1999).
11. A. Seppala, I. Suominen and E. Ristolainen, in: *Proceedings of the First International IEEE Conference on Polymers and Adhesives in Microelectronics and Photonics*, Potsdam, Germany, p. 196 (2001).
12. R. A. Matula, *J. Phys. Chem. Ref. Data* **8**, 1147 (1979).
13. R. Holm, *Electric Contacts: Theory and Application*. Springer-Verlag, New York, NY (1967).
14. E. Rabinowicz and D. Tabor, *Proc. Royal Soc. London A* **208**, 455 (1951).

Mechanics of Adhesively Bonded Flip-Chip-on-Flex Assemblies. Part II: Effect of Bump Coplanarity on Manufacturability and Durability of Non-conducting Adhesive Assemblies

D. Farley^a, A. Dasgupta^{a,*} and J. F. J. Caers^b

^a CALCE, Mechanical Engineering Dept., University of Maryland, College Park, MD 20742, USA

^b Philips Applied Technologies, Electronic Packaging & Thin Film, High Tech Campus 7, WDX-3A 0.262, 5656 AE Eindhoven, The Netherlands

Abstract

This is Part II of a two-part paper on the mechanics of adhesively-bonded Flip-Chip-on-Flex (FCOF) assemblies. Part I dealt with the use of anisotropic conductive adhesives (ACAs) while this paper deals with the use of non-conducting adhesives (NCAs). The central concern here is the influence of bump coplanarity on the manufacturability and durability of the assembly. The assembly is first analyzed with global/local nonlinear finite element models to assess the effect of bump coplanarity on the maximum force needed to achieve reliable bonding. The number of bumps at the low end of the manufacturing height tolerance is parametrically increased to quantify the effect on the bonding force. Results confirm that the bonding force required is inversely proportional to the number of ‘short’ bumps in the assembly.

Next, the bonding and adhesive curing process is simulated in detail with finite element models, in order to assess the residual pre-stress between matching interconnect bumps, since this compressive contact stress may be important to the long-term performance of the FCOF assembly. The nonlinearities addressed in the model include elastic–plastic properties of gold, viscoplastic properties of the NCA and evolution of contact area between the mating bumps. Results show that it is necessary to model the viscoplasticity of the NCA to obtain realistic predictions, and that the residual compressive pre-stress between the mating bumps increases as the percentage of ‘short’ bumps increases in the assembly.

Keywords

FCOF, non-conductive adhesive, gold bump, copper bump, fabrication pressure, residual pre-stress, contact force, viscoplasticity, elastic–plastic deformation, curing shrinkage, contact surface area

1. Introduction

In the push for Pb-free interconnect technologies, adhesively-bonded interconnect assemblies have emerged as a viable alternative for low-temperature applications.

* To whom correspondence should be addressed: Tel.: +1 301 405 5251; e-mail: dasgupta@umd.edu

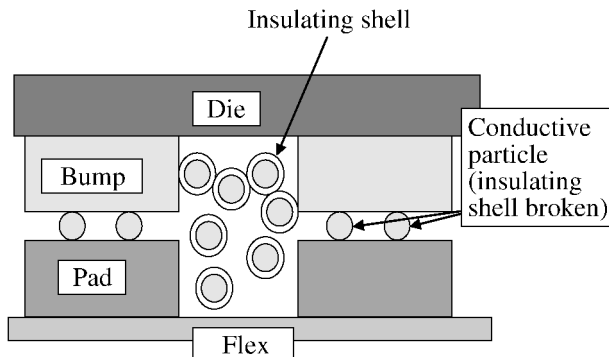


Figure 1. ACA schematic [1].

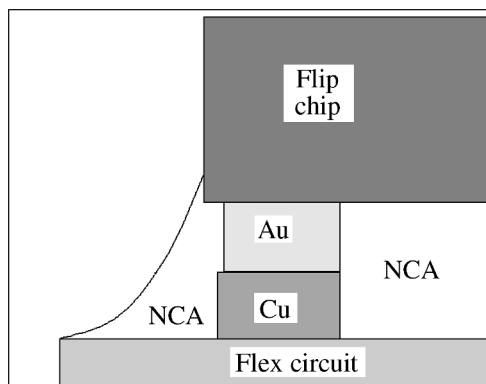


Figure 2. NCA schematic.

Adhesives not only offer lower process temperatures compared to Pb-free solders (*curing versus reflow*), but also require fewer process steps, and have the ability to accommodate much smaller pitches, as in Flip-Chip-on-Flex (FCOF) assemblies. In this technology, the interconnect is usually between gold bumps on the silicon die and gold-plated copper bumps on a flex substrate (Figs 1 and 2). Conductive adhesives (CAs) (Fig. 1) or non-conductive adhesives (NCAs) (Fig. 2), are used as an underfill to bond the die to the flex substrate. The CA shown in Fig. 1 is an anisotropic conductive adhesive (ACA) with higher conductivity across facing bumps than between adjacent bumps. Some other technologies use isotropic conductive adhesives (ICAs).

Part I [1] of this two-part series had discussed durability issues in a FCOF bonded with an ACA. Small (2–3 µm diameter) conductive particles used in ACAs are often trapped between the mating interconnect bumps to complete the connection (Figs 1 and 3). However, when very small pitches are used (30 µm in some cases), there is a finite possibility of particles concentrating between adjacent interconnect bumps

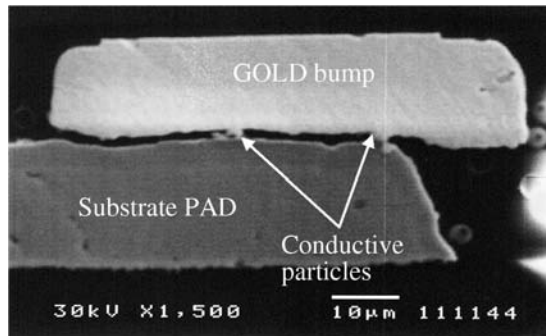


Figure 3. FCOF ACA interconnect with conductive particles completing the circuit.



Figure 4. FCOF NCA interconnect.

and causing a short during compression and bonding. NCAs are considered a viable alternative for such small pitches, and are the focus of this study.

The current paper (Part II of this two-part series) discusses fabrication issues for reliable interconnection with a NCA. As seen in Figs 2 and 4, the primary electrical path in NCAs depends on direct face-to-face contact between mating bumps, as there are no conductive particles to bridge any gaps between them. The remainder of this introductory section describes the fabrication process, followed by a literature review.

1.1. NCA Fabrication Process and Modeling

According to one school of thought, the primary performance criterion in FCOF joints bonded with NCAs is the compressive stress that develops between the mating metal bumps due to chemical and thermomechanical shrinkage of the NCA during the curing process. Competing models, discussed in Part I [1] of this series, are predicated on mechanical/metallurgical bonding occurring between the bond-pads. This theory is explored in this study because of reports in the literature about progressive increase in the mean resistance of an adhesively-bonded FCOF system under thermal cycling [2–4], eventually reaching failure threshold at time, t_f . This increase of contact resistance is believed to be caused by the gradual cyclic decrease in compressive force holding the mating interconnect pairs together, due to stress relaxation mechanisms in the viscoelastic epoxy, as shown schematically in Fig. 5. The initial state of this compressive contact pre-stress (at time = 0) is the residual stress generated by the adhesive bonding process.

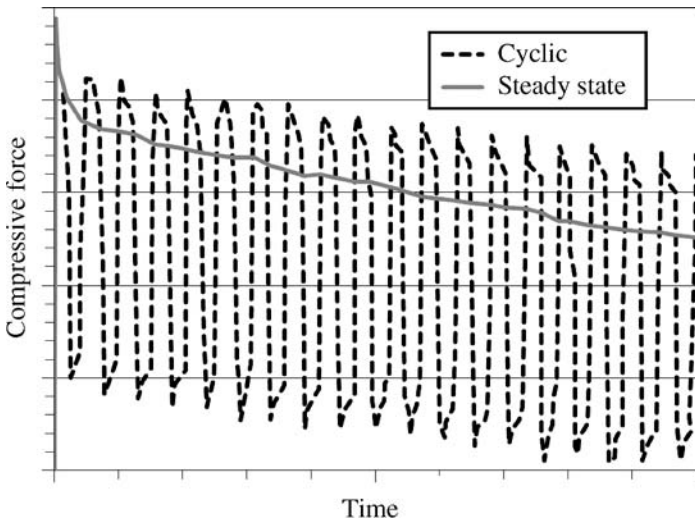


Figure 5. Degradation of compressive force as a function of time [5].

The usable life, therefore, depends on the magnitude of the initial contact resistance and on the rate of cyclic increase in the contact resistance. From a mechanical point of view, some key drivers for durability are the magnitude of the initial contact pre-stress and the rate of cyclic viscoelastic relaxation of the contact stress.

The residual compressive pre-stress is strongly dependent on the NCA properties as well as on the fabrication pressure. The fabrication pressure is more important in NCAs than in ACAs since the lack of conductive particles in NCAs makes it essential that all mating bumps make robust face-to-face contact. This can be seen, comparing Fig. 1 through Fig. 4. Ensuring full contact in all mating pairs is not always easy as there are inherent variabilities in the interconnect bump heights (the 'Au' and 'Cu' of Fig. 2) due to manufacturing tolerances. These varying gaps between the mating pairs must be closed by plastically deforming 'tall' bumps with compressive mechanical bonding force so that all the 'short' mating bumps can be brought into contact during the fabrication step. The resulting contact stress, after fabrication and cool-down, is referred to as the 'residual stress' or 'pre-stress'. The magnitude of the compressive contact stress is key to achieving low contact resistance for successful electrical performance. This study uses finite element modeling to first determine the fabrication force required to overcome the lack of coplanarity, and then the resulting pre-stress remaining after fabrication. Other works in literature have used methods such as interferometry to measure package warpage on a sub-micrometer scale [6] which gives insight into the amount of residual stress developed during the fabrication. The present study instead uses detailed nonlinear predictive modeling. The validity of such modeling approaches has been demonstrated in the literature by comparing modeling results with experimental measurements [6, 7].

This study, therefore, uses nonlinear finite element modeling to investigate:

- (1) The compressive force required during fabrication to compensate for lack of coplanarity of the bumps and to ensure that all interconnects have been brought into contact.
- (2) The residual compressive stress developed at the interface of mating interconnect bumps at the end of fabrication, once the epoxy has been cured and the compressive bonding force and heat have been removed.

1.2. Summary of Literature

The use of adhesively-bonded flip-chip technology started to become widespread around 1999 [8]. Much work has been done since then to quantify the reliability and durability, usually for specific package styles. In cyclic thermal loading studies, these works have mostly focused on cycles to failure, contact resistance, and effects of different bonding forces and bonding temperatures. An extensive literature search has been conducted to understand the nature and history of interconnect failure mechanisms in adhesively-bonded flip-chip assemblies.

Many of these studies typically test a specific package geometry for a specified accelerated test sequence and simply report package-specific pass-fail reliability data without going into sufficient detail of failure mechanisms or acceleration factors [3, 4, 7, 9–16].

Mercado *et al.* studied the failure mechanisms of packages bonded with an anisotropic conductive film (ACF), but concluded that the reliability was strongly dependent on moisture and, therefore, ignored temperature cycling [17]. Simulation techniques have been used in conjunction with experimental results, in an attempt to fully characterize adhesively-bonded flip-chips [6, 7].

Several studies have explored the relationship between interconnect resistance and compressive force [5, 7, 15, 18]. Chan and Luk [19] and Li and Treliant [4] pursued relating bonding pressure and bonding temperature to the reliability of adhesively-bonded flip-chips. Chan and Luk based their conclusions regarding required bonding pressure on the amount of ACA particle deformation. They also reported that the optimal bonding temperature for ACAs was 200°C. Temperatures higher than 200°C resulted in higher interconnect resistance for their architecture. Fu *et al.* [20] agreed with Chan and Luk's work, citing particle deformation as an important factor, and added that particle location in the interface was also important. The resistance of an interconnect increases as the particle distance grows from the center of the bump.

The works of Chan and Luk [19] and Yeo *et al.* [21] confirmed the dependence of resistance on temperature, but Yeo *et al.* conceded that more work was needed to fully understand the failure mechanisms. Haase *et al.* [1] found that the contact resistance in their Au–Au interconnect system did not degrade through 1000 temperature cycles (20–115°C). Li and Treliant did report slight degradation in their Au–Ni system [4] under temperature cycling, although it was not significant; they found an increase from about 35 mΩ to about 45 mΩ of contact resistance after 500 cycles from –55°C to +125°C.

Wu *et al.* looked into the impact of bump height on interconnect reliability, concluding that higher bumps resulted in higher ACF stress [22]. But they also concluded that higher ACF stress was a negative attribute, resulting in delamination failures.

DMA (dynamic mechanical analyzer) is a fairly common tool for measuring the properties of epoxies to obtain master stress relaxation curves associated with viscoelastic shift functions [23]. Simon *et al.* developed an analytical model to describe the development of mechanical properties during cure, using a combination of time-temperature superposition, time-crosslink density superposition and elasticity of the polymer network [24]. Cusano *et al.* reported a novel refractive index technique to monitor the development of epoxy cure [25] that can be used to fully understand the extent of cure in an epoxy in a fabrication profile. Bockenheimer *et al.* studied thermal aging in epoxies, reporting that 40°C aging leaves bulk mechanical properties intact, while 60°C aging leads to a phase separation [26].

While many of these studies have looked at the varying aspects of durability degradation, and some have characterized it, none has specifically focused on the development of the ‘initial’ contact stresses. This study examines the necessary fabrication pressure, and the resulting pre-stress of a NCA-bonded FCOF package.

The two FCOF architectures used in this study for investigating the fabrication pressure and residual stresses are described in Section 2. The analysis methods and results are described in Section 3. Summary and conclusions are presented in Section 4.

2. FCOF Architectures

Two different FCOF architectures were used for investigating the necessary bonding pressure and the resulting pre-stress state when using NCAs. These package styles and their materials are described in this section.

2.1. Geometry

For the first step in this study (determination of minimum required compressive bonding force), a rectangular flip-chip with a large aspect ratio was used. The chip was 15 mm long and 1.5 mm wide, and 0.5 mm thick. It had 1000 Au bumps, arranged in a 30-μm-pitch perimeter array, but only along the two long sides of the chip. The Au bumps had a 20 μm square footprint and were 15 μm tall. The flexible substrate used in this phase was 0.05 mm thick, with 18 μm thick Cu traces. The copper bumps had a finish of nickel/immersion gold. The manufacturing tolerance on coplanarity of bump height was ±2 μm. This architecture is termed ‘Configuration 1’ in the remainder of this paper.

For the second step (determination of residual stress after bonding), an 8 mm square flip-chip was used. This chip also had a perimeter array, but it was around all four sides and the pitch measured 300 μm. There were 56 I/Os, and each Au bump had a 80 μm square footprint at the contact surface and were 21 μm tall. The

manufacturing tolerance on the bump height was $\pm 0.7 \mu\text{m}$ in this case. The flexible substrate used in this phase has 18 μm high Cu traces, that measure 0.025 mm wide. This architecture is termed ‘Configuration 2’ in the remainder of this paper.

2.2. Materials

Both architectures included a silicon chip, flex circuit, and mating pairs of Au–Cu interconnects. There was no adhesive in the first step of the study, when the required mechanical compressive force was assessed. The epoxy was introduced in the second step, when the residual stress developed during curing of the NCA epoxy was modeled.

In both steps, the silicon chip and the flexible substrate are modeled as elastic materials. The corresponding elastic properties are listed in Table 1. Gold [27] and copper [28] in the interconnects are modeled as elastic–plastic materials with stress strain curves seen in Figs 6 and 7, respectively. Since the mechanical compression step in the FCOF fabrication process is relatively fast, rate-dependent material be-

Table 1.
Elastic properties of materials used

	CTE (μ/C°)	ν	E (GPa)
Au	14.2	0.291	66.7
Cu	17.4	0.3	120
Epoxy	400	0.3	3.3
Flex	23	0.3	4.3

ν is Poisson’s ratio and E is the Young’s modulus.

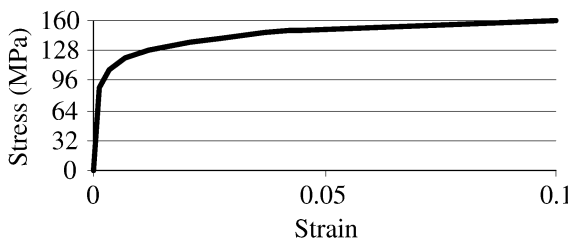


Figure 6. Elastic–plastic constitutive model for gold [26].

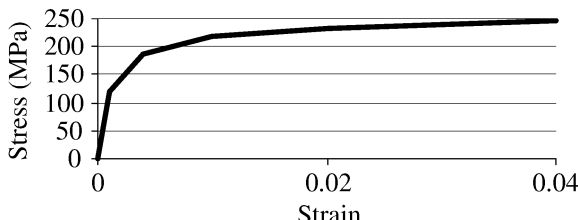


Figure 7. Elastic–plastic constitutive model for copper [27].

havior is not modeled. The rate-dependent behavior will become important later in this paper, when residual stresses due to adhesive curing are modeled.

For the residual stress determination in Step 2, the material properties of the silicon die, flex substrate and the gold and copper bumps are identical to those used in Step 1. The new material in Step 2 is the NCA epoxy, which is modeled as a viscoelastic material.

The viscoelastic NCA epoxy is modeled with a Prony series expansion, with Williams–Landel–Ferry (WLF) shift factors, as follows:

$$G(t) = G_{\text{inf}} + \sum_{i=1}^N G_i e^{-t/\lambda_i} = G_{\text{inf}} + \sum_{i=1}^N C_i (G_0 + G_{\text{inf}}) e^{-t/\lambda_i}, \quad (1)$$

$$G_0 = E_0/2(1+\nu), \quad G_\infty = E_\infty/2(1+\nu), \quad (2)$$

where G_{inf} is the final modulus, G_0 is the initial modulus, and G_i and λ_i are the relaxation moduli and relaxation times, respectively. This study uses a six-term Prony series representation. The temperature effect is introduced through reduced time, $\xi(t)$, defined as:

$$\xi(t) = \int_0^t \frac{d\tau}{a_T(T(\tau))}, \quad (3)$$

where a_T , the shift factor at time t , is approximated by the WLF equation:

$$\log a_T = \frac{-C_1(T - T_{\text{ref}})}{C_2 + (T - T_{\text{ref}})}, \quad (4)$$

where T_{ref} is the reference temperature, and C_1 and C_2 are empirical constants at T_{ref} . The viscoelastic material constants for the NCA are taken from the literature [28].

3. Modeling Approach and Results

This section describes the methodology used to determine the two important aspects of fabricating reliable NCA-bonded FCOF assemblies: compressive bonding force and residual contact stress.

3.1. Compressive Bonding Force

One of the key manufacturability concerns in adhesively-bonded flip-chip technology is that the maximum bonding force, needed to overcome lack of coplanarity when bonding high-I/O flip-chips with NCAs, may be prohibitively high. Fortunately, this can be estimated reasonably well at the design phase with computer modeling, provided the elastic–plastic properties of the bump materials (Au and Cu) are well known. This mechanical bonding step also sets up the initial condition that eventually determines the compressive residual stress in the interconnect at the end of the bonding process.

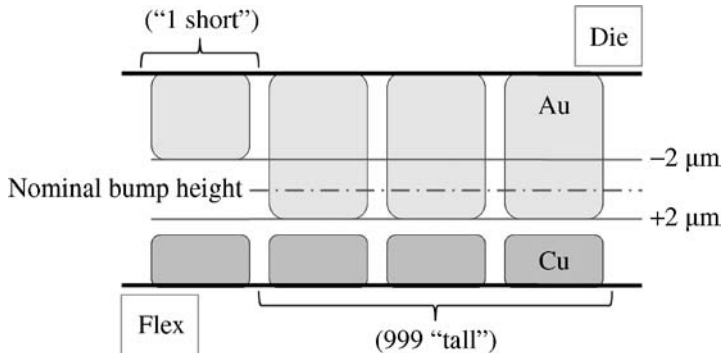


Figure 8. Schematic representing the worst-case scenario of 999 ‘tall’ bump pairs and one ‘short’.

3.1.1. Objective

This section illustrates simulation-based estimation of the total bonding force needed to bond a high-I/O flip-chip on a flex-circuit substrate with NCA. The geometry is that of Configuration 1 described in Section 2.1. The dimensional tolerance of the interconnect bump height is $\pm 2 \mu\text{m}$. Assuming the variation of the height of the Cu traces on the flexible substrate is minimal, it follows that the worst case scenario (maximum bonding force) would be a situation where one bump is at the low end of the height tolerance band ($-2 \mu\text{m}$ on the chip bump) whilst the rest are at the high end ($+2 \mu\text{m}$). Therefore the bonding force would have to plastically compress 999 bump pairs by $4 \mu\text{m}$, until the one short pair comes into contact (shown schematically in Fig. 8). It is this upper bound estimate of the maximum required compressive force that is of interest for manufacturability assessment. If the required force is too large then reliable interconnection cannot be achieved by the fabrication process. A finite element modeling approach is used here to estimate this worst-case bonding force.

3.1.2. Model Strategy

The finite element model developed to assess the bonding force is described in this section. In view of the high-I/O, a global/local modeling strategy is used to minimize the computational resources, as seen schematically in Fig. 9. The ‘local model’ is a detailed representation of a representative repeated unit of the assembly. In this study, the repeated unit is a mating pair of gold and copper bond-pads. The axial (compressive) and transverse (shear) stiffnesses of the bump pair are computed in the local model and incorporated as an equivalent beam in the global model of the entire Flip-Chip-on-Flex (FCOF) assembly, so that the numerous mating interconnect units can be represented in compact simplified form.

This global/local method is quite versatile and will also be used in Step 2 of this investigation, to assess the residual stress in the joint after the adhesive is cured. The features of the local and global models are described below, followed by discussion of the results of the maximum compressive bonding force estimation. The model

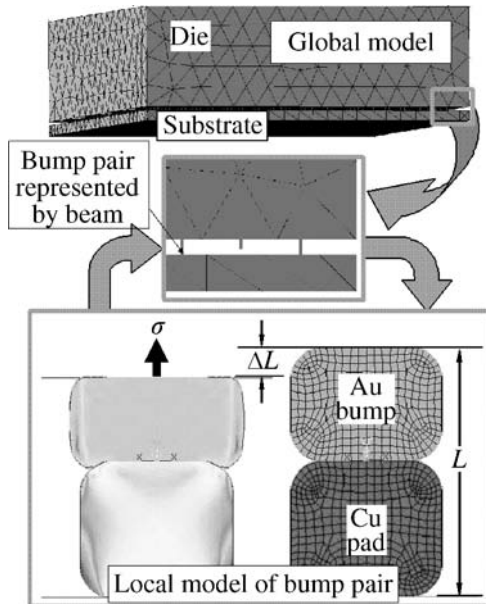


Figure 9. Global/local methodology schematic, where ΔL is the compression distance and σ is the residual stress.

details for the residual stress estimation are somewhat different and are discussed in a subsequent section.

3.1.3. Local Model

The local model is a 2D, plane strain FEA representation of a single mating gold–copper interconnect pair. In the finite element model, the gold and copper bumps are separated by contact elements at the surface, to prevent interpenetration at the interface. Due to the elastic–plastic properties, the gold experiences very large deformations, thus changing the contact area at the interface and creating a nonlinear situation. Eight-noded quadratic finite elements are used in the model. There are 16 098 nodes in the axial (compressive) case and 8057 nodes in the transverse (shear) case.

Boundary Conditions and Loading: The two load cases considered here (axial compression and transverse shear) are shown in Figs 10 and 11, respectively. The shear case is necessary because the mismatch in the Poisson's ratio between the flex and the silicon can lead to significant shearing of the extreme corner interconnect pairs in this die with high aspect ratio.

As discussed above, the first load case consists of 4 μm of compression at the top surface, to account for the manufacturing tolerance of $\pm 2 \mu\text{m}$ in the height of the gold bumps. The second load case consists of transverse 4 μm deflection of the top surface, in order to generate nominal shear loading. In both cases, the bottom surface of the copper is constrained from displacement, and the top of the gold

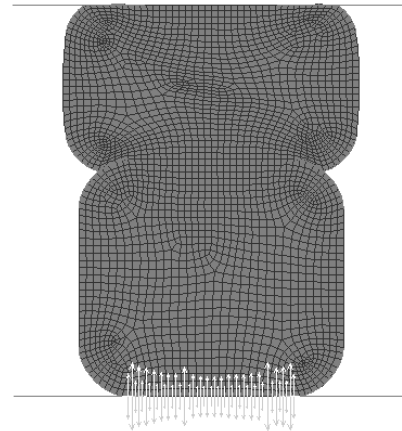


Figure 10. Local model for axial compression.

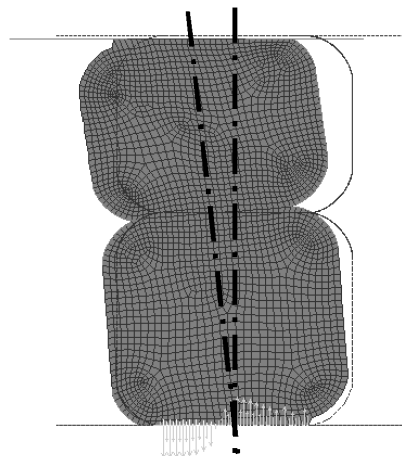


Figure 11. Local model for transverse shear.

surface is constrained to remain horizontal. Contact elements are used at the lower corners of the copper to prevent interpenetration between the Cu bump and the flex underneath.

Results of Local Model: The outputs of the local model are load–displacement curves for axial compression and transverse shear loading. Effective stress–strain curves are derived from these load–displacement curves, by using the average stress distribution through the local model. These effective stress–strain curves are shown in Fig. 12 for axial loading and in Fig. 13 for shear loading. These effective properties will be used later in the global model, as discussed below.

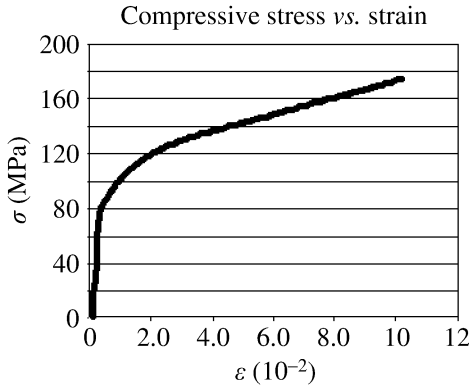


Figure 12. Compressive axial effective stress (σ)–strain (ε) curve of an interconnect, from the local model.

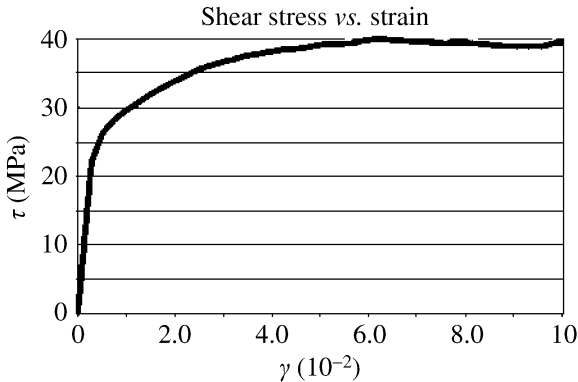


Figure 13. Shear stress (τ)–strain (γ) effective stress–strain curve of an interconnect, from the local model.

3.1.4. Global Model

A finite element representation of the entire FCOF assembly is developed, with the 1000 interconnects under the Si die modeled with the equivalent beams derived from the local models described above. The axial compression case gives the stress-strain curve to assign to the beam, and the shear case gives the G (shear modulus) value. Due to symmetry, only one quarter of the assembly is modeled. One interconnect in the quarter region is modeled to be 4 μm shorter than the remaining interconnects. Thus this model represents a total of four short interconnects in the overall assembly. A schematic representation of the global model can be seen in Fig. 14. The model consists of 25 724 3D, 20-noded quadratic hexahedral (brick) elements, and 1150 3D, 2-noded, shear-deformable (Timoshenko beam) beam elements for the interconnects. There are a total of 51 492 nodes.

Boundary Conditions and Loading: The assembly is compressed by 4 μm in the out-of-plane direction, to assess the compressive force necessary to plastically

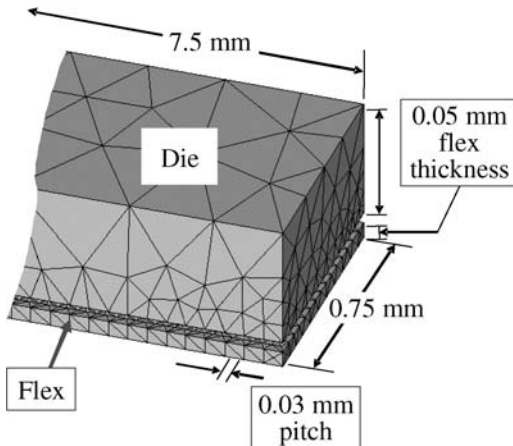


Figure 14. Close-up of the end of the 3D global model. A quarter model was used to take advantage of the near symmetry of the package.

deform the ‘tall’ bumps sufficiently to ensure full connection of the ‘short’ interconnects. During the loading, the bottom face of the flex is constrained in the out-of-plane direction, but in-plane Poisson expansion is allowed. Symmetric boundary conditions are applied on the two planes of symmetry of this quarter model.

Results of Global Model: The results of the global model analysis shows that a force of 122 N is needed in the out-of-plane direction to plastically compress all 996 ‘tall’ interconnects by 4 μm and make contact in the 4 ‘short’ (initially ‘open’) interconnects. This predicted bonding force is in excellent agreement with forces measured during FCOF fabrication. The results of the global finite element model also show that the Poisson mismatch causes less than 0.27 μm horizontal misalignment in the corner interconnect. This misalignment is well within acceptable limits.

Following this initial global analysis, two more parametric studies were conducted, by increasing the number of ‘short’ interconnects from 4 to 40 and finally to 400. The corresponding bonding forces are presented as nonlinear functions of the vertical displacement, in Fig. 15. As a sanity-check, the force required for 4 μm deflection is plotted against the number of ‘open’ bumps, in Fig. 16. The dotted line is an extrapolation of the data to verify that the required compressive bonding force decreases linearly with the number of ‘short’ interconnects and decreases to zero when all the bumps are equally ‘short’.

These data are useful for assessing the bonding force, when the statistical distributions of bump heights are known. These bonding forces are also useful as inputs in Step 2 below, when assessing the residual stresses developed in the interconnects during curing of the NCA epoxy. Section 3.2 discusses the procedure for assessing this residual stress.

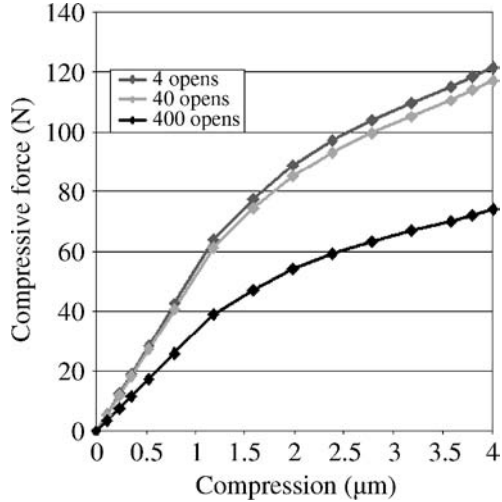


Figure 15. Compressive force/deflection curves for the parametrics of global model showing how much bump compression results from how much compressive force on the system.

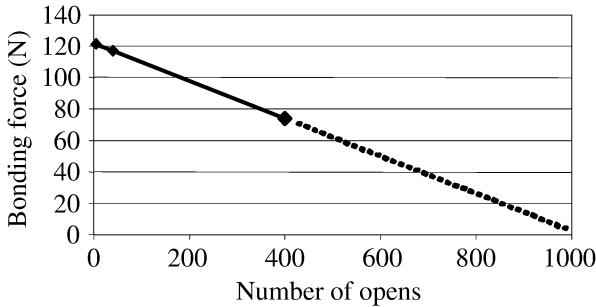


Figure 16. Linear relationship between bonding force and number of opens. The dotted line represents an extrapolation of the trend from the simulation results.

3.2. Residual Stress Determination

In this section, numerical assessments are provided of the compressive residual stress that develops in the interconnect during the bonding process. As shown schematically in Figs 17 and 18, during fabrication, bonding pressure and heat are applied to the chip while the adhesive cures. The adhesive undergoes chemical shrinkage during the curing. After the adhesive is cured, the compressive force is released, and the assembly is cooled to room temperature. The chemical and thermal volume reductions of the cured adhesive create a residual compressive stress on the interconnects. This residual stress is important for achieving acceptable contact resistance.

The focus of this phase of the study is the determination of the residual compressive stress in the interconnect through simulation of the bonding and curing process. As discussed in Section 1.1, this step is an important precursor to any

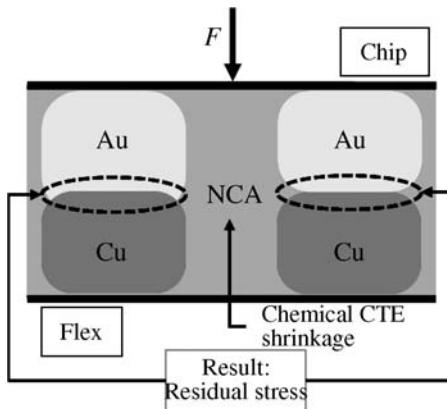


Figure 17. NCA RVE (representative volume element) schematic.

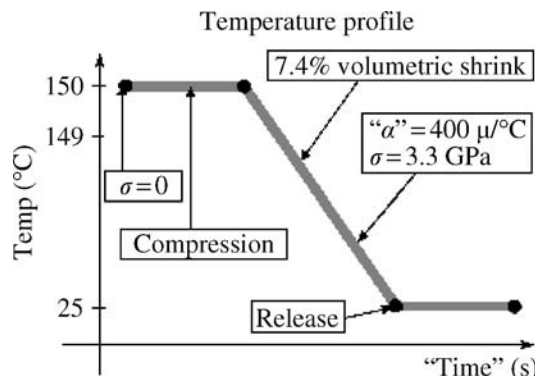


Figure 18. Schematic of the temperature profile used during the fabrication process of the NCA-bonded FCOF system, showing stages of compression, chemical shrinkage and release. A false ‘ α ’ is used in simulation to mathematically induce chemical shrinkage.

durability study because cyclic changes may cause gradual relaxation of this compressive stress with an accompanying increase in the contact resistance. The focus here is on understanding the effects of the nonlinear material properties of gold on the contact surface area evolution during the bonding compression, and on the rate-dependent properties of the epoxy during the cool-down after curing. These simulation results can be used in conjunction with thermal cycling experiments to assess the durability of the FCOF interconnect assembly.

3.2.1. Objective

To obtain insight into the durability of an adhesively-bonded FCOF interconnect pair, the compressive residual stress developed in the matching pair during the fabrication process needs to be estimated. This residual contact force serves as the initial condition for the cyclic degradation experienced during temperature cycling.

3.2.2. Model Strategy

Computational models are developed to simulate the fabrication process. Once again, a two-step global/local finite element model is used. The global model uses a simplified reduced-order schematic representation of the complex architecture, in the interest of computational efficiency. These models were subjected to the temperature profile shown in Fig. 18. The epoxy experiences large amount of volumetric shrinkage during the curing process due to processes such as outgassing. This chemical shrinkage of the epoxy is mimicked in the simulation by suitably tailoring the coefficient of thermal expansion (CTE), α . The chemical shrinkage is 7.4% over a temperature change of 185°C, so the CTE is selected to be 400 ppm/°C. In comparison, the thermal shrinkage of the epoxy is much smaller and is, therefore, neglected. In essence, the CTE used in simulation actually becomes a ‘coefficient of chemical expansion’.

Complexities arise in the simulation due to the nonlinearities and transient phenomena inherent in the bonding process. These include: (a) large amount of plastic deformation in the gold; (b) evolution of the contact surface between the metal bumps during the initial mechanical compression phase of the bonding process; (c) evolution of the mechanical stiffness of the epoxy during the curing and polymerization process and (d) the viscoelasticity of the NCA. The strategies for addressing these nonlinearities are discussed below.

- (A) *Gold plasticity*: The gold is quite soft and undergoes large amounts of plastic deformation, in accordance with Fig. 6. These model properties are used in the simulation model and the resulting large nonlinear deformations are incrementally captured.
- (B) *Contact surface evolution*: ‘Contact elements’ are used in the finite element model, between the bump interconnect pairs. These are needed in the mathematical formulation of finite elements to prevent the bumps from interpenetrating when they come into contact during the loading. The change in contact surfaces, with changes in contact forces, directly requires nonlinear solving methods.
- (C) *Evolution of the epoxy stiffness during polymerization*: A computational process known as ‘element birth and death’ is used in the finite element model to capture the fact that the epoxy gains stiffness and load-bearing capability only after it polymerizes from a viscous melt state to a viscoelastic solid state. ‘Element birth and death’ refers to activation and deactivation of element stiffness during the simulation. ‘Killing’ an element does not delete it, but assigns it a negligible stiffness value ($\sim 1 \times 10^{-6}$ Pa) and also zeroes out the corresponding contribution to the force vector in the finite element equations. When the element is ‘born’ (or reborn), it has no strain history and no initial strain. In this model, the elements representing the epoxy are allowed to be ‘born’ only after sufficient time has been spent at the curing temperature. This is a simplified representation of the gradual increase of the epoxy stiffness. The resulting

'jump' from near-zero to full stiffness in the model representation adds to the fragility of the convergence of the analysis.

- (D) *Viscoelasticity of the NCA:* The addition of viscoelastic properties to the epoxy constitutive model brings an added dependence on time and temperature to the simulation. Nonlinear simulations rely on time stepping to march toward a solution. Consequently, the time steps must be sufficiently small such that the solution data at the end of each substep are within an accepted range of the actual solution.

The process used in the numerical simulation to mimic the bonding process is described below. Some modeling simplifications have been clearly necessary, compared to the actual physical process. The compressive bonding force is first ramped from zero to maximum value, over 10 s. At this point, the force is held constant as the epoxy elements are allowed to be 'born' over one second of simulated time. The resulting 'jump' in structural stiffness causes a small plateau in the force history plots shown later in Figs 20 and 21. For the next twenty seconds, the force is held constant and the temperature is brought from 210°C to 25°C, which induces the chemical shrinkage effects *via* the tailored CTE. Finally, the compressive force is gradually ramped back down to zero over five seconds.

The fabrication process is simulated using a simplified global/local finite element modeling methodology. To reduce the computational burden, a representative volume element (RVE) is defined using a unit cell of one pitch length. This unit cell contains half of one 'tall' and half of one 'short' interconnect pair. The terms 'tall' and 'short' are used to describe bumps that are at the extremes of the manufacturing tolerances of the bump elevation from the chip. A 'tall' bump is taller than a 'short' bump by the maximum manufacturing tolerance (0.7 µm in this study). The two simplified global and local model configurations are described below.

3.2.3. Global Model

This model uses four one-dimensional elastic–plastic linear elements for the metal bumps separated by 984 two-dimensional four-noded plane strain quadrilaterals representing the epoxy that fills the intervening pitch (Fig. 19). There are 3137 nodes. Instead of explicitly modeling the die, it is replaced with rigid boundary conditions at the top end.

The width of the bumps is 80 µm. Only half of each of two adjacent bumps is modeled within the RVE of one pitch length. The height of the gold bump, nominally, is 21 µm. The bump on the right is 'short' in terms of the manufacturing tolerance while the bump on the left is 'tall'. The height of the copper bump is 18 µm, and the flex is 25 µm thick. 'Gap' contact elements are used to prevent interpenetration of the initially 'open' bumps into the flex.

The out-of-plane (Z-direction) thicknesses are scaled to represent the entire three-dimensional FCOF structure. Parametric studies are conducted by varying the number of 'short' and 'tall' bump pairs. This is accomplished by changing the out-of-plane depth of each bump pair (and the flex under the bump), in proportion

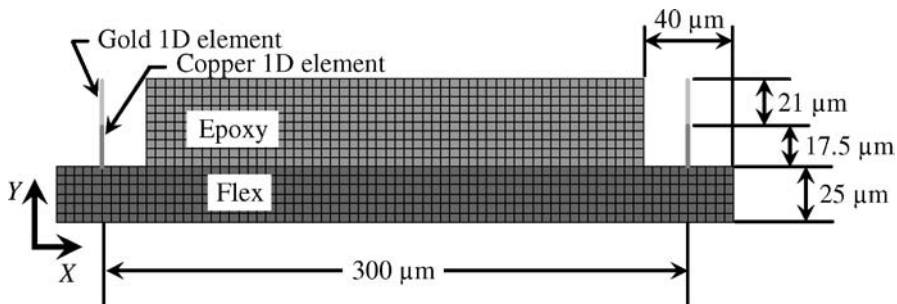


Figure 19. Global model: representative pitch length using ‘total’ out-of-plane depth and cross-sectional areas to describe the residual forces developed in the interconnect pairs.

to the number of bumps represented. The out-of-plane depth of the epoxy (and the flex under the epoxy) are held constant to represent the full footprint of the epoxy. The epoxy is modeled first as an elastic material, and then as a viscoelastic material to assess the effect of stress relaxation on the residual compressive stress that develops in the interconnect.

Boundary Conditions and Loading for Global Model: The bottom surface is constrained in the vertical direction and the sides of the flex are constrained in the horizontal direction. The top surface of the epoxy and the metal bumps are coupled to move together vertically to mimic the constraint from a stiff die. Since the metal bumps in the model are connected to the flex at a single node, constraint equations are used to distribute the compression forces over all the nodes that fall within the physical footprint of the bump. This is accomplished by coupling these nodes on the top surface of the flex to move with the bottom node of the bar element representing the copper bump.

Compressive bonding forces are first applied so that the ‘tall’ bumps deform sufficiently (0.7 μm) for the ‘short’ bumps to touch. Continued compressive loading for another 0.7 μm makes all bumps deform together. Then the epoxy is cured at 210°C to allow polymerization and appropriate volumetric shrinkage. The heat and compression tool is then removed allowing elastic springback and thermal shrinkage.

Results of the Global Model: Figures 20 and 21 show the force history for the case of 28 ‘short’ bumps, without and with the viscoelastic effects included, respectively. The model with the elastic epoxy predicts that both bump types, ‘tall’ and ‘short’, develop over 0.8 N of force per bump at the end of fabrication. When the viscoelastic behavior is included, the ‘short’ bumps develop almost 30% less force after fabrication. Since lower compressive force implies greater contact resistance, the viscoelasticity must be included to obtain a worst-case prediction of the interconnect performance.

The deformed geometry of the global models at the end of the full process can be seen in Figs 22 and 23, for the global model with 55 ‘short’ bumps. The results

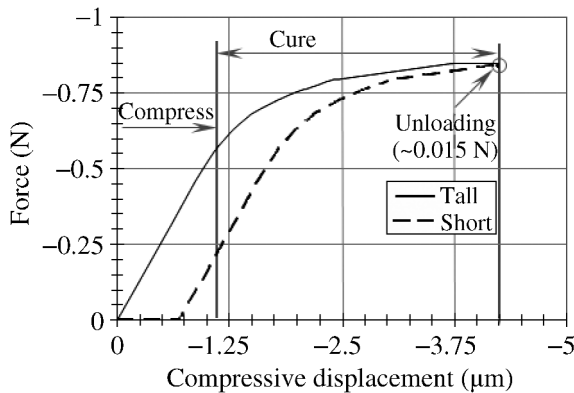


Figure 20. Force history of average force in each bump type during fabrication simulation, without including viscoelastic effects in the epoxy, for the global model with 28 ‘short’ bumps.

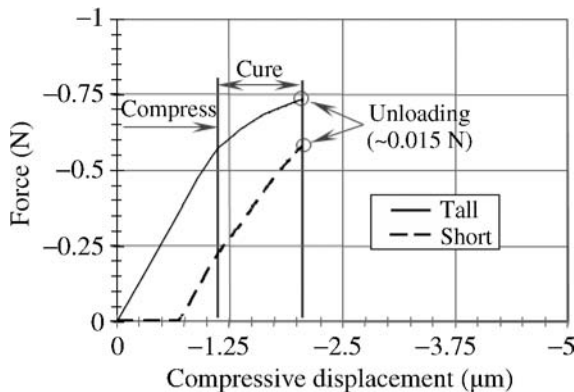


Figure 21. Force history of average force in each bump type during fabrication simulation including viscoelastic effects in the epoxy, for the global model with 28 ‘short’ bumps.

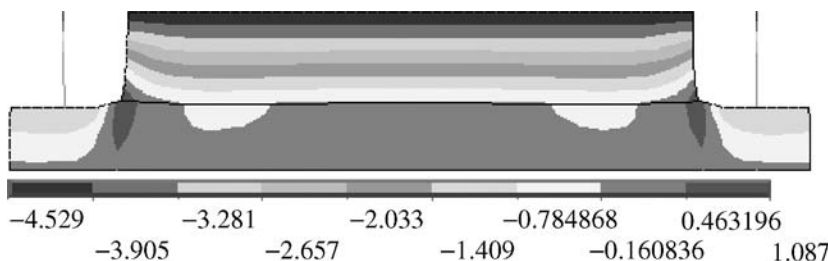


Figure 22. Y -Direction deformation contour plot without including viscoelastic effects in the epoxy, for the global model with 55 ‘short’ bumps (contour values are in μm) corresponding with Fig. 20.

show that including the viscoelastic relaxation reduces the maximum compressive deformation by over 90%.

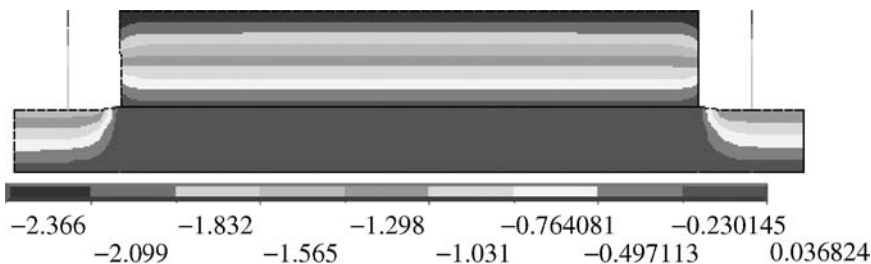


Figure 23. Y-Direction deformation contour plot including viscoelastic effects in the epoxy, for the global model with 55 ‘short’ bumps (contour values are in μm) corresponding with Fig. 21.

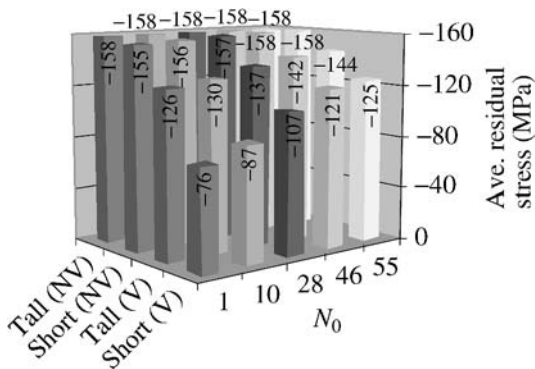


Figure 24. Parametric study of average residual stress after fabrication, as a function of number of short bumps (N_0). ‘NV’ and ‘V’ refer to the cases without and with viscoelastic effects in the epoxy.

Figure 24 shows histograms of the changes in the average residual compressive stress per bump as the number of ‘short’ bumps is varied. Results are presented without and with the epoxy viscoelasticity included. As expected, inclusion of viscoelasticity reduces the average residual compressive contact stress. Also as expected, the ‘short’ bumps have lower residual stresses than the ‘long’ bumps and the compressive residual stresses for each category of bump increase as the number of ‘short’ bumps increases. Force/bump and total force in the whole system are illustrated in Fig. 25 for the viscoelastic case. Figure 25 shows the residual force/bump and the total force caused by NCA shrinkage during curing. The minimum contact force occurs when half the bumps are ‘short’.

Parametric variation of the stiffness of the flex substrate for 28 ‘short’ bumps shows (Fig. 26) that the worst-case average residual contact stresses (in the short bumps) increases by 25% as the flex stiffness is increased by 50%. This logically follows, as a softer flex would produce less resistance to the compression of the metals and therefore contribute to a lesser magnitude of stress development at the bump interface.

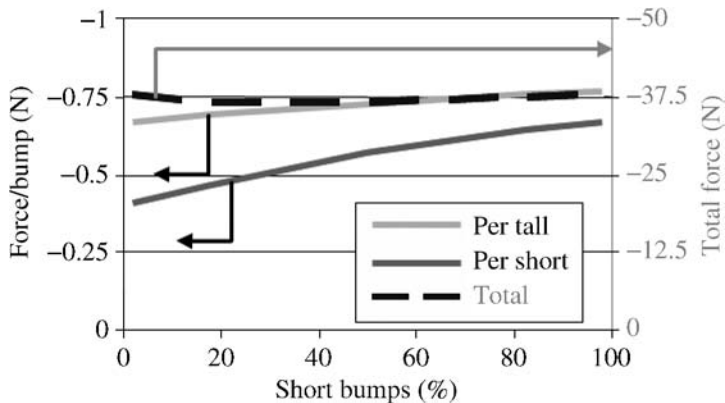


Figure 25. Final force/bump and total force in all bumps (with viscoelastic effects).

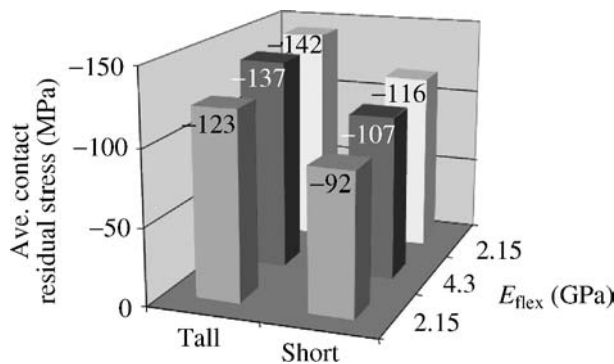


Figure 26. Residual stresses as a function of flex-stiffness, for the case of 28 ‘short’ bumps.

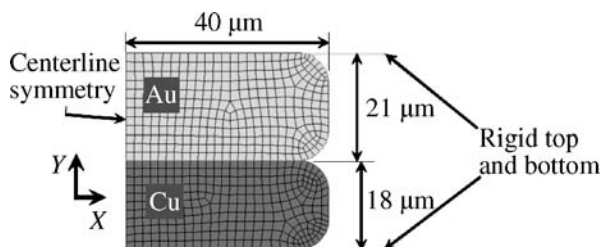


Figure 27. Local model: one interconnect pair consisting of the gold bump of the flip-chip and copper trace of the flexible substrate.

3.2.4. Local Model

One interconnect bump pair is modeled using 2D 4-noded quadrilateral elements, with the bumps separated by contact elements to prevent interpenetration. The stress distribution at the interface is thus assessed (Fig. 27). The out-of-plane thickness was parametrically varied from that of one bump to that of 55 bumps, for both the ‘tall’ and ‘short’ cases. There are 668 elements and 1934 nodes.

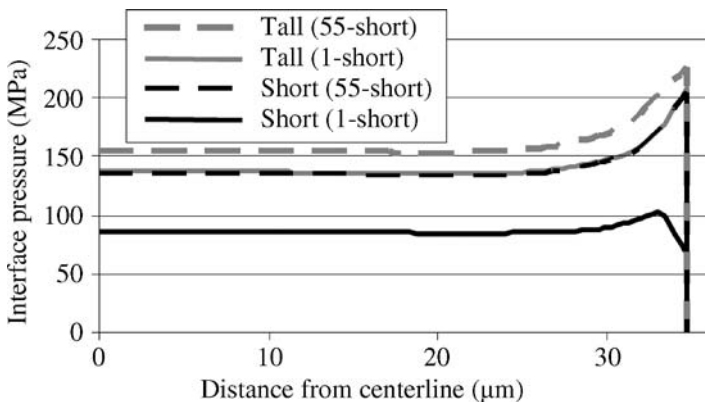


Figure 28. Pressure distribution across bump interface in ‘short’ and ‘tall’ bumps for the upper bound (55 ‘short’ bumps) and the lower bound (1 ‘short’ bump) configurations.

Boundary Conditions and Loading: The right edge of the model is constrained for symmetry, the bottom of the model is constrained against vertical movement, and the top edge is coupled to move together. The deformation history of the bumps, obtained from the global model, is applied as boundary conditions to the local model.

Results of the Local Model: The goal is to see the distribution of the interface stress.

The local model data, seen in Fig. 28 shows that a fairly uniform distribution of stress develops across the surface of the individual bump interfaces. Once again, it’s easy to see that the ‘short’ bumps develop a lesser residual compressive contact force and that the contact force increases as the number of ‘short’ bumps increases.

4. Summary and Conclusions

Finite element models have been developed to simulate the effect of selected fabrication parameters on the reliability of adhesively-bonded FCOFs. First, the effect of bump coplanarity on required bonding pressure is parametrically assessed. The worst-case bonding force (when a small minority of the bumps are ‘short’ compared to the rest) is found to be in excess of 120 N. Parametric studies are conducted to assess how the bonding force decreases with decreasing number of ‘short’ interconnects. In the second section, the residual stresses during bonding and curing are numerically estimated, as this contact pre-stress can be important to reliability under thermal cycling. Neglecting the viscoelastic effects in the epoxy results in inaccurate results for compressive stress estimation in the FCOF interconnects. Once the viscoelastic effects are included, however, trends emerge in how much the stress development is dependent on the coplanarity manufacturing variabilities of the bumps on the flip-chip. Additionally, the effect of the stiffness of the flexible substrate is also assessed.

The global/local methodology developed here works well for studying contact stress at the interconnect bump interface. The two-step (global/local) modeling strategy increases computational manageability. However, it is difficult to experimentally verify these values as direct instrumentation at this small scale would most likely result in altering the state of stress.

The viscoelastic model data show that the residual stress in the bump interface at the end of fabrication depends on the percent of ‘short’ bumps that exist in the system prior to fabrication, resulting in smaller residual stress for all ‘short’ bumps than all ‘tall’ bumps. This is confusing as it would seem that once they are *all* categorized as ‘short’, this would be the same as all ‘tall’ bumps. However, since the compressive force is chosen with the nominal geometry in mind, the compressive force used at 100% tall would be different than the compressive force used at 100% short for the same package.

The immense plastic deformation far into the plastic regime in the gold shows that the residual contact stress in the metal bumps is very sensitive to the stress-strain behavior and to the ultimate strength of the gold. Therefore, the accuracy of the model depends heavily on the accuracy of the gold properties.

Acknowledgement

This work was funded by the members of the EPSC consortium of the Center for Advanced Life Cycle Engineering, at the University of Maryland.

References

1. J. Haase, D. Farley, P. Iyer, P. Baumgartner, A. Dasgupta and J. F. J. Caers, *J. Adhesion Sci. Technol.* **22**, 1733 (2008).
2. J. F. J. Caers, X. J. Zhao, E. H. Wong, C. K. Ong, Z. X. Wu and R. Ranjan, in: *Proceedings of the 53rd IEEE Electronic Components and Technology Conference*, New Orleans, LA, p. 1176 (2003).
3. F. Ferrando, J. F. Zeberli, P. Clot and J. M. Chenuz, in: *Proceedings of the 4th International Conference on Adhesive Joining and Coating Technology in Electronics Manufacturing*, Espoo, Finland, p. 205 (2000).
4. L. Li and F. Treliant, in: *Proceedings of the 4th International Conference on Adhesive Joining and Coating Technology in Electronics Manufacturing*, Espoo, Finland, p. 129 (2000).
5. J. F. J. Caers, X. J. Zhao, H. G. Sy, E. H. Wong and S. G. Mhaisalkar, in: *Proceedings of the 54th IEEE Electronic Components and Technology Conference*, Las Vegas, NV, p. 106 (2004).
6. C. Jang, S. Han, K. Yeongkook, H. Kim, Y. Samson, S. Cho and C. Han, in: *Proceedings of the 6th International Conference on Thermal, Mechanical and Multi-Physics Simulation and Experiments in Micro-Electronics and Micro-Systems*, Berlin, Germany, p. 566 (2005).
7. K. N. Chiang, C. W. Chang and J. D. Lin, in: *Proceedings of the 3rd Electronics Packaging Technology Conference*, Singapore, p. 110 (2000).
8. T. W. Ellis, *Gold Bulletin* **37**, 66 (2004).
9. R. Aschenbrenner, R. Miessner and H. Reichl, in: *Proceedings of the The 1st IEEE International Symposium on Polymeric Electronics Packaging*, Norrkoping, Sweden, p. 86 (1997).

10. Y. C. Chan, K. C. Hung, C. W. Tang and C. M. L. Wu, in: *Proceedings of the 4th International Conference on Adhesive Joining and Coating Technology in Electronics Manufacturing*, Espoo, Finland, p. 141 (2000).
11. L. Frisk and E. Ristolainen, *Microelectronics Reliability* **45**, 583 (2005).
12. J. Pajonk, in: *Proceedings of the 29th International Electronics Manufacturing Technology Symposium*, San Jose, CA, p. 165 (2004).
13. L. Teh, C. Wong, S. Mhaisalkar, K. Ong, P. Teo and E. Wong, *Electronic Mater.* **33**, 271 (2004).
14. M. Teo, S. G. Mhaisalkar, E. H. Wong, T. Poi-Siong, C. C. Wong, O. Kristine, G. Chin Foo and T. Lay Kuan, *IEEE Trans. Packaging Technologies* **28**, 157 (2005).
15. M.-J. Yim, J.-S. Hwang, W. Kwon, K. W. Jang and K.-W. Paik, *IEEE Trans. Electronics Packaging Manuf.* **26**, 150 (2003).
16. C. Yin, H. Lu, C. Bailey and Y.-C. Chan, *IEEE Trans. Electronics Packaging Manuf.* **27**, 254 (2004).
17. L. L. Mercado, J. White, V. Sarihan and T. Y. T. Lee, *IEEE Trans. Packaging Technologies* **26**, 509 (2003).
18. H. Christiansen, M. Gulliksen, H. Haugerud and R. Friberg, in: *Proceedings of the 3rd International Conference on Adhesive Joining and Coating Technology in Electronics Manufacturing*, Binghamton, NY, p. 345 (1998).
19. Y. C. Chan and D. Y. Luk, *Microelectronics Reliability* **42**, 1195 (2002).
20. Y. Fu, Y. Wang, X. Wang, J. Liu and Z. Lai, *IEEE Trans. Advanced Packaging* **23**, 15 (2000).
21. A. Yeo, M. Teo and C. Lee, in: *Proceedings of the 6th Electronics Packaging Technology Conference*, Singapore, p. 92 (2004).
22. C. M. L. Wu, J. Liu and N. H. Yeung, in: *Proceedings of the 4th International Conference on Adhesive Joining and Coating Technology in Electronics Manufacturing*, Espoo, Finland, p. 101 (2000).
23. M. Hojjati, A. Johnston, S. V. Hoa and J. Denault, *Appl. Polym. Sci.* **91**, 2548 (2004).
24. S. L. Simon, G. B. Mckenna and O. Sindt, *J. Appl. Polym. Sci.* **76**, 495 (2000).
25. A. Cusano, V. Buonocore, G. Breglio, A. Calabr, M. Giordano, A. Cutolo and L. Nicolais, *Appl. Optics* **39**, 1130 (2000).
26. C. Bockenheimer, D. Fata and W. Possart, *J. Appl. Polym. Sci.* **91**, 361 (2004).
27. S. Hannula, J. Wanagel and L. Che-Yu, *IEEE Trans. Components, Hybrids, and Manufacturing Technology* **6**, 494 (1983).
28. S. Liu, Y. H. Mei, S. G. Zhou and J. S. Zhu, in: *Proceedings of the 27th International Symposium on Microelectronics*, Boston, MA, p. 576 (1994).

Fatigue Behavior of Electrically Conductive Adhesives

Bin Su and Jianmin Qu*

The George W. Woodruff School of Mechanical Engineering, Georgia Institute of Technology,
801 Ferst Drive NW, Atlanta, GA 30332-0405, USA

Abstract

The fatigue behavior of an isotropic conductive adhesive made of epoxy matrix with silver flakes is studied by performing fatigue tests. Repetitive tensile and compressive strains are applied to the conductive adhesive while the electrical resistivity is constantly monitored *in situ*. It is found that resistivity of the conductive adhesive increases as more fatigue cycles are applied. The electrical resistivity may increase by more than 100% before any visible fracture of the sample can be observed. Based on 100% increase of the resistivity as the electrical failure criterion, the strain amplitude *versus* number of cycles to electrical failure data can be fitted to a power law model. Experimental results also show that strain amplitude, strain ratio and strain rate all have an effect on the electrical fatigue life of conductive adhesives. Microscopic images of the failed conductive adhesive samples show that electrical failure is caused by the debonding of silver flakes from epoxy matrix. Further examination shows that the debonding typically occurs along the direction of the maximum shear stress.

Keywords

Conductive adhesive, fatigue, electrical failure

1. Introduction

In electronic packaging technologies such as surface mounting, the interconnection joints connect the component and the substrate as well as serve as both mechanical and electrical connections. The joints are required to accommodate relative displacements between the component and the board induced by temperature changes. Another source of thermal displacement is temperature gradients, which also lead to relative displacements between components and substrates.

Very often the interconnection joints do not fail at temperature extremes, but fail under cyclic temperature changes or thermal fatigue. The fatigue behavior of PbSn solder has been investigated extensively, while the study of fatigue failure of electrically conductive adhesives (ECAs) is somewhat inadequate. Conductive adhesives have a different fatigue behavior from a metal solder. Not only the polymer matrix

* To whom correspondence should be addressed. Tel.: +1-404-894-5687; Fax: +1-404-894-0186; e-mail: jq@gatech.edu

has different properties compared with a metal, but also the failure of conductive adhesives can be of two types: electrical and mechanical, and either can precede the other. This is different from solder, where electrical failure is always accompanied by mechanical failure. In conductive adhesives the joints can still maintain mechanical strength after the electrical conductivity has deteriorated to an unusable value [1]. Keusseyan and Dilday [2] suggested that since the function of conductive adhesives includes both mechanical bonding and electrical connection, mechanical strength measurements alone do not characterize the interconnection properties of conductive adhesives for surface mount applications.

It is found that both the stress ratio and load frequency have an effect on the fatigue life of conductive adhesives. Gomatam and Sancaktar [3] tested adhesive joints made of smooth stainless steel 304 adherends bonded with electrically conductive adhesives. They found that the stress ratio had a strong effect on fatigue life. The fatigue life of the joint decreases considerably as the frequency of the cyclic loading is decreased.

The fatigue life is also affected by the joint geometry [3]. Mo *et al.* [4] found that the standoff height significantly influences the maximum von Mises stress at the knee of the conductive adhesive joint during thermal cycling.

When debonding occurs, it could be at the interface or in the adhesive. Constable *et al.* [1] found in their experiments that debonded specimens had fatigue failures that all occurred at the interface between the adhesives and surface finishes. Kitazaki and Hata [5] and Sancaktar and Zhang [6] showed that interfacial failure becomes the more likely mode of failure in adhesive joints when the loading rate is increased. Gomatam and Sancaktar [7] found that interfacial failure corresponds to high cyclic load and low load ratio, while the cohesive failure corresponds to high load ratio and low cyclic load.

Researchers have proposed life prediction models for conductive adhesives, but most of these models have been developed with respect to mechanical failure. Gomatam and Sancaktar [8] obtained fatigue life *versus* load amplitude curves (the S-N curves) based on experiments. By proper normalization, they showed that these curves could be used for different environmental conditions and stress states.

In this study, we have investigated the electrical fatigue behavior of conductive adhesives through mechanical fatigue tests. The conductive adhesive samples were stencil-printed on the surface of a printed wiring board (PWB). The four-point push/pull beam bending test was conducted, so that the compressive/tensile stress could be exerted on the conductive adhesive samples. By bending the beam repetitively, a cyclic uniaxial stress was applied on the conductive adhesive samples. The resistance of the conductive adhesive sample was monitored during the fatigue tests. An electrical fatigue failure criterion is proposed in term of the resistivity increase. Using the fatigue test data, a power law type fatigue model is used to relate the number of cycles to failure to the compressive/tensile strain amplitude. The effect of strain ratio on the fatigue life of conductive adhesives is studied by varying the magnitude of the compressive or tensile strain. Tests were also performed to show

the effect of strain rate on the fatigue life of conductive adhesives. The microstructure of the conductive adhesive samples was examined before and after fatigue tests to ascertain the failure mechanism.

2. Experimental Procedure

2.1. Materials

The conductive adhesive used in this study was made of a thermoset epoxy resin and silver flake fillers. The resin consisted of epoxy, hardener and catalyst, which were bisphenol-F (DGEBF) Epon 862 from Hexion Specialty Chemicals, Inc., Columbus, OH, USA, methylhexa-hydrophthalic anhydride (MHHPA) from Lindau Chemicals, Inc., Columbia, SC, USA, and 1-cyanoethyl-2-ethyl-4-methylimidazole, from Shikoku Chemicals Corp., Kagawa, Japan, respectively. The weight ratio of epoxy:hardener:catalyst was 1:0.84:0.0184. The silver flakes were SF 26LV, from Ferro Corporation, Cleveland, OH, USA, with an average length of flakes being 10 μm . The weight ratio of silver and epoxy resin in the conductive adhesive was 4:1, corresponding to an approximate volume fraction of silver of 30%. After mixing, the epoxy resin and silver flakes were mildly blended with an applicator stick for 5 min until a thorough mixture was obtained.

2.2. Fatigue Tests on Conductive Adhesives

A four-point beam bending experiment was designed to load the conductive adhesive with cycling tensile and compressive stresses. The load frame was model SSTM-500, made by the United Calibration Company, Huntington Beach, CA, USA. An illustration of the experiment is shown in Fig. 1. The conductive adhesive samples were applied on the top surface of the beam, as shown in Fig. 2. Since the thickness of the conductive adhesive was very thin compared to the thickness of the beam, it was assumed that the conductive adhesive samples would have the same strain as the top layer of the beam. In our test, four conductive adhesive samples were applied between the two inner fixtures on the top surface of the beam. As the bending moment between the two inner fixtures is constant, these four conduc-

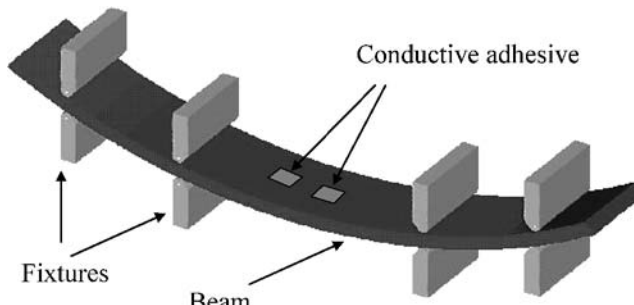


Figure 1. Schematic illustration of the four-point beam bending test.

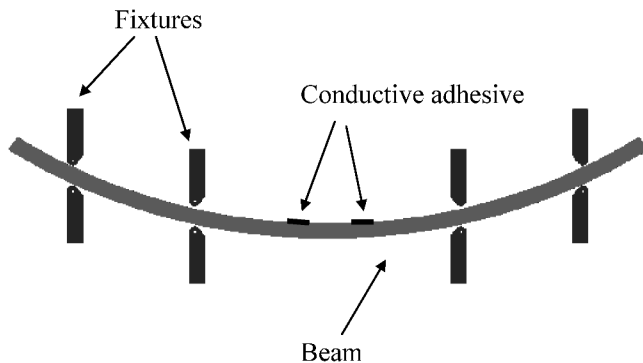


Figure 2. Side view of the four-point bending test.

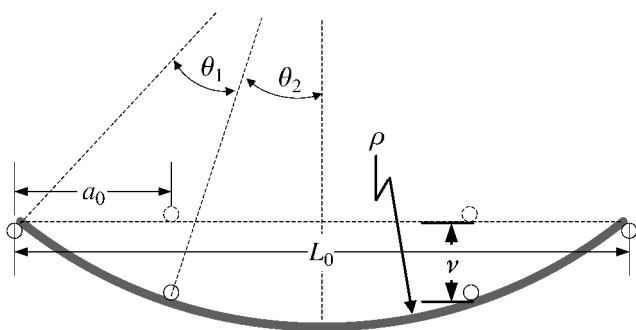


Figure 3. Geometry of the bent beam.

tive samples were subjected to the same magnitude of compressive/tensile strain during the test.

Four special fixtures were used to conduct the four-point push/pull beam bending test. These fixtures constrain the movement of the beam in both upward and downward directions. The outer two fixtures are fixed, and only the two inner fixtures were movable. When the inner two fixtures move down, they exert a compressive stress on the upper surface of the beam, and when they move up a tensile stress is exerted on the upper surface of the beam. Thus by controlling the movement of the crosshead a continuously varying cycling stress is applied to the conductive adhesive samples. Furthermore, by varying the maximum upward and downward displacement of the crosshead, an asymmetrical loading with different maximum tensile and compressive stresses can be applied.

The strain of the top surface layer of the beam and the conductive adhesive samples can be calculated based on the geometry of the bent beam, which is shown in Fig. 3. In the plot, ρ is the radius of the neutral plane of the bent beam, v is the crosshead displacement, a_0 is the length of the beam between the outer fixture and inner fixture before bending, L_0 is the length of the beam between the two outer

fixtures before bending, and θ_1 and θ_2 are the two angles corresponding to the two sections of the bent beam.

The crosshead displacement v can be read from the tester, and a_0 and L_0 can be measured before the beam is bent, which are 103.1 mm and 26.3 mm, respectively. Assuming the radius is constant along the beam after it has been bent, then the radius ρ of the neutral plane of the bent beam and the two angles θ_1 and θ_2 are determined from the following equations:

$$\rho \cos \theta_2 = v + \rho \cos(\theta_1 + \theta_2), \quad (1)$$

$$\sin \frac{\theta_1 + \theta_2}{2} = \frac{\sqrt{(\frac{L_0}{2})^2 + [\rho(1 - \cos(\theta_1 + \theta_2))]^2}}{2\rho}, \quad (2)$$

$$\sin \frac{\theta_1}{2} = \frac{\sqrt{a_0^2 + v^2}}{2\rho}. \quad (3)$$

The strain ε of the top layer of the beam and the conductive adhesive samples can be calculated by

$$\varepsilon = \frac{t}{2\rho}, \quad (4)$$

where t is the thickness of the beam.

In our fatigue tests the beams were cut from copper-clad FR4 boards (printed circuit boards), which were obtained from LPKF Laser & Electronics North America, Wilsonville, OR, USA. The printed circuit board was used to facilitate the resistance measurement of the conductive adhesive samples, which will be discussed later. The beam has a length of 131 mm, width 19 mm and thickness 2.375 mm.

For a given value of the maximum displacement of the crosshead, the radius of the neutral plane of the beam and the maximum compressive/tensile strain of the conductive adhesive samples are calculated. Their values are listed in Table 1.

Table 1.

Maximum crosshead displacement and corresponding compressive/tensile strain of the conductive adhesive samples

	Maximum crosshead displacement v (mm)				
	5.0	6.0	8.0	10.0	12.0
Radius of neutral plane of the bent beam ρ (mm)	205.4	172.6	132.2	108.6	93.3
Maximum compressive/tensile strain ε of conductive adhesive samples	5.8×10^{-3}	6.9×10^{-3}	9.0×10^{-3}	10.9×10^{-3}	12.7×10^{-3}

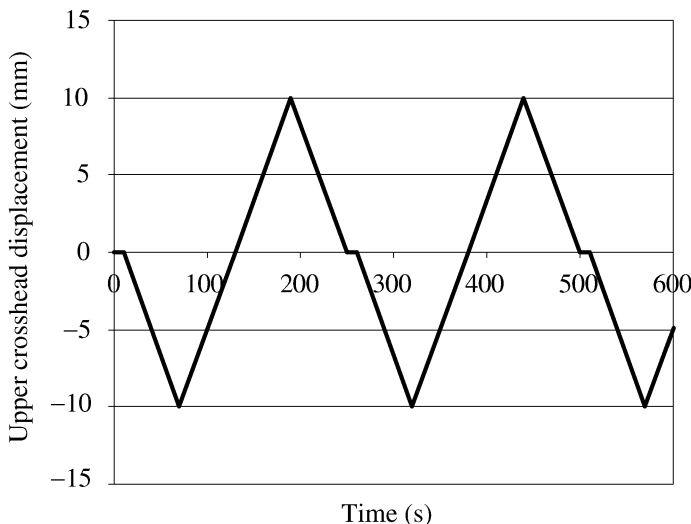


Figure 4. Upper crosshead displacement curve (crosshead speed: 10 mm/min, maximum crosshead displacement: 10 mm).

The fatigue test was strain-controlled for the conductive adhesive samples. The fatigue test was conducted in the following manner. At the beginning of each cycle the crosshead was held still for 10 s. During this 10-s period, the resistance value of the conductive adhesive sample remains constant. This allows to record the resistance at the end of each cycle. Then the crosshead moved down and applied a compressive strain on the conductive adhesive. After reaching the maximum downward displacement, the crosshead moved up and loaded the upper surface of the beam with tensile stress. When the maximum upward displacement was reached, the crosshead returned down to the zero displacement location. The displacement *vs.* time plot of the upper crosshead of the load frame is shown in Fig. 4. The short horizontal plateaus in Fig. 4 correspond to the 10-s hold period at the beginning of each cycle.

The strain rate applied to the conductive adhesive samples can be varied by adjusting the speed of the crosshead movement. The relationship between the displacement of the crosshead and the compressive/tensile strain of the upper surface of the beam is not strictly linear, but very close to a linear one, as shown in Fig. 5. So a constant speed of the crosshead will result in an approximately constant strain rate for the conductive adhesive samples in the fatigue test. The speeds of the crosshead and corresponding strain rates are shown in Table 2.

2.3. Resistance Measurement of Conductive Adhesive Samples

The two primary functions of the conductive adhesive are mechanical adhesion and electrical conduction. In fatigue tests, the fatigue failure should be defined based not only on the mechanical strength of the conductive adhesive but also on the electrical conduction, whichever happens first. Hence the resistance of the conductive adhe-

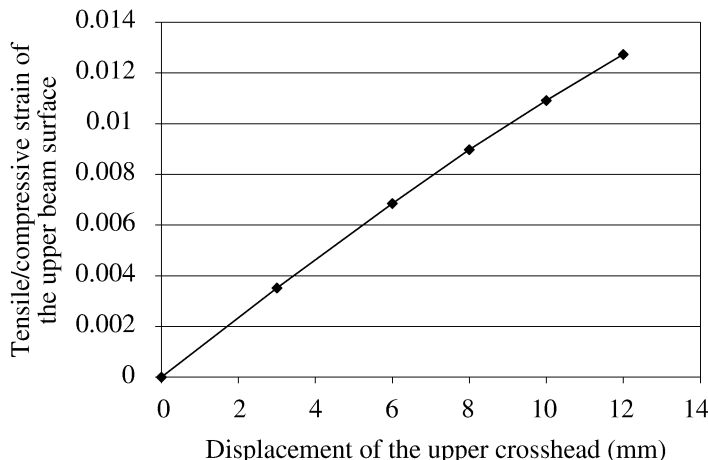


Figure 5. Compressive/tensile strain of the upper beam surface vs. displacement of the upper crosshead.

Table 2.

Crosshead speeds and corresponding strain rates

Speed of the crosshead (mm/min)	6	8	10	15
Strain rate of the upper beam surface ($\times 10^{-4} \text{ s}^{-1}$)	1.1	1.5	1.8	2.7

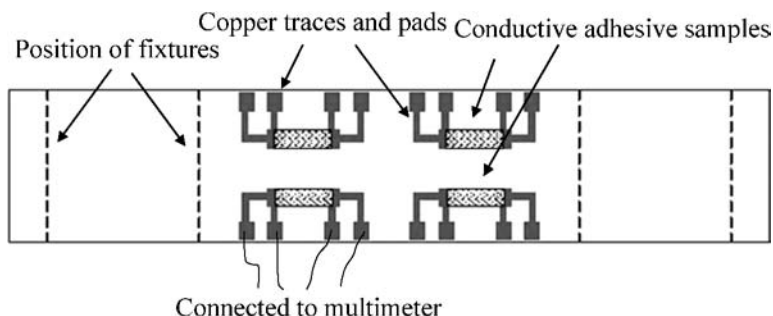


Figure 6. The layout of the upper surface of the PCB beam.

sive samples was measured and monitored during the entire process of the fatigue test.

A custom-made printed circuit board was used as the beam to facilitate the resistance measurement of the conductive adhesive samples. The layout of the upper surface of the beam is shown in Fig. 6.

The copper traces are in a pattern such that the resistance of the conductive adhesive sample can be measured by the four-point measurement method. A scanner

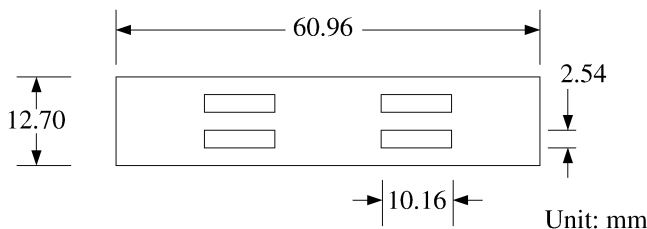


Figure 7. Stencil for application of conductive adhesives.

card was used to measure the resistances of all four samples at the same time. The 16 leads (4 leads \times 4 samples) are connected to the scanner card, which is connected to the digital multimeter. Every time a “measure” instruction is sent to the digital multimeter, the scanner card switches the inner relays and the resistances of the conductive adhesive samples are measured one by one. The scanner card is a 10-channel Model 2000-SCAN Scanner Card from Keithley, Cleveland, OH, USA. The digital multimeter is Keithley Model 2001, with a resolution of $1 \mu\Omega$. The time interval between each scan was 2 s, and after each scan all four resistance values were recorded into the computer. The resistance measurement and the fatigue tests started at the same time, so that the entire resistance change during the fatigue test was captured.

The conductive adhesive was applied to the upper surface of the PCB beam by a custom-made stainless steel stencil, as shown in Fig. 7. The PWB was cleaned thoroughly by acetone and sandpaper and dried before the application of conductive adhesive. The thickness of the stencil is 0.178 mm. The paste-form conductive adhesive was applied through the slots of the stencil using a stainless steel squeegee, then the PWBs were placed into a convection oven at 150°C for 3 h to ensure full cure of the conductive adhesive samples. After the conductive adhesive samples were cooled down in dry room temperature for about 2 h the fatigue tests were performed. The average size of the conductive adhesive samples was 2.5 mm wide, 7.6 mm long (the distance between the copper pads on the PCB beam) and 0.170 mm thick.

A scanning electron microscope was used to examine the microstructure of the conductive adhesive samples before and after fatigue tests.

3. Results and Discussion

The fatigue tests on conductive adhesive samples were done using the four-point push/pull beam bending test. The resistance values of all conductive adhesive samples were simultaneously recorded. It is found that the resistance value of the conductive adhesives increases when more cycles are applied, but no visible mechanical damage is observed. Clearly the electrical conduction failure happens before any mechanical failure.

A failure criterion is proposed to define the electrical failure of the conductive adhesive in terms of electrical conduction. The fatigue life of the conductive adhesive is found to be related to the strain range applied, and the relation can be fitted by a power law equation. The fatigue life is also dependent on the strain ratio and strain rate.

Through microscopic examination of the cross-sections of the conductive adhesive samples before and after fatigue tests, it is found that the interface between the epoxy matrix and silver flakes is damaged by fatigue tests. Consequently, electrical conductivity of the conductive adhesive is affected.

3.1. Resistance Change of Conductive Adhesive Samples in Fatigue Tests

The resistance of the conductive adhesive samples was closely monitored during the fatigue test. It is found that the resistance of conductive adhesive sample is significantly influenced by both the compressive and tensile strains. The resistance of a conductive adhesive sample measured during a fatigue test is shown in Fig. 8.

In Fig. 8, the resistance of the conductive adhesive sample is plotted as a function of time. The spikes in the resistance values correspond to time periods in which the conductive adhesive sample is subjected to tensile strains. The rising part of the spike is due to the upward movement of the load frame crosshead, which applies an increasing tensile strain to the conductive adhesive sample. When the tensile strain reaches the maximum value, the resistance value also reaches the largest value, i.e., the top point of the spike. When the tensile strain decreases, the resistance value decreases correspondingly. It can be seen that as the fatigue test continues, the highest resistance values, i.e., the heights of the spikes, also increase.

The data between the two circles in Fig. 9 correspond to the resistance values of the conductive adhesive in one fatigue cycle. The portion of the curve between the

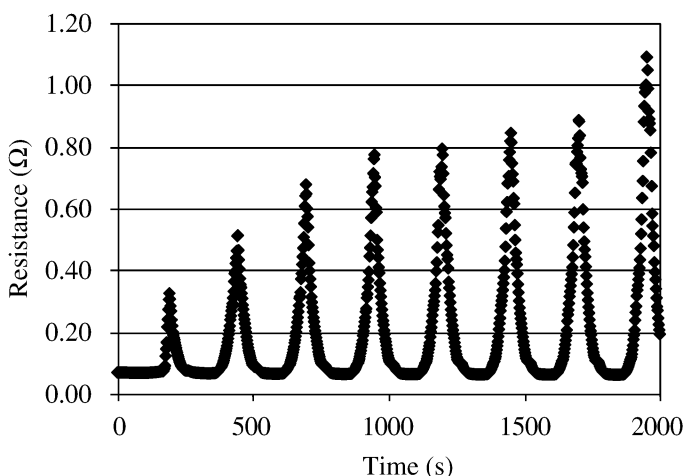


Figure 8. Representative resistance change of a conductive adhesive sample during fatigue test (strain ratio = -1).

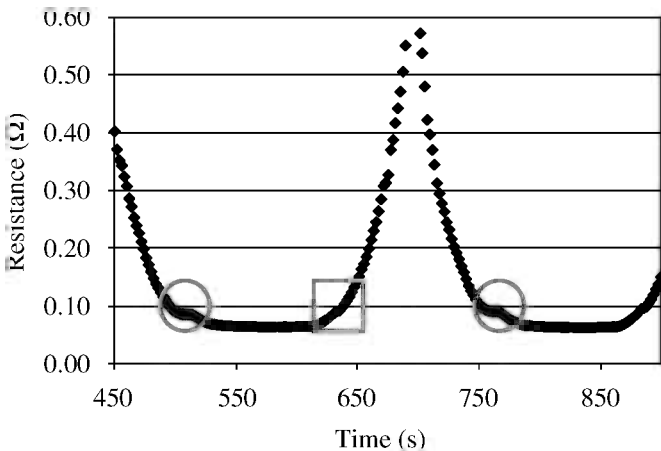


Figure 9. Resistance change of a conductive adhesive sample in one cycle of the fatigue test (strain ratio = -1).

square and the right circle corresponds to the period when tensile strain is exerted on the conductive adhesive sample, i.e., the spike in Fig. 8. The portion of the curve between the left circle and the square corresponds to the period of the fatigue test when compressive strain is applied to the conductive adhesive sample.

The effects of compressive strain and tensile strain on the resistance can be seen from Figs 8 and 9. Clearly the magnitude of the resistance decreases because the compressive strain is much smaller than the resistance increase caused by the tensile strain. The magnitudes of the compressive and tensile strains are the same, yet the magnitudes of the resistance change are very different. This phenomenon can be explained as follows. The conduction of the conductive adhesive is achieved through the interconnections of the silver flakes, and the resistance of the conductive adhesive is the total resistance of the resistor network formed by all the contact resistances between flakes. The contact resistance depends on the contact pressure, and when the contact pressure is increased the contact resistance becomes smaller because of the enlargement of the contact area and the decrease of the tunnel resistivity. The tunnel resistivity — contact pressure relationship is not linear, as shown in [9]. The tunnel resistivity decreases faster at first, then slows down and approaches a steady value as contact pressure increases. Therefore, for the same magnitudes of tensile and compressive stresses the tensile stress causes a much larger resistance increase of the conductive adhesives than the compressive stress in the fatigue test.

The average of the resistance values measured during the first 10-s hold time of each fatigue cycle is taken as the resistance value of the conductive adhesive before that cycle. This resistance value increases as the number of fatigue cycles is increased, which can be seen in figure by comparing the two resistance values in the two circles. As more and more fatigue cycles are applied to the conductive adhesive sample, its resistance value grows higher and higher. A typical resistivity change of

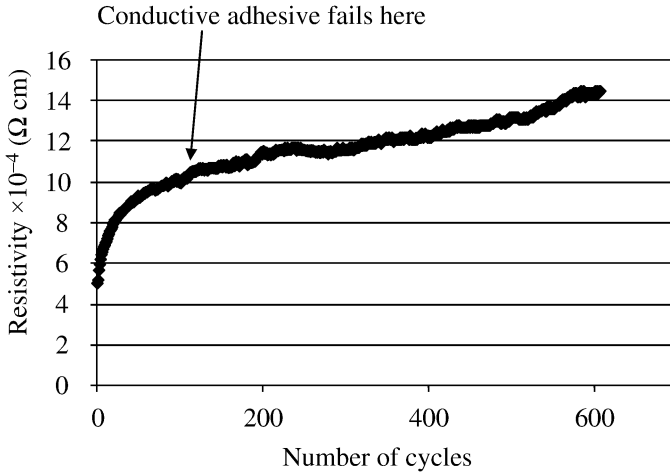


Figure 10. Resistivity of a conductive adhesive sample in fatigue test.

a conductive adhesive sample is shown in Fig. 10, in which the resistivity is plotted *versus* the number of fatigue cycles. The resistivity ρ is calculated by equation (5) based on the measured resistance value R , length L and cross-sectional area A of the conductive adhesive sample:

$$\rho = \frac{RA}{L}. \quad (5)$$

The resistivity of the conductive adhesive sample keeps on increasing as more and more fatigue cycles are applied, hence an electrical failure criterion needs to be defined in terms of electrical conduction for conductive adhesives to be usable as an interconnection material in electronic packaging. The average resistivity of the conductive adhesive samples before fatigue tests is found to be around $5 \times 10^{-4} \Omega \text{ cm}$. It is proposed that the bulk resistivity should be less than $1 \times 10^{-3} \Omega \text{ cm}$ [10]. Therefore, the electrical conduction failure criterion for the conductive adhesive samples in this study is defined as a 100% increase of the resistivity value. The failure point of the conductive adhesive sample is shown in Fig. 10.

No breakage or delamination of the conductive adhesive from the PWB beam is observed even after the resistivity has increased by 100%, which means that the electrical conduction failure happens well before the mechanical failure. Microscopy examination confirms this observation.

3.2. Fatigue Life Models of Conductive Adhesives

A number of fatigue tests were conducted on conductive adhesive samples with different strain magnitudes being applied. The resistances of the conductive adhesive samples are monitored throughout the fatigue test, and the number of cycles to failure (100% increase of resistivity) is recorded. The strain amplitude and the corresponding fatigue lives of four conductive adhesive samples are listed in Table 3.

Table 3.

Strain amplitudes and corresponding fatigue lives of conductive adhesive samples

	Strain amplitude			
	0.7×10^{-2}	0.9×10^{-2}	1.1×10^{-2}	1.3×10^{-2}
Fatigue lives of four conductive adhesive samples (cycles to failure)	2125	576	191	48
	2312	662	228	40
	1983	681	208	37
	2123	671	231	35
Average fatigue life	2136	648	215	40

The strain rate of these tests is $1.8 \times 10^{-4} \text{ s}^{-1}$, and the maximum compressive and tensile strains are equal, i.e., completely reversed strains are applied.

To utilize the experimental data, a fatigue life model for the electrical failure of conductive adhesives is required. The Coffin–Manson model is probably the most popular empirical fatigue life model, which has been successful on several common materials including PbSn solder. The Coffin–Manson model assumes that the plastic strain causes the fatigue damage in the material subjected to low cycle fatigue, and the plastic strain range of the material in fatigue test is used as the basis for life prediction. For conductive adhesives, it is found that the fatigue life before electrical conduction failure can be fitted by a power law model as well. The power law model can be written as:

$$\frac{\Delta\varepsilon}{2} = \varepsilon'_f(2N_f)^c, \quad (6)$$

where $\Delta\varepsilon/2$ is the strain amplitude, N_f is the number of cycles to electrical failure, and ε'_f and c are two constant parameters.

Although the forms are similar, equation (6) has different meaning from that of the Coffin–Manson equation. The Coffin–Manson equation considers the plastic deformation where fatigue cracks begin, and it is often used on materials that show local yielding. For our fatigue tests, the failure is electrical instead of mechanical. This electrical conduction failure is caused by the debonding of silver flakes from epoxy matrix, which will be shown later by microscopy examination. The damage caused by fatigue tests is on the interface between silver and epoxy rather than in the epoxy matrix. Hence by using the power law relationship of equation (6) the electrical fatigue life is related to the interfacial property of silver–epoxy by strain amplitudes instead of with local plastic strain.

The fatigue life data in Table 3 are well fitted by the power law relationship in equation (6) using the strain amplitude, and the fitted strain amplitude — fatigue life line is shown in Fig. 11. The two parameters for the Coffin–Manson model are

$$c = -0.1604, \quad (7)$$

$$\varepsilon'_f = 0.0273.$$

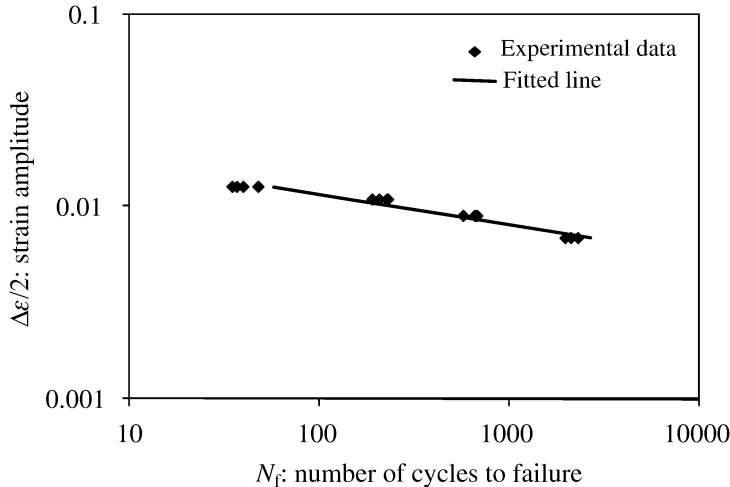


Figure 11. Fitted power law fatigue model with zero mean strain (strain ratio $R = 0$).

It can be seen from Fig. 11 that when the strain amplitude is increased, the fatigue life of the conductive adhesive sample is decreased. This is a fatigue behavior similar to most PbSn solder materials.

3.3. Influence of Strain Ratio on Fatigue Life of Conductive Adhesives

To study the effect of tensile and compressive stresses on the fatigue life of conductive adhesives, different strain ratios are applied in the fatigue tests. The strain ratio R is defined as the ratio between the minimum and the maximum strain (compressive strain is defined as negative and tensile strain as positive):

$$R = \frac{\varepsilon_{\min}}{\varepsilon_{\max}}. \quad (8)$$

The strain ratio, its corresponding maximum compressive and tensile strain, and the corresponding fatigue lives of four conductive adhesive samples are shown in Table 4. The strain rate for all the fatigue tests in Table 4 is $1.8 \times 10^{-4} \text{ s}^{-1}$.

The fatigue data of conductive adhesive samples under different strain ratios are also shown in Fig. 12. The conductive adhesive sample that is subjected to only compressive stress does not fail even after 2000 cycles and is not shown in Fig. 12.

When the conductive adhesive sample is subjected to only the compressive strain, its resistance does not increase significantly even after 2000 cycles. When tensile strain is applied all conductive adhesives fail below 1000 cycles. The tensile stress facilitates the resistance increase of the conductive adhesive.

It can be seen that the strain ratio, or different combinations of the tensile and compressive strains, has a significant effect on the fatigue life of conductive adhesives. From Table 4 it can be seen that for the same strain range, the fatigue life of conductive adhesives is longer when the strain ratio is reduced. The decrease of strain ratio is caused by the increase of the compressive strain and decrease of the

Table 4.

Strain ratios and corresponding fatigue lives of conductive adhesive samples

Strain range ($\Delta\epsilon$)	Strain ratio R			
	0	$-\infty$	-0.53	-1.89
Maximum compressive/tensile strain	0/0.011	-0.011/0	-0.006/0.011	-0.011/0.006
Fatigue lives of four conductive adhesive samples (cycles to failure)	754 681 703 727	>2000 >2000 >2000 >2000	403 343 419 370	806 775 766 754
Average fatigue life (cycles to failure)	716	>2000	384	775

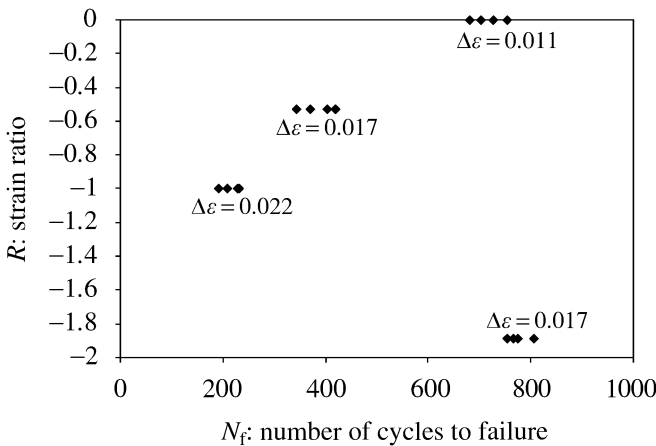


Figure 12. The fatigue life of conductive adhesive samples under different strain ratios.

tensile strain. Since the tensile strain induces fatigue failure faster than the compressive strain, the fatigue life is prolonged when the strain ratio is smaller.

It should be noted that the fitted fatigue life model shown in Fig. 11 and equation (7) is obtained based on fatigue test data with zero mean strain, i.e., with $R = 0$. Since strain ratio affects the fatigue life of conductive adhesives significantly, for fatigue tests with strain ratio $R \neq 0$ the two coefficients c and ε'_f in the power law model equation (6) will be different from those shown in equation (7). To include the effect of strain ratio in the fatigue life model, fatigue tests with different mean strain values should be performed. Based on such fatigue test data, a set of different values of coefficients c and ε'_f can be fitted and used to predict the life of conductive adhesive joints subjected to fatigue loading with non-zero strain ratio.

3.4. Influence of Strain Rate on the Fatigue Life of Conductive Adhesives

Fatigue tests were also performed with different crosshead speeds to study the effect of strain rate. The different strain rates tested are listed in Table 2. The fatigue lives of conductive adhesive samples under different strain rates are listed in Table 5 and plotted in Fig. 13. The strain range used in these tests was 0.011 with strain ratio $R = 0$.

Figure 13 shows significant strain rate effect on the fatigue life of conductive adhesives. At smaller strain rates the conductive adhesive fails at fewer fatigue cycles. When the strain rate is increased from 1.1×10^{-4} to $2.7 \times 10^{-4} \text{ s}^{-1}$, the fatigue life increases from 147 to 559 cycles, a 280% increase of the fatigue life. Therefore, to increase the fatigue life of conductive adhesives, slow strain rate should be avoided. The fact that the conductive adhesive fails faster at a lower strain rate is an indicator that creep might be involved. With higher strain rate there is less time for creep to happen and hence the conductive adhesive fails more slowly. This behavior of the

Table 5.

Strain rates and corresponding fatigue lives of conductive adhesive samples

	Strain rate ($\times 10^{-4} \text{ s}^{-1}$)			
	1.1	1.5	1.8	2.7
Fatigue lives of four conductive adhesive samples (cycles to failure)	156	171	191	558
	152	151	228	519
	148	165	208	575
	132	176	150	585
Average fatigue life (cycles to failure)	147	165	194	559

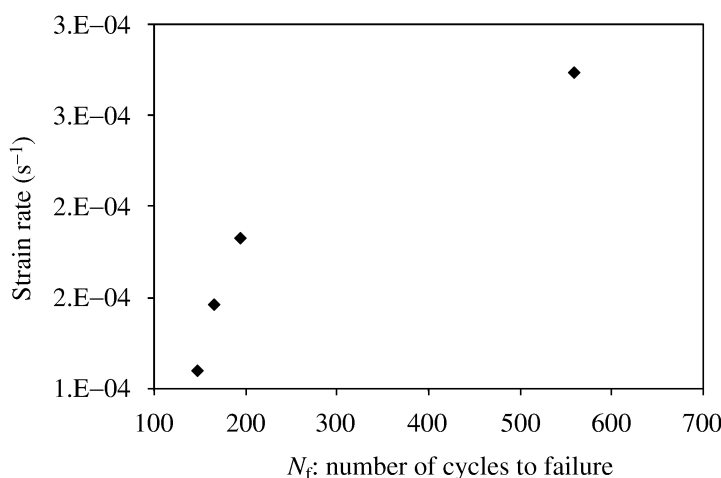


Figure 13. Strain rates and corresponding average fatigue lives of conductive adhesive samples with zero mean strain.

reduction of number of cycles to failure with lower strain rates is similar to that for solder materials.

3.5. Failure Mechanism of Conductive Adhesives in Fatigue Tests

To study the failure mechanism of conductive adhesives, the cross-section of the conductive adhesive sample as shown in Fig. 14 was examined by a scanning electron microscope (SEM) before and after fatigue tests.

Figure 15 shows the SEM micrograph of a conductive adhesive sample before fatigue tests, and Fig. 16 shows a conductive adhesive sample after fatigue tests.

Significant difference can be identified between the good and failed conductive samples. The conductive adhesive sample after fatigue test shown in Fig. 16 exhibits many cavities, which are marked by circles. These cavities were caused by the falling off of silver flakes from the epoxy matrix. In Fig. 15 no cavities are observed in the good conductive adhesive sample. Obviously the interface between the silver flakes and the epoxy matrix is damaged during the fatigue test.

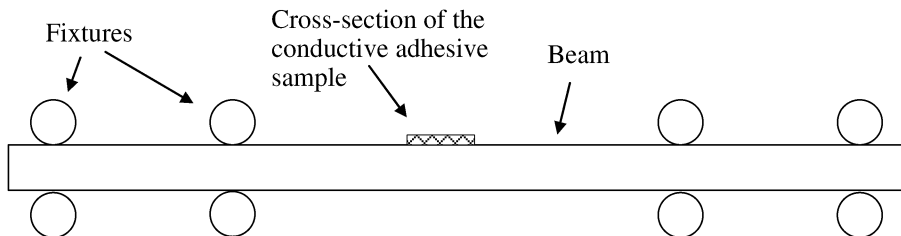


Figure 14. Cross-section of a conductive adhesive sample.

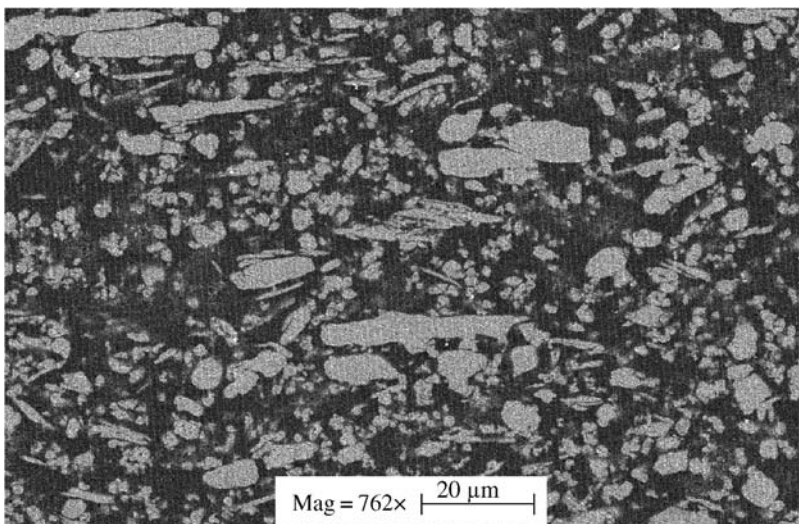


Figure 15. Cross-section of a conductive adhesive sample before fatigue tests.

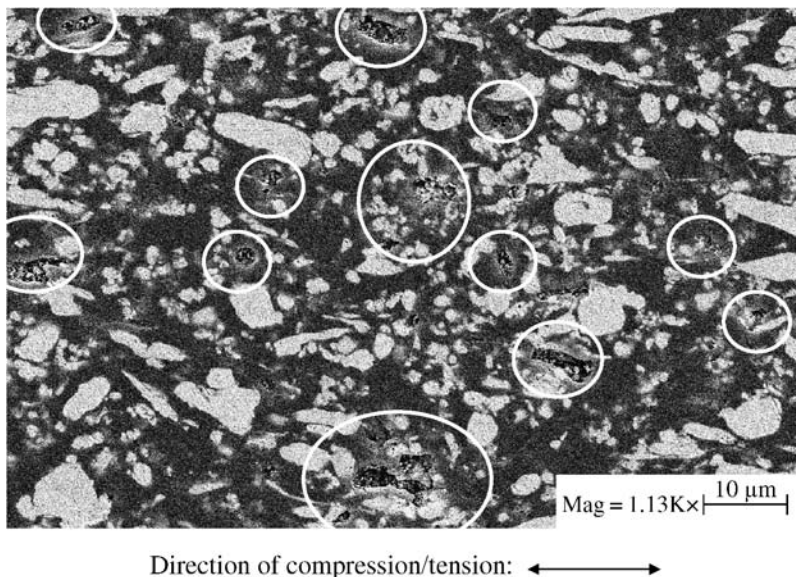


Figure 16. Cross-section of a conductive adhesive sample in fatigue test after 228 cycles (failed), strain rate = $1.1 \times 10^{-4} \text{ s}^{-1}$, strain amplitude = 0.019, strain ratio = -1.

After the adhesion between the silver flakes and epoxy matrix is lost, the epoxy matrix no longer holds the silver flakes as tight as before fatigue tests. The contact pressure between the silver flakes is reduced, causing the contact resistance between silver flakes to increase. The total resistance of the conductive adhesive consequently is increased. As more fatigue cycles are performed, more and more silver flakes lose adhesion with the epoxy matrix. The number of interconnections between silver flakes is reduced and the contact resistance between flakes becomes higher. At a certain number of fatigue cycles, the resistivity has increased to over two times the original resistivity value, and the conductive adhesive is regarded as failed. Since the electrical conduction failure is caused by the debonding of epoxy–silver interface, the interfacial adhesion between epoxy and silver flakes is critical to the fatigue life of conductive adhesives.

The interfacial debonding of the flakes from the epoxy matrix can be observed under a microscope. An SEM picture of a silver flake in the conductive adhesive sample after fatigue test is shown in Fig. 17. It can be seen that the interface between the silver flake and the epoxy matrix has been partially damaged. With more fatigue cycles, the crack between the flake and epoxy matrix will propagate and finally cause a complete debonding of the silver flake. The debonding of silver flakes could be due to the weak adhesion between the epoxy and silver flakes, but the direct cause of the damage is fatigue loading.

It should be noted that no large cracks are found in the SEM images. Although there are cracks and debonding between the epoxy matrix and the silver flakes, but these are all along the epoxy–silver interface. The fatigue test has not caused large

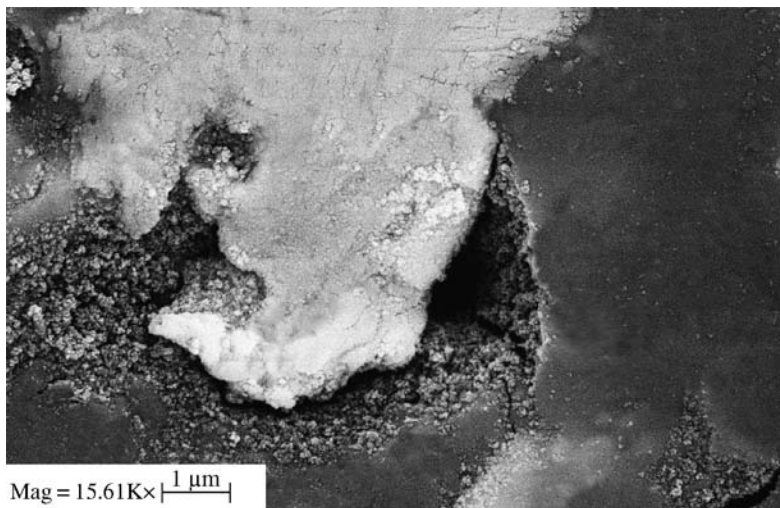


Figure 17. A silver flake in a conductive adhesive sample after fatigue test of 575 cycles.

cracks that propagate through the conductive adhesive. Considering that there is also no breakage and peeling off of conductive adhesive samples from the PCB, the damage done to the conductive adhesive sample by fatigue tests is mainly electrical. The electrical resistance increases to a large value well before major mechanical damage has developed. Therefore the fatigue failure should be considered in terms of electrical conduction rather than mechanical adhesion or breakage.

To observe the development of the debonding of silver flakes, two SEM micrographs were taken during the fatigue test and after fatigue test, as shown in Figs 16 and 18, respectively. Figure 18 shows the flakes in the early stage of the fatigue test, and Fig. 16 shows the flakes after the fatigue test. By comparing these two images, it can be seen that in Fig. 18 the debonding between the flakes and the epoxy matrix is just beginning to appear. Not only is the number of the cavities fewer but also the size is smaller compared with the SEM image after fatigue failure as shown in Fig. 16.

To verify that the electrical failure mechanism of debonding was general and not particular to the conductive adhesive samples used in our test, fatigue tests were also performed on a commercial conductive adhesive material: Loctite 3889 from Henkel Loctite Corporation, Rocky Hill, CT, USA. The microscopy examination of the cross section of the conductive adhesive samples after electrical fatigue failure showed similar phenomenon of debonding between silver flakes and epoxy matrix. In other words, the epoxy–silver interfacial debonding seems to be a common failure mechanism for conductive adhesives under fatigue loading.

4. Summary

In this paper, the fatigue behavior of conductive adhesives was studied by performing fatigue tests. It was found that the number of cycles to electrical failure is related

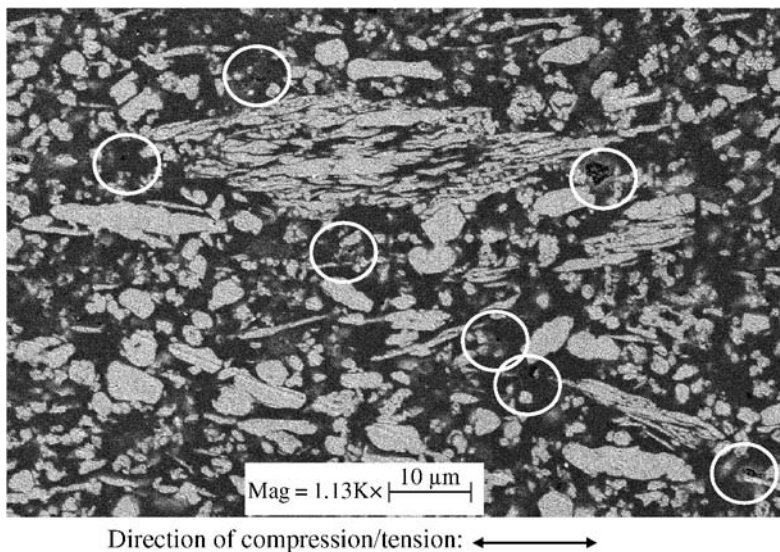


Figure 18. Cross-section of a conductive adhesive sample in fatigue test after 40 cycles (not failed), strain rate = $1.1 \times 10^{-4} \text{ s}^{-1}$, strain amplitude = 0.02, strain ratio = -1.

to the strain amplitude through a power law equation. In addition, test data showed that the strain ratio and strain rate both have a significant effect on the fatigue life of conductive adhesives, and tensile strain has a more detrimental effect on the electrical failure. In all the tests, no visible fracture of sample was observed before the electrical resistivity had increased by 100%, which was defined as the threshold for electrical failure.

The failure mechanism of conductive adhesives was found by scanning electron microscopy examination. The SEM images of conductive adhesives after fatigue tests show debonding of silver flakes from the epoxy matrix. The interfacial adhesion between silver flakes and the epoxy matrix is impaired by the fatigue test. With flakes being partially debonded, the contact pressure and contact area between silver flakes are reduced, which, in turn, increase the contact resistance between silver flakes. As a result the total resistance is increased. Some of the SEM images seem to show that the debonding of silver flakes appears mostly along the 45° direction to the compressive/tensile load direction, where the maximum shear stress occurs, suggesting a shear dominant failure mechanism. However, this is only a speculation and more work is needed to fully understand the exact failure mechanism and mode.

More work is needed to predict the electrical fatigue life of conductive adhesives in electronic packaging. Our fatigue tests were performed with uniaxial tensile and compressive loadings, and the fatigue life model was fitted using uniaxial strain range. However, in electronic packaging, conductive adhesive joints are often subjected primarily to shear deformation. To predict the fatigue life of the conductive adhesive joints using our fatigue life model, some conversion needs to be per-

formed. A finite element analysis needs to be performed first to determine the strain distribution in the conductive adhesive joint. Then the von Mises equivalent strain can be calculated for a local point, and be applied in the fatigue life model to predict the fatigue life of the conductive adhesive joint. If the stress concentration is induced by the joint geometry, mechanical failure can happen before electrical failure. Therefore, both mechanical and electrical failures should be considered for conductive adhesive joints with complex shapes. Also in electronic packaging the coupled thermomechanical fatigue should be considered, instead of mechanical fatigue only. The change of the material property, especially the property change of the epoxy matrix under different temperatures, should be considered when predicting the fatigue life of conductive adhesive joints. In summary, more investigation is yet to be done to predict the fatigue life of conductive adhesive joints.

Acknowledgements

The work was supported, in part, by the NSF Packaging Research Center at Georgia Tech. J. Q. was also partially supported by the Changjiang Professorship at Beijing University and by the Harbin Institute of Technology.

References

1. J. H. Constable, T. Kache, H. Teichmann, S. Muhle and M. A. Gaynes, *IEEE Trans. Components Packaging Technol.* **22**, 191–199 (1999).
2. R. L. Keusseyan and J. L. Dilday, *Int. J. Microcircuits Electronic Packaging* **17**, 236–242 (1994).
3. R. Gomatam and E. Sancaktar, in: *Proceedings of the International Symposium and Exhibition on Advanced Packaging Materials Processes, Properties and Interfaces*, Braselton, GA, pp. 6–12 (2001).
4. Z. Mo, Z. Lai, S. Li and J. Liu, *Soldering Surface Mount Technol.* **16**, 48–52 (2004).
5. Y. Kitazaki and T. Hata, *J. Adhesion* **4**, 123–133 (1972).
6. E. Sancaktar and P. Zhang, *Trans. ASME, J. Mech. Design* **112**, 605–619 (1990).
7. R. R. Gomatam and E. Sancaktar, *J. Adhesion Sci. Technol.* **18**, 731–750 (2004).
8. R. R. Gomatam and E. Sancaktar, *J. Adhesion Sci. Technol.* **20**, 87–104 (2006).
9. B. Su and J. Qu, in: *Proceedings of the International Symposium and Exhibition on Advanced Packaging Materials Processes, Properties and Interfaces*, Irvine, CA, pp. 75–78 (2005).
10. M. Zwolinski, J. Hickman, H. Rubin, Y. Zaks, S. McCarthy, T. Hanlon, P. Arrowsmith, A. Chaudhuri, R. Hermansen, S. Lau and D. Napp, *IEEE Trans. Components Packaging Manuf. Technol. Part C* **19**, 241–250 (1996).

Aspect Ratio and Loading Effects of Multiwall Carbon Nanotubes in Epoxy for Electrically Conductive Adhesives

Jing Li^a, Janet K. Lumpp^{a,*}, Rodney Andrews^b and David Jacques^b

^a Electrical and Computer Engineering Department, 453 F. Paul Anderson Tower,
Lexington, KY 40506-0046, USA

^b Center for Applied Energy Research, University of Kentucky, Lexington, KY 40506, USA

Abstract

Isotropic conductive adhesives (ICAs) filled with metal particles are commercially available as alternatives to solder joining in electronic packaging. Replacing metal fillers with multiwall carbon nanotubes (MWCNTs) offers the potential benefits of being corrosion resistant, high strength and lightweight. Traditional metal filled ICAs require high metal loading to ensure electrical conductivity, which may cause problems with respect to reliability and strength to weight ratio. The ultra-high aspect ratio and surface area of multiwall carbon nanotubes induce a low percolation threshold of less than 0.25 wt% in epoxy. MWCNTs dispersed in epoxy increase the thermal diffusivity of the polymer by a factor of 2 to 3 and decrease the volume resistivity to less than $10 \Omega \text{ cm}$ for loadings up to 12 wt%. Lap shear strength decreases with increased MWCNT loading. The dependences of electrical, thermal and mechanical properties on loading and aspect ratio of MWCNTs are reported, and the electrical conduction mechanism is discussed.

Keywords

Isotropic conductive adhesive, multiwall carbon nanotubes, MWCNTs, percolation threshold, epoxy

1. Introduction

Printed circuit board and component fabrication technologies require an array of materials to be assembled into mechanically robust and electrically functional final products. Electronic assemblies typically use solder alloys to both electrically and mechanically connect the components to the circuit board. Solder is applied as solder paste by screen printing, stencil printing or pressure dispensing, then a reflow oven activates the flux and melts the solder. Molten solder is also used in wave soldering of surface mount and through-hole components. Both wave soldering and solder reflow rely on molten solder wetting on metal surfaces to define shape of the solder joints and to prevent short circuit bridging across insulated spaces between

* To whom correspondence should be addressed. Tel.: (859) 257-4985; Fax: (859) 257-3092; e-mail: jklumpp@uky.edu

metal features. In manufacturing facilities worldwide, the traditional tin–lead solder alloys are being replaced by lead-free materials in response to the international Restriction on the use of Hazardous Substances (RoHS) legislation.

Even before RoHS, metal filled isotropic conductive adhesives were commercially available as viable alternatives to soldering for die attach and component assembly. ICA material properties are significantly different than solder and depend on the choice of polymer matrix composition. For example, ICA products may be thermoplastic or thermosetting and may wet both conductor and insulator surfaces. The same dispensing methods used for solder paste are employed to apply an ICA to printed circuit boards with appropriate process control tolerances to prevent bridging. As composite materials, the polymer matrix of an ICA provides adhesion to the circuit board pads and component leads while compressing the conductive particles together to form the electrical path. Traditional metal filled ICAs require 25% to 30% volume fraction (up to 80 wt%) metal to overcome the percolation threshold and ensure electrical conductivity [1]. Such a high volume fraction of filler degrades the mechanical properties of the polymer matrices. With conventional metal filled conductive adhesives, only a small portion of the shear strength of polymer matrices can be retained. When the fillers are randomly distributed cylinders, the critical volume fraction for percolation is inversely proportional to the product of the aspect ratio and surface area [2]. Low percolation thresholds are expected, therefore, with long narrow filler particles providing large surface areas for particle to particle contact.

High aspect ratio, large surface area multiwall carbon nanotubes have the potential as ICA filler particles to reach the percolation threshold with small volume fraction loading. The MWCNTs used in the present study have aspect ratios from 250 to 2500. MWCNTs are electrically conductive independent of synthesis method and have extremely high strength to weight ratio offering the potential to improve the stiffness of the polymer matrix. In recent years, electrical and mechanical properties have been investigated for MWCNT/polymer composites. Sandler *et al.* [3] reported the percolation threshold of MWCNTs in epoxy as low as 0.0025 wt%. Meincke *et al.* [4] reported the percolation threshold for MW-CNT/polyamide/ABS composite lies between 2 and 3 wt% and a 27% increase in Young's modulus for MWCNT/polyamide/ABS composite with 7 wt% loading of MWCNTs.

New ICA compositions developed for the microelectronics industry will need to be compatible with glass, polymer, ceramic and metal surfaces. For component attachment, the ICA may need to adhere to the copper interconnect with a surface finish applied, glass/polymer composite board, solder mask insulator coating, thick film chip resistors, ceramic chip capacitor, integrated circuit package bodies made of polymer, ceramic or metal and component leads. Metal surface finishes may include plated metals, flash evaporation coatings, dip coatings, or organic solderability preservatives. MWCNT filled conductive adhesives will have to be tested

on each of the possible surfaces and endure a battery of standard reliability tests to fully develop a commercially viable composition.

At this stage in our research efforts, we are focusing on optimizing the volume resistivity and processability of carbon nanotube filled epoxies. Prior results presented in several conference papers [5–8] addressed dispersibility, loading and potlife of MWCNTs into several different resins to demonstrate their potential application in electronic assemblies. Replacing metal fillers with MWCNTs has the potential benefits of being lead free, corrosion resistant, high-mechanical strength and lightweight. In this work, epoxy/MWCNT composites with different loadings of MWCNTs were prepared. Electrical, mechanical and thermal properties were tested. Accelerated aging testing was also carried out.

2. Experimental

2.1. Materials

The epoxy resin and curing agent used in this study were diglycidyl ether bisphenol-F (Epon 862, Shell Chemical, USA) and methyl hexahydro phthalic anhydride (MHHPA, Miller-Stephenson Chemical, USA). Cyanoethyl-2-ethyl-4-methylimidazole (2E4MZ-CN, Shikoku Chemical, Japan) was used as a catalyst. MWCNTs were obtained from the University of Kentucky Center for Applied Energy Research (CAER) with average lengths of 50 μm and average diameters of 20 nm yielding an aspect ratio of approximately 2500. The chemical vapor deposition growth conditions are described in reference [9]. Shatter-milled short MWCNTs were prepared by grinding the MWCNTs in a shatter mill for 10 min. Figure 1a and 1b is transmission electron microscope (TEM, JEOL 2010F, Japan) images showing that MWCNTs can be broken and tips opened by shatter milling.

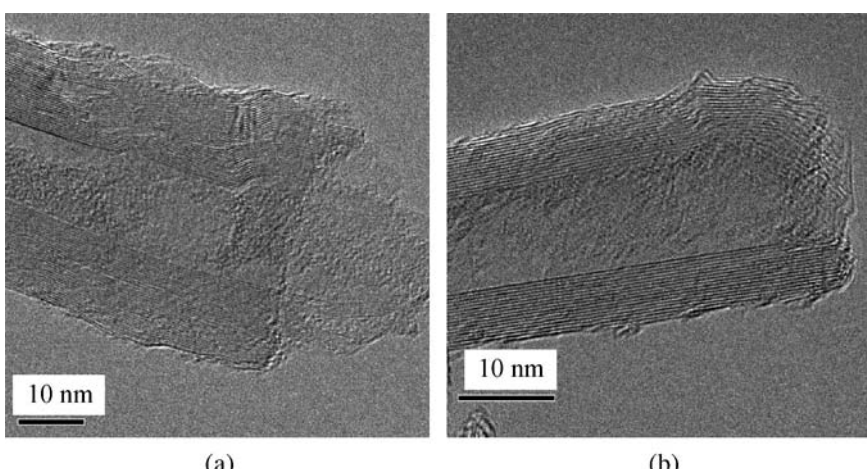


Figure 1. TEM micrographs of (a) broken, shatter-milled MWCNTs and (b) open-ended shatter-milled MWCNTs.

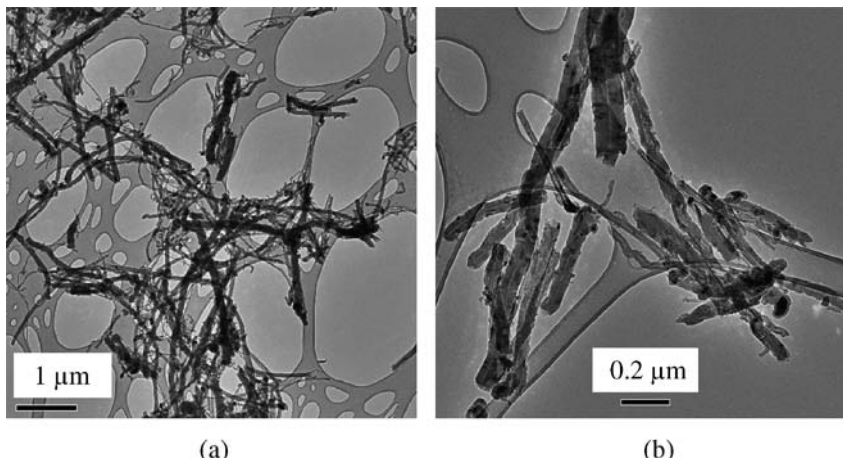


Figure 2. (a) and (b) TEM micrographs of shatter-milled MWCNTs.

Figure 2a and 2b are TEM images demonstrating that the average length of shatter-milled MWCNTs is less than 5 μm.

2.2. Preparation of Epoxy/MWCNT Compositions

Epoxy was prepared by mixing the resin, curing agent and catalyst at a weight ratio of 100:85:0.5, respectively. The batch size was 10 grams. A planetary mixer (AR-250, Thinky Inc., Japan) was used to mix MWCNTs into epoxy for 30 min. The planetary mixer generates large continuous centripetal forces (up to 400G) by compound motion of the revolving centrifuge and the counter-rotation of the material container. The high shear mixing action achieves uniform distribution and removes air bubbles from the mixture at the same time. No blending tool was required and each batch was mixed in a new clean polyethylene container to prevent contamination.

2.3. Volume Resistivity Measurement

To measure the volume resistivity, the mixed epoxy/MWCNT composites were stencil-printed onto aluminum oxide substrates (4 × 4 inch, CoorsTek, USA). On the stencil pattern were five $1 \times 1 \text{ cm}^2$ openings and two substrates were printed for each epoxy/MWCNT loading, thereby ten squares for each loading were printed. Samples were held at 80°C for 4 h to outgas and then cured at 150°C for 30 min. The volume resistivity of each sample was calculated by multiplying the sheet resistance by the average thickness of the epoxy/MWCNT composite layer. A four-point probe tester (Signatone, USA) was used to measure the sheet resistance for each square. A stylus profilometer (Alpha-Step 500, Tencor, USA) was used to scan each square in four directions to obtain the average thickness. Figure 3 illustrates the volume resistivity measurement sample. Volume resistivity for each of the ten

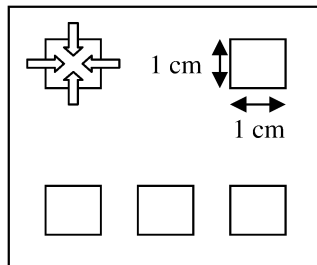


Figure 3. Sample design for volume resistivity measurement with $1 \times 1 \text{ cm}^2$ stencil-printed pads. Arrows indicate scan directions for stylus profilometer thickness measurements.

squares was calculated and averaged to determine the volume resistivity for each loading.

2.4. Contact Resistance Measurement

To measure the contact resistance of MWCNT filled ICAs, daisy chain patterns were etched on 1-ounce copper clad FR-4 printed circuit boards (PCBs) (D&L Products, USA) and 1206 size zero-ohm resistors (DigiKey, USA) were assembled onto the daisy chains. 10 zero-ohm resistors constitute each daisy chain with 4 daisy chains on each board. A multimeter (HP 3478A, USA) was used to measure the resistance for each daisy chain on the test board. The mean value of resistance for each daisy chain was calculated and divided by 20 to determine the average resistance per contact for each set of 10 resistors.

2.5. Scattering Parameter Measurement

RT/Duroid 5880 (Rogers, USA) high frequency board was used to etch S-parameter measurement test vehicles. Microstrip lines were patterned on the 1-ounce copper double-side high frequency board. On each test pattern, a zero-ohm resistor was attached across the gap in the microstrip line using the MWCNT/epoxy composite. A network analyzer (HP 8753D, USA) was used to measure the S-parameters for each test sample in the frequency range of 50 MHz to 3 GHz. Measured S-parameters for solder joints, commercially available Ag filled ICA, and epoxy/MWCNT composites with different MWCNT loadings were compared.

2.6. Lap Shear Strength Measurement

To evaluate the mechanical degradation of the polymer matrix caused by adding MWCNTs, a lap shear test was conducted using an Instron 4442 tensile tester (Instron, USA). The test sample was prepared by attaching two copper clad-printed circuit board tabs using the epoxy/MWCNT composite. The lap area was $0.635 \times 0.635 \text{ cm}^2$. Figure 4 illustrates the test sample. Eight samples were prepared to determine the average lap shear strength for each loading of MWCNTs. Tabs were milled from bare-printed circuit boards using a MITS FP-21T milling machine.

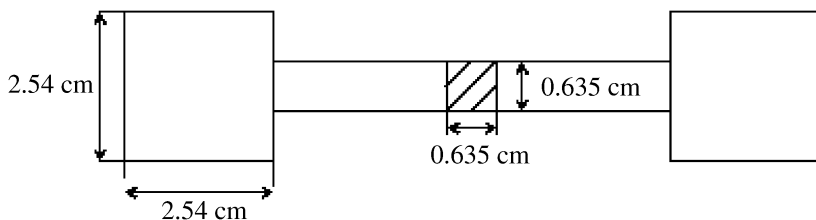


Figure 4. Lap shear test samples cut from copper clad-printed circuit board material.

2.7. Thermal Diffusivity Measurement

Thermal diffusivity analysis for the MWCNT filled conductive adhesives was conducted by using a laser flash apparatus (NETSCH, USA). Pure epoxy and epoxy/MWCNT composites with different loadings were cured in a Teflon die 1.27 cm diameter and a diamond saw cut 0.15 cm thick discs to make the test samples. Thermal diffusivity of samples at different temperatures were measured and compared.

2.8. Accelerated Aging Test

To evaluate the impact of humidity and temperature on the volume resistivity of epoxy/MWCNT composites, an 85°C/85% relative humidity accelerated aging test was conducted in an environmental chamber (Bryant, USA). Stencil-printed samples for volume resistivity measurement were placed in the 85°C/85% environment for 96 h, removed and measured to compare with the volume resistivity values measured before accelerated aging testing.

3. Results and Discussion

Volume resistivities of epoxy/MWCNT composites with different loadings were measured. Figure 5 plots volume resistivity as function of the MWCNT loading. The largest reduction in volume resistivity is observed at 0.25 wt%, which means the MWCNTs start forming interconnected path before the loading reaches 0.25 wt%. Thus the percolation threshold is less than 0.25 wt%. In preparing all the batches, it was observed that viscosity increased with increased MWCNT loading. At loadings above 12 wt% as-produced MWCNTs, the epoxy/MWCNT composite becomes too viscous to process by screen printing, stencil printing, or pressure dispensing.

Figure 6a and 6b shows SEM micrographs of the top surface and fracture cross-section, respectively. From the top surface micrograph (Fig. 6a), it is difficult to determine whether MWCNTs are exposed on the top surface of the composite. By comparison, in Fig. 6b, randomly dispersed MWCNTs can be seen protruding from the fracture cross-section. To determine if the resistance of the epoxy/MWCNT composite was mainly caused by the lack of exposed MWCNTs on the surface, argon plasma (Plasma-Preen II862, Plasmatic Systems, Inc., USA) was used to etch

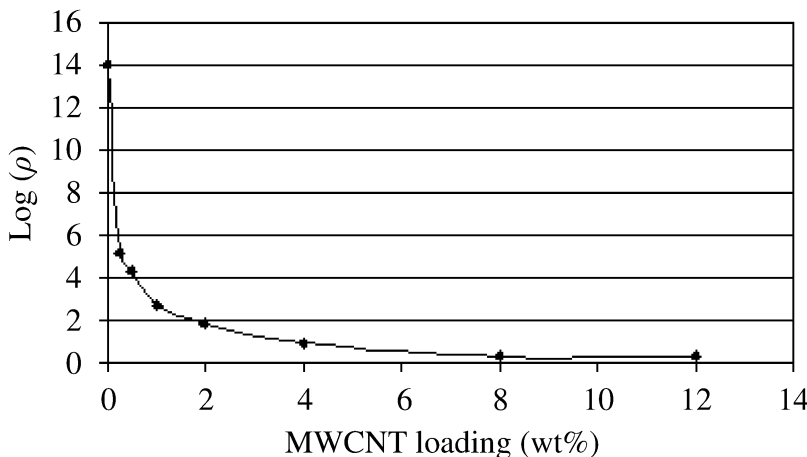


Figure 5. Log (ρ) volume resistivity *versus* MWCNT loading for as-produced high aspect ratio MWCNTs in epoxy.

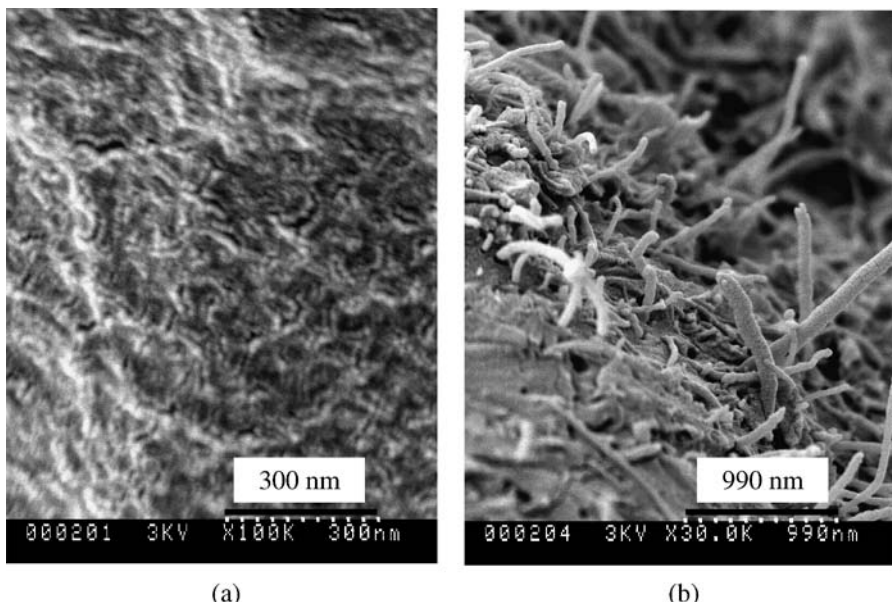


Figure 6. SEM micrographs of (a) top surface and (b) fracture cross-section of 4 wt% loading of as-produced MWCNTs in epoxy.

the epoxy layer on the surface of epoxy/MWCNT composites. The argon airflow rate was 3 cubic feet per minute and power was 900 W. Figure 7 is the SEM micrograph for the epoxy/MWCNT composite surface after plasma etching for 8 min. Volume resistivity measurement samples for 8 wt% MWCNT loading were exposed to argon plasma for 4, 8 and 16 min. A four-point probe tester was used to evaluate the voltage drop with the same current injected. After 4 and 8 min of argon plasma

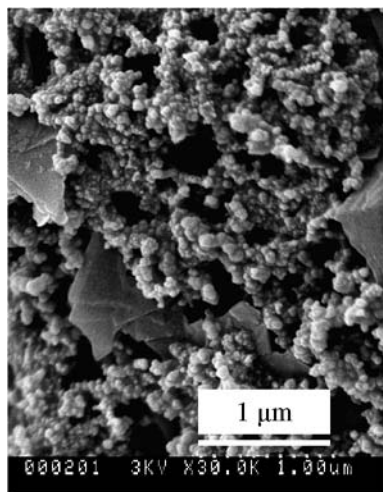


Figure 7. SEM micrograph for 8 wt% as-produced MWCNT/epoxy composite after argon plasma etching for 8 min.

Table 1.

Volume resistivities of epoxy/MWCNT composites mixed with different ratios of ‘a’, as-produced, and ‘s’, shatter-milled, MWCNTs with a total loading of 12 wt%

Loading (wt%)	a	s	a	s	a	s	a	s	a	s	a	s	
	12	0	10	2	8	4	6	6	4	8	2	10	
Volume resistivity ($\Omega \text{ cm}$)	2.17		0.96		2.05		5.07		7.48		24.17		149.45

etching, no change in the four-point probe voltage reading was observed. After etching for 16 min, the voltage reading was reduced by an average of 4%. No measurable change in thickness was detected by the surface profilometer, therefore the decrease in volume resistivity of the epoxy/MWCNT composite due to plasma etching can only be estimated as 4%. Based on the four-point probe and SEM analyses, etching the thin epoxy surface layer on the bulk epoxy/MWCNT surface decreased the volume resistivity marginally and it can be concluded that the volume resistivity of epoxy/MWCNT composite is not dominated by the epoxy layer on the surface of epoxy/MWCNT composite.

To evaluate the effect of MWCNT size on volume resistivity, the total weight percent of both as-produced MWCNTs and shatter-milled MWCNTs was set at 12 wt%, and measured volume resistivities for different ratios of as-produced and shatter-milled MWCNTs were compared. The aspect ratio of as-produced MWCNTs is approximately 2500 while the aspect ratio of shatter-milled MWCNTs is less than 250. In Table 1, ‘a’ represents as-produced MWCNTs and the ‘s’ represents shatter-milled MWCNTs. In preparing samples, it was observed that at the

same weight percent loading, epoxy/MWCNT composites made with shatter-milled MWCNTs and combinations of long and short MWCNTs had much lower viscosity than the composites made with only as-produced MWCNTs. The maximum loading of only shatter-milled MWCNTs that can be mixed into epoxy is approximately 36 wt%. At higher loadings, the viscosity is too high for printing or dispensing. With 36 wt% loading of shatter-milled MWCNTs, the measured volume resistivity of epoxy/MWCNT composite is $11.96 \Omega \text{ cm}$. From Table 1, it can be concluded that MWCNTs with high aspect ratio form electrically conductive paths more easily than MWCNTs with low-aspect ratio, and mixing high and low-aspect ratio MWCNTs can improve both the conductivity and processability.

Figure 8 shows the result for the contact resistance measurements for 2, 4 and 8 wt% MWCNT loadings. It can be seen that the value of contact resistance and standard deviation both reduce with increasing MWCNT loading but are still fairly large for electronic applications. It was observed that pressure on the components during curing effectively reduced the contact resistance. By applying pressure during curing, contact area is enlarged while the height between pads is reduced so that more contact points between pads and MWCNTs are achieved. In the future work, the relationship between the applied pressure and the contact resistance will be evaluated.

The highest conductivity achieved in our MWCNT/epoxy samples is on the order of 10^0 S/cm , which is still not as high as for commercially available metal filled ICAs. In conductive adhesives, there are three major factors affecting the conductivity of the composite: intrinsic conductivity of the filler particles, dimension (aspect ratio) of the filler particles and the contact resistance between the particles. MWCNTs with small size and high aspect ratio can form more contacts than large metal particles with the same weight percent loading, making it easier for MWCNTs to form conductive networks in the composite. Therefore, the percolation threshold of MWCNT/epoxy composite is extremely low. When the conductive filler in the composite has formed a percolated network, the resistance of the composite is determined by the intrinsic conductivity of the filler particles

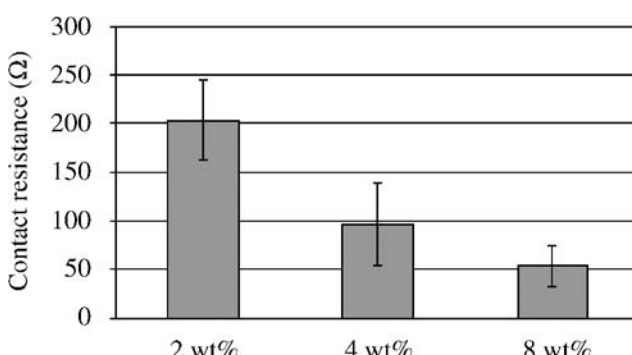


Figure 8. Average contact resistances for 2, 4 and 8 wt% loading of as-produced MWCNTs in epoxy.

and the contact resistances between the filler particles. The intrinsic conductivity of MWCNTs is on the order of 10^3 S/cm [10] while the conductivity of silver, the most commonly used filler in metal filled ICAs, is 6.3×10^5 S/cm [11]. Consequently, the intrinsic resistance of the filler particles in MWCNT/epoxy composite is larger than for a commercially available ICA.

The contact resistance (R_c) consists of two factors, the constriction resistance (R_{cr}) and the tunneling resistance (R_t). When two conductive filler particles come into contact with each other, constriction resistance is caused by constriction of electron flow through the small contact area. The R_{cr} is inversely proportional to the diameter of the contact area. Quantum-mechanical tunneling occurs when the distance between two conductive filler particles in the composite is small (on the order of 10 nm or less). The R_t is proportional to the distance between the conductive filler particles and work function of the filler particle [12]. The work function of silver is 4.3 eV [11] while the work function of MWCNTs is 4.95 eV [13]. Therefore, the tunneling resistance between filler particles is larger for MWCNTs than silver particles. In compositions where the polymer matrix shrinks during the curing process, a certain amount of pressure is applied to the metal filler particles by the matrix which decreases the distance between the metal particles and increases the diameter of the contact area. However, the shrinkage of the matrix during curing of the MWCNT/epoxy composite does not move the MWCNTs as much due to lack of cross-link bonding between MWCNTs and epoxy. Therefore, the contact resistance between MWCNTs in the cured MWCNT/epoxy composite is much larger than the contact resistance between silver particles in the cured silver filled ICA. For each percolated linkage in MWCNT/epoxy composite, the intrinsic conductivity of the filler particle is smaller than the silver filled ICA and the contact resistance between the filler particles is larger than silver filled ICA. Hence MWCNT/epoxy composites in our experiments (less than 6 vol%) have higher contact resistance than commercially available metal filled ICAs (above 25 vol%) although the percolation threshold of MWCNTs in epoxy is much lower than that of metal.

Figure 9a and 9b shows the comparison of measured scattering parameters S_{11} and S_{21} for solder joints, MWCNT/epoxy composites and silver filled ICA. S_{11} and S_{21} are the input reflection coefficient and forward transmission coefficient of the 50Ω terminated output. It can be concluded that MWCNT filled ICAs have comparable AC performance to tin-lead solder and commercially available silver filled ICA in this configuration and frequency range.

Figure 10 shows the comparison of lap shear strength for epoxy/MWCNT composites and commercially available silver filled ICA (80 wt% silver loading, Epoxy Tech., USA). By comparison, it can be seen that a higher lap shear strength was achieved with lower loadings, while for the same weight percent loading, the mixtures of as-produced and shatter-milled MWCNTs yielded higher lap shear strength.

Figure 11 shows the measured thermal diffusivity of neat epoxy and epoxy/MWCNT composites. At the same temperature, the thermal diffusivity in-

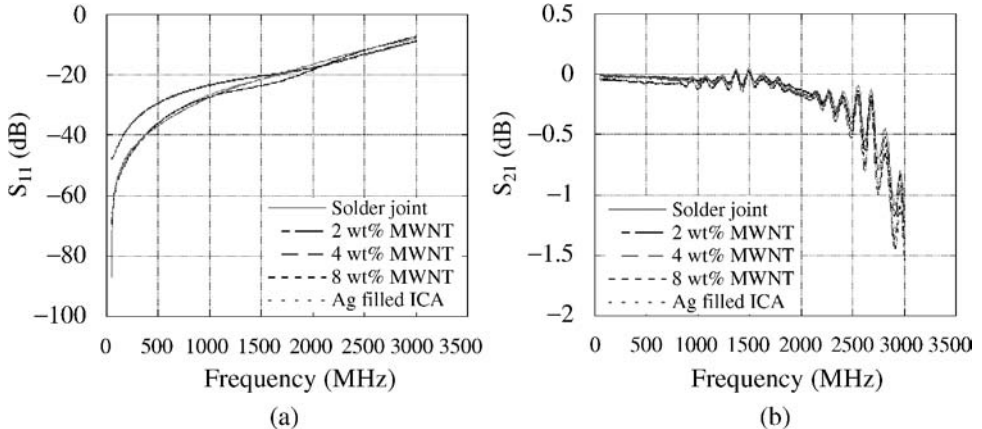


Figure 9. (a) S_{11} and (b) S_{21} AC scattering parameters for solder, silver filled adhesive and MWCNT filled epoxies from 50 MHz to 3 GHz.

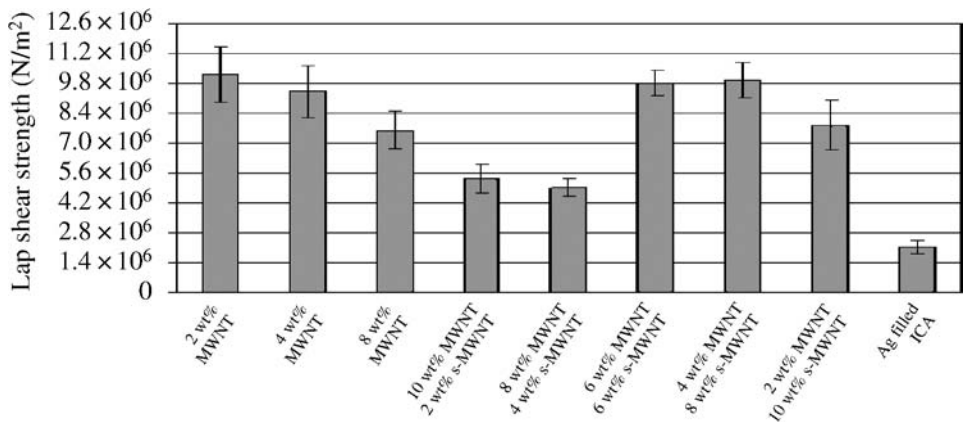


Figure 10. Comparison of lap shear strength for silver filled ICA and various ratios of as-produced and 's', shatter-milled, MWCNTs in epoxy.

creases with increasing MWCNT loading. For the same loading, the thermal diffusivity decreases with increasing temperature. It was observed that the increase in thermal diffusivity is limited even though MWCNTs individually have a high thermal conductivity. Two factors contributing to the low thermal conductivity are the lack of significant contact area between MWCNTs dispersed in the matrix and that heat is not effectively transferred by tunneling. As a result, the epoxy works as a thermally insulating layer between the MWCNTs.

Volume resistivity measurement samples for 4 wt% MWCNT loading were used to perform an accelerated aging test. Volume resistance change with aging time is shown in Fig. 12.

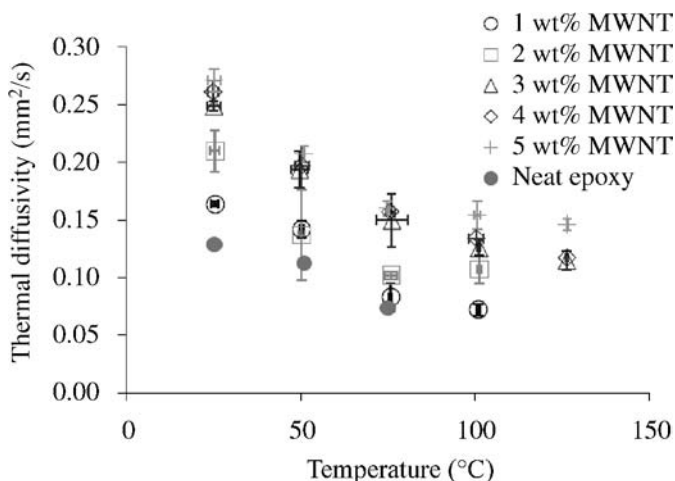


Figure 11. Laser flash thermal diffusivity analysis results for as-produced MWCNTs in epoxy.

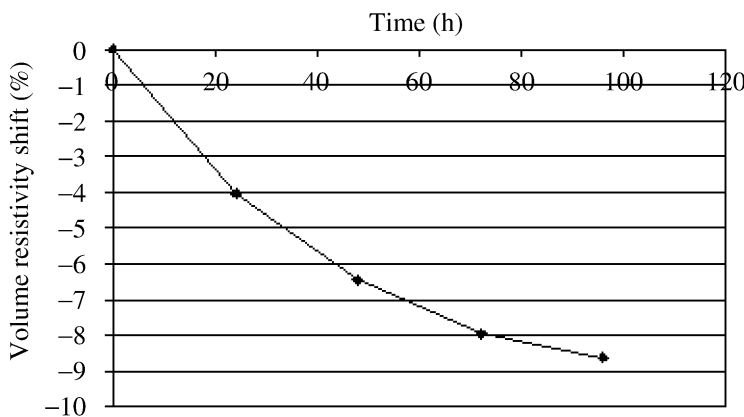


Figure 12. Shift in volume resistivity for 4 wt% as-produced MWCNTs measured every 24 h for a total of 96 h accelerated aging in 85% RH and 85°C.

4. Conclusions

The results of this work indicate that epoxy/MWCNT composites have a significantly lower percolation threshold than a metal filled ICA. Replacing metal fillers in ICA with MWCNTs improves the lap shear strength and the strength to weight ratio. AC scattering parameters measured for epoxy/MWCNT composites are competitive with solder and silver filled ICAs. Thermal diffusivity of the epoxy increases with the addition of MWCNTs. Varying the fractions of long and short MWCNTs in the composite improves both the volume resistivity and processability of the mixture. Preliminary accelerated aging tests show a decrease in volume resistivity as a result of 85°C/85% RH exposure. The conduction mechanism in the epoxy/MWCNT composite is influenced by the intrinsic conductivity of the

MWCNTs and the contact resistance between MWCNTs. The contact resistance is determined by shrinkage of the matrix, distance between particles and the work function of the MWCNTs. Consequently, the contact resistance and volume resistivity are not yet comparable to commercially available metal filled ICAs. In future work, MWCNT treatment and functionalized MWCNT will be studied to improve metallic contacts with MWCNT/epoxy composite and decrease contact resistance within the composite.

Acknowledgements

This research was sponsored by Kentucky NASA EPSCoR and the Army Research Laboratory under Cooperative Agreement Number W911NF-04-2-0023. The views and conclusions contained in this document are those of the authors and should not be interpreted as representing the official policies, either expressed or implied, of the Army Research Laboratory or the US Government. The US Government is authorized to reproduce and distribute reprints for Government purposes notwithstanding any copyright notation hereon.

The authors would like to thank Dr. Mark Meier for assistance in shatter milling the MWCNTs and Dr. Dali Qian for micrographs.

References

1. J. H. Lau, C. P. Wong, N. C. Lee and S. W. R. Lee, *Electronics Manufacturing with Lead-free, Halogen-free & Conductive Adhesive Materials*. McGraw Hill, New York, NY (2003).
2. I. Balberg, C. H. Anderson, S. Alexander and N. Wagner, *Phys. Rev. B* **30**, 3933–3943 (1984).
3. J. K. W. Sandler, J. E. Kirk, A. J. Kinloch, M. S. P. Shaffer and A. H. Windle, *Polymer* **44**, 5893–5899 (2003).
4. O. Meincke, D. Kaempfer, H. Weickmann, C. Fridrich, M. Vathauer and H. Warth, *Polymer* **45**, 739–748 (2004).
5. J. Li, J. K. Lumpp and E. Grulke, in: *Proc. 2003 IMAPS International Microelectronics and Packaging Symposium*, Boston, MA, pp. 35–38 (2003).
6. J. Li and J. K. Lumpp, in: *Proc. 2006 IEEE Aerospace Conference*, Big Sky, MT, paper #1519 (2006).
7. J. Li and J. K. Lumpp, in: *Proc. 2006 IMAPS International Microelectronics and Packaging Symposium*, San Diego, CA, pp. 100–104 (2006).
8. J. Li and J. K. Lumpp, in: *Proc. 2007 IEEE Aerospace Conference*, Big Sky, MT, paper #1349 (2007).
9. R. Andrews, D. Jacques, A. M. Rao, F. Derbyshire, D. Qian, X. Fan, E. C. Dickey and J. Chen, *Chem. Phys. Lett.* **303**, 467–474 (1999).
10. K. Kanetoa, M. Tsuruta, G. Sakai, W. Y. Cho and Y. Ando, *Synthetic Metals* **103**, 2543–2546 (1999).
11. Robert C. Weast (Ed.), *Handbook of Chemistry and Physics*. CRC Press (1984).
12. G. R. Ruschau and R. E. Newnham, *J. Composite Mater.* **26**, 2727–2735 (1992).
13. M. Shirashi and M. Ata, *Carbon* **39**, 1913–1917 (2001).

This page intentionally left blank

Part 3

Characterization and Properties

This page intentionally left blank

Novel Techniques for Characterization of Fast-Cure Anisotropic Conductive and Non-conductive Adhesives

Mary Teo *

Infineon Technologies Asia Pacific Pte Ltd, Assembly & Interconnect Technology, 168 Kallang Way,
Singapore 349253

Abstract

Anisotropic conductive adhesives (ACAs) and non-conductive adhesives (NCAs) are widely used in adhesive flip chip technology. Typically, ACAs and NCAs are formulated to achieve a complete cure in less than 60 s when curing between 180 and 250°C. The fast-cure characteristic of these adhesives poses great difficulties for conventional cure characterization techniques. In this study, novel cure monitoring techniques including Modulated Differential Scanning Calorimetry (MDSC), Dielectric Analysis (DEA) and Fibre Bragg Grating (FBG) techniques were evaluated. Cure-related properties in terms of adhesion strength and cure shrinkage were characterized. Findings showed that MDSC is an improved method for analyzing partial-cured samples compared to conventional Differential Scanning Calorimetry (DSC). It was also demonstrated that cure monitoring of these fast-cure materials was feasible using both DEA and FBG techniques. Adhesion study showed good correlation of adhesion strength and failure modes with degree of cure. Failure mode changes from mixed to cohesive mode at 50% degree of cure. Above 90% degree of cure, adhesion strength was found to surpass the shear strength of silicon substrate. These results clearly emphasize the importance of cure optimization to attain sufficient adhesion strength of these adhesives. For cure shrinkage measurement, feasibility of both FBG and Thermomechanical Analysis (TMA) techniques was demonstrated. In summary, this study has demonstrated the applicability of several techniques for cure behaviour characterization of fast-cure ACA and NCA materials. Key findings from this work represent a significant step towards cure process optimization for the development of reliable adhesives for flip chip interconnects.

Keywords

Conductive adhesives, fast-cure, cure monitoring, cure shrinkage, adhesion, process optimization

1. Introduction

Flip chip interconnects formed using adhesives have been recognized as a promising substitute for solder interconnects because of their fine-pitch, lead-free and low-temperature processing capabilities. The two leading candidates for adhesive flip chip technology include anisotropic conductive adhesives (ACAs) and non-

* Tel.: +65 68664058; Fax: +65 68400626; e-mail: mary.teo@infineon.com

conductive adhesives (NCAs) [1, 2]. Both ACAs and NCAs are comprised of a fast-cure thermosetting epoxy matrix, with ACAs also containing a small amount of electrically conductive particles. Unlike a solder flip chip joint, an adhesive interconnect is a non-metallurgical joint and its reliability performance depends largely on the adhesion strength and resultant compressive force arising from the applied load during flip chip bonding, adhesive cure shrinkage and thermal shrinkage during the cool-down process. The compressive force is essential to establish stable and low resistance electrical connections [3, 4]. Of the three factors mentioned, cure shrinkage is the most complex to determine, and has attracted considerable interest in recent years [5–9]. For adhesion strength measurement, the most commonly used techniques are die shear test and lap shear test [10, 11]. It has been highlighted in several studies that adhesion strength is largely influenced by degree of cure of the adhesive [12–18]. Therefore, an optimized cure process is critical to achieve the ultimate performance and reliability of these adhesive joints.

Typically, ACAs and NCAs are formulated to achieve a complete cure in less than 60 s when curing between 180 and 250°C. The fast-cure characteristic of these adhesives poses great difficulties for conventional cure characterization techniques. Currently, there is no well-established method for cure monitoring of such fast-cure materials even though cure characterization of ACAs and NCAs is crucial for development of reliable adhesive flip chip joints.

Differential Scanning Calorimetry (DSC) is widely used for cure kinetics study of polymeric materials. There are two main methods for DSC cure kinetics study: isothermal cure and dynamic scan [20, 21]. Due to the equipment stabilization time (typically a few minutes) and difficulty to establish a cure model for commercial adhesives, DSC cure kinetics is not suitable for characterization of fast-cure ACAs and NCAs [19]. The other method, which is more tedious, is to prepare samples with different cure profiles and measure the residual heat. An optimized cure profile is established when no residual heat can be detected. However, conventional DSC has some limitations for analyzing partial-cured samples. One common problem encountered is when the glass transition temperature (T_g) overlaps with the temperature range of the residual heat exotherm, rendering difficulties in analysis of results. The Modulated DSC (MDSC) can circumvent this limitation by separating the heat flow of reversing reactions such as T_g from non-reversing reactions such as curing [22].

Two other techniques for cure monitoring are the Dielectric Analysis (DEA) and Fibre Bragg Grating (FBG) techniques. Both techniques have high sensitivity for cure monitoring and high potential for *in situ* measurements since the sensors can be embedded into the adhesive during actual process. DEA uses electrodes in contact with the adhesive to monitor the intrinsic electrical properties of the material due to chemical and physical changes during cure [21, 22]. High resolution strain measurement using embedded FBGs is also increasingly being investigated for monitoring cure progress and process-induced strains [24]. To the knowledge of the author, there is currently very limited literature on the use of FBG technique

for cure monitoring and shrinkage measurement of ACAs and NCAs. So far, cure shrinkage measurement for conductive adhesives has only been reported using the Thermomechanical Analysis (TMA) [6–9].

The objective of this study was to establish the methodologies to characterize the fast-cure behaviour of ACA and NCA materials. To overcome limitations of conventional cure characterization methods, novel cure monitoring techniques such as MDSC, DEA and FBG were evaluated. Cure shrinkage measurements were conducted using both FBG and TMA techniques. The correlation between degree of cure, adhesion strength and failure mode was also established.

2. Experimental

2.1. Materials

Four ACA and NCA materials, listed in Table 1, were evaluated in this study. The selected materials included two non-conductive pastes (NCPs), one anisotropic conductive paste (ACP) and one anisotropic conductive film (ACF).

2.2. Degree of Cure Characterization Using MDSC

In this study, the cure temperature was predefined at 220°C. Degree of cure characterization was conducted to determine the cure duration required. Cure durations of 5, 10, 15, 20, 30 and 40 s were evaluated. Samples for analysis were prepared using the actual flip chip bonder (Panasonic KME FB35W-M). Two aluminium blocks ($10 \times 10 \times 1$ mm thick) with Teflon tapes on both sides were used to sandwich the adhesive, as illustrated in Fig. 1. After curing for the required duration, the adhesive was removed for analysis. MDSC experiments were conducted on a TA Instruments 2910 MDSC equipment using a heating rate of 5°C/min, a modulation amplitude of $\pm 1^\circ\text{C}$ and a modulation period of 60 s. The size of the sample used in the analysis was typically about 5 mg.

2.3. Adhesion Study

Adhesion strength at various degrees of cure was evaluated by the die shear test. The test samples (4 × 4 mm silicon die on 10 × 10 mm silicon substrates) were prepared using the actual flip chip bonder (Panasonic KME FB35W-M). A customized fixture

Table 1.
Some information on ACA and NCA materials

Material	Type	Recommended cure profile
1	NCP	220°C/5 s
2	NCP	240°C/4 s
3	ACP	200°C/10–15 s
4	ACF	220°C/5 s

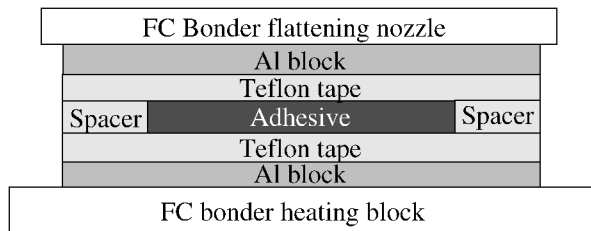


Figure 1. Sample preparation for degree of cure analysis.

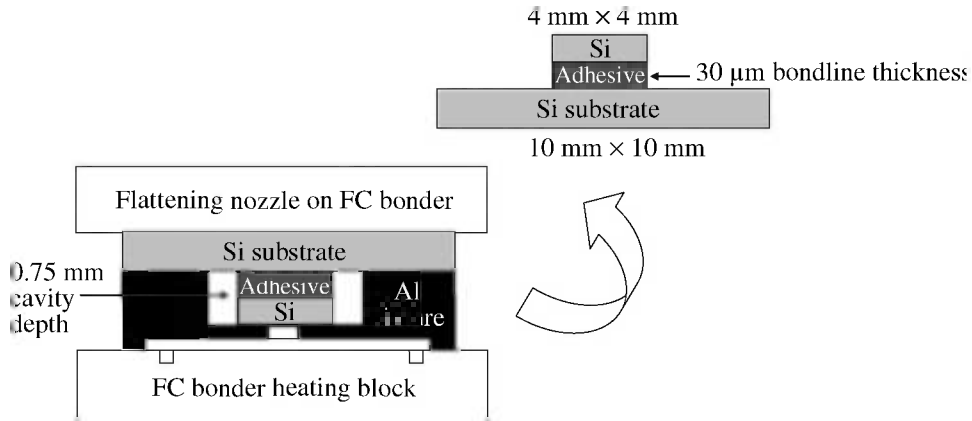


Figure 2. Sample preparation for adhesion test.

was used to prepare the test samples with a controlled adhesive bondline thickness of $30 \mu\text{m}$ with minimum fillet, as shown in Fig. 2. The cure durations at 220°C were 5, 10, 20, 30 and 40 s. Die shear test was conducted on a Dage 4000 shear tester using a shear speed of $100 \mu\text{m}/\text{s}$. For each cure duration, 5 samples were sheared and the failure modes observed under an optical microscope at $20\times$ magnification.

2.4. Evaluation of In Situ Cure Monitoring Techniques

The two potential techniques for *in situ* cure monitoring are DEA and FBG. In this feasibility study, instead of incorporating the sensors in the flip chip bonder, cure monitoring was conducted using a preheated oven maintained at 220°C .

DEA experiments were conducted using a Netzsch DEA 231/1 equipment with a sampling rate of 55 ms. A thin layer of adhesive was spread onto an interdigitated sensor (Netzsch INDEX 066S) for measurement purpose. Data collection was started before the sensor with the adhesive was placed in the preheated oven to avoid missing the initial cure reaction.

The setup for FBG experiments includes an FBG interrogation unit (ElectroPhotonics Corporation FLS 3100) used to illuminate the Bragg grating and monitor the reflected wavelength and a PC with real-time data capture *via* a National Instruments data acquisition card with a data interval of 10–35 ms. For FBG measure-

ments, a sealant mold ($40 \times 80 \times 3$ mm) was first formed on an aluminium base covered with Teflon impregnated fabric. V-shaped grooves were cut to accommodate short lengths of Teflon tubings to ensure placement of the FBG sensors to allow free fibre expansion and contraction. A thin-film platinum resistance thermocouple (PRT) was placed close to the FBG for temperature monitoring, as shown in Fig. 3. After the mold was filled with the adhesive, the FBG was pulled tautly and then allowed to relax to its natural length. Similarly, data capture was initiated before the sample was introduced into the preheated oven to avoid missing any critical curing event.

2.5. Cure Shrinkage Characterization

The FBG and TMA techniques were used for cure shrinkage measurements. The same experiment as used for FBG cure monitoring also provided cure shrinkage results in terms of FBG strains. The experimental setup used for TMA is illustrated in Fig. 4. The adhesive was sandwiched between two silicon slides. TMA experiments were conducted on a TA Instruments 2940 TMA unit with a heating rate of $5^{\circ}\text{C}/\text{min}$ and an applied load of 0.5 N.

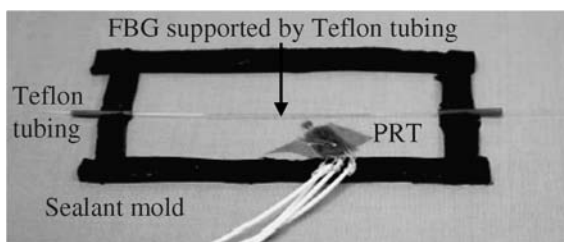


Figure 3. Setup for FBG measurement.

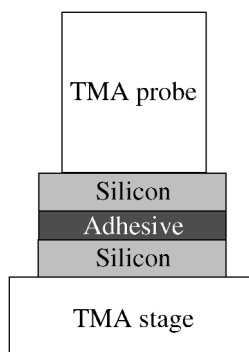


Figure 4. Setup for TMA measurement.

3. Results and Discussion

3.1. DSC and MDSC Analyses

The MDSC results obtained for a partial-cured sample are presented in two ways to illustrate how MDSC improves the analysis of partial-cured sample. A typical result obtainable from a conventional DSC experiment is shown in Fig. 5. Notice how the overlapping T_g transition makes it difficult to determine the area of the residual heat exotherm accurately. Figure 6 shows the result obtained with an MDSC run,

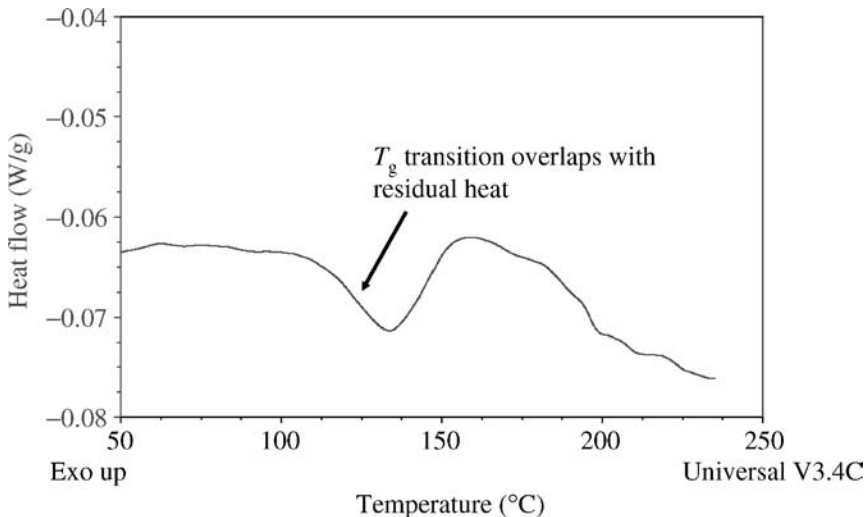


Figure 5. Conventional DSC result.

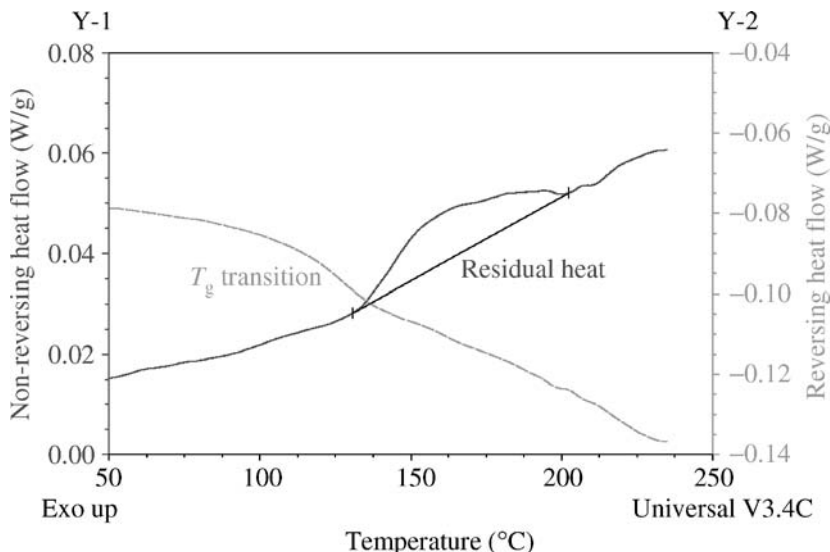


Figure 6. MDSC results show separation of T_g transition and residual heat exotherm.

where the total heat flow can be separated into reversing and non-reversing heat flows. With the separation of the reversing T_g transition, the analysis of the residual heat can be done with more certainty. Therefore, the MDSC is clearly an improved technique over conventional DSC for partial-cured sample analysis.

3.2. Degree of Cure from MDSC Analysis

The degree of cure (DOC) can be calculated using equation (1) by comparing the total heat of reaction for the as-received uncured sample to the residual heat for a partial-cured sample. Figure 7 shows typical MDSC results used for degree of cure calculation. The degree of cure as a function of curing duration for the 4 adhesives investigated is presented in Fig. 8. The required cure duration is determined by selecting the time taken to achieve >90% degree of cure. It can be seen from Table 2 that the required cure duration is typically longer than the recommended curing profiles from the suppliers. This further emphasizes the need for cure process optimization of these ACA and NCA adhesives:

$$\text{DOC}(\%) = 100 * \frac{\Delta H_T - \Delta H_R}{\Delta H_T}, \quad (1)$$

where ΔH_T = area under the curve for as-received sample, ΔH_R = area under the curve for partial-cured sample.

3.3. Adhesion Study

The die shear test results for all four materials show that adhesion strength increases with the degree of cure, and it plateaus close to 90% degree of cure. Examination of the failure mode reveals a mixed mode failure (interfacial and cohesive) at low degree of cure and the failure mode becomes cohesive failure at 50% degree of cure,

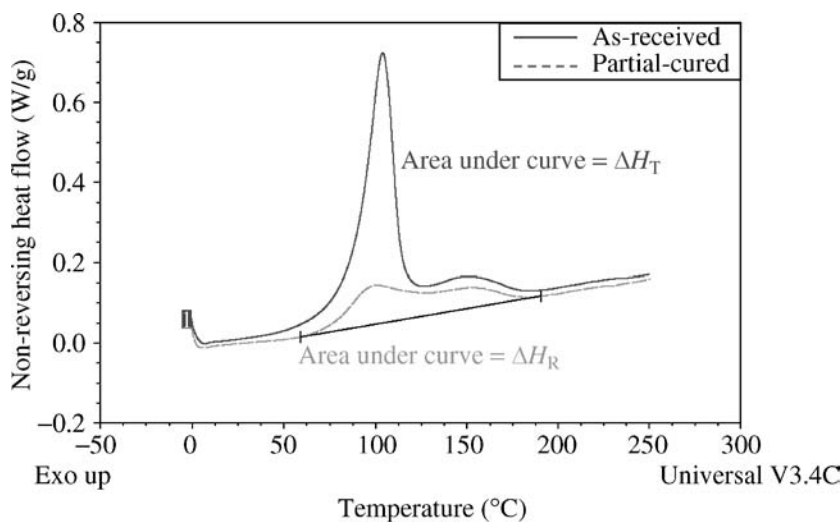


Figure 7. MDSC results for degree of cure analysis.

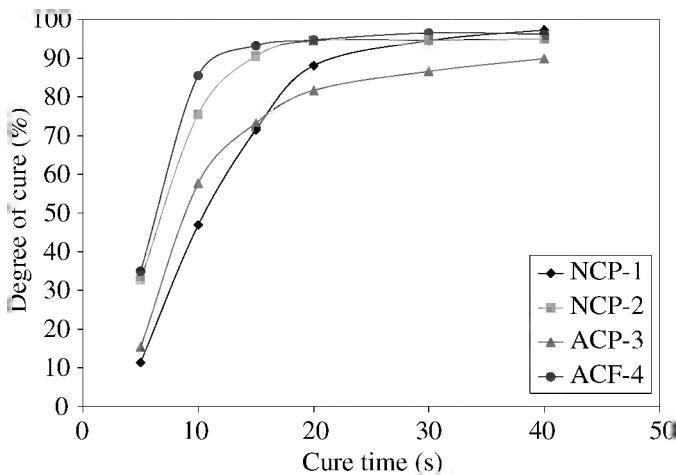


Figure 8. Degree of cure as a function of cure time for the four adhesive investigated.

Table 2.

Cure time required at 220°C to achieve >90% degree of cure

Material	Recommended cure profile	Cure time required
NCP-1	220°C/5 s	30 s
NCP-2	240°C/4 s	15 s
ACP-3	200°C/10–15 s	40 s
ACF-4	220°C /5 s	15 s

as shown in Fig. 9. Silicon failure is predominantly observed above 90% degree of cure and thus implies that adhesion strength surpasses shear strength of the silicon substrate. Hence, it is clear that an optimized cure progress is critical to attain sufficient adhesion for these fast-cure adhesives.

3.4. Feasibility of In Situ Cure Monitoring Techniques

The two potential *in situ* cure monitoring techniques evaluated were DEA and FBG. For this study, cure monitoring was conducted in a preheated oven maintained at 220°C to evaluate the feasibility of both techniques for such fast-cure materials.

A typical DEA result is shown in Fig. 10. The ion viscosity (IV) is a measure of the mobility of ions in the material, and is directly related to material viscosity prior to gelation and to rigidity after gelation [24]. When curing starts, the ion viscosity starts to increase, until it reaches a plateau where curing is then completed. The cure duration is taken as the time between the minimum and maximum of the ion viscosity. The DEA was able to detect this clear transition for all the four adhesives tested.

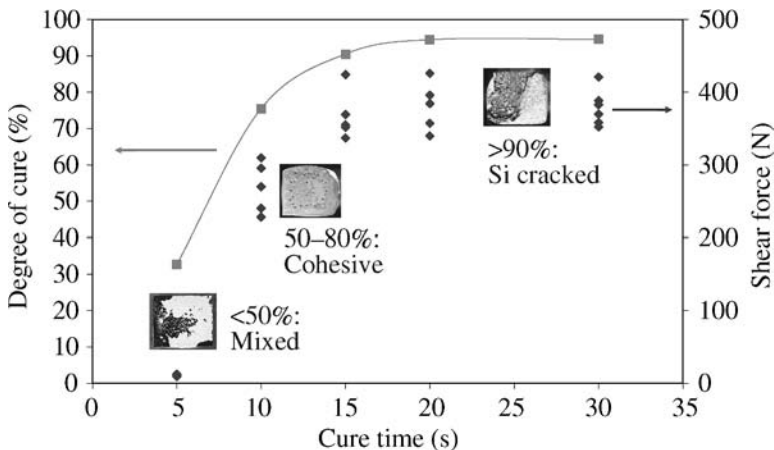


Figure 9. Adhesion strength and failure modes at different degrees of cure.

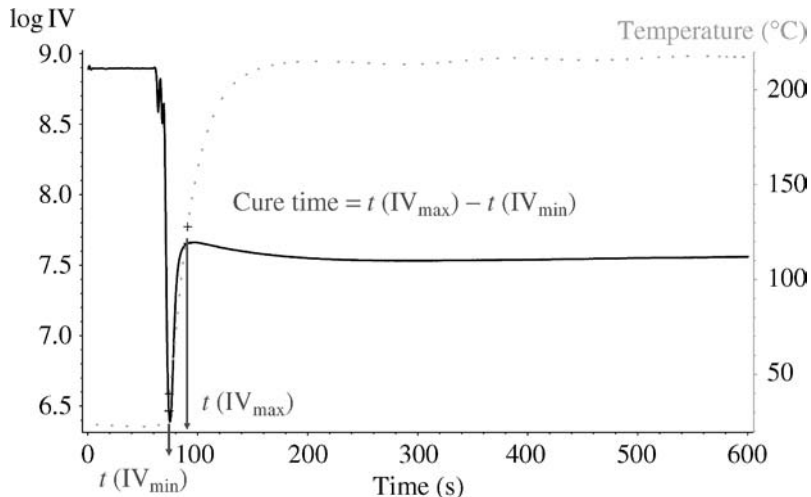


Figure 10. Typical DEA result showing cure time taken as the time between minimum and maximum of ion viscosity (IV).

A typical FBG result is shown in Fig. 11. The Platinum Resistance Thermometer (PRT) temperature shows a sharp increase upon entering the oven. The FBG sensor shows no strain since the material has low viscosity and does not impart any strain to the FBG sensor. As the viscosity increases until gel point, the FBG sensor deviates from the zero strain value where cure shrinkage is expected to occur at this stage. However, the large temperature exothermic spike overlaps with the cure shrinkage stage and camouflages the expected compressive cure shrinkage strain. Due to these competing processes, the determined cure shrinkage is a conservative estimate of the absolute cure shrinkage. After cure completion, the strain again increases due

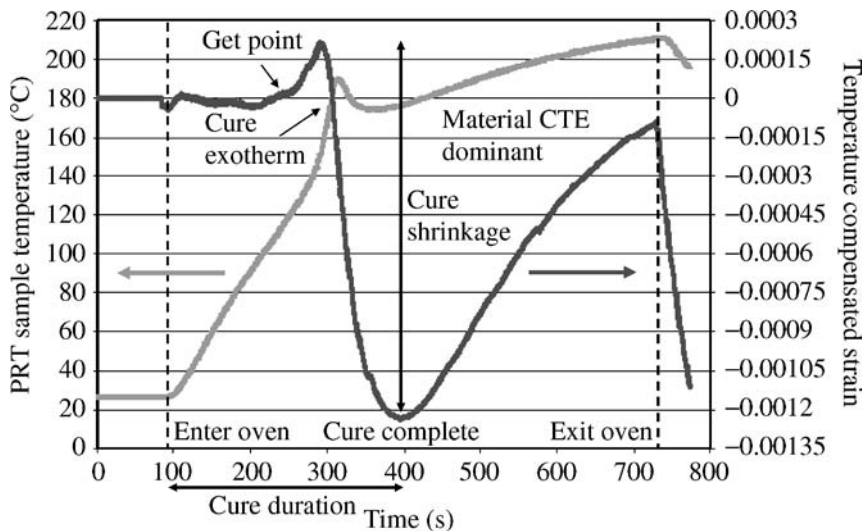


Figure 11. Typical FBG result showing cure duration taken as the time to reach minimum strain.

to the dominating CTE effect from the cured adhesive. Therefore, the cure duration is taken as the time to reach minimum strain.

Results from both DEA and FBG techniques show that fast-cure characterization is feasible within certain accuracy. However, the use of a preheated oven in the current study did not reflect true isothermal cure monitoring at the desired 220°C. Since both DEA and FBG sensors can be incorporated into the actual flip chip bonder, both techniques have high potential for *in situ* cure monitoring and cure process optimization of these fast-cure adhesives.

3.5. Cure Shrinkage Derived from FBG and TMA Analyses

The overlay of the TMA and DSC results for a paste adhesive is shown in Fig. 12. There is an initial shrinkage due to viscosity drop of the paste material with increasing temperature as shown in Region I. Once curing starts, as indicated by the cure onset from DSC result, cure shrinkage becomes the predominant factor in Region II. After curing is completed, an expansion is detected due to the Coefficient of Thermal Expansion (CTE) effect from the cured adhesive as indicated by Region III.

The overlay of the TMA and DSC results for the ACF film material is shown in Fig. 13. Since the film is in B-stage, there is no initial shrinkage. Instead, the initial expansion is due to the CTE of the B-stage film as represented by Region I. Once the cure onset temperature is reached, cure shrinkage of the adhesive can be detected in Region II. Similarly, after cure completion, an expansion is again detected due to the CTE of the cured film as in Region III.

A comparison of the cure shrinkage measurements from FBG and TMA techniques is provided in Table 3. The correlation factor R^2 , calculated based on equa-

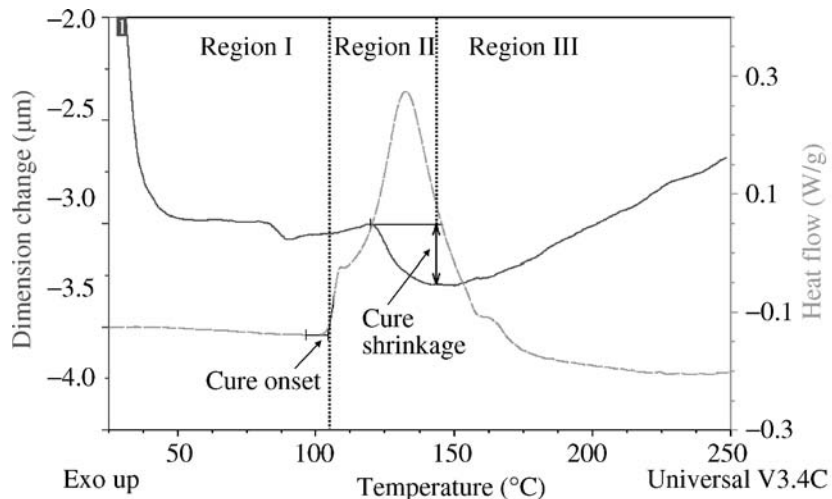


Figure 12. TMA and DSC results for ACP. Region I represents initial shrinkage due to viscosity drop, Region II is dominated by the ACP cure shrinkage, Region III is dominated by CTE of the cured ACP.

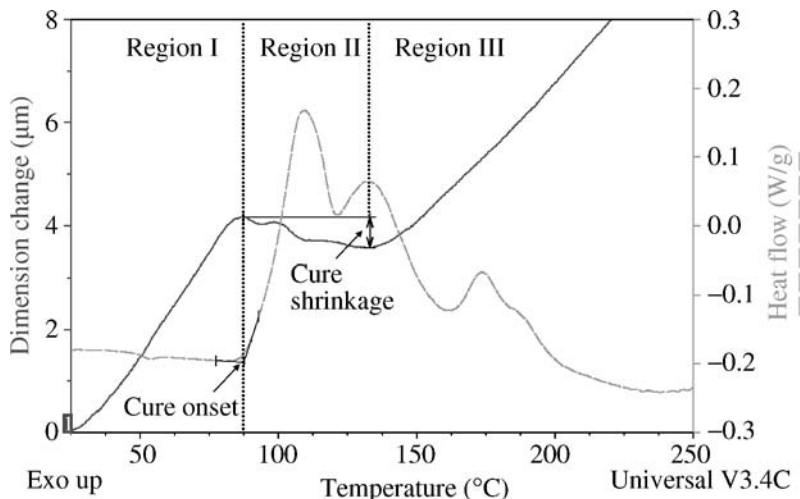


Figure 13. TMA and DSC results for ACF. Region I represents initial expansion due to CTE of the B-staged ACF, Region II is dominated by the ACF cure shrinkage, Region III is dominated by CTE of the cured ACF.

tion (2), is 0.83. Therefore, cure shrinkage results obtained from both techniques were in good agreement, with the measured shrinkage for the four adhesives following the same trend:

$$\text{NCP-2} \sim \text{ACP-3} > \text{NCP-1} > \text{ACF-4},$$

$$R^2 = \left[\frac{\sum(x - \bar{x})(y - \bar{y})}{\sqrt{\sum(x - \bar{x})^2 \sum(y - \bar{y})^2}} \right]^2, \quad (2)$$

Table 3.
Cure shrinkage results

Material	TMA shrinkage (%)	FBG shrinkage (μ strain)
NCP-1	2.0	1147
NCP-2	4.4	3526
ACP-3	3.3	3932
ACF-4	0.9	556

where x and y = data in array 1 and array 2 respectively, \bar{x} and \bar{y} = mean of data in array 1 and array 2, respectively.

4. Conclusion

In this study, several novel techniques were evaluated for cure characterization of fast-cure ACA and NCA materials. Degree of cure analysis showed that MDSC was an improved method for analyzing partial-cured samples compared to conventional DSC. Adhesion study showed that shear strength increases with the degree of cure, with failure mode changing from mixed to cohesive at 50% degree of cure. Above 90% degree of cure, the adhesion strength was found to surpass the shear strength of silicon substrate. Hence, it is clear that an optimized cure process is critical to attain sufficient adhesion for these fast-cure adhesives. It was also demonstrated that it is feasible to apply DEA and FBG techniques in cure characterization for these fast-cure adhesives. It is worth noting that both DEA and FBG techniques have potential for *in situ* cure monitoring since the sensors can be embedded into the adhesive during the flip chip bonding process. For cure shrinkage measurement, feasibility of FBG was demonstrated in addition to using TMA which has been reported in prior work. Cure shrinkage results obtained using both techniques were found to be in good agreement. In summary, this study has demonstrated the feasibility of several methodologies for cure behaviour characterization of fast-cure ACA and NCA materials. Key findings from this work represent a significant step towards cure process optimization for the development of reliable adhesive flip chip interconnects.

Acknowledgements

The author would like to thank Dr Harald Preu (Infineon, Regensburg, Germany) for conducting the DEA analysis, and Maria Lodeiro (National Physical Laboratory, UK) for conducting the FBG analysis. Special thanks to Yu Hong (Nanyang Technological University, Singapore) for his helpful discussion on TMA measurements. Finally, the author would like to thank the management of Infineon Technologies Pte Ltd for supporting this work.

References

1. J. Liu, in: *Proc. 1996 International Electronics Packaging Society Conf.*, pp. 483–501 (1996).
2. J. Liu, Z. Lai, H. Kristiansen and C. Khoo, in: *Proc. 3rd IEEE International Conference on Adhesive Joining and Coating Technology in Electronics Manufacturing*, pp. 1–18 (1998).
3. R. R. Gomatam and E. Sancaktar, *J. Adhesion Sci. Technol.* **18**, 1245–1261 (2004).
4. E. Sancaktar and Y. Wei, *J. Adhesion Sci. Technol.* **10**, 1221–1235 (1996).
5. K. W. Lee, H. J. Kim, M. J. Yim and K. W. Paik, in: *Proc. 56th IEEE Electronic Components and Technology Conf.*, pp. 918–923 (2006).
6. H. Yu, S. G. Mhaisalkar and E. H. Wong, *J. Electronic Mater.* **34**, 1177–1182 (2005).
7. H. Yu, S. G. Mhaisalkar and E. H. Wong, *J. Mater. Res.* **20**, 1324–1329 (2005).
8. W. S. Kwon, S. Y. Yang, S. B. Lee, K. W. Paik, in: *Proc. 55th IEEE Electronic Components and Technology Conf.*, pp. 1468–1474 (2005).
9. D. Lu, Q. K. Tong and C. P. Wong, in: *Proc. 6th IEEE International Symposium of Advanced Packaging Materials*, pp. 2–10 (1999).
10. K. L. DeVries and P. R. Borgmeier, in: *Handbook of Adhesive Technology*, A. Pizzi and K. L. Mittal (Eds), pp. 65–91. Marcel Dekker, New York, NY (1994).
11. S. Luo and C. P. Wong, *J. Adhesion Sci. Technol.* **18**, 275–285 (2004).
12. L. Cao, Z. Lai and J. Liu, in: *Proc. 2004 IEEE CPMT High Density Microsystem, Design, Packaging and FA Conf.*, pp. 254–258 (2004).
13. C. G. L. Khoo, J. Liu, M. Agren and T. Hjertberg, in: *Proc. 1996 International Electronics Packaging Society Conf.*, pp. 483–501 (1996).
14. D. Klosterman, L. Li and J. E. Morris, *IEEE Trans. CPMT-A* **21**, 23–31 (1998).
15. M. J. Rizvi, Y. C. Chan, C. Bailey, H. Lu and A. Sharif, *J. Soldering Surface Mount Technol.* **17**, 40–48 (2005).
16. S. X. Wu, C. Zhang, C. P. Yeh, S. Willie and K. Wyatt, in: *Proc. 47th IEEE Electronic Components and Technology Conf.*, pp. 550–553 (1997).
17. M. A. Uddin, M. O. Alam, Y. C. Chan and H. P. Chan, *J. Microelectronics Reliability* **44**, 505–514 (2003).
18. H. Yu, S. G. Mhaisalkar, E. H. Wong, L. K. Teh and C. C. Wong, *IEEE Trans. CPT* **29**, 71–79 (2006).
19. Y. C. Chan, M. A. Uddin, M. O. Alam and H. P. Chan, *J. Electronic Mater.* **32**, 131–136 (2003).
20. D. N. S. Hon, in: *Handbook of Adhesive Technology*, A. Pizzi and K. L. Mittal (Eds), pp. 129–150. Marcel Dekker, New York, NY (1994).
21. Thermal Analysis Review: DSC Kinetics Methods, TA Instruments Application Note TA073.
22. Modulated Differential Scanning Calorimetry (MDSC) Compendium: Basic Theory and Experimental Considerations, TA Instruments Application Note TA210.
23. J. W. Kwon, W. S. Chin and D. G. Lee, *J. Adhesion Sci. Technol.* **17**, 2111–2130 (2003).
24. M. J. Lodeiro and M. G. Gain, *Application of Dielectric and Fibre Bragg Grating Strain Measurements to Cure Monitoring*, National Physical Laboratory Measurement Note MATC (MN) 53 (2003).

This page intentionally left blank

Chemorheology of Epoxy/Nickel Conductive Adhesives During Processing and Cure

Jianguo Zhou and Erol Sancaktar*

Department of Polymer Engineering, The University of Akron, Akron, OH 44325-0301, USA

Abstract

Epoxy/nickel adhesives can be used as integrated circuit (IC) packaging material due to their lower cost than epoxy/silver adhesives with acceptable electrical conductivity. In this work, chemorheological behaviors of Epon 830/Ni/diethylenetriamine (DETA) adhesives were investigated during processing and cure, as a function of shear rate, resin conversion, Ni volume fraction and temperature. A strongly nonlinear characteristic of filled epoxy/Ni systems was revealed, and a steady shear had to be employed for chemorheological analyses. A strongly non-Newtonian flow behavior was observed for epoxy/Ni adhesives also during cure. The power law model, Castro–Macosko model, Liu model and the Arrhenius model adequately describe, respectively, the effects of shear rate, resin conversion, filler volume fraction and temperature on chemoviscosity. A comprehensive model combining these individual models predicts the isothermal chemoviscosity data well and the nonisothermal data reasonably. A modified comprehensive model was also proposed in this work to improve the model fit to nonisothermal experimental data.

Keywords

Epoxy/Ni conductive adhesives, chemorheological behavior, steady shear, chemoviscosity modeling

1. Introduction

Application of Ni/epoxy conductive adhesives to integrated circuit (IC) packaging is closely related to their chemorheological behavior during processing and cure, which includes effects, at least, from temperature, shear rate, resin conversion and filler concentration in adhesives. Due to the complexity of the flow and gelation behaviors of highly filled thermosets, trial-and-error method has been traditionally employed, leading to high design and raw material costs. A scientific chemorheological model for this process will clearly be important for the design, process control and optimization purposes.

Electrically conductive adhesives have gained significant attention during the last decades due to their increased usage in electronics industry to replace lead soldering [1–18]. Theoretical and experimental studies have been performed on basic conduc-

* To whom correspondence should be addressed. Tel.: (330) 972-5508; e-mail: erol@uakron.edu

tion mechanisms [1–8]; the effects of particle size, shape and type [3–8]; behavior in the bonded form [5, 7–15]; processing effects, such as pressure [1, 3, 8], adhesive film thickness [2, 4, 7], silver coating [3, 4, 6], anisotropic alignment of nickel particles in magnetic field [16]; as well as the possibility of using polymeric emeraldine salt particles as conductive fillers [17]. Ni/epoxy conductive adhesives can be used in integrated circuit (IC) packaging due to their lower cost than Ag/epoxy adhesives, with acceptable electrical conductivity, high thermal conductivity and low thermal expansion. Furthermore, silver-filled conductive adhesives suffer from the problem of silver migration, which may lead to failure in electrical conduction [18]. Because of highly filled nature of thermosets, their chemorheological behavior becomes complicated and much research work is still needed to describe it accurately. It is well known that process conditions affect the mechanical performance of thermosetting adhesives in general [19–23], and mechanical as well as conductive performance of electrically conductive adhesives in particular [5, 7–15].

Halley and Mackay [24] presented an extensive review of common chemorheological techniques and measurement systems for unfilled and filled thermoset resins. Wang *et al.* [25] developed a combined model for the traditional four-parameter model and modified WLF model for an epoxy-terminated poly(phenylene ether ketone) (E-PEK) and 4,4'-diaminodiphenyl sulfone (DDS) system in both isothermal and nonisothermal cure cycles. They also established a new five-parameter chemorheological model by introducing a proportionality factor in the four-parameter model to make the new model fit the experimental results well during the actual stepwise temperature cure cycle. Karkanas and Partridge [26] related a one-to-one relationship of T_g and resin conversion to cure kinetics of epoxy/amine systems, and employed a modified WLF equation to model the viscosity profiles at different isothermal cure temperatures with a very good degree of accuracy, by introducing a reference temperature in the WLF equation as an adjustable parameter. Ivankovic *et al.* [27] studied the curing kinetics and chemorheology of a low-viscosity laminating epoxy/anhydride system, developing a modified Kamal kinetic model and proposing a combination of WLF and Castro and Macosko models to describe the system viscosity as a function of temperature and resin conversion. The same viscosity model from isothermal data was employed to predict the viscosity change during the nonisothermal temperature cure cycle.

Filled thermosetting resins are two-phase systems, and their rheological behavior is determined by the properties of both phases, as well as by the interactions between the matrix and the filler. Ng and Manas-Zloczower [28] investigated the effects of silica filler loadings on the reaction kinetics and rheological behavior of epoxy-molding compounds by isothermal parallel plate rheometry, and found the accelerating effect of filler on gelation and improvement of heat transfer for the system during cure. Halley [29] summarized a thorough chemorheological analysis of a typical IC packaging thermoset material, which included novel isothermal and nonisothermal multiwave parallel plate chemorheology, and the effect of experimental time at each frequency was considered. It is worth noting that in Halley's work,

the original Cox–Merz rule [30] was confirmed and applied to correlate dynamic viscosities to steady shear viscosities. More recently, Dehnke *et al.* [31] applied chemorheology and kinetic measurements to establish a process window for a solventless epoxy injection pultrusion system, and developed viscosity expressions as a function of temperature, degree of cure and filler content. Ganguli *et al.* [32] conducted chemorheological studies to characterize the effect of organically modified silicates on the cure behavior of cyanate ester resin nanocomposites, and suggested the catalytic effect of clay on curing as revealed by decreases in gel times and activation energies of cure. The filler concentration effect, however, has not been incorporated into a complete chemorheological model so far to predict the viscosity as a function of temperature, shear rate, resin conversion and filler concentration during processing and cure of highly filled thermoset resins.

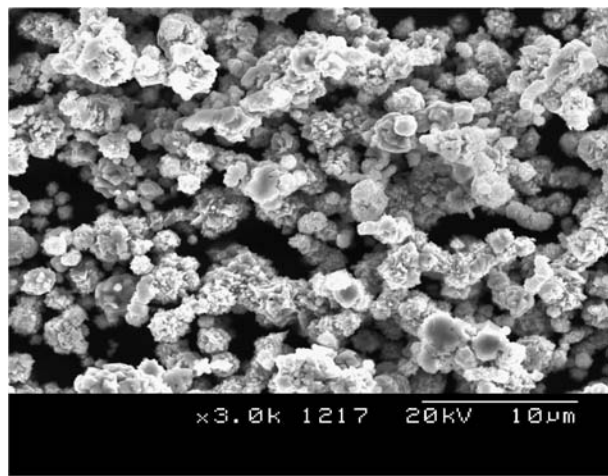
A nonlinear response is also typical of many highly filled thermosetting resins, as noted by Malkin [33] who expressed doubts about the validity of dynamic shear tests for many highly filled materials due to their complex nonlinear nature. Actually, for highly filled epoxy/nickel systems in this study, there is no linear viscoelastic region over the whole dynamic (oscillating) strain and frequency ranges within the instrument limit. Thus, unlike many other chemorheological studies, a steady shear had to be employed here, instead, to investigate the effect of shear rate on the viscosity change.

The objective of this study was, therefore, to characterize and model the chemorheological viscosity as a function of temperature, shear rate, resin conversion and filler concentration for highly filled epoxy/nickel/DETA conductive adhesive systems during processing and cure. This chemorheological study was performed by means of differential scanning calorimetry (DSC) and steady shear parallel plate rheometry in both isothermal and nonisothermal temperature cure cycles. To our knowledge, this is the first study on the chemorheology of highly filled epoxy/nickel conductive adhesives and incorporation of the filler concentration effect under steady shear into a comprehensive chemorheological model.

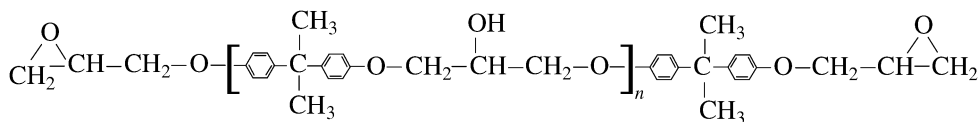
2. Experimental

2.1. Materials

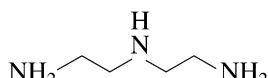
The highly filled conductive adhesives used in this study were Epon 830/Ni systems with 50%, 55% and 60 wt% of Ni. These three filler concentrations are above the electrical conductivity percolation threshold. The diglycidyl ether of bisphenol A (DGEBA) epoxy resin, Epon 830, as received from Miller–Stephenson (Danbury, CT) has epoxide equivalent weight of 190–198, viscosity of 16.8 Pa s and density of 1.16 g/cm³ at 25°C. The Ni 102 flakes (Fig. 1(a)), with an average diameter of 3 µm and apparent density of about 2.2 g/cm³, were used as received from Atlantic Equipment Engineers, Division of Micron Metals, Inc. (Bergenfield, NJ). The curing agent, diethylenetriamine (DETA) was received from Resolution Performance Products (Houston, TX) with molecular weight of 103 g/mol. The chemical



(a)



(b)



(c)

Figure 1. (a) Morphology of the nickel flakes used in this study and chemical structures of (b) the epoxy resin, Epon 830: $n = 0.17$ and (c) curing agent, DETA.

structures of epoxy resin and curing agent are presented in Fig. 1(b) and 1(c), respectively.

Epon 830 was thoroughly mixed with nickel flakes according to the desired filler weight ratios at room temperature, followed by the addition of diethylenetriamine (DETA) as the hardener at the mass ratio of 12 phr and mixed for another 2 min. This freshly prepared mixture was used for differential scanning calorimetry (DSC) and parallel plate rheometry measurements in both isothermal and nonisothermal temperature cures.

2.2. Characterization

2.2.1. DSC Measurements

The calorimetric measurements were done on TA MDSC 2920 equipment (TA Instruments, New Castle, DE) in a nitrogen atmosphere. The sample size was about 10 mg. Due to relatively small heat flow generated during cure at room temperature in DSC, resin conversions, α , of samples cured at room temperature (25°C)

for different time periods were measured from their residual heat through another dynamic temperature scan and calculated as:

$$\alpha = \frac{H_T - H_R}{H_T}, \quad (1)$$

where H_T is the total reaction heat obtained by dynamic scan of uncured sample from -10 to 300°C at a heating rate of $10^\circ\text{C}/\text{min}$, and H_R is the residual reaction heat of partially cured epoxide samples after 25°C cure for certain time periods. Here, the total reaction heat obtained for Epon 830/DETA system was 23.9 kcal/mol of epoxide, similar to the value obtained by other researchers on Epon 828/diamine system [28].

Dynamic DSC measurements can also provide useful kinetic information over a broad temperature range. The kinetic parameters can possibly be obtained from one scan trace. It is generally assumed that in curing reaction the heat evolved is directly proportional to the resin conversion, and the cumulative heat generated during the dynamic DSC measurement can be related to the resin conversion by:

$$\alpha = \frac{1}{H_T} \int_0^t \left(\frac{dH}{dt} \right) dt, \quad (2)$$

where α is the resin conversion at time t or temperature T , dH/dt is the heat flow rate per unit mass from DSC, and H_T is the total reaction heat for 100% resin conversion. A temperature scan from 25 to 300°C at a heating rate of $10^\circ\text{C}/\text{min}$ was employed and the conversion data obtained could be utilized in parallel plate rheometry measurements during similar nonisothermal temperature cures.

2.2.2. Rheometry

The rheological characterization was carried out using an Advanced Rheometric Expansion System (ARES) (Rheometric Scientific, Inc., Piscataway, NJ) dynamic viscosity spectrometer. Parallel plates with a diameter of 25 mm were used, covered by a layer of $11\text{ }\mu\text{m}$ thick high density polyethylene (HDPE) film for easier cleaning. Preliminary oscillation frequency and strain sweeps were conducted to determine the linear viscoelastic region and check the validity of the Cox–Merz rule. Dynamic time sweep was also employed to determine the gel point of neat resin by the moduli crossover method (shear storage modulus, G' = shear loss modulus, G'' or loss tangent, $\tan \delta = 1$). An angular frequency (ω) of 1 rad/s and an initial strain of 30% were applied. As the cure proceeded, the strain was progressively reduced to maintain the torque within the range of transducer response. The viscoelastic properties of the sample during cure, including the complex dynamic viscosity (η^*), and G' and G'' were monitored.

Isothermal and nonisothermal steady shear experiments were performed in an ARES rheometer under conditions identical to those in DSC. They were first carried out on samples of different resin conversions under isothermal cure and then extended to the nonisothermal temperature cure cycle. A gap of 0.5 mm was used throughout and about 2-min time was needed to reach the chamber temperature

equilibrium after the sample was inserted. A range of steady shear rates between 0.1 to 1.0 s⁻¹ was utilized throughout the study. The nonisothermal rheometry measurements were performed over a temperature range between 25 and 100°C at a ramp rate of 10°C/min, and the steady viscosity data were recorded until the torque exceeded the transducer response limit.

3. Results and Discussion

3.1. Basic Rheology

Due to the complexity of highly filled thermoset conductive adhesives, basic rheology of the material was investigated prior to extensive chemoviscosity tests. These preliminary measurements may include determination of linear viscoelastic region in dynamic shear measurement, validity of the Cox–Merz rule, and the presence of wall slip.

3.1.1. Linear Viscosity Region

Dynamic strain sweep tests were first undertaken to investigate the effect of strain ($\gamma\%$) on the dynamic viscosity (η^*) of Epon 830/Ni systems with 50 and 60 wt% of Ni without cure at room temperature, and to identify the linear viscoelastic region, where the viscosity was independent of strain. Figure 2 shows the strain effect on the dynamic viscosity for two weight ratios of Ni and at three oscillation frequencies (1, 10 and 100 rad/s). It is clear that there is no linear viscoelastic region over the whole investigated strain (0.05–100%) and frequency ranges (1–100 rad/s) within the instrument limit. The dynamic viscosity is found to be highly strain-dependent

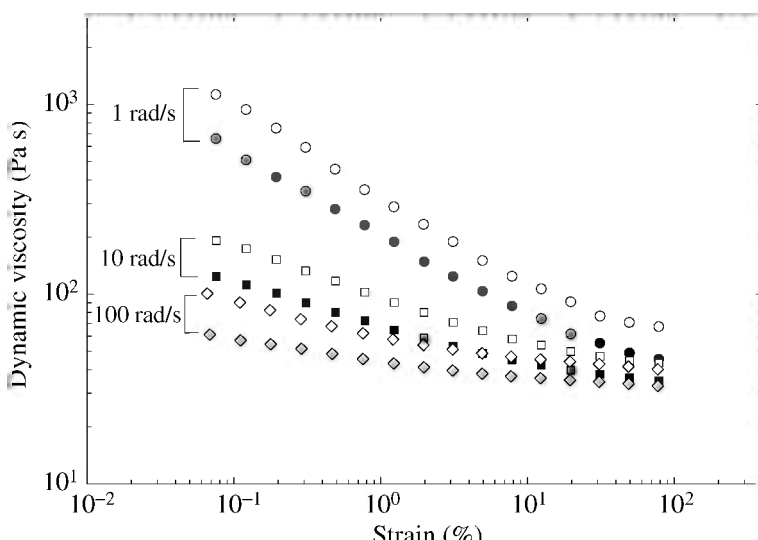


Figure 2. Effect of strain on dynamic viscosity, η^* , at three frequencies for Epon 830/Ni systems without cure at RT, where open symbols represent 60 wt% of Ni and filled symbols 50 wt% of Ni.

here as well as during cure (data not shown). Such a phenomenon is typical of many highly filled thermoset materials just as previously noted by Malkin [33].

3.1.2. Validity of the Cox–Merz Rule

Investigation on the validity of the Cox–Merz rule for presently studied systems was undertaken by comparing the responses from dynamic viscosity and steady shear sweep experiments. The Cox–Merz rule states that the steady viscosity is equal to the dynamic viscosity at equivalent shear rates or frequencies, as $\eta(\dot{\gamma}) = \eta^*(\omega)$. This rule has been confirmed for many materials, including some filled epoxy resin systems [29, 34]. Also, a modified Cox–Merz relationship was first found by Philipoppoff [35] and later by others for highly filled materials [36, 37], stating that the steady shear viscosity is equal to the dynamic viscosity at equivalent effective shear rates, as $\eta(\dot{\gamma}) = \eta^*(\gamma\omega)$, where γ is the dynamic shear strain amplitude.

However, a comparison between the dynamic and steady shear viscosities for Epon 830/Ni systems in this study indicates no clear correlation between them. As shown in Fig. 3, neither the original Cox–Merz rule nor the modified Cox–Merz rule holds over the whole investigated frequency and strain ranges, further emphasizing the strong nonlinear nature of highly filled thermoset resins, while the Cox–Merz rule holds for the unfilled Epon 830/DETA system during cure (data not shown here). Due to this strong nonlinearity, steady shear measurements had to be utilized for subsequent chemorheological analyses in this work.

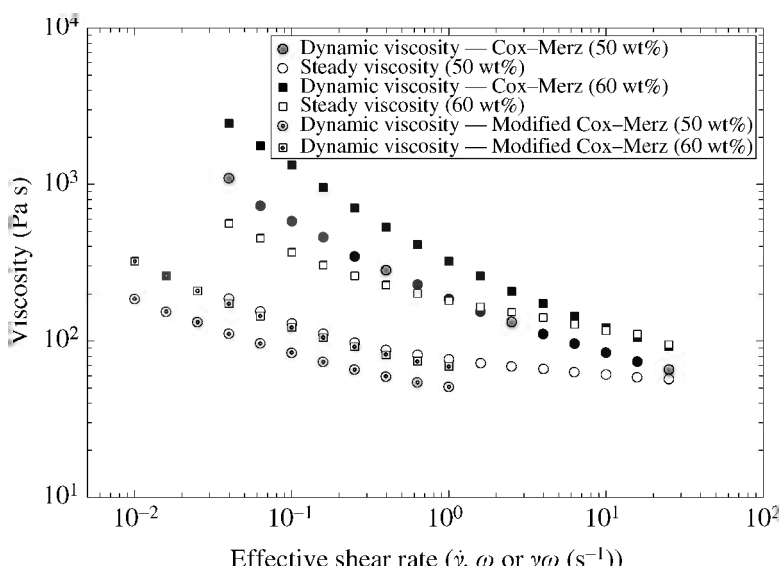


Figure 3. Comparison of the steady shear viscosity, η (shear rate, $\dot{\gamma}$, s^{-1}), dynamic viscosity, η^* (frequency, ω , s^{-1}), and dynamic viscosity, η^* (effective frequency, $\gamma\omega$, s^{-1}) based on Cox–Merz and modified Cox–Merz rules for Epon 830/Ni systems with 50 and 60 wt% of Ni without cure at RT. The strain employed in dynamic shear measurement was 1%.

3.1.3. Wall Slip

Steady shear sweeps were carried out at different gaps between the two parallel plates of the ARES rheometer to detect the presence of wall slip. If slip is present, the measured steady viscosity will increase as the gap increases and the slip velocity can be characterized [38]. Figure 4(a) and 4(b) shows the effects of gap on the steady viscosity for Epon 830/Ni systems with 50 and 60 wt% of Ni at room temperature (similar behavior was observed for 55 wt%, data not shown here). The shear rate range used was 0.01–10 s⁻¹ and the gap was varied from 0.5 to 1.5 mm.

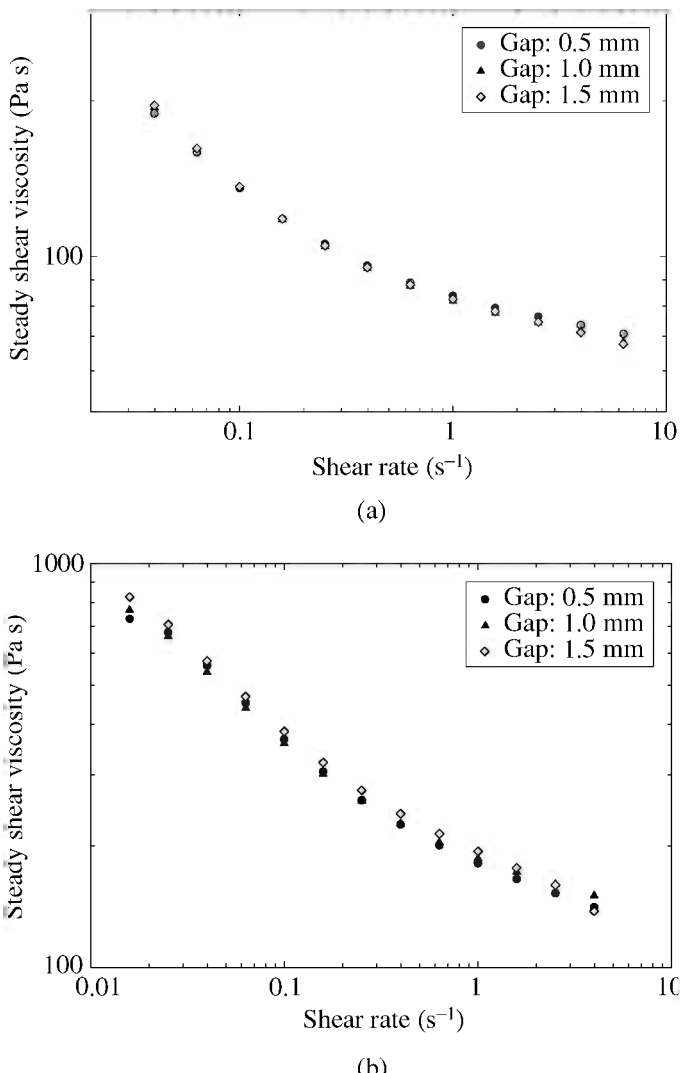


Figure 4. Effect of the rheometer plates gap on the steady shear viscosity for Epon 830/Ni systems with (a) 50 wt% and (b) 60 wt% of Ni, without cure at RT.

Clearly, there is no significant viscosity change by varying the gap over the limited shear rate range (sample fracture occurs at high rates) for epoxy/nickel systems, even at 60 wt% of Ni. Therefore, 0.5 mm gap was used throughout for convenience and the steady viscosity data could be utilized directly in the subsequent chemorheological analysis.

3.2. Gel Point

The gel point is defined as the time or temperature at which covalent bonds connect across the network and an infinite network is formed. When gelation initiates, the resin viscosity rises rapidly and an irreversible transition from a viscous liquid to an elastic solid occurs. Gelation does not inhibit the cure reaction. As the resin is cured beyond the gel point, the modulus of the network continues to increase until the network vitrifies, where the glass transition temperature (T_g) equals the cure temperature (T_c) and further reaction is prohibited due to the formation of a rigid glass.

Several methods have been proposed to detect the gel point, including independency of loss tangent on frequency, crossover of G' and G'' , inflection in G'' , and infinite steady viscosity [39]. For sub- T_g low temperature cure, vitrification possibly sets in close to the gel point and interferes with gelation, thus making rheological determination of the gel point complicated with moduli crossover never reached [39]. In this work, the moduli crossover method was employed and a crossover point was obtained for Epon 830/DETA system cured at room temperature (RT), as shown in Fig. 5, which indicates that a time interval may exist between the vitrification and gelation.

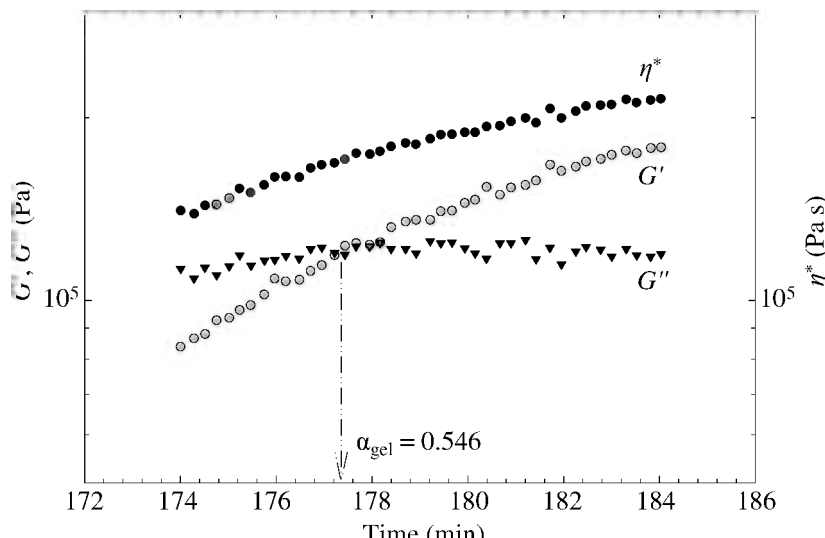


Figure 5. Gel conversion, α_{gel} , determination from crossover of G' and G'' for neat Epon 830/DETA (12 phr) system cured at RT. The dynamic viscosity, η^* , variation with time is also shown. The diameter of parallel plates is 25 mm and the gap used is 0.5 mm.

In Fig. 5, the crossover point occurs at a resin conversion level of 0.546, as calculated through the residual reaction heat from DSC. This roughly obtained value comes close to the theoretical value of 0.531, predicted for the system by using Flory's classical theory of gelation [40] as:

$$\alpha_{\text{gel}} = \frac{1}{[r(f-1)(g-1)]^{1/2}}, \quad (3)$$

where α_{gel} is the gel conversion, i.e., the resin conversion at the gel point; r is the stoichiometric ratio; f is the functionality of epoxide and g is the functionality of the amine curing agent. For current Epon 830/DETA (12 phr) system examined, r , f and g are 0.89, 2 and 5, respectively. These results indicate that the use of G'/G'' crossover method is probably appropriate.

The presence of filler was found to accelerate the curing reaction in filled thermoset resins, yet the gel conversions are about the same [28, 32]. Furthermore, the cure temperature generally does not change the gel conversion either. Therefore, the value of gel conversion obtained for neat epoxy was used throughout for all filled Epon 830/Ni/DETA adhesives, and at different cure temperatures in this work.

3.3. Chemorheological Tests

3.3.1. Isothermal Chemoviscosity

Isothermal chemoviscosity tests were first undertaken to examine the effects of steady shear rate ($\dot{\gamma}$), resin conversion (α) and nickel volume fraction (Φ) on the chemoviscosity of Epon 830/Ni/DETA systems at room temperature (25°C). Temperature effect was then incorporated within the temperature range of 30–50°C. These individual effects were first investigated by fits to individual models and then combined into a comprehensive model. Due to instrument limitations, the tests were conducted under the steady shear mode within the shear rate range of 0.3–1 s⁻¹, the resin conversion range of 0.06–0.36 and Ni volume fraction range of 0.35–0.44, corresponding to 50–60 wt%.

Shear Rate Effect. As discussed above, due to the lack of clear correlation between the dynamic and steady shear viscosities over the whole shear rate and strain ranges, steady shear had to be employed for the present chemorheological study. The shear rate range, however, was restricted by both instrument torque response limitation and sample fracture at high shear rates. Furthermore, relatively long time to stress equilibrium at low rates, as well as the shear and measurement times in one shear cycle, which need to be as small as possible during cure, also restrict the shear rate range. Thus, the shear rate range of 0.3–1 s⁻¹ was employed, and the time period used for four rates during one shear cycle (0.3, 0.5, 0.8 and 1 s⁻¹) was 10 s. The total time for the rheometer to complete one shear cycle was less than 25 s.

The shear rate effect on chemoviscosity, η_{sr} , has been described by the power law model, given by the following equation, at different resin conversions

($\alpha = 0.06\text{--}0.36$) and Ni volume fractions ($\Phi = 0.35\text{--}0.44$) at room temperature, for our data:

$$\eta_{sr} = A\dot{\gamma}^{n-1}, \quad (4)$$

where A is the power law constant and n is the power law index.

Figure 6(a) shows the shear rate effect on neat Epon 830/DETA system cured at room temperature (RT) with different resin conversions. As expected, the neat polymer system exhibits Newtonian flow behavior during cure, while the highly filled Epon 830/Ni/DETA systems exhibit strong pseudoplastic flow at all three filler volume fractions, as shown in Fig. 6(b) for the typical Epon 830/Ni/DETA system with 39.2 vol% of Ni. We attribute this observed flow behavior change to polymer–nickel particle interactions as well as resistance to flow brought about by the presence of high concentration of relatively large and anisotropic nickel particles in the polymer matrix.

From Fig. 6(b), it is evident that the power law model describes the shear rate effect quite well, and the model parameters at different conditions are displayed in Table 1. As expected, the power law constant A increases with the level of cure and the filler volume fraction. The power law index, n , increases with the level of cure. This may be because the shear thinning effect becomes less as the crosslinked network proceeds and confines the movement of Ni particles. On the other hand, the index remains approximately constant with respect to change in filler volume fraction over the realistic filler concentration range we studied (Table 1).

The power law index, n , is depicted as a function of resin conversion at three volume fractions of Ni in Fig. 7, where the dashed line represents a quadratic fit:

$$n(\alpha) = -0.0178 + 4.2317 \cdot \alpha - 4.387 \cdot \alpha^2, \quad R^2 = 0.995 \quad (5)$$

and the solid line represents a linear fit:

$$n(\alpha) = 0.1314 + 2.377 \cdot \alpha, \quad R^2 = 0.971. \quad (6)$$

For simplicity, we employed linear fitting in the subsequent chemoviscosity modeling. It is worth noting that an average constant value of n over the conversion range in the model does not reflect the shear rate effect on chemoviscosity well.

Conversion Effect. The Castro–Macosko model [41–43] was employed in this work to describe the effect of resin conversion on the chemoviscosity, η_c , during cure, as follows:

$$\eta_c = C \left[\frac{\alpha_{gel}}{\alpha_{gel} - \alpha} \right]^{(d+e \cdot \alpha)}, \quad (7)$$

where C , d and e are constants and α_{gel} is the resin conversion at the gel point ($= 0.546$).

Figure 8(a) depicts the Castro–Macosko model fit, which predicts the viscosity very well for neat Epon 830/DETA system cured at RT, as:

$$\eta_c = 1.74 \cdot \left(\frac{0.546}{0.546 - \alpha} \right)^{12.00 - 15.07 \cdot \alpha}, \quad R^2 = 0.999. \quad (8)$$

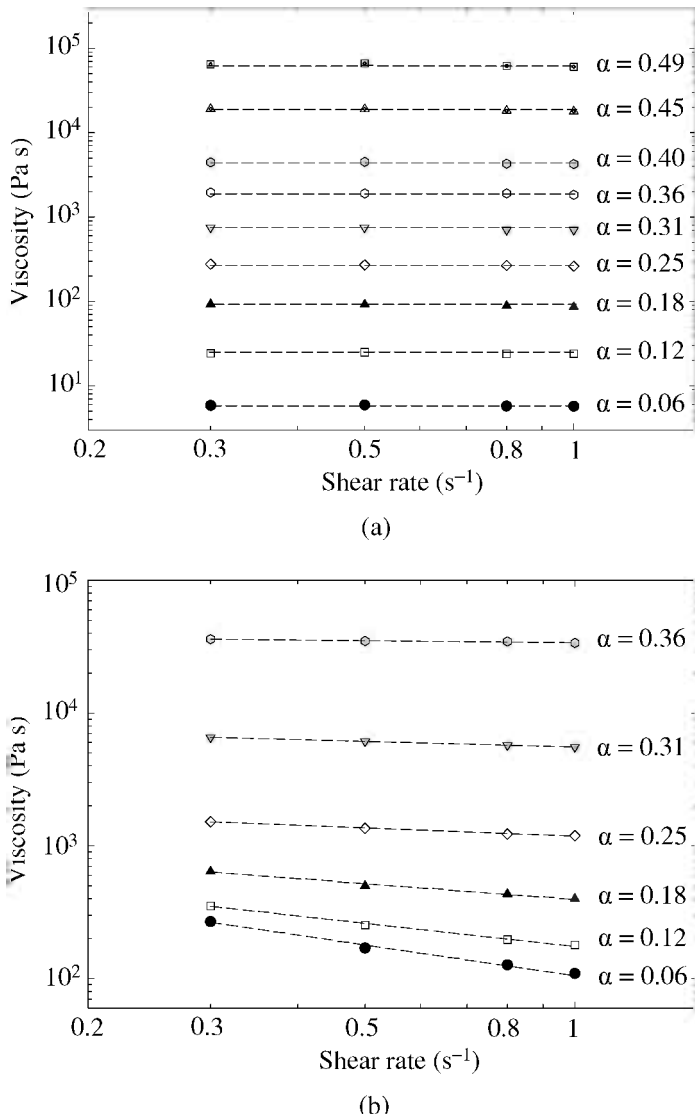


Figure 6. Effect of the shear rate on the steady shear viscosity at different resin conversions, α , for (a) neat Epon 830/DETA system cured at RT and (b) Epon 830/Ni/DETA system with 39.2 vol% Ni, as characterized by the power law model (----). A strong non-Newtonian flow behavior was observed for filled systems.

Note that the constant 1.74, which is the initial mix viscosity of epoxy and curing agent at zero resin conversion ($\alpha = 0$) derived from equation (8), is in good agreement with the value in the specification sheet for a similar material (1.5–2.0 Pa s). Note also that the shear rate effect can be removed from the model fit because of the Newtonian flow nature of the neat Epon 830/DETA system.

Table 1.

Power law model, equation (4), parameters from fits to isothermal data at room temperature, illustrating the shear rate effect

Shear rate effect conditions	<i>A</i>	<i>n</i> (<i>n</i> - 1)
34.6 vol%		
$\alpha = 0.06$	82.45	0.25 (-0.75)
$\alpha = 0.12$	131.3	0.41 (-0.59)
$\alpha = 0.18$	280.1	0.60 (-0.40)
$\alpha = 0.25$	846.8	0.77 (-0.23)
$\alpha = 0.31$	3750	0.87 (-0.13)
$\alpha = 0.36$	24 589	0.92 (-0.08)
39.2 vol%		
$\alpha = 0.06$	104.5	0.23 (-0.77)
$\alpha = 0.12$	173.7	0.42 (-0.58)
$\alpha = 0.18$	392.0	0.60 (-0.40)
$\alpha = 0.25$	1180	0.80 (-0.20)
$\alpha = 0.31$	5541	0.86 (-0.14)
$\alpha = 0.36$	33 852	0.95 (-0.05)
44.2 vol%		
$\alpha = 0.06$	179.9	0.23 (-0.77)
$\alpha = 0.12$	314.1	0.42 (-0.58)
$\alpha = 0.18$	738.1	0.61 (-0.39)
$\alpha = 0.25$	2101	0.78 (-0.22)
$\alpha = 0.31$	10 825	0.89 (-0.11)
$\alpha = 0.36$	58 436	0.92 (-0.08)

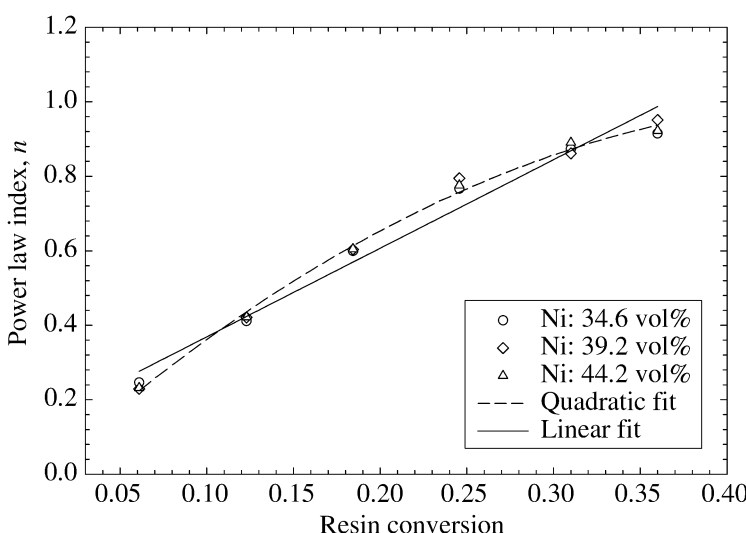


Figure 7. The power law index, *n*, as a function of resin conversion, α , for Epon 830/Ni/DETA systems cured at RT with (○) 34.6, (◊) 39.2 and (Δ) 44.2 vol% of Ni.

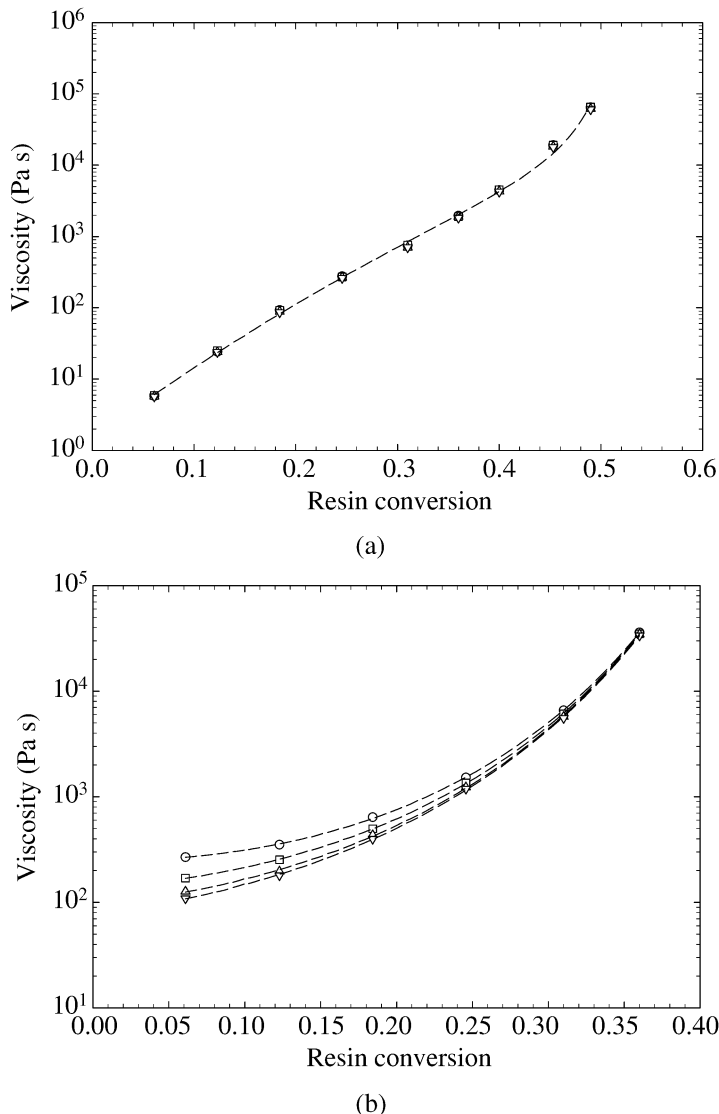


Figure 8. Fits of the Castro–Macosko model (---) to (a) Neat Epon 830/DETA system cured at RT and (b) Epon 830/Ni/DETA system with 39.2 vol% of Ni, at the steady shear rates of (\circ) 0.3, (\square) 0.5, (Δ) 0.8 and (∇) 1 s^{-1} .

Figure 8(b) shows the typical fits of the Castro–Macosko model to Epon 830/Ni/DETA system with 39.2 vol% of Ni at four steady shear rates. It is evident that this model still describes the cure effect for filled systems quite well. Table 2 lists the model parameters obtained at different conditions. As expected, the initial constant C decreases with the shear rate and increases with the filler volume frac-

Table 2.

Castro–Macosko model, equation (7), parameters from fits to isothermal data at room temperature, illustrating the cure effect

Cure effect conditions	<i>C</i>	<i>d</i>	<i>e</i>
34.6 vol%			
0.3 (s^{-1})	210.5	-0.93	15.01
0.5 (s^{-1})	120.6	0.17	13.31
0.8 (s^{-1})	80.33	1.03	11.87
1.0 (s^{-1})	65.80	1.51	10.98
39.2 vol%			
0.3 (s^{-1})	254.2	-0.39	13.81
0.5 (s^{-1})	140.2	0.90	11.72
0.8 (s^{-1})	95.57	1.64	10.58
1.0 (s^{-1})	78.49	2.12	9.70
44.2 vol%			
0.3 (s^{-1})	411.0	0.21	12.42
0.5 (s^{-1})	233.5	1.34	10.71
0.8 (s^{-1})	151.6	2.35	8.89
1.0 (s^{-1})	127.2	2.71	8.28
Neat epoxy			
0.3–1 (s^{-1})	1.74	12.00	-15.07

tion. The other two coefficients (*d* and *e*) also show some variations with the shear rate and volume fraction.

Ni Volume Fraction Effect. Addition of solid fillers into polymers alters the rheological characteristic of the polymer matrix, i.e., increases the suspension viscosity, η . With the assumption of spherical, noninteracting rigid particles in a dilute solution, the first η – Φ equation was proposed by Einstein [44] as:

$$\eta_r = 1 + 2.5 \cdot \Phi, \quad (9)$$

where η_r is the relative viscosity defined as the ratio of suspension viscosity to the suspending medium viscosity, and Φ is the solid filler volume fraction. However, for highly filled suspensions, particle interactions, size distribution and, most critically, the maximum packing density (Φ_m) have to be taken into account. The value of Φ_m is also altered by many factors in a given suspension, such as particle size distribution, particle agglomeration, particle irregularity, as well as the shear rate applied [45, 46].

From inspection of the basic relationship between viscosity and concentration equations, Liu [46] proposed a simple and reliable empirical model for the determination of Φ_m and viscosity interrelationship for a variety of ceramic suspensions and shear conditions. This model covers a wide spectrum of material parameters

such as particle size, shape, distribution, particle chemistry, solvent chemistry, as well as the corresponding matrix fluids, as follows:

$$\eta_r = [a(\Phi_m - \Phi)]^{-n}, \quad (10)$$

where η_r is the relative viscosity, n is a flow-dependent parameter, which takes the value 2, a and Φ_m are suspension-specific parameters, which can be experimentally determined for a given suspension *via* a single $1 - \eta_r^{-1/2} \sim \Phi$ plot through the use of a few viscosity *versus* concentration data points. A linear relationship is generally found in this plot, as

$$1 - \eta_r^{-1/2} = a \cdot \Phi + b, \quad (11)$$

where a is the slope, b is the intercept value and $\Phi_m = \frac{1-b}{a}$.

Therefore, the Φ_m for the currently studied Epon 830/Ni systems can be obtained using equation (11), as shown in Fig. 9. A value of 0.594 is obtained for Φ_m , which is rather close to the value observed in the steady shear experiment, and this value is used throughout this work by assuming that it roughly holds at all investigated conditions. A value of 1.66 was obtained for a , which is actually a function of resin conversion during cure. Thus, we can express the suspension viscosity during cure, simply as:

$$\eta = \eta_m(\alpha) [a(\alpha) \cdot (\Phi_m - \Phi)]^{-2} = F(\alpha) [0.594 - \Phi]^{-2}, \quad (12)$$

where η_m is the polymer matrix viscosity and F is the resulting constant at certain resin conversion level.

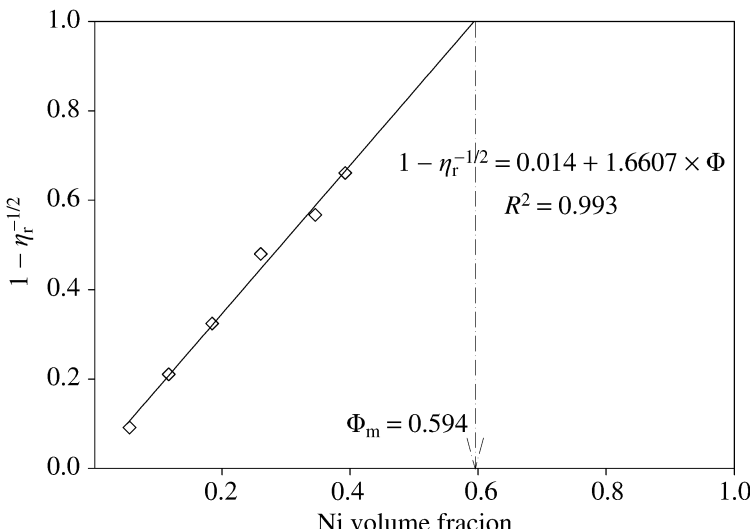


Figure 9. The $1 - \eta_r^{-1/2} \sim \Phi$ (volume fraction) relationship of Epon 830/Ni systems for determination of the maximum packing density, Φ_m . The steady shear rate of 1 s^{-1} was employed here at room temperature and without cure.

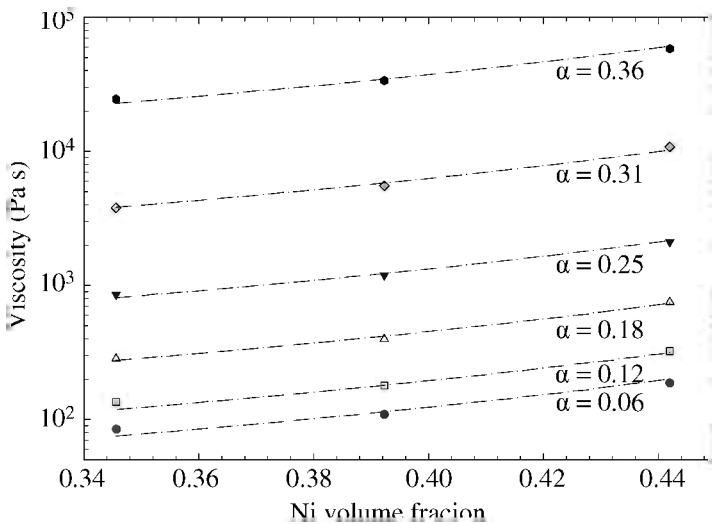


Figure 10. Effect of Ni volume fraction, Φ , on the chemoviscosity of Epon 830/Ni/DETA systems cured at RT with different resin conversions. The shear rate of 1 s^{-1} was used. The dashed lines are the Liu model fits and α is the resin conversion level (from top to bottom: 0.36, 0.31, 0.25, 0.18, 0.12 and 0.06).

Figure 10 depicts the effects of Ni volume fraction on the chemoviscosity of Epon 830/Ni/DETA systems cured at RT with different resin conversion levels at the typical shear rate of 1 s^{-1} , as well as the Liu model fits based on equation (12). From these fits, it is evident that the Liu model describes the volume fraction effect well. Table 3 displays the model parameters obtained at different conditions. As expected, the constant F increases with the resin conversion level and decreases with the shear rate.

Thermal Effect. The Arrhenius model, given in the following equation, is assumed to hold and was employed here to fit the effect of temperature on the chemoviscosity, η_T , of Epon 830/Ni/DETA systems at different conditions during cure:

$$\eta_T = G \cdot \exp\left(\frac{H}{T}\right), \quad (13)$$

where G is the pre-exponential factor, which is a function of Ni volume fraction, resin conversion and shear rate during cure; $H = E/R$ is the activation temperature [29], with E and R the flow activation energy and universal gas constant, respectively. For simplicity, H assumes a single constant value independent of the process conditions during cure.

Figure 11 is a typical Arrhenius model fit for Epon 830/Ni/DETA system with 34.6 vol% of Ni at four shear rates ($0.3, 0.5, 0.8$ and 1 s^{-1}). Three isothermal temperatures, $30, 40$ and 50°C , were investigated with zero resin conversion during measurements. The Arrhenius model fits the data well, and the average activation temperature obtained here, H , is 3180 K . Obviously, this activation temperature is

Table 3.

Liu model, equation (12), parameters from fits to isothermal data at room temperature, illustrating the volume fraction effect

Volume fraction effect conditions	Parameter F	Resin conversion	Parameter F
0.3 s^{-1}			
$\alpha = 0.06$	11.35	$\alpha = 0.25$	65.16
$\alpha = 0.12$	15.21	$\alpha = 0.31$	274.2
$\alpha = 0.18$	27.23	$\alpha = 0.36$	1535
0.5 s^{-1}			
$\alpha = 0.06$	7.30	$\alpha = 0.25$	56.62
$\alpha = 0.12$	10.79	$\alpha = 0.31$	256.5
$\alpha = 0.18$	21.68	$\alpha = 0.36$	1489
0.8 s^{-1}			
$\alpha = 0.06$	5.37	$\alpha = 0.25$	52.48
$\alpha = 0.12$	8.50	$\alpha = 0.31$	241.6
$\alpha = 0.18$	18.24	$\alpha = 0.36$	1442
1 s^{-1}			
$\alpha = 0.06$	4.64	$\alpha = 0.25$	49.89
$\alpha = 0.12$	7.31	$\alpha = 0.31$	236.1
$\alpha = 0.18$	17.02	$\alpha = 0.36$	1406

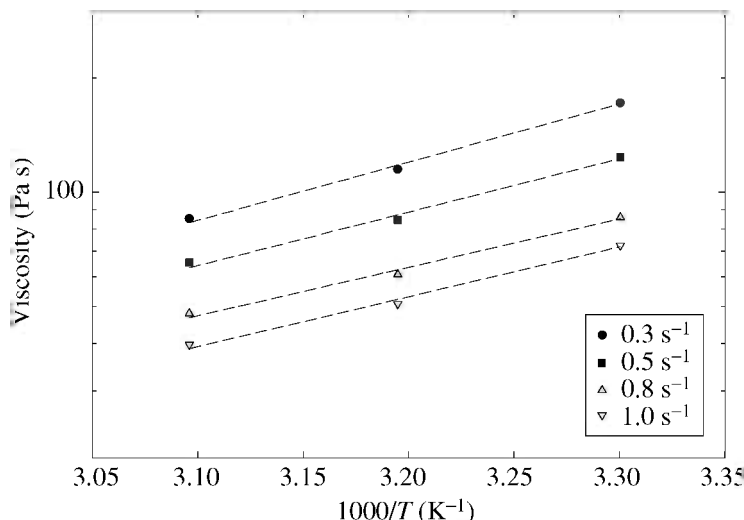


Figure 11. The Arrhenius model fits (---) of viscosity *versus* temperature relationship for typical Epon 830/Ni/DETA system with 34.6 vol% of Ni and zero resin conversion at four shear rates.

unrealistic for polymer-based materials, and should only be considered as a curve fitting parameter.

Comprehensive Modeling. The chemoviscosity of Epon 830/Ni/DETA systems during processing and cure at RT is a function of Ni volume fraction, shear rate and resin conversion level. A comprehensive model may then be represented by the combination of the power law (shear rate effect), Castro–Macosko model (conversion effect) and Liu model (Ni volume fraction effect), as the following equation:

$$\eta(\Phi, \dot{\gamma}, \alpha) = A \cdot (\Phi_m - \Phi)^{-2} \cdot \dot{\gamma}^{C_0 + C_1 \cdot \alpha} \cdot \left[\frac{\alpha_{\text{gel}}}{\alpha_{\text{gel}} - \alpha} \right]^{D+E \cdot \alpha}, \quad (14)$$

where A , C_0 , C_1 , D and E are model constants that can be determined by multivariable nonlinear regression analysis of isothermal data; Φ_m and α_{gel} are 0.594 and 0.546 for our systems, respectively.

Table 4 displays these comprehensive model parameters obtained, and Fig. 12(a) shows the typical model fits for Epon 830/Ni/DETA system with 39.2 vol% of Ni cured at RT using different conditions. This model fit is quite good for the isothermal chemoviscosity data at RT.

By incorporating the isothermal temperature effect, the general form of our comprehensive model can be obtained as follows:

$$\begin{aligned} \eta(T, \Phi, \dot{\gamma}, \alpha) \\ = A \cdot \exp\left(\frac{B}{T}\right) \cdot (\Phi_m - \Phi)^{-2} \cdot \dot{\gamma}^{C_0 + C_1 \cdot \alpha} \cdot \left[\frac{\alpha_{\text{gel}}}{\alpha_{\text{gel}} - \alpha} \right]^{D+E \cdot \alpha}, \end{aligned} \quad (15)$$

where B is the activation temperature and the other coefficients are the same as in equation (14).

A new set of model parameters from fits to isothermal data using equation (15) are also given in Table 4. Figure 12(b) shows a typical fit of this model to Epon 830/Ni/DETA system with 39.2 vol% of Ni and cured at RT using different cure times. It can be seen that our general model still predicts the viscosity well.

3.3.2. Nonisothermal Chemoviscosity

In order to model realistic industrial processes, which usually have broad temperature range, nonisothermal tests were also undertaken in this work. A nonisothermal

Table 4.

Comprehensive model parameters from isothermal data at room temperature (RT) and in a general form

Isothermal parameters — RT (equation (14))				
A (Pa s)	C_0	C_1	D	E
3.50	-0.84	2.29	1.77	10.61
Isothermal parameters — general form (equation (15))				
A (Pa s)	B	C_0	C_1	E
2.65E-3	2185	-0.79	2.09	11.91

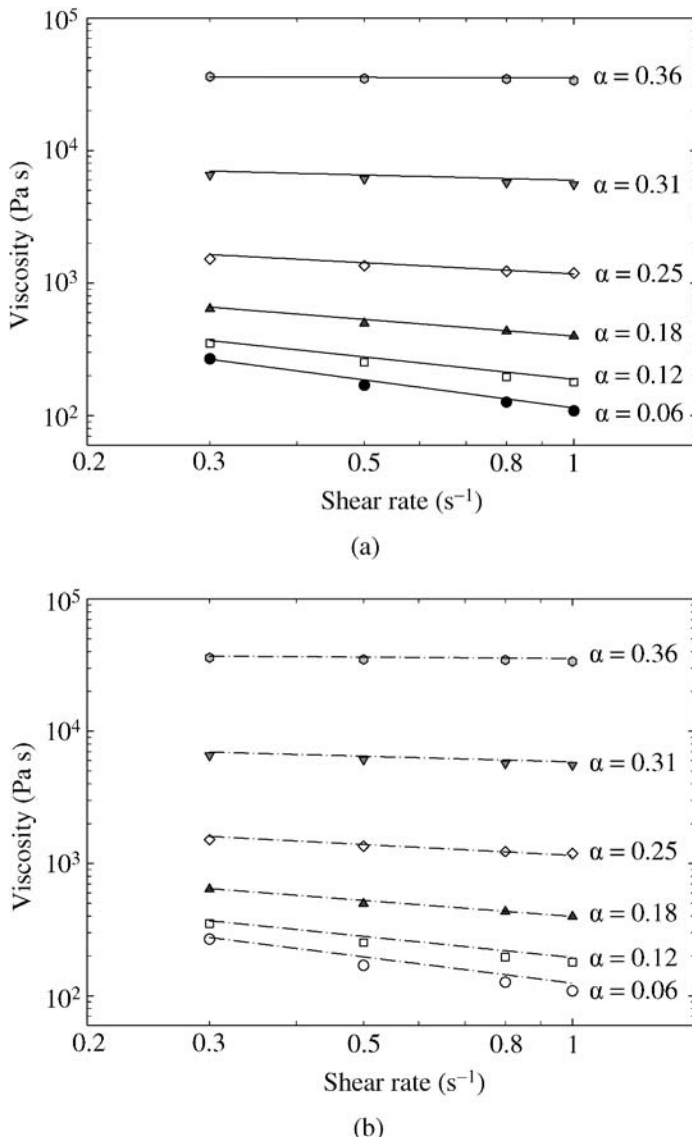


Figure 12. Fits of the comprehensive model: (a) equation (14) fits to isothermal data of Epon 830/Ni/DETA system and (b) equation (15) fits to isothermal data in a general form. The adhesive systems were cured at RT at six resin conversion levels ($\alpha = 0.06\text{--}0.36$) and 39.2 vol% of Ni.

temperature ramp identical to that in DSC (25–300°C at 10°C/min), with steady shear rate range of 0.3–1 s^{-1} , and Ni volume fractions of 34.6 and 44.2 vol%, were employed.

The overall isothermal chemoviscoelasticity model, based on equation (15), may be first extended to nonisothermal temperature cure cycle through nonlinear regression analysis of nonisothermal data. Table 5 displays the model parameters obtained

Table 5.

Comprehensive model parameters from nonisothermal data and for a modified form

Nonisothermal parameters (equation (15))											
A (Pa s)	B	C ₀	C ₁	D	E						
4.06E-7	5071	-0.57	-0.57	-0.41	3.99						
Nonisothermal parameters — modified form (equation (16))											
A (Pa s)	B	C ₀	C ₁	D ₀	D ₁	D ₂	D ₃	E ₀	E ₁	E ₂	E ₃
6.13E-4	2838	-0.53	0.27	-372.9	-3.49	35.39	1.06	-483.8	5.96	-37.46	1.20

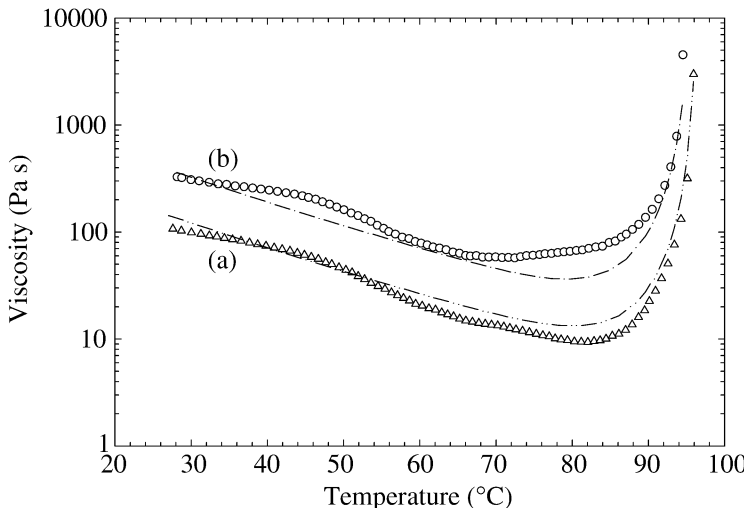


Figure 13. Fits of the comprehensive model, equation (15), to nonisothermal cure data of Epon 830/Ni/DETA systems with (a) 34.6 and (b) 44.2 vol% of Ni. The shear rate and heating rate (dT/dt) employed were 1 s^{-1} and $10^\circ\text{C}/\text{min}$, respectively.

from the fit, and Fig. 13 shows a typical fit of this model to Epon 830/Ni/DETA systems with 34.6 and 44.2 vol% of Ni during nonisothermal cure at the shear rate of 1 s^{-1} .

From Fig. 13, it can be seen that a minimum viscosity appears around 84°C at this heating rate, which indicates that the viscosity increase due to cure effect is initially overwhelmed by the viscosity decrease due to thermal effect as the temperature increases. Also, from the fit it is seen that this comprehensive model still predicts the viscosity data reasonably well, as shown in Fig. 13. The observed deviation of the fit from the experimental data suggests that some modifications may be needed.

In fact, nonisothermal temperature cure is a process different from isothermal cure. The reaction kinetics, total reaction order, and the reaction energy for epoxy systems may not be constant and same, but process-dependent. Consequently, some

modifications may need to be made to our model to reflect effects of such differences.

By allowing parameters D and E , which are no longer average constant values at all conditions in equation (15), to change with temperature during nonisothermal cure, an improvement in the model predictability may be expected. Furthermore, as previously discussed, both of these parameters also show some variations with the volume fraction (Φ) and shear rate ($\dot{\gamma}$). Therefore, we propose a modified comprehensive model in the following form:

$$\eta(T, \Phi, \dot{\gamma}, \alpha) = A \cdot \exp\left(\frac{B}{T}\right) \cdot (\Phi_m - \Phi)^{-2} \cdot \dot{\gamma}^{C_0 + C_1 \cdot \alpha} \cdot \left[\frac{\alpha_{\text{gel}}}{\alpha_{\text{gel}} - \alpha} \right]^{D^* + E^* \cdot \alpha},$$

where

$$\begin{aligned} D^* &= D_0 + D_1 \cdot \dot{\gamma} + D_2 \cdot \Phi + D_3 \cdot T, \\ E^* &= E_0 + E_1 \cdot \dot{\gamma} + E_2 \cdot \Phi + E_3 \cdot T. \end{aligned} \quad (16)$$

A noticeable improvement in fits can be found using our modified comprehensive model given by equation (16). Table 5 displays the adjustable model parameters obtained by regression of nonisothermal data at the heating rate of 10°C/min. Figure 14(a) and 14(b) illustrate the improved model fits to Epon 830/Ni/DETA systems with 34.6 and 44.2 vol% of Ni at three shear rates (0.3, 0.7 and 1.0 s⁻¹). It is evident that this modification is effective in improving the comprehensive model fits to Epon 830/Ni/DETA systems during nonisothermal temperature cure.

4. Conclusions

Chemorheological behavior of the highly filled Epon 830/Ni/DETA systems was found to be rather complicated due to the presence of high volume fraction of filler. No linear viscoelastic region could be observed within the investigated strain and frequency ranges in dynamic shear measurements, and neither the Cox–Merz rule nor the modified Cox–Merz rule could be employed, even though the Cox–Merz rule was valid for the neat epoxy system. Therefore, steady shear had to be used for the chemorheology analysis in this work.

A strong non-Newtonian flow is assumed by filled resins, especially at the early stage of cure, while the neat epoxy shows Newtonian flow behavior. Power law model, Castro–Macosko model, Liu model and Arrhenius model can be individually employed to describe, respectively, the effects of shear rate, resin conversion, Ni volume fraction and temperature on the chemoviscosity. A combination of these four individual models predicts the isothermal chemoviscosity well, and also fits the nonisothermal data reasonably. A modified model was also proposed to improve the model fit to nonisothermal experimental data.

Future work should include extension of the low shear rates currently used to a more realistic high shear rate range, and the determination of the corresponding

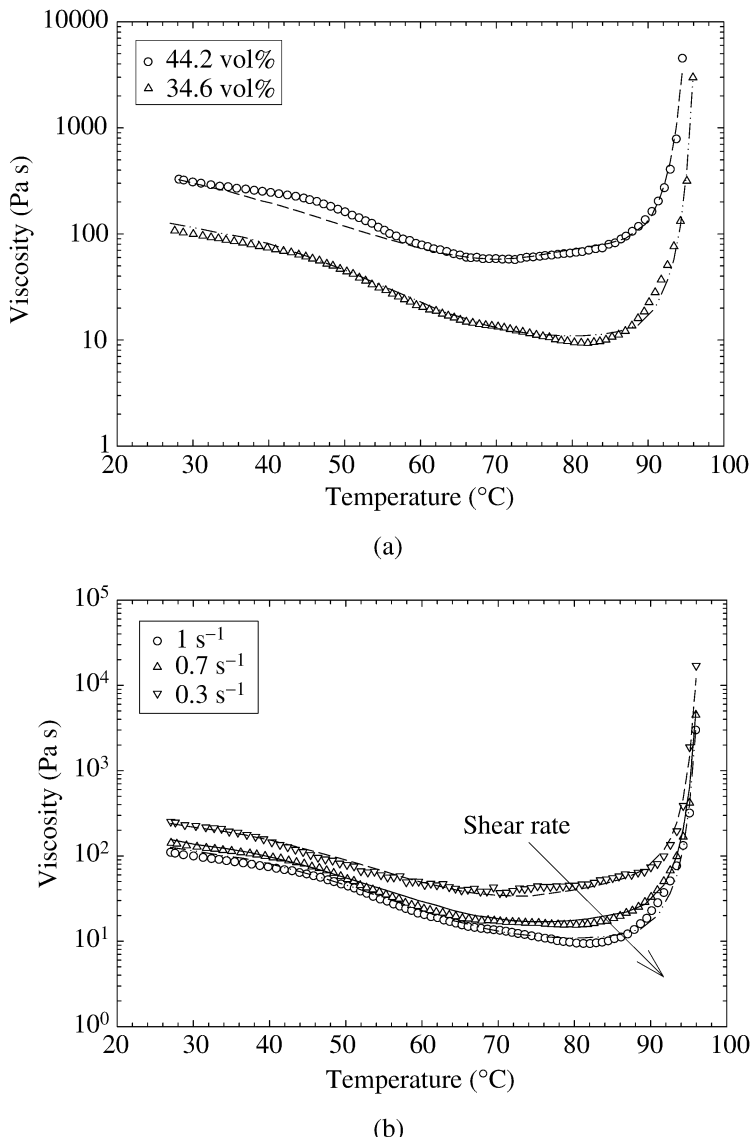


Figure 14. Fits of the modified comprehensive model, equation (16), to nonisothermal data of Epon 830/Ni/DETA systems with (a) 34.6 and 44.2 vol% of Ni, at the shear rate of 1 s^{-1} and at (b) three shear rates of 0.3, 0.7 and 1 s^{-1} , with 34.6 vol% of Ni. The heating rate (dT/dt) was $10^\circ\text{C}/\text{min}$.

high shear rate viscosities. More information on the effects of resin and filler properties on their chemorheological behavior will also be helpful.

References

1. E. Sancaktar and Y. Wei, *J. Adhesion Sci. Technol.* **10**, 1221–1235 (1996).

2. Y. Wei and E. Sancaktar, *J. Adhesion Sci. Technol.* **10**, 1199–1219 (1996).
3. E. Sancaktar and N. Dilsiz, *J. Adhesion Sci. Technol.* **13**, 679–693 (1999).
4. E. Sancaktar and N. Dilsiz, *J. Adhesion Sci. Technol.* **13**, 763–771 (1999).
5. E. Sancaktar, Y. Wei and M. A. Gaynes, *J. Adhesion* **56**, 229–246 (1996).
6. N. Dilsiz, R. Partch, E. Matijevic and E. Sancaktar, *J. Adhesion Sci. Technol.* **11**, 1105–1118 (1997).
7. R. Gomatam and E. Sancaktar, *J. Adhesion Sci. Technol.* **18**, 1225–1244 (2004).
8. R. Gomatam and E. Sancaktar, *J. Adhesion Sci. Technol.* **18**, 1245–1262 (2004).
9. R. Gomatam and E. Sancaktar, *J. Adhesion Sci. Technol.* **20**, 87–104 (2006).
10. R. Gomatam and E. Sancaktar, *J. Adhesion Sci. Technol.* **20**, 69–86 (2006).
11. R. Gomatam and E. Sancaktar, *J. Adhesion Sci. Technol.* **20**, 53–68 (2006).
12. R. Gomatam and E. Sancaktar, *J. Adhesion Sci. Technol.* **19**, 659–678 (2005).
13. R. Gomatam and E. Sancaktar, *J. Adhesion Sci. Technol.* **18**, 1833–1848 (2004).
14. R. Gomatam and E. Sancaktar, *J. Adhesion Sci. Technol.* **18**, 849–881 (2004).
15. R. Gomatam and E. Sancaktar, *J. Adhesion Sci. Technol.* **18**, 731–750 (2004).
16. E. Sancaktar and N. Dilsiz, *J. Adhesion Sci. Technol.* **11**, 155–166 (1997).
17. E. Sancaktar and C. Liu, *J. Adhesion Sci. Technol.* **17**, 1265–1282 (2003).
18. E. Sancaktar, P. Rajput and A. Khanolkar, *IEEE Trans. Compon. Packag. Technol.* **28**, 771–780 (2005).
19. H. Jozavi and E. Sancaktar, *J. Adhesion* **18**, 25–48 (1985).
20. E. Sancaktar and P. Zhang, *J. Mech. Design* **112**, 605–619 (1990).
21. E. Sancaktar and D. Beachtle, *J. Adhesion* **42**, 65–85 (1993).
22. E. Sancaktar, *J. Adhesion Sci. Technol.* **9**, 119–142 (1995).
23. E. Sancaktar, *Appl. Mech. Rev.* **49**, S128–S138 (1996).
24. P. J. Halley and M. E. Mackay, *Polym. Eng. Sci.* **36**, 593–609 (1996).
25. Q. Wang, T. He, P. Xia, T. Chen and B. Huang, *J. Appl. Polym. Sci.* **66**, 799–808 (1997).
26. P. I. Karkanas and I. K. Partridge, *J. Appl. Polym. Sci.* **77**, 2178–2188 (2000).
27. M. Ivankovic, L. Incarnato, J. M. Kenny and L. Nicolais, *J. Appl. Polym. Sci.* **90**, 3012–3019 (2003).
28. H. Ng and I. Manas-Zloczower, *Polym. Eng. Sci.* **33**, 211–216 (1993).
29. P. J. Halley, *J. Appl. Polym. Sci.* **64**, 95–106 (1997).
30. W. P. Cox and E. H. Merz, *J. Polym. Sci.* **28**, 619–622 (1958).
31. L. M. Dehnke, Permadi and J. M. Castro, *J. Appl. Polym. Sci.* **82**, 601–610 (2001).
32. S. Ganguli, D. Dean, K. Jordan, G. Price and R. Vaia, *Polymer* **44**, 6901–6911 (2003).
33. A. Y. Malkin, *Adv. Polym. Sci.* **96**, 69–97 (1990).
34. D. Heskamp, H. C. Broecker and M. H. Pahl, *Chem. Eng. Technol.* **21**, 149–153 (1998).
35. W. Philippoff, *Trans. Soc. Rheology* **10**, 317–334 (1966).
36. D. Doraiswamy, A. N. Mujumdar, I. Tsao, A. N. Beris, S. C. Danforth and A. B. Metzner, *J. Rheology* **35**, 647–685 (1991).
37. A. I. Isayev and X. Fan, *J. Mater. Sci.* **29**, 2931–2938 (1994).
38. A. Yoshimura and R. K. Prud'homme, *J. Rheology* **32**, 53–67 (1988).
39. I. Kroutilová, L. Matějka, A. Sikora, K. Souček and L. Staš, *J. Appl. Polym. Sci.* **99**, 3669–3676 (2006).
40. D. Harran, M. F. Grenier-Loustalot and P. H. Monge, *Europ. Polym. J.* **24**, 225–230 (1988).
41. J. M. Castro and C. W. Macosko, *SPE ANTEC Proc.* **26**, 434–438 (1980).
42. J. M. Castro and C. W. Macosko, *AICHE J.* **28**, 250–260 (1982).
43. J. M. Castro, C. W. Macosko and S. J. Perry, *Polym. Commun.* **25**, 82–87 (1984).

44. A. Einstein, in: *Investigations on the Theory of the Brownian Movement*, R. Furth (Ed.), p. 49. Dover Publications, New York, NY (1956).
45. C. R. Wildemuth and M. C. Williams, *Rheol. Acta* **24**, 75–91 (1985).
46. D.-M. Liu, *J. Mater. Sci.* **35**, 5503–5507 (2000).

This page intentionally left blank

Temperature Characterization in Anisotropic Conductive Film Adhesive Bonding

Robert L. D. Zenner^a, Cameron T. Murray^{a,*} and Carl Fisher^b

^a Electronics Markets Materials Division, 3M Company, 3M Center, Maplewood, MN 55144, USA

^b Corporate Research Materials Laboratory, 3M Company, 3M Austin Center,
6801 River Place Boulevard, Austin, TX 78726, USA

Abstract

An accurate assessment of the bonding temperature values in the adhesive layer during Anisotropic Conductive Film bonding is complicated by several factors related to small dimensions, large temperature gradients, and inherent-thermal perturbations caused by the measurement technique. Thermal modeling simulations were used to characterize the temperature values and evaluate their influences on the dynamic temperature variation through the bonding process used for thin electronic devices. These simulations reveal the degree of temperature gradient through the electronic assembly layers and within the adhesive, the effects of design changes, and the significance of equipment parameters on the temperatures reached during bonding. The simulations show that the adhesive temperature can vary by more than 30°C across the characteristic sizes both of the total bond area and along or between the individual circuit traces. Also, the heat transfer through the layers showed changes due to the device design and bonding equipment base material choice of 40 to 80°C in some cases. Therefore, thermocouples in the adhesive used to measure the temperature must use very fine wire size and require meticulous precision in positioning to insure accuracy and reproducibility in the adhesive bonding conditions to enable the highest yield and reliability.

Keywords

Anisotropic conductive film adhesive, temperature, thermal model thermocouple, bonding, thin electronic assembly

1. Introduction

Anisotropic conductive film (ACF) adhesives are used in the assembly of electronic devices that generally require connections between flexible printed circuits or integrated circuit chips and various next-level interconnects such as printed circuit boards, flat panel displays, flexible printed circuits, or touch screens, to list a few common examples. These ACF materials typically require the use of hot bar bonding equipment that applies heat and pressure through the flexible printed circuit or integrated circuit chip to compress together the corresponding connecting pads

* To whom correspondence should be addressed. Tel.: 651-736-9294; Fax: 651-733-8305; e-mail: ctmurray1@mmm.com

thus trapping conductive particles in the adhesive to create an electrical current path while simultaneously causing the adhesive thermosetting resin to undergo cure by holding for a sufficient time.

The performance of a thermosetting ACF is measured by reliability tests measuring both the bond strength and electrical contact resistance. The level of thermosetting resin cure (determined by the bonding temperature and time) affects the final bond strength reliability while the uniformity of conductive particle trapping and residual compression (determined by the bonding temperature, time and pressure) affect the electrical contact resistance reliability.

In the past, ACFs were developed to be bonded within a range of bonding conditions that included high temperature (greater than 180°C) with high bonding pressure (greater than 3 MPa). There are emerging applications for which the bonding conditions become potentially limiting toward the viability of ACF materials that previously enjoyed the greater process latitude. New assembly applications such as for plastic touch screens or plastic displays present new upper-end restrictions on bonding temperature and pressure to insure high yield. These plastic devices typically are based on polyester-type materials that may undergo physical property changes at temperatures greater than 150°C [1].

Inherent in the process of ACF bonding is the ability to accurately set the bonding conditions with real parts in an assembly operation. Typically, pressure and time are quite easy to measure reproducibly and control with good accuracy; but temperature in the bondline, though easily measured in general, has proven elusive in terms of measurement reproducibility, accuracy or control. This is due, in large part, to the very rapid bonding cycle times (less than 20 s) prevailing in the ACF products. The actual temperatures in the bondline are often undergoing continuous increase through the short bond cycle time and this can lead to varying levels of uncertainty in the measured temperature values but other factors may also contribute to such uncertainty.

This elusiveness in the temperature consistency in the bondline combined with the emerging applications that show greater sensitivity to temperature exposure demand improvements in the understanding of the thermal conditions during the bonding process.

In this paper we will use thermal modeling simulations to characterize the temperature values during the thermoset bonding process. We will examine the influence of the small dimension of the circuitry, the large temperature gradients and the bonding equipment on the dynamic temperature variation through the bonding process.

2. Measurement of ACF Bonding Temperature

The basic construction used to measure bond temperatures includes a thermocouple placed between a top layer flexible printed circuit and a bottom layer next-level interconnect or device (such as: printed circuit board, glass or plastic flat panel dis-

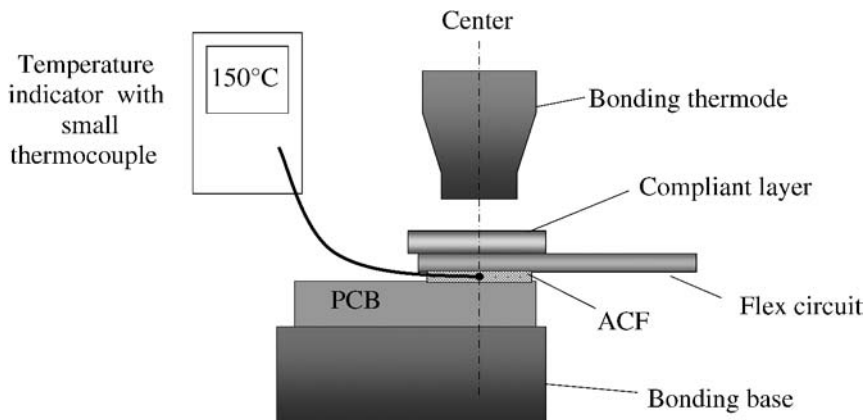


Figure 1. Schematic drawing of the thermocouple embedded test sample for measuring the bondline temperature in an ACF bond. The industry calls this assembly a lay-up of parts. The thermode is a heated metal bar with a flat bottom used to apply the heat and pressure to the parts during assembly.

play, glass or plastic touch screen, another flexible printed circuit or similar item). Figure 1 shows a typical temperature measurement system (or lay-up) and bonder with its heated metal bar (thermode) and bonding base or stage. The lay-up features the thermocouple inserted into the stack of parts at the ACF level, either as a temporarily constructed adhesiveless dry lay-up or embedded and cured in the ACF adhesive as a permanently constructed structural lay-up. In either case, the inclusion of the thermocouple will alter the temperature to some extent, adding to the difficulty in achieving absolute characterization of the temperature. The thermocouple embedded test sample is positioned in the bonding equipment as would normally be the case for production parts and the thermocouple is connected to a temperature indicator. The setpoint temperature of the bonding thermode is adjusted so that the measured temperature shown on the temperature indicator is within the target range required to bond the ACF product.

In most electronic assemblies that use ACF the thickness of the various layers is very low:

- Flexible printed circuits — 0.025–0.075 mm.
- ACF material — less than 0.050 mm.
- Next-level interconnect or device — less than 1.0 mm.

Also, the bonding base typically acts as a large heat sink in direct contact with the electronic assembly. Further, the addition of the thermocouple itself may impart a significant perturbation to the electronic assembly. These thermocouples have diameter of at least 0.125 mm, obviously much greater than the ACF thickness in which they are embedded. These pose some potential difficulties affecting ACF bondline temperature characterization.

While thermocouples are easy to use, relatively accurate and reliable in most applications, they are also susceptible to significant variation in measurement repeatability. Measured values can show significant changes due to slight deviation in positioning or for measurements in very thin materials of low thermal conductivity. Therefore, these embedded test samples might be best used only as a rough guide to the actual temperature or as a tool for coarse verification of the bond conditions. The measurements can also be less reliable due to subtle issues that may limit this accuracy.

The issues that most limit the accuracy, repeatability and correlation to actual ACF temperature of thermocouple embedded test samples are as follows:

1. Temperature measurements with thermocouples can be affected by the heat transfer around the thermocouples [2]. The important parameters are the convection coefficient around the sample being measured as well as around the thermocouple and the relative thermal conductivities of the sample and thermocouple. The thickness of most thermocouples is quite large in comparison with the ACF thickness. The ACF layer in a typical bonding application is less than 50 µm thick, whereas the thermocouple probe tips are typically greater than 50 µm thick. The greater thickness of the thermocouple compared to the surrounding adhesive means that the heat flow path is significantly perturbed and the heat flux will be concentrated through the small area where the thermocouple is protruded, so that the measured temperature does not represent the uniformly spreading heat through the various layers of the actual electronic assembly with a resultant increase in the ‘measured’ temperature.
2. The thermocouple thickness will also cause the measured temperature value to differ from the average temperature in the ACF layer. Since the typical size of a thermocouple exceeds the thickness of the ACF layer, this temperature measurement will tend to give the reading at the ACF surface closest to the thermode, which corresponds to a maximum value.
3. The thermocouple leads near the probe tip act as heat sinks [3]. For this situation, where the convection is negligible, the result is that the large difference in thermal conductivity between the thermocouple metal and the polymer layer causes significant heat flow down the thermocouple leads, with a resultant decrease in the ‘measured’ temperature.
4. Thermocouple placement is important. These bondline regions have alternating metal circuit lines and spaces that are, respectively, regions with materials of high and low thermal conductivity. Due to this arrangement of alternating thermal conductivities (copper trace, space and copper trace), the local temperature can vary, perhaps dramatically. The long copper circuit line traces with high thermal conductivity and the adhesive near these circuit lines do not heat-up as rapidly as the adhesive and support layer between the circuit traces, so the temperature at a point centered on the traces will be lower than the temperature

at a point centered in the space between traces. Depending upon whether the thermocouple probe tip is positioned directly over a circuit line, directly in the space between the circuit lines, or partially in the line or in the space location can lead to differences in the measured temperature.

5. The rapid cycle time for these ACF materials can result in the measured temperature profiles never reaching equilibrium. This leads to challenges in catching a correct temperature value over a steep slope of the temperature *vs* time curve. This can be further complicated if the temperature indicator refresh rate for output values does not display values at a rate high enough to capture data accurately.
6. Other sources of temperature variability not addressed in this paper are the thermode temperature stability, the thermode-to-base planarity control, and time dependent effects such as gradual change of base equilibrium temperature from repeated use.

The arrangement shown in Fig. 1 with a thermocouple placed carefully in the center of the bond region is the method that is used to characterize the bond temperature and prepare the bonding equipment for assembly despite these limitations to the accuracy. This test set-up can deliver reliable and accurate measurements of the ACF bondline temperature when used with the necessary attention to detail. An example of the temperature *vs* time profile for a typical electronic assembly is shown in Fig. 2. These tests with the carefully positioned thermocouple will provide a very good approximation to actual temperature values for many electronic assemblies. Increased accuracy may be a more critical concern for the case of the

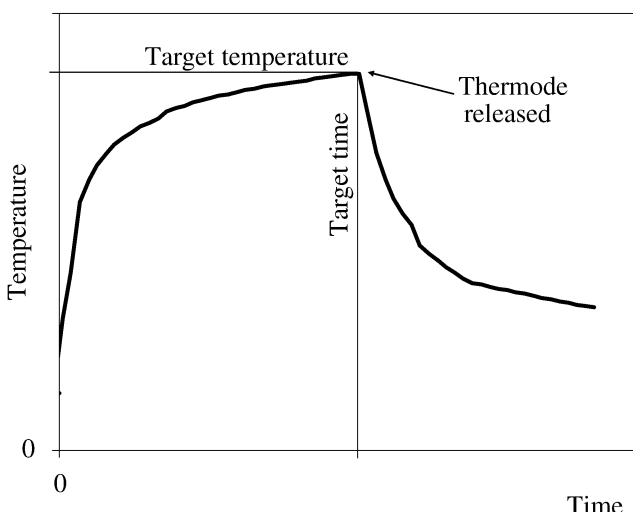


Figure 2. Representative plot of a typical temperature *vs* time profile for ACF bonded to electronic assembly showing actual temperatures measured by a thermocouple.

emerging plastic touch screen and plastic flat panel display applications. To better understand the thermal characteristics in these critical applications thermal modeling techniques are required due to the limitations to the accuracy that can arise.

3. Thermal Modeling Simulation Details of Computational Design

Transient heat transfer simulations were carried out using Icepak 4.3 (ANSYS Inc., Canonsburg, PA). Icepak is a 3D finite-volume computational fluid dynamics code with conjugate heat transfer. Icepak uses the ICEM™ meshing package and the FLUENT™ solver. The ACF assembly to be modeled is broken up into blocklike elements, each block is a computational mesh and the energy equation is solved in each mesh to satisfy the first law of thermodynamics. For these simulations, the air-flow solver was turned off because the short duration (15 s) and small computational domain (<5 mm in height) would not give the natural convection air-flow field time to develop — thus the temperature profiles are due to the conduction through the different layers of the polymer stack. Each of the layers of the stack was modeled as a solid rectangular block with physical and thermal properties obtained from handbooks or direct measurements. The properties of the ACF, for example, were obtained from internal DMA and thermal conductivity measurements. Perfect contact between each of the layers was assumed. This is a reasonable assumption because of the relative softness of the polymer materials and the pressure exerted by the thermode during bonding. To reduce the size of the solution matrix, *z*-axis symmetry was assumed. In addition, only 20 of the metal (copper) traces were modeled, rather than the 50 or so that exist in the some systems. The metal trace layout was based on a flexible printed circuit with 5 mm metal line length and 0.5 mm line pitch (0.25 mm traces and 0.25 mm spaces). It was considered that the traces further away from the symmetry axis would have little or no effect on the temperature in the region of interest. The thermode was modeled as a planar heat source at a fixed temperature.

Icepak uses the concept of the computational domain as a closed cabinet where all of the walls are impervious and adiabatic. For this problem, however, all of the walls were maintained at the fixed ambient temperature, and the cabinet was made large enough to minimize thermal conduction errors. The validity of these assumptions could be evaluated by viewing the temperature gradient at the boundaries. A significant gradient ($>5^{\circ}\text{C}/\text{mm}$) is an indication that the boundary may be too close to the heat-generating object and may be driving the solution. For these simulations, the temperature gradient at the upper wall was always much less than $0.1^{\circ}\text{C}/\text{mm}$ for the $300 \text{ mm} \times 300 \text{ mm} \times 200 \text{ mm}$ computational domain, thus the assumptions are appropriate. Each block of the model was subdivided with a minimum of three mesh elements on the edge of each block. The ACF layer (block), however, was modeled with seven elements to better capture the temperature gradient through this material. The total number of elements in these simulations ranged from about 250 000 to 300 000. The problems were solved with a fixed transient

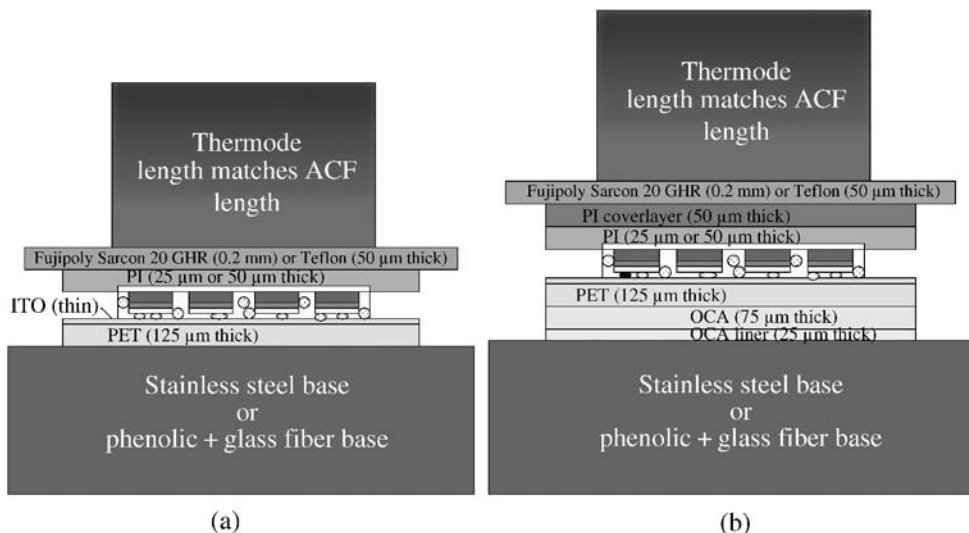


Figure 3. Schematic drawings of the modeling simulation designs. In (a) the simplified assembly plastic touch screen design ACF bonding model is depicted. In (b) the more realistic assembly plastic touch screen design ACF bonding model is depicted which includes several other layers often found in real assemblies (coverfilm for the polyimide film, an optically clear adhesive (OCA) and the OCA liner).

time step of 0.002 s, with the data saved every 50 time steps. Up to 100 iterations were allowed at each time step to achieve a converged solution. The solution time for each ACF bond simulation was about 8 hours for the 15-second bond cycle. In all thermal simulations that follow, the output graphs are plotted at the 10-second point during the bonding cycle.

The basic design of the model features an ACF bonding application of a polyimide (PI)-based flexible printed circuit attached to an indium-tin-oxide (ITO) coated polyester (PET) film used to simulate a simplified plastic touch screen assembly (see Fig. 3a). This basic design was also augmented with the addition of more layers as is typically found in actual plastic touch screen sub-assemblies (see Fig. 3b). These added layers included a coverlayer on the top of flexible printed circuit and an optically clear adhesive (OCA) to the base of the polyester with the attached release liner. The physical properties of all materials used in these simulations are shown in Table 1.

4. Thermal Modeling Simulations of ACF Bonding Temperatures

ACF bonds are completed in a cycle time of 5 to 20 s using a bonder which has a heated metal bar (thermode) which applies both heat and pressure for the specified time. Figure 3 shows a Simplified Assembly of a flexible printed circuit being bonded with an ACF to a plastic touch screen (shown as a polyester film coated with a very thin layer of indium-tin-oxide) or, as a closer mock-up to a real touch screen,

Table 1.

Physical properties of materials used in thermal simulations

Material	Density (kg/m ³)	Thermal conductivity (W/m K)	Specific heat capacity (J/kg K)	Thickness (μm)
G10 Phenolic	1800	1	1450	> 10 000
Stainless steel	8200	15	480	> 10 000
OCA liner	1250	0.2	1250	25
OCA	1350	0.25	1250	75
PET	1350	0.2	1900	125
Copper	5300	390	380	40
ACF	1050	0.75	1650	50
PI	1420	0.35	1100	25
Coverlayer	1100	0.15	1400	50
Teflon	2200	0.25	1000	50
Sarcon HGR	2360	0.7	1000	200

a Realistic Assembly includes the simplified assembly with coverlayer added to the flexible printed circuit and an optically clear adhesive with a liner added to the polyester. There is a bonding platform supporting these components which affects the heat flow through the stack. In addition, there is a compliant layer between the thermode and the parts to provide uniform pressure distribution and helps to uniformly distribute the temperature in the bondline. As a result of the thermal resistance of the various parts, the thermode is heated to a temperature significantly above the desired bondline temperature, as the heat flows through the assembly into the base support platform.

The issues cited in the Section 2 highlighted the challenges that could be encountered in trying to measure ACF bondline temperature accurately, reproducibly, and with good correlation to the actual bonding case. As a more detailed representation of the temperatures throughout the bond region is desired, the thermal model described in the previous section has been used to examine various bonding options. This modeling simulation presents an opportunity to examine the effects of several possible variables either in a modeling design that resembles a real assembly or in one based on a more simplified test vehicle. The following additional variations in the settings were examined by these thermal modeling simulations:

The Simplified Assembly thermal model was used to examine the following effects:

- Platform base material (thermally conductive stainless steel or a non-conductive glass resin composite called G10 Phenolic).
- Polyimide film thickness in the flexible printed circuit base material (25 or 50 μm).

- Compliant layer material (Teflon™ film or thermally conductive silicone rubber — Fujipoly Sarcon™).

The Representational Assembly thermal model was used to examine the following effects:

- Platform base material (thermally conductive stainless steel or a non-conductive glass resin composite called G10 Phenolic).
- Thermode setpoint temperature for the stainless steel base case (295°C, 330°C and 365°C).

4.1. Simplified Assembly Touch Screen Design

4.1.1. Effect of Bonding Equipment Base Material

The bonding equipment used to assemble electronic devices includes both a heated thermode and corresponding base or fixture designed to provide good planarity control to insure uniformity of bonding pressure over all of the contacting pads to be joined. The base or fixtures are made of metal or other materials depending on the application. In some cases the base is formed with a quartz platform that will allow for a visual path to assist in the alignment of the flexible printed circuit to a transparent device. This is particularly useful for flat panel display assembly. The thermal properties of the base or fixture material may affect the overall heat distribution and stability. The residual stress after bonding is known to be strongly influenced by a large thermal gradient in the case of ACF attachment of integrated circuit chips to glass for flat panel display applications [4]. The thermal gradient may be controlled, to some extent, by bias heating of the base or fixture. Also, there can be a gradual increase in the base temperature following many repeated bonds at a high throughput rate even in the absence of a base heater.

Figure 4 shows the ACF bondline temperatures after 10 s application of the thermode heat and pressure for the case of the simplified assembly touch screen design (schematic layout shown in Fig. 3a). The temperatures shown start at right at the surface of the bonding thermode operated at a setpoint temperature of 295°C. The profile shows a drop in temperature through the various layers moving from right-to-left to the base materials. The graph shows the case of the simplified assembly comparing a phenolic base below the touch screen with a stainless steel base below the touch screen. The model predicts significant differences in the temperatures for this change in base material where the phenolic base (acting somewhat like a thermal insulator) leads to smaller thermal gradient through the layers compared to the metal base (acting as an effective heat sink) which leads to a larger and more rapid drop in the temperature through the layers. A further feature revealed by the data is the prediction that in both cases there is a significant thermal gradient through every layer of the bond. Also, the target adhesive layer temperature is reached at a lower thermode setpoint using the more insulating phenolic base than for the more thermally conductive steel base as found in the case of actual temperature measurements with the embedded thermocouple test parts.

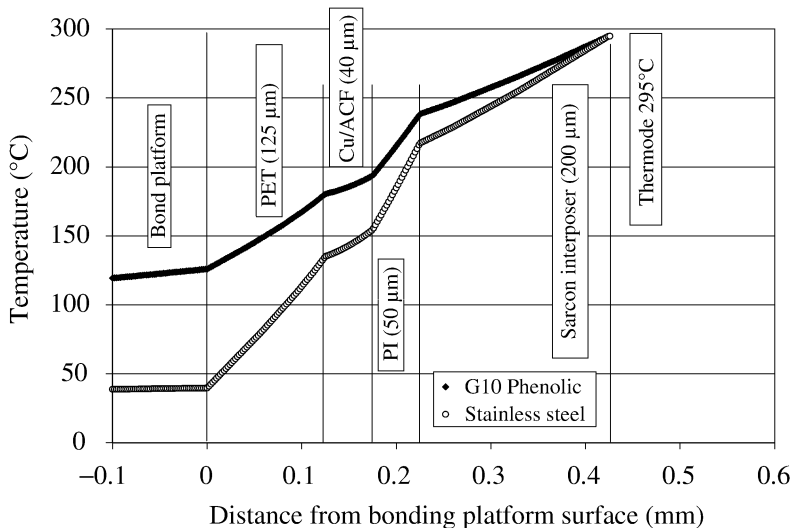


Figure 4. Simulated model showing the instantaneous temperature profile (y-axis) through the cross-sectional assembly layers (x-axis) along the thermode centerline for ACF bond using a simplified assembly touch screen design (Fig. 3a). Graph shows calculations comparing a phenolic base (solid diamond) vs stainless steel base (open circles) for a thermode setpoint of 295°C and a bond time of 10 s.

In Fig. 5 the same setup as simulated in Fig. 4 is shown but in this graph the temperature profiles experienced at mid-height in the ACF layer plotted along the thermode width direction. At the midpoint of the thermode width the temperatures are at a maximum value that corresponds to the middle of the Cu/ACF region shown in Fig. 4. The midpoint temperature for the case of the phenolic base is about 180°C while the midpoint temperature for the steel base is about 140°C. There is a significant thermal gradient occurring from the centerline of the thermode out toward the thermode edges. Regardless of base material the temperature has dropped by over 30°C for displacement to edge of the thermode width. The temperature gradient in Fig. 5 on the x -direction temperature profiles is not linear, we see changes in the slope at ± 2 mm. These humps arise in the model because the data points in Fig. 5 are taken on a line that is midway between two metal traces where there is a large difference in thermal conductivity and heat capacity between the ACF and the metal traces.

4.1.2. Effect of Flexible Printed Circuit Polyimide Backing Thickness

Variations in the component materials or dimensions are often encountered in high-volume electronics assembly. For instance, there may be several suppliers of flexible printed circuits used for any given application where large unit volumes are needed. Different suppliers may offer different options in the constructions that include change of materials or thickness as examples. These changes are also a source of significant variation in the thermal conditions during bonding.

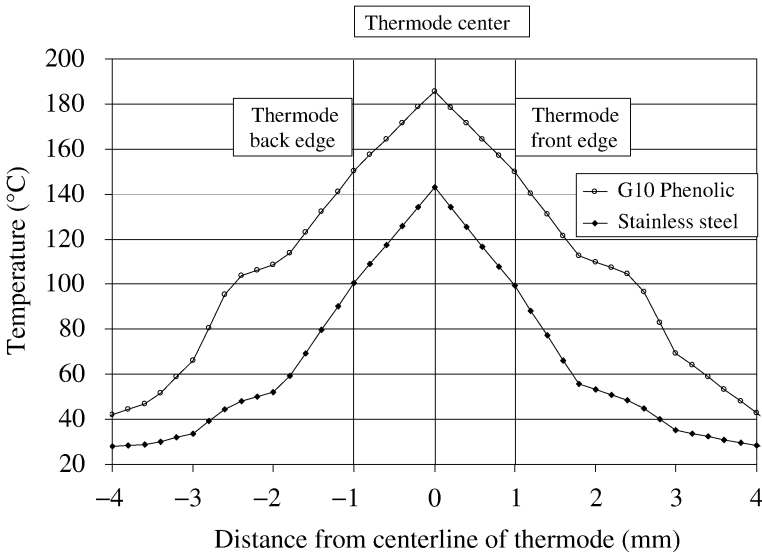


Figure 5. Simulated model showing the instantaneous temperature profile (y-axis) across assembly width (x-axis) using simplified assembly touch screen design (Fig. 3a). The temperature plotted comes from the calculation made in the center of ACF layer and at center of thermode length. The thermode edges and center are marked with solid lines. Graph shows calculations comparing phenolic base (solid diamonds) vs stainless steel base (open circles) for a thermode setpoint of 295°C and a time of 10 s.

Shown in Fig. 6 is a comparison of flexible printed circuit polyimide thickness (25 µm vs 50 µm) after 10 s application of the thermode heat and pressure again for the case of the simplified assembly touch screen design (Fig. 3a). The model predicts that temperature drop through the thickness of the polyimide was about 20°C for the 25 µm thick and 45°C for the 50 µm thick polyimide layers. This thickness difference translates to a change in the bonding temperature within the ACF layer of about 25°C for this constant thermode temperature setting of 295°C. (The gradient within the ACF layer remains very similar in all reported simulations.)

4.1.3. Effect of Compliant Interposer Material

A compliant interposer is placed between the thermode and flexible printed circuit to help evenly distribute the heat and pressure over all of the bond pads and bond area. The selection of interposer material is application dependent, for example flex to glass bonding uses different materials than flex to board bonds. The most critical considerations for compliant layer are the relative flatness of the layers and the differences in the thermal conductivity of the highly heterogeneous system [5].

In Fig. 7 a comparison of interposer material (and thickness) is shown for the case of the simplified assembly touch screen design (Fig. 3a) after 10 s application of the thermode heat and pressure. This model compares a thin Teflon™ (50 µm) film with the Sarcon™ (200 µm) rubber. The prediction reveals how, even compared to very thin Teflon™, the heat transfer through the Sarcon™ material will give

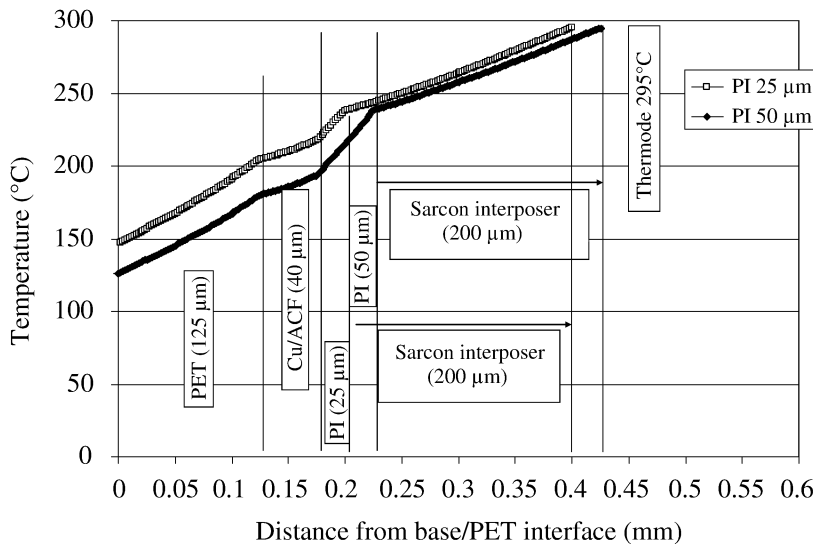


Figure 6. Simulated model showing the instantaneous temperature profile (y-axis) through the cross-sectional assembly layers (x-axis) along the thermode centerline for ACF bond using a simplified assembly touch screen design (Fig. 3a). Graph shows calculations comparing polyimide flexible printed circuit thickness 25 μm (open boxes) vs 50 μm (closed diamonds) for a thermode setpoint of 295°C and a bond time of 10 s.

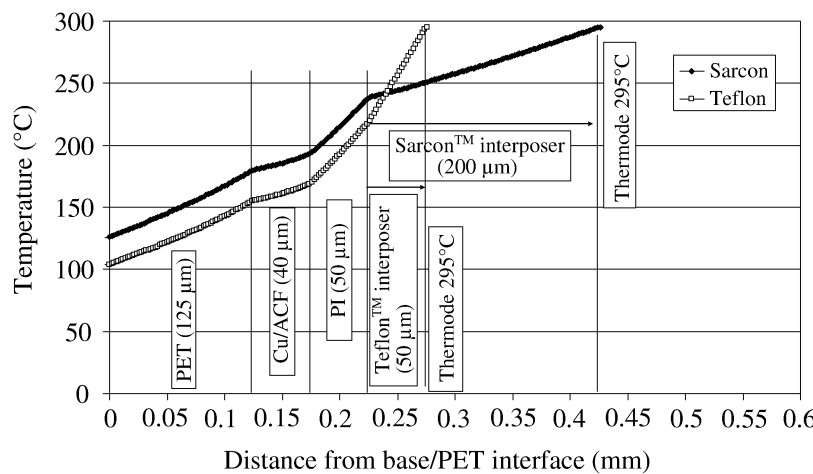


Figure 7. Simulated model showing the instantaneous temperature profile (y-axis) through the cross-sectional assembly layer (x-axis) along the thermode centerline for ACF bond using a simplified assembly touch screen design (Fig. 3a). Graph shows calculations comparing 50 μm thick Teflon™ interposer (open boxes) vs 200 μm thick Sarcon™ interposer (closed diamonds) for a thermode setpoint of 295°C and a time of 10 s.

a higher ACF bond temperature for a given thermode setpoint condition. The actual interposer thickness during an actual ACF bond would likely involve some level

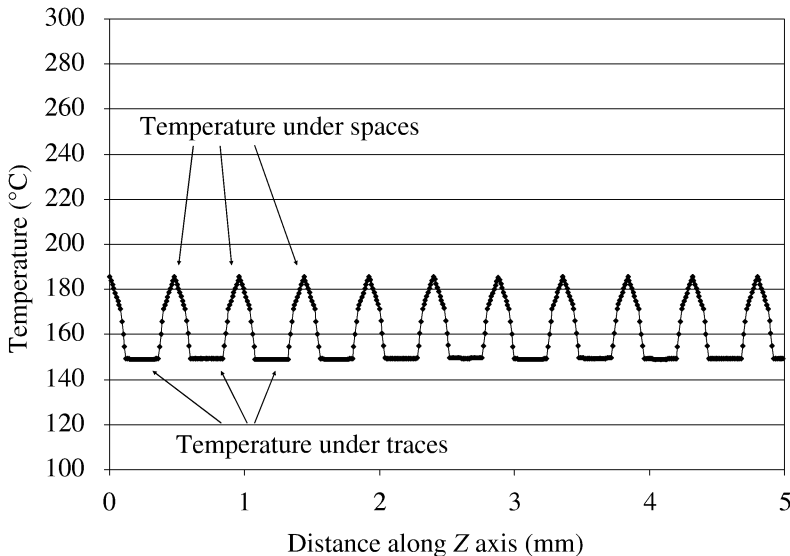


Figure 8. Simulated model showing the instantaneous temperature profile (y-axis) across the bond length (x-axis) at mid-height in the ACF layer, centered along thermode length for ACF bond using a simplified assembly touch screen design (Fig. 3a). Graph shows calculations for 200 μm thick SarconTM interposer (closed diamonds) and a thermode setpoint of 295°C at a time of 10 s. The pattern seen is a result of the pattern of traces on the PI circuit.

of deformation of the TeflonTM material and compression of the SarconTM material that can change the heat transfer. This simulation does not account for such effects.

Figure 8 shows the same setup as simulated in Fig. 7 for the case of the SarconTM interposer but this view is a cross-section along the thermode length at mid-height in the ACF layer. The temperature in the ACF below the traces is much lower compared to the temperature in the space region demonstrating how much of an effect the metal circuit lines have on the simulated temperature. This highlights the importance of thermocouple placement for real part thermal characterization as the metal traces conduct away some of the heat, while the spaces between these traces do not.

4.2. Representational Assembly Touch Screen Design

4.2.1. Effect of Bonding Equipment Base Material

In Fig. 9 a comparison of base material again was considered but in this case for the representational assembly touch screen design (Fig. 3b, but without the polyimide coverlayer) after 10 s application of the thermode heat and pressure. This model compares the thermally insulating phenolic base with the more thermally conductive steel base. At the constant thermode setpoint temperature the predicted ACF layer temperature differed by about 50°C. This simulation also shows the difference in the thermal gradients through the layers comparing the conductive vs insulating base materials. This shows that the touch screen base materials (polyester and optically clear adhesive) will tend to be at higher temperature for the case

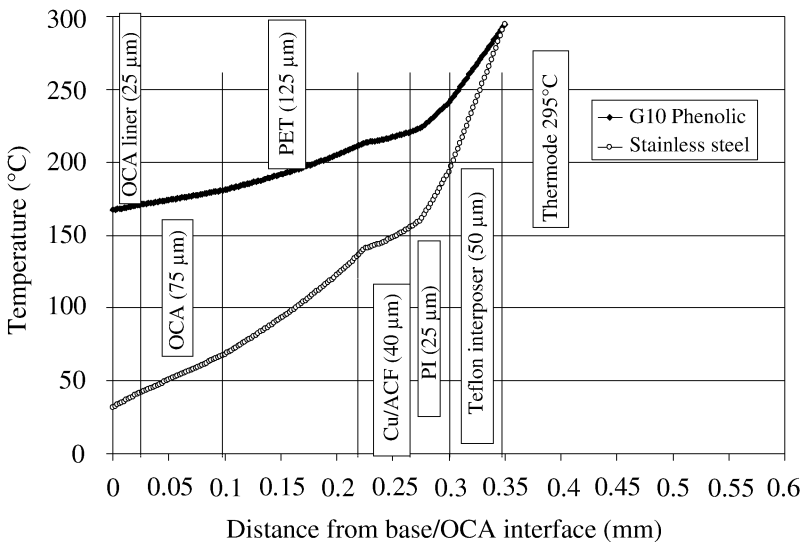


Figure 9. Simulated model showing the instantaneous temperature profile (y-axis) through the cross-sectional assembly layers (x-axis) along the thermode centerline for ACF bond using the representational assembly touch screen design (Fig. 3b). Graph shows calculations comparing phenolic base (solid diamonds) vs stainless steel base (open circles) for a thermode setpoint of 295°C and a time of 10 s.

of the phenolic base compared with the case of the steel base. Typically, such a temperature difference will be compensated for by changing the thermode setpoint temperature.

4.2.2. Effect of Bonding Equipment Thermode Temperature Setpoint

In Fig. 10 a comparison of thermode setpoint temperatures is shown again for the case of the representational assembly touch screen design (Fig. 3b) after 10 s application of the thermode heat and pressure. This model compares thermode setpoint temperatures of 295, 330 and 365°C. The model in this case also shows the inclusion of a polyimide coverlayer positioned on the top-side of the flexible printed circuit. The model predicts that the presence of this coverlayer imparts a staggering temperature drop of at least 100°C through the 50 μm thickness of this layer alone. This is a complicating issue as the setpoint temperature increase of 70°C shows only about a 20°C increase in the predicted temperature in the ACF layer.

In Fig. 11 the same setup as simulated in Fig. 10 is shown but in this graph the temperature profile experienced within the ACF layer is plotted along the thermode width direction. At the midpoint of the thermode width, the temperatures are at a maximum value that corresponds to the middle of the Cu/ACF region shown in Fig. 10. The midpoint temperatures for this simulation range from about 80°C to 100°C corresponding to the range of thermode setpoint temperatures selected. Again, there is a significant thermal gradient, the temperature dropping on either side of the x-axis origin of the plot, which is the centerline of the thermode width.

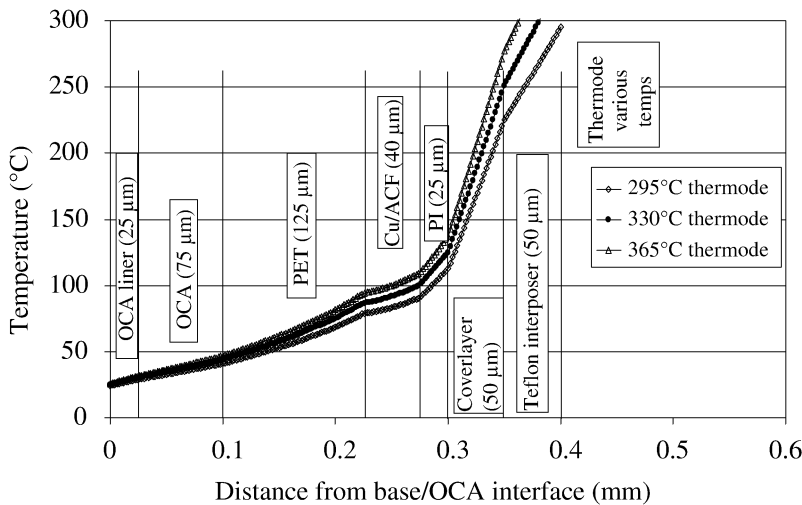


Figure 10. Simulated model showing the instantaneous temperature profile (y-axis) through the cross-sectional assembly layers (x-axis) along the thermode centerline for ACF bond using the representational assembly touch screen design (Fig. 3b). Graph shows calculations comparing thermode setpoint temperatures of 295 $^{\circ}\text{C}$ (open diamonds), 330 $^{\circ}\text{C}$ (closed squares) and 365 $^{\circ}\text{C}$ (open triangles) at 10 s.

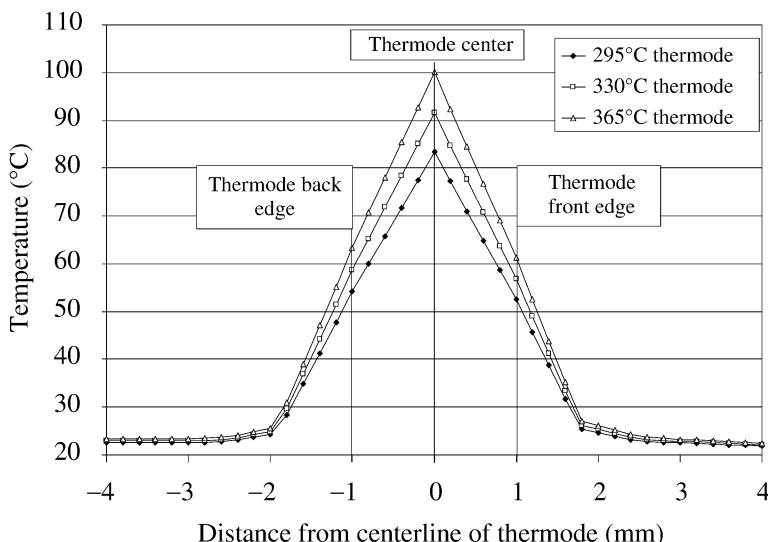


Figure 11. Simulated model showing instantaneous temperature profile (y-axis) across assembly bond length using the representational assembly touch screen design (Fig. 3b). The temperature plotted comes from the calculation made in the center of ACF layer and at center of thermode length. The thermode edges and center are marked with solid lines. Graph shows calculations comparing thermode setpoint temperatures of 295 $^{\circ}\text{C}$ (closed diamonds), 330 $^{\circ}\text{C}$ (open squares) and 365 $^{\circ}\text{C}$ (open triangles) at 10 s.

Regardless of setpoint temperature, the simulated temperature has dropped by over 30°C from the thermode center to the edge of the thermode width. (Note this temperature drop compares very closely to the simulated case shown in Fig. 5 regardless of the difference in the design of the model, the change of base material, or the addition of the coverlayer. Although both simulations include the same flexible printed circuit layer having the same metal circuit design.)

5. Summary and Conclusions

These simulations show some of the more important considerations for ACF bonds to devices such as plastic touch screen or plastic flat panel displays. The predictions reveal that the thermal gradients are very large through the layers in these devices. Typically, the change in temperature through a polyester layer directly below the ACF is at least 50°C. The ACF temperature always is shown to be at least 10–20°C higher than the PET top surface layer located directly below the ACF. In addition, the temperature gradient continues through the thickness of the PET thus insuring that there is only little likelihood of incurring damage to the PET device.

The design of the assembly is important to the resulting temperatures through each layer during bonding. The difference in flexible printed circuit material thickness and the addition of a coverlayer changed the temperature in the ACF layer. The temperature drop through 50 µm thick polyimide flexible printed circuit was at least 40°C with the insulating base and over 70°C with the metal base. The simulation that included the 50 µm thick polyimide coverlayer showed over 100°C drop in this layer. This reiterates that any change in the overall design may cause an unforeseen change in the ACF layer temperature, affecting the cure and bond reliability. Also, the added OCA layers effectively make the base layer somewhat more insulating.

Bonding equipment base material was shown to cause a dramatic change to the temperature gradient through all layers. The thermally conductive base acts as a very efficient heat sink and produces very steep gradients. On the contrary, the thermally insulating base reduces this gradient. As a consequence, to achieve the target ACF layer temperature the thermode setpoint temperature must be adjusted to much higher temperature setting for the metal base. One advantage to using the metal base is to help insure, by virtue of the very steep temperature gradient, that the PET layer will be at a much lower temperature than the ACF layer to help avoid potential damage. Further, the efficiency of the metal base heat sink will help to keep the actual bonding temperatures through all layers more stable through multiple cycles in high-volume production.

Thermocouple placement is important. The temperature measured by these thermocouples is affected by their placement relative to the circuit lines as well as relative to the centerline of the bonding thermode. According to these simulations, a thermocouple underneath a circuit line or quite far from the thermode centerline can result in a more than 30°C difference compared with being located between the traces or perfectly centered. The choice of location for the thermocouple em-

bedded test sample depends on the need to determine the minimum temperature or maximum temperature. Knowing the minimum temperature can permit achieving adequate ACF adhesive cure, so placement of the thermocouple should be under a trace and at the edge of the thermode bonding area. Knowing the maximum temperature can help to avoid thermal degradation, and the maximum would be detected by a thermocouple placed between traces and in the centerline of the thermode. Accurate placement of the thermocouple and reproducibly locating the embedded test sample relative to the bonding thermode is necessary to achieving identical temperature settings over time.

The details highlighted in this discussion clearly indicate how it is so challenging to measure temperatures without inevitable inaccuracies or uncertainties. The simulations have provided clear evidence of the main trends and key factors that need to be carefully considered. Overall, the temperature measurement reproducibility and accuracy can be improved by painstaking attention to the following considerations:

- The need to minimize the thermocouple size.
- The need to exercise extreme accuracy in the placement of the thermocouple, and understand that the placement will affect the measurements.
- The need to check the temperature regularly using embedded test samples to monitor the bonding conditions. However, through repeated use these test samples may suffer some degradation and, in some cases, will require periodic replacement.

This provides the possibility of attaining the highest yield and highest reliability when using ACF materials for the assembly of leading edge electronic devices within highly limiting process restrictions.

References

1. W. A. MacDonald, M. K. Looney, D. MacKerron, R. Eveson, R. Adam, K. Hashimoto and K. Rakos, *J. SID* **15**, 1075–1083 (2007).
2. J. P. Holman, *Experimental Methods for Engineers*, 3rd edn. McGraw Hill Higher Education, New York, NY (1978).
3. H. Shaukatullah and A. Claassen, in: *Proc. IEEE SEMI-THERM Symposium*, San Jose, CA, pp. 97–105 (2003).
4. H.-C. Chang, C.-L. Ho, W.-C. Chen and S.-S. Yang, *IEEE Transactions on Components and Packaging Technologies* **29**, 557–588 (2006).
5. J. Ge, I. Saarinen and P. Savolainen, in: *Proc. IEEE 2006 Electronic Components and Technology Conference*, San Diego, CA, pp. 1499–1503 (2006).

This page intentionally left blank

Operating Temperature of Anisotropic Conducting Film Adhesives

Ranjith Divigalpitiya *

3M Canada Company, 1840 Oxford Street East, London, Ontario, Canada N5V 3R6

Abstract

Polymeric adhesive materials used in anisotropic conducting films (ACFs) are thermally the weakest link in them; they have to be able to withstand the temperature resulting from the current flow in them for reliable operation of devices using ACFs. The current carrying capacity of an ACF is, thus, limited by the thermo-mechanical performance of the polymer material used. A simple thermal model is presented to estimate the operating temperature of anisotropic conducting adhesive films in terms of current, conducting particle density, particle size and resistance of the ACF. The model can be used to predict the current carrying capacity of electrically conductive adhesives if the thermal performance of polymeric resin is known.

Keywords

Anisotropic conductive adhesive, ACF, temperature, heat transfer

1. Introduction

Anisotropic conductive film (ACF) adhesives are made with electrically conducting particles dispersed in an adhesive matrix. The adhesive bonds two substrates while the conducting particles provide paths for the electrical current from one substrate to the other [1]. Since ACFs carry current in electronic applications, an inevitable question arises regarding the effect of the current conducted *via* the conducting filler particles on the polymeric resin. The polymeric resin is the weakest component in the system, in general, with respect to thermal stability. When an electrical current is passed in a conductor, heat is generated due to Joule heating. The performance of an ACF is dependent upon the temperature and its thermo-mechanical properties. For example, the adhesive will soften at a certain temperature, and if the current heats up the ACF to that temperature, then it is likely that the electrical bond will have a high chance of failure. Even though it is important to understand the limits of operation of ACF in this context, very little work has been reported in literature thus far [2]. In the work regarding the temperature of electrical contacts, what is routinely cited

* Tel.: 519-451-2500-2175; Fax: 519-452-6763; e-mail: rdivigalpitiya@mmm.com

is the maximum temperature estimated for metallic contacts with the theory (called the Ψ - Θ theorem) formulated by Holm [3], and later by Jones [4]. However, this maximum temperature estimation is done independent of heat transfer and assumes “lagged” (or completely insulated) samples with the condition that the vector flow of energy everywhere is zero [4]. This flow condition is not met in many practical scenarios.

The other possible route to estimating the operating temperature is thermal analysis using finite element analysis [2]. However, an analytical method, which is useful in examining the effects of many parameters to understand the behavior of an ACF, is missing in the literature. In the present work, we will describe a simple steady-state thermal model which takes thermal transfer across contacts into account. Using this simple model we can estimate the operating temperature of an ACF as a function of current carried by it and examine the effects of other relevant parameters. We will show that the model can be used to estimate the current carrying capacity of ACFs as well.

2. Model

Let us consider an ACF with solid, electrically conducting, metallic particles embedded in a polymeric resin. For example, the ACF will be used between two copper pads in the case of bonding two flex circuits together. This is shown schematically, in cross section, in Fig. 1. Conducting particles are considered as rigid solid particles in this case as opposed to coated resin particles which are deformable. The contact pads (circuit traces) made of copper could be on a polyimide film.

In the idealized structure shown in Fig. 1, all conducting particles are considered to be identical in size and uniformly distributed in the adhesive. To simplify calculations, let us consider one conducting particle, as shown in Fig. 1, in a rectangle of width L (dashed lines); we will consider this rectangle as a “unit cell”. Conceptually, the unit cell can be translated in x and y directions, in constant

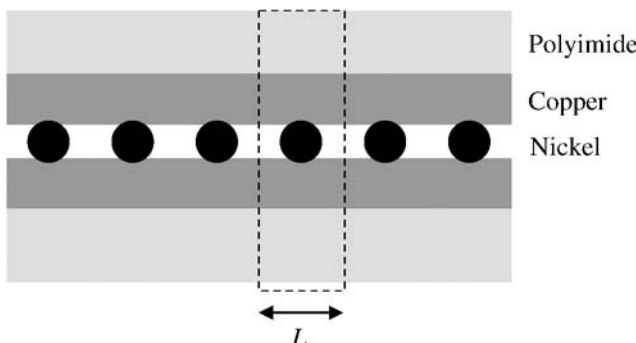


Figure 1. A schematic diagram of an anisotropic conducting adhesive film with nickel particles (shown as ●) used to bond two copper pads. The rectangle marked in dashed lines can be considered as a unit cell.

displacements, and generate the complete ACF bond. Considering typical sizes of conducting particles used in ACFs ($1\text{--}50\ \mu\text{m}$) in relation to the dimensions of flex circuits ($5\text{--}40\ \text{mm}$), we can assume that the sample extends to infinity in both x and y directions. The model is applicable to ACF bonds formed between pads which are much larger than the conducting particles in them such that the sample can be considered infinite with respect to the particles. This indicates that the model will be more suitable for applications such as smartcard bonding, flex-to-flex bonding but not to flip-chip applications where only a handful of particles are present in a bonding pad. The last case can be accommodated with some simple modifications to the boundary conditions which will be discussed in a later section.

To illustrate the model better, consider a three-dimensional diagram of the unit cell as shown in Fig. 2. For uniformly distributed particles of diameter D , we will assume that the distance between the particles (center to center) is two diameters, thus, $L = 2D$. Any desirable value can be used for the cell size L which, in practice, is determined by the size and the number density of conducting particles in the adhesive.

Since all conducting particles are considered identical, by considering a single cell we can understand the behavior of the system. A potential difference applied between the top and bottom conductors drives a current through the particle. This current will generate heat in the conducting parts of the structure due to Joule heating. Heat, thus produced, will be conducted away from the cell solely by top and bottom surfaces. Since the cells are considered identical, the temperatures on both sides of a side-wall between adjacent cells are the same, so we can ignore heat conduction from four sides of a unit cell. Thus, with identical cells, the boundary

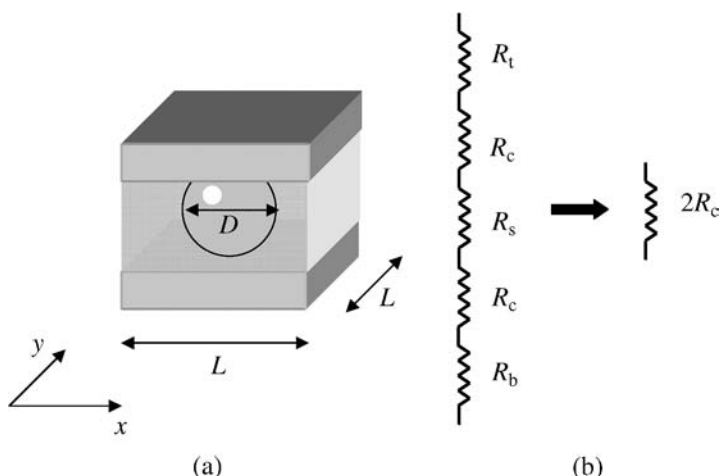


Figure 2. (a) A schematic diagram of a unit cell. This unit can be translated in both x and y directions in multiples of fixed increments of L to generate the ACF between two flex pads. (b) A simplified equivalent circuit of the unit cell showing the approximation used, where R_t resistance of top pad, R_c constriction resistance, R_s resistance of spherical particle and R_b resistance of bottom pad.

conditions for solving the electro-thermal problem are simplified. The steady state temperature of the cell is then the temperature of the ACF.

We neglect the edge effects in the simple model in which the attempt is to capture the average thermal behavior of the system. We note that the above model is equivalent to considering a free-standing sample whose thickness is much less than its lateral dimension. In this case, the heat loss from the periphery is justifiably neglected since the loss rate is proportional to the cross-sectional area; the periphery has a smaller cross-sectional area than the top and bottom surfaces. Following the same logic, we have ignored any edge conduction to or from external contacts as well.

At the steady state condition, the Joule heating in the conductors is balanced by the amount of heat lost by convection from top and bottom surfaces. This equilibrium condition determines the temperature of the idealized ACF bond.

If the total electrical resistance of the unit cell is R and the current through the cell is I , then, using Newton's law of cooling [5], we can write,

$$I^2 R = h_t A(T - T_0) + h_b A(T - T_0), \quad (1)$$

where T is the temperature of the adhesive (unit cell), T_0 is the ambient temperature, A is the surface area of the cell, h_t and h_b are the heat transfer coefficients of the top and bottom surfaces, respectively [5, 6]. The left-hand side of equation (1) is the electrical power (energy per unit time) consumed by the structure generating heat.

A simplifying assumption is that the heat transfer coefficient of the top surface is the same as that of the bottom surface. For example, if the bonded flex circuits are held vertically, this condition is satisfied. Substituting $h_t = h_b = h$ in equation (1) we obtain

$$I^2 R = 2hA(T - T_0). \quad (2)$$

Equation (2) can be rewritten as

$$T = T_0 + \frac{I^2 R}{2hA}. \quad (3)$$

Equation (3) clearly indicates the relationship of equilibrium temperature of the adhesive bond with the experimental parameters. I is an externally controlled (independent) variable whereas A and R represent the system parameters which will be determined by, essentially, the size and type of conducting particles, and the number density of the particles in the bond. An important feature of this simple model is that it shows how the cell resistance determines the adhesive temperature in a predictable way. We will examine the implications of equation (3) below.

We notice that equation (3) is also independent of the current carrying mechanism of the ACFs: it represents a very general approach to the thermal problem. At present, there is a controversy in the literature [7, 8] regarding the exact nature of conduction mechanism of an ACF. The presence of an extraneous material, such as an oxide, at the particle/contact pad interface as well as possible tunneling via insulative barrier materials have been discussed in the literature [7, 8]. This subject

will be examined elsewhere in detail; however, at least in the case of ACFs comprised of insulative spheres coated with a thin electrically conducting layer, the role of interfacial materials is only marginal. The reason for this was shown recently [9] where the contact resistance was calculated analytically as well as with finite element analysis as a function of the amount of insulative material at the particle/pad interface. In this study it was shown that the effect of the presence of an insulating material at the particle/pad contact interface on the total resistance was very minimal at best. In the case of solid conducting particles, however, the resistance is somewhat affected by interfacial materials [9]. So, depending on the situation, one needs to use the correct form of resistance in equation (3) to estimate the equilibrium temperature of the adhesive.

Alternatively, the measured resistance of an ACF can be used in equation (3) for more accurate prediction of temperature. Such values are available in a recent publication [8].

Next, we will find a relation between the temperature T and material parameters of the ACF by writing appropriate expressions for R and A and substituting them in equation (3). Ignoring contaminants at the interface between the metallic particles and bonding pads, let us express the resistance of the cell as

$$R = R_t + R_c + R_s + R_c + R_b, \quad (4)$$

where R_t , R_c , R_s and R_b represent the resistance of top pad, constriction resistance at the contact with the particle and the pad, resistance of the spherical metallic particle, and the resistance of the bottom pad, respectively (see Fig. 2(b)).

Assuming that the top and bottom pads are electrically identical, equation (4) can be written as:

$$R = 2(R_b + R_c) + R_s, \quad (5)$$

since $R_t = R_b$. In a typical situation, it can be verified that R_c dominates over R_s and R_b since $a \ll L$ and $a \ll D$. Thus, $R_c \gg R_b$ and R_s and equation (5) simplifies to

$$R = 2R_c. \quad (6)$$

If the radius of the contact circle at the particle/pad interface is a , then R_c can be written as [10]

$$R_c = (\rho_b + \rho_s)/4a, \quad (7)$$

where ρ_b and ρ_s are the resistivities of pad material and particle material, respectively. Substituting for R_c in equation (6) from equation (7) we obtain

$$R = (\rho_b + \rho_s)/2a. \quad (8)$$

If δ is the depth of indentation of the spherical particle in the pad, and D is the diameter of the particle, then using the geometric relation $a = \sqrt{(D - \delta)\delta}$ (Fig. 3) we can rewrite equation (8) as

$$R = (\rho_b + \rho_s)/2\sqrt{(D - \delta)\delta}. \quad (9)$$

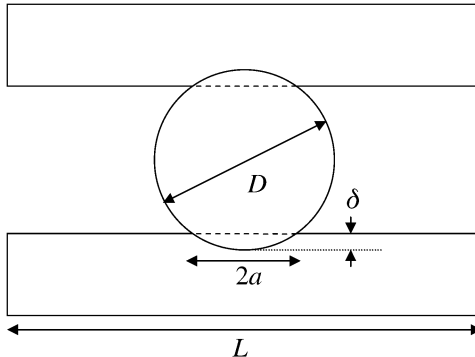


Figure 3. A schematic cross-sectional diagram of the geometry of a rigid sphere indenting two contact pads. D is the diameter of the particle making an indentation δ which corresponds to a contact circle of radius a (dashed lines); they satisfy the relation $a = \sqrt{(D - \delta)\delta}$.

If N is the number density of particles present in the ACF bond, expressed in units of particles per unit area, and assuming the particles are distributed uniformly in a square lattice, the dimension L is given by $L = 1/\sqrt{N}$. Since $A = L^2$, we obtain

$$A = 1/N. \quad (10)$$

Now we can substitute for R and A in equation (3) from equations (9) and (10) and finally obtain for copper pads and nickel particles

$$T = T_0 + \frac{I^2 N (\rho_{\text{Cu}} + \rho_{\text{Ni}})}{2h\sqrt{(D - \delta)\delta}}. \quad (11)$$

Equation (11) expresses the equilibrium temperature of the adhesive in terms of current, particle size, depth of indentation and electrical parameters of the components in the adhesive.

In practice, during application of an ACF, a prescribed pressure is used [11] to ensure that electrical contacts are made by conducting particles with the pads. This bonding pressure determines the indentation δ . In the analysis below we will use different values of D , size of particles and other parameters in equation (11) and examine their effect on the operating temperature of ACFs. In present treatment of the thermal problem of ACFs we ignore the temperature dependence of the electrical resistivity; however, one can substitute for $\rho_b(T)$ and $\rho_s(T)$ with known temperature coefficients of resistivities of materials involved in equation (11) and solve for T if desired.

3. Analysis and Discussion

First, we will calculate the resistance of a unit cell using equation (9) as a function of particle size to determine the range of resistance values to be used in equation (3).

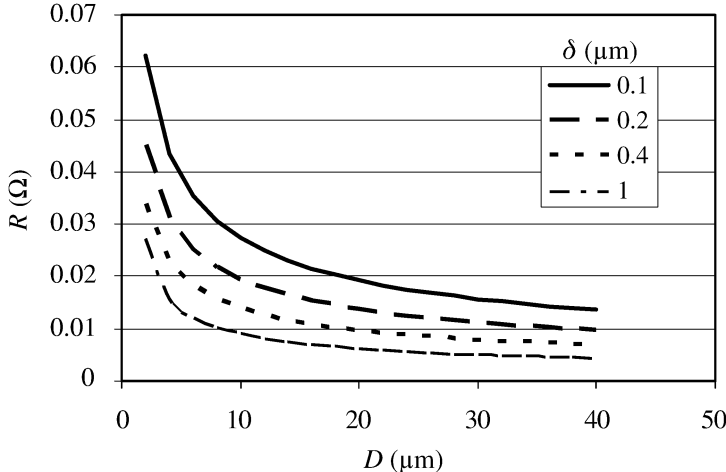


Figure 4. Estimated resistance R of a unit cell as a function of particle size D for different values of δ using equation (9). Following parameters are used: $\rho_b = 1.7 \times 10^{-8} \Omega \text{ m}$ and $\rho_s = 7.3 \times 10^{-8} \Omega \text{ m}$.

The results from equation (9), the calculated resistance of a unit cell as a function of particle size for various depths of indentation, are shown in Fig. 4.

As the depth of penetration or, in other words, the degree of indentation of the metallic particles in the contact pads is increased the resistance decreases as expected due to the increase of effective contact area. And, for the same reason, R decreases with increasing particle size. Figure 4 shows that the variation due to the particle size is small because of its square root dependence (see equation (9)).

Before we carry out any further calculations, we have to select a coefficient of heat transfer for the top and bottom surfaces. In electronic applications, typically, h for natural convection in air is taken as $5 \text{ W/m}^2 \text{ K}$ [6].

Figure 5 shows the effect of h on the operating temperature of the ACF, and as expected, cooling the contacts with an air flow, for instance, will increase h and, thus, reduce the temperature. It is worth noting that at the low current values ($< 5 \times 10^{-3} \text{ A}$), the effect of varying the convective heat transfer coefficient is not very significant and the ACF bond seems to maintain a constant temperature irrespective of the thermal transfer characteristics: the effect of h is more pronounced at higher currents than with lower values. In all subsequent calculations, we will use $5 \text{ W/m}^2 \text{ K}$ for the heat transfer coefficient h .

With the range of resistance values determined using equation (9) (see Fig. 4), now we can examine the resulting temperatures in the ACF by substituting those values for R in equation (3). Figure 6 shows the calculated variation of the operating temperature as a function of resistance of a unit cell for the case of particles of size $10 \mu\text{m}$. Several values of current passing through the particle are shown. According to equation (9), the current I has a larger effect on the steady state temperature than the particle size D .

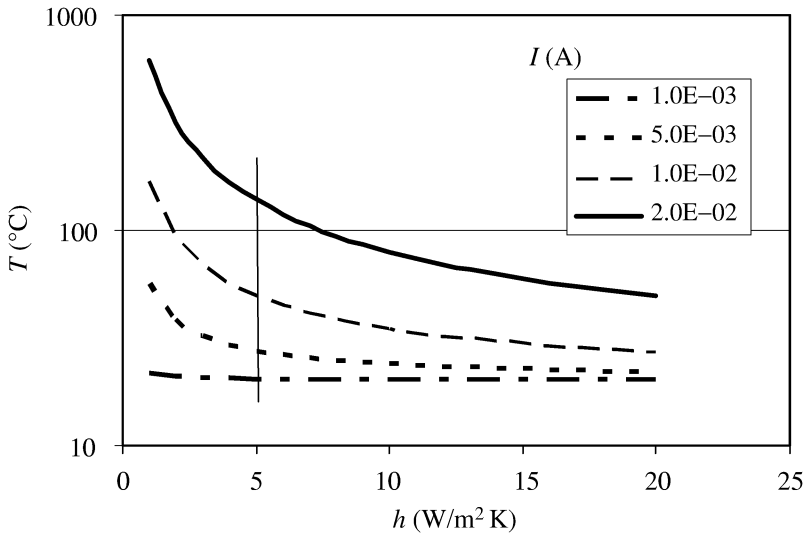


Figure 5. The calculated operating temperature T of an ACF with particles of diameter $D = 10 \mu\text{m}$ as a function of heat transfer coefficient h for various values of current I flowing through a unit cell. The total current in the sample is simply the number of conducting particles in the sample multiplied by this current. The case of natural convection in air ($h = 5 \text{ W/m}^2 \text{ K}$) is shown with a vertical line.

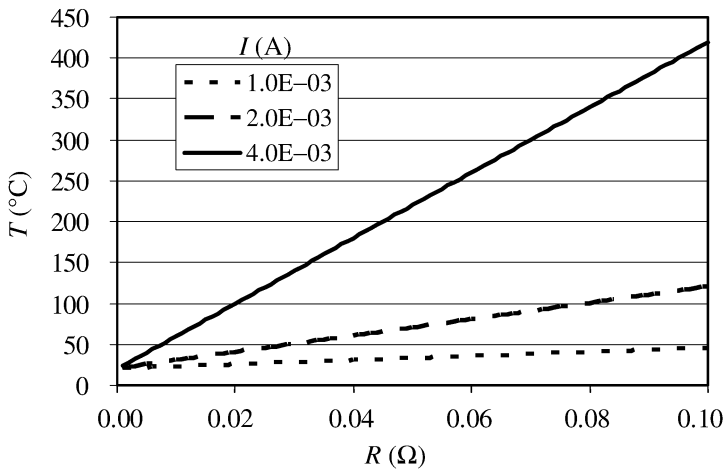


Figure 6. The calculated operating temperature T of an ACF as a function of the resistance R of its unit cell for different levels of current I flowing through it (equation (3): $h = 5 \text{ W/m}^2 \text{ K}$; $D = 10 \mu\text{m}$; $L = 20 \mu\text{m}$; $A (=L^2) = 4.0 \times 10^{-10} \text{ m}^2$).

Results of calculations using equations (9) and (11) are shown in Table 1 for different particle sizes with a constant current of 10^{-2} A flowing through each particle. Four unit cell sizes, which represent four different number densities of particles, are used in the calculation. The corresponding particle number density is also shown along with the calculated temperature, for comparison. The advantage

Table 1.

Calculated resistance R (equation (9)) and the corresponding operating temperature (equation (11)) of an ACF adhesive which contains mono-sized particles carrying a current of 10^{-2} A via one particle. The indentation (δ) made by the particle on the pads is set at 1 μm depth and $h = 5 \text{ W/m}^2 \text{ K}$

D (μm)	a (μm)	R (Ω) $\times 10^{-3}$	$L = 2D$	$L = 4D$	$L = 8D$	$L = 16D$
			T ($^\circ\text{C}$) ($N \#/\text{m}^2$)			
4	1.73	15.65	2465 (1.56E+10)	631 (3.91E+09)	173 (9.77E+08)	58 (2.44E+08)
10	3.00	9.04	246 (2.50E+09)	77 (6.25E+08)	34 (1.56E+08)	24 (3.91E+07)
40	6.24	4.34	27 (1.56E+08)	22 (3.91E+07)	20 (9.77E+06)	20 (2.44E+06)

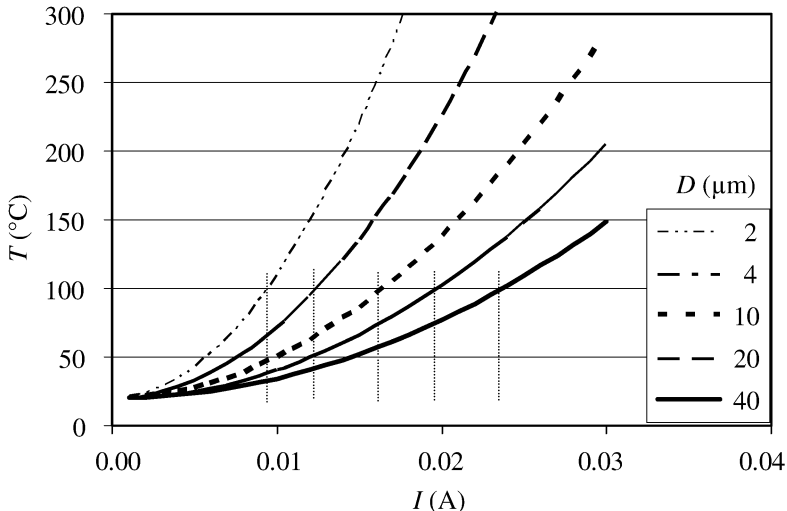


Figure 7. The calculated operating temperature T of an ACF as a function of current I flowing through a unit cell for different sizes of particles D (equation (11): $h = 5 \text{ W/m}^2 \text{ K}$, $\delta = 1 \mu\text{m}$).

of using large particles (40 μm) in the ACF to maintain lower temperature is seen with this result.

Now we will use equation (11) and examine the dependence of particle size on the operating temperature for various amounts of current through the particle. The expected parabolic or quadratic dependence on current due to Joule heating is seen in equation (11) and the resulting curves are shown in Fig. 7.

The other parameters in equation (11) that can have an influence on the operating temperature of the ACF is the number density of conducting particles N . In Fig. 8, we show the effect of N on the temperature of the adhesive at various values of

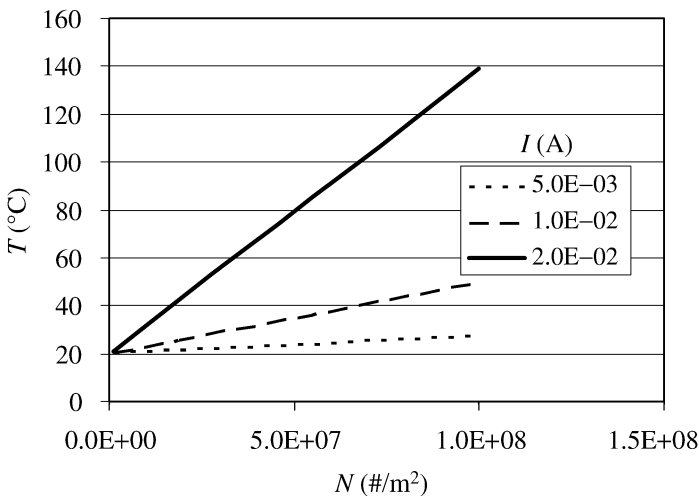


Figure 8. Calculated variation of temperature T of an ACF with particles of diameter 10 μm as a function of the number density N for different levels of current I flowing through it (equation (11): $h = 5 \text{ W/m}^2 \text{ K}$; $\delta = 1 \mu\text{m}$).

current flowing through a particle of diameter of 10 μm . A linear dependence of temperature on N and a strong influence of current are clearly seen in Fig. 8.

In practice, the thermal behavior of the adhesive used in ACF is known. For example, the glass transition temperature T_g in the case of a thermosetting polymer or the softening temperature in the case of a thermoplastic (hot-melt) adhesive can be measured experimentally. These parameters will set the limit of operation of the adhesive in applications. Alternatively, one can design an adhesive to have the T_g or the softening temperature well above the predicted temperature due to the current the ACF is expected to carry. For example, if the softening temperature of the adhesive is around 100°C, then Fig. 7 shows the current a particle of given size can carry, marked with vertical dashed line. Any current above this critical value will produce higher temperature in the adhesive resulting in potential bond failure provided there is no external mechanical support keeping the bond constrained.

If the particle number density in an ACF sample is known, then it is a simple matter to estimate the current carrying capacity of the ACF by multiplying the above critical current value with the number of particles in the bond area. Table 2 shows an example of such an estimate of the current carrying capacity of an adhesive limited by its softening point, which is assumed to be around 100°C, using equation (9). With the values used, we find that the current carrying capacity increases only slowly with increasing particle size: an order of magnitude increase in size increases the current capacity only by two folds.

Equation (11) shows that the current I and the particle number desnity N in the ACF have a larger effect on its operating temperature than the particle size D or the indentation δ . This behavior is seen in Figs 7 and 8. As expected, the higher the

Table 2.

Estimated value of the critical current through a particle in an ACF adhesive, whose softening temperature is around 100°C, for particles of different sizes determined with the aid of equation (11) and Fig. 7 with $N = 10^8/\text{m}^2$

Particle size (μm)	Critical current for a particle (A)	Estimated current carrying capacity (A/m^2)
2	9.5×10^{-3}	0.95×10^6
4	12.5×10^{-3}	1.25×10^6
10	17.0×10^{-3}	1.70×10^6
20	20.0×10^{-3}	2.00×10^6
40	24.0×10^{-3}	2.40×10^6

glass transition temperature or the softening temperature of the adhesive, the higher the current carrying capacity of ACF.

We indicated that the model is more applicable to cases where the sample is relatively large compared to the conducting particles; hence, it is only marginally suitable for flip-chip applications where a very small number of particles are present in a bonding pad ("bump") of relatively small size. This situation can be addressed by the model by simply modifying equation (1) using the appropriate heat transfer coefficient (h_t) and the operating temperature of the chip instead of the ambient temperature.

4. Conclusions

The steady-state thermal model described above allows us to estimate the operating temperature of an ACF adhesive and examine the effects of material and external parameters on it. ACFs with smaller conducting particles have higher temperatures than those with large particles at the same current load. Increasing the number of particles in a bond increases the temperature. The convective cooling effect of a "forced" system is understood with the steady-state model in terms of the heat transfer coefficients of the surfaces. The current carrying capacity of an ACF does not vary drastically as the particle size is increased.

One can select a polymeric adhesive to operate below a certain threshold temperature by selecting experimentally accessible relevant parameters such as the size of the particles, number density of the particles, and resistance of the metallic particles according to the model, for a given current.

Acknowledgement

I wish to thank Prof. Kanthi Kaluarachchi of the Department of Physics and Astronomy, University of Western Ontario for reading the manuscript and making valuable suggestions.

References

1. C. T. Murray, R. L. Rudman, M. B. Sabade and A. V. Pocius, *MRS Bulletin* **28**, 449 (2003).
2. C. N. Oguibe, S. H. Mannan, D. C. Whalley and D. J. Williams, *IEEE Trans. Compon. Packag. Technol.* **21**, 235 (1998).
3. R. Holm, *Electrical Contacts*. Springer-Verlag, Berlin (1967).
4. F. L. Jones, *The Physics of Electrical Contacts*. Clarendon Press, Cambridge, UK (1957).
5. J. M. Coulson and J. F. Richardson, *Coulson & Richardson's Chemical Engineering*, 6th edn. Butterworth Heinemann, London (1999).
6. A. Bejan and A. D. Kraus, *Heat Transfer Handbook*, p. 958. Wiley, New York, NY (2003).
7. M. Chin, K. A. Iyer and S. J. Hu, *IEEE Trans. Compon. Packag. Technol.* **27**, 317 (2004).
8. J. H. Constable, *IEEE Trans. Compon. Packag. Technol.* **29**, 494 (2006).
9. R. Divigalpitiya, *IEEE Trans. Compon. Packag. Technol.* **31**, 222 (2008).
10. R. S. Timsit, *IEEE Trans. Compon. Packag. Technol.* **22**, 85 (1999).
11. R. Divigalpitiya and P. Hogerton, *J. Microelectronics Electronic Packaging* **1**, 194 (2004).

Geometric Effects on Multilayer Generic Circuits Fabricated Using Conductive Epoxy/Nickel Adhesives

Jianguo Zhou and Erol Sancaktar*

Department of Polymer Engineering, University of Akron, Akron, OH 44325-0301, USA

Abstract

Epoxy/nickel adhesives can be used as integrated circuit (IC) packaging materials due to their lower cost than epoxy/silver adhesives with acceptable electrical conductivity. In this work, conductive epoxy/Ni adhesives were prepared by the solution method and filled into holes connecting the multilayers of a novel prototype designed for use in electronic components in circuit boards, in order to study the geometric effects on the prototype's electrical resistance. An empirical equation was obtained for the contact resistance (R_c) measured after cure. We also show that Ohm's law adequately describes the effects of the bulk adhesive resistance (R_b) on prototype's electrical resistance.

Keywords

Epoxy/Ni conductive adhesives, generic circuits, electrical resistance, multilayer hole structure, geometry

1. Introduction

Electrically conductive adhesives have attracted significant attention during the last decades due to their increased usage in electronics industry to replace lead soldering [1–18]. The major applications are die attachment, liquid crystal display and surface-mounted assembly of packaged components on printed wiring boards. In general, conductive adhesive pastes are formulated by mixing polymeric resins (such as epoxies, silicones and polyimides) and highly conductive metallic fillers. Theoretical and experimental studies have been performed on basic conduction mechanisms [2–9]; the effects of particle size, shape and type [4–9]; behavior in the bonded form [6, 8–16]; processing effects, such as pressure [2, 4, 9], adhesive film thickness [3, 5, 8], silver coating [4, 5, 7], anisotropic alignment of nickel particles in magnetic field [17]; as well as the possibility of using polymeric emeraldine salt particles as conductive fillers [18]. So far, the most popular conductive adhesive formulation has been silver (Ag) particles in epoxy resin [19–22]. Nickel fillers with lower cost than silver and comparatively less oxidation, and better thermal stabil-

* To whom correspondence should be addressed. Tel.: (330) 972-5508; e-mail: erol@uakron.edu

ity than copper, offer an alternative to silver fillers, while the copper-filled systems may be unstable after exposure to elevated temperatures due to oxide growth on the particle surfaces [23]. Furthermore, silver-filled conductive adhesives suffer from the problem of silver migration, which may lead to failure in electrical conduction [24].

It is well known that process conditions affect the mechanical performance of thermosetting adhesives in general [25–29], and mechanical as well as conductive performances of electrically conductive adhesives in particular [6, 8–16].

High density electronic components of different electrical resistances, which can be manufactured as multilayer plate structures, are promising in their potential applications to circuit boards. In this work, epoxy/Ni flake adhesive was prepared by the solution method and then filled into a simplified multilayer hole model structure, a prototype of new electronic components in circuit boards, in order to study the geometric effects on the prototype's electrical resistance. Information on variations of electrical resistance *via* the geometric change from such a model structure of novel design will be very interesting and useful, prior to design and manufacturing of a new generation of electronic components in circuit boards.

2. Experimental

2.1. Materials

Aromatic epoxy, Epon 830 (diglycidyl ether of bisphenol A (DGEBA)) was received from Miller-Stephenson (Danbury, CT) with an epoxide equivalent weight of 190–198, viscosity of around 16.8 Pa s, and specific gravity of 1.16 at 25°C.

Ni 102 flakes were received from Atlantic Equipment Engineers, Division of Micron Metals, Inc. (Bergenfield, NJ) with an average diameter of 3 µm, and were etched using 10% hydrochloric acid to remove the nickel oxide on the surfaces and improve the electrical conductivity (Fig. 1(a)).

The curing agent, diethylenetriamine (DETA) was received from Resolution Performance Products (Houston, TX), and used at 12 phr for Epon 830/Ni flake system. The adhesive samples were cured at 150°C for 30 min.

2.2. Sample Preparation

We found that the solution method for incorporating conductive particles into the liquid epoxy resin provided the most uniform and the highest bulk adhesive electrical conductivity compared to other processing methods, such as two-roll mill and mechanical mixer dispersion methods (data not shown here). Hence, the solution mixing method was employed to prepare electrically conductive epoxy/Ni adhesives in this study.

For this purpose, epoxy was first dissolved in acetone until a homogeneous solution was obtained. Then, nickel flakes were added and mixed according to the desired weight ratio, which was followed by the addition of curing agent and fur-

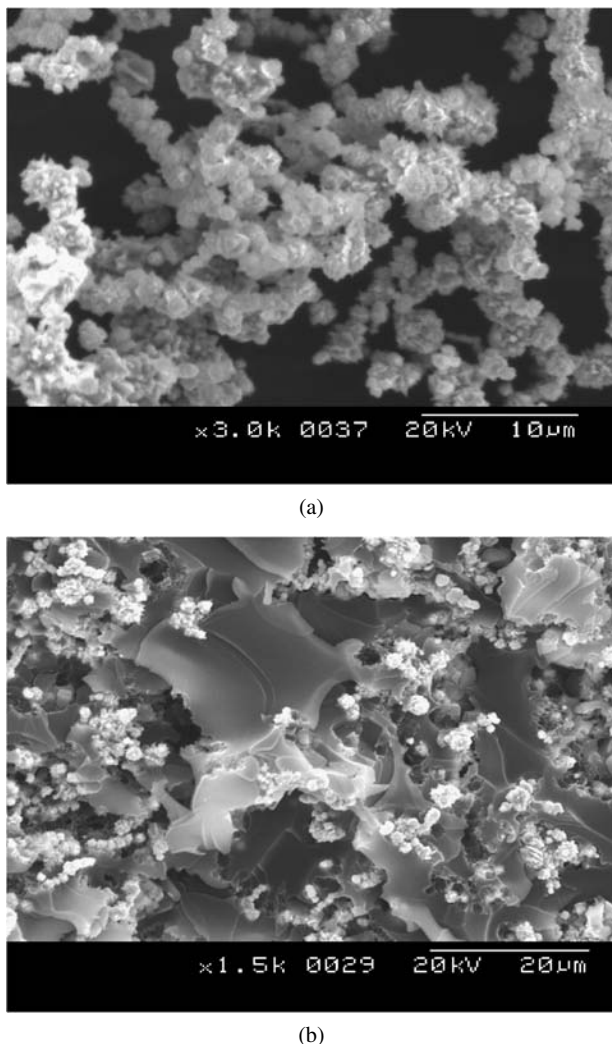


Figure 1. Scanning electron microscope images of (a) acid etched nickel flakes used in this study and (b) fracture surface of Epon 830/Ni/DETA adhesive with 50 wt% of Ni.

ther stirring. Any air bubbles and residual solvent resulting from sample preparation could be removed in vacuum at room temperature within 20 min. The resin conversion after this process, in general, was less than 8%, and the epoxy gel content of pastes, after cure at 150°C for 30 min, showed no significant difference between different nickel weight ratios. Figure 1(b) shows the micrograph of Epon 830/Ni/DETA adhesive with 50 wt% Ni, typically prepared by this process and after cure. The bulk adhesive electrical conductivity was measured using the four-probe method by Keithley 580 Micro-ohmmeter (Cleveland, OH) as schematically shown in Fig. 2.

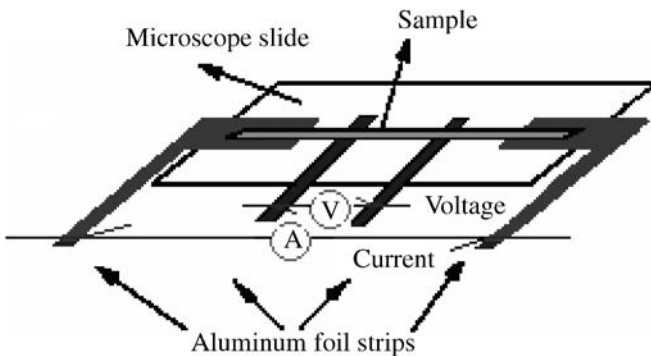


Figure 2. Schematic depiction of the four-point probe method for bulk adhesive electrical conductivity measurements.

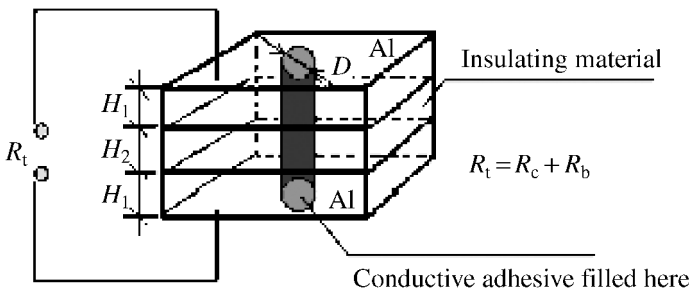


Figure 3. Schematic illustration of generic multilayer plate hole structure bonded with a conductive adhesive. H_1 is Al plate thickness, H_2 is the hole depth and D is the hole diameter. R_t is the total electrical resistance measured between the top and bottom Al plates, R_c is the contact resistance at the interface between the bulk adhesive and the Al plate in the hole, and R_b is the bulk adhesive resistance contributed by the cylindrical adhesive bulk of length H_2 and diameter D .

2.3. Design and Measurement

Figure 3 illustrates the novel design of a simplified multilayer hole model structure used in this study, where D is the hole diameter, H_1 is the aluminum (Al) plate thickness and H_2 is the hole depth. The insulating material is one or multiple pieces of Grade XX Garolite sheets (McMaster-Carr, Aurora, OH). The structural electrical resistance, R_t , measured between the top and bottom Al plates, includes the contact resistance, R_c , at the interface between the bulk adhesive and the Al plate in the hole (Fig. 3), and the bulk adhesive resistance, R_b , contributed by the cylindrical adhesive bulk of length H_2 and diameter D (Fig. 3). By changing the structure geometry, namely, D , H_1 or H_2 , different electrical resistances, R_t , are obtained. When any of the geometric dimensions were not varied as investigated parameters, their values were: $H_1 = 1.98$ mm, $H_2 = 3.18$ mm and $D = 2.74$ mm. We call specimen with these dimensions ‘base sample’.

During experiments, epoxy/Ni/DETA adhesives prepared at room temperature were filled into the hole structure, and clamps were used to fix the bonded samples.

A mounting tape was used to cover the hole at both sides, during cure in an oven preheated at 150°C for 30 min.

3. Results and Discussion

3.1. Bulk Adhesive Resistivity and Bonded Sample Resistance Changes During Cure

Complicated physical and chemical changes can happen during cure. Figure 4(a) and 4(b) shows changes of the bulk resistivity, for Epon 830/Ni/DETA adhesive with 50 wt% of Ni, and the base sample resistance, respectively, during cure at 150°C for 30 min. Obviously, intimate particle contact caused by curing reaction probably occurs between 7–9 min, as shown in Fig. 4(a), which leads to a dramatic decrease in both bulk electrical resistivity and bonded sample resistance. This implies the formation of a three-dimensional connected network as well as an approaching percolation threshold at this Ni concentration.

We think that the resistivity increase during the early stage is caused by thermal expansion of resin matrix, which pushes the nickel particles away from each other. The resistance decreases in the bonded sample as cooling starts, possibly due to the continuous cure and bulk shrinkage at lower temperatures, resulting in a tighter packing of Ni particles, as shown in Fig. 4(b).

The 60 wt% Ni adhesive provides lower bulk resistivity, as shown in Fig. 5. Furthermore, a slower change of bulk resistivity is obtained with cure time (Fig. 5(a)). The Ni concentration of 60 wt% is above the percolation threshold, thus providing this behavior. It is interesting that after about 26 min of cure, the bulk resistivity does not change while the bonded sample resistance continues to decrease instead. Obviously, interfacial contact effect exists, which can be roughly attributed to the difference between Al plate and epoxy in their thermal diffusivity a ($a = \lambda/\rho C_p$, where λ is the thermal conductivity, ρ is the density, and C_p is the heat capacity) and heat expansion coefficient α , values.

The resin has a larger heat expansion coefficient than the Al plate, but its thermal diffusivity is about one thousandth of the latter, thus resulting in much longer time for the resin to reach the ambient temperature during cure. This leads to a lack of effective interfacial contact between the bulk adhesive and Al plate, and continues until the cure is close to completion, thus leading to an increase of resistance within the first 26 min. After this, the bulk material continues to expand for some time, resulting in a more intimate interfacial contact. Hence, the bonded sample resistance decreases during the late cure stage, as shown in Fig. 5(b).

3.2. Geometric Effects

Measurements of the total electrical resistance between the top and bottom Al plates after cure were carried out after the bonded samples were cured at 150°C for 30 min, at which time the heat was turned off and the samples cooled in the furnace to room

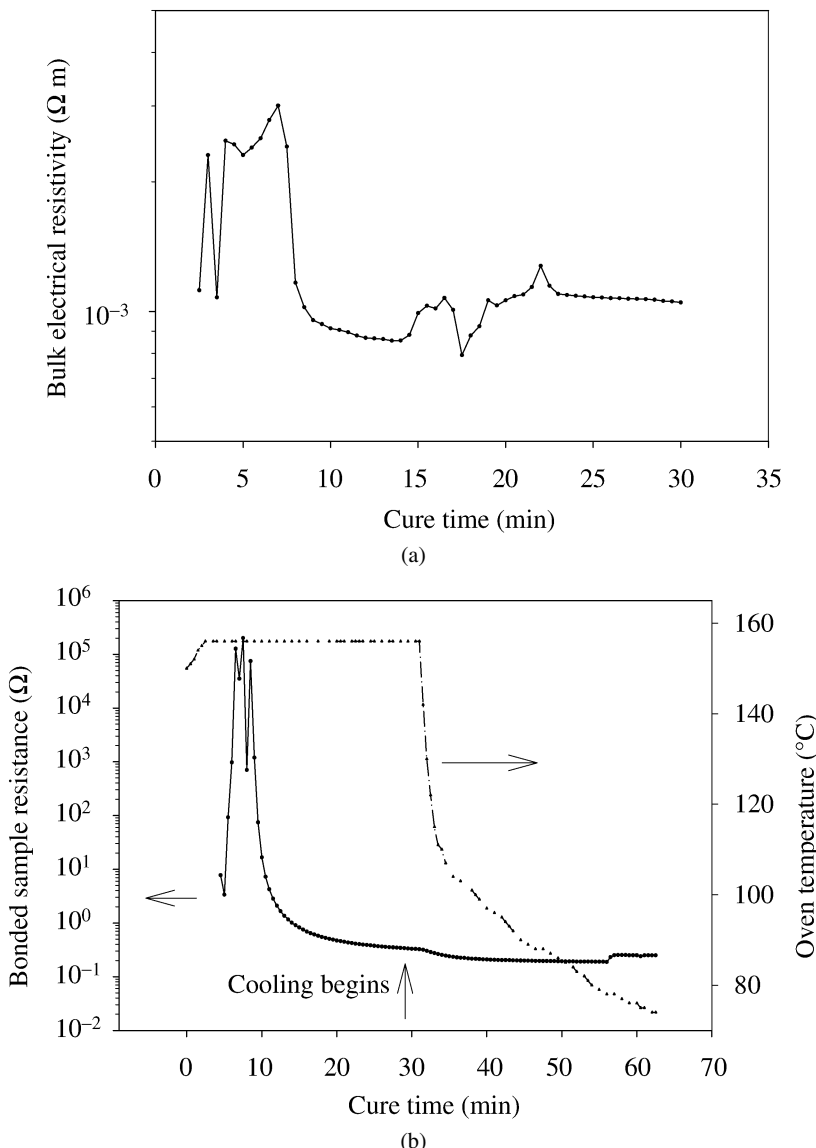


Figure 4. Changes of (a) the bulk resistivity and (b) the bonded sample electrical resistance with cure time, for Epon 830/Ni adhesive with 50 wt% of Ni during cure at 150°C for 30 min. The dashed line in (b) shows the oven temperature profile.

temperature. Generally, the fluctuations in resistance readings thus obtained were within 10%. As previously mentioned, the total resistance, R_t , includes the contact resistance, R_c , at the bulk adhesive-Al plate interfaces, and the bulk adhesive resistance, R_b , from the hole depth H_2 .

In order to separate the contact resistance from the bulk adhesive resistance, Garolite sheets were first replaced with a piece of insulating 80 μm thick Mylar

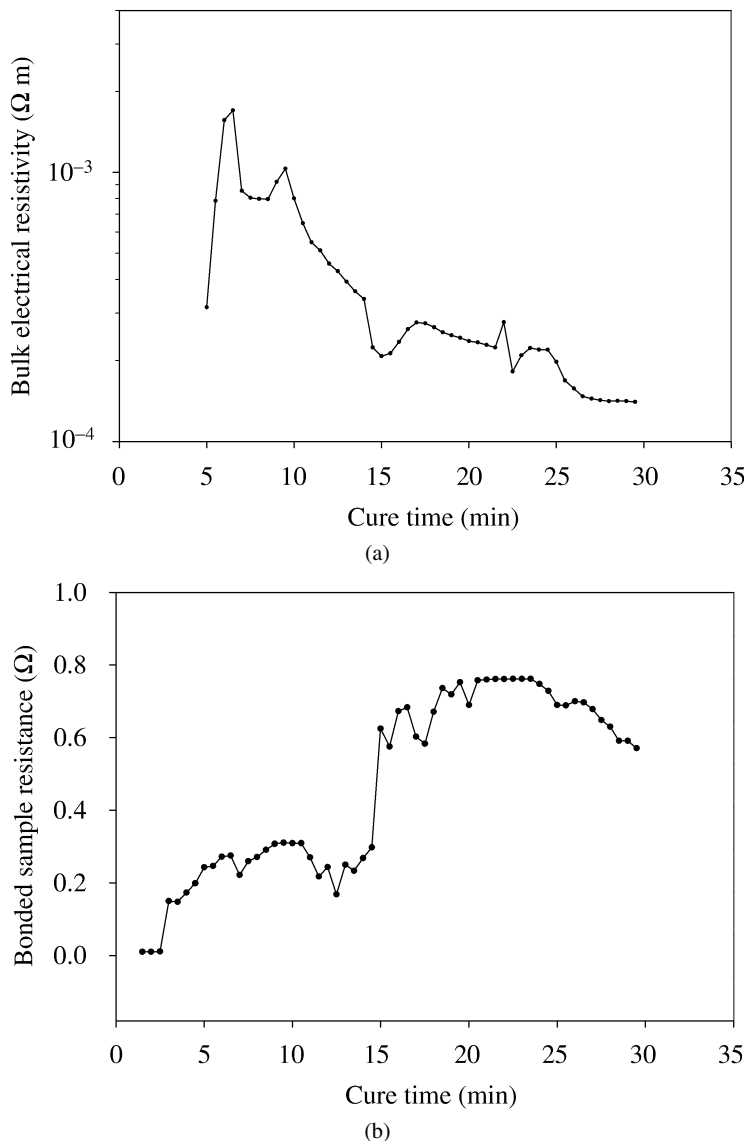


Figure 5. Changes of (a) the bulk resistivity and (b) the bonded sample resistance with cure time, for Epon 830/Ni adhesive with 60 wt% of Ni during cure at 150°C for 30 min.

film. Therefore, the contribution of the bulk adhesive resistance, R_b , to the total structural resistance, R_t , could be neglected. Figure 6(a) depicts the change of contact resistance, R_c , with the hole diameter, D , at the plate thickness of 1.98 mm. Figure 6(b) further shows this change on a logarithmic scale at two plate thicknesses. The bulk adhesive used is Epon 830/Ni/DETA with 60 wt% of Ni, and it was cured at 150°C for 30 min.

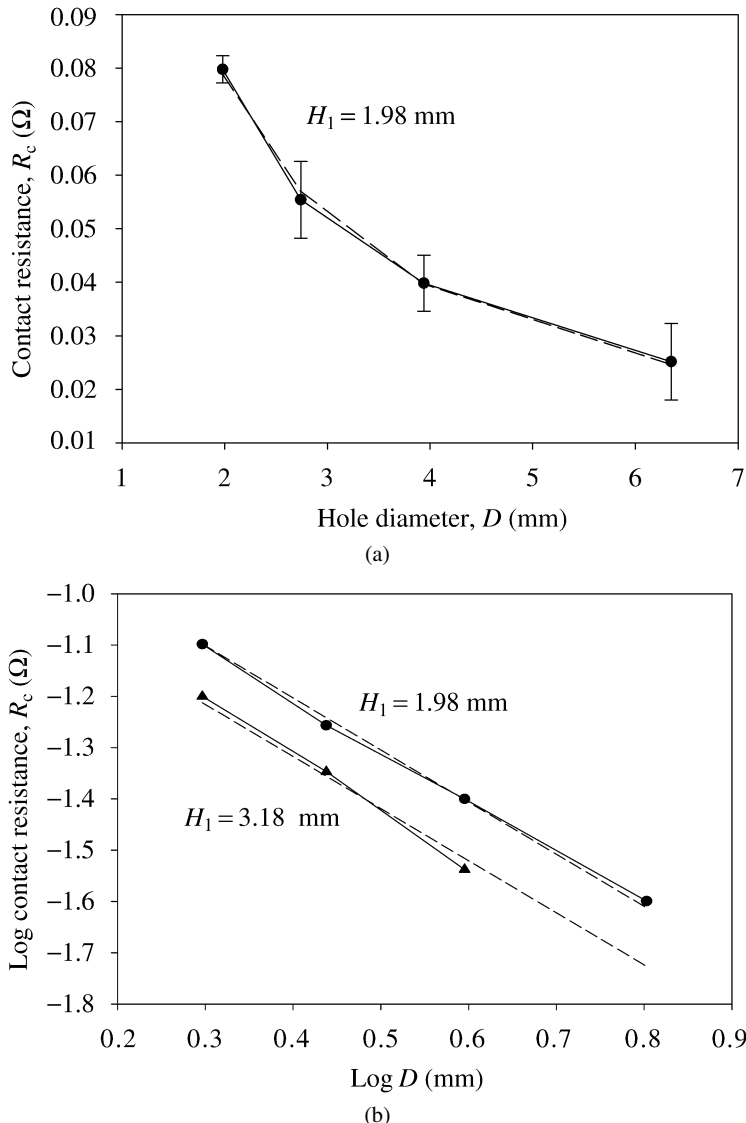


Figure 6. Changes in the contact resistance, R_c , with the hole diameter, D , using plate thicknesses of: (a) 1.98 mm and (b) both 1.98 mm and 3.18 mm, on a logarithmic scale. The dashed lines denote the fits to equation (1).

An empirical relationship can be initially proposed between the contact resistance R_c , the hole diameter D , and the plate thickness H_1 , based on a regression analysis of the experimental data in Fig. 6, as follows:

$$R_c = 10^{-0.632} / (D^{1.016} \cdot H_1^{0.555}), \quad R^2 = 0.994. \quad (1)$$

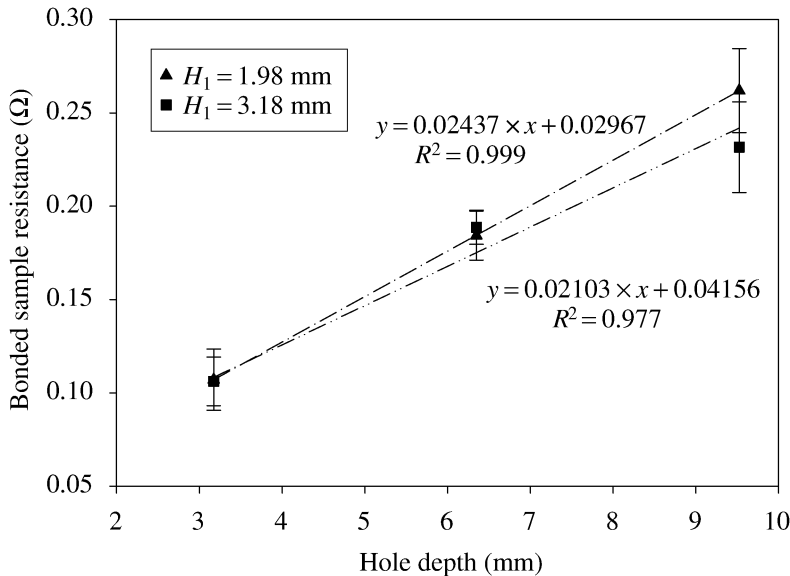


Figure 7. Effect of the hole depth, H_2 , on the bonded sample total resistance, R_t , using a hole diameter of 2.74 mm. H_1 is the Al plate thickness.

For simplicity, equation (1) can be rewritten as:

$$R_c = 0.233/(D \cdot \sqrt{H}), \quad R^2 = 0.955. \quad (2)$$

It is worth noting that this relationship was obtained for the Epon 830/Ni/DETA system with 60 wt% of Ni, cured at 150°C for 30 min. Different equations can possibly result at other conditions. Also, the physical principle or mechanism behind this relationship needs to be further investigated.

When the Al plate thickness remains the same, any variation in the hole depth leads to the total resistance change simply due to a change in the bulk adhesive resistance. Figure 7 demonstrates the effect of the hole depth, H_2 , as caused by bulk adhesive resistance, on the total electrical resistance, R_t , at the hole diameter of 2.74 mm for 60 wt% Ni adhesive. Within experimental error, a good linearity was observed, which implies the applicability of Ohm's law with the predicted slope $4\rho/\pi D^2$, where, ρ is the bulk adhesive electrical resistivity and D is the hole diameter.

Consequently, the contact resistance, R_c , after cure, can thus be described by the empirical relationship we propose, and Ohm's law describes the bulk adhesive resistance, R_b . Both resistances constitute the total electrical resistance measured between the top and bottom Al plates.

4. Conclusions

A novel design of multilayer hole-structure was employed to investigate the geometric effects of the holes connecting the multilayers of a novel prototype designed

for use in electronic components in circuit boards on their electrical resistances. The bonded sample resistance not only depends on the bulk adhesive electrical resistance, but also on the interfacial contact between the adhesive and the adherend. An empirical relationship was proposed between the contact resistance (R_c), the hole diameter (D), and the plate thickness (H_1), for Epon 830/Ni/DETA adhesive after cure with 60 wt% of Ni as the filling material. Ohm's law adequately describes the hole depth effect on the component's electrical resistance.

References

1. B. T. Alpert and A. J. Schoenberg, *Electronic Packag. Prod.* **31**, 130–132 (Nov. 1991).
2. E. Sancaktar and Y. Wei, *J. Adhesion Sci. Technol.* **10**, 1221–1235 (1996).
3. Y. Wei and E. Sancaktar, *J. Adhesion Sci. Technol.* **10**, 1199–1219 (1996).
4. E. Sancaktar and N. Dilsiz, *J. Adhesion Sci. Technol.* **13**, 679–693 (1999).
5. E. Sancaktar and N. Dilsiz, *J. Adhesion Sci. Technol.* **13**, 763–771 (1999).
6. E. Sancaktar, Y. Wei and M. A. Gaynes, *J. Adhesion* **56**, 229–246 (1996).
7. N. Dilsiz, R. Partch, E. Matijevic and E. Sancaktar, *J. Adhesion Sci. Technol.* **11**, 1105–1118 (1997).
8. R. Gomatam and E. Sancaktar, *J. Adhesion Sci. Technol.* **18**, 1225–1244 (2004).
9. R. Gomatam and E. Sancaktar, *J. Adhesion Sci. Technol.* **18**, 1245–1262 (2004).
10. R. Gomatam and E. Sancaktar, *J. Adhesion Sci. Technol.* **20**, 87–104 (2006).
11. R. Gomatam and E. Sancaktar, *J. Adhesion Sci. Technol.* **20**, 69–86 (2006).
12. R. Gomatam and E. Sancaktar, *J. Adhesion Sci. Technol.* **20**, 53–68 (2006).
13. R. Gomatam and E. Sancaktar, *J. Adhesion Sci. Technol.* **19**, 659–678 (2005).
14. R. Gomatam and E. Sancaktar, *J. Adhesion Sci. Technol.* **18**, 1833–1848 (2004).
15. R. Gomatam and E. Sancaktar, *J. Adhesion Sci. Technol.* **18**, 849–881 (2004).
16. R. Gomatam and E. Sancaktar, *J. Adhesion Sci. Technol.* **18**, 731–750 (2004).
17. E. Sancaktar and N. Dilsiz, *J. Adhesion Sci. Technol.* **11**, 155–166 (1997).
18. E. Sancaktar and C. Liu, *J. Adhesion Sci. Technol.* **17**, 1265–1282 (2003).
19. T. W. Giants, *J. Adhesion Sci. Technol.* **12**, 593–613 (1998).
20. K. Feldmann and R. Luchs, *Surface Mount Technol.* **12**, 74–78 (1998).
21. D. Lu, Q. K. Tong and C. P. Wong, *IEEE Trans. Electronics Packag. Manuf.* **22**, 223–227 (1999).
22. M. Zwolinski, J. Hickman, H. Rubin, Y. Zakes, S. McCarthy, T. Hanlon, P. Arrowsmith, A. Chaudhuri, R. Hermansen, S. Lau and D. Napp, *IEEE Trans. Compon. Packag. Manuf. Technol., Part C* **19**, 241–250 (1996).
23. J. C. Bolger and S. L. Morano, *Adhesives Age* **27**, 17–20 (June 1984).
24. E. Sancaktar, P. Rajput and A. Khanolkar, *IEEE Trans. Compon. Packag. Technol.* **28**, 771–780 (2005).
25. H. Jozavi and E. Sancaktar, *J. Adhesion* **18**, 25–48 (1985).
26. E. Sancaktar and P. Zhang, *J. Mech. Design* **112**, 605–619 (1990).
27. E. Sancaktar and D. Beachtle, *J. Adhesion* **42**, 65–85 (1993).
28. E. Sancaktar, *J. Adhesion Sci. Technol.* **9**, 119–142 (1995).
29. E. Sancaktar, *Appl. Mech. Rev.* **49**, S128–S138 (1996).

Stable and Unstable Capillary Flows of Highly-Filled Epoxy/Nickel Suspensions

Jianguo Zhou and Erol Sancaktar*

Department of Polymer Engineering, The University of Akron, Akron, OH 44325-0301, USA

Abstract

Epoxy/nickel adhesives can be used as integrated circuit (IC) packaging materials due to their lower cost than epoxy/silver adhesives with acceptable electrical conductivity. In this study, stable and unstable capillary flows of highly-filled epoxy/Ni suspensions were investigated with and without cure at room temperature, *via* the capillary rheometry and syringe extrusion. Variations of the bulk electrical conductivity in these processes were discussed as well. Axial filtration of the polymer binder occurs under a static pressure for a cured epoxy/Ni system, Epon 815 C/Ni/diethylenetriamine (DETA) adhesive with 50 wt% of Ni in the syringe, resulting in an unstable flow and a cross-sectional filler concentration or electrical conductivity gradient. In dynamic capillary extrusion, lower resin viscosity and apparent shear rates enhance the flow instability and filtering of polymeric binder for epoxy/Ni suspensions with 75 wt% of Ni, thus facilitating a change in bulk electrical conductivity during processing. With increasing shear rates, both average force and force oscillation frequency increase. Incorporation of Ni nanopowder promotes a stable flow, yet the occurrence of agglomerates somewhat nullifies this advantage. Additionally, different rheological behaviors result as cure proceeds with different resins. Also, occurrence of the agglomerates leads to flow instability during processing with cure.

Keywords

Epoxy/Ni suspension, conductive adhesive, flow instability, rheology

1. Introduction

Electrically conductive adhesives have attracted significant attention during the last decades due to their increased usage in electronics industry to replace lead soldering [1–18]. Theoretical and experimental studies have been performed on basic conduction mechanisms [1–8]; the effects of particle size, shape and type [3–8]; behavior in the bonded form [5, 7–15]; processing effects, such as pressure [1, 3, 8], adhesive film thickness [2, 4, 7], silver coating [3, 4, 6], anisotropic alignment of nickel particles in magnetic field [16]; as well as the possibility of using polymeric emeraldine salt particles as conductive fillers [17]. Ni/epoxy conductive adhesives can be used

* To whom correspondence should be addressed. Tel.: (330) 972-5508; e-mail: erol@uakron.edu

in integrated circuit (IC) packaging due to their lower cost than Ag/epoxy adhesives, with acceptable electrical conductivity, high thermal conductivity and low thermal expansion. Furthermore, silver-filled conductive adhesives suffer from the problem of silver migration, which may lead to failure in electrical conduction [18]. It is well known that process conditions affect the mechanical performance of thermosetting adhesives in general [19–23], and mechanical as well as conductive performances of electrically conductive adhesives in particular [5, 7–15].

Understanding the rheological behavior of highly-filled epoxy/Ni suspensions with and without cure, as well as their effect on the bulk electrical conductivity change during processing, would be very useful for design and manufacturing. Rheology of concentrated suspensions, in general, is very complex, which is often accompanied by shear thinning, thixotropy, yield, flow instability and wall slip. All these effects complicate the investigation of rheological properties and appropriate modeling of their rheological behavior.

Development of the flow instabilities during the capillary flow of concentrated suspensions filled with solids was reported by Kalyon and coworkers [24–26], where the axial migration of the matrix in pressure driven flows, i.e., during capillary flow and extrusion processing, were first observed, and filtering of polymer matrix, periodic mat formation and break-up mechanism were proposed and related to a critical shear stress, below which flow instabilities occurred. Effects of temperature and surface roughness of the particles on the rheological behavior were also examined. Isayev and Fan [27] studied the steady and oscillatory flows of highly-filled silicon–polypropylene ceramic compounds based on the first harmonics of stresses. By conducting shear-flow experiments, they observed work-hardening in the very low shear rate region, stress oscillation in the high shear rate region, as well as yield behavior. Suwardie *et al.* [28] observed viscoplasticity, plug flow, wall slip and flow instabilities associated with axial migration of the low viscosity binder under an imposed pressure gradient for ceramic suspension with 50% by volume of silicon carbide in a wax binder.

Wall slip is likely to occur at high solid loading levels [29, 30]. In such cases, slip velocity *versus* wall shear stress data can be obtained using the Mooney method [31]. Direct measurement techniques to characterize the wall slip include magnetic resonance imaging [32], laser Doppler anemometry [33] and the visualization technique [34]. Kalyon [34] assumed that an apparent slip layer exists and consists solely of the binder, with its thickness being independent of the flow rate. As a first approximation, the apparent slip layer thickness is related to the particle diameter and the ratio of the volume loading level to the maximum packing fraction of the particles.

In this experimental study, stable and unstable capillary flows of highly-filled epoxy/Ni suspensions, both with and without cure, were investigated over different weight ratios of Ni particles in the capillary rheometer and also in the syringe, together with variations of the bulk electrical conductivity developed in these processes. Such knowledge can be very useful for processing of highly-

filled epoxy/Ni conductive adhesives and their specific application to integrated circuits.

2. Experimental

2.1. Materials

The epoxy resins used in this study, which include both Epon 830 and Epon 815C received from Miller-Stephenson, Danbury, CT, are Newtonian and their shear viscosity values at 25°C are 16.8 and 0.9 Pa s, respectively. Ni 102 flakes, received from Atlantic Equipment Engineers, Bergenfield, NJ, have an average diameter of 3 µm (Fig. 1(a)), and nickel oxide on their surfaces can be etched away with 10% hydrochloric acid to obtain improved electrical conductivity (Fig. 1(b)). Ni nanopowder, received from Inframet Advanced Materials LLC, Farmington, CT, with an average diameter of 80 nm, was also employed in this study in etched and unetched forms. Larger agglomerates of Ni particles, generated during etching, were additionally used to examine their effect on the rheological behavior of filled resins. Diethylenetriamine (DETA), received from Resolution Performance Products, Houston, TX, was used as the curing agent at 12 phr in epoxy/Ni systems.

2.2. Sample Preparation

The solution blending was employed to prepare epoxy/Ni suspensions or electrically conductive pastes in this study [35]. Epoxy was first dissolved in acetone until a homogeneous solution was obtained. Then, nickel particles were added and mixed according to the desired weight ratio. For studies involving conductive pastes with cure, this step was followed by the addition of curing agent and further stirring.

Any air bubbles and the residual solvent resulting from sample preparation could be removed in vacuum at room temperature within 20 min. Resin conversion after

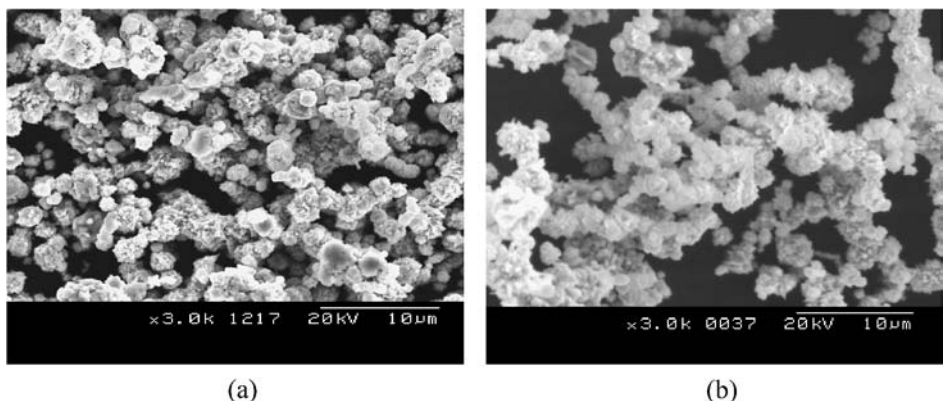


Figure 1. Morphology of (a) as-received and (b) etched Ni flakes used in this study.

this process for conductive paste preparation was less than 8%, in general, and the epoxy gel content of pastes after cure at 150°C for 30 min, was not significantly different between different nickel weight ratios.

2.3. Characterization

2.3.1. Rheology

Rheological behavior of conductive adhesives extruded through a narrow passage under static pressure was first investigated on Epon 815C/Ni(etched)/DETA system with 50 wt%, or 34 vol% of Ni. The as-prepared conductive paste was filled into a 5 ml syringe with an inner diameter of 11.9 mm (Becton Dickinson & Co., Franklin Lakes, NJ) attached to a needle of 0.5 mm inner diameter and 25 mm length. The static pressure was kept constant at 524 kPa and applied to the bulk adhesive in the syringe for 30 min at room temperature. Figure 2 schematically shows the device employed as well as some typical phenomena that happen during this process.

The dynamic extrusion process through a narrow passage was conducted in an Instron capillary rheometer 3211, as well as in syringes for epoxy/Ni suspensions with 75 wt%, or 61 vol% of Ni. Different resin viscosities, apparent shear rates, filler concentrations and particle sizes were used to investigate their effects on the rheological behavior. Effects of particle agglomeration, etching as well as cure process on the rheological behavior were examined *via* syringes as well. During syringe extrusion, the plunger speed was controlled by the Instron rheometer, as schematically illustrated in Fig. 3. All experiments were run at room temperature.

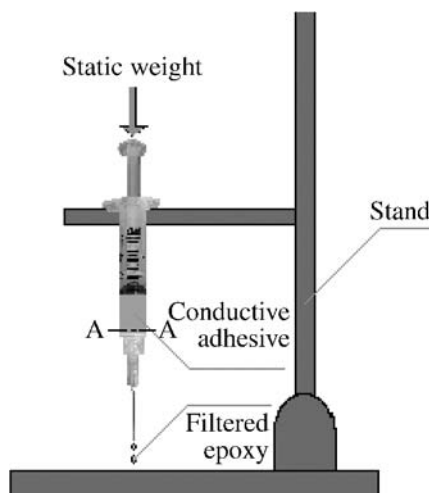


Figure 2. Schematic illustration of the device for investigation of the rheological behavior of Epon 815C/Ni/DETA adhesive with 50 wt% of Ni, through a narrow passage in syringe under static pressure of 524 kPa. A–A shows the location where the filler concentration distribution over the cross-section was examined after filtering of epoxy for 30 min at room temperature.

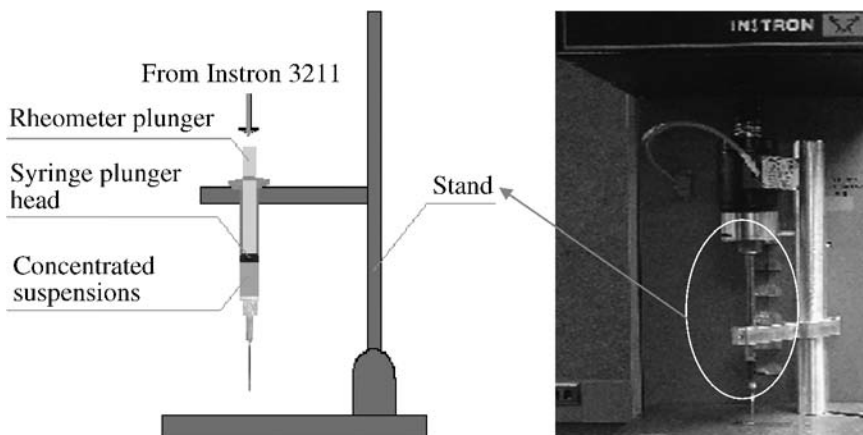


Figure 3. Schematic illustration (left) of the device for investigation of the dynamic extrusion process of highly-filled epoxy/Ni systems through a narrow passage in syringe, with and without cure. The plunger speed was controlled by Instron capillary rheometer 3211 (right).

2.3.2. Thermogravimetric Analysis and Differential Scanning Calorimetry

The filler concentration gradient formed in bulk epoxy/Ni systems due to processing was examined by TGA (TA Instruments TGA 2050, New Castle, DE) at a heating rate of 10°C/min to 700°C. The resin conversions at room temperature for various time periods were measured utilizing DSC (TA Instruments MDSC 2920, New Castle, DE) at a heating rate of 10°C/min to 300°C. All the measurements were under nitrogen atmosphere.

2.3.3. Bulk Morphology

The bulk morphology of epoxy/Ni systems was characterized using a Hitachi (Tokyo, Japan) S2150 scanning electron microscope (SEM) operating at 20 kV.

2.3.4. Electrical Conductivity

The bulk electrical conductivity of epoxy/Ni adhesives was measured after cure using the standard four-probe method by a Keithley 580 Micro-ohmmeter (Cleveland, OH).

3. Results and Discussion

3.1. Rheological Behavior of Conductive Adhesives in Syringe Under Static Pressure

As depicted in Figs 2 and 4, filtering of the polymeric binder occurred for Epon 815C/Ni(etched)/DETA adhesive with 50 wt% of Ni under static pressure of 524 kPa, as the bulk slowly cured at room temperature. Clear liquid epoxy emerged from the needle, shortly after the application of static pressure until the experiment was stopped at 30 min.

Figure 4 shows the nickel particle concentration distribution over the syringe cross-section (A–A) near the capillary entrance, as obtained by thermogravimetric

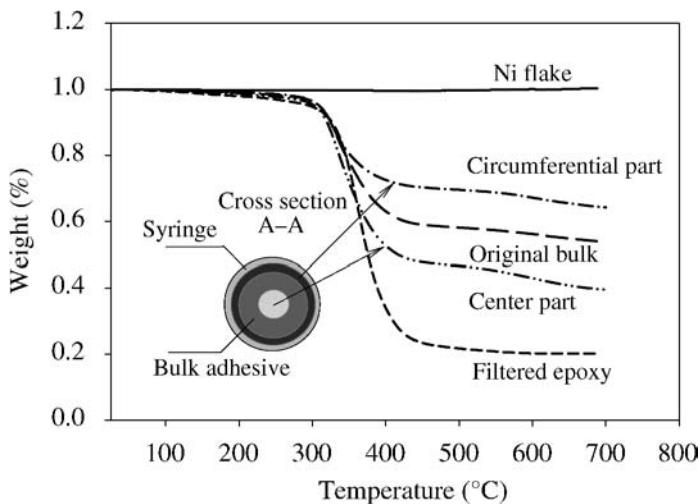


Figure 4. Analysis of the Ni particle concentration distribution over the cross-section A–A by TGA. The insert picture depicts the typical locations with different filler concentrations over the cross-section after 30 min of polymeric binder filtration.

analysis (TGA) after 30 min of filtering. The epoxy-rich region near the syringe axis and solid particle-rich region near the syringe inner wall are referred as ‘center part’ and ‘circumferential part’, respectively.

Apparently, a higher particle concentration is obtained in the circumferential part than either in the center part or in the original bulk. The bulk electrical conductivities measured after post-cure at 150°C for 30 min using the standard four-probe method are about 894.9 S/cm for the circumferential part and 559.2 S/cm for the original bulk. Continuous filtering and depletion of polymer binder along the syringe axis in the syringe reservoir is responsible for this filler concentration gradient over the cross-section.

Figure 5(a)–(d) further shows SEM micrographs of original adhesive, filtered epoxy and bulk materials from these different cross-sectional locations, where different microstructures or nickel particle distributions can be observed. Higher filler concentration is evident in the circumferential part.

As pressure-induced filtration continues, the polymeric binder is depleted in the axial flow direction and the solid concentration further increases in the syringe reservoir. This can result in a compacted particle aggregation structure or increased bulk electrical conductivity in the reservoir, filler concentration gradient along the axis, reduced filtration, as well as an unstable flow as cure proceeds under static pressure.

3.2. Flow Instability of Highly-Filled Epoxy/Ni Suspensions During Capillary Flow

An Instron capillary rheometer (Instron 3211), with barrel diameter of 9.525 mm, capillary diameter of 1.593 mm and length to diameter ratio of 19.3, was employed

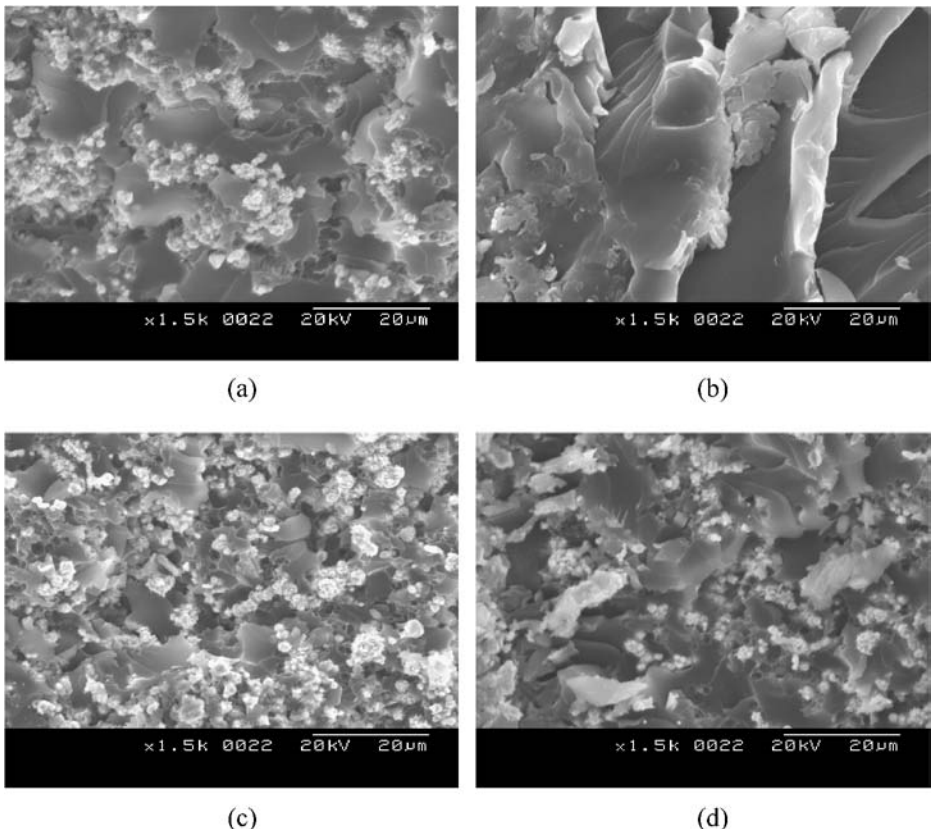


Figure 5. SEM images of (a) epoxy/Ni adhesive prior to filtering, (b) filtered epoxy and bulk materials from (c) the circumferential part and (d) center part, after 30 min of filtration under 524 kPa static pressure.

in this study. The force curves were initially read from the chart paper and re-plotted thereafter. The same amount of suspension was loaded in each run, and a firm and slow loading pattern was used on samples to avoid air bubbles in the rheometer barrel reservoir. The flow of the extrudates emerging from the capillary was photographed using a digital camera, in order to obtain visual records of the extrudate shapes upon extrusion.

Syringes attached to a needle were employed for similar purposes as well. Pastes were filled into the syringe reservoir smoothly to avoid any air bubbles in the mixture. The plunger force curves were recorded on Instron rheometer chart paper for further analysis. The extrusion process continued until the plunger reached the syringe cavity bottom or until syringe breakage under excessive plunger force.

3.2.1. Flow Instability in Capillary Rheometer

The plunger force *versus* time curves, as recorded using the capillary rheometer during extrusion, are shown in Fig. 6(a)–(d) for Epon 830/Ni suspension with

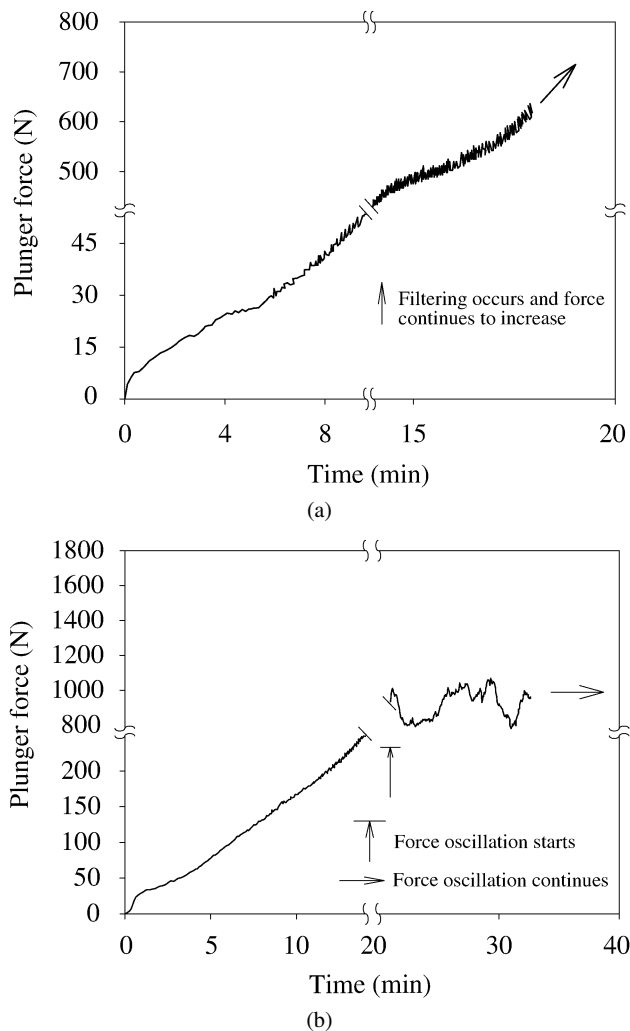
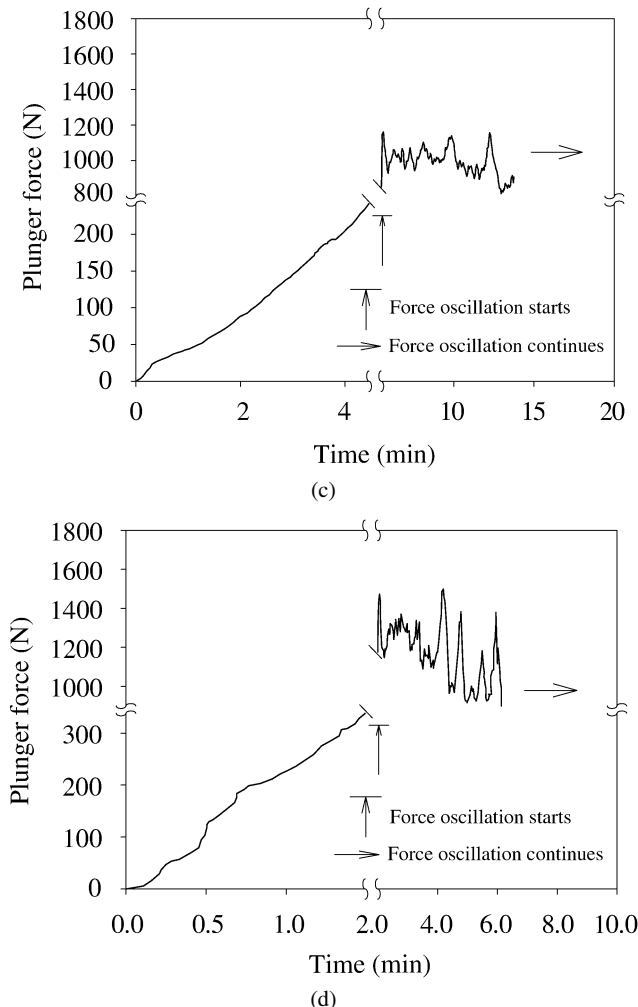


Figure 6. Variation of plunger force with time and apparent shear rate in Instron capillary rheometer for Epon 830/Ni suspension with 75 wt% of Ni, at apparent shear rates of (a) 2.3, (b) 7.6, (c) 22.8 and (d) 76.1 s^{-1} .

75 wt% of Ni at various apparent shear rates. They are all characterized by time-periodic force oscillations, which occur during the late phases of the extrusion process.

It is worth noting that, at the lowest apparent shear rate of 2.3 s^{-1} , filtration and force oscillation appear earlier, even during the initial extrusion stage, as shown in Fig. 6(a) and curve A in Fig. 7. Figure 7 illustrates the details of plunger force versus time curves in Fig. 6 during the initial and late stages. The insert pictures in Fig. 7 show the corresponding extrudate shapes emerging from the die exit at various apparent shear rates. Figure 7 reveals that filtration of the polymeric binder

**Figure 6.** (Continued).

is observed only at the lowest apparent shear rate of 2.3 s^{-1} , while no filtration occurs at the other three shear rates used. This can be ascribed to “lower apparent shear rate effect” on flow instability and filtration during unstable capillary flow of highly-filled concentrated suspensions, which is probably accompanied by a continuous change in the bulk electrical conductivity. This general finding is consistent with the earlier investigations [24–26].

It can also be seen that the plunger force increases approximately proportionally to the apparent shear rate during the initial stage. The average plunger force continues to increase in an unbounded way in the case of the lowest shear rate, i.e., 2.3 s^{-1} . Yet, with the other three shear rates used, it reaches a definite time-periodic force oscillation stage later, without filtration of the polymeric binder. In this late

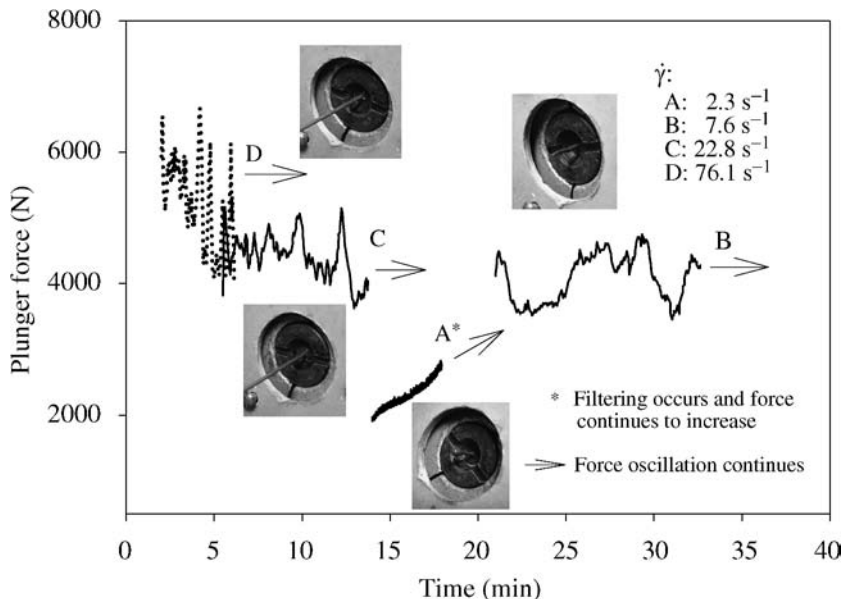


Figure 7. Variation of plunger force with time and apparent shear rate, $\dot{\gamma}$, in Instron capillary rheometer for Epon 830/Ni suspension with 75 wt% of Ni during the late stage. Filtration of the polymeric binder occurs only at the lowest shear rate (A). As the shear rate increases, both the average plunger force and force oscillation frequency increase. The insert pictures show the extrudates emerging from the exit at various apparent shear rates.

stage, the greater the apparent shear rate, the greater is the average plunger force and the frequency of oscillation. Actually, transition between the stable and unstable flows occurs at a critical stress, and is accompanied by the appearance of a thin matrix layer on the extrudate surface to different extents. Such transition can lead to changes in the extrudate electrical conductivity during extrusion, and extrudates with increasing filler concentration and electrical conductivity can appear in time as depletion of the matrix continues in the barrel.

Compared to Epon 830/Ni suspension with 75 wt% of Ni, low viscosity resin system, Epon 815C/Ni with 75 wt% of Ni, shows filtering of polymeric matrix at all three apparent shear rates investigated, and a much stronger force oscillation with high frequency can be observed at low shear rates. The oscillation amplitude grows with time as well, as shown in Fig. 8(a). With increasing shear rate, the average force increases quickly with time, yet without a strong force oscillation over the whole extrusion process. At the highest apparent shear rate of 76.1 s^{-1} , one period of relatively smooth extrusion accompanied by a somewhat continuous flow appears during the late stage prior to the plunger force limit, as shown in Fig. 8(c) and curve C in Fig. 9. Apparently, as with the Epon 830/Ni system, a higher apparent shear rate facilitates stable processing of Epon 815C/Ni system with 75 wt% of Ni during capillary flow.

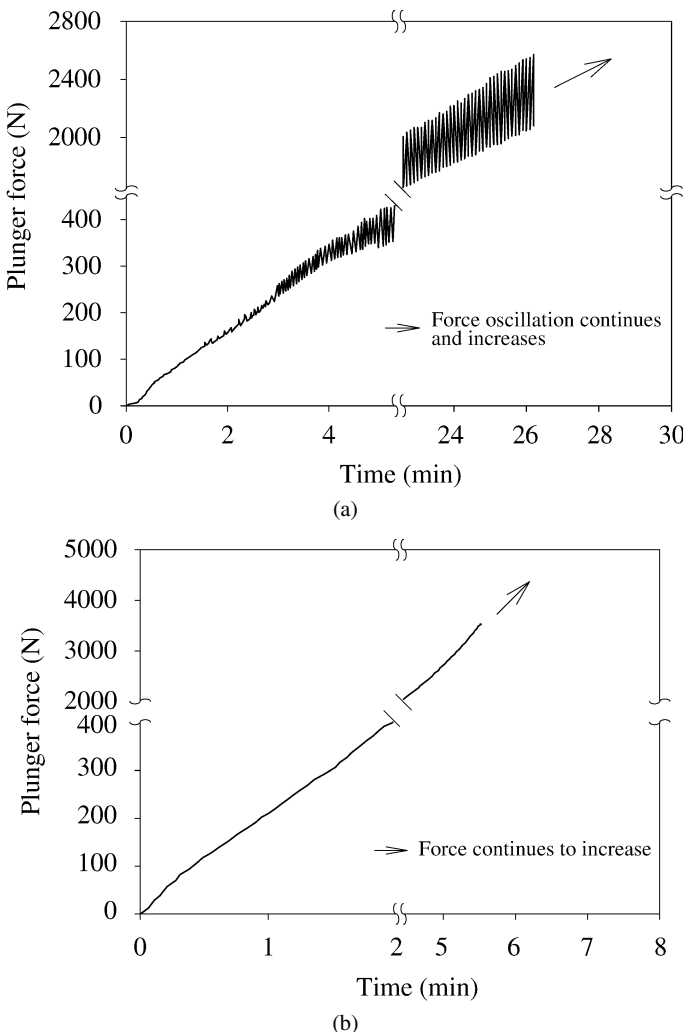


Figure 8. Variation of plunger force with time and apparent shear rate in Instron capillary rheometer for Epon 815C/Ni suspension with 75 wt% of Ni, at apparent shear rates of (a) 7.6, (b) 22.8 and (c) 76.1 s^{-1} .

Figure 9 shows the late stage of the plunger force *versus* time curves in Fig. 8, and the inserts illustrate extrudates emerging from the die exit with filtration at different apparent shear rates. The image of a compressed Ni–epoxy cylinder at the die entrance, created as a result of the depletion of matrix after extrusion under up to 22.24 kN plunger force and apparent shear rate of 76.1 s^{-1} is also included in the inserts. The calculated cylinder density is around 5.8 g/cm^3 , while the Ni flakes have a density of 2.2 g/cm^3 in as-received powder form. The calculated wt% of Ni in the cylinder is about 92.3%, by assuming a fully compact cylinder of Ni particles and

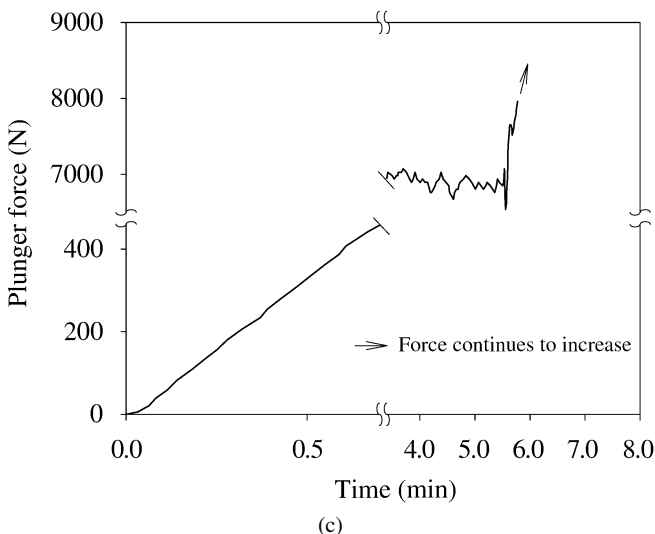


Figure 8. (Continued).

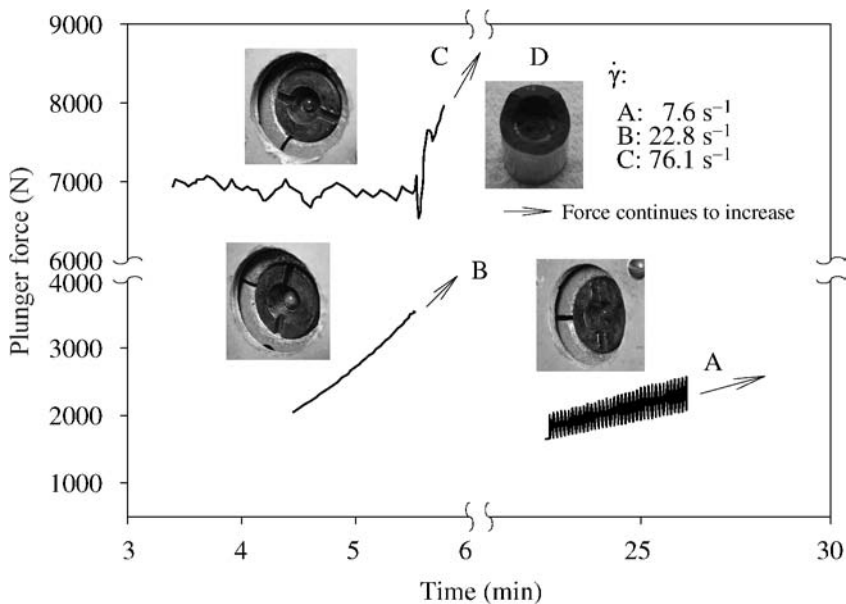


Figure 9. Variation of plunger force with time and apparent shear rate, $\dot{\gamma}$, in Instron capillary rheometer for Epon 815C/Ni suspension with 75 wt% of Ni during the late stage. Filtration of the polymeric binder as well as stronger plunger force occur at all apparent shear rates in comparison to Epon 830/Ni suspension, which has higher viscosity (Fig. 7). A typical compressed epoxy–Ni cylinder, created at the die entrance as a result of the depletion of polymeric matrix after extrusion, is also shown in the insert picture (D). Extrudates at the capillary exit are also shown in insert pictures with corresponding plunger force curves.

epoxy resin. Also, the calculated electrical resistivity is around 5.85×10^{-5} (Ω cm), while it is 0.68×10^{-5} (Ω cm) for pure Ni.

As the filler concentration is decreased, i.e., to 70 wt%, or 55 vol% of Ni, it can be seen again that higher resin viscosity renders an improved processability. This is verified by the continuous stable flow of Epon 830/Ni suspension at apparent shear rate of 7.6 s^{-1} . For the Epon 815C/Ni system, however, unstable flow with periodic plunger force oscillation and polymeric matrix filtration is observed, and a much larger pressure is necessary for the extrusion process (data not shown). A lower filler concentration of around 62.7 wt%, or 47 vol% is found to result in stable flow without any filtration or force oscillation for the Epon 815C/Ni system.

Periodic mat formation, filtering of polymer matrix, and mat breakup under certain conditions can be responsible for the general time dependence and oscillation of the plunger force. A simplified model has been developed for the capillary flow of highly-filled concentrated suspensions, in order to analyze the effects of various suspension characteristics and geometric parameters on flow stability [26]. In the presence of a plug flow at high shear stress, filtering will occur followed by unstable flow, if the average velocity of the liquid with respect to the filler particles, \bar{V} , is higher than or of the same order of magnitude as the slip velocity, V_s . The relationship between \bar{V} and the wall shear stress, τ_w , can be derived from Ergun's filtering analysis of the liquid through a packed bed [36], as follows:

$$\bar{V} = \left[\frac{D_p^2}{37.5\mu D} \left(\frac{1}{\Phi} - 1 \right)^2 \right] \tau_w, \quad (1)$$

where D_p is an equivalent particle diameter, μ is the viscosity of the liquid medium, D is the diameter of the tube and Φ is the particle volume fraction.

The relationship between the apparent wall slip velocity, V_s , and the wall shear stress, τ_w , can be obtained from experimental measurements using the Mooney method. Intersection of the plots of $V_s - \tau_w$ and equation (1) suggests a critical wall stress, τ_{cr} , below which \bar{V} is greater than V_s , and filtering and unstable flow occur [26]. Increase in the matrix viscosity, tube diameter, and decrease in the filler particle size are generally found to shift τ_{cr} to smaller values, and therefore promote stable flows.

3.2.2. Flow Instability in Syringe

Syringes provide an alternative method for rheological study of highly-filled epoxy/Ni suspensions during capillary flow. Syringes are particularly useful in studying extrusion processes with cure, since they are disposable. In general, compared to capillary rheometer, a syringe provides higher shear rates due to its larger barrel to needle diameter ratio. The plunger force, however, cannot be too high because of the mechanical strength limitation of plastic syringes. Furthermore, the capillary flow through the needle may not be uniform if syringe deformation occurs under large plunger forces.

Figure 10(a) and 10(b), respectively, show plunger force traces obtained at various plunger speeds in syringes for Epon 830/Ni and Epon 815C/Ni systems with

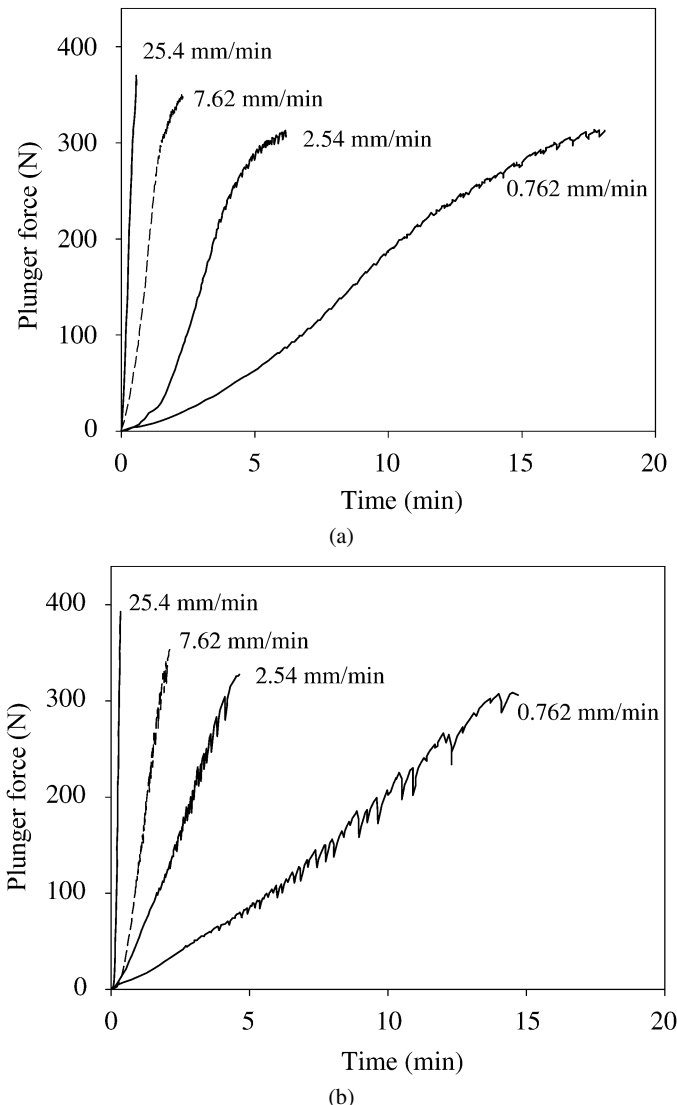


Figure 10. Variation of plunger force with time and plunger speed in syringes for (a) Epon 830/Ni and (b) Epon 815C/Ni systems with 75 wt% of Ni.

75 wt% of Ni. Up to the plunger force limit for syringes, no obvious flow out of the needle or filtering of polymeric binder occurs. Yet, it is interesting that evidently stronger oscillation and somewhat larger average plunger force are still observed in the Epon 815C/Ni system at all plunger speeds, as compared to the Epon 830/Ni system.

When Ni nanopowder is incorporated in the paste, instead of Ni flakes, in the same 75 wt% proportion, a continuous stable flow can be obtained during capillary flow in the syringe, as shown in curve e in Fig. 11. This can be ascribed to the

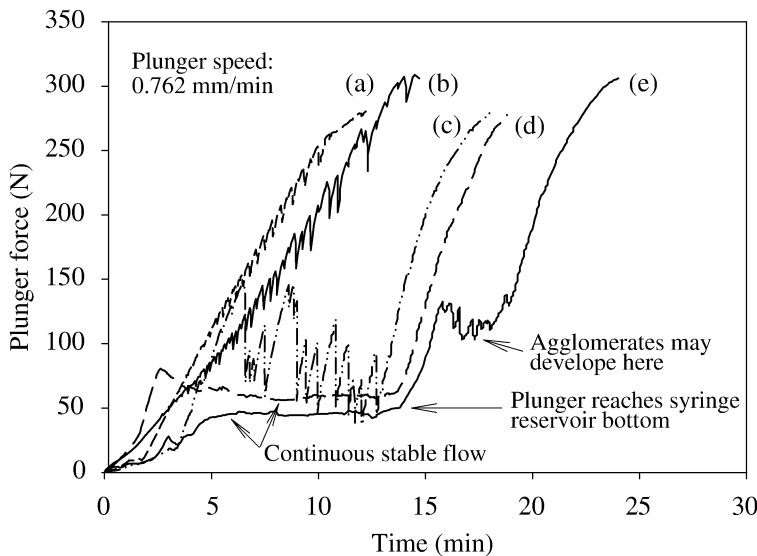


Figure 11. Variation of plunger force with time in syringes for Epon 815C/Ni systems with 75 wt% of Ni, using (a) Ni flakes, etched, (b) Ni flakes, as-received, (c) Ni nanopowder, etched and agglomerated, (d) Ni nanopowder, etched and (e) Ni nanopowder, as-received. The plunger speed is 0.762 mm/min.

particle size effect, as well as the spherical shape of the particles, which minimizes interlocking among flakes in highly-filled suspensions. Moreover, compared to the as-received Ni nanopowder, a larger plunger force is required for extruding etched Ni nanopowder paste, as shown in curve d in Fig. 11. Similar phenomenon happens for etched Ni flakes, as shown in curve a in Fig. 11. This could be explained by the stronger bonding between the etched particles and polymeric matrix.

Incorporation of etched Ni nanopowder with larger or more agglomerates, however, leads to an unstable flow with strong force oscillations, as shown in curve c in Fig. 11. The presence of larger particles or more agglomerates contributes to the loss of the processing advantage gained by incorporation of Ni nanopowder, and leads to instability during capillary flow in syringes. Reduced particle–matrix interfacial area as well as interactions between agglomerates may be responsible for this change. Figure 12(d) shows one typical SEM micrograph of such a paste.

Figure 12 illustrates the morphologies for as-received Ni nanopowder (a), in highly-filled paste with 75 wt% of Ni, before (b) and after extrusion through the syringe (c), and in paste with etched and agglomerated nanoparticles before extrusion through the syringe (d). It is interesting that finer particles as well as less or smaller aggregates result after extrusion through the syringe, as shown in Fig. 12(c). High shear force at the apparent shear rate of 115.1 s^{-1} can be responsible for pulverizing the particles and their aggregates to the finer structure observed after extrusion. The small inner diameter of the needle probably acts as a sieve for achievement of such a finer particle structure as well.

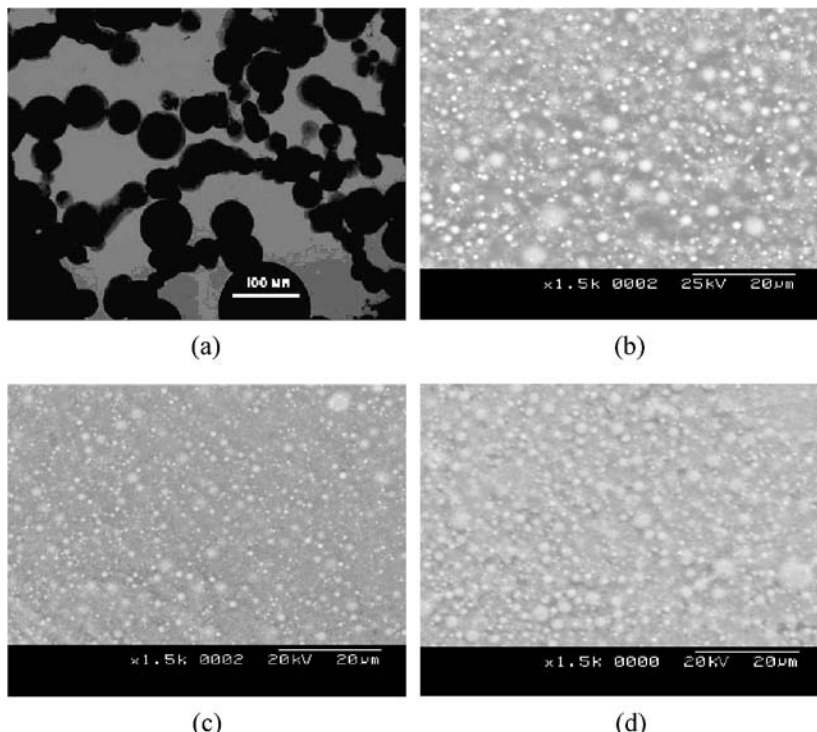


Figure 12. Morphology of Ni nanopowder and its pastes with Epon 815C at 75 wt% of Ni, before and after extrusion through the syringe. TEM micrograph of as-received Ni nanopowder, courtesy of the supplier (a) and SEM images of Ni nanopowder(as-received)/Epon 815C paste, before (b) and after (c) extrusion through the syringe and (d) Ni nanopowder(etched and agglomerated)/Epon 815C paste before extrusion through the syringe. The plunger speed is 0.762 mm/min corresponding to shear rate 115.1 s^{-1} .

3.3. Rheological Behavior of Conductive Adhesives in the Syringe During Cure

Pastes studied in this section are electrically conductive epoxy/Ni adhesives, Epon 815C/Ni/DETA and Epon 830/Ni/DETA systems, with 50 wt% of Ni at different extents of particle agglomeration. Unless noted otherwise, Ni particles here are as-received Ni flakes.

As cure proceeds, the rheological behavior of bulk material varies. Figure 13 illustrates such a change during cure for Epon 815C/Ni/DETA system with 50 wt% of Ni, where polymeric binder filtering occurs up to resin conversion of 0.19, and increased rate of plunger force change can be observed with increasing resin conversion.

In Fig. 14, plots of plunger force *versus* time curves for Epon 830/Ni/DETA system with 50 wt% of Ni are presented as a function of cure (extrusion) time. The plunger speed employed in each measurement is 2.54 mm/min. Similar to the case without cure, the higher matrix viscosity in Epon 830/Ni/DETA system is found to generate smaller plunger force, as compared to Epon 815C system at the same

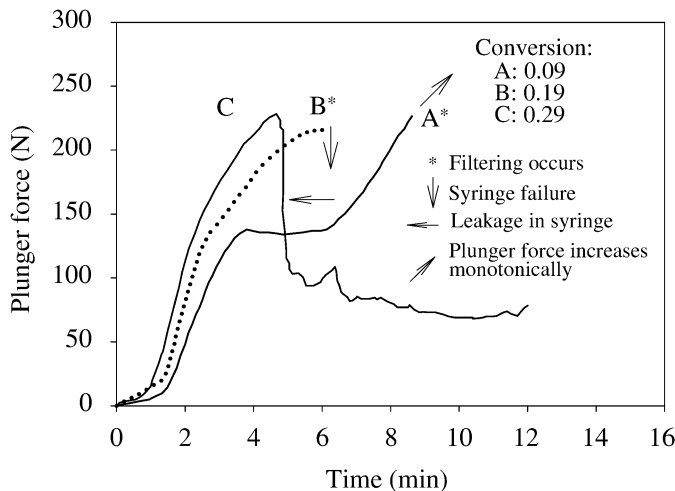


Figure 13. Variation of plunger force with time and resin conversion at room temperature in syringes at the plunger speed of 2.54 mm/min for Epon 815C/Ni/DETA adhesive with 50 wt% of Ni. Syringe leakage occurs for samples with resin conversion larger than 0.29.

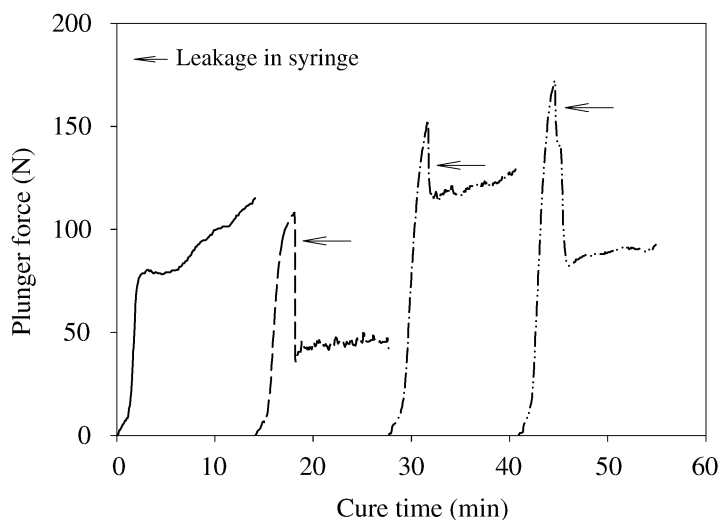


Figure 14. Syringe plunger force *versus* cure time for Epon 830/Ni/DETA adhesive with 50 wt% of Ni, cured at room temperature for different durations. These durations correspond to periods shown between the origin and the intercepts on the horizontal axis. The syringe plunger speed in each measurement is 2.54 mm/min.

plunger speed and similar resin conversion. Also, no filtering of polymeric matrix occurs in this process. Additionally, the maximum plunger force during extrusion, prior to sample leakage in the syringe, seems to increase as cure continues.

Like extrusion of Ni nanopowder paste with agglomerates, Epon 830/Ni/DETA pastes with 50 wt% of Ni, containing etched and more agglomerated Ni flakes,

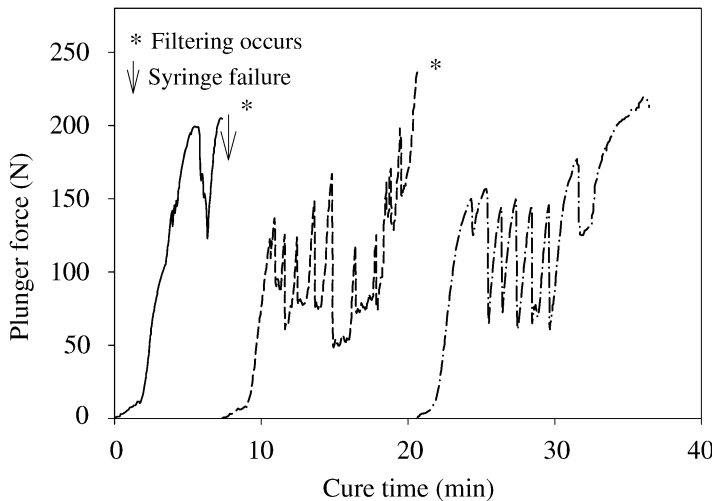


Figure 15. Syringe plunger force *versus* cure time for Epon 830/Ni(etched and agglomerated)/DETA adhesive with 50 wt% of Ni, cured at room temperature for different durations. These durations correspond to periods shown between the origin and the intercepts on the horizontal axis. The syringe plunger speed in each measurement is 2.54 mm/min.

present both larger plunger forces and pronounced force oscillations over the whole process, as shown in Fig. 15 when compared with Fig. 14. It is also worth noting that filtering of polymeric binder again occurs up to the cure time of 20 min. Obviously, agglomerates or larger particles in pastes are prone to bring about filtering of polymeric binder, force oscillations, as well as larger plunger forces necessary for extrusion.

To verify this pronounced effect of agglomerates, ultrasonic bath (Branson 2510, Danbury, CT) was employed for 3 h at room temperature during paste preparation, in order to remove or considerably reduce the size of existing agglomerates. The results indicate that rheological behavior similar to that in Fig. 14 can be obtained after this treatment, as shown in Fig. 16. In both cases, a continuous stable flow occurs at first, and it is then followed by a large increase in plunger force, causing paste leakage from the syringe. Obviously, the size of agglomerates could be much reduced or even eliminated after ultrasonic treatment, leading to plunger forces approximately equal or even smaller than those in Fig. 14.

Effect of agglomerates on suspension properties, including electrical conductivity can be complicated, depending on the ingredient characteristics, i.e., particle size distribution, and processing conditions, i.e., thermo-mechanical history. Agglomeration induced by moderate shear forces or increased ionic concentrations under certain conditions, for instance, surmounts the energy barrier and forms a conductive network in carbon black-filled epoxy suspensions [37]. Similarly, with increased degree of mixing, the smaller finite graphite particle clusters can convert a polymer binder suspension from conductive to insulating, and result in decreases in

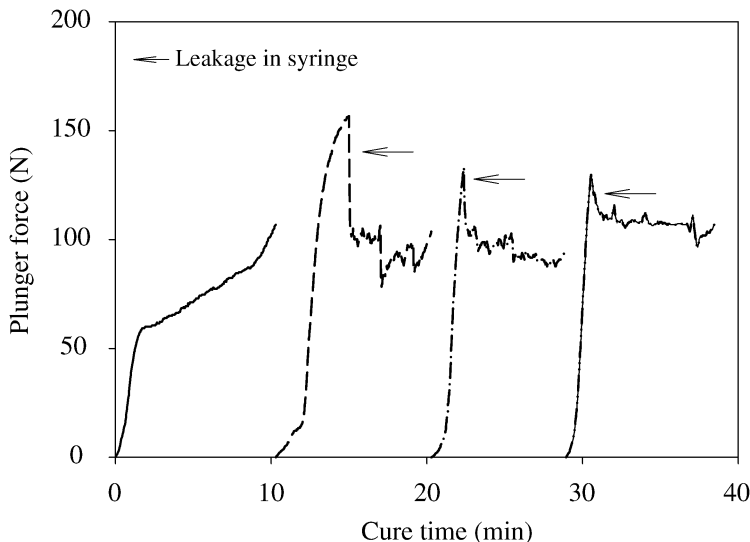


Figure 16. Syringe plunger force *versus* cure time for Epon 830/Ni(etched plus ultrasonic treatment)/DETA adhesive with 50 wt% of Ni, cured at room temperature for different durations. These durations correspond to periods shown between the origin and the intercepts on the horizontal axis. The syringe plunger speed in each measurement is 2.54 mm/min.

storage modulus and viscosity [38]. Control of material characteristics and processing routes is essential to the desired reproducible material properties.

4. Conclusions

The rheological behavior of epoxy/Ni conductive adhesives, and the variations in their electrical conductivity during processing have been investigated in this work. Polymer binder migration is observed under the static pressure for Epon 815C/Ni/DETA adhesive with 50 wt% of etched Ni, during cure. Such binder migration leads to unstable flow and electrical conductivity gradients after extrusion.

Lower resin viscosity and shear rates facilitate the flow instability and filtering of polymeric binder during dynamic capillary flow of epoxy/Ni suspensions with 75 wt% of Ni, thus leading to a change in the bulk electrical conductivity during processing. As the shear rate increases, the average plunger force and force oscillation frequency increase. Ni concentrations of 70 and 62.7 wt% give rise to stable flows in Epon 830/Ni and Epon 815C/Ni systems, respectively.

Incorporation of Ni nanopowder in the suspension results in a stable capillary flow at 75 wt% of Ni. Occurrence of agglomerates somewhat nullifies this advantage. Different rheological behaviors result as cure proceeds with different resins. The particle agglomerates bring about flow instabilities during cure as well.

References

1. E. Sancaktar and Y. Wei, *J. Adhesion Sci. Technol.* **10**, 1221–1235 (1996).
2. Y. Wei and E. Sancaktar, *J. Adhesion Sci. Technol.* **10**, 1199–1219 (1996).
3. E. Sancaktar and N. Dilsiz, *J. Adhesion Sci. Technol.* **13**, 679–693 (1999).
4. E. Sancaktar and N. Dilsiz, *J. Adhesion Sci. Technol.* **13**, 763–771 (1999).
5. E. Sancaktar, Y. Wei and M. A. Gaynes, *J. Adhesion* **56**, 229–246 (1996).
6. N. Dilsiz, R. Partch, E. Matijevic and E. Sancaktar, *J. Adhesion Sci. Technol.* **11**, 1105–1118 (1997).
7. R. Gomatam and E. Sancaktar, *J. Adhesion Sci. Technol.* **18**, 1225–1244 (2004).
8. R. Gomatam and E. Sancaktar, *J. Adhesion Sci. Technol.* **18**, 1245–1262 (2004).
9. R. Gomatam and E. Sancaktar, *J. Adhesion Sci. Technol.* **20**, 87–104 (2006).
10. R. Gomatam and E. Sancaktar, *J. Adhesion Sci. Technol.* **20**, 69–86 (2006).
11. R. Gomatam and E. Sancaktar, *J. Adhesion Sci. Technol.* **20**, 53–68 (2006).
12. R. Gomatam and E. Sancaktar, *J. Adhesion Sci. Technol.* **19**, 659–678 (2005).
13. R. Gomatam and E. Sancaktar, *J. Adhesion Sci. Technol.* **18**, 1833–1848 (2004).
14. R. Gomatam and E. Sancaktar, *J. Adhesion Sci. Technol.* **18**, 849–881 (2004).
15. R. Gomatam and E. Sancaktar, *J. Adhesion Sci. Technol.* **18**, 731–750 (2004).
16. E. Sancaktar and N. Dilsiz, *J. Adhesion Sci. Technol.* **11**, 155–166 (1997).
17. E. Sancaktar and C. Liu, *J. Adhesion Sci. Technol.* **17**, 1265–1282 (2003).
18. E. Sancaktar, P. Rajput and A. Khanolkar, *IEEE Trans. Compon. Packag. Technol.* **28**, 771–780 (2005).
19. H. Jozavi and E. Sancaktar, *J. Adhesion* **18**, 25–48 (1985).
20. E. Sancaktar and P. Zhang, *J. Mech. Design* **112**, 605–619 (1990).
21. E. Sancaktar and D. Beachtle, *J. Adhesion* **42**, 65–85 (1993).
22. E. Sancaktar, *J. Adhesion Sci. Technol.* **9**, 119–142 (1995).
23. E. Sancaktar, *Appl. Mech. Rev.* **49**, S128–S138 (1996).
24. D. M. Kalyon, P. Yaras, B. Aral and U. Yilmazer, *J. Rheology* **37**, 35 (1993).
25. P. Yaras, D. M. Kalyon and U. Yilmazer, *Rheol. Acta* **33**, 48 (1994).
26. U. Yilmazer, C. G. Gogos and D. M. Kalyon, *Polym. Composites* **10**, 242 (1989).
27. A. I. Isayev and X. Fan, *J. Mater. Sci.* **29**, 2931 (1994).
28. H. Suwardie, R. Yazici, D. M. Kalyon and S. Kovenklioglu, *J. Mater. Sci.* **33**, 5059 (1998).
29. A. I. Isayev, in: *Advances in Ceramics*, G. L. Messing, K. S. Mazdiyasni, J. W. McCauley and R. A. Haber (Eds), Ceramic Powder Science, Vol. 21, pp. 601–613. American Ceramic Society, Westerville, OH (1987).
30. G. A. Vinogradov, G. B. Froishteter and K. K. Trilisky, *Rheol. Acta* **17**, 156 (1978).
31. M. Mooney, *J. Rheology* **2**, 210 (1931).
32. M. Han and C. Kim, *J. Rheology* **43**, 1157 (1999).
33. S. C. Jana, B. Kapoor and A. Acrivos, *J. Rheology* **39**, 1123 (1995).
34. D. M. Kalyon, *J. Rheology* **49**, 621 (2005).
35. J. Zhou and E. Sancaktar, in: *Proceedings of the 2007 ASME International Mechanical Engineering Congress and Exposition on CD-ROM, Reliability, Failure Prevention, and Stress Analysis*, E. Sancaktar (Ed.), No. IMECE2007-34401. ASME, New York, NY (2007).
36. S. Ergun, *Chem. Eng. Prog.* **48**, 89 (1952).
37. R. Schueler, J. Petermann, K. Schulte and H.-P. Wentzel, *J. Appl. Polym. Sci.* **63**, 1741 (1997).
38. D. M. Kalyon, D. Dalwadi, M. Erol, E. Birinci and C. Tsengoglu, *Rheol. Acta* **45**, 641 (2006).

Electrical Properties of Copper-Filled Electrically Conductive Adhesives and Pressure-Dependent Conduction Behavior of Copper Particles

Yung-Sen Lin * and Sheng-Shiang Chiu

Department of Chemical Engineering, Feng Chia University, No. 100, Wenhwa Rd,
Seatwen, Taichung, Taiwan 407, ROC

Abstract

This study focuses on the effects of particle composition, particle shape, particle size and oxidizing temperature on the electrical properties of copper-filled electrically-conductive adhesives (CFECAs) and the pressure-dependent conduction behavior of compressed copper particles (CCPs). Silver-coated copper particles and un-coated copper particles of both spherical and flake-shaped types were oxidized at 30°C, 175°C and 240°C for two hours. The copper particles were dispersed in an epoxy matrix for CFECAs or compressed in a mold for CCPs. Silver-coated copper particles showed significantly greater oxidation resistance than un-coated copper particles since the silver coating provides good oxidation resistance at temperatures lower than 175°C. Thermogravimetric Analysis (TGA), X-ray diffraction (XRD) and Auger Electron Spectroscopy were used to observe how metal oxides such as Ag₂O and Cu₂O affected the electrical properties of CFECAs and the conduction behavior of CCPs. The electrically-conductive adhesives (ECAs) filled with flake-shaped copper particles offer better electrical conduction than the ECAs filled with spherical copper particles.

Keywords

Copper particles, oxidation, particle shape, silver coating, Auger electron spectroscopy, electrical conduction, conductive adhesive

1. Introduction

To meet the demand for small, light, thin, high-performance semiconductor components, there has recently been a great deal of effort in miniaturization. To achieve this, the I/O pin count of the devices must increase and the I/O pin pitch of the devices must decrease. Hence, PWBs (Printed Wiring Boards) with higher wiring densities are essential. It is difficult for conventional PWBs with mechanically drilled plated-through-holes to meet high density interconnection requirement. To

* To whom correspondence should be addressed. Tel.: 886-4-24517250, ext. 3659; Fax: 886-4-24510890;
e-mail: yslin@fcu.edu.tw

augment the packing efficiency of PWBs, the microvias in PWB dielectric parts are formed by laser drilling. The space created by the drilling is filled with ECAs, and this part provides interconnections between metal layers [1–4].

ECAs are primarily comprised of polymeric matrices and metal particles. ECAs can be categorized by particle loading into anisotropically-conductive adhesives (ACAs), anisotropically-conductive films (ACFs) and isotropically-conductive adhesives (ICAs). For an ICA, the loading level of conductive particles exceeds the percolation threshold, providing electrical conductivity in x -, y - and z -directions, which is typically on the order of 15–25 vol% concentration. For ACA and ACF, on the other hand, the loading level of conductive particles is far below the percolation threshold, and the low-volume loading is insufficient for inter-particle contact; this prevents conductivity in the X – Y plane of the adhesive. Therefore, ACA and ACF offer single directional electrical conduction along the vertical Z -axis when pressure and heat are applied [5].

The electrical properties of ECAs and the mechanisms involved in the formation of ECAs have been examined in a number of studies [6–11]. A variety of conductive particles such as Al [12], Ag [13–25], Pd [26], Cu [27–30], Zn, Cr, Mg [31], Ni [32–35], carbon black [36], carbon fiber [37] and various graphites [38, 39] have been dispersed in polymers in order to create ECAs. Silver particles of spherical and flake-shaped types are the most widely used metallic fillers for ECAs [40]. Silver has the drawback of being comparatively expensive. Aluminum particles are widely used in the adhesives industry as a reinforcing filler and for decoration, but aluminum particles cannot be used to make ECAs because of the thin oxide film which insulates the particle contact points. Gold particles are occasionally used for special electronic assembly operations. Gold-filled adhesives are much more expensive and, moreover, demonstrate a much lower electrical conductivity than silver-filled ones [40]. Pure palladium particles are not produced since palladium is available in limited quantity. Therefore, to fabricate low-cost ECAs, copper particles are blended into epoxy. Metallic fillers generally suffer from the oxidation of the metallic particles and from the deterioration of the electrical properties of the ECAs due to the non-conductive nature of such oxide layers. Copper is readily oxidized at relatively low temperatures, and has no self-protective layer to prevent further oxidation [41, 42]. Therefore, the means to prevent copper oxidation must be developed in order to use copper fillers in ECAs. This study investigated the effects of silver coating to enhance the oxidation resistance of copper particles in air and to improve the conduction of ICA type CFECAs and CCPs. Silver-coated and un-coated copper fillers were oxidized at 30°C, 175°C and 240°C for two hours and studied in order to measure their effects on the electrical properties of CFECAs and conduction behavior of CCPs.

The electrical properties of ECAs are dependent on the contact between particles, which is affected by the concentration, shape and size distribution of the conductive particles [43]. This report examines CFECAs to determine whether there is any relationship between the particle shape, either flake or sphere and the

CFECAs' electrical properties. Thermogravimetric Analysis (TGA), X-ray diffraction (XRD) and Auger Electron Spectroscopy are utilized to determine the particle composition and examine how the specific metal oxides on the surfaces of copper particles affect the electrical properties of CFECAs and conduction behavior of CCPs.

2. Experimental

2.1. Materials and Sample Preparation

Commercially available un-coated copper particles and silver-coated copper particles were utilized to examine the electrical properties of CFECAs and the conduction behavior of CCPs. Un-coated copper particles (product number 800) and silver-coated copper particles (product numbers 106 and 107) were obtained from Ferro Electronic Materials Systems, South Plainfield, New Jersey. SEM images as shown in Fig. 1a-c indicate that un-coated copper particles #800 are spherical; silver-coated particles #106 are flake-shaped; and silver-coated copper particles #107 are spherical [44]. Un-coated copper particles #800 contain less than

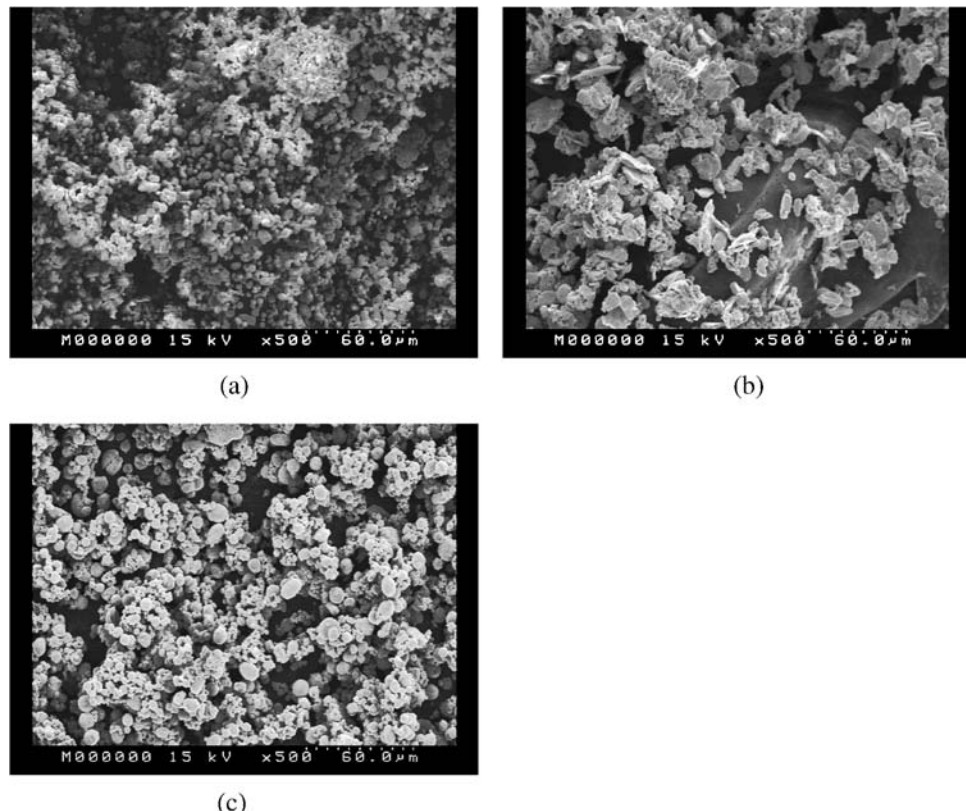


Figure 1. SEM images ($\times 500$) of (a) #800, (b) #106 and (c) #107 particles [44].

1150 ppm of oxygen. Silver-coated copper particles #106 contain 9.4% silver and silver-coated copper particles #107 contain 10.1% silver. The surface area of un-coated copper particles #800 is $0.26\text{ m}^2/\text{g}$. The surface areas of silver-coated copper particles #106 and #107 are $0.52\text{ m}^2/\text{g}$ and $0.23\text{ m}^2/\text{g}$, respectively. Particle size distributions for un-coated copper particles #800 and silver-coated copper particles #106 and #107, determined by laser light scattering, are shown in Fig. 2a–c [44, 45]. The average particle size for un-coated copper particles #800 is approximately 5 μm . The average particle size for both silver-coated copper particles #106 and #107 is approximately 10 μm . The silver coating is electrolytically plated onto the surface of each copper particle to yield a typical thickness of 0.07–0.1 μm .

The electrical properties of ECAs are greatly affected by the particle shape of conductive particles that can be described by their aspect ratio [46]. The aspect ratio of conductive particles such as silver-coated copper particles can be calculated based on the formula: $D_{\text{ave}}/t_{\text{ave}}$. D_{ave} is the average particle diameter of $\sim 10\text{ }\mu\text{m}$ for all products and t_{ave} is the average particle thickness of $\sim 1.7\text{ }\mu\text{m}$ for silver-coated copper particles #106. The aspect ratios of flake-shaped #106 particles, and spherical #107 particles are 6 and 1, respectively. The effects of the particle shape on the electrical properties of #106 and #107 in CFECAAs and CCPs were investigated.

In this study, copper particles were oxidized at 30°C, 175°C and 240°C for two hours prior to being dispersed in the polymer matrix for the CFECAAs or being compressed in a mold for the CCPs. Oxidation temperature of 175°C is the typical curing temperature for the CFECAAs. However, oxidation temperature of 240°C is used for snap-cured adhesives.

The copper particles (12%–50% by volume) were mixed into epoxy for preparation of CFECAAs. Using an EXAKT ‘Triple Roller Mill’ (E. J. Payne Ltd., London, UK), the following materials were blended: novolac epoxy resin used as a binder, anhydride used as a curing agent, methylimidazole used as an accelerator and copper particles used as fillers.

Prior to casting CFECA onto a glass slide 2.54 cm wide, two strips of 3M Scotch® tape (25.4 μm thick) were placed on the glass slide with a gap of 0.254 cm. Then the CFECA was spread onto the glass slide to form a film 2.54 cm long, 0.254 cm wide and 20–22 μm thick, and curing was carried out at 175°C for two hours. The thickness of the cured film was determined by Scanning Electron Microscopy (SEM) on the cross-section of the film. The typical thickness of the cured films was 16–18 μm .

To study the electrical conductivity of CFECAAs for the interconnected copper layers of PWBs, the CFECAAs were also filled into the *via* which had a hole diameter of 200 μm in the dielectric (75 μm thick) and cured at 175°C for two hours.

2.2. Volume Resistivity Measurement

The electrical properties of cured CFECAAs and conduction behavior of CCPs were described by their electrical resistivities. Low electrical resistivities mean good electrical properties for cured CFECAAs and good conduction behavior for CCPs.

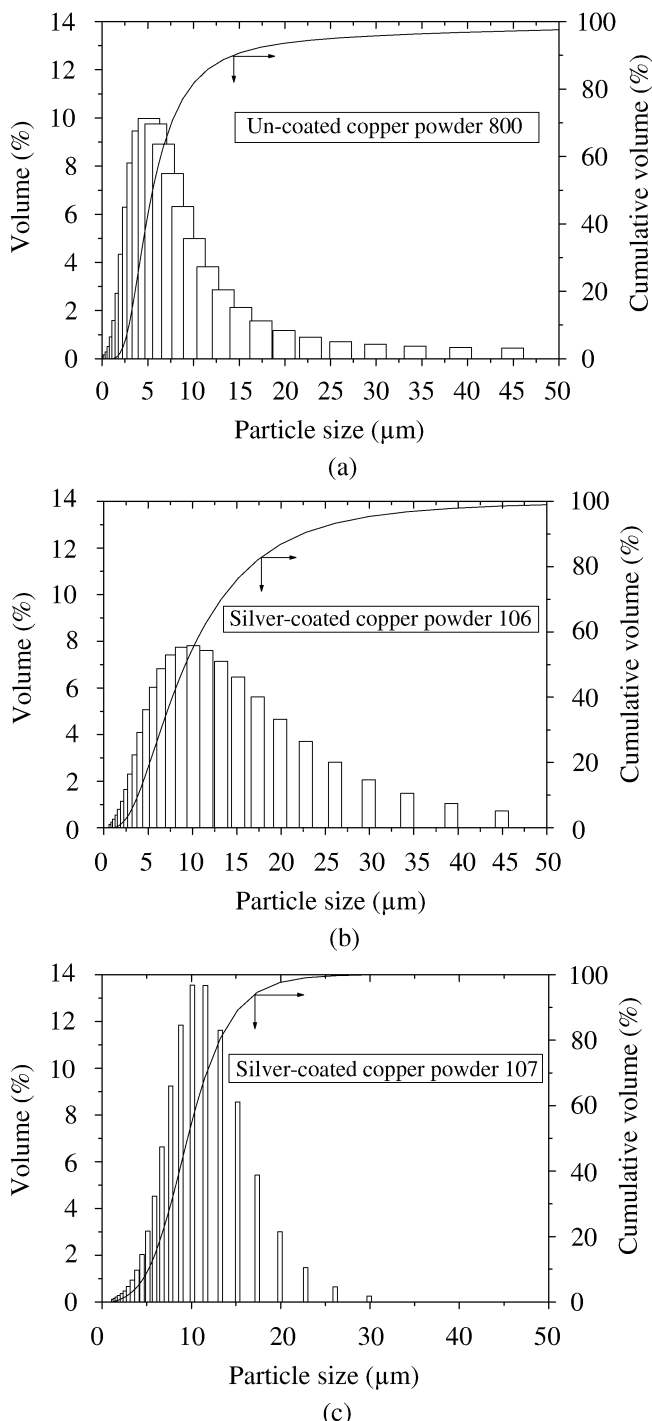


Figure 2. Particle size distributions of (a) #800, (b) #106 and (c) #107 particles [44, 45].

The electrical resistivities of cured CFECAs and CCPs were confirmed by their volume resistivities. A tungsten four-point probe with a tip diameter of 50 μm and a gap of 0.159 cm between the probes was applied to the cured films to determine their resistance an applying a current. The volume resistivities of the cured CFECAs and CCPs were calculated by:

$$\text{Volume resistivity } (\Omega \text{ cm}) = [\text{Resistance } (\Omega) \times \text{area } (\text{cm}^2)] / [\text{length } (\text{cm})].$$

The volume resistivities of cured CFECAs and CCPs reported in this study were taken as the arithmetic average of five replicate measurements. In this study, the variation in volume resistivities of cured CFECAs and CCPs was less than 10%.

2.3. Characterization Techniques

Morphology of copper particles in CFECAs and CCPs was observed by a Hitachi model S-2700 Scanning Electron Microscope (SEM). A 15 keV acceleration voltage was used to scan the sample surfaces.

Two machines were connected to each other to observe and calculate the contact areas of the surfaces of copper particles in CCPs (Olympus BH2-UMA Optical Microscope and a Media Cybernetic 41N30000-13348 analyzer with Image-Pro Plus software).

To evaluate the oxidation of Cu particles, the weight gain of Cu particles, dependent on temperature, was monitored by TGA (PERKIN ELMER TGA 7). The temperature range used for Cu particles was from 30°C to 480°C, at a heating rate of 20°C/min, and air flow was used for purging at 30 ml/min.

Auger electron spectroscopy (AES) has a high resolution for carbon, oxygen, silver and copper. AES data were collected by both surveying the surface and using an in-depth X-ray high resolution mode examination of the samples by a VG Scientific 310 D instrument. This X-ray system is equipped with a Mg anode (X-ray source) with an operational voltage of 3 kV and an operational current of 8 mA. Data was recorded at 45° collection angle and at a sputter rate of 1 Å/s.

X-ray diffraction data on the disc-shaped specimen were collected in a Sintage X-4000 (Sintage Ltd., USA). The X-ray generator was operated at 35 kV and 30 mA with Cu K α radiation. The diffractometer scan speed was four degrees per minute. The Bragg angle, 2θ , varied from 20° to 80°.

3. Results and Discussion

3.1. Volume Resistivity of CFECAs

The volume resistivities of #106, #107 and #800 CFECAs are shown in Table 1 [45]. The highest volume resistivity in this study is $10^{-1.4}$ Ω cm, from #800 at 23°C. Also at 23°C, #106 gives $10^{-2.8}$ Ω cm and #107 gives $10^{-2.4}$ Ω cm. At every temperature, #800 has the highest volume resistivity, #107 has moderate volume resistivity, and #106 has the lowest resistivity. Higher temperatures produce higher volume resistivities. However, temperatures between 175°C and 240°C produce

Table 1.

Volume resistivities of #106, #107 and #800 CFECA when particles were oxidized at various oxidation temperatures for two hours [45]

Oxidation temperature (°C)	Volume resistivity ($\Omega \text{ cm}$)		
	106	107	800
23	$10^{-2.8}$	$10^{-2.4}$	$10^{-1.4}$
125	$10^{-2.7}$	$10^{-2.4}$	$10^{-0.3}$
150	$10^{-2.6}$	$10^{-2.4}$	$10^{0.1}$
175	$10^{-2.6}$	$10^{-2.3}$	$10^{0.5}$
200	$10^{-2.3}$	$10^{-2.1}$	$10^{1.2}$
240	$10^{-1.6}$	$10^{-1.3}$	$10^{3.0}$
300	$10^{5.2}$	$10^{6.0}$	$10^{7.1}$

sharper increases in volume resistivity, and above 240°C cause more dramatic effects. Hence, silver coating improves oxidation resistance for copper particles at temperatures from 23°C to 175°C.

Figure 2a shows the particle size distribution for un-coated copper particles #800. 5 μm is the most frequent size for #800. Figure 2b and 2c illustrates the particle size distributions for silver-coated copper particles #106 and #107 [44, 45]. A particle size of 10 μm is the most frequent for both #106 and #107. However, the volume resistivities of #106 CFECA are slightly lower than those of #107 CFECA, as shown in Table 1 [45]. Figure 3a and 3b presents the SEM images of #106 and #107 CFECA [45]. #106, with flake-shaped particles, offers a greater contact area for the copper particles in the ECAs and a more electrically-conductive path than #107, which has spherical particles.

Figure 3c shows an SEM image of #800 CFECA [45]. #800 has spherical particles. Compare this with the SEM image of #107 CFECA in Fig. 3b. The contact area of #800 in CFECA is lower than the contact area of #107 in CFECA. The smaller contact area of the #800 in CFECA is due to the fact that the un-coated particles are smaller than the silver-coated particles. 5 μm is the most frequent size for #800 (see Fig. 2a), which is much smaller than the particle size of 10 μm for #107 (see Fig. 2c). However, the volume resistivities of #800 CFECA are much higher than those of #107 CFECA, as shown in Table 1. Not only the particle composition but also its size affect the volume resistivities of CFECA, as shown in Table 1. The lower conductivity of copper in comparison to silver, and the smaller contact area result in higher volume resistivities for #800 CFECA as compared to the volume resistivities of #107 CFECA.

A dielectric-filled via (DFV) is a circuit board mainly composed of dielectric material, such as fiber glass, uses ECA as a conductor to fill its via. Figure 4 shows volume resistivities for DFVs using #106 and #107 CFECA. From 30°C to 175°C, #106 DFVs have lower volume resistivities than #107 DFVs. For oxidation tem-

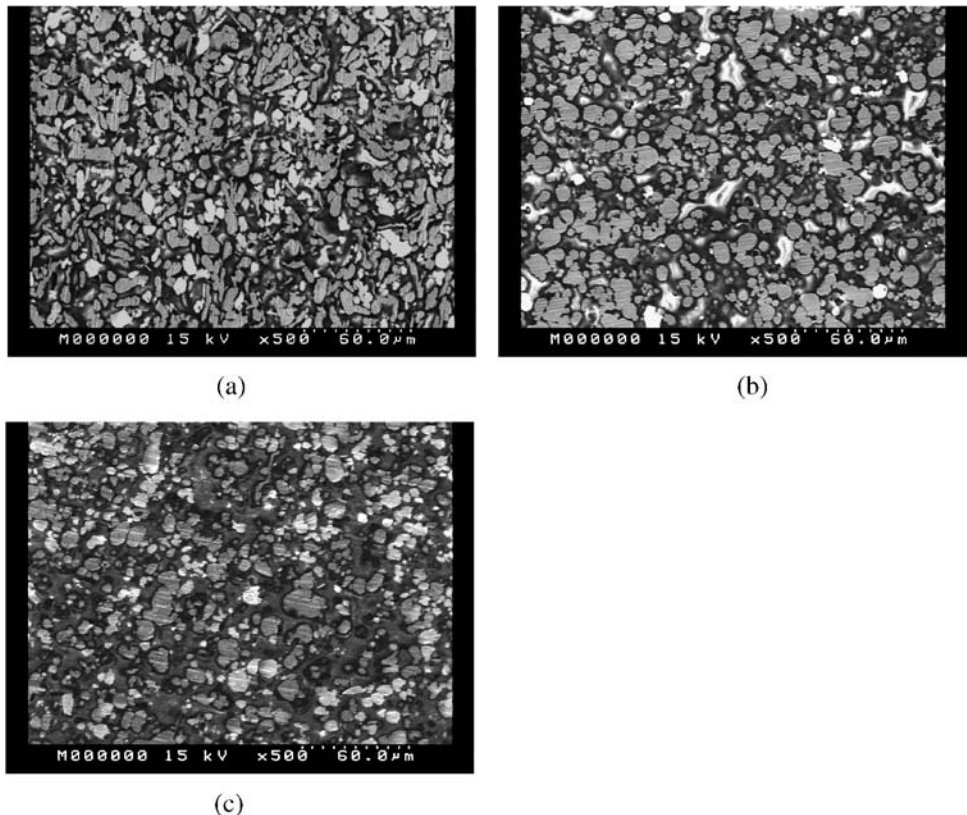


Figure 3. SEM images ($\times 500$) of (a) #106, (b) #107 and (c) #800 CFECA [45].

peratures of 175°C – 220°C , the resistivity values of #106 and #107 DFVs become closer. For oxidation temperatures above 240°C , volume resistivities are similar for #106 and #107 DFVs. The SEM images in Fig. 5 show that the #106 flakes provide a greater contact area and a more conductive path than #107 spheres.

3.2. Critical Volume Fraction of CFECA

The electrical properties of adhesives are understood in terms of percolation phenomenon. When sufficient amount of conductive fillers was loaded into an insulating polymer matrix, the adhesives transformed from insulators to conductors resulting in continuous linkages of filler particles. This is shown graphically in Fig. 6. When the volume fraction of filler is increased, the probability of continuity increases until it reaches the critical volume fraction V_c . Then the electrical resistivity of the composite material is low and comparable to the resistivity of pure filler material [47].

The volume resistivities of CFECA are plotted as functions of the volume fractions of #106 and #107 in CFECA as shown in Fig. 7. Figure 7 shows the rapid decrease in volume resistivity of CFECA from $1.6 \times 10^5 \Omega \text{ cm}$ to $6.3 \times 10^{-4} \Omega \text{ cm}$

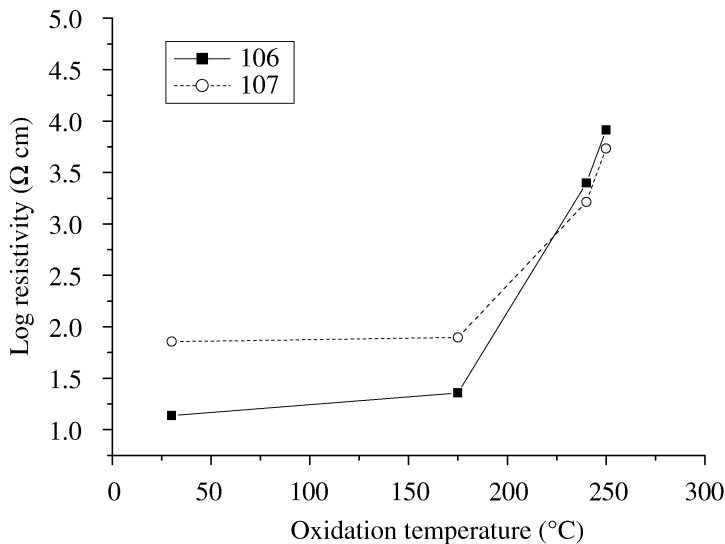


Figure 4. Plots of volume resistivity of DFV filled with #106 and #107 CFECA as a function of oxidation temperature.

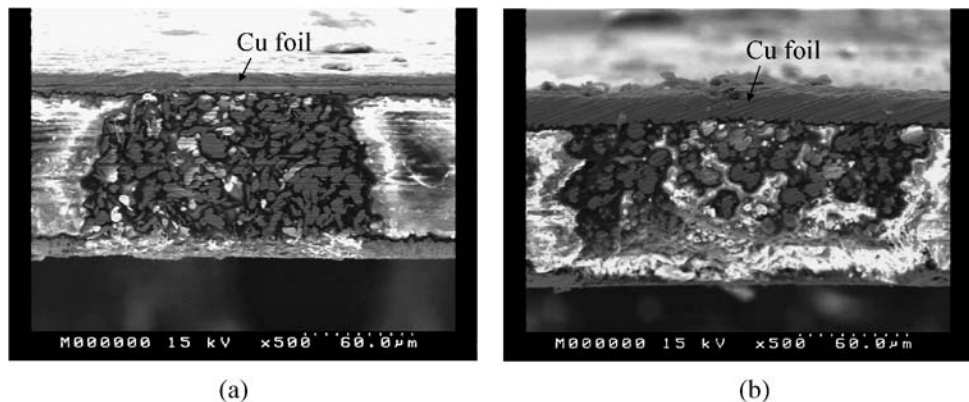


Figure 5. SEM images ($\times 500$) of cross-sections of DFV filled with (a) #106 and (b) #107 CFECA.

as the volume fraction of #106 increases to V_c . The same is true for #107 CFECA, where the corresponding decrease is from $3.2 \times 10^5 \Omega \text{ cm}$ to $2 \times 10^{-3} \Omega \text{ cm}$. The V_c values of #106 and #107 in CFECA are 0.131 and 0.157. The further increases in volume fractions for #106 and #107 in CFECA from V_c to a volume fraction of 0.5 slightly decreases the CFECA volume resistivities to $1.6 \times 10^{-6} \Omega \text{ cm}$ and $5 \times 10^{-6} \Omega \text{ cm}$, respectively. Lower V_c values and lower volume resistivities for #106 CFECA in comparison to #107 CFECA were observed.

#106 flakes with an average length of 10 μm and a volume fraction of 0.204, when mixed in epoxy and cured, provided more contact area than #107 spheres of

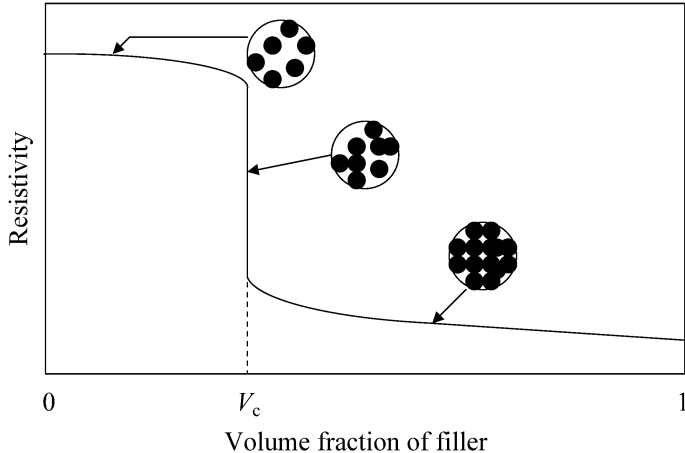


Figure 6. Electrical resistivity of ECAs plotted as a function of volume fraction of filler in terms of percolation phenomenon [47]. The formation of the first complete particle linkage results in a sharp drop in electrical resistivity at a critical volume fraction V_c . When the volume fraction of filler is less than V_c , particle linkage is not completed which results in a high electrical resistivity. If the volume fraction of filler is above V_c , more particle linkages are achieved and thus a low electrical resistivity is measured.

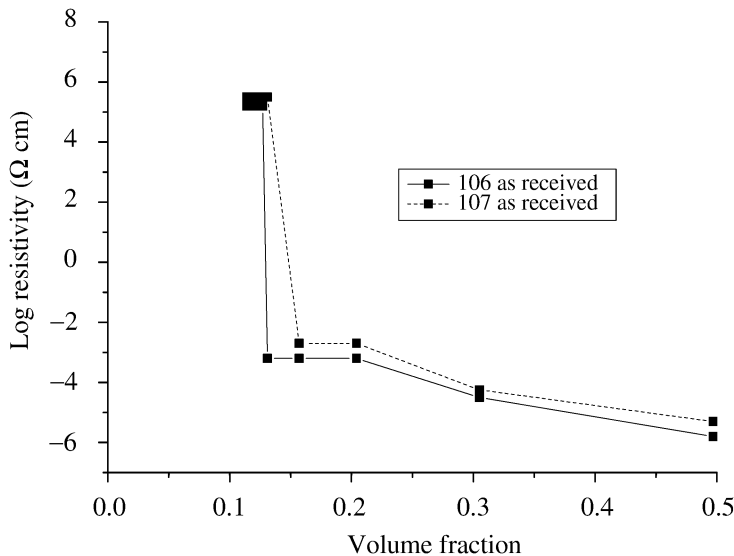


Figure 7. Volume resistivity of #106 and #107 CFECA plotted as a function of particle volume fraction in the ECA [44].

diameter 10 μm as shown in Fig. 3a and 3b. Conductive fillers which can achieve high contact areas produce ECAs with low volume resistivities.

Franey *et al.* [48] observed that the volume resistivity of an ECA was $\sim 1 \times 10^{-4} \Omega \text{ cm}$ when the volume fraction of silver particles in the ECA was 0.22. Mori

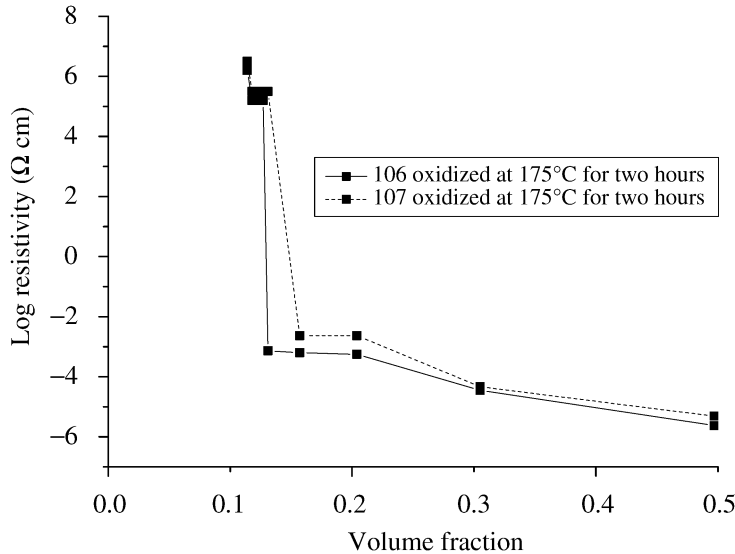


Figure 8. Volume resistivity of #106 and #107 CFECAs plotted as a function of particle volume fraction in the ECA when particles are oxidized at 175°C for two hours [44].

et al. [28] found that the volume resistivity of an ECA was $1 \times 10^{-3} \Omega \text{ cm}$ when the volume fraction of copper particles in the ECA was 0.2. In this study, the volume resistivities of ECAs are 1×10^{-4} – $1 \times 10^{-3} \Omega \text{ cm}$ when the volume fractions of silver-coated copper particles such as #106 and #107 are 0.131 and 0.157, as shown in Fig. 7. The results of this study show that both #106 and #107 are acceptable-conductive fillers for production of CFECAs.

Figure 8 shows plots of volume resistivities of CFECAs in #106 and #107, after #106 and #107 were oxidized at 175°C for two hours, dispersed in epoxy and cured to produce CFECAs. The V_c values of #106 and #107 remained at 0.131 and 0.157, respectively. This shows the V_c values of #106 and #107 were not influenced by oxidation at 175°C for two hours. The volume resistivity of #106 CFECAs is slightly increased from $6.3 \times 10^{-4} \Omega \text{ cm}$ to $7.2 \times 10^{-4} \Omega \text{ cm}$ after oxidation at 175°C for two hours. When #107 is used, the volume resistivity is increased from $2 \times 10^{-3} \Omega \text{ cm}$ to $2.3 \times 10^{-3} \Omega \text{ cm}$.

Figure 9 shows plots of volume resistivities of CFECAs containing #106 and #107, after #106 and #107 were oxidized at 240°C for two hours, mixed into epoxy and cured to produce CFECAs. The V_c values of #106 and #107 and the volume resistivities at V_c all increased as oxidation temperature increased from 175°C to 240°C. The V_c values of #106 and #107 increased from 0.131 and 0.157 to 0.247 and 0.406, respectively. The volume resistivity of #106 CFECAs at V_c is increased from $6.3 \times 10^{-4} \Omega \text{ cm}$ to $2.9 \times 10^{-3} \Omega \text{ cm}$. For #107 the corresponding increase was from $2 \times 10^{-3} \Omega \text{ cm}$ to $9.8 \times 10^{-3} \Omega \text{ cm}$.

Oxidation below 175°C results in good oxidation resistance both for #106 and #107 particles. These low temperatures also result in stable V_c values and volume

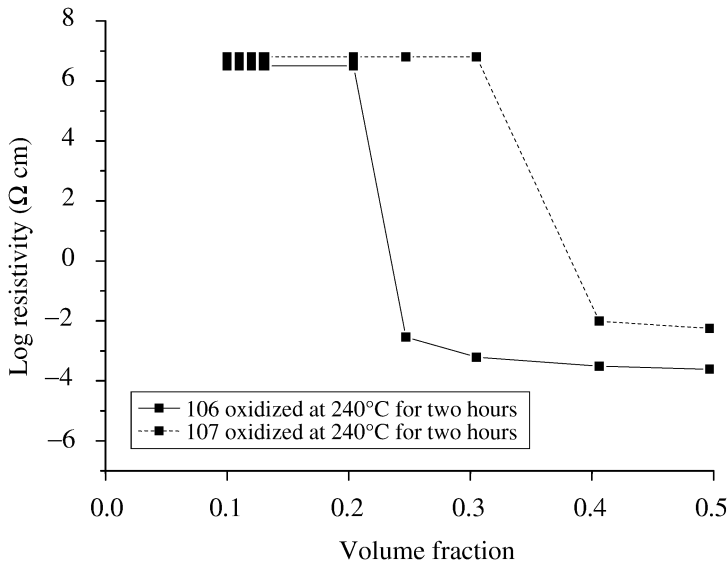


Figure 9. Volume resistivity of #106 and #107 CFECAs plotted as a function of particle volume fraction in the ECA when particles are oxidized at 240°C for two hours [44].

resistivities of $9.4 \times 10^{-5} \Omega \text{ cm}$ for #106 and $3.49 \times 10^{-4} \Omega \text{ cm}$ for #107. Oxidation at 240°C does not allow good oxidation resistance for both #106 and #107. All oxidation was done in ambient air.

3.3. Volume Resistivity of CCPs

The efficiency of electrical conduction in particle-filled conductive adhesives is largely dependent on the interparticle conduction. Sancaktar and Dilsiz [49] discussed the pressure-dependent conduction behavior with particles such as Ni particles, Ni flakes, Ag particles, Ni filaments, magnetite spindles and Cu particles. In order to gain insight into the pressure-dependent conduction behavior of Cu particles, this study tested #800, #106 and #107 particles.

#800 particles were oxidized at temperatures of 30°C to 175°C and at 240°C for two hours; they were compressed in a mold at pressures ranging from 1 MPa to 50 MPa; and their volume resistivities are shown in Fig. 10. The volume resistivities of CCPs decreased as compression pressure increased from 1 MPa to 50 MPa. When #800 particles were oxidized at a temperature of 30°C for two hours prior to being compressed, the volume resistivity of #800 CCPs decreased strongly from $3.1 \times 10^3 \Omega \text{ cm}$ to $1.4 \times 10^{-6} \Omega \text{ cm}$ as compression pressure increased from 1 MPa to 50 MPa. For a given particle level, the samples oxidized at higher temperatures had higher volume resistivities. As the oxidation temperature increased from 30°C to 175°C and 240°C, the volume resistivities of #800 CCPs significantly increased from $1.4 \times 10^{-6} \Omega \text{ cm}$ to $3.2 \times 10^{-4} \Omega \text{ cm}$ and $1.4 \times 10^4 \Omega \text{ cm}$ at a compression pressure 50 MPa. The volume resistivity increase causes a lower conduction. Hence, the conduction of #800 CCPs is largely decreased as oxidation temperature

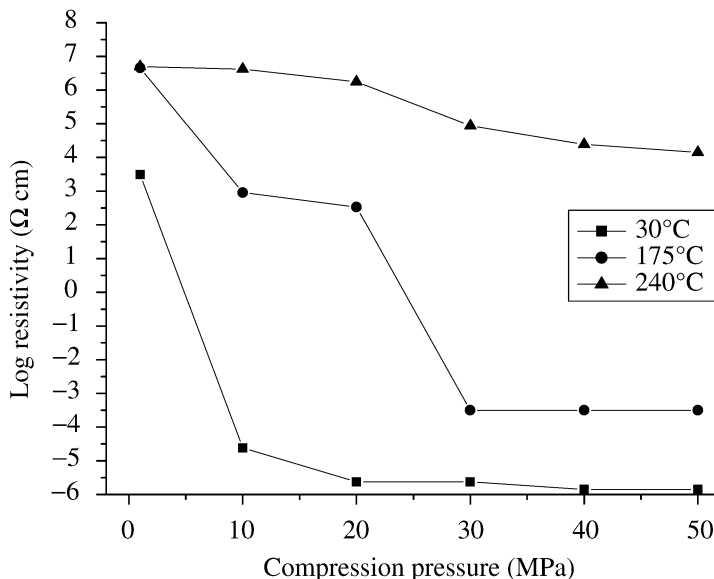


Figure 10. Volume resistivity of #800 CCPs as a function of compression pressure when particles are oxidized at 30°C, 175°C and 240°C for two hours.

increased from 30°C to 240°C and decreased as compression pressure increased from 1 MPa to 50 MPa.

For #106 and #107 particles oxidized at temperatures of 30°C and 175°C for two hours prior to being compressed, Fig. 11a and 11b shows that the volume resistivities of #106 and #107 CCPs decreased considerably as compression pressures increased from 1 MPa to 10 MPa, and decreased only slightly as pressures increased from 11 MPa to 50 MPa. When a certain compression pressure (1–50 MPa) was applied, only a negligible difference in volume resistivities for #106 and #107 CCPs between 30°C-oxidized particles and 175°C-oxidized particles was measured, as shown in Fig. 11a and 11b. This indicates #106 and #107 particles have good oxidation resistance in ambient air at oxidation temperatures 30–175°C. As the oxidation temperature increased from 175°C to 240°C, the volume resistivities of #106 and #107 CCPs were highly increased as a certain compression pressure was applied. For #106 and #107 particles oxidized at temperature of 240°C for two hours prior to being compressed at the compression pressures of 1–39 MPa, Fig. 11a and 11b shows the volume resistivities of #106 CCPs are lower than those of #107 CCPs. #106, with flake-shaped particles (Fig. 1b), has higher aspect ratio than #107, which has spherical particles (Fig. 1c). Contact area between particles in #106 CCP was higher than that in #107 CCP. This indicates that the higher the contact areas between conductive particles, the lower the volume resistivities of CCP. When compression pressure was increased to 40–50 MPa, both #106 and #107 CCPs had almost the same volume resistivities, as consistent contact areas between conductive particles were produced.

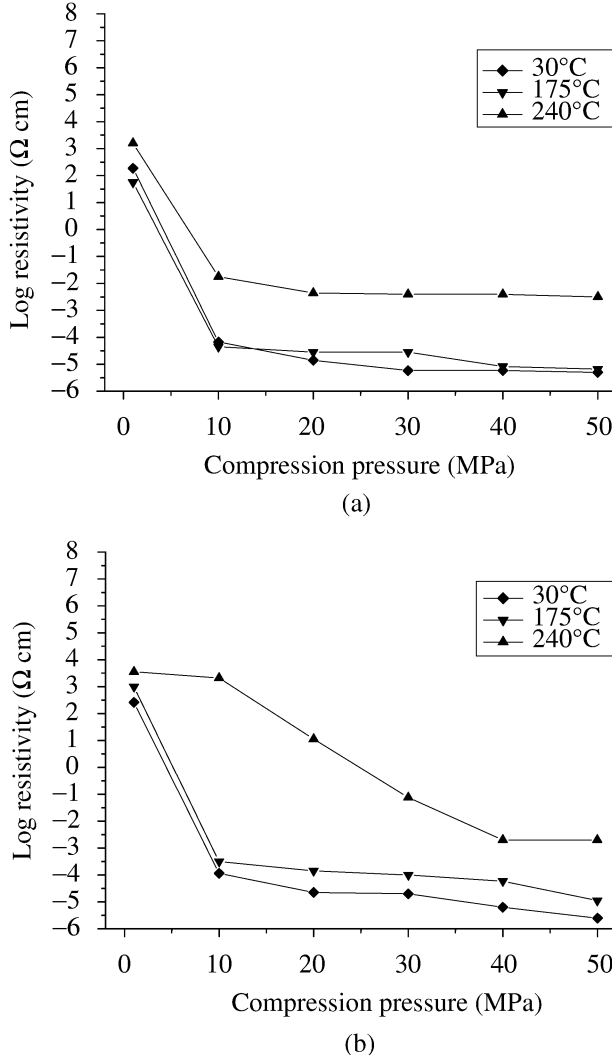


Figure 11. Volume resistivities of (a) #106 and (b) #107 CCPs as a function of compression pressure when particles are oxidized at 30°C, 175°C and 240°C for two hours.

Figure 12 shows that contact areas of #106, #107 and #800 increased as compression pressure increased. The mirror image of this trend is that the volume resistivities are decreased as compression pressure is increased. When the compression pressure increased from 1 MPa to 5 MPa, the volume resistivities and the contact areas of #106, #107 and #800 CCPs remained at the same values. The volume resistivities of #106, #107 and #800 are decreased because the contact areas are increased at compression pressure increased from 6 MPa to 24 MPa. When the compression pressure increased from 25 MPa to 50 MPa, the volume resistivities and the contact areas of #106, #107 and #800 CCPs remained at the same values. Why

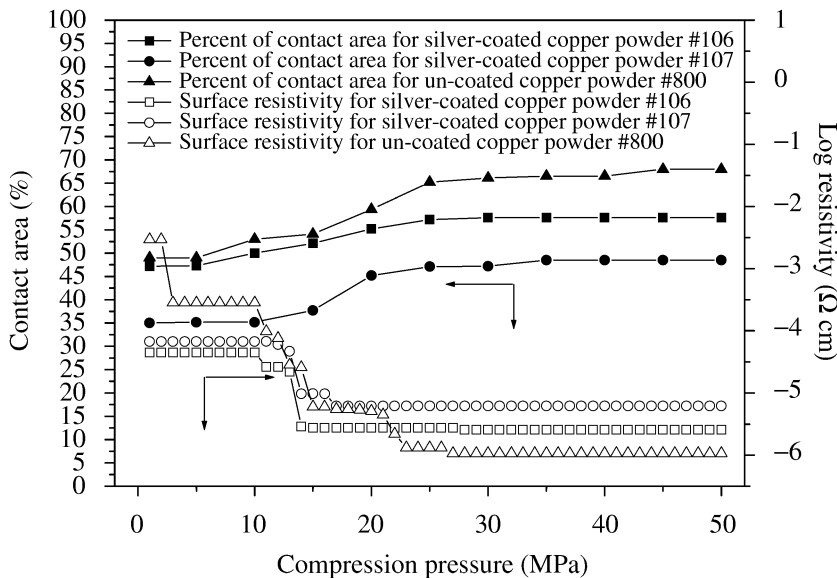


Figure 12. Contact area (%) and volume resistivity of #106, #107 and #800 plotted as a function of compression pressure when particles are oxidized at 30°C for two hours.

does #800 show high volume resistivities at low compression pressures between 1 MPa and 5 MPa and then show low volume resistivities at high compression pressures between 25 MPa and 50 MPa? At the low compression pressures from 1 MPa to 5 MPa, silver coating provides a better electrical conduction, the volume resistivities of #106 and #107 are lower than that of #800, even though #800 offers a higher contact area than #106 and #107. The volume resistivities of #800 are much smaller than those of #106 and #107 at compression pressures between 25 MPa and 50 MPa. #800 CCPs provide high contact areas because #800 particles are smaller (these spherical particles are 5 µm in diameter on average as shown in Fig. 2a) than particles in #106 (flake-shaped particles with an average length of 10 µm as shown in Fig. 2b) and #107 (10 µm diameter spheres as shown in Fig. 2c). The higher contact areas of #800 particles result in their volume resistivities being lower than #106 and #107. Figure 13a–c supports this hypothesis. When #106 and #107 particles are compressed at pressures between 1 MPa and 50 MPa, #106 shows lower volume resistivities than #107. #106 particles have more contact areas than those of #107 particles because #106 has flake-shaped particles and #107 has spherical particles.

3.4. Growth of Oxides of Copper Particles

The oxide growth of #106, #107 and #800 particles was determined by TGA. Figure 14 shows that #800 particles are gradually oxidized at temperatures from 30°C to 240°C and rapidly oxidized at temperatures higher than 240°C. This resulted in

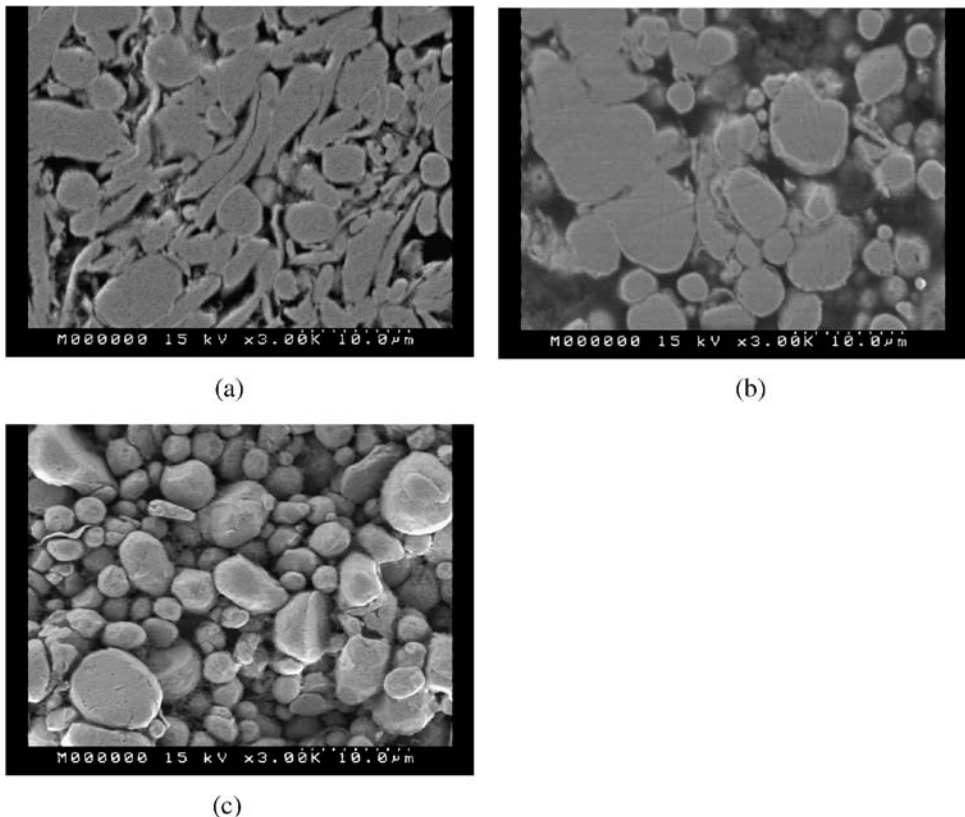


Figure 13. SEM images ($\times 3000$) of (a) #106, (b) #107 and (c) #800 CCPs when particles are compressed at a pressure of 50 MPa.

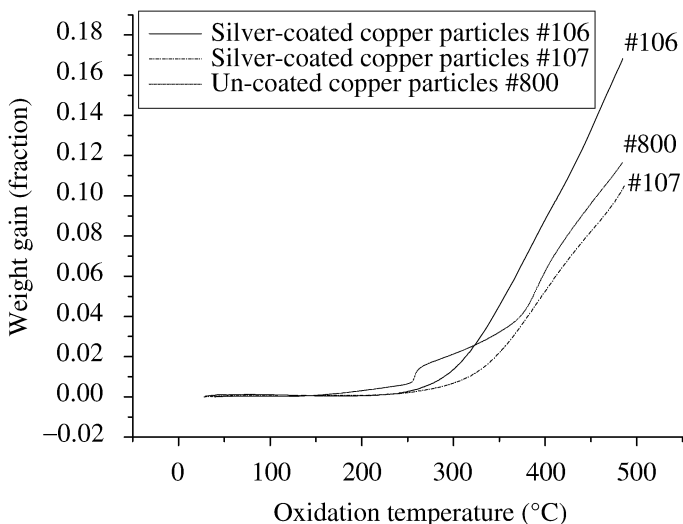


Figure 14. TGA curves of #800, #106 and #107 particles [44].

gradual and then rapid increase in the volume resistivities of #800 ECAs as shown in Table 1.

Figure 14 shows #106 and #107 particles are not oxidized from 30°C to 175°C, slightly oxidized from 175°C to 240°C, gradually oxidized from 240°C to 340°C and rapidly oxidized from 340°C to 480°C. There are no weight gains of #106 and #107 particles from oxidation at temperatures from 30°C to 175°C as shown in Fig. 14, which results in no increase in the volume resistivities of #106 and #107 CFECAs as shown in Table 1. There is a slight weight gain of #106 and #107 particles from oxidation from 175°C to 240°C as shown in Fig. 14, which results in slight increase in the volume resistivities of #106 and #107 CFECAs as shown in Table 1. The gradual increase in weight of #106 and #107 particles for oxidation from 240°C to 300°C as shown in Fig. 14, which results in gradual increase in the volume resistivities of #106 and #107 CFECAs as shown in Table 1.

Figure 14 shows gradual oxidation of #800 particles but #106 and #107 show negligible oxidation with temperature rise from 30°C to 240°C. This indicates that the silver coating on the surfaces of copper particles can offer additional oxidation resistance in the temperature range from 30°C to 240°C.

Figure 14 shows that #106 particles are easier to oxidize than #107 if the temperature rises above 240°C. However, the volume resistivities of #106 CFECAs are lower than those of #107 CFECAs as shown in Table 1. Flake-shaped #106 particles (see Fig. 3a) provide greater contact areas than spherical #107 particles (see Fig. 3b), which results in #106 CFECAs having the lower volume resistivities (see Table 1).

3.5. Metal Oxides of Copper Particles

The metal oxides of #106, #107 and #800 particles were examined by Auger electron spectroscopy and XRD. After #800 particles were oxidized at 30°C for two hours, the oxygen concentration (fraction) of #800 particles decreased from 0.08 at the surface to 0.02 at a depth of 65 nm, as shown in Fig. 15a. When #800 particles were oxidized at 175°C for two hours, the atomic concentration (fraction) of oxygen decreased from 0.23 at the surface to 0.07 at a depth of 250 nm, as shown in Fig. 15b. This indicates that more oxygen migrates from the #800 particles surfaces to their interior when the oxidation temperature is increased from 30°C to 175°C. High levels of Cu were found to be oxidized to Cu₂O because high intensities of Bragg angle 36.49° in the XRD curves were measured in Fig. 16. When oxidation temperature was increased from 30°C to 175–240°C, the formation of Cu₂O on the #800 particle surfaces causes an increase in the volume resistivities of CFECAs and CCPs, as shown in Table 1 and Fig. 10. An increase in the volume resistivities of CFECAs and CCPs results in a decrease in the conduction of CFECAs and CCPs. However, Fig. 16 does not show formation of Cu₂O on the #800 particle surfaces when #800 particles are oxidized at 30°C for two hours. This is because it is being beyond the resolution of XRD. Hence, the conduction of CFECAs and CCPs decreases mainly due to the formation of more Cu₂O at the #800 particle surfaces and

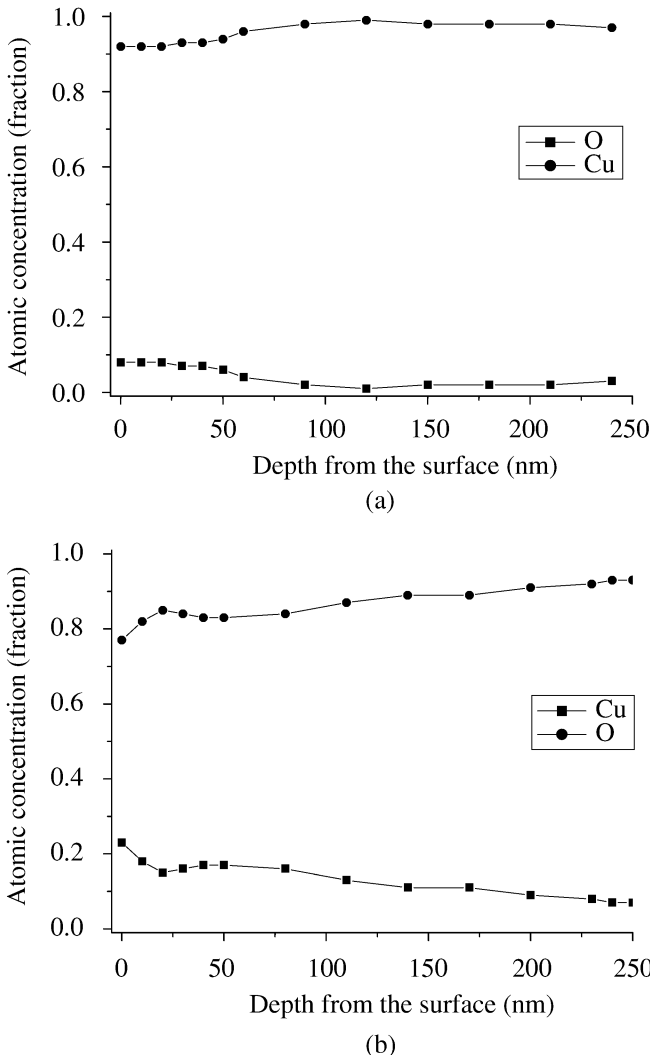
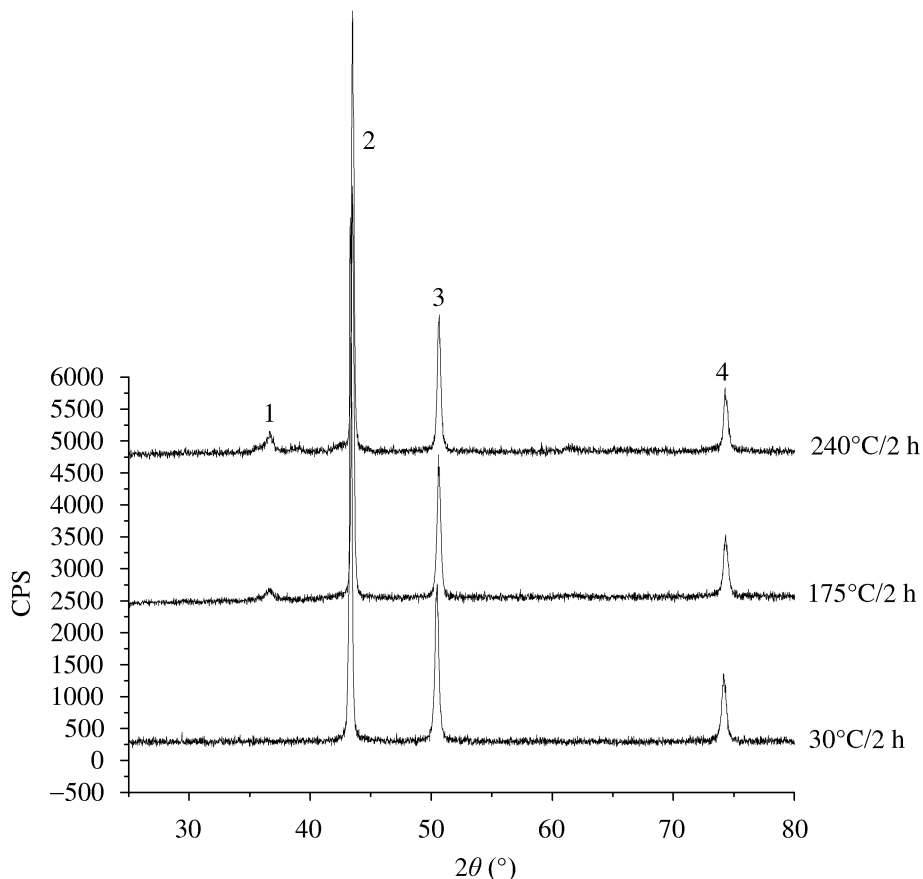


Figure 15. Atomic concentrations of Cu and O for #800 particles after being oxidized at (a) 30°C and (b) 175°C for two hours plotted as a function of the depth from the surface.

migration to their interior as oxidation temperatures increases from 30°C to 175°C and 240°C.

The Auger electron spectra of #107 particle surfaces are shown in Fig. 17. Figure 17 indicates that only silver, oxygen and carbon are observed in #107 particle surface layers when #107 is oxidized at 175°C for two hours. When the oxidation temperature is increased from 175°C to 240°C, not only silver, oxygen and carbon are observed, but also Cu is observed on #107 particle surface layers. Figure 18a and 18b illustrates that the copper migrates from the interior to the surface as temperature increases from 175°C to 240°C. For enhancing the weatherabil-



Peak number	1	2	3	4
2θ	36.49	43.37	50.5	74.17
Element/oxide	Cu_2O	Cu	Cu	Cu
Miller index	(1 1 1)	(1 1 1)	(2 0 0)	(2 2 0)

Figure 16. Elements and oxide for #800 particles after oxidized at various temperatures for two hours as determined by XRD.

ity of silver-coated copper particles, an organic coating is applied onto the surfaces of silver-coated copper particles, which results in the carbon observed in Fig. 18a and 18b. When #107 particles were oxidized at 175°C and 240°C for two hours, Fig. 18a and 18b shows only organic coatings in the top 26 nm and 13 nm layers, respectively. Figure 19 shows the element and oxide for #107 particles after oxidation at various temperatures for two hours as determined by XRD. Only AgO is formed on #107 when #107 particles are oxidized at 30°C and 175°C for

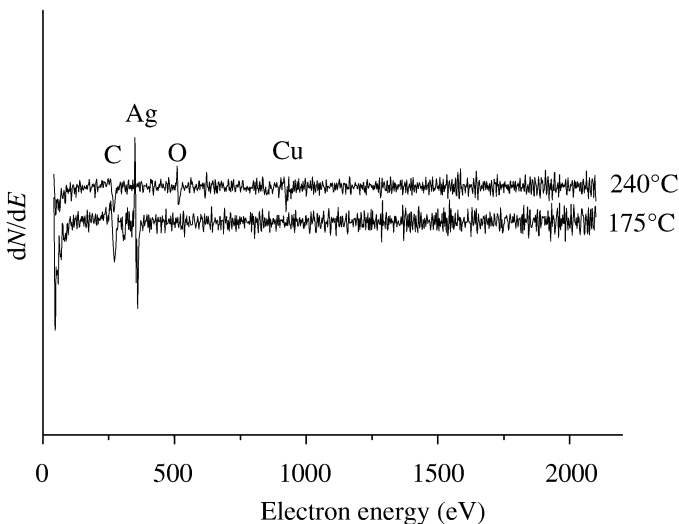


Figure 17. Auger electron spectra of the surface of #107 particles after oxidized at 175°C and 240°C for two hours [44].

two hours. Cu₂O and AgO are formed on #107 when #107 particles are oxidized at 240°C for two hours. Wang and Xie [50] claimed that the diffusion coefficient between silver and copper increased with the increase in temperature from 225°C to 340°C. For #107 particles oxidized at 175°C for two hours, the diffusion coefficient between silver and copper is still not high enough to allow copper to migrate from #107 particle interior to its surface layer. After oxidation of #107 particles at 240°C for two hours, the diffusion coefficient between silver and copper becomes high enough to allow copper to migrate from the interior of #107 particles to their surface layers.

Table 1 and Fig. 11b show the low-volume resistivities of CFECAs and CCPs for #107 particles, even when oxidized at temperatures from 30°C to 175°C. This indicates that #107 particles have good conduction behavior, even when oxidized at temperatures from 30°C to 175°C. Hence, the conduction of CFECAs and CCPs for #107 particles, shown in Table 1 and Fig. 11b, is not affected by AgO. The volume resistivities of CFECAs and CCPs for #106 particles follow the same pattern. The volume resistivities of CFECAs and CCPs for #106 and #107 particles increase with the temperatures rise from 175°C to 240°C. This is due to the Cu₂O formed onto #106 and #107 particle surfaces when oxidized at 240°C for two hours. The formation of Cu₂O on #106 and #107 particle surfaces results in increases of the V_c to 0.247 and 0.406, respectively.

4. Conclusion

Silver-coated copper has good oxidation resistance at temperatures lower than 175°C by hindering copper diffusion from the interior to the surface of particles

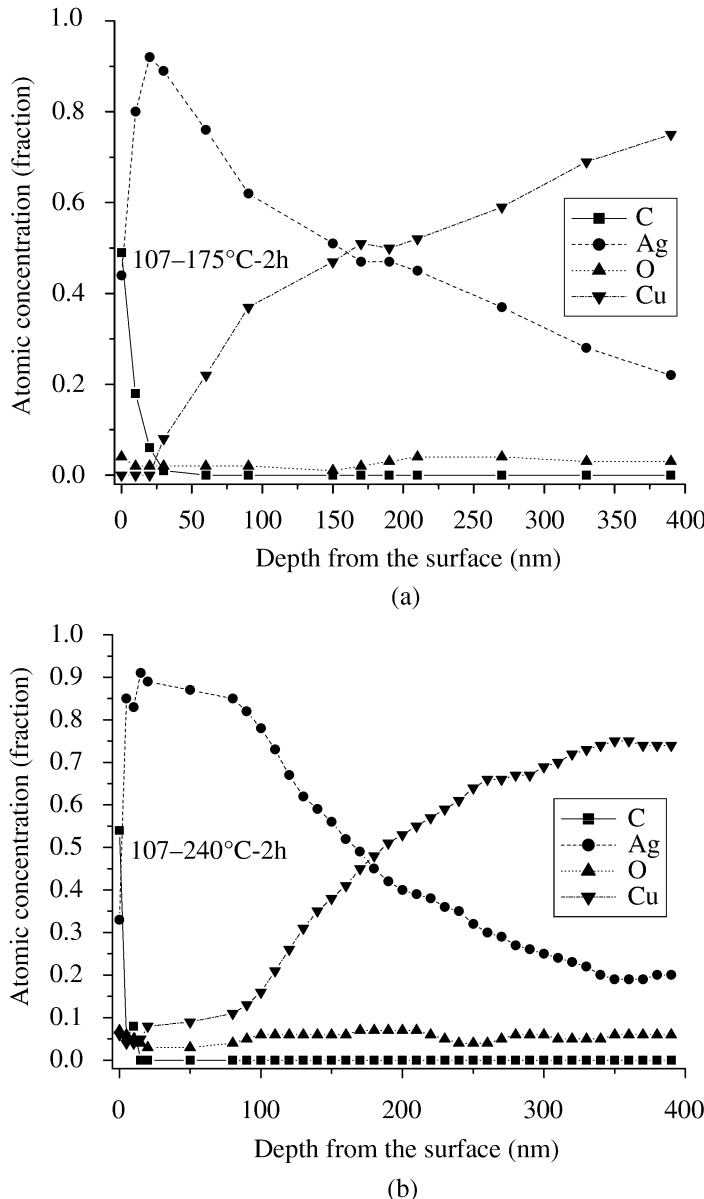
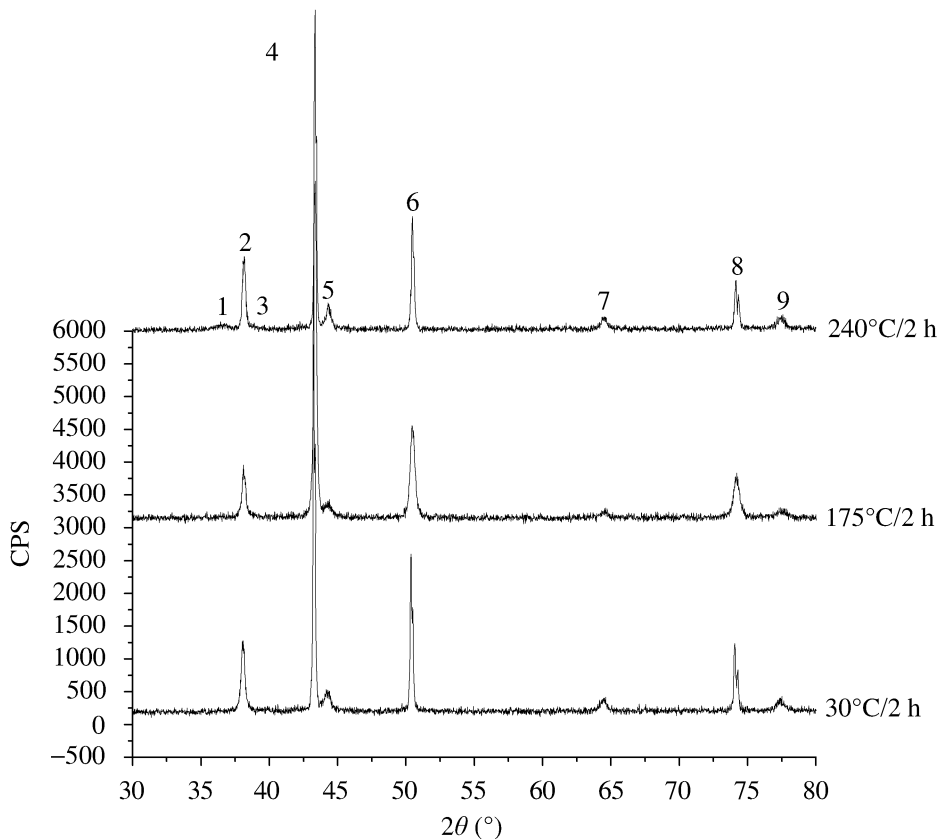


Figure 18. Atomic concentrations of C, Ag, O and Cu for #107 particles after being oxidized at (a) 175°C and (b) 240°C for two hours plotted as a function of the depth from the surface [44].

#106 and #107. This prevents Cu₂O formation on the particle surfaces. CFECAs and CCPs remain at low-volume resistivities. Volume resistivities of CFECA and CCPs are independent of the formation of AgO on the surfaces of silver-coated copper particles #106 and #107.



Peak number	1	2	3	4	5	6	7	8	9
2θ	36.49	38.17	38.75	43.37	44.32	50.5	64.51	74.17	77.5
Element/oxide	Cu ₂ O	Cu	AgO	Cu	Cu	Cu	AgO	Cu	Ag
Miller index	(1 1 1)	(1 1 1)	(1 0 0)	(1 1 1)	(2 0 0)	(2 0 0)	(0 2 3)	(2 2 0)	(1 1 1)

Figure 19. Elements and oxide for #107 particles after oxidized at various temperatures for two hours as determined by XRD [44].

The critical volume fractions of silver-coated copper particles #106 and #107 in conductive adhesives are only slightly affected by particle shape at oxidation temperatures 30°C–175°C but are strongly affected by particle shape at oxidation temperature of 240°C. Flake-shaped copper particles #106 show a lower critical volume fraction of CFECAAs than spherical #107 particles since a higher contact area is provided.

The conduction behavior of CCPs is strongly affected by compression pressure, oxidation temperature and particle composition and is only slightly affected by par-

ticle size and particle shape. When a higher compression pressure is applied onto the smaller size and flake-shaped particles, a better conduction behavior of CCPs is produced because of higher contact areas formed.

Acknowledgement

The authors wish to thank the National Science Council of the Republic of China for supporting this research under contract NSC91-2745-P-214-003.

References

1. S. K. Kang, S. Buchwalter, N. La Bianca, J. Gelmore, S. Purushothaman, K. Papathomas and M. Poliks, in: *Proc. 50th IEEE Electronic Components and Technology Conference*, Las Vegas, NV, USA, pp. 887–891 (2000).
2. S. K. Kang, S. L. Buchwalter, N. C. LaBianca, J. Gelmore, S. Purushothaman, K. Papathomas and M. Poliks, *IEEE Trans. Compon. Packag. Technol.* **24**, 431–435 (2001).
3. T. Suzuki, S. Tomekawa, T. Ogawa, D. Andoh, M. Tanahashi and T. Ishida, in: *Proc. IMAPS Int. Symp. on Advanced Packaging Materials, Processes, Properties and Interfaces*, Braselton, GA, USA, pp. 23–28 (2001).
4. S. Tomekawa, T. Suzuki, Y. Nakatani, F. Echigo and D. Andoh, *Proc. SPIE* **4428**, 93–97 (2001).
5. Y. Li and C. P. Wong, *Mater. Sci. Eng. R.* **51**, 1–35 (2006).
6. F. Bueche, *J. Appl. Phys.* **43**, 4837–4848 (1972).
7. S. M. Aharoni, *J. Appl. Phys.* **43**, 2463–2465 (1972).
8. B. E. Springett, *J. Appl. Phys.* **44**, 2925–2926 (1973).
9. S. Etemad, X. Quan and N. A. Sanders, *Appl. Phys. Lett.* **48**, 607–609 (1986).
10. X. Quan, *J. Polym. Sci., Part B: Polym. Phys.* **25**, 1557–1559 (1987).
11. A. Mikrajuddin, F. G. Shi, S. Chungpaiboonpatana, K. Okuyama, C. Davidson and J. M. Adams, *Mater. Sci. Semicond. Process* **2**, 309–319 (1999).
12. D. M. Bigg, *Polym. Eng. Sci.* **19**, 1188–1192 (1979).
13. C. T. Lo, K. S. Chou and W. K. Chin, *J. Adhesion Sci. Technol.* **15**, 783–792 (2001).
14. B. L. Roos-Kozel and F. M. Casavecchia, *Solid State Technol.* **27**, 167–170 (August 1984).
15. A. J. Lovinger, *J. Adhesion* **10**, 1–15 (1979).
16. S. M. Wentworth, B. L. Dillaman, J. R. Chadwick, C. D. Ellis and R. W. Johnson, *IEEE Trans. CPMT Part A* **20**, 52–59 (1997).
17. D. Klosterman, L. Li and J. E. Morris, *IEEE Trans. CPMT Part A* **21**, 23–31 (1998).
18. D. Lu and C. P. Wong, *IEEE Trans. Electron. Packag. Manuf.* **23**, 185–190 (2000).
19. M. Yamashita and K. Suganuma, *J. Mater. Sci. Lett.* **22**, 1311–1313 (2003).
20. S. B. Rane, T. Seth, G. J. Phatak, D. P. Amalnerkar and M. Ghatpande, *J. Mater. Sci.: Mater. Electron.* **15**, 103–106 (2004).
21. H.-W. U. Chiang, C.-L. Chung, L.-C. Chen, Y. I. Li, C. P. Wong and S.-L. I. Fu, *J. Adhesion Sci. Technol.* **19**, 565–578 (2005).
22. Y. Li, K.-S. Moon and C. P. Wong, *J. Appl. Polym. Sci.* **99**, 1665–1673 (2006).
23. R. R. Gomatam and E. Sancaktar, *J. Adhesion Sci. Technol.* **20**, 53–68 (2006).
24. Y. Li and C. P. Wong, in: *Proc. 56th IEEE Electronic Components and Technology Conference*, San Diego, CA, USA, pp. 924–931 (2006).
25. S. M. Pandiri, *Adhesives Age* **30**, 31–35 (1987).

26. R. Kuzel, I. Krivka, J. Kubat, J. Prokes, S. Nespurek and C. Klason, *Synthetic Metals* **67**, 255–261 (1994).
27. D. Das, S. Basu and A. Paul, *J. Mater. Sci.* **15**, 1719–1723 (1980).
28. K. Mori, Y. Okai, H. Yamada and Y. Kashiwaba, *J. Mater. Sci.* **28**, 376–372 (1993).
29. H. Dong, Z. Zhang and C. P. Wong, *J. Adhesion Sci. Technol.* **19**, 87–94 (2005).
30. R. N. Das, J. M. Lauffer and F. D. Egitto, in: *Proc. 56th IEEE Electronic Components and Technology Conference*, San Diego, CA, USA, pp. 112–118 (2006).
31. K.-S. Moon, S. Liong, H. Li and C. P. Wong, *J. Electron. Mater.* **33**, 1381–1388 (2004).
32. R. R. Gomatam and E. Sancaktar, *J. Adhesion Sci. Technol.* **18**, 1245–1261 (2004).
33. R. R. Gomatam and E. Sancaktar, *J. Adhesion Sci. Technol.* **18**, 1225–1243 (2004).
34. C. F. Goh, H. Yu, S. S. Yong, S. G. Mhaisalkar, F. Y. C. Boey and P. S. Teo, *Mater. Sci. Eng. B* **117**, 153–158 (2005).
35. C. F. Goh, Z. H. Gan, S. G. Mhaisalkar, F. Y. C. Boey, A. M. Gusak and P. S. Teo, *J. Appl. Phys.* **100**, 1–5 (2006).
36. S. Miyauchi and E. Togashi, *J. Appl. Polym. Sci.* **30**, 2743–2751 (1985).
37. M. Park, C. Choe, J. Kim, S. Lim, H. Ko and V. S. Mironov, *J. Appl. Polym. Sci.* **84**, 1040–1048 (2002).
38. M. L. Clingerman, J. A. King, K. H. Schulz and J. D. Meyers, *J. Appl. Polym. Sci.* **83**, 1341–1356 (2002).
39. D. M. Kalyon, E. Birinci, R. Yazici, B. Karuv and S. Walsh, *Polym. Eng. Sci.* **42**, 1609–1617 (2002).
40. J. C. Bolger and S. L. Morano, *Adhesives Age* **27**, 17–20 (1984).
41. Y. S. Gong, C. Lee and C. K. Yang, *J. Appl. Phys.* **77**, 5422–5425 (1995).
42. Y. Z. Hu, R. Sharangpani and S.-P. Tay, *J. Vac. Sci. Technol. A* **18**, 2527–2532 (2000).
43. G. Yu, M. Q. Zhang and H. M. Zeng, *J. Appl. Polym. Sci.* **70**, 559–566 (1998).
44. Y.-S. Lin and S.-S. Chiu, *Polym. Eng. Sci.* **44**, 2075–2082 (2004).
45. Y.-S. Lin and S.-S. Chiu, *J. Appl. Polym. Sci.* **93**, 2045–2053 (2004).
46. G. R. Ruschau and R. E. Newnham, *J. Composite Mater.* **26**, 2727–2735 (1992).
47. G. R. Ruschau, S. Yoshikawa and R. E. Newnham, *J. Appl. Phys.* **72**, 953–959 (1992).
48. J. P. Franey, T. E. Graedel, G. J. Gualtieri, G. W. Kammlott, D. L. Malm, L. H. Sharpe and V. Tierney, *J. Mater. Sci.* **19**, 3281–3286 (1984).
49. E. Sancaktar and N. Dilsiz, *J. Adhesion Sci. Technol.* **13**, 679–693 (1999).
50. R. Wang and B. Xie, *Nucl. Instrum. Meth. Phys. Res. B* **198**, 197–200 (2002).

Experimental Investigation and Micropolar Modelling of the Anisotropic Conductive Adhesive Flip-Chip Interconnection

Yan Zhang^{a,b}, Johan Liu^{a,c,*}, Ragnar Larsson^b and Itsuo Watanabe^d

^a Key Laboratory of Advanced Display and System Applications, Ministry of Education & SMIT Center, School of Mechatronics Engineering and Automation, Shanghai University, Shanghai 200072, China

^b Department of Applied Mechanics, Chalmers University of Technology, SE-412 96 Gothenburg, Sweden

^c SMIT Center, Department of Microtechnology and Nanoscience, Chalmers University of Technology, SE-412 96 Gothenburg, Sweden

^d Advanced Interconnect Material Division, Hitachi Chemical Co., Ltd., 1150 Goshomiyama, Chikusei-shi Ibaraki, 308-8524 Japan

Abstract

A conductive adhesive is a promising interconnection material for microsystem packaging. The interconnect features are of great importance to system responses under various loading conditions. The flip-chip packaging system with anisotropic conductive film (ACF) joint under thermal loadings has been investigated both experimentally and theoretically. The displacement distributions have been measured by an interferometer, which could provide the in-plane whole-field deformation observation. The interconnection is of much smaller scales compared with the neighbouring components such as the chip and substrate, and there are even finer internal structures involved in the joint. The wide scale range makes both experimental observation and conventional simulation difficult. A micropolar model is thus developed. Utilizing the homogenization, this model requires low computation resource. Combination of this model with a second-order model was able to produce a highly efficient and valid prediction of the packaging system response under thermal and mechanical loadings. Comparison of the micropolar model simulation and experimental data shows good agreement.

Keywords

ACF, micropolar model, interconnect, interferometry

* To whom correspondence should be addressed. Tel.: +46-31-772 3067; Fax: +46-31-772 3622; e-mail: jliu@chalmers.se

1. Introduction

1.1. Flip-Chip Interconnection

Flip-chip technology is a significant development in surface mount technology (SMT) to improve cost, reliability and productivity in electronic packaging industry. In this technology, the semiconductor chip is turned upside down, i.e. active face down and hence called flip-chip, and bonded directly to a printed circuit board (PCB) or chip carrier substrate, in which all I/Os are connected simultaneously. Flip-chip interconnection is the connection of an integrated circuit chip to a carrier or substrate, which provides the shortest chip-to-packaging interconnection distance and has superiorities such as minimum resistance and minimum capacitance. Electrical performance and, consequently, the system reliability are highly dependent on the interconnection features. As a result, interconnection behaviour is a key issue in the long-term performance of a microsystem.

When the packaged system is powered up, it is subjected to a temperature change. The system consists of components of various materials deforming at different rates. Due to the mismatch in the coefficients of thermal expansion (CTE) among different materials, i.e. thermal gradient in the system, and due to geometric constraints, thermal-induced stresses and strains are generated in various parts of the system [1]. Thermal loading from either environmental or internal heat in system operation will have some impact on the interconnect behaviour. With the increase of device power dissipation and decrease of package size, the heat generated becomes serious, and the thermomechanical deformation of the interconnect becomes more complicated.

Flip-chip bonding usually involves solder or conductive adhesive interconnections to make the electrical and mechanical connections between the chip I/Os and the substrate. Anisotropic conductive adhesives (ACAs) are widely used as interconnection materials due to their advantages such as low processing temperature, fine pitch capability, compatibility with a wide range of substrates, flexible and simple processing and therefore low cost, environmental compatibility and so on. Their applications include flexible circuit interconnects, smart card applications, organic displays and so on. In spite of the multi-application of ACAs, only limited work has been done on the mechanical properties with respect to component/interconnect size decreasing from mm to μm , and even less attention has been paid to the micro-scale influences of the internal structures in the ACA interconnection.

This paper investigates the ACF flip-chip joints both experimentally and theoretically. In the experiments, the system deformation was measured by Moiré interferometry, which provides deformation information under various thermal loading conditions. Moreover, based on the interconnect structure characteristics, an interface model has been developed. Here the model was set up within the micropolar theory and utilized the homogenization idea. The micro-scale effects of constituents in the interconnect and the coupling between micro- and macro-scale responses was reflected by the stiffness coefficients. Simulation based on this interface model pro-

vides valid prediction of the packaging which includes the internal microstructure contributions and, at the same time, low computation cost.

1.2. Moiré Interferometry

In-plane Moiré interferometry is an optical measurement method, providing whole-field displacement contour maps with sub-wavelength sensitivity. It can provide abundant displacement data, which permits reliable determination of normal and shear strains. Moreover, the Moiré interferometry is characterized by excellent qualities including real time, high sensitivity, high spatial resolution, and high signal-to-noise ratio. These features make the method ideally suitable for microelectronics devices, especially those with complex geometries. The optical arrangement and operation mechanism had been described in detail by Post and Wood [2]. As applications of this Moiré interferometry method, the deformation fields of ball grid array (BGA) packaging under different thermal loadings had been observed [3–9], among which Shi and Wang [9] focused on the thermal deformation of a single solder ball. Ham and co-workers [10, 11] investigated electronic conductive film deformation under thermal cycling. The existing literature shows that Moiré interferometry can provide accurate information for studying the deformation of microsystem assemblies, and can be applied with confidence to thermomechanical deformation analysis as well as verification of numerical simulations.

2. Experimental Details

2.1. Moiré Interferometry

The instrument used in the present study was a Multi-function Macro Micro Moiré Interferometer (WTI 4M-120, USA), as shown in Fig. 1. The 4M-120 used was a compact system utilizing a cross-line grating and various mirrors to produce the four incident beams. A similar instrument had also been used by other researchers [7, 12]. The schematic diagram of the 4M optical arrangement is illustrated in Fig. 2. The laser light was of a wavelength of 633 nm. As shown in Fig. 2, a diverging laser

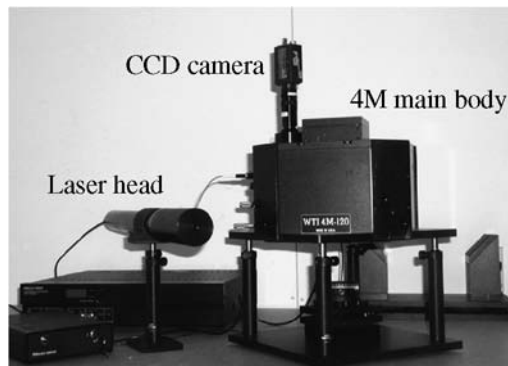


Figure 1. Multi-function Macro Micro Moiré Interferometer.

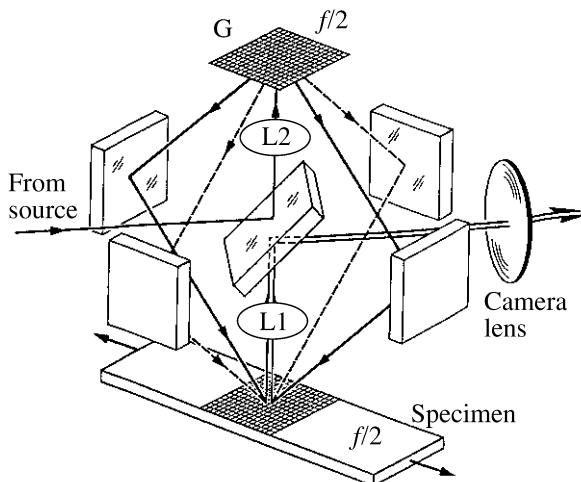


Figure 2. Schematic diagram of the 4M optical arrangement.

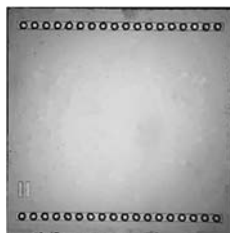


Figure 3. Chip in ACF bonding (active face).

beam as the laser source was directed by the 45° mirrors to pass through a collimation lens L2 and then the collimated beam struck a cross-line diffraction grating G at normal incidence. First, a cross-line grating (with frequency $f_g = 1200$ lines/mm) was adopted to set the null field before specimen measurement. The four beams were redirected by the four vertical mirrors to strike the grating at an angle of incidence α (with the relation $\sin \alpha = \lambda f/2$, where λ is the wavelength and f is the virtual grating frequency). After the null field setting, a virtual grating at the frequency $f = 2400$ lines/mm was formed by these four incident beams.

The specimen with replicated grating on the considered surface was measured when the null field was set. Light diffraction by the specimen grating was collected by the camera lens, which focused images of the Moiré patterns onto the record plane of the CCD camera.

2.2. Sample Preparation

The assembly specimen used in the experiments was a flip-chip system with anisotropic conductive film (ACF) joint. Figure 3 shows the photograph of the chip with the dimensions $0.28 \times 0.28 \times 0.02$ cm. The bumps on the chip were $60 \mu\text{m}$ in diameter and $18 \mu\text{m}$ in height. Figure 4 is the photograph of the substrate, here only

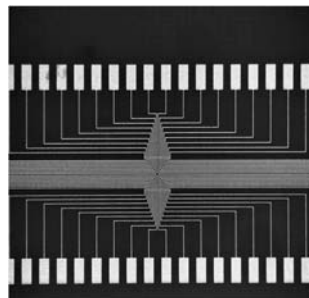


Figure 4. Center area of the substrate in ACF bonding.

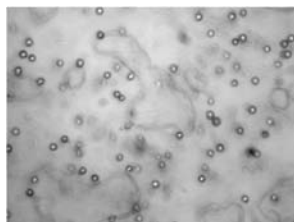


Figure 5. Particle distribution in ACF (particle diameter 5 μm).

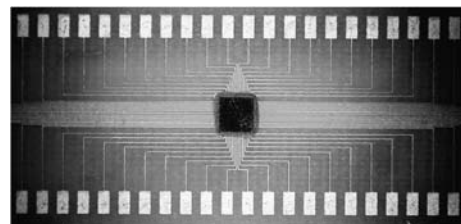


Figure 6. Bonded system with ACF flip-chip joint (top view).

the center area is shown. Figure 5 is the conductive particle distribution in the ACF, where the particles are Au-plated plastic with diameter 5 μm . It can be observed that the particles are uniformly distributed in the adhesive matrix with a relatively low volume fraction. Figure 6 is the bonded system with ACF joint.

It can be inferred from the literature [10, 11] as well as from our experimental observation that the chip is a quite ‘rigid’ body with uniform deformation along the measured direction. Therefore, in the following experimental observations, the measurement was carried out on the chip surface, which could also provide data for evaluating the later modelling work.

For specimen preparation, a high frequency grating mold of $f_s = 1200$ lines/mm cross-line grating with single layer aluminium was used for replication of the specimen grating. The grating was replicated on the specimen surface at temperature $T_0 = 65^\circ\text{C}$ and then cooled down to $T_1 = 20^\circ\text{C}$. Thereafter, a thermal loading with the same temperature excursion was applied once more on the specimen to study the

thermal cycling effect. The grating deformed together with the specimen, so the specimen displacement was recorded by the grating and measured by the 4M Interferometer system.

3. Experimental Results and Discussion

During the experimental observations, the Moiré interferometry produced fringes when the deformed specimen grating interfered with the virtual reference grating. The fringe patterns on the chip surface are shown in Fig. 7. Figure 7(a) provides the sketch map showing the bump positions on the chip. Figure 7(b) and 7(c) is the U - and V -field fringe patterns after the first thermal loading, and Fig. 7(d) is the V -field fringe pattern after the second thermal loading (thermal cycling). Here the image contrast has been enhanced to provide clearer views.

The resulted fringe patterns generate contour maps of the displacement fields. From the fringe distribution in Fig. 7(b), it can be inferred that the deformation increases when going further away from the center point, while the top and bottom boundaries of the chip have a constraining effect on the deformation field, showing as the inflection points of the fringe curves. The fringe orders reflect the displacement magnitudes in the corresponding measurement direction. Comparing Fig. 7(b) with Fig. 7(c), it can be seen that the fringe density in the x_1 direction

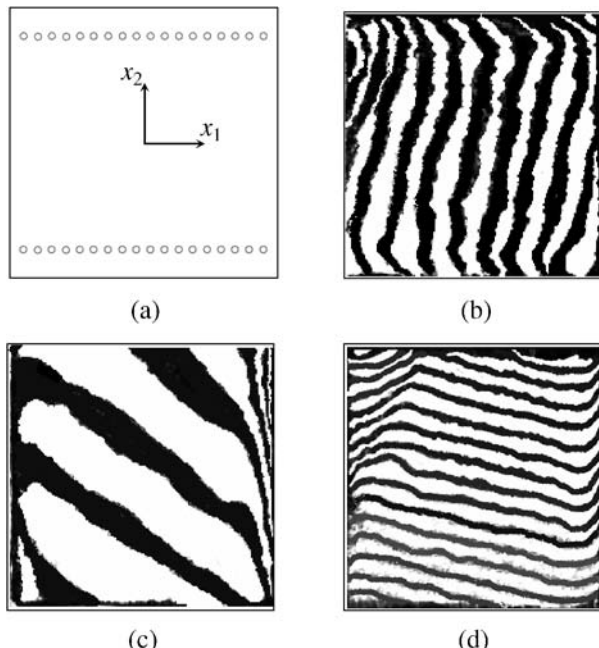


Figure 7. Chip geometry and fringe patterns: (a) sketch map of the chip bump location, (b) fringe pattern after first thermal loading (x_1 direction), (c) fringe pattern after first thermal loading (x_2 direction) and (d) fringe pattern after second thermal loading (x_2 direction).

is higher than that in the x_2 direction by about 2–3 orders. This may be attributed to the geometry of the substrate, which is rectangular with a high length-to-width ratio, and the expansion in the x_1 direction is higher than that in the x_2 direction. Figure 7(c) and 7(d) shows that the fringe density along the x_2 direction after first thermal loading is much lower than that after the second loading, corresponding to changes in deformation degree.

Thermal loading causes deformations of the assembly components, which can be quantitatively determined from the fringe patterns. The relationship between fringe order N and displacement U in the observation direction is $U = 1/fN$, where f is the frequency of the virtual reference grating. Here $f = 2400$ lines/mm, providing a basic sensitivity of $0.417\text{ }\mu\text{m}$ per fringe order. When the corresponding strain is required, it can be extracted from the displacement fields by the small strain relationship as $\epsilon = \partial U / \partial x = 1/f[\partial N / \partial x]$.

During the deformation calculation, the origin of the coordinates is set at the center of the chip, as shown in Fig. 7(a). Figure 8 presents the deformations calculated from Fig. 7(b) with $x_1 = 0$ setting to be the neutral line. Here the center line denotes the displacement distribution along $x_2 = 0$, and the top and bottom bump lines denote the displacement distributions along the two bump lines shown in Fig. 7(a). Figure 9 shows the corresponding strain profiles. The deformation profiles show the elongation trend of the chip along the top-left to bottom-right diagonal, where the maximal displacement appears in the top left corner. As the displacement distributions are nearly linear, the strains are almost constant.

The deformation in the x_2 direction after thermal cycling increases about three times more than that after the first thermal loading, indicated by the fringe densities in Fig. 7(c) and 7(d). This increase shows the impact of heat accumulation after each thermal cycle. Consequently, the component deformation will increase dramatically

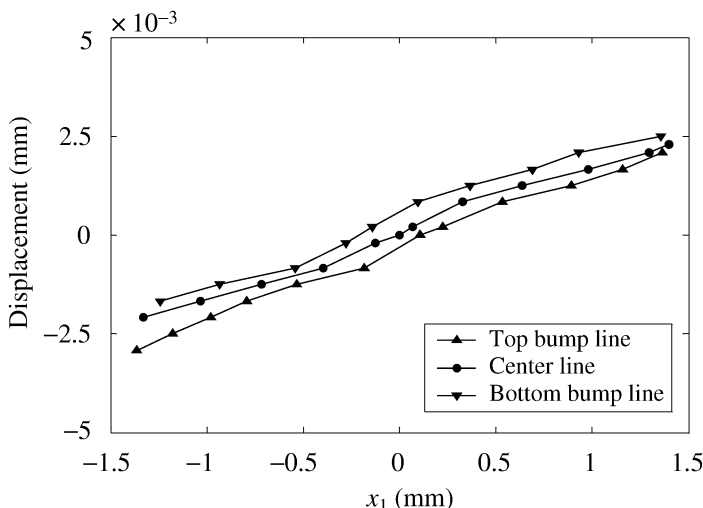


Figure 8. Displacement distributions after first thermal loading (x_1 direction).

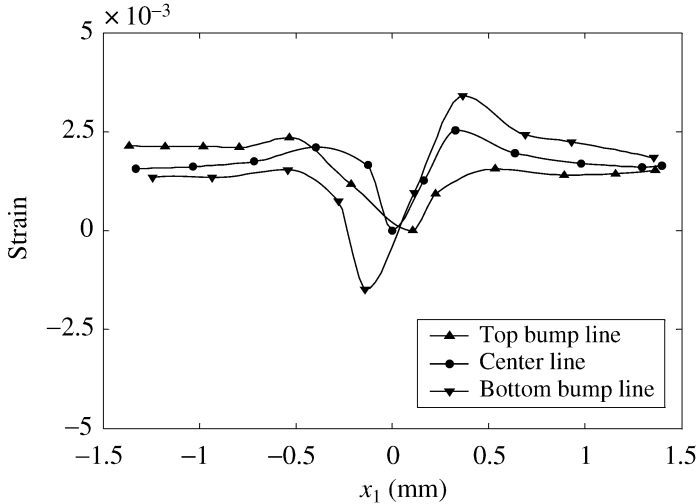


Figure 9. Strain distributions after first thermal loading (x_1 direction).

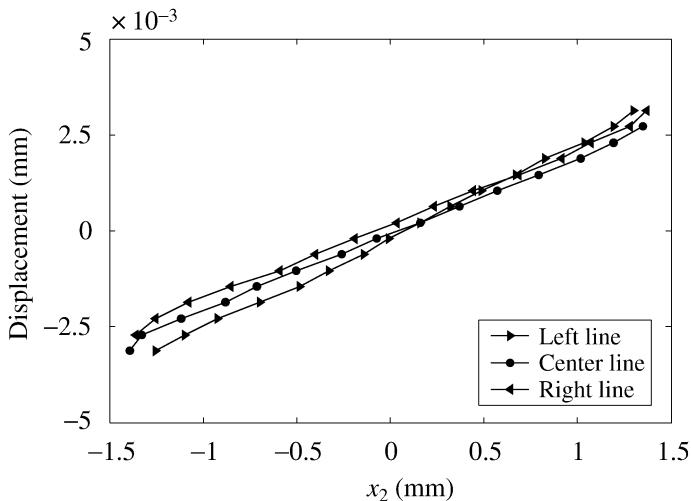


Figure 10. Displacement distributions after second thermal loading (x_2 direction).

after several thermal cycles. Figure 10 is the displacement in the x_2 direction calculated from Fig. 7(d), where the distributions along the center-line ($x_1 = 0$), left boundary and right boundary lines are shown. Figure 11 shows the corresponding strain distributions. The deformation on left side is higher, and the expansion in the x_2 direction is more than that in the x_1 direction. Combining the expansion trends in the x_1 and x_2 directions, it can be inferred that the chip deformation was not symmetric, and the top-right corner experienced the least displacement.

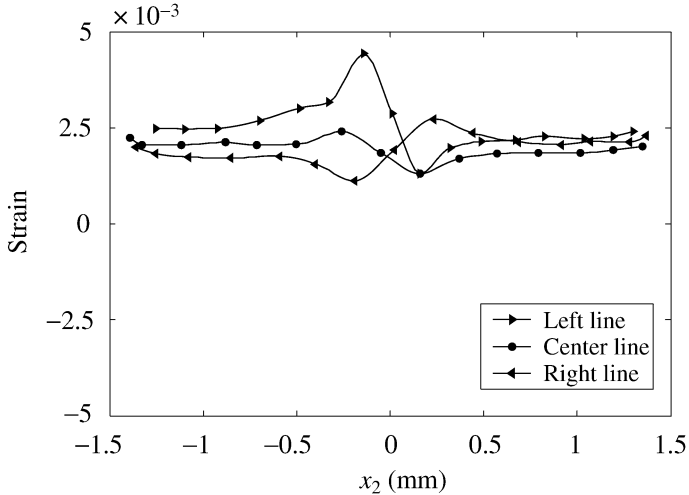


Figure 11. Strain distributions after second thermal loading (x_2 direction).

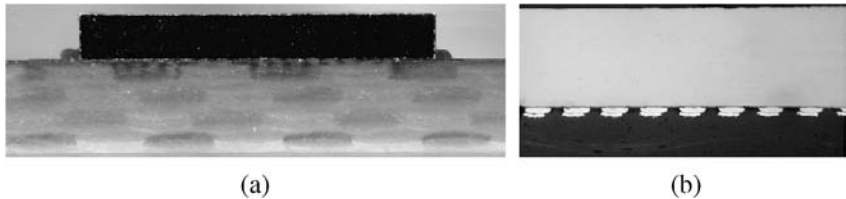


Figure 12. (a) Cross-section of the ACF interconnect; (b) a closer view of the interconnect interface.

4. Micropolar Model and Simulation

For flip-chip assembly with an ACF joint, electrical conduction between the chip and the substrate is achieved through the conductive particles trapped between the corresponding electrodes of the chip and the substrate, and the mechanical bonding is accomplished after the adhesive has cured. Figure 12 shows the cross-section of the experimental specimen. Figure 12(a) gives a global view including both the chip and substrate, and Fig. 12(b) provides a closer view of the interconnection area indicating the size difference between the internal structures at the interface and the adherends.

Prediction of the system response under thermal and mechanical loadings must include the interconnect as well as small size internal structures. The wide difference in component sizes makes the conventional computation method expensive, and even impossible in some cases. A homogenization model was thus developed to provide a highly efficient way for numerical simulation.

The packaging system could be treated as a layered structure, in which the interconnect layer has a much smaller size/thickness than its neighbors. To include this size difference in the model, micropolar theory was utilized because of its ability to reflect micro-scale influences. Due to the heterogeneous interface, discon-

tinuity was introduced. Then the variables in the model such as the displacement $\mathbf{u} = \mathbf{u}(\mathbf{x}, t)$ and the rotation $\theta = \theta(\mathbf{x}, t)$ were expressed in the format of continuous parts and discontinuous parts:

$$\mathbf{u} = \mathbf{u}_c(\mathbf{x}, t) + Hs(\mathbf{x})\mathbf{d}_u(\mathbf{x}, t), \quad (1)$$

$$\theta = \theta_c(\mathbf{x}, t) + Hs(\mathbf{x})d_\theta(\mathbf{x}, t) \quad (2)$$

here the subscript c refers to the continuous part, and $\mathbf{d}_u = \mathbf{u} - \mathbf{u}_c$, $d_\theta = \theta - \theta_c$. The interface area was treated as a strong discontinuity in the considered continuum and the Heaviside function Hs was considered centering at the discontinuity boundary. Since the Dirac delta function δ_S was locally undefined at the interface, the regularization concept [13–15] was introduced into the interface model. Hs was regularized with regard to the interface thickness k so that δ_S equaled $1/k$ when the material point was in the interface area and became zero in the vicinity of the interface. The regularized degrees of freedom become:

$$\mathbf{u} = \mathbf{u}_c + Hs_r\mathbf{d}_u, \quad (3)$$

$$\theta = \theta_c + Hs_r d_\theta. \quad (4)$$

The induced gradients were also expressed as regularized continuous parts and discontinuous parts as:

$$\mathbf{l}_r = \mathbf{u} \otimes \nabla = \mathbf{l}_{cr} + \delta_{Sr}\mathbf{d}_u \otimes \mathbf{n}, \quad (5)$$

$$\mathbf{k}_r = \nabla \theta = \mathbf{k}_{cr} + \delta_{Sr}d_\theta \mathbf{n}, \quad (6)$$

$$\boldsymbol{\varepsilon}_r = \boldsymbol{\varepsilon}_{cr} + \delta_{Sr}\mathbf{d}_u \otimes \mathbf{n}. \quad (7)$$

Here the strain includes both the mechanical action (stress induced) and thermal effect, $\boldsymbol{\varepsilon} = \boldsymbol{\varepsilon}^{\text{mechanical}} + \boldsymbol{\varepsilon}^{\text{thermal}}$. Then the momentum balance relations can be established, as shown in [19].

In the regularized kinematic fields, the stored internal energy was expressed as $\rho\dot{e} = \dot{e}_c + \delta_{Sr}\dot{e}_d$. Set the Helmholtz free energy ψ as the same expression, i.e. $\psi = \psi_c + \delta_{Sr}\psi_d$. Localization of the global entropy inequality expression is as

$$(\dot{e}_c - \dot{\psi}_c) - \delta_{Sr}(\dot{e}_d - \dot{\psi}_d) \geq 0, \quad (8)$$

then the entropy inequalities were obtained as:

$$\dot{e}_c - \dot{\psi}_c = \boldsymbol{\sigma}^t : \boldsymbol{\varepsilon}_c + \mathbf{m}^t : \mathbf{k}_c - \dot{\psi}_c \geq 0, \quad (9)$$

$$\dot{e}_d - \dot{\psi}_d = \mathbf{t} \cdot \mathbf{d}_u + t_m d_\theta - \dot{\psi}_d \geq 0, \quad (10)$$

where $\boldsymbol{\sigma}^t$ is the true stress tensor, \mathbf{m}^t is the couple stress tensor, \mathbf{t} is the traction vector and t_m is the couple stress traction. Taking minimum values of the inequality expressions, the constitutive state equations for the true stress tensor and the couple stress tensor can be obtained as:

$$\boldsymbol{\sigma}^t = \frac{\partial \psi_c}{\partial \boldsymbol{\varepsilon}_c}, \quad \mathbf{m}^t = \frac{\partial \psi_c}{\partial \mathbf{k}_c}, \quad (11)$$

and the constitutive relations for the interface as:

$$\mathbf{t} = \frac{\partial \psi_d}{\partial \mathbf{d}_u}, \quad t_m = \frac{\partial \psi_d}{\partial d_\theta}. \quad (12)$$

The prototype model including the thermal influence can be considered as:

$$\psi_c = \frac{1}{2} K (\varepsilon_{vc} - \alpha \cdot \Delta T)^2 + G(\mathbf{e}_c : \mathbf{e}_c + l_c^2 \mathbf{k}_c : \mathbf{k}_c), \quad (13)$$

$$\psi_d = \frac{1}{2} k_n (d_{un} - k \cdot \alpha \cdot \Delta T)^2 + \frac{1}{2} k_t d_{ut}^2 + k_{t\theta} d_{ut} d_\theta + \frac{1}{2} k_\theta d_\theta^2, \quad (14)$$

where ε_v is the volumetric strain, \mathbf{e} is the deviatoric strain, α is the coefficient of thermal expansion, ΔT is the temperature difference, K is the elastic bulk modulus, G is the shear modulus, l_c is the characteristic length of the considered structure, k is the interconnect characteristic length, d_{un} and d_{ut} are components of the discontinuous displacement vector \mathbf{d}_u with relations $d_{un} = \mathbf{d}_u \cdot \mathbf{n}$ and $d_{ut} = \mathbf{d}_u \cdot \mathbf{m}$, where \mathbf{n} and \mathbf{m} are the normal and tangential vectors of the interface, k_n , k_t , k_θ and $k_{t\theta}$ are the stiffness coefficients. Combining equations (13) and (14) with equations (11) and (12), the stress tensor and couple stress tensor relations are obtained as:

$$\begin{pmatrix} \sigma^t \\ \mathbf{m}^t \end{pmatrix} = \begin{pmatrix} K\mathbf{I} \otimes \mathbf{I} + 2G\mathbf{I}^{dev} & 0 \\ 0 & 2Gl_c^2\mathbf{I} \end{pmatrix} \begin{pmatrix} \boldsymbol{\varepsilon}_c \\ \mathbf{k}_c \end{pmatrix} + \begin{pmatrix} -\alpha \cdot \Delta T \mathbf{I} \\ 0 \end{pmatrix} \quad (15)$$

and the constitutive state equations for the interface as:

$$\begin{pmatrix} \mathbf{t} \\ t_m \end{pmatrix} = \begin{pmatrix} k_n \mathbf{n} \otimes \mathbf{n} + k_t \mathbf{m} \otimes \mathbf{m} & k_{t\theta} \mathbf{m} \\ k_{t\theta} \mathbf{m}^t & k_\theta \end{pmatrix} \begin{pmatrix} \mathbf{d}_u \\ d_\theta \end{pmatrix} + \begin{pmatrix} -k_n \cdot \alpha \cdot \Delta T \cdot k \mathbf{n} \\ 0 \end{pmatrix}, \quad (16)$$

where \mathbf{I} is the second-order unit tensor, \mathbf{I} is the fourth-order unit tensor, and \mathbf{I}^{dev} is the fourth-order deviatoric operator defined as $\mathbf{I}^{dev} = \mathbf{I} - 1/3\mathbf{I} \otimes \mathbf{I}$. To determine the stiffness coefficients k_n , k_t , k_θ and $k_{t\theta}$ in the developed interface model, knowledge of the interconnect internal structure response is necessary.

The bumps, conductive particles and pads constitute typical internal structures in the ACA interconnection, and the constituents responses dominate the interconnection behaviour under external loading. Figure 13 shows some examples of the cross-sections of the internal structures in a flip-chip interconnect. Different constituent geometries and materials such as the size of the particle and electrodes, nature of the particle (whether pure metal or metal-coated plastic) produce various bonding situations, which as a result produce different interconnect performances and influences on the long-term reliability of the system. For example, Fig. 13(a) is a case with insufficient particle deformation, so the electrical conduction is not stable after the interconnection experiences thermal/mechanical loading. Figure 13(b) is a case of metal conductive particle and the bonding is quite good. Figure 13(d)–(f) is internal structures of various geometries and materials.

As the constituent sizes in the internal structures are so small (the conductive particles in commercial ACAs are usually μm size, and nano-scale particles

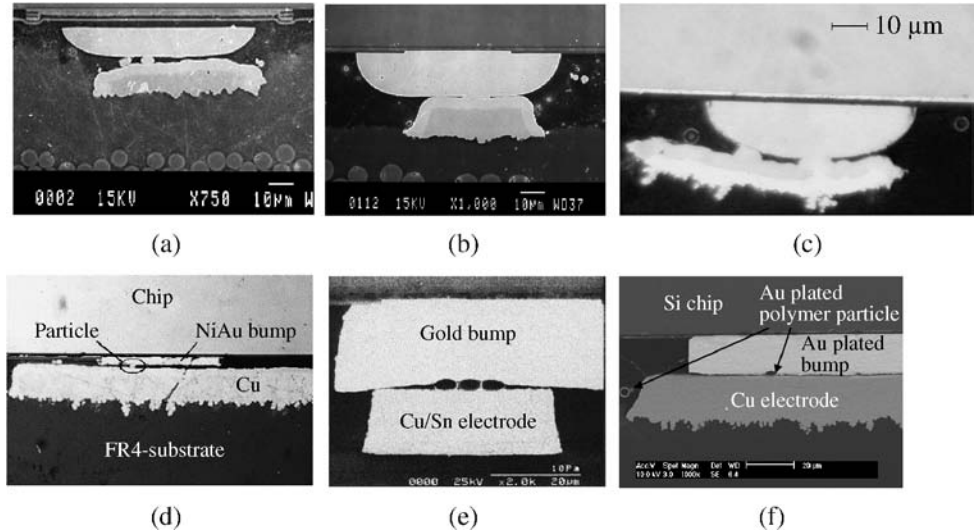


Figure 13. Various cross-sections of an ACA flip-chip interconnect: (a), (b) and (c) are observations from our group, and (d), (e) and (f) are from [16, 17] and [18], respectively.

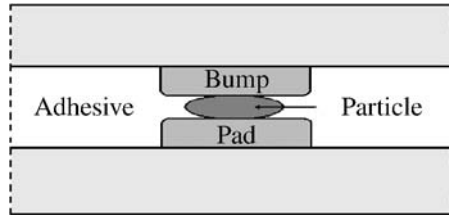


Figure 14. Representative structure in the ACA flip-chip joint.

have already been developed [20]), it is very difficult for experimental measurements or conventional simulation methods to obtain information about the internal constituents response during the interconnection deformation. Furthermore, the particles are of micro or nano sizes, which are orders of magnitude smaller than other constituents. This size difference may contribute to interconnection behaviour, and the microscopic and macroscopic deformations play different roles in the interface response. A second-order model zooming in on the representative structure of the ACA interconnect, as shown in Fig. 14, had been developed to include macro- and micro-responses [21].

The basic idea of the second-order model was to express the displacement $\mathbf{u}(\mathbf{x})$ and rotation $\boldsymbol{\theta}(\mathbf{x})$ in the Taylor series expansions around a material point $\bar{\mathbf{x}}$ as:

$$\mathbf{u} = \bar{\mathbf{l}} \cdot \mathbf{x} + \frac{1}{2} \bar{\mathbf{g}} : (\mathbf{x} \otimes \mathbf{x}) + \mathbf{u}_f(\mathbf{x}), \quad (17)$$

$$\boldsymbol{\theta} = \bar{\boldsymbol{\theta}} + \boldsymbol{\theta}_f(\mathbf{x}), \quad (18)$$

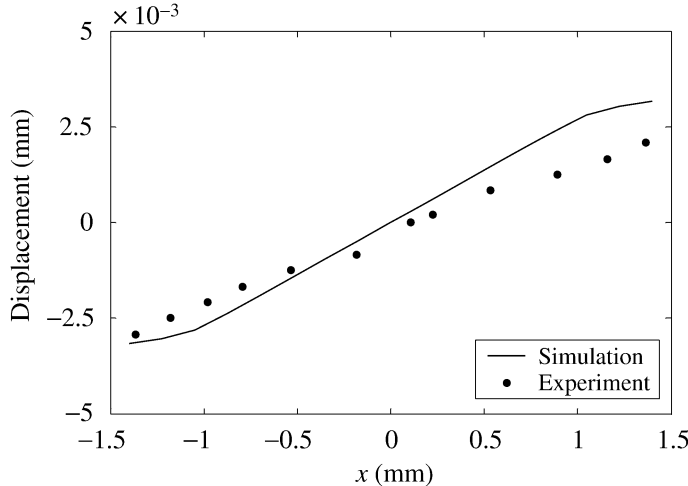


Figure 15. Displacement distributions along chip top from numerical simulation and experimental observation.

in which the top bar denotes the macroscopically-related quantities, and the subscript f stands for the fluctuation field. In equation (17), $\bar{\mathbf{I}}(\bar{\mathbf{x}}) = \bar{\mathbf{u}} \otimes \nabla = \bar{\boldsymbol{\varepsilon}} + \text{spn}(\bar{\theta})$ is the displacement gradient, and $\bar{\mathbf{g}}(\bar{\mathbf{x}}) = \bar{\mathbf{I}}(\bar{\mathbf{x}}) \otimes \nabla$ is the second displacement gradient that reflects the higher-order description of the deformation fields. Then the corresponding kinematics, momentum balance relations, energy balance and entropy inequality were established.

The stiffness coefficients k_n, k_t, k_θ cannot be expressed explicitly, but their values can be obtained by considering unit size deformations with the second-order model. The developed interface model was implemented with finite element method (FEM), and the geometrical and material parameters were chosen according to experimental conditions. A thermal loading with the same temperature change as that in the experiments was applied to the flip-chip bonded system with ACF joint. Comparison of chip deformation from numerical simulation and experimental measurements is shown in Fig. 15, and the good agreement validates the theoretical model. This also provides proof for the higher efficiency and lower computation cost of the developed micropolar interface model.

5. Concluding Remarks

An ACF bonded system under thermal loading was measured by an in-plane Moiré interferometer. The fringe patterns under different loading conditions were recorded, and the displacement and strain distributions were obtained quantitatively. Due to the geometries of system components, the deformation magnitudes along different directions show much difference, and thus displacement distributions are nonsymmetrical. The deformation degree increases by about one order after a thermal cycle.

For the flip-chip packaging with ACF joint, the interconnect is at least orders of magnitude less in size compared to the adherends. Furthermore, there are finer scale internal structures in the interconnect that made experimental work difficult and conventional computation expensive. A theoretical interface model has been developed in micropolar frame to include size influences of fine structures in the interconnect, and homogenization idea was adopted so that the model became less time-consuming. The model, with aid of another higher-order model to include macro- and micro-responses of internal structures, was applied to predict the behavior of ACF interconnect system, and the numerical results show good agreement with experimental measurements.

Acknowledgements

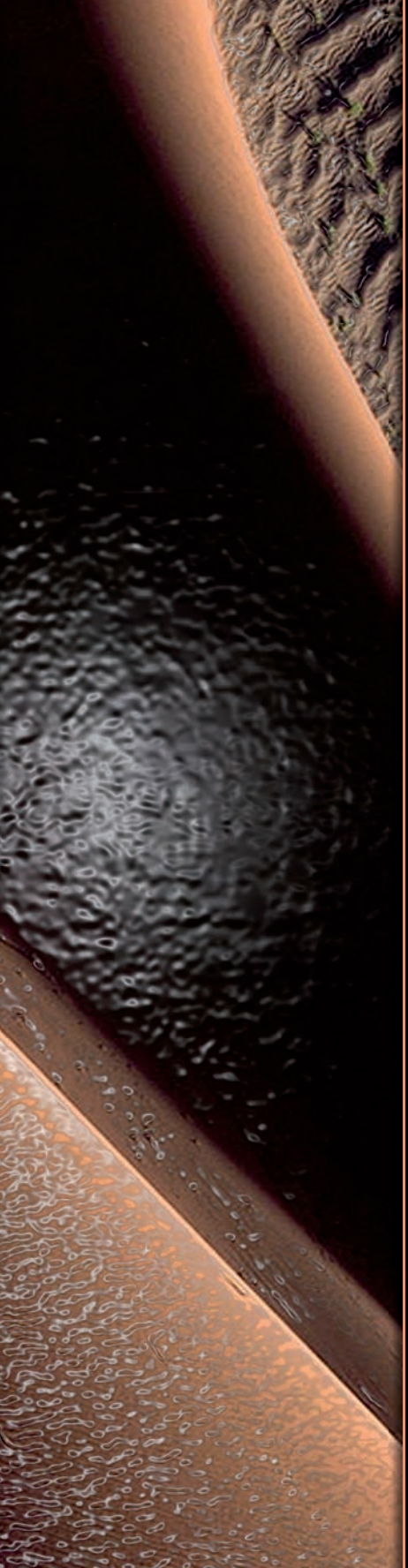
This work was supported by the National Natural Science Foundation of China (Grant No. 10702037). Also support from the Innovative Foundation of Shanghai University is greatly appreciated.

References

1. R. Tummala, *Fundamentals of Microsystem Packaging*. McGraw-Hill, New York, NY (2001).
2. D. Post and J. D. Wood, *Experimental Mechanics* **29**, 318–322 (1989).
3. B. Han, *Experimental Mechanics* **38**, 278–288 (1998).
4. B. Han and D. Post, *Experimental Mechanics* **32**, 38–41 (1992).
5. J. Joo, K. Oh, S. Cho and B. Han, in: *Proc. 3rd International Symposium on Electronic Materials and Packaging*, Cheju Island, Korea, pp. 421–427 (2001).
6. J. Zhu, D. Zou, F. Dai and S. Liu, in: *Proc. 19th IEEE/CPMT International Electronics Manufacturing Technology Symposium*, Austin, TX, USA, pp. 75–83 (1996).
7. S. Liu, J. Wang, D. Q. Zou, X. Y. He and Z. F. Qian, in: *Proc. 48th IEEE Electronic Components and Technology Conference*, Seattle, WA, USA, pp. 1345–1353 (1998).
8. E. A. Stout, N. R. Sottos and A. F. Skipor, *IEEE Trans. Advanced Packaging* **23**, 637–645 (2000).
9. X. Q. Shi and Z. P. Wang, in: *Proc. 52nd IEEE Electronic Components and Technology Conference*, San Diego, CA, USA, pp. 183–191 (2002).
10. W. S. Kwon, S. J. Ham and K. W. Paik, *Microelectronics Reliability* **46**, 589–599 (2006).
11. T. K. Hwang, S. J. Ham and S. B. Lee, in: *Proc. International Symposium on Electronic Materials & Packaging (EMAP 2000)*, Hong Kong, China, pp. 358–363 (2000).
12. S. Liu, J. Zhu, D. Zou and J. Benson, *IEEE Trans. Components, Packaging, and Manufacturing Technology-Part A* **20**, 505–512 (1997).
13. J. Larsson and R. Larsson, *Intl. J. Solids Structures* **33**, 7131–7257 (2000).
14. N. E. Josson and R. Larsson, *Composite Structures* **53**, 409–417 (2001).
15. R. Larsson, *Computer Methods in Applied Mechanics and Engineering* **193**, 3173–3194 (2004).
16. D. Wojciechowski, J. Vanfleteren, E. Reese and H. W. Haggard, *Microelectronics Reliability* **40**, 1215–1226 (2000).
17. G. Sarkar, S. Mridha, T. T. Chong, W. Y. Tuck and S. C. Kwan, *J. Mater. Process. Technol.* **89–90**, 484–490 (1999).
18. M. J. Yin, H. J. Kim, C. K. Chung and K. W. Paik, in: *Proc. 56th IEEE Electronic Components and Technology Conference*, San Diego, CA, USA, pp. 338–343 (2006).

19. Y. Zhang, R. Larsson, J. Y. Fan and J. Liu, in: *Proc. 7th IEEE Conference on High Density Microsystem Design, Packaging and Component Failure Analysis (HDP05)*, Shanghai, China, pp. 115–119 (2005).
20. J. Liu, Swedish Patent No. 0601323-9 (2006).
21. R. Larsson and Y. Zhang, *J. Mech. Phys. Solids* **55**, 819–841 (2007).

This page intentionally left blank



With all the environmental concerns and constraints today and stricter future regulations, there is a patent need to replace materials noxious to the environment by environmentally-friendly alternatives. Electrically conductive adhesives (ECAs) are one such example. ECAs offer an excellent alternative to lead-solder interconnects for microelectronic packaging applications. ECAs are used in electronics for laptop computers, camcorders, watch electronics, hard-drive suspensions and a myriad of electronic equipments. Environmentally-friendly ECAs offer many advantages vis-à-vis solder, such as simple and low-temperature processing conditions, better thermo mechanical performance and finer pitch.

This book is based on the two Special Issues of the *Journal of Adhesion Science and Technology* (JAST vol. 22, no. 8-9 and vol. 22, no. 14) dedicated to this topic. The book contains a total of 21 papers (reflecting overviews and original research) and is divided into three parts as follows: Part 1: Introduction and Recent Developments, Part 2: Mechanical, Durability and Reliability Aspects and Part 3: Characterization and Properties.



VSP
www.brill.nl